DISSERTATION

WILDFIRE IMPACTS ON SOIL ORGANIC MATTER BIODEGRADABILITY, METABOLOMICS, AND BIOGEOCHEMICAL CARBON CYCLING

Submitted by

Jacob VanderRoest

Department of Chemistry

In partial fulfillment of the requirements

For the Degree of Doctor of Philosophy

Colorado State University

Fort Collins, Colorado

Spring 2026

Doctoral Committee:

Advisor: Thomas Borch

Megan Willis
Nancy Levinger
Corey Broeckling

ABSTRACT

WILDFIRE IMPACTS ON SOIL ORGANIC MATTER BIODEGRADABILITY, METABOLOMICS, AND BIOGEOCHEMICAL CARBON CYCLING

Wildfires are natural ecosystem disturbances that are beneficial to adapted environments. However, global wildfire activity has deviated from historical patterns primarily due to urban expansion into wildland areas, forest management strategies, and climate change. Wildfires are now more intense and frequent, burning larger areas across Earth and impacting air, water, and soil quality. Wildfires impact soil quality by changing the composition of soil organic matter (SOM): a heterogenous mixture of organic molecules in soil ranging from small metabolites to larger lignin-like compounds that comprises two-thirds of Earth's terrestrial carbon stores. SOM serves as critical sustenance supporting soil microbial metabolism and activity, especially SOM that is more biodegradable (i.e. the SOM can be physically accessed, metabolized, and mineralized to CO_2 by soil microbes). A key component of biodegradable SOM is the soil metabolome: the assemblage of soil metabolites (e.g. amino acids, organic acids, peptides and saccharides) that drive microbial protein production, cellular energy generation, and soil nutrient cycling. Thus, SOM biodegradability and soil metabolites influence soil carbon cycling and contribute to a healthy, productive soil system. However, the impacts of wildfires on SOM biodegradability and soil metabolite content are largely unknown. Alterations to SOM biodegradability and metabolites could impact microbial activity, biogeochemical nutrient cycling, and the propensity for burned soils to act more as carbon sources rather than carbon sinks. Therefore, the work in this dissertation investigated post-fire SOM biodegradability and soil metabolite contents and was driven by the

following questions: How do wildfires impact soil metabolomics, and how do abundances of soil metabolites change after fire? Does SOM become more or less biodegradable after wildfires? These questions were answered across experimental scales from laboratory to field investigations and by using a comprehensive suite of analytical instrumentation.

First, we conducted a controlled soil burning experiment using pyrocosms: steel containers filled with soil over which vegetation is burned to simulate a wildfire. The objectives of this study were to 1) characterize SOM and microbial community composition throughout the first month following fire, 2) identify postfire shifts in the soil metabolome and metabolite abundances, and 3) determine how changes in SOM composition correspond to microbial community structure. Using microbial amplicon (16S/ITS) sequencing and gas chromatography-mass spectrometry, heterotrophic microbes (*Actinobacteria, Firmicutes,* and *Proteobacteria*) and specific metabolites (glycine, protocatechuate, citric acid cycle intermediates) were enriched in burned soils, indicating that burned soils can contain a variety of substrates that support microbial metabolism. Molecular formulas assigned by 21 T Fourier transform ion cyclotron resonance mass spectrometry revealed that SOM in burned soil was lower in molecular weight and featured 20 to 43 % more nitrogen-containing molecular formulae than SOM in unburned soil. We also measured higher water extractable organic carbon concentrations and higher CO_2 respiration in burned soils, implying that the SOM in burned soils may be more biodegradable than the SOM in unburned soils. The observed enrichment of biodegradable SOM, metabolites, and microbial heterotrophs illustrates the resilience of these soils to severe burning, providing important implications for postfire soil microbial activity and carbon cycling.

To further explore the impacts of wildfires on soil metabolites, we conducted a laboratory-based, soil heating experiment with the following overarching objective: evaluate how soil

metabolite contents change under varying fire intensities. Soils from a lodgepole pine forest, mixed conifer forest, and spruce-fir forest were heated to 150 °C, 250 °C, and 450 °C, and the metabolite contents of the soils were analyzed with gas chromatography-mass spectrometry and liquid chromatography-mass spectrometry. The metabolite contents drastically changed at each heating temperature, indicating that soils burned by wildfires of different intensity conditions will feature disparate metabolite assemblages. Soils heated to 150 °C were enriched in amino acids and peptides while soils heated to 250 °C were enriched in aromatic metabolites, organic acids, and nitrogen-containing saccharides. Surprisingly, 43 to 52 % of the detected metabolites across the three forested ecosystems were significantly more abundant in the heated soils compared to the control soils. These results indicate that soils burned by wildfires (especially of lower intensity) may feature an enriched metabolite pool that could provide essential nutrients for post-fire microbial activity.

Lastly, we conducted a field study to determine if our laboratory- and controlled burned-based results were observed in soil burned by an actual wildfire and to address the following objectives: 1) evaluate what metabolites are enriched in burned soil and if SOM is more biodegradable in burned soil from a natural wildfire, 2) determine how differences in soil metabolites and SOM biodegradability may influence short-term soil carbon mineralization and soil CO_2 respiration, and 3) assess whether burned soils act more as carbon sinks or carbon sources. We sampled soil from unburned, low severity, and high severity areas from a 2024 Colorado wildfire ~1.5 months post-fire. Ninety-six percent of the putatively identified metabolites were either statistically similar or significantly greater in abundance in burned soils compared to unburned soils. Biological oxygen demand incubations and soil CO_2 flux measurements exhibited on average 2.0 to 2.6x greater microbial metabolism of SOM and 1.4 to 2.5x greater CO_2 fluxes,

respectively, from burned soils relative to unburned soils, suggesting that SOM from burned soil is more biodegradable than from unburned soil. This heightened SOM biodegradability could cause greater microbial metabolism and CO_2 emissions from wildfire-impacted soil, potentially shifting post-fire environments from being carbon sinks to carbon sources.

Overall, this dissertation used a variety of experimental approaches and instrumentation to discover that burned soils can be enriched in metabolites, SOM from burned soils can be more biodegradable than corresponding unburned soils, and burned soils may act as carbon sources immediately after fire due to this metabolite enrichment and biodegradability enhancement. These results shift our understanding of post-fire SOM composition, and our conceptual understanding of SOM from burned soils should now include a highly reactive pool comprised of enriched metabolites and more biodegradable SOM. This increased biodegradable SOM content could cause post-fire soils to act more like carbon sources, potentially intensifying both climate change and wildfire activity.

ACKNOWLEDGEMENTS

My educational journey truly began at Saugatuck High School. Thank you to the entire Saugatuck High School staff and the following teachers and mentors in particular that prepared me for college and beyond: Bradley Smit, Christina Lewis, Elizabeth Terhaar, Jeff Walker, Angelina Bauer, and Rick Bauer. Beyond Saugatuck High School, thank you to the Hope College Chemistry and Geological and Environmental Sciences departments for offering undergraduate research opportunities, providing genuine mentorship, and encouraging me to enroll in graduate school. Specifically, Dr. Jeffrey Johnson, Dr. Jon Peterson, Michelle Gibbs, and Dr. Steven Bouma-Prediger were instrumental in my Hope College experience. Go Dutch!

Thank you to the Colorado State University chemistry department for providing me the opportunity to earn a doctoral degree. Thank you to my PhD committee comprised of Dr. Megan Willis, Dr. Nancy Levinger, Dr. Corey Broecking, and Dr. Thomas Borch. Dr. Megan Willis provided excellent advice for me while navigating the first year of graduate school. Dr. Nancy Levinger was an excellent sounding board throughout my PhD experience and provided helpful suggestions for my National Science Foundation Graduate Research Fellowship Program application. Overall, this dissertation would not have been possible without Dr. Corey Broeckling. I was not familiar with metabolomics at all when I entered graduate school. Through the grace and help of Dr. Broeckling, metabolomics became a pivotal component of this dissertation. Thank you.

I have been blessed with exceptional collaborations ranging from local educational programs to national laboratories. Thank you to the Wilkins research lab at Colorado State University (specifically Julie Fowler, Kya Sparks, and Dr. Mike Wilkins) for conducting all the microbial analyses in this dissertation and opening my eyes to the wonders of interdisciplinary

collaboration. Thank you to the U.S. Forest Service Rocky Mountain Research Station (particularly Isabel McPherson, Tim Fegel, and Dr. Charles Rhoades) for analyzing soil samples with a suite of instruments, providing guidance for project design, and offering their lab for biological oxygen demand incubations. I'd like to specifically thank Dr. Charles Rhoades for offering stupendous writing suggestions and demonstrating what it means to be a writer. Thank you to the EcoCore lab at Colorado State University and to Danuel Reuss for training me on their elemental analyzer and Shimadzu TOC-L instrument. Thanks to Dr. Robert Young for paving the way for Fourier transform ion cyclotron resonance mass spectrometry analysis within the Borch lab. Thank you to the National High Magnetic Field Laboratory, Dr. Amy McKenna, and Dr. Lydia Babcock-Adams for their collaboration with Fourier transform ion cyclotron resonance mass spectrometry analysis. Thank you to the Heart J Center (specifically Laura Armstrong, Silas Binkley, and Angela Stanford) for providing us with field access to the Alexander Mountain Fire burn scar. Chapter 5 of this dissertation would not have happened if it weren't for their generosity and collaboration. Lastly, thank you to the Analytical Resource Core (specifically Dr. Claudia Boot, Dr. Prithwiraj De, Dr. Nathan Montgomery, and Paul Mathews) for providing instrumentation and offering invaluable insight into mass spectrometry analysis.

Thank you to the Colorado State University School of Global Environmental Sustainability (especially Aleta Weller) for collaborating with educational outreach activities with the Graduate Student Chapter of the Student Sustainability Center. Additionally, thank you for providing me the opportunity to attend the 2023 United Nations Climate Change Conference (COP 28) in Dubai, United Arab Emirates and for selecting me for the Diana Wall Sustainability Leadership Fellows program. Thank you to the Colorado State University Office of Vice President for Research for

selecting me for the Vice President for Research Graduate Fellowship Program. Thank you to the U.S. Department of Agriculture and U.S. National Science Foundation for funding.

I am very grateful for the Borch lab at Colorado State University in which I conducted my dissertation research. Thank you to prior Borch lab members (specifically Dr. Holly Roth and Dr. William Bahureksa) that provided guidance and support during my first two years of my PhD. Thank you to Dr. Sean Fettrow and Dr. Martin Kurek for their mentorship during the final years of my PhD. Thanks to my fellow Borch lab members Dr. Marin Wiltse, Huma Tariq Malik, Adam Norris, Kerry Miller, Anne Harper, Chelsea Zhao, and Amelia Skinner for contributing to an exceptional lab culture. The final year of my PhD was exceedingly enjoyable, largely due to those lab members fostering an environment that I was excited to work in.

Thank you to Dr. Thomas Borch for being my PhD advisor. Due to Thomas's generosity, I had opportunities to travel to international conferences, collaborate with researchers at national labs, prioritize educational outreach extracurricular activities, and have an exceptional PhD experience. Thomas pushed me beyond my academic comfort zone to embrace challenges and tackle projects that seemed too ambitious initially. I'm appreciative of Thomas's patience as I steadily developed into a scientist throughout my PhD in his lab as well. While my time in Thomas's lab is drawing to a close, my time as a collaborator and friend of Thomas has only just begun.

Beyond the academic realm, I am grateful for friends and family that provided so much love and surplus value during my time in graduate school. Despite moving about 1,000 miles away from my home state of Michigan, friends from back home continuously provided support and much needed humor. Special thanks go to Erik Schoonover, Jacob Kelley, Nate Vorhees, Luke Shoemaker, Dan Chalice, Connor Hotary, Ray Bartlett, Max McQueary, and Corey Gorgas. Thanks

to the following social groups in Fort Collins, CO that enriched my life outside of academia: Fort Collins Running Club, Fort Collins Salsa Collective, Comedy Fort Improv Classes offered by Bart Sumner, and the Fort Collins First United Methodist Church led by Pastor Brad Laurvick. Thank you to the friends that I've made in Fort Collins for going on memorable adventures and making my PhD journey a well-rounded experience, particularly Alex Fenton, Richard Reyes, Ashley Banuelos, Max Eggenberger, Yezzen Khazindar, Carl Patterson-Markowitz, Yaman Peksenar, and Kai Brantley.

Thank you to my partner Hannah Burke. Due to Hannah, the final year of my PhD was defined by excitement, tenderness, and joy. From singing "Vienna" together at Scrumpy's Bar on a given Saturday to going for long walks at Riverbend Ponds, thank you for adding so much to my life and helping me grow into a man. I am thrilled that I am your boyfriend, partner, and teammate. I love you, Hannah.

Thank you to the VanderRoest family. Moving from Michigan to Colorado reinforced how important you all are to me. Thank you to Molly VanderRoest for bringing such life and energy to our family. Thank you to Adrianna VanderRoest for enriching our family with your sincerity and spirit. Thank you to Nathan VanderRoest for being the best older brother that a younger brother could ask for. Lastly, thank you to Dr. Jim VanderRoest and Karla VanderRoest for your commitment to being the best parents that you could be. Thank you for thoroughly providing for me physically, financially, educationally, and emotionally. It is without hesitation that this dissertation, and everything that I've done educationally and professionally to this point, is dedicated to you two. Your son has, currently does, and will always love you.

The following song lyric from "Kathy's Song" written by Paul Simon encapsulates my reverence for everyone that has helped me: "There, but for the grace of you, go I." This dissertation

was possible because of the courteous goodwill and grace that I received from everyone acknowledged here and beyond. With admiration and appreciation, thank you.

DEDICATION

This dissertation is dedicated to Dr. James Mark VanderRoest and Karla Paulette VanderRoest

TABLE OF CONTENTS

CHAPTER 1: INTRODUCTION

1.1 WILDFIRE ACTIVITY IS INCREASING IN THE 21ST CENTURY

Wildfires alter ecosystems and can impart essential benefits onto adapted environments.[1] Wildfires remove invasive species, help eliminate diseases and pests, form open habitats for shade-intolerant plants, add inorganic nutrients into the soil, and drive soil formation.[1,2] However, global wildfire activity has drastically changed during the 21st century and has deviated from historical fire regimes (i.e. generalized description of fire characteristics like fire severity, fire intensity, fire frequency, and burn area).[3–5] For example, while global burn area has declined since 2001 primarily because of decreasing African savannah burning, every other wildfire-prone continent has featured increasing extreme wildfire events and burn area with ~367 million ha burning globally in 2024 alone.[6] Wildfires are becoming more severe in which fire severity refers to the degree of surface organic matter consumption from fire.[7–10] Fire intensity (i.e. energy released during burning) has increased globally throughout 21st century.[7,11] In fact, extreme wildfire events characterized by high intensity conditions have more than doubled in frequency from 2003 to 2023.[11] This increase in high intensity fire frequency extends to overall wildfire frequency, as well. Since 1984, the frequency of global wildfires has doubled, expanding the fire weather season by 14 days (a 27 % increase) from 1979 to 2019.[10,12] Thus, wildfires are a prevalent force shaping global ecosystems and will continue to do so in the future.[3,13]

These global trends in wildfire activity are also occurring within the United States. Average fire events in the United States were up to four times the size and triple the frequency in the 2000s compared to the 1980s through 1990s.[14] In the western United States, wildfire-burned area has doubled over the past four decades,[15] and 3 million ha were burned by nearly 65,000 fires in 2022

alone.[16] Understanding the factors contributing to this increased wildfire activity and the resultant impacts are critical for adapting to an increasingly fire-prone world.

Many compounding factors have caused increased wildfire activity including climate change, wildland-urban interface expansion, and forest management strategies. Climate change has caused hotter, drier conditions that exacerbate wildfire severity, intensity, and frequency.[5,11,15,17–19] These arid conditions result in drier vegetative fuel which is more susceptible to ignition and burning at hotter temperatures.[15,20,21] Overall, human-caused climate change contributed to an estimated additional 4.2 million ha of wildfire burn area from 1984 to 2015 in the western United States.[18] Climate change is also coupled with the expansion of the wildland-urban interface (WUI). The WUI is defined as "the area where houses are in or near wildland vegetation."[22] Globally, 3.5 billion people live within the WUI.[23] Within the United States, the number of houses and people in the WUI increased by 12.7 million and 25 million, respectively, from 1990 to 2010.[22] Now, approximately one in three U.S. houses are located in the WUI.[22] This increased human population near wildland areas likely increases wildfire ignition rates in which ~80 % of wildfires are already human-caused, contributing to greater wildfire activity.[22,24,25] In addition to WUI expansion, certain forest management strategies, such as fire suppression, can contribute to larger, more severe wildfires. Fire suppression is a strategy that prioritizes preventing wildfires and suppressing a wildfire as fast as possible once ignited.[26] Starting in the 1930s, federal land managers promoted fire suppression which effectively prevented wildfires from starting and spreading.[4,26] For example, from 2000 to 2023, USD 1.9 billion were spent by the United States Forest Service and Department of Interior Agencies towards fire suppression efforts, resulting in ~98 % of wildfires being suppressed before they grew larger than 100 acres.[27,28] However, fire suppression can lead to decadal accumulation of vegetative fuel on forest floors, increasing the

likelihood of larger, more severe wildfires after ignition.[4,29,30] Such massive wildfires have been prolific in Colorado in which the 20 largest wildfires in Colorado history have all occurred since 2001.[31] Whether driven by climate change, WUI expansion, and/or forest management strategies, wildfire activity has been increasing in the 21st century and is projected to intensify in the future with burn areas in the western United States expected to increase by 50 to 100 % in the next 50 years.[32] Thus, studying wildfire impacts on ecosystems is essential to better understand how wildfire activity will shape the quality of Earth's air, water, and soil and alter global biogeochemical cycles.

Wildfires directly influence the global carbon cycle by emitting CO_2 during vegetation burning. For example, the 2023 Canadian wildfires emitted 657 Tg of carbon into the atmosphere which was greater than the individual 2023 fossil fuel-related carbon emissions of every country on Earth other than China, United States, and India. Such wildfire carbon emissions are offsetting greenhouse gas reduction efforts. In California, wildfire CO_2 equivalent emissions in 2020 were approximately two times greater than California's total greenhouse gas emissions reductions since 2003.[33] In other words, all of California's efforts towards reducing their greenhouse gas footprint were completely wiped out by a single wildfire season. While wildfires act as carbon sources during burning due to vegetation combustion, the extent to which post-fire environments act as carbon sources vs. carbon sinks is less known. Wildfire activity is already decreasing the effectiveness of land carbon sinks, and climate change will further curtail the ability of burned areas to sequester carbon.[34] A major carbon sequester is soil which contains ~ 2500 Pg of total carbon worldwide which is 3.1 times greater than atmospheric carbon content.[35] Approximately 70% of this total global topsoil carbon is exposed to fire.[36] Therefore, wildfires may drastically impact soil carbon cycling and the propensity of burned environments to act as carbon sources vs

carbon sinks. Thus, investigating how and to what extent wildfires alter soil carbon chemistry is essential.

1.2 WILDFIRES CHANGE SOIL ORGANIC MATTER COMPOSITION

Soil acts as the intersection of the atmosphere, biosphere, and pedosphere, featuring a diverse array of minerals, water, bacteria, fungi, plants, roots, and soil organic matter. These soil components are directly impacted by wildfires by changing soil mineralogy,[37] decreasing microbial community diversity,[38,4,39–41] increasing soil pH,[40,42–50] decreasing soil C/N ratios,[48,49,51–55] and altering soil organic matter (SOM) composition.[56] SOM is a highly complex mixture of organic compounds ranging in size from smaller metabolites (e.g. organic acids and peptides) to bigger proteinaceous compounds. SOM is considered one of the most complex natural mixtures on Earth and is a substantial carbon sink.[57] In fact, two-thirds of the terrestrial carbon in the world is stored in SOM (~Pg gigatons of organic carbon) which is double the amount of carbon in the atmosphere.[57,58] Thus, SOM plays critical roles in global carbon dynamics, soil biogeochemical cycling, and sustaining soil microbiology.[17] Soil microbial communities consume SOM as a food source, fueling microbial metabolism and activity. For microbial consumption of SOM to occur, SOM needs to be biodegradable which we operationally define as SOM that is physically accessible, can be thermochemically oxidized, and can be mineralized to CO_2 by soil microbes.[59,60] Terms such as “bioavailability” and “lability” have been used to describe the propensity to which SOM is consumed by microbes,[38,61–63] but we will use “biodegradability” to incorporate both the environmental[60] and thermodynamic[59] factors that influence microbial SOM consumption. SOM biodegradability ranges from more persistent organic molecules (such as condensed aromatics) to more readily biodegradable molecules like sugars and organic acids. A key component of the readily biodegradable SOM pool is the soil metabolome.

The soil metabolome is an assemblage of metabolites within a soil sample. Metabolites are smaller (< 1500 Da) compounds such as amino acids, organic acids, peptides, and saccharides that are key components of microbial protein production, cellular energy generation (e.g. the citric acid cycle and adenosine triphosphate [ATP] production), and soil nutrient cycling. The investigation of metabolites is called "metabolomics", and the measured metabolite content of a given sample can be designated as the "metabolite profile" or "metabolome." Metabolites are most typically detected with gas chromatograph-mass spectrometry (GC-MS) and/or liquid chromatography-mass spectrometry with recent advances in Fourier transform ion cyclotron resonance-mass spectrometry (FT ICR-MS).[64–66] Metabolite identification is often performed with either targeted or nontargeted mass spectrometry analysis featuring the use of authentic standards or library databases, respectively, for identification.[67] Identification confidence is frequently reported using the Schymanski index which ranges from Level 1 to Level 5 in order of decreasing identification confidence.[68] Level 1 and Level 2 indicate a probable structure and identity of the metabolite determined with either using an authentic standard or by performing library database comparisons, respectively. Level 3 reports a chemical ontology (e.g. saccharide-like, organic acid). Level 4 indicates that the molecular formula of the metabolite is known. Level 5 reports only the mass of a detected metabolite. Level 2 or 3 identified metabolites can be referred to as "annotated" metabolites.[69] Over 80,000 studies on metabolomics have been published from 1998 to 2023,[70] and 8% of all published metabolomics studies have examined soil metabolomics as of 2022.[71] Overall, metabolites propel soil carbon and nutrient cycling, microbial activity, and microbial metabolism, making metabolites a critical component of SOM.[65,66,71–77]

Wildfires alter SOM composition resulting in SOM often becoming more enriched in nitrogen and more aromatic.[52,56] Surficial soil temperatures typically range from ~50 to 1500 °C

during wildfires. These temperatures heat the underlying soil and cause aliphatic molecules to degrade and carboxylic acid functional groups to oxidize, leaving behind more stable aromatic compounds.[42] Pyrogenic organic matter (i.e. thermochemically altered organic matter produced from incomplete combustion often present in burned soils) can also be formed from elevated soil temperatures ranging from ~300 to 700 °C with estimates suggesting that 116-385 Tg of condensed pyrogenic organic matter is generated annually.[2,61,78,79] While aromatic molecules and pyrogenic organic matter are well-studied components of SOM in burned soils,[79] the soil metabolome within burned soils is drastically understudied.

Wildfire impacts on soil metabolomics are largely unknown. Lower molecular weight molecules (such benzene and furfural) have been detected (Level 2 or 3 on the Schymanski index) in burned soils by utilizing pyrolysis GC-MS, but changes in the abundances of those detected metabolites due to fire were often not reported.[80–85] A laboratory experiment was conducted where pyrogenic organic matter was added to soil after which individual metabolites were detected and quantified on a relative basis (total ion current normalization); however, the metabolite identities were not determined (Level 4 and Level 5 on the Schymanski Index was only achieved).[86] Thus, the first knowledge gap of this dissertation is that there is a lack of studies characterizing soil metabolite responses to wildfires at high identification confidence (level 3 or higher on the Schymanski Index) coupled with individual metabolite abundance quantification (Figure 1.1). Therefore, how wildfires influence amino acids, organic acids, and saccharides, which drive microbial activity and soil carbon cycling, remain unknown. Addressing that knowledge gap will enable a deeper understanding of how wildfires impact both post-fire biogeochemical cycling and SOM biodegradability.

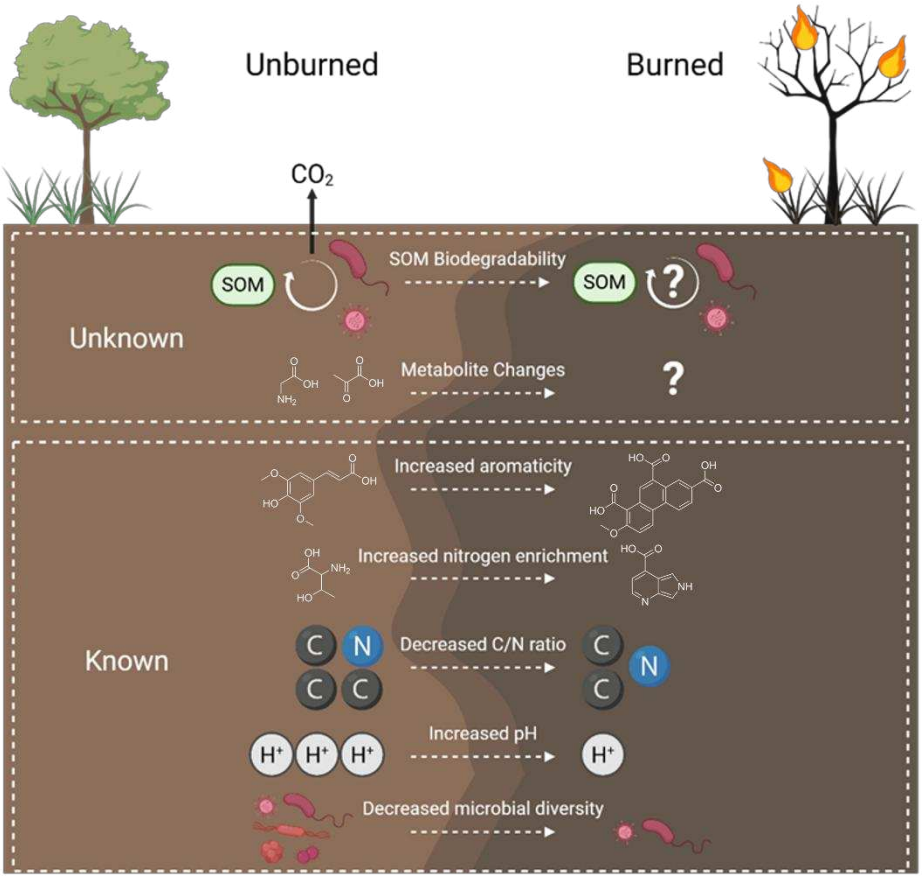

Figure 1.1. Conceptual diagram outlining major knowledge gaps presented in this dissertation.

SOM biodegradability from burned soils is not well understood either. Traditionally, increased aromaticity and pyrogenic organic matter content are thought to make SOM from burned soils more persistent with the half-lives of pyrogenic organic matter reaching millennial timeframes.[87–89] This SOM dominated by persistent organic molecules would cause post-fire SOM to be fairly unreactive and contribute minimally to biogeochemical carbon cycling. However, lab-based investigations have observed 1) pyrogenic organic matter decomposition by microbes can occur over the timeframe of 10 days,[62,63,90–92] 2) that a SOM microbial decomposition priming effect can be initiated by the presence of pyrogenic organic matter,[86] and 3) that pyrogenic organic matter decay rates can be thermodynamically faster than that of natural dissolved organic matter pools.[48,93] Thus, pyrogenic organic matter may be more biodegradable than originally presumed.

However, such studies looking at pyrogenic organic matter are only examining a subset of SOM within burned soil, not the entire SOM mixture which is comprised of proteins, lignin-like compounds, and metabolites in addition to pyrogenic organic matter. Thus, the second knowledge gap of this dissertation is the lack of studies examining the biodegradability of the entire, holistic SOM pool within burned soils (Figure 1.1). In other words, there is not a strong consensus on whether wildfires make SOM more or less biodegradable. Understanding post-fire SOM biodegradability would provide insights into post-fire SOM microbial consumption influencing microbial activity, soil recovery, and soil CO_2 emissions.

1.3 STUDYING WILDFIRE IMPACTS ON SOIL ORGANIC MATTER REQUIRES COMPREHENSIVE EXPERIMENTAL DESIGNS AND A SUITE OF CHEMICAL INSTRUMENTATION

To thoroughly investigate the metabolite content and biodegradability of SOM in burned soils, multiple experimental techniques and instrumentation need to be employed. Wildfire impacts on SOM can be studied across experimental scales, ranging from controlled muffle furnace heating to extensive field campaigns.[94] Using muffle furnaces to simulate wildfires provides heightened control over experimental variables (e.g. soil type and heating temperature) and are widely available.[37,49,52,94–98] Muffle furnaces can be limited, however, by their small experimental scale and since radiation from electrical components is used to generate heat rather than burning vegetation. For increasing scale, incorporating vegetation burning, and still providing some control over experimental variables, pyrocosms can be used.[99] Pyrocosms are metal containers of soil placed into the ground, and vegetation is burned over the soil to simulate a wildfire.[99] Pyrocosms provide control over experimental variables (e.g. selecting soil and forest litter type) and more realistic conditions due to vegetation burning compared to using a muffle furnace at the cost of

losing control of exact heating temperatures. Lastly, field campaigns in wildfire-impacted ecosystems provide the most representative, accurate assessment of wildfire impacts on SOM; however, wildfire-impacted areas can be difficult to access due to location, sampling permission acquisition, and permitting. Thus, conducting a combination of these experimental approaches provides the most thorough assessment of wildfire impacts on SOM.

Comprehensively evaluating SOM changes due to wildfires requires broad analytical instrumentation such as pyrolysis GC-MS, spectroscopy-based approaches (e.g. excitation-emission matrix [EEM] fluorescence spectroscopy), FT ICR-MS, traditional GC-MS, and LC-MS. Pyrolysis GC-MS takes a soil sample, pyrolyzes it (often to ~500 °C), and the molecules that volatize out of the soil are analyzed via gas chromatography often coupled with a quadrupole mass analyzer.[80–85] Therefore, the analytical scope of pyrolysis GC-MS is restrained to non-derivatized, volatile molecules within soil. EEM fluorescence spectroscopy utilizes the chromophore and fluorophore substrates within SOM to assess aromaticity, molecular weight, and the degree of SOM humification.[46,100–102] While this method is relatively quick, accessible, and requires little sample preparation, the targeted molecules represent a small portion of the overall SOM pool because only chromophoric and fluorophoric compounds are detected.[103,104] To capture a broader suite of SOM molecules, FT ICR-MS can be employed and has been a primary tool for post-fire SOM analysis for the past decade.[38,46,96,103,105–115] FT ICR-MS assigns molecular formulae across a broad mass range (175 – 1200 Da) at high mass accuracy (sub-ppm mass measurement error) with high mass resolving power (up to 3,000,000 at m/z 200).[103,116] Electrospray ionization is commonly used as the ionization source which is ideal for SOM due to the prevalence of carboxylic acid moieties within SOM that readily deprotonate.[103] FT ICR-MS only provides metabolite identification confidence up to Level 3 on the Schymanski index with van Krevelen plot

analysis.[68,117–119] Achieving metabolite identification with higher confidence (i.e. Level 2 on the Schymanski index) requires traditional GC-MS (meaning not pyrolysis GC-MS) and/or LC-MS since those approaches feature more robust library databases for metabolite identification compared to FT ICR-MS.[65,66,71–77] Traditional GC-MS also enhances metabolite volatility via derivatization, increasing the likelihood of amino acid, organic acid, and saccharide detection compared to pyrolysis GC-MS which does not feature derivatization.[73] While ideal for metabolite identification and quantification, traditional GC-MS and/or LC-MS have not been utilized to identify and quantify the abundances of individual metabolites within burned soil, limiting our understanding of post-fire soil metabolomics. Overall, utilizing multiple instrumental approaches would help account for the limitations of any singular instrument, advance characterization of metabolite contents, and address the first knowledge gap of this dissertation related to post-fire soil metabolomics.

SOM biodegradability in burned soils can be assessed using soil CO_2 respiration measurements and experimental incubations. Soil CO_2 respiration can be measured either in the field or in the laboratory, and more soil CO_2 microbial respiration can be indicative of more biodegradable SOM.[120–122] Experimental incubations feature a microbial inoculum spiked into soil-water extracts followed by measuring changes in oxygen or dissolved organic carbon concentrations.[98,123–126] The more oxygen and/or dissolved organic carbon consumption, the more biodegradable the SOM. Employing these two techniques would help address the second knowledge gap of this dissertation related to how wildfires impact SOM biodegradability holistically.

This dissertation outlines multiple studies exploring SOM composition from burned soils, specifically examining the soil metabolome and SOM biodegradability. The chapters herein

address the following pertinent research questions: How do wildfires impact soil metabolomics, and how do abundances of soil metabolites change after fire? Does SOM become more or less biodegradable after wildfires? How do these changes in soil metabolite content and SOM biodegradability influence biogeochemical carbon cycling and the propensity of burned soils to act more as carbon sources rather than as carbon sinks? These questions were answered using a suite of analytical instrumentation across scales ranging from laboratory experiments to field investigations.

1.4 PUBLICATIONS, PRESENTATIONS, AWARDS, AND FELLOWSHIPS

This dissertation begins with a review paper published in *Nature Reviews Earth & Environment* that I co-authored outlining major knowledge gaps within the field of wildfire impacts on soil chemistry (Chapter 2).[92] Chapter 3 describes a mesocosm-scale experiment using pyrocosms which was published in *Environmental Science & Technology*.[127] Chapter 4 provides a deeper evaluation of soil metabolomics in soils from three forested ecosystems heated in a muffle furnace and is in preparation to be submitted to *Environmental Science & Technology*. Chapter 5 describes a field-based study examining how the 2024 Alexander Mountain Fire in Colorado influenced SOM biodegradability and soil metabolite contents and is in preparation to be submitted to *Nature Geoscience*. For Chapters 3-5, I am/will be the first-author for the associated publications. Supplementary information for Chapters 2-5 can be found in Appendices A-D.

I have contributed to five additional publications. I was the sole author on a publication titled “Using pyrocosms to determine fire impacts on soil molecules” which was published in *Nature Reviews Earth & Environment* as a part of the “Tools of the Trade” article series.[128] The work in Appendix E “Characterization of Burned Soil Organic Matter via Sequential Solvent Extractions and 21 T FT-ICR Mass Spectrometry with Electrospray and Atmospheric Pressure

Photoionization" was published in *Analytical Chemistry*.[105] The work in Appendix F "Determination of Soil Contamination at the Wildland-Urban Interface after the 2021 Marshall Fire in Colorado, USA" was published in *Environmental Science & Technology*.[129] The work in Appendix G "Role of permafrost thaw transitions in biogeochemical nitrogen cycling" was published in *Soil & Environmental Health*.[130] I was also a co-author for a publication titled "Advancing sustainable water use across the agricultural life cycle in the USA" which was published in *Nature Water*.[131] A coauthored manuscript determining the impacts of the 2025 Los Angeles Fires on disinfection byproduct formation titled "Enrichment of Disinfection Byproduct Precursors in Fire-Affected Soils from the 2025 Eaton Fire in Los Angeles, California" is in review for *Environmental Science & Technology Water*. An additional coauthored manuscript evaluating how the 2020 Cameron Peak Fire in Colorado influenced watershed dissolved organic matter composition and disinfection byproduct formation potential titled "Changes in Molecular Chemistry of Stream Organic Matter and Disinfection Byproduct Precursors Following Initial Post-Fire Rainstorms" is in review for *Environmental Science & Technology*. Lastly, I contributed to five coauthored manuscripts that are in preparation for submission that have the following respective objectives: 1) determine differences in SOM composition from experimentally burned soils collected from lodgepole pine and aspen forests, 2) evaluate per- and polyfluoroalkyl substances contamination in soil and building debris burned by the 2025 Los Angeles Fires, 3) identify what metabolites can be released from burned vegetation and how that influences watershed biogeochemistry, 4) elucidate how organic matter in acid mine drainage interacts with toxic metals, and 5) characterize the composition and biodegradability of the metabolomic profile of Amazon River dissolved organic matter during the peak wet season. According to CRediT criteria, my collective roles in these coauthored manuscripts include conceptualization,

methodology, formal analysis, investigation, writing – review and editing, visualization, and supervision. Overall, the work I've conducted as a PhD student will culminate in 16 publications.

This body of research has been shared in presentations at various scientific meetings including the 2022 American Geophysical Union Hydrology Days Conference at Colorado State University (oral presentation); 2022 American Society of Agronomy, Crop Science Society of America, and Soil Science Society of America International Annual Meeting in Baltimore, MD (oral presentation); the 2023 13th North American Fourier Transform Mass Spectrometry Conference in Key West, FL (oral presentation); the 2023 Graduate Student Showcase at Colorado State University (poster presentation); the 2023 American Geophysical Union Annual Conference in San Francisco, CA (poster presentation); the 2024 American Chemical Society Meeting in Denver, CO (oral presentation); the University of Colorado-Boulder Environmental Engineering Seminar Series in 2024 (invited oral presentation); a Pacific Northwest National Laboratory river corridor science focus area meeting in 2024 (invited virtual oral presentation); and the 2025 Goldschmidt Conference in Prague, Czech Republic (oral presentation). I also served as the lead organizer and co-presider for a symposium at the 2024 American Chemical Society Meeting in Denver, CO titled "Chemical Footprint of Wildfires: Impacts on Soil, Water, and Air Quality" where I led a team of professors from Colorado State University, University of Colorado-Boulder, and Texas A&M University.

These publications and presentations have received the following awards: **the 2021 Maciel Fellowship Award** (awarded to incoming Colorado State University chemistry graduate students who exhibited outstanding academic record and recommendations), **the first place Hydrology Days Student Showcase award** (awarded to the best four-minute "lightning talk" at the 2022 American Geophysical Union Hydrology Days conference), **the second place award for Soil**

Chemistry Division Oral Presentation Student Competition (awarded to the second-best oral presentation given by a graduate student at the 2022 American Society of Agronomy, Crop Science Society of America, and Soil Science Society of American International Annual Meeting in Baltimore, MD), **2023 National Science Foundation Graduate Research Fellowship Program Honorable Mention award**, **the 2023 Lee Sommer Excellence in Leadership Award** (awarded to a graduate student associated with the Colorado State University Soil and Crop Sciences Department who has demonstrated scientific excellence and a strong commitment to leadership to benefit communities from the campus to international levels), **the 2023 College of Natural Sciences Outstanding Scholar Award** (awarded to graduate students who exemplify Colorado State University's commitment to cutting-edge research at the Colorado State University Graduate Student showcase poster session), **the 2024 Outstanding Student Presentation Award** (awarded to the most exceptional presentations during the 2023 American Geophysical Union meeting in which only the top 2 to 4 % of presentations are given this award), **the 2024 Ellen Gonter Graduate Student Research Paper award** (awarded to graduate students who submit the highest quality research papers to an American Chemical Society journal and was awarded to my first-author publication in *Environmental Science & Technology* titled "Fire Impacts on the Soil Metabolome and Organic Matter Biodegradability." This is the highest award given to students by the Division of Environmental Chemistry of the American Chemical Society), and **the 2025 C. Michael Elliott Scholarship** (award to high achieving graduate students within the Colorado State University Chemistry Department). I have also been accepted into the following fellowship programs at Colorado State University: the Diana Wall Sustainability Leadership Fellows Program within the School of Global and Environmental Sustainability and the Vice President for Research Graduate Fellows Program.

CHAPTER 1 REFERENCES

(1) Pausas, J. G.; Keeley, J. E. Wildfires as an Ecosystem Service. *Front. Ecol. Environ.* **2019**, *17* (5), 289–295. https://doi.org/10.1002/fee.2044.

(2) Santín, C.; Doerr, S. H. Fire Effects on Soils: The Human Dimension. *Philos. Trans. R. Soc. B Biol. Sci.* **2016**, *371* (1696), 20150171. https://doi.org/10.1098/rstb.2015.0171.

(3) Sayedi, S. S.; Abbott, B. W.; Vannière, B.; Leys, B.; Colombaroli, D.; Romera, G. G.; Słowiński, M.; Aleman, J. C.; Blarquez, O.; Feurdean, A.; Brown, K.; Aakala, T.; Alenius, T.; Allen, K.; Andric, M.; Bergeron, Y.; Biagioni, S.; Bradshaw, R.; Bremond, L.; Brisset, E.; Brooks, J.; Brugger, S. O.; Brussel, T.; Cadd, H.; Cagliero, E.; Carcaillet, C.; Carter, V.; Catry, F. X.; Champreux, A.; Chaste, E.; Chavardès, R. D.; Chipman, M.; Conedera, M.; Connor, S.; Constantine, M.; Courtney Mustaphi, C.; Dabengwa, A. N.; Daniels, W.; De Boer, E.; Dietze, E.; Estrany, J.; Fernandes, P.; Finsinger, W.; Flantua, S. G. A.; Fox-Hughes, P.; Gaboriau, D. M.; M.Gayo, E.; Girardin, Martin. P.; Glenn, J.; Glückler, R.; González-Arango, C.; Groves, M.; Hamilton, D. S.; Hamilton, R. J.; Hantson, S.; Hapsari, K. A.; Hardiman, M.; Hawthorne, D.; Hoffman, K.; Inoue, J.; Karp, A. T.; Krebs, P.; Kulkarni, C.; Kuosmanen, N.; Lacourse, T.; Ledru, M.-P.; Lestienne, M.; Long, C.; López-Sáez, J. A.; Loughlin, N.; Niklasson, M.; Madrigal, J.; Maezumi, S. Y.; Marcisz, K.; Mariani, M.; McWethy, D.; Meyer, G.; Molinari, C.; Montoya, E.; Mooney, S.; Morales-Molino, C.; Morris, J.; Moss, P.; Oliveras, I.; Pereira, J. M.; Pezzatti, G. B.; Pickarski, N.; Pini, R.; Rehn, E.; Remy, C. C.; Revelles, J.; Rius, D.; Robin, V.; Ruan, Y.; Rudaya, N.; Russell-Smith, J.; Seppä, H.; Shumilovskikh, L.; T.Sommers, W.; Tavşanoğlu, Ç.; Umbanhowar, C.; Urquiaga, E.; Urrego, D.; Vachula, R. S.; Wallenius, T.; You, C.; Daniau, A.-L.

Assessing Changes in Global Fire Regimes. *Fire Ecol.* **2024**, *20* (1), 18. https://doi.org/10.1186/s42408-023-00237-9.

(4) McLauchlan, K. K.; Higuera, P. E.; Miesel, J.; Rogers, B. M.; Schweitzer, J.; Shuman, J. K.; Tepley, A. J.; Varner, J. M.; Veblen, T. T.; Adalsteinsson, S. A.; Balch, J. K.; Baker, P.; Batllori, E.; Bigio, E.; Brando, P.; Cattau, M.; Chipman, M. L.; Coen, J.; Crandall, R.; Daniels, L.; Enright, N.; Gross, W. S.; Harvey, B. J.; Hatten, J. A.; Hermann, S.; Hewitt, R. E.; Kobziar, L. N.; Landesmann, J. B.; Loranty, M. M.; Maezumi, S. Y.; Mearns, L.; Moritz, M.; Myers, J. A.; Pausas, J. G.; Pellegrini, A. F. A.; Platt, W. J.; Roozeboom, J.; Safford, H.; Santos, F.; Scheller, R. M.; Sherriff, R. L.; Smith, K. G.; Smith, M. D.; Watts, A. C. Fire as a Fundamental Ecological Process: Research Advances and Frontiers. *J. Ecol.* **2020**, *108* (5), 2047–2069. https://doi.org/10.1111/1365-2745.13403.

(5) Hagmann, R. K.; Hessburg, P. F.; Prichard, S. J.; Povak, N. A.; Brown, P. M.; Fulé, P. Z.; Keane, R. E.; Knapp, E. E.; Lydersen, J. M.; Metlen, K. L.; Reilly, M. J.; Sánchez Meador, A. J.; Stephens, S. L.; Stevens, J. T.; Taylor, A. H.; Yocom, L. L.; Battaglia, M. A.; Churchill, D. J.; Daniels, L. D.; Falk, D. A.; Henson, P.; Johnston, J. D.; Krawchuk, M. A.; Levine, C. R.; Meigs, G. W.; Merschel, A. G.; North, M. P.; Safford, H. D.; Swetnam, T. W.; Waltz, A. E. M. Evidence for Widespread Changes in the Structure, Composition, and Fire Regimes of Western North American Forests. *Ecol. Appl.* **2021**, *31* (8). https://doi.org/10.1002/eap.2431.

(6) Kolden, C. A.; Abatzoglou, J. T.; Jones, M. W.; Jain, P. Wildfires in 2024. *Nat. Rev. Earth Environ.* **2025**, *6* (4), 237–239. https://doi.org/10.1038/s43017-025-00663-0.

(7) Keeley, J. E. Fire Intensity, Fire Severity and Burn Severity: A Brief Review and Suggested Usage. *Int. J. Wildland Fire* **2009**, *18* (1), 116–126. https://doi.org/10.1071/wf07049.

(8) Parson, A.; Robichaud, P. R.; Lewis, S. A.; Napper, C.; Clark, J. T. Field Guide for Mapping Post-Fire Soil Burn Severity. *Gen Tech Rep RMRS-GTR-243 Fort Collins CO US Dep. Agric. For. Serv. Rocky Mt. Res. Stn. 49 P* **2010**. https://doi.org/10.2737/RMRS-GTR-243.

(9) Lopez, A. M.; Avila, C. C. E.; VanderRoest, J. P.; Roth, H. K.; Fendorf, S.; Borch, T. Molecular Insights and Impacts of Wildfire-Induced Soil Chemical Changes. *Nat. Rev. Earth Environ.* **2024**, *5*, 431–446. https://doi.org/10.1038/s43017-024-00548-8.

(10) Jones, M. W.; Abatzoglou, J. T.; Veraverbeke, S.; Andela, N.; Lasslop, G.; Forkel, M.; Smith, A. J. P.; Burton, C.; Betts, R. A.; Van Der Werf, G. R.; Sitch, S.; Canadell, J. G.; Santín, C.; Kolden, C.; Doerr, S. H.; Le Quéré, C. Global and Regional Trends and Drivers of Fire Under Climate Change. *Rev. Geophys.* **2022**, *60* (3), 1–76. https://doi.org/10.1029/2020rg000726.

(11) Cunningham, C. X.; Williamson, G. J.; Bowman, D. M. J. S. Increasing Frequency and Intensity of the Most Extreme Wildfires on Earth. *Nat. Ecol. Evol.* **2024**, *8*, 1420–1425. https://doi.org/10.1038/s41559-024-02452-2.

(12) Mansoor, S.; Farooq, I.; Kachroo, M. M.; Mahmoud, A. E. D.; Fawzy, M.; Popescu, S. M.; Alyemeni, M. N.; Sonne, C.; Rinklebe, J.; Ahmad, P. Elevation in Wildfire Frequencies with Respect to the Climate Change. *J. Environ. Manage.* **2022**, *301*, 113769. https://doi.org/10.1016/j.jenvman.2021.113769.

(13) Clarke, H.; Nolan, R. H.; De Dios, V. R.; Bradstock, R.; Griebel, A.; Khanal, S.; Boer, M. M. Forest Fire Threatens Global Carbon Sinks and Population Centres under Rising Atmospheric Water Demand. *Nat. Commun.* **2022**, *13* (1), 1–10. https://doi.org/10.1038/s41467-022-34966-3.

(14) Iglesias, V.; Balch, J. K.; Travis, W. R. U.S. Fires Became Larger, More Frequent, and More Widespread in the 2000s. *Sci. Adv.* **2022**, *8* (11), eabc0020. https://doi.org/10.1126/sciadv.abc0020.

(15) Higuera, P. E.; Cook, M. C.; Balch, J. K.; Stavros, E. N.; Mahood, A. L.; St. Denis, L. A. Shifting Social-Ecological Fire Regimes Explain Increasing Structure Loss from Western Wildfires. *PNAS Nexus* **2023**, *2*, 1–11. https://doi.org/10.1093/pnasnexus/pgad005.

(16) Villarruel, C. M.; Figueroa, L. A.; Ranville, J. F. Quantification of Bioaccessible and Environmentally Relevant Trace Metals in Structure Ash from a Wildland–Urban Interface Fire. *Environ. Sci. Technol.* **2024**, *58* (5), 2502–2513. https://doi.org/10.1021/acs.est.3c08446.

(17) Zhang, Y.; Biswas, A. The Effects of Forest Fire on Soil Organic Matter and Nutrients in Boreal Forests of North America: A Review; Springer Singapore, 2017; pp 465–476.

(18) Abatzoglou, J. T.; Williams, A. P. Impact of Anthropogenic Climate Change on Wildfire across Western US Forests. *Proc. Natl. Acad. Sci.* **2016**, *113* (42), 11770–11775. https://doi.org/10.1073/pnas.1607171113.

(19) Potapov, P.; Tyukavina, A.; Turubanova, S.; Hansen, M. C.; Giglio, L.; Hernandez-Serna, A.; Lima, A.; Harris, N.; Stolle, F. Unprecedentedly High Global Forest Disturbance Due to Fire in 2023 and 2024. *Proc. Natl. Acad. Sci.* **2025**, *122* (30), e2505418122. https://doi.org/10.1073/pnas.2505418122.

(20) Seager, R.; Hooks, A.; Williams, A. P.; Cook, B.; Nakamura, J.; Henderson, N. Climatology, Variability, and Trends in the U.S. Vapor Pressure Deficit, an Important Fire-Related Meteorological Quantity. **2015**. https://doi.org/10.1175/JAMC-D-14-0321.1.

(21) Sedano, F.; Randerson, J. T. Multi-Scale Influence of Vapor Pressure Deficit on Fire Ignition and Spread in Boreal Forest Ecosystems. *Biogeosciences* **2014**, *11* (14), 3739–3755. https://doi.org/10.5194/bg-11-3739-2014.

(22) Radeloff, V.; Helmers, D.; Kramer, H.; Mockrin, M.; Alexandre, P.; Bar-Massada, A.; Butsic, V.; Hawbaker, T.; Martinuzzi, S.; Syphard, A.; Stewart, S. Rapid Growth of the US

Wildland-Urban Interface Raises Wildfire Risk. *Proc. Natl. Acad. Sci.* **2018**, *115*, 3314–3319. https://doi.org/10.1073/pnas.171885011.

(23) Schug, F.; Bar-Massada, A.; Carlson, A. R.; Cox, H.; Hawbaker, T. J.; Helmers, D.; Hostert, P.; Kaim, D.; Kasraee, N. K.; Martinuzzi, S.; Mockrin, M. H.; Pfoch, K. A.; Radeloff, V. C. The Global Wildland–Urban Interface. *Nature* **2023**, *621* (7977), 94–99. https://doi.org/10.1038/s41586-023-06320-0.

(24) Jain, M.; Saxena, P.; Sharma, S.; Sonwani, S. Investigation of Forest Fire Activity Changes Over the Central India Domain Using Satellite Observations During 2001–2020. *GeoHealth* **2021**, *5* (12). https://doi.org/10.1029/2021gh000528.

(25) Balch, J. K.; Bradley, B. A.; Abatzoglou, J. T.; Nagy, R. C.; Fusco, E. J.; Mahood, A. L. Human-Started Wildfires Expand the Fire Niche across the United States. *Proc. Natl. Acad. Sci.* **2017**, *114* (11), 2946–2951. https://doi.org/10.1073/pnas.1617394114.

(26) *U.S. Forest Service Fire Suppression*. foresthistory.org. https://foresthistory.org/research-explore/us-forest-service-history/policy-and-law/fire-u-s-forest-service/u-s-forest-service-fire-suppression/#:~:text=Until%20around%201970%2C%20federal%20land,could%20aid%20in%20fire%20suppression. (accessed 2026-01-21).

(27) *Suppression Costs*. https://www.nifc.gov/fire-information/statistics/suppression-costs (accessed 2026-01-26).

(28) Avitt, Andrew. *The 98% Suppression Rate: Analyzing Extreme Wildfire Behavior*. https://www.fs.usda.gov/r05/newsroom/stories/98-suppression-rate-analyzing-extreme-wildfire-behavior (accessed 2026-01-26).

(29) Prichard, S. J.; Hessburg, P. F.; Hagmann, R. K.; Povak, N. A.; Dobrowski, S. Z.; Hurteau, M. D.; Kane, V. R.; Keane, R. E.; Kobziar, L. N.; Kolden, C. A.; North, M.; Parks, S.

A.; Safford, H. D.; Stevens, J. T.; Yocom, L. L.; Churchill, D. J.; Gray, R. W.; Huffman, D. W.; Lake, F. K.; Khatri-Chhetri, P. Adapting Western North American Forests to Climate Change and Wildfires: 10 Common Questions. *Ecol. Appl.* **2021**, *31* (8). https://doi.org/10.1002/eap.2433.

(30) Kreider, M. R.; Higuera, P. E.; Parks, S. A.; Rice, W. L.; White, N.; Larson, A. J. Fire Suppression Makes Wildfires More Severe and Accentuates Impacts of Climate Change and Fuel Accumulation. *Nat. Commun.* **2024**, *15* (1), 2412. https://doi.org/10.1038/s41467-024-46702-0.

(31) *Historical Wildfire Information*. https://dfpc.colorado.gov/sections/wildfire-information-center/historical-wildfire-information (accessed 2026-01-26).

(32) Rust, A. J.; Hogue, T. S.; Saxe, S.; McCray, J. Post-Fire Water-Quality Response in the Western United States. *Int. J. Wildland Fire* **2018**, *27* (3), 203–216. https://doi.org/10.1071/wf17115.

(33) Jerrett, M.; Jina, A. S.; Marlier, M. E. Up in Smoke: California's Greenhouse Gas Reductions Could Be Wiped out by 2020 Wildfires. *Environ. Pollut.* **2022**, *310*, 119888.

(34) Burton, C. A.; Kelley, D. I.; Burke, E.; Mathison, C.; Jones, C. D.; Betts, R. A.; Robertson, E.; Teixeira, J. C. M.; Cardoso, M.; Anderson, L. O. Fire Weakens Land Carbon Sinks before 1.5 °C. *Nat. Geosci.* **2024**, *17* (11), 1108–1114. https://doi.org/10.1038/s41561-024-01554-7.

(35) *Soil Carbon Storage | Learn Science at Scitable*. https://www.nature.com/scitable/knowledge/library/soil-carbon-storage-84223790/ (accessed 2026-02-06).

(36) Pellegrini, A. F. A.; Harden, J.; Georgiou, K.; Hemes, K. S.; Malhotra, A.; Nolan, C. J.; Jackson, R. B. Fire Effects on the Persistence of Soil Organic Matter and Long-Term Carbon Storage. *Nat. Geosci.* **2021**, *15*, 5–13. https://doi.org/10.1038/s41561-021-00867-1.

(37) Namayandeh, A.; Lamb, C.; Sarabia, J. L.; Shakouri, M.; Lopes, E.; Lezama Pacheco, J.; Honeyman, A.; Coker, A.; Stewart, B.; Tikoo, S.; Peak, D.; Fendorf, S. Nonlinear Redox Transformations of Chromium in Soil during Wildfire Heating: The Critical Role of Iron Mineralogy. *Environ. Sci. Technol.* **2025**, *59* (50), 27623–27634. https://doi.org/10.1021/acs.est.5c10407.

(38) Nelson, A. R.; Narrowe, A. B.; Rhoades, C. C.; Fegel, T. S.; Daly, R. A.; Roth, H. K.; Chu, R. K.; Amundson, K. K.; Young, R. B.; Steindorff, A. S.; Mondo, S. J.; Grigoriev, I. V.; Salamov, A.; Borch, T.; Wilkins, M. J. Wildfire-Dependent Changes in Soil Microbiome Diversity and Function. *Nat. Microbiol.* **2022**, *7* (9), 1419–1430. https://doi.org/10.1038/s41564-022-01203-y.

(39) Pulido-Chavez, M. F.; Alvarado, E. C.; DeLuca, T. H.; Edmonds, R. L.; Glassman, S. I. High-Severity Wildfire Reduces Richness and Alters Composition of Ectomycorrhizal Fungi in Low-Severity Adapted Ponderosa Pine Forests. *For. Ecol. Manag.* **2021**, *485*, 118923.

(40) Fowler, J. A.; Nelson, A. R.; Bechtold, E. K.; Paul, R.; Wettengel, A. M.; McNorvell, M. A.; Stevens-Rumann, C. S.; Fegel, T. S.; Anderson, E.; Rhoades, C. C.; Wilkins, M. J. Pile Burns as a Proxy for High Severity Wildfire Impacts on Soil Microbiomes. *Geoderma* **2024**, *448*, 116982. https://doi.org/10.1016/j.geoderma.2024.116982.

(41) Caifa, M. V.; Nelson, A. R.; Borch, T.; Roth, H. K.; Fegel, T.; Rhoades, C. C.; Wilkins, M. J.; Glassman, S. I. Distinct Fungal and Bacterial Responses to Fire Severity and Soil Depth across a Ten-Year Wildfire Chronosequence in Bettle-Killed Lodgepole Pine Forests. *For. Ecol. Manag.* **2023**, *544*, 121160.

(42) Knicker, H. How Does Fire Affect the Nature and Stability of Soil Organic Nitrogen and Carbon? A Review. *Biogeochemistry* **2007**, *85* (1), 91–118. https://doi.org/10.1007/s10533-007-9104-4.

(43) Roshan, A.; Biswas, A. Fire-Induced Geochemical Changes in Soil: Implication for the Element Cycling. *Sci. Total Environ.* **2023**, *868*, 161714.

(44) Zimmerman, S.; Frey, B. Soil Respiration and Microbial Properties in an Acid Forest Soil: Effects of Wood Ash. *Soil Biol. Biochem.* **2002**, *34* (11), 1727–1737.

(45) Memoli, V.; Panico, S. C.; Santorufo, L.; Barile, R.; Di Natale, G.; Di Nunzio, A.; Toscanesi, M.; Trifuoggi, M.; De Marco, A.; Maisto, G. Do Wildfires Cause Changes in Soil Quality in the Short Term? *Int. J. Environ. Res. Public. Health* **2020**, *17* (15), 5343. https://doi.org/10.3390/ijerph17155343.

(46) Zhu, S.; Yang, P.; Yin, Y.; Zhang, S.; Lv, J.; Tian, S.; Jiang, T.; Wang, D. Influences of Wildfire on the Soil Dissolved Organic Matter Characteristics and Its Electron-Donating Capacity. *Water Res.* **2024**, *266*, 122382. https://doi.org/10.1016/j.watres.2024.122382.

(47) Zheng, X.; Zhang, Y.; Deng, Y.; Cui, X. Effects of Wildfire on the Adsorption-Desorption of Soil Free Amino Acids in a Dahurian Larch Forest in Northeast China. *J. Soil Sci. Plant Nutr.* **2024**. https://doi.org/10.1007/s42729-024-02027-x.

(48) Johnson, D. B.; Yedinak, K. M.; Sulman, B. N.; Berry, T. D.; Kruger, K.; Whitman, T. Effects of Fire and Fire-Induced Changes in Soil Properties on Post-Burn Soil Respiration. *Fire Ecol.* **2024**, *20* (1). https://doi.org/10.1186/s42408-024-00328-1.

(49) Araya, S. N.; Meding, M.; Berhe, A. A. Thermal Alteration of Soil Physico-Chemical Properties: A Systematic Study to Infer Response of Sierra Nevada Climosequence Soils to Forest Fires. *SOIL* **2016**, *2* (3), 351–366. https://doi.org/10.5194/soil-2-351-2016.

(50) Rhoades, C. C.; Fegel, T. S.; Fowler, J. A.; Starr, B.; Wilkins, M. J. Rapid Changes in the Chemistry of Ash and Underlying Soil Layers after Pile Burning in a Subalpine Forest. *Trees For. People* **2025**, *22*, 101035. https://doi.org/10.1016/j.tfp.2025.101035.

(51) Francos, M.; Ubeda, X.; Pereira, P.; Alcañiz, M. Long-Term Impact of Wildfire on Soils Exposed to Different Fire Severities. A Case Study in Cadiretes Massif (NE Iberian Peninsula). *Sci. Total Environ.* **2018**, *615*, 664–671.

(52) Bahureksa, W.; Young, R. B.; McKenna, A. M.; Chen, H.; Thorn, K. A.; Rosario-Ortiz, F. L.; Borch, T. Nitrogen Enrichment during Soil Organic Matter Burning and Molecular Evidence of Maillard Reactions. *Environ. Sci. Technol.* **2022**, *56* (7), 4597–4609. https://doi.org/10.1021/acs.est.1c06745.

(53) Su, W.-Q.; Yu, M.; Lin, J.; Tang, C.; Xu, J. Fire Decreases Gross Mineralization Rate but Does Not Alter Gross Nitrification Rate in Boreal Forest Soils. *Soil Biol. Biochem.* **2022**, *175*, 108838. https://doi.org/10.1016/j.soilbio.2022.108838.

(54) Krichels, A. H.; Stephens, E. Z.; Reid, C.; Barriga, M. F. P.; Ordoñez, M. E.; McLaren, J. R.; Kargul, M.; Larios, L.; Glassman, S. I.; Homyak, P. M. Wildfire-Induced Losses of Soil Particulate and Mineral-Associated Organic Carbon Persist for Over 4 Years in a Chaparral Ecosystem. *Glob. Change Biol.* **2025**, *31* (8), e70404. https://doi.org/10.1111/gcb.70404.

(55) Kelly, J.; Doerr, S. H.; Ekroos, J.; Ibáñez, T. S.; Islam, Md. R.; Santín, C.; Soares, M.; Kljun, N. No Recovery of Soil Respiration Four Years after Fire and Post-Fire Management in a Nordic Boreal Forest. *Agric. For. Meteorol.* **2025**, *364*, 110454. https://doi.org/10.1016/j.agrformet.2025.110454.

(56) González-Pérez, J. A.; González-Vila, F. J.; Almendros, G.; Knicker, H. The Effect of Fire on Soil Organic Matter—a Review. *Environ. Int.* **2004**, *30* (6), 855–870. https://doi.org/10.1016/j.envint.2004.02.003.

(57) Simpson, M. J.; Simpson, A. J. The Chemical Ecology of Soil Organic Matter Molecular Constituents. *J. Chem. Ecol.* **2012**, *38* (6), 768–784. https://doi.org/10.1007/s10886-012-0122-x.

(58) Wu, M.; Li, P.; Li, G.; Liu, K.; Gao, G.; Ma, S.; Qiu, C.; Li, Z. Using Potential Molecular Transformation To Understand the Molecular Trade-Offs in Soil Dissolved Organic Matter. *Environ. Sci. Technol.* **2022**. https://doi.org/10.1021/acs.est.2c01137.

(59) LaRowe, D. E.; Van Cappellen, P. Degradation of Natural Organic Matter: A Thermodynamic Analysis. *Geochim. Cosmochim. Acta* **2011**, *75* (8), 2030–2042. https://doi.org/10.1016/j.gca.2011.01.020.

(60) Schmidt, M. W. I.; Torn, M. S.; Abiven, S.; Dittmar, T.; Guggenberger, G.; Janssens, I. A.; Kleber, M.; Kögel-Knabner, I.; Lehmann, J.; Manning, D. A. C.; Nannipieri, P.; Rasse, D. P.; Weiner, S.; Trumbore, S. E. Persistence of Soil Organic Matter as an Ecosystem Property. *Nature* **2011**, *478* (7367), 49–56. https://doi.org/10.1038/nature10386.

(61) Graham, E. B.; Song, H.-S.; Grieger, S.; Garayburu-Caruso, V. A.; Stegen, J. C.; Bladon, K. D.; Myers-Pigg, A. N. Potential Bioavailability of Representative Pyrogenic Organic Matter Compounds in Comparison to Natural Dissolved Organic Matter Pools. *Biogeosciences* **2023**, *20* (16), 3449–3457. https://doi.org/10.5194/bg-20-3449-2023.

(62) Goranov, A. I.; Wozniak, A. S.; Bostick, K. W.; Zimmerman, A. R.; Mitra, S.; Hatcher, P. G. Microbial Labilization and Diversification of Pyrogenic Dissolved Organic Matter. *Biogeosciences* **2022**, *19* (5), 1491–1514. https://doi.org/10.5194/bg-19-1491-2022.

(63) Bostick, K. W.; Zimmerman, A. R.; Goranov, A. I.; Mitra, S.; Hatcher, P. G.; Wozniak, A. S. Biolability of Fresh and Photodegraded Pyrogenic Dissolved Organic Matter From Laboratory-Prepared Chars. *J. Geophys. Res. Biogeosciences* **2021**, *126* (5), 1–17. https://doi.org/10.1029/2020jg005981.

(64) Cochran, D.; Powers, R. Fourier Transform Ion Cyclotron Resonance Mass Spectrometry Applications for Metabolomics. *Biomedicines* **2024**, *12* (8), 1786. https://doi.org/10.3390/biomedicines12081786.

(65) Baran, R.; Brodie, E. L.; Mayberry-Lewis, J.; Hummel, E.; Da Rocha, U. N.; Chakraborty, R.; Bowen, B. P.; Karaoz, U.; Cadillo-Quiroz, H.; Garcia-Pichel, F.; Northen, T. R. Exometabolite Niche Partitioning among Sympatric Soil Bacteria. *Nat. Commun.* **2015**, *6* (1), 8289. https://doi.org/10.1038/ncomms9289.

(66) Swenson, T. L.; Karaoz, U.; Swenson, J. M.; Bowen, B. P.; Northen, T. R. Linking Soil Biology and Chemistry in Biological Soil Crust Using Isolate Exometabolomics. *Nat. Commun.* **2018**, *9* (1). https://doi.org/10.1038/s41467-017-02356-9.

(67) Manz, K. E.; Feerick, A.; Braun, J. M.; Feng, Y.-L.; Hall, A.; Koelmel, J.; Manzano, C.; Newton, S. R.; Pennell, K. D.; Place, B. J.; Godri Pollitt, K. J.; Prasse, C.; Young, J. A. Non-Targeted Analysis (NTA) and Suspect Screening Analysis (SSA): A Review of Examining the Chemical Exposome. *J. Expo. Sci. Environ. Epidemiol.* **2023**, *33* (4), 524–536. https://doi.org/10.1038/s41370-023-00574-6.

(68) Schymanski, E. L.; Jeon, J.; Gulde, R.; Fenner, K.; Ruff, M.; Singer, H. P.; Hollender, J. Identifying Small Molecules via High Resolution Mass Spectrometry: Communicating Confidence. *Environ. Sci. Technol.* **2014**, *48* (4), 2097–2098. https://doi.org/10.1021/es5002105.

(69) Zweigle, J.; Tisler, S.; Bevilacqua, M.; Tomasi, G.; Nielsen, N. J.; Gawlitta, N.; Lübeck, J. S.; Smilde, A. K.; Christensen, J. H. Prioritization Strategies for Non-Target Screening in Environmental Samples by Chromatography – High-Resolution Mass Spectrometry: A Tutorial. *J. Chromatogr. A* **2025**, *1751*, 465944. https://doi.org/10.1016/j.chroma.2025.465944.

(70) Bifarin, O. O.; Yelluru, V. S.; Simhadri, A.; Fernández, F. M. A Large Language Model–Powered Map of Metabolomics Research. *Anal. Chem. 97* (27), 14088–14096. https://doi.org/10.1021/acs.analchem.5c01672.

(71) Bhattacharjya, S.; Ghosh, A.; Sahu, A.; Agnihotri, R.; Pal, N.; Sharma, P.; Manna, M. C.; Sharma, M. P.; Singh, A. B. Utilizing Soil Metabolomics to Investigate the Untapped Metabolic Potential of Soil Microbial Communities and Their Role in Driving Soil Ecosystem Processes: A Review. *Appl. Soil Ecol.* **2024**, *195*, 105238.

(72) McGivern, B. B.; Tfaily, M. M.; Borton, M. A.; Kosina, S. M.; Daly, R. A.; Nicora, C. D.; Purvine, S. O.; Wong, A. R.; Lipton, M. S.; Hoyt, D. W.; Northen, T. R.; Hagerman, A. E.; Wrighton, K. C. Decrypting Bacterial Polyphenol Metabolism in an Anoxic Wetland Soil. *Nat. Commun.* **2021**, *12* (1). https://doi.org/10.1038/s41467-021-22765-1.

(73) Swenson, T. L. Untargeted Soil Metabolomics Methods for Analysis of Extractable Organic Matter. *Soil Biol. Biochem.* **2015**, *80*, 189–198. https://doi.org/doi:10.1016/j.soilbio.2014.10.007.

(74) Withers, E.; Hill, P. W.; Chadwick, D. R.; Jones, D. L. Use of Untargeted Metabolomics for Assessing Soil Quality and Microbial Function. *Soil Biol. Biochem.* **2020**, *143*, 107758. https://doi.org/10.1016/j.soilbio.2020.107758.

(75) Li, W.; Liu, X.; Xia, Q.; Gao, Z.; Zheng, W.; Zhai, B.; Yang, Z. Untargeted Metabolomics to Study Changes in Soil Microbial Community in Response to Tillage Practices. *Appl. Soil Ecol.* **2024**, *199*, 105409.

(76) Brown, R. W.; Chadwick, D. R.; Zang, H.; Jones, D. L. Use of Metabolomics to Quantify Changes in Soil Microbial Function in Response to Fertiliser Nitrogen Supply and Extreme Drought. *Soil Biol. Biochem.* **2021**, *160*, 108351. https://doi.org/10.1016/j.soilbio.2021.108351.

(77) Lai, X.; Duan, W.; Zhang, W.; Peng, Z.; Wang, X.; Wang, H.; Qi, X.; Pi, H.; Chen, K.; Yan, L. Integrative Analysis of Microbiome and Metabolome Revealed the Effect of Microbial Inoculant on Microbial Community Diversity and Function in Rhizospheric Soil under Tobacco Monoculture. *Microbiol. Spectr.* **2024**, *12* (8). https://doi.org/10.1128/spectrum.04046-23.

(78) Woolet, J.; Whitman, T. Pyrogenic Organic Matter Effects on Soil Bacterial Community Composition. *Soil Biol. Biochem.* **2020**, *141*, 107678. https://doi.org/10.1016/j.soilbio.2019.107678.

(79) Bird, M. I.; Wynn, J. G.; Saiz, G.; Wurster, C. M.; McBeath, A. The Pyrogenic Carbon Cycle. *Annu. Rev. Earth Planet. Sci.* **2015**, *43* (1), 273–298. https://doi.org/10.1146/annurev-earth-060614-105038.

(80) Chen, H.; Wang, J.-J.; Ku, P.-J.; Tsui, M. T.-K.; Abney, R. B.; Berhe, A. A.; Zhang, Q.; Burton, S. D.; Dahlgren, R. A.; Chow, A. T. Burn Intensity Drives the Alteration of Phenolic Lignin to (Poly) Aromatic Hydrocarbons as Revealed by Pyrolysis Gas Chromatography–Mass Spectrometry (Py-GC/MS). *Environ. Sci. Technol.* **2022**, *56* (17), 12678–12687. https://doi.org/10.1021/acs.est.2c00426.

(81) De La Rosa, J. M.; González-Pérez, J. A.; González-Vázquez, R.; Knicker, H.; López-Capel, E.; Manning, D. A. C.; González-Vila, F. J. Use of Pyrolysis/GC–MS Combined with

Thermal Analysis to Monitor C and N Changes in Soil Organic Matter from a Mediterranean Fire Affected Forest. *CATENA* **2008**, *74* (3), 296–303. https://doi.org/10.1016/j.catena.2008.03.004.

(82) Jiménez-González, M. A.; De La Rosa, J. M.; Jiménez-Morillo, N. T.; Almendros, G.; González-Pérez, J. A.; Knicker, H. Post-Fire Recovery of Soil Organic Matter in a Cambisol from Typical Mediterranean Forest in Southwestern Spain. *Sci. Total Environ.* **2016**, *572*, 1414–1421. https://doi.org/10.1016/j.scitotenv.2016.02.134.

(83) Faria, S. R.; De La Rosa, J. M.; Knicker, H.; González-Pérez, J. A.; Keizer, J. J. Molecular Characterization of Wildfire Impacts on Organic Matter in Eroded Sediments and Topsoil in Mediterranean Eucalypt Stands. *CATENA* **2015**, *135*, 29–37. https://doi.org/10.1016/j.catena.2015.07.007.

(84) Jiménez-Morillo, N. T.; de la Rosa, J. M.; Waggoner, D.; Almendros, G.; González-Vila, F. J.; González-Pérez, J. A. Fire Effects in the Molecular Structure of Soil Organic Matter Fractions under Quercus Suber Cover. *CATENA* **2016**, *145*, 266–273.

(85) Jiménez-Morillo, N. T.; Almendros, G.; De la Rosa, J. M.; Jordán, A.; Zavala, L. M.; Granged, A. J. P.; González-Pérez, J. A. Effect of a Wildfire and of Post-Fire Restoration Actions in the Organic Matter Structure in Soil Fractions. *Sci. Total Environ.* **2020**, *728*, 138715. https://doi.org/10.1016/j.scitotenv.2020.138715.

(86) Zeba, N.; Berry, T. D.; Fischer, M. S.; Traxler, M. F.; Whitman, T. Soil Carbon Mineralization and Microbial Community Dynamics in Response to Pyrogenic Organic Matter Addition. *Soil Biol. Biochem.* **2024**, *191*, 109328.

(87) Liang, B.; Lehmann, J.; Solomon, D.; Sohi, S.; Thies, J. E.; Skjemstad, J. O.; Luizao, F. J.; Engelhard, M. H.; Neves, E. G.; Wirick, S. Stability of Biomass-Derived Black Carbon in Soils. *Geochim. Cosmochim. Acta* **2008**, *72*, 6069–6078.

(88) Zimmerman, A. R. Abiotic and Microbial Oxidation of Laboratory-Produced Black Carbon (Biochar). *Environ. Sci. Technol.* **2010**, *44* (4), 1295–1301. https://doi.org/10.1021/es903140c.

(89) Kuzyakov, Y.; Subbotina, I.; Chen, H.; Bogomolova, I.; Xu, X. Black Carbon Decomposition and Incorporation into Soil Microbial Biomass Estimated by 14C Labeling. *Soil Biol. Biochem.* **2009**, *41*, 210–219.

(90) Monika S. Fischer; Frances G. Stark; Timothy D. Berry; Nayela Zeba; Thea Whitman; Matthew F. Traxler. Pyrolyzed Substrates Induce Aromatic Compound Metabolism in the Post-Fire Fungus, Pyronema Domesticum. *Front. Microbiol.* **2021**, *12*, 1–12.

(91) De La Rosa, J. M.; Miller, A. Z.; Knicker, H. Soil-Borne Fungi Challenge the Concept of Long-Term Biochemical Recalcitrance of Pyrochar. *Sci. Rep.* **2018**, *8*. https://doi.org/10.1038/s41598-018-21257-5.

(92) Lopez, A. M.; Avila, C. C. E.; VanderRoest, J. P.; Roth, H. K.; Fendorf, S.; Borch, T. Molecular Insights and Impacts of Wildfire-Induced Soil Chemical Changes. *Nat. Rev. Earth Environ.* **2024**, *5*, 431–446. https://doi.org/10.1038/s43017-024-00548-8.

(93) Johnson, D. B.; Woolet, J.; Yedinak, K. M.; Whitman, T. Experimentally Determined Traits Shape Bacterial Community Composition One and Five Years Following Wildfire. *Nat. Ecol. Amp Evol.* **2023**, *7* (9), 1419–1431. https://doi.org/10.1038/s41559-023-02135-4.

(94) Brucker, C. P.; Livneh, B.; Minear, J. T.; Rosario-Ortiz, F. L. A Review of Simulation Experiment Techniques Used to Analyze Wildfire Effects on Water Quality and Supply. *Environ. Sci. Process. Impacts* **2022**, *24* (8), 1110–1132. https://doi.org/10.1039/d2em00045h.

(95) Cawley, K. M.; Hohner, A. K.; Podgorski, D. C.; Cooper, W. T.; Korak, J. A.; Rosario-Ortiz, F. L. Molecular and Spectroscopic Characterization of Water Extractable Organic Matter from Thermally Altered Soils Reveal Insight into Disinfection Byproduct Precursors. *Environ. Sci. Technol.* **2017**, *51* (2), 771–779. https://doi.org/10.1021/acs.est.6b05126.

(96) Zhang, Q.; Wang, Y.; Guan, P.; Zhang, P.; Mo, X.; Yin, G.; Qu, B.; Xu, S.; He, C.; Shi, Q.; Zhang, G.; Dittmar, T.; Wang, J. Temperature Thresholds of Pyrogenic Dissolved Organic Matter in Heating Experiments Simulating Forest Fires. *Environ. Sci. Technol.* **2023**, *57*, 17291–17301.

(97) Hohner, A. K.; Rhoades, C. C.; Wilkerson, P.; Rosario-Ortiz, F. L. Wildfires Alter Forest Watersheds and Threaten Drinking Water Quality. *Acc. Chem. Res.* **2019**, *52* (5), 1234–1244. https://doi.org/10.1021/acs.accounts.8b00670.

(98) Promi, S. I.; Gardner, C. M.; Hohner, A. K. Biodegradability of Unheated and Laboratory Heated Dissolved Organic Matter. *Environ. Sci. Process. Impacts* **2024**. https://doi.org/10.1039/d3em00383c.

(99) Bruns, T. D.; Chung, J. A.; Carver, A. A.; Glassman, S. I. A Simple Pyrocosm for Studying Soil Microbial Response to Fire Reveals a Rapid, Massive Response by Pyronema Species. *PLoS ONE* **2020**, *15* (3), 1–20.

(100) Fischer, S. J.; Fegel, T. S.; Wilkerson, P. J.; Rivera, L.; Rhoades, C. C.; Rosario-Ortiz, F. L. Fluorescence and Absorbance Indices for Dissolved Organic Matter from Wildfire Ash and

Burned Watersheds. *ACS EST Water* **2023**, *3* (8), 2199–2209. https://doi.org/10.1021/acsestwater.3c00017.

(101) Ohno, T. Fluorescence Inner-Filtering Correction for Determining the Humification Index of Dissolved Organic Matter. *Environ. Sci. Technol.* **2002**, *36* (4), 742–746. https://doi.org/10.1021/es0155276.

(102) Yin, G.; Guan, P.; Wang, Y.-H.; Zhang, P.; Qu, B.; Xu, S.; Zhang, G.; He, C.; Shi, Q.; Wang, J. Temporal Variations in Fire Impacts on Characteristics and Composition of Soil-Derived Dissolved Organic Matter at Qipan Mountain, China. *Environ. Sci. Technol.* **2024**. https://doi.org/10.1021/acs.est.4c00446.

(103) Bahureksa, W.; Tfaily, M. M.; Boiteau, R. M.; Young, R. B.; Logan, M. N.; McKenna, A. M.; Borch, T. Soil Organic Matter Characterization by Fourier Transform Ion Cyclotron Resonance Mass Spectrometry (FTICR MS): A Critical Review of Sample Preparation, Analysis, and Data Interpretation. *Environ. Sci. Technol.* **2021**, *55* (14), 9637–9656. https://doi.org/10.1021/acs.est.1c01135.

(104) Rosario-Ortiz, F. L.; Korak, J. A. Oversimplification of Dissolved Organic Matter Fluorescence Analysis: Potential Pitfalls of Current Methods. *Environ. Sci. Amp Technol.* **2017**, *51* (2), 759–761. https://doi.org/10.1021/acs.est.6b06133.

(105) Roth, H. K.; McKenna, A. M.; Aguilera, M. L.; VanderRoest, J. P.; Chen, H.; Borch, T. Characterization of Burned Soil Organic Matter via Sequential Solvent Extractions and 21 T FT-ICR Mass Spectrometry with Electrospray and Atmospheric Pressure Photoionization. *Anal. Chem.* **2025**, *97* (43), 24040–24049. https://doi.org/10.1021/acs.analchem.5c04154.

(106) Roth, H. K.; Borch, T.; Young, R. B.; Bahureksa, W.; Blakney, G. T.; Nelson, A. R.; Wilkins, M. J.; McKenna, A. M. Enhanced Speciation of Pyrogenic Organic Matter from

Wildfires Enabled by 21 T FT-ICR Mass Spectrometry. *Anal. Chem.* **2022**, *94* (6), 2973–2980. https://doi.org/10.1021/acs.analchem.1c05018.

(107) Roth, H. K.; Nelson, A. R.; McKenna, A. M.; Fegel, T. S.; Young, R. B.; Rhoades, C. C.; Wilkins, M. J.; Borch, T. Impact of Beaver Ponds on Biogeochemistry of Organic Carbon and Nitrogen along a Fire-Impacted Stream. *Environ. Sci. Process. Amp Impacts* **2022**. https://doi.org/10.1039/d2em00184e.

(108) Roth, H. K.; McKenna, A. M.; Simpson, M. J.; Chen, H.; Srikanthan, N.; Fegel, T.; Nelson, A. R.; Rhoades, C. C.; Wilkins, M. J.; Borch, T. Effects of Burn Severity on Organic Nitrogen and Carbon Chemistry in High-Elevation Forest Soils. *Soil Environ. Health* **2023**, 100023.

(109) Jimenez-Morillo, N. T.; Gonzalez-Perez, J. A.; Almendros, G.; De la Rosa, J. M.; Waggoner, D. C. J.; Zavala, L. M.; Gonzalez-Vila, F. J. H. Ultra-High Resolution Mass Spectrometry of Physical Speciation Patterns of Organic Matter in Fire-Affected Soils. *J. Environ. Manage.* **2018**, *225*, 139–147.

(110) Wozniak, A. S.; Mitra, S.; Goranov, A. I.; Zimmerman, A. R.; Bostick, K. W.; Hatcher, P. G. Effects of Environmental Aging on Wildfire Particulate and Dissolved Pyrogenic Organic Matter Characteristics. *Am. Chem. Soc. Earth Space Chem.* **2024**, *8*, 104–118.

(111) Myers-Pigg, A. N.; Grieger, S.; Roebuck Jr., J. A.; Barnes, M. E.; Bladon, K. D.; Bailey, J. D.; Barton, R.; Chu, R. K.; Graham, E. B.; Homolka, K. K.; Kew, W.; Lipton, A. S.; Scheibe, T.; Toyoda, J. G.; Wagner, S. Experimental Open Air Burning of Vegetation Enhances Organic Matter Chemical Heterogeneity Compared to Laboratory Burns. *Environ. Sci. Technol.* **2024**, *58*, 9679−9688.

(112) Zhang, Q.; Wang, Y.; Zhang, Y.; Zhang, J.; Hou, F.; He, C.; Shi, Q.; Zhang, G.; Wang, J. Heating-Induced Changes in Content and Molecular Characteristics of Pyrogenic Dissolved Organic Matter across Soil Types. *Environ. Sci. Technol.* **2025**, *59* (8), 3937–3948. https://doi.org/10.1021/acs.est.4c08306.

(113) Cawley, K. M.; Hohner, A. K.; Podgorski, D. C.; Cooper, W. T.; Korak, J. A.; Rosario-Ortiz, F. L. Molecular and Spectroscopic Characterization of Water Extractable Organic Matter from Thermally Altered Soils Reveal Insight into Disinfection Byproduct Precursors. *Environ. Sci. Technol.* **2017**, *51* (2), 771–779. https://doi.org/10.1021/acs.est.6b05126.

(114) Zhang, Z.; Cui, X.; Qu, X.; Fu, H.; Tao, S.; Zhu, D. Revealing Molecular Structures of Nitrogen-Containing Compounds in Dissolved Black Carbon Using Ultrahigh-Resolution Mass Spectrometry Combined with Thermodynamic Calculations. *Environ. Sci. Technol.* **2024**, *58* (27), 11998–12007. https://doi.org/10.1021/acs.est.4c01829.

(115) Goranov, A. I.; Wozniak, A. S.; Bostick, K. W.; Zimmerman, A. R.; Mitra, S.; Hatcher, P. G. Microbial Labilization and Diversification of Pyrogenic Dissolved Organic Matter. *Biogeosciences* **2022**, *19* (5), 1491–1514. https://doi.org/10.5194/bg-19-1491-2022.

(116) Bahureksa, W.; Borch, T.; Young, R. B.; Weisbrod, C. R.; Blakney, G. T.; McKenna, A. M. Improved Dynamic Range, Resolving Power, and Sensitivity Achievable with FT-ICR Mass Spectrometry at 21 T Reveals the Hidden Complexity of Natural Organic Matter. *Anal. Chem.* **2022**, *94* (6), 2973–2980. https://doi.org/10.1021/acs.analchem.2c02377.

(117) Kim, S.; Kramer, R. W.; Hatcher, P. G. Graphical Method for Analysis of Ultrahigh-Resolution Broadband Mass Spectra of Natural Organic Matter, the Van Krevelen Diagram. *Anal. Chem.* **2003**, *75* (20), 5336–5344. https://doi.org/10.1021/ac034415p.

(118) Laszakovits, J. R.; Mackay, A. A. Data-Based Chemical Class Regions for Van Krevelen Diagrams. *J. Am. Soc. Mass Spectrom.* **2022**, *33*, 198–202. https://doi.org/10.1021/jasms.1c00230.

(119) van Krevelen, D. W. Graphical-Statistical Method for the Study of Structure and Reaction Processes of Coal. *Fuel* **1950**, *29*, 269–284.

(120) Pinto, A. D. S. Soil Emissions of N2O, NO, and CO2 in Brazilian Savannas: Effects of Vegetation Type, Seasonality, and Prescribed Fires. *J. Geophys. Res.* **2002**, *107* (D20). https://doi.org/10.1029/2001jd000342.

(121) Sánchez-García, C.; Santín, C.; Doerr, S. H.; Strydom, T.; Urbanek, E. Wildland Fire Ash Enhances Short-Term CO2 Flux from Soil in a Southern African Savannah. *Soil Biol. Biochem.* **2021**, *160*, 108334. https://doi.org/10.1016/j.soilbio.2021.108334.

(122) Cotrufo, M. F.; Soong, J. L.; Horton, A. J.; Campbell, E. E.; Michelle; Wall, D. H.; Parton, W. J. Formation of Soil Organic Matter via Biochemical and Physical Pathways of Litter Mass Loss. *Nat. Geosci.* **2015**, *8* (10), 776–779. https://doi.org/10.1038/ngeo2520.

(123) Fegel, T.; Boot, C. M.; Broeckling, C. D.; Baron, J. S.; Hall, E. K. Assessing the Chemistry and Bioavailability of Dissolved Organic Matter From Glaciers and Rock Glaciers. *J. Geophys. Res. Biogeosciences* **2019**, *124* (7), 1988–2004. https://doi.org/10.1029/2018jg004874.

(124) Fegel, T. S.; Boot, C. M.; Covino, T. P.; Elder, K.; Hall, E. K.; Starr, B.; Stegen, J.; Rhoades, C. C. Amount and Reactivity of Dissolved Organic Matter Export Are Affected by Land Cover Change from Old-growth to Second-growth Forests in Headwater Ecosystems. *Hydrol. Process.* **2021**, *35* (8). https://doi.org/10.1002/hyp.14343.

(125) Moody, C. S.; Worrall, F. Sub-Daily Rates of Degradation of Fluvial Carbon from a Peat Headwater Stream. *Aquat. Sci.* **2016**, *78* (3), 419–431. https://doi.org/10.1007/s00027-015-0456-x.

(126) Worrall, F.; Howden, N. J. K.; Burt, T. P. BOD as a Measure of Fluvial Organic Matter Lability—The Decoupling of O_2 Consumption From CO_2 Production. *J. Geophys. Res. Biogeosciences* **2021**, *126* (12). https://doi.org/10.1029/2021jg006401.

(127) VanderRoest, J. P.; Fowler, J. A.; Rhoades, C. C.; Roth, H. K.; Broeckling, C. D.; Fegel, T. S.; McKenna, A. M.; Bechtold, E. K.; Boot, C. M.; Wilkins, M. J.; Borch, T. Fire Impacts on the Soil Metabolome and Organic Matter Biodegradability. *Environ. Sci. Technol.* **2024**, *58*, 4167–4180. https://doi.org/10.1021/acs.est.3c09797.

(128) VanderRoest, J. P. Using Pyrocosms to Determine Fire Impacts on Soil Molecules. *Nat. Rev. Earth Environ.* **2024**, *5*, 415. https://doi.org/10.1038/s43017-024-00562-w.

(129) Jech, S.; Adamchak, C.; Stokes, S. C.; Wiltse, M. E.; Callen, J.; VanderRoest, J.; Kelly, E. F.; Hinckley, E.-L. S.; Stein, H. J.; Borch, T.; Fierer, N. Determination of Soil Contamination at the Wildland-Urban Interface after the 2021 Marshall Fire in Colorado, USA. *Environ. Sci. Technol.* **2024**, *58* (9), 4326–4333. https://doi.org/10.1021/acs.est.3c08508.

(130) Logan, M. N.; Patzner, M. S.; Vanderroest, J. P.; McGivern, B. B.; Srikanthan, N.; Simpson, M. J.; McKenna, A. M.; Wrighton, K. C.; Bryce, C.; Kappler, A.; Borch, T. Role of Permafrost Thaw Transitions in Biogeochemical Nitrogen Cycling. *Soil Amp Environ. Health* **2025**, *3* (2), 100148. https://doi.org/10.1016/j.seh.2025.100148.

(131) Malik, H. T.; Zvulunov, Y.; Kinnebrew, E.; Gates, T. K.; Evett, S. R.; VanderRoest, J. P.; Radian, A.; Chi, J.; Abhijith, G. R.; Mueller, N. D.; Ostfeld, A.; Fang, L.; Borch, T. Advancing

Sustainable Water Use across the Agricultural Life Cycle in the USA. *Nat. Water* **2025**, *3* (6), 655–667. https://doi.org/10.1038/s44221-025-00450-7.

CHAPTER 2: MOLECULAR INSIGHTS AND IMPACTS OF WILDFIRE-INDUCED SOIL CHEMICAL CHANGES[1]

2.1. INTRODUCTION

Wildfires are natural environmental disturbances that burn millions of acres each year[1]. Wildfires can benefit fire-adapted biomes by driving soil formation, managing pests and diseases, and promoting habitat heterogeneity, biodiversity, and seed germination[2–4]. However, fire weather seasons have lengthened by 27% since 1979, leading to an increase in the occurrence of high-severity fires and the total area burned each year; the area of extratropical and high-latitude forests being burned each year increased by over 50% from 2001 to 2019[1]. During 2001–2019, an average area of 4.1 million km^2 was burned annually across the world, constituting ~3% of vegetated surface area1 (**Figure 2.1**). Additionally, high-severity wildfires are projected to become more frequent under climate change[1,5,6]. Thus, fire-driven transformations in surface soils could be exacerbated as these environmental disturbances become more common and more severe.

Wildfires directly affect soil properties, in ways ranging from landscape-scale changes to molecular alterations; these impacts are influenced by burn severity (**Box 2.1**). High-severity wildfires can leave landscapes barren for days to years, increasing soil hydrophobicity in the short term (1–5 years post fire) and making soils vulnerable to erosion and nutrient loss[7,8]. Such changes can reduce the ability of soil to support vegetation and can contribute to long-term destabilization of ecosystems. Soil physical changes are coupled with transformations in soil chemistry. For example, fires with low burn severities can create nutrient-rich surface soils by increasing the

---

[1]Reproduced with permission from Springer Nature. Lopez, A. M.; Avila, C. C.; VanderRoest, J. P.; Roth, H. K.; Fendorf, S.; Borch, T. Molecular Insights and Impacts of Wildfire-Induced Soil Chemical Changes. Nature Reviews Earth and Environment 2024, 5, 431-446. https://doi.org/10.1038/s43017-024-00548-8. Copyright 2024, Springer Nature

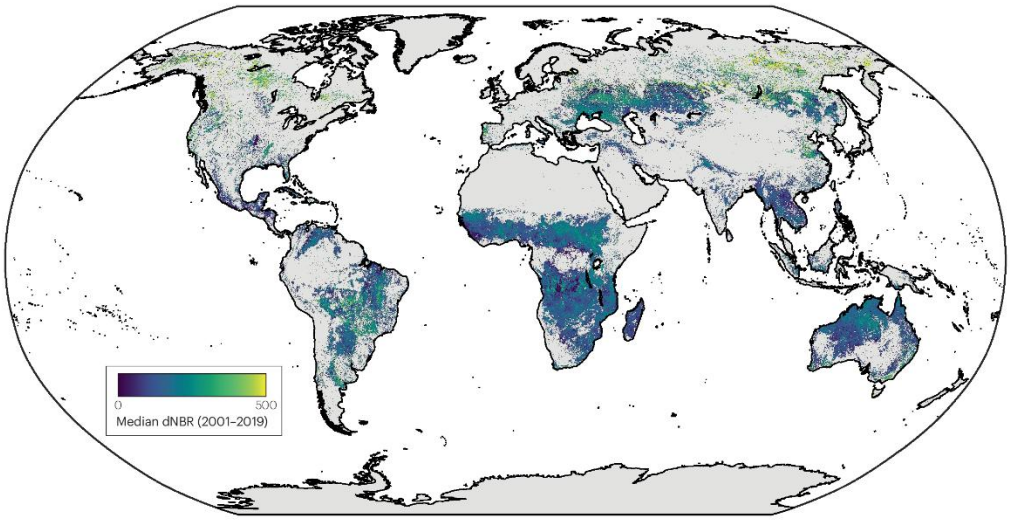

Figure 2.1. Distribution of global burn severity. Median difference of normalized burn ratio (dNBR; pre-fire NBR minus post-fire NBR) for fire events between 2001 and 2019 as an estimate for burn severity, with 0 indicating unburned conditions and 500 indicating high burn severity. Data from the MOSEV database[201]. Pixel resolution is 500 m. Note that some pixels contain multiple fire events. Regions of high median burn severity include high-latitude ecosystems; however, high-severity wildfires are projected to become more frequent under climate change in many regions across the globe.

concentration of aliphatic organic compounds[9] and plant-available phosphorus and nitrogen[10–13]. Additionally, wildfires induce molecular changes in the organic and inorganic components of soils (including soil minerals and heavy metals), contributing to the release of seed germination promoters or inhibitors, and changes in the toxicity and mobility of metals in soil and ash[14–16], which can result in degraded air and water quality. These molecular-scale chemical changes in burned soils must be explored to understand their impact on ecosystem and human health.

Trends in the total organic and metal content of pre-fire and post-fire soils[17–23] and the role of erosion in transporting this material have been extensively explored[19,21,24,25], but it remains unclear how fire-induced changes in organic matter and metal speciation influence their fate, transport and potential health threats. Controlled experiments, such as laboratory-based heating simulations, and field observations after natural wildfires provide insight into these impacts. For

Box 2.1

Metrics to assess wildfires

Fire intensity and burn severity are often used to describe the extent of wildfires and can be estimated using different proxies.

Fire intensity
Fire intensity refers to the amount of energy released during a fire. The highest intensities (greatest increases in temperature) often occur in areas where there is an abundant fuel supply. Intensity can vary across a landscape and with fire weather conditions[22]. Flame length is used as a proxy for fire intensity.

Burn severity
Often used interchangeably with fire severity, burn severity is a measure of the loss or decomposition of organic matter aboveground and belowground caused by fire and is positively correlated with fire intensity[203]. Various observations and measurements are used to assess burn severity (as shown in the figure)[204].

- **Vegetation ash colour:** Brown to black ash indicates low burn severity, whereas white or grey ash indicates high burn severity and more complete biomass combustion.
- **Soil redness rating:** Soils get redder with increasing fire intensity and combustion completeness, owing to the thermal transformation of Fe (oxy)hydroxides (including goethite and ferrihydrite) to haematite above ~300 °C, even at low Fe (oxy) hydroxide abundances (<1wt%)[205]. Reddened soil is often observed where fallen logs and large branches have completely burned.
- **Other soil properties:** High burn severity often causes increased magnetic susceptibility, heightened soil erodibility, water repellency, and loss of soil structure and fine roots[22].
- **Ecosystem properties:** The degree of canopy and ground cover consumed by fire, such as tree mortality and scorch height, increases with burn severity.
- **Difference of normalized burn ratio:** dNBR=pre-fire NBR−post-fire NBR (where NBR is an index using shortwave-infrared and near-infrared reflection). High dNBR values indicate high burn severity. dNBR can be determined using satellite imagery and can resolve areas affected by wildfire and approximate burn severity on a regional scale that can be assessed globally.

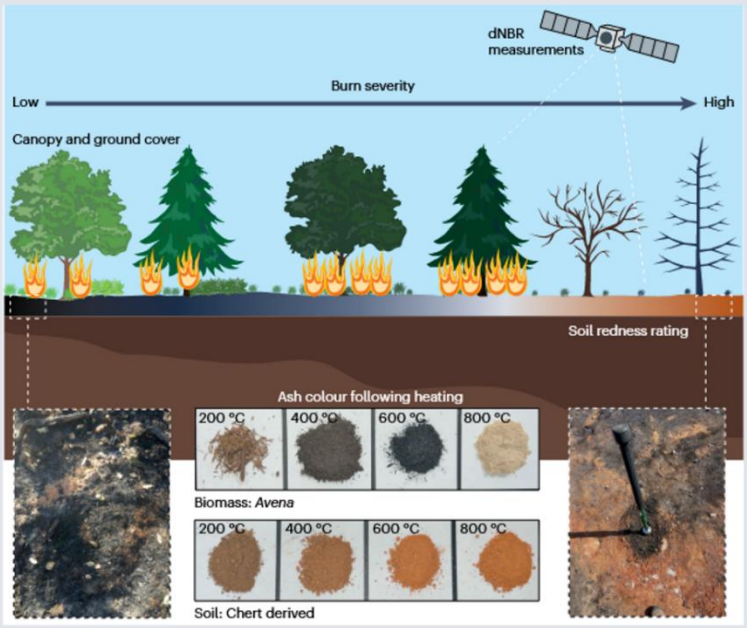

example, laboratory simulations (including muffle furnace and blowtorch methods) allow physicochemical analyses and precise manipulations of burn temperature and duration. However, the heterogeneity of soils in natural landscapes complicates thermal reactions because burn temperature and duration can differ widely across scales. Therefore, both laboratory simulations and field observations are needed to elucidate soil chemical changes and their impacts during and after fire.

In this Review, we evaluate data from laboratory-based simulations and field observations to explore how wildfires affect soil organic matter (SOM) and metal speciation, and how those alterations influence post-fire conditions. We then discuss how these molecular-level changes

affect revegetation, water quality, and air quality, and we discuss implications for human and ecosystem health. We exclude the impact of fire on soils in wetland and boreal ecosystems containing thick peat or permafrost layers[26,27]. Additionally, this Review focuses on chemical transformations and does not specifically address alterations in physical processes. Finally, we provide suggestions for future investigations, including using mass spectrometry to analyse low-molecular-weight organic molecules in burned soils, identifying sources of toxic metals in post-fire particulate matter, and expanding geographical locations of future research.

2.2. FIRE AS A CATALYST

Wildfires can have immediate impacts on soil organic and inorganic chemistry. For example, fires can induce changes in SOM redox properties, composition and N content, alter soil minerals and contribute to the addition of ash to soil from burning vegetation, as discussed here (**Table A1**).

2.2.1 FACTORS INFLUENCING FIRE-INDUCED REACTIONS

Temperature is a primary driver for many molecular transformations and can catalyse chemical reactions across a fire intensity gradient. Reaction pathways also depend on oxygen availability and are often differentiated as combustion (oxygen-abundant) or pyrolysis (oxygen-limited). The duration of heating also influences reaction times, molecular products, and, thus, the overall biogeochemical response of soil to fire[28–32]. However, the effect of fire duration has currently been investigated less than the effect of fire intensity (temperature), and the rate of cooling has largely not been explored.

Soil heating is locally heterogeneous, influenced by the micrometre-scale characteristics of soil (including moisture, organic matter, mineralogy and texture) and the overlying fire conditions (including fuel type, temperature and duration)[20,22,33,34] (**Figure 2.2**). Moist soils yield

lower temperatures than dry soils when heated, but the heat penetrates deeper in moist soils owing to the large heat capacity and thermal conductivity of water. By contrast, dry soils exhibit high temperatures in the uppermost portion of the soils but limited heat transfer with depth. Additionally, fuel conditions (such as vegetation type, density of fire, fuel moisture, distance of flames to soil, and fire weather) and soil or ash characteristics (for example, the ash thickness, SOM content, porosity and mineralogy) also influence heat transfer in soil. These spatial heterogeneities in soil heating generate O_2-rich and O_2-deficient microenvironments in which combustion and pyrolysis, respectively, can occur[34].

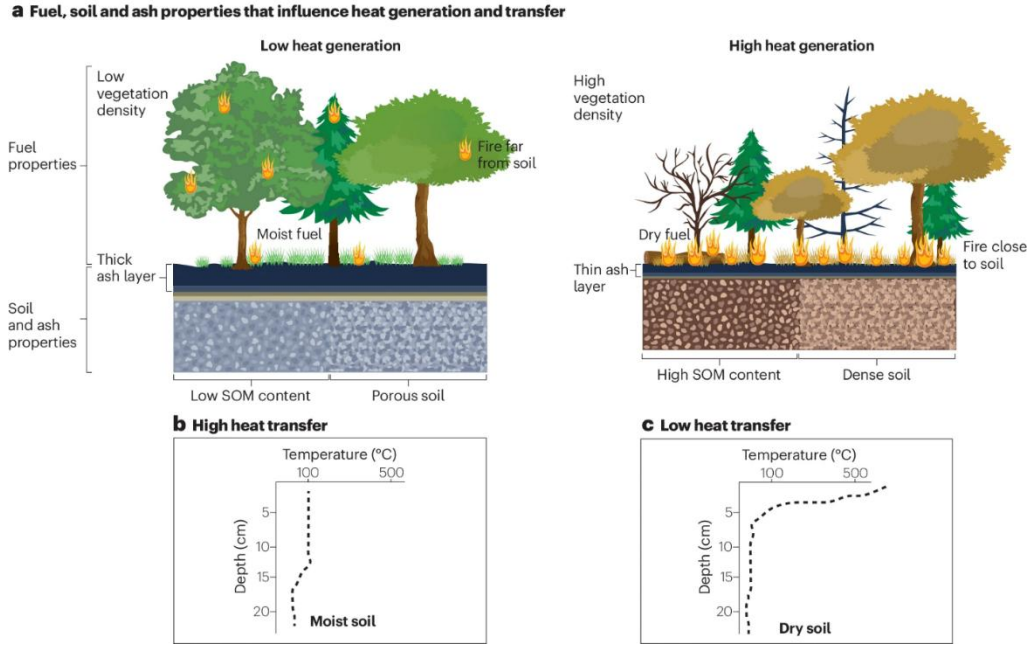

Figure 2.2. Factors affecting heat generation and transfer. **a**, Factors that contribute to low (left) or high (right) heat generation during wildfires. **b**, Heat transfer profile for moist pre-fire soil conditions. **c**, Heat transfer profile for dry pre-fire soil conditions. Factors such as fuel properties and soil and ash properties dictate the overall burn and fire intensity (heat generation) experienced aboveground and belowground, and soil moisture further influences heat transfer. Combined, these factors contribute to distinct post-fire soil chemical changes. SOM, soil organic matter.

2.2.2 ORGANIC MATTER TRANSFORMATIONS

Thermal reactions during wildfires drive chemical alterations in SOM, forming pyrogenic organic matter (PyOM, organic matter that has been thermochemically altered)[30] (**Table A1**).

During fast-moving wildfires, aboveground vegetation can experience short periods of high temperatures (>600 °C), favouring the formation of black ash by partial combustion, which is rich in PyOM. However, temperatures belowground differ from those experienced aboveground. Soil temperatures in low-severity and moderate-severity wildfires generally do not exceed ~350–450 °C (ref. 35), resulting in the partial combustion of biomass and SOM along with the formation of ash containing a mixture of PyOM and inorganic compounds including nutrients[36]. At higher soil burn temperatures (>450 °C), SOM mineralization becomes more prevalent, leading to the formation of ash with lower PyOM and higher inorganic mineral concentrations including carbonates[37].

The burning of vegetation and SOM can induce the formation of polycyclic aromatic hydrocarbons (PAHs), a class of hundreds of organic compounds consisting of two or more merged benzene rings[38,39]. PAHs and their metabolites are carcinogenic, and some compounds (for example naphthalene) can inhibit post-fire seed germination[14,40,41]. Soils burned by wildfires can have up to double the concentration of $\sum_{16}$PAH (sum of the US Environmental Protection Agency's 16 priority compounds) of unburned soils. Interestingly, there is no apparent link between post-fire $\sum_{16}$PAH concentrations and vegetation types (broad-leaf, conifer, shrub)[42]. At high fire intensities (above 500 °C), PAHs often follow divergent pathways in which some compounds volatilize and others increase in aromaticity to form environmentally more persistent structures[43] (**Figure 2.3**). Therefore, PAH concentrations following low-intensity fires are 163% and 168% higher than after moderate and high-intensity fires, respectively[42].

Fires influence the redox properties of SOM by altering surface functional groups and C matrices. PyOM can serve as an electron donor, fueling post-fire soil microbial growth and influencing metal biogeochemical cycling[44]. Alternatively, PyOM can behave as a terminal

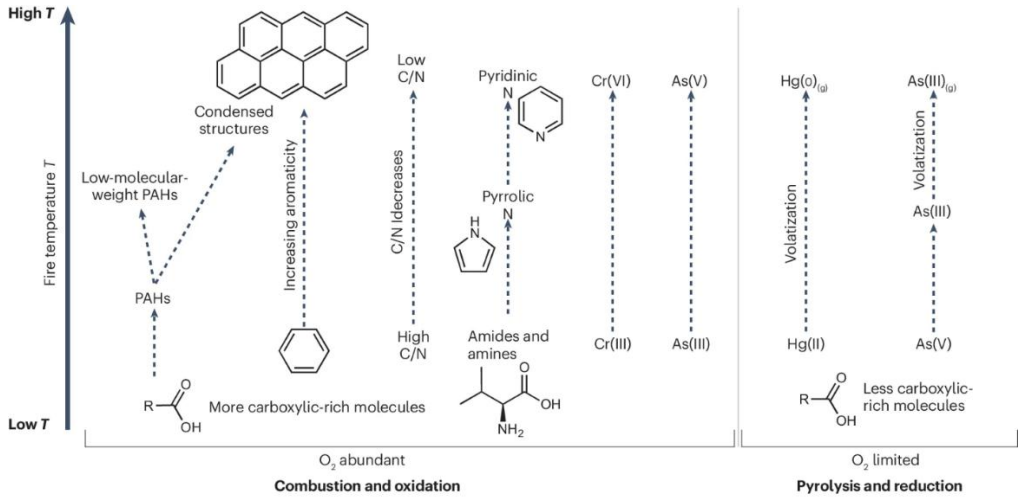

Figure 2.3. The effect of temperature on chemical transformations in O_2-abundant and O_2-limited environments. More carboxylic acids are produced in O_2-rich conditions (left) than in O_2-limited conditions (right). Under increasing fire intensities, combustion produces polycyclic aromatic hydrocarbons (PAHs), increases aromaticity of organic compounds, reduces C/N ratios, produces pyrrolic and/or pyridinic N, and oxidizes Cr and As. When O_2 is limited, As and Hg can be reduced and volatilized.

electron acceptor when other thermodynamically favourable electron acceptors are not present, such as under anaerobic conditions. Across a fire intensity gradient of 200–800 °C, dissolved PyOM generated from pyrolysed grass and wood has a larger electron-donating capacity than electron-accepting capacity. However, the overall electron exchange capacity (sum of electron-donating and electron-accepting capacities) decreases with increasing burn temperature[44]. Under low fire intensities (200 °C), dissolved PyOM from wood has a larger electron-donating capacity than that from grass products, owing to high lignin content and contributions from phenol functional groups in wood[44].

Fires also influence the redox properties of SOM through the generation of environmentally persistent free radicals (EPFRs)[45,46]. EPFRs form through the burning of organic compounds and can remain bound to charcoal surfaces for years after fire. In the aqueous phase, EPFRs can further react to form reactive oxygen species (ROS)[45,46]. The abundance of EPFRs produced depends on the burn conditions, including maximum fire temperature and O_2 availability.

For example, flaming conditions often produce more EPFRs than smouldering fires[46]. Additionally, the increased abundance of EPFRs in field-collected charcoal samples from global burned landscapes with high aromaticity and low O/C ratios indicates that intermediate temperatures and woody fuels increase the production of EPFRs[45]. Charcoal collected from burned sites characterized by extreme high temperatures and long combustion times contains a low abundance of EPFRs, probably owing to the loss of O functional groups[45].

Wildfires also induce transformations in organic N, altering N bioavailability and reactivity in post-fire soils. For example, combustion of two subalpine soil samples from northern Colorado in a muffle furnace at temperatures ≥225 °C increased the number of N-containing SOM molecules by 20–32%, lowering the C/N ratio of the SOM[47,48]. Organic N in unburned soils can be converted to pyrrolic, pyridinic and quaternary forms as the burn temperature increases[49–51]. Nitrogen-containing aromatic compounds have high thermodynamic stability, leading to a potential reduction of the amount of bioavailable N in postfire soils depending on local microbial and vegetation compositions[52]. The Maillard reaction pathway, which involves the condensation of amino acids and sugars[47,51], is thought to be responsible for the formation of N-containing aromatic compounds during wildfires. However, further work is required to elucidate the pathways contributing to the formation of N-containing aromatic PyOM and track how organic N is cycled and transformed within a post-fire soil environment.

Wildfires can also increase the concentration of water-extractable organic carbon in soils, augmenting the solubility of the post-fire SOM. For example, soil samples burned at 250 °C contain more water-extractable C than unburned soil and soils burned at >250 °C (refs. 47,48,53). Thus, PyOM released by lower-intensity burns (~250 °C) could be more mobile than that produced

at higher burn intensities, increasing the leaching of PyOM out of fire-impacted areas and potentially leading to a larger impact on downstream water quality.

2.2.3 INORGANIC MINERALS IN ASH AND SOIL

High burn severities (**Box 2.1**) can lead to the formation of grey and white ash, which is rich in inorganic matter. The quantity of white ash produced depends on fuel type, fuel abundance and fire conditions[36]. For example, average concentrations of inorganic C increase from 7.5 g kg^{-1} in ash formed by low-severity fire to 12.3 g kg^{-1} in ash derived from high-severity fire[54]. The complex composition of plants and soil minerals can also lead to fire-induced formation of hundreds of primary and secondary products, including metal oxides, hydroxides, chlorides and carbonates[20,36,55–57].

Biomass burning and mineral reactions are interlinked in surface soils during wildfires. The contribution of soil to the surface ash layer depends on burn severity, making it difficult to infer the origin of inorganic minerals, which are derived either from burning biomass or from altered soil minerals. Within unburned soils, trace elements, such as heavy metals, are adsorbed on or substituted within minerals and organic matter. Trace metal cations also occur in (oxy)hydroxides and as structural impurities. During mineral heating and transformations, structurally bound metal ions are redistributed and can partition onto mineral surfaces, increasing post-fire solubility[58]. Alternatively, metal ions can be reincorporated into thermally altered minerals[59].

Plants also assimilate soil-borne heavy metal(loid)s, including Fe, Mn, Cr, Ni and As. The extent of metal uptake and partitioning within plant structures varies between plant species, environmental and soil conditions, and elements[60]. Although metals typically constitute a minor fraction of the chemical composition of biomass[36,61], high-severity fires leave behind ash with high

metal concentrations[36], especially Ca, Fe and Al (ref. 54). For example, the average concentrations of Fe and Ca in global ash samples from high-severity fires are 20.1 g kg^{-1} and 53.6 g kg^{-1}, respectively, compared with 11.7 g kg^{-1} and 37.5 g kg^{-1} in ash from low-severity fires[54].

At burn temperatures between 300 °C and 800 °C, plant-derived Ca, Na, K and Mg form molten oxides and carbonates[56]. The formation of these carbonates alters the thermodynamic viability of redox transformations, such as the oxidation of Cr(III) to Cr(VI)[62]. Calcite ($CaCO_3$) and fairchildite ($K_2Ca(CO_3)_2$), which are inorganic matter constituents in ash, are formed by the oxalate transformation of Ca or by the reaction of Ca with atmospheric CO_2. The concentration of calcite and fairchildite in ash increases with fire severity. The increase in soil alkalinity during high-intensity wildfires with temperatures above 750 °C is partly caused by Ca carbonate further decomposing and generating CaO, in addition to K_2O (ref. 63).

Fire temperature and duration affect mineral particle size[64], morphology[64], and solubility[58], although the exact response of these critical particle properties varies and must be evaluated further. In general, with increasing temperatures (up to 700 °C), inorganic matter in ash decreases in particle size and increases in surface area[65]. The outcome is an increase in PM2.5 (the number of particles with an aerodynamic diameter less than 2.5 μm) and in particle reactivity.

There can be complex trends in fire-induced changes in particle size during wildfires, particularly for Fe (and probably also Mn) hydroxides and oxyhydroxides[66,67]. Oxidative heating transforms Fe(III) hydroxides and oxyhydroxides, such as ferrihydrite and goethite, into oxides of haematite or maghaemite (the latter being magnetic)[62,68,69]. The particle size and surface area of these firegenerated minerals can also change[59]. For example, at low temperatures (<500 °C), goethite transforms to a porous haematite structure, increasing its surface area. However, at higher temperatures (>500 °C) the particle size of goethite increases as the irregular porous haematite

structure becomes more ordered and surface area decreases[59], which is in contrast to the decreases in the particle size with increasing fire severity observed in the field[65]. This apparent contradiction can be explained by accounting for both the complexity of particles within soils and ash and, in particular, the role of silicates interacting with metal (hydr)oxides. For example, in a mixed-phase experiment initially containing ferrihydrite and montmorillonite, particle size decreased with temperature, with more nanosized haematite particles being produced at high temperatures because interactions with clay minerals prevented aggregation[64].

Unlike oxidative conditions during combustion, reducing conditions during pyrolysis can produce various particle chemistries for redox-active metals. For example, during pyrolysis, Fe(III) can be reduced and converted to phases composed of Fe(II), such as magnetite or wüstite, and even to phases composed of Fe(0)[70]. The metal particle chemistry of wildfires is beginning to be revealed, with extensive research on coal combustion[71–74], industrial waste incineration[75–77], and structural fires (fires involving a building or other structure)[78,79] providing insight on the potential changes in metal speciation and particle size and chemistry resulting from wildfires.

2.2.4 FORMATION OF METAL(LOID) TOXINS

As plant and soil minerals are thermally altered, metals can undergo oxidation and reduction reactions, potentially forming species that are more toxic than those present in unburned soils and vegetation (**Table A1**). Specifically, wildfires can catalyse redox transformations of Cr, As and Hg, altering their toxicity and thus possible threat to human health. For example, in unburned soils, Cr predominantly exists as Cr(III), but it can be oxidized under high temperatures to its toxic hexavalent state, Cr(VI), which is a known class-1 carcinogen[80] (**Figure 2.3**). Conversely, the reduction of As(V) to As(III) during the pyrolysis stage of fires increases the toxicity of As.

The oxidation or reduction of metals is complex and depends on oxygen availability, temperature, heating duration, and mineralogy[69,81,82]. Cr and As illustrate the nonlinear and complex alteration of metals that can occur during wildfires. Heating synthetic mixtures of Cr(III)-containing ferrihydrite, goethite and haematite results in the formation of Cr(VI)[82,83], but the extent of oxidation depends on the temperature and Cr-host phase[82]. With the exception of Cr-bearing goethite, the amount of Cr(VI) produced decreases at high temperatures (>600 °C). Additionally, the proportion of the reactive Cr(VI) (including dissolved and surface-exchangeable forms) that is produced decreases at high burn temperature, possibly owing to increased particle size, Cr stability, and mineral transformations during rapid cooling[76,82]. The formation of Cr(VI) is also inhibited by the absence of O_2 (ref. 84), indicating that pyrolysis does not lead to Cr(III) oxidation and thus does not increase Cr toxicity. The effect of heating duration on Cr-bearing minerals has not yet been tested; however, increased heating durations or combustion times are likely to enhance the formation of Cr(VI).

Conversely, As(V) reduction occurs[78] during pyrolysis (**Figure 2.3**), although the As(III) formed tends to be short-lived in oxygenated postfire environments. Between 200 °C and 400 °C, As(V) is rapidly reduced to As(III) in organic-rich soils, with reoxidation back to As(V) being promoted at higher temperatures and longer heating durations[69]. Both As(V) and As(III) phases were observed in ash nanoparticles collected after a wildfire, suggesting that As(V) reduction and As(III) oxidation both occurred[78].

Both natural and anthropogenic metal(loid) sources can contribute to wildfire-induced toxins[85,86]. Anthropogenic As sources (such as pesticides, smelting, coal from combustion, mining and wood preservatives) can contribute to As release during wildfires[78,87–89]. For example, soil and ash collected from burned homes after wildfires in California contained 2–81 times as much As

(predominantly As(V)) as did unburned wildland areas[79,90]. Although anthropogenic Cr sources, which are similar to those of As, can be problematic, natural sources can also have a substantial effect. Mafic and ultramafic geologies and their metamorphic equivalents, such as serpentinite, lead to soil Cr(III) concentrations of 200–60,000 mg kg^{-1} (2,650 mg kg^{-1} average), which contrast with those of metal-poor geologies, such as granites, often having soil Cr(III) concentrations less than 200 mg kg^{-1} (ref. 91).

Biomass burning can serve as an additional source of metal toxins, depending on the vegetation type[61]. Common biomass ash constituents (such as Ca, Na, K and Mg oxides) can enhance the oxidation of Cr(III) in plants and form highly soluble $CaCrO_4$, Na_2CrO_4, K_2CrO_4 and $MgCrO_4$ phases[16,76,77,84]. For example, heating grass species to 500 °C and 900 °C led to the conversion of 23% and 58%, respectively, of the total Cr in the ash to Cr(VI), suggesting that these increases in Cr(VI) are caused by the oxidation of Cr(III) through biomass burning[16].

Volatilization contributes to the transport of Hg during wildfires[88,89]. During pyrolysis, particle-bound Hg(II) is reduced and volatilized as gaseous Hg(0), contributing to global Hg transport through the re-emission of Hg in smoke[92–95] (**Figure 2.3**). However, particulate-Hg species comprise less than 15% of total Hg emissions during fires. The amount of Hg emitted following wildfires depends more on plant species, stand age, SOM and fire severity than on soil parent material[92–95]. For example, densely vegetated ecosystems with infrequent fire, such as forests, accumulate high fuel loads and large amounts of Hg through dry and wet deposition; thus, such ecosystems account for much of the remaining proportion of the total Hg released during wildfires[96–99].

Similarly, volatilization also contributes to the transport of As. For example, As(V) was reduced and subsequently emitted as arsine gas (AsH_3) during the burning of an As hyper-

accumulating plant (brake fern, *Pteris vittata*), even at temperatures less than 400 °C (ref. 100). The production of AsH_3 increased as temperatures increased from 100 °C to 800 °C (ref. 100). Large amounts of biomass can promote pyrolysis, leading to the production of AsH_3 at (pyrolysis) temperatures above 150–200 °C (ref. 101). Interestingly, negligible As was released when rice straw plants with trace As levels (~0.1–12 mg kg^{-1}) were heated to individual temperature targets or when temperature increased stepwise by 100 °C and held for 30 min from 300–900 °C (refs. 102,103). However, As emissions from burning biomass with greater As concentrations have been observed during prescribed burns of rice (*Oryza sativa*) straw, which is a common agricultural practice that heats soil to temperatures between 350 °C and 630 °C (ref. 104).

2.3. POST-FIRE SOIL CONDITIONS

The transformation of contaminants and metastable products (such as mineral dehydration and rehydration and PyOM interactions) in soils following wildfires can affect the environmental fate and transport of these components. Environmental conditions post fire, such as precipitation or extended dry periods, can further transform these products. For example, depending on burn severity, soil hydrophobicity promotes landscape-scale erosion and flooding during heavy precipitation[105]. As with the geomorphological impacts of post-fire conditions, precipitation can also induce biogeochemical reactions that affect soils for weeks to months after wildfires[106]. Various post-fire soil changes occur in mineral hydration, organo–mineral interactions, microbially mediated PyOM decomposition, and redox cycling, as discussed here.

2.3.1 HYDRATION AND DEHYDRATION

After wildfires, ash and soil contain a mixture of fire-altered particles that differ in reactivity and can mix with subsurface particles that did not experience heating. Reaction products formed at high temperatures are often thermodynamically unstable under ambient climate, with

their lifetimes depending on the temperature and humidity[57]. Thermally altered minerals can revert to their pre-fire phases by rehydration, rehydroxylation or carbonation. Rehydration influences the physical characteristics of minerals including the size and surface area, ultimately altering their surface reactivity. However, the capacity for mineral rehydration decreases with increasing temperature. During rehydration, these minerals can undergo dissolution or recrystallization[107]. Minerals that lose large amounts of mass during heating are most susceptible to water incorporation, forming rehydroxylated minerals, which differs from water being adsorbed to mineral surfaces[108,109]. A mixture of dehydroxylated and partly rehydroxylated phases can persist in post-fire soils with distinct reactivities. Consequently, dehydroxylation can decrease nutrient availability in soils by leading to minerals that strongly absorb nutrients such as P (as phosphate)[107].

Post-fire soil biogeochemical processes, such as rehydration, dehydroxylation, or carbonation, induce further alterations in the surface area and functional groups of minerals in the soil. These changes can influence the reactivity of these minerals, which can affect nutrient and toxin availability. Low-severity to moderate-severity fires induce the formation of more water-extractable elements than high-intensity fires[36]. For example, chloride salts in vegetation ash formed by hydration, hydroxylation, and carbonation dissolve readily in water regardless of pH, whereas carbonate and oxides formed by hydration have increased solubility under acidic conditions. After severe wildfires, the loss of SOM and the formation of dehydrated phyllosilicate minerals with collapsed interlayers reduce soil cation exchange owing to a decrease in adsorption sites.

2.3.2 ORGANO-MINERAL INTERACTIONS

Interactions between PyOM and soil minerals, such as metal oxides and oxyhydroxides[110,111], in post-fire soils can increase the stability of PyOM by preventing abiotic and biotic oxidation[112,113]. For example, the chemical oxidation and biodegradation of laboratory-generated PyOM decreased by 42.5% and 49.4%, respectively, when mixed with kaolinite[64,113]. Additionally, concentrations of benzene polycarboxylic acids, which are PyOM biomarkers, are correlated with concentrations of organically bound Al (R^2 = 0.737) and Fe (R^2 = 0.573), suggesting that increasing the concentration of organically bound metals or minerals decreases the degradation of PyOM[114–116].

Post-fire surface soils are typically well oxygenated, which increases the susceptibility of PyOM functional groups to oxidation and increases PyOM polarity, solubility and reactivity. For example, post-fire dissolved organic carbon (DOC) concentrations increase with increasing O/C ratios (indicative of oxidation level) of PyOM because PyOM with high oxidation levels has increased polarity and is therefore more water soluble[117]. PyOM with many O-containing functional groups, such as carboxylic acids, typically has a negative surface charge in environmental conditions, owing to functional group dissociation reactions[117]. This negative surface charge augments soil cation exchange capacity, enhancing the retention of plant-available nutrients, and influences PyOM–mineral interactions in post-fire soils through cation bridging. Divalent cations (such as Ca^{2+} and Mg^{2+}) electrostatically bridge oxidized, negatively charged PyOM to negatively charged clay surfaces. Thus, calcic soils can increase the stability of PyOM. Ligand exchange and van der Waals forces are also potential drivers of PyOM–mineral interactions.

PyOM can mediate electron transfer to minerals through its C matrices or by charging and discharging its surface functional groups. This electron transfer can influence the biogeochemical cycling of redox-active metals such as Fe and Mn (refs. 44,118–120), affecting mobility. After low-severity and moderate-severity wildfires, the formation of specific functional groups in PyOM influences redox properties between PyOM and soil minerals[119]. For example, phenol, quinone, and hydroquinone groups and aromatic C can accept and donate electrons[44,118–121]. Phenolic groups can be irreversibly oxidized, whereas quinones can be reversibly reduced. Condensed aromatic C, which is formed during wildfires, becomes the dominant source of electron shuttling owing to its high electrical conductivity[118]. Such mechanisms make electron transfer between laboratory-generated PyOM and common soil minerals such as Mn oxides, Fe oxides and Fe chloride[118,121] thermodynamically favourable. For example, laboratory-generated, wood-derived PyOM at concentrations of 5 and 10 g PyOM l^{-1} can donate electrons during the Fe(III) reduction of ferrihydrite[121].

2.3.3 MICROBIAL DEGRADATION OF PYOM

Thermodynamic calculations and laboratory experiments[122–127] suggest that PyOM is less resistant (that is, more susceptible) to microbial degradation than previously thought. A 2008 analysis of PyOM with solid-state nuclear magnetic resonance spectroscopy, near-edge X-ray absorption fine structure spectroscopy, and X-ray photoelectron spectroscopy of Brazilian soils suggested that PyOM remains stable in soils for centuries to millennia[128]. However, thermodynamic calculations using representative PyOM and unburned dissolved organic matter (DOM) compounds published in 2023 demonstrate substantial overlap between the predicted metabolic rates of PyOM and DOM microbial degradation[127]. Thus, PyOM might not be as markedly resistant to microbial degradation as previously presumed, especially when compared

with unburned DOM. Additionally, SOM from high-severity fires has lower Gibbs free energy of oxidation than SOM from low-severity fires and unburned areas, suggesting that high-severity fires reduce the energy required for organic matter oxidation[129].

Laboratory measurements also support the notion of enhanced PyOM biodegradability. PyOM produced by pyrolysing sewage sludge and pinewood was degraded by *Fusarium oxysporum* and *Pyronema domesticum* fungi within 120 and 57 days, respectively[125,126]. Additionally, upwards of 25% of C content and 25–67% of aromatic content from charred oak leachates was biomineralized by a soil-derived microbial consortium within 10 days[123,124]. However, it is unclear whether these results accurately represent PyOM degradation within burned soils, which are influenced by complex environmental factors such as organo–mineral interactions and soil redox conditions[112,113,130]. Thus, future research on PyOM microbial degradation should incorporate these environmental factors to account for soil complexity. Despite this uncertainty, these laboratory measurements clearly indicate that PyOM can be more susceptible to microbial degradation than inferred from previous observations[128,131].

Multiple explanations for the susceptibility of PyOM to microbial degradation have been proposed, including enzyme-mediated degradation. For example, monooxygenase and dioxygenase enzymes released by post-fire soil microorganisms could aid the degradation of aromatic PyOM[125,129]. The genes related to these aromatic PyOM degradation pathways have been found to be upregulated by *Leotiomycetes* and *Coniochaeata ligniaria* fungi from wildfire-burned soils[129] and *Pyronema* fungi exposed to pyrolysed pinewood[125]. Intermediate products formed in these degradation pathways, namely catechol and protocatechuate, can then be microbially degraded to succinyl-coenzyme A and acetyl-coenzyme A, which feed into the citric acid cycle[125,129,132]. Such results imply that microbial degradation of aromatic PyOM can produce labile

metabolites that can be funnelled into central microbial metabolic pathways. Thus, PyOM could have a more important role in soil biochemical cycling than previously presumed.

ROS and EPFRs could also contribute to aromatic PyOM degradation[124,126]. Microbial exoenzymes generate ROS, such as hydroxyl radicals, which can oxidize condensed aromatic PyOM into smaller molecules[124,126]. Thereafter, these degraded compounds can be further oxidized to catechol and protocatechuate, feeding into the degradation pathways described above[125,129]. ROS can also be formed by EPFRs derived from PyOM in post-fire soils[45,46]. These EPFRs can persist for years following wildfires, effectively extending the impact of a wildfire on PyOM degradation and soil biochemical cycling.

Additionally, nitrogen from PyOM can be microbially degraded into a plant-available form and incorporated into plant biomass. For example, after 72 hours of incubation, 10% of the ^{15}N in ^{15}N-enriched PyOM mixed in calcareous soil (classified under the US Department of Agriculture system to the great group level as Rhodoxeralf) incubated with rye grass seeds was incorporated into new grass biomass, likely owing to the degradation of pyrrolic N (ref. 133). Thus, beyond serving as a carbon and energy source for microorganisms, PyOM could also provide a nutrient source for pioneer vegetation in burned areas. Overall, PyOM, which can remain stable across millennial timescales, can also be degraded within weeks and months under laboratory conditions[125,128]. Thus, to thoroughly evaluate the efficacy of PyOM as a carbon sink, further research on PyOM biodegradability that accounts for the complexity of soil matrices must be conducted.

2.3.4 REDOX CYCLING OF METAL TOXINS

Post-fire shifts in the dynamics of the soil microbial community and the reactivity of minerals and SOM regulate the cycling of metal toxins, such as Cr, As and Hg. Abiotic and biotic

redox reactions can either mitigate transport of these metal toxins in post-fire environments or increase their abundance and therefore increase the risk of exposure.

Post-fire soil is typically oxygenated; thus, fire-generated As(III) is often short-lived because it is oxidized by PyOM or through microbially mediated pathways. Phenol, semiquinone, and nitrogenous functional groups can mediate As(III) oxidation. For example, electron-donating phenol groups and semiquinone radicals and electron-accepting quinones of PyOM formed by moderate-severity fires can oxidize As(III) directly or through the production of hydrogen peroxide[134]. The reduction of quinone produces phenols or semiquinone radicals, which can further react with As(III). In PyOM generated by high-severity fire, As(III) can also be oxidized through reactions with pyridinic or pyrrolic N, phenol groups, and semiquinone radicals[134]. In all postfire conditions, reducing conditions favour the reduction of As(V) to As(III), which is mobilized in soil porewater, contributing to possible As leaching and increased concentrations of aqueous As(III) in shallow groundwater. However, research on post-fire changes to groundwater quality remains sparse[135].

Fire-generated Cr(VI) weakly adsorbs to soil minerals in alkaline conditions and is easily displaced by other oxyanions, including phosphate and sulfate. These changes could potentially make Cr(VI) more susceptible to leaching into surface waters, threatening aquatic habitats and drinking water sources[136]. Measurements of the amount of aqueous Cr(VI) formed after laboratory heating have been used to estimate the potential post-fire risk of freshwater Cr(VI) pollution in Cr-rich environments in New Caledonia[136]. However, further field measurements of aqueous Cr(VI) following wildfires and precipitation events are needed to verify whether such leaching occurs.

Dissolved Cr(VI) can be reduced to Cr(III), which is less soluble and more benign than Cr(VI). The abiotic coupling of Cr(VI) reduction and Fe(II) oxidation (including Fe(II) phases

formed during wildfires) can result in the rapid precipitation of amorphous, mixed Cr(III)–Fe(III) hydroxides[137,138], immobilizing Cr in surface soils and decreasing health threats. Increased PyOM in post-fire soils can also promote Cr(VI) reduction by directly donating electrons to Cr(VI)[139–141] or by transferring electrons to proximal Fe(III) minerals producing Fe(II), which secondarily reduces Cr(VI) to Cr(III)[142].

With limited post-fire precipitation, fire-generated Cr(VI) can persist in soils. For example, elevated Cr(VI) concentrations in soil and ash were observed compared with unburned areas nearly a year after a severe wildfire in a serpentine chaparral[86], owing to continued dry conditions and below-average precipitation over an 11-month period. Additionally, increased soil pH from alkaline salts in ash formed by high-severity fire inhibits the adsorption of Cr(VI) onto soil minerals and can augment post-fire Cr(III) oxidation by O_2 (ref. 143), increasing the abundance of Cr(VI). Oxidation of Cr(III) can also be aided by Mn(III) or Mn(IV) oxides, which are often present in ash following biomass combustion[142].

The duration of the post-fire threat from Hg depends on the rate of Hg oxidation. Wildfire-derived black and white ash are not effective adsorbents of gaseous Hg (ref. 144), and gaseous Hg emissions only persist for a short period after wildfires before being oxidized to Hg(II)[145]. Ash-associated Hg in post-fire soils is less bioavailable than Hg in unburned vegetation litter[144]. Additionally, aromatic PyOM[146] and sulfide functional groups[144,147] adsorb Hg, reducing its bioavailability. Therefore, less than 1% of ash-associated Hg is expected to be released or methylated in post-fire soils[146].

2.4 ECOSYSTEM AND HUMAN HEALTH IMPACTS

Wildfire-driven changes in soil chemistry can affect revegetation, water quality, and air quality, as discussed in this section.

2.4.1 REVEGETATION

Wildfire-induced changes in soil health, which encompasses the chemical, physical, and biological properties of soil, can determine the success of revegetation and influence the post-fire recovery of an ecosystem. Many factors influence revegetation, including changes in soil pH, toxic metal concentrations, nutrient availability, and SOM transformations. For example, karrikins — a family of carboxylate esters (**Figure 2.4**) — promote the seed germination of plants such as *Arabidopsis*[14]. Karrikins can form under both combustion and pyrolysis conditions[14,148,149], making them a potentially common germination promoter regardless of fire type[150]. Other molecular classes produced by fires, such as PAHs, inhibit seed germination[14,150] (**Figure 2.4**). Mass spectrometry and other advanced analytical methods should be used to target these germination-promoting and germination-inhibiting species in fire-impacted soils and unravel the factors driving or preventing post-fire revegetation.

2.4.2 WATER QUALITY

Post-fire water quality is difficult to predict, owing to the confounding effects of several factors, including the rate of vegetation recovery, sediment availability, basin morphology, and precipitation patterns[151–153]. The variables that influence long-term soil and vegetation recovery are understudied for many ecosystem types[154], making it hard to predict the duration of decreases in water quality. Fires also influence hydrological processes, leading to increased evaporative losses, reduced soil infiltration[19], and increased runoff[155]; again, the extent to which these processes are influenced is difficult to predict, owing to landscape and fire heterogeneity. Landslides, debris flows, floods, and the introduction of particulate and dissolved contaminants to streams can also decrease post-fire water quality[105,156,157]. For example, sediment transport in freshet is increased by 2–100 times following fire[158,159]. Increases in sediment and dissolved PyOM

can be exacerbated by post-wildfire storms and spring snowmelt[153,160], increasing turbidity in nearby water bodies and increasing the cost of water treatment and fixing damaged infrastructure[161–164].

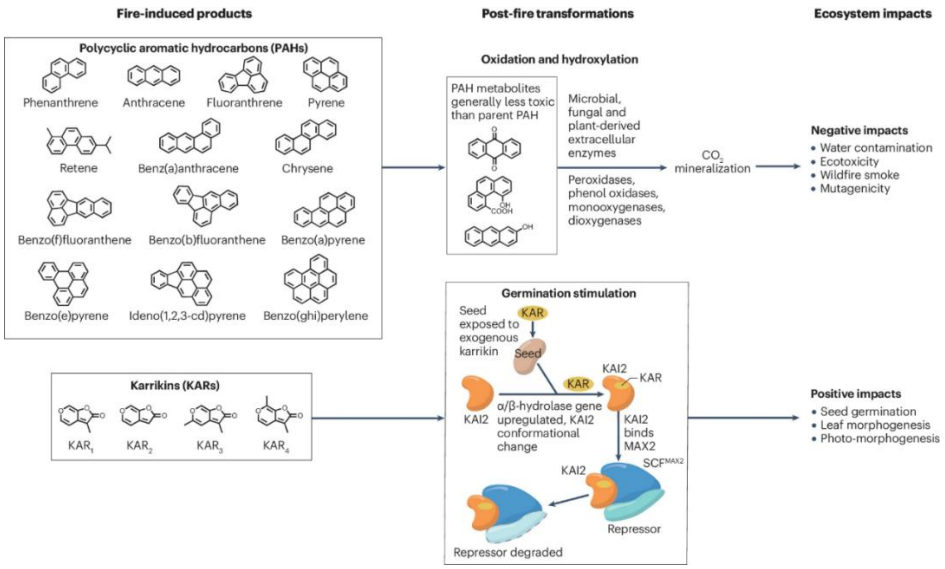

Figure 2.4. The ecosystem impacts of wildfire products. The structures of polycyclic aromatic hydrocarbons (PAHs) and karrikins (KARs) formed by fire. PAHs can be oxidized via microbial, fungal, and plant-derived extracellular enzymes, leading to eventual mineralization to CO_2. KARs can degrade growth-repressing proteins by first binding to an α/β-hydrolase receptor protein called karrikin insensitive 2 (KAI2), inducing a change in the KAI2 shape. This conformation change then allows KAI2 to bind to the F-box protein more axillary growth 2 (MAX2), which is a subunit of the Skp, Cullin, F-box containing complex (SCF complex). This MAX2-SCF complex (identified as SCFMAX2) then degrades a growth repressor, improving seed germination, leaf morphogenesis, and photomorphogenesis. Thus, fire-induced products can have positive and negative ecosystem impacts. The proposed karrikin signal transduction mechanism is adapted from ref. 150 under a Creative Commons licence CC BY 4.0, and adapted with permission from ref. 202, Elsevier.

Erosion is a primary mechanism for the post-fire transport of pollutants, including charred organic compounds, nutrients, and heavy metals, to nearby water bodies. The combustion of forest vegetation and organic-rich soil increases post-fire erosion and decreases water quality, owing to decreased soil stability from the loss of aboveground vegetation and roots[151]. The chemical composition and concentrations of key nutrients in eroded material are influenced by burn severity, time since fire, and hydrology[54,151,153,165,166]. However, the effects of burn extent in the watershed,

burn severity, and post-fire precipitation events are often neglected in predictions of post-fire water quality. Therefore, integrated approaches, which incorporate landscape-level physical changes with chemical observations and climate, must be developed to assess the impact of fire on water quality.

Wildfire-induced nutrient export is a key concern for surface water management[153] because municipalities could be required to adapt treatment methods to handle increased N and P, sediment, and DOM concentrations[90,151,165,167]. Nitrogen fluxes in burned regions are 2–250 times as large as in undisturbed areas. Additionally, P fluxes could be up to 400 times as large in burned watersheds as they are in unburned watersheds[25,151]. Elevated nutrient concentrations in surface waters can persist for over a decade following severe fires[155,166,168] but typically return to pre-fire levels within 5 years[169]. Areas with historic low-intensity fires are particularly vulnerable to increased eutrophication, owing to the large amounts of N and P that are transported into streams and rivers when plant nutrient demand decreases and soil nutrient availability increases[22,170,171].

The primary mechanism of transport is specific to each nutrient or contaminant. Dissolved N leachate (primarily in the form of nitrate and ammonium) from burned watersheds can fertilize and pollute streams, lakes, and reservoirs, putting drinking water infrastructure, aquatic ecosystems, and recreational activities at risk[172]. Meanwhile, sediment erosion is the primary vector of P transport in aquatic ecosystems[173,174], which can also contribute to eutrophication and harmful algal blooms[175]. Nitrogen, P, and other nutrients (such as potassium or calcium) are often identified as potential contaminants in fire-affected catchments; however, the concentrations of these other nutrients are not widely regulated. Thus, the potential negative impacts of postfire nutrient fluxes should be explored more thoroughly to optimize post-fire responses by water quality managers.

The effects of fire on surface water toxicity vary between trophic levels and are influenced by the input of organic and inorganic compounds from burned watersheds[176]. There have been conflicting findings on the effects of aqueous ash extracts (AEA) on organisms such as *Daphnia magna*, *Danio rerio*, and *Aliivibrio fischeri* (**Table A2**). Acute toxicity was observed on *Daphnia magna* for AEA from three out of six ecosystems[177]. For example, *Daphnia magna* was negatively affected by AEA from burned Australian eucalypt stands (pH 11.1) but not by AEA from Spanish heathland (pH 9.1), demonstrating the influence of overstorey vegetation type and the relationship between pH and ash toxicity[177]. Further, eucalyptus AEA from soil surfaces is toxic across trophic levels, negatively affecting *Danio rerio*, *Salamandra salamandra*, *Rana iberica*, and human cells[178–181], potentially owing to the presence of dissolved metals[178–180] and methoxy phenols[181]. However, overland flow from a burned (75%) eucalyptus plantation had no effect on *Daphnia magna* despite high PAH concentrations[182]. Erosion-mediated dilution could mitigate the toxicity of AEA in some scenarios. Fires also increase the concentration of PAHs and metals in the soil, which can be transported to nearby water bodies[36,38,136], but the transport and fate of such compounds are highly complex and must be further analysed to accurately predict fire-driven contaminant risks.

The effect of burn severity on organisms is less clear than the effect of AEA concentrations. Increasing fire severity led to increased soil toxicity for *A. fischeri* in aqueous soil extracts from a burned lodgepole pine forest, potentially owing to the formation of N-heterocycles and PAHs or the release of heavy metals during burning[52]. Additionally, fire severity negatively affected the community composition of soil arthropods in a mixed hardwood forest in the southern United States, but the fire products did not have any effect on aquatic arthropods[183]. Aquatic arthropods in southern Australian artesian springs were also unaffected for 2 years after a fire[184]. However,

differences in the aquatic macroinvertebrate assemblage structures were observed between reference and burned catchments 8 years after a fire in the Rocky Mountains, indicating that post-fire toxicity can vary between regions[185]. Given the dynamic nature of aquatic systems, research covering a range of spatial and temporal scales is needed to understand these contrasting results.

DOM from burned watersheds can form carcinogenic disinfection by-products (DBPs) through chlorination during water treatment[48,186,187]. DBPs have been detected in post-fire municipal water samples and are often attributed to increased concentrations of DOC and suspended solids in local fire-impacted watersheds, which require more coagulants and disinfectants during treatment, augmenting DBP formation. Nitrogenous DBPs (N-DBPs) are not regulated[135], and cell chronic cytotoxicity and acute genotoxicity assays suggest that N-DBPs could pose greater health risks than carbonaceous DBPs, owing to the heightened biomolecular nucleophilic substitution (S_N2) reactivity of N-DBPs which increases displacement of halogen atoms[188]. Leachates from burned organic matter produce more N-DBPs than unburned organic matter during chlorination[48,186,187], possibly owing to N-enrichment in PyOM. Additionally, the formation of haloacetonitrile (an N-DBP) was positively correlated with the watershed burned area in water samples collected 12 years after a fire, highlighting the persistence of harmful N-DBP precursors in post-fire environments[189].

2.4.3 SMOKE AND POST-FIRE DUST

In fire-affected soils, the composition and speciation of wind-dispersible particles influence toxicity. Airborne particulate matter comprises silt-sized (2–50 μm) and clay-sized (<2 μm) particles, including PM10 (particles of <10 μm aerodynamic diameter) and PM2.5. Clay-sized particles have high surface area and dominate adsorption sites for surface-associated toxins and nutrients[86,190], and they can be transported by wind or water. When inhaled, PM2.5 can penetrate

the lungs and be absorbed into the bloodstream, increasing the risk of cancer[191–193] and oxidative stress.

The relative composition and toxicity of wildfire smoke are poorly understood[194] and vary with ecosystem type[195] and fire temperature. Metals are among the hundreds of different types of toxins present in airborne particulate matter during and after high-severity wildfires. Superparamagnetic magnetite and maghaemite have also been observed in spherical particles ranging from 0.1 to 2 μm in diameter following wildfires and, owing to the fine particle size, can be resuspended, with implications for direct toxicity and oxidative stress[70]. Additionally, fire-generated PAHs (particularly those with low molecular weight such as naphthalene and phenanthrene), Hg, and As can be emitted as gases and transported long distances[196–198] or redistributed on the soil surface within ash[199].

The duration of dust emissions and exposure caused by wildfire is likely to increase as worsening droughts delay revegetation in burned ecosystems. Therefore, ash and surface toxins will persist across widespread and sparsely covered wildland landscapes for increasing periods. Increased dust emissions have been linked with large wildfires globally, occurring for days to months after fires[8]. Future work further examining the composition, mineralogy, and formation mechanisms of fire-generated fine particulates in surface soils is warranted.

2.5 SUMMARY AND FUTURE PERSPECTIVES

Wildfires can catalyse various molecular transformations, affecting the chemical properties of post-fire soil (**Figure 2.5**). For example, PyOM contains both beneficial and toxic compounds, such as karrikins, PAHs, and N-containing aromatic compounds, and PyOM is more soluble and biodegradable than previously estimated. Wildfires can also alter the oxidation state of soil-borne metals, generating hazardous and/or mobile species. Additionally, fire-induced and redox-induced

changes in SOM can alter the speciation and toxicity of metal(loid)s, such as Cr and As. Fires can also affect ecosystem and human health; for instance, PyOM can promote the growth of some fire-adapted plant species while inhibiting others. The presence of PyOM in water can also lead to the formation of carcinogenic DBPs during post-fire water treatment. Despite this progress towards elucidating the chemical transformations and subsequent effects of fire-impacted soil, persistent knowledge gaps remain.

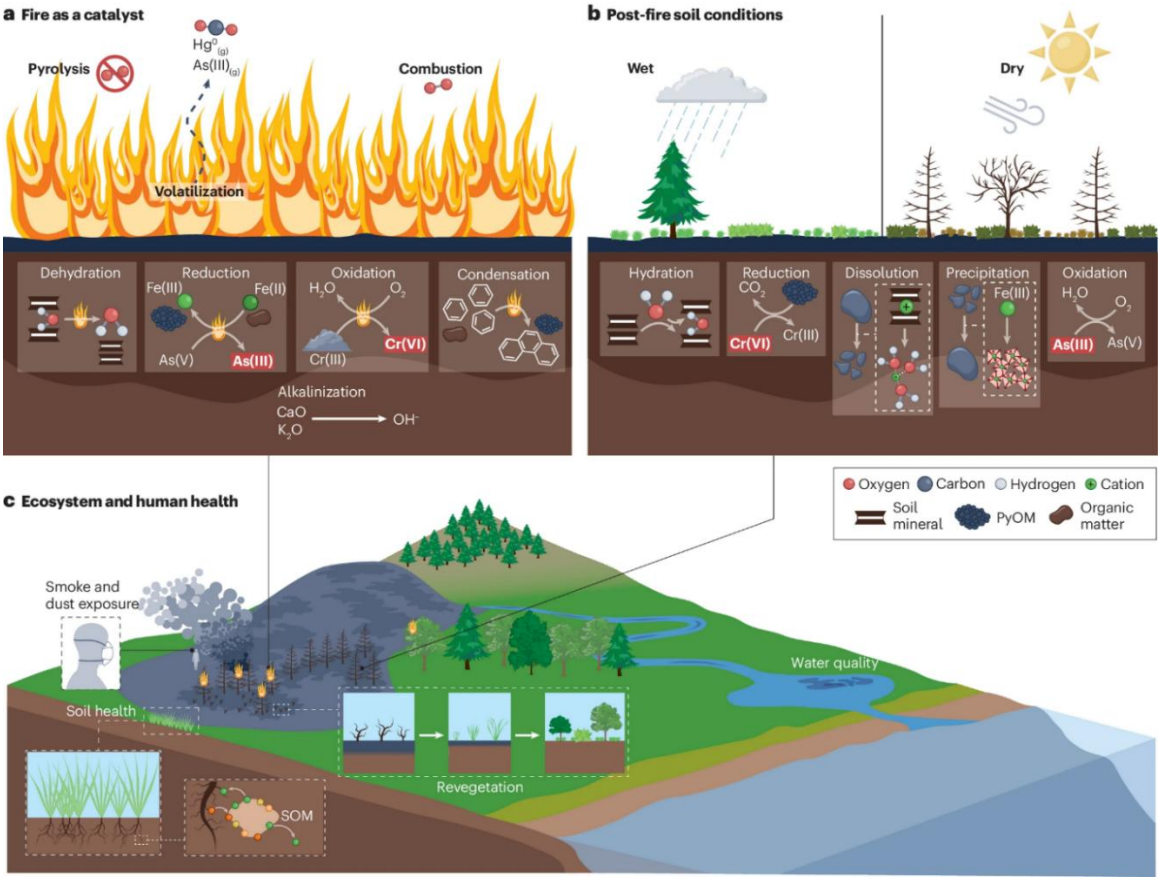

Figure 2.5. Wildfire-induced chemical changes and their impacts. **a**, Chemical reactions that occur during fire, with toxic species indicated by a red box. **b**, Chemical reactions that occur after fire. **c**, The effects of the processes in **a** and **b** on ecosystems and human health. Fire-induced organic and inorganic speciation changes during fire and environmental conditions post fire can influence soil characteristics and broader ecosystem and human health. PyOM, pyrogenic organic matter; SOM, soil organic matter.

Integrated approaches to explicitly assess the impact of fire on water quality must be developed to guide water treatment strategies. For example, it is not clear which PyOM molecules act as DBP precursors and what mechanisms are responsible for DBP formation. Additionally, there are no standard procedures for treating source water from burned watershed, despite known increases in DBP concentrations post fire[200] because most municipalities choose to divert this water rather than treating it. Identifying DBP precursors and establishing protocols for treating fire-impacted source water could allow optimized treatment of water from burned watersheds to mitigate the formation of harmful DBPs. These approaches are particularly needed in regions where water scarcity makes water managers reluctant to divert water that originates from or flows through burned areas. Similarly, the molecular characteristics of metal toxins in post-fire soils that influence aqueous mobility and longevity remain elusive. Identifying these characteristics, especially in fine (nano)particulates, could improve understanding of post-fire transport of metal toxins through watersheds.

Techniques to analyse low-molecular-weight organic molecules in burned soils are also needed. Combining targeted and non-targeted mass spectrometry approaches will provide a broader understanding of the molecules that regulate post-fire revegetation, DBP formation, C and N cycling, and toxicity. For example, targeting karrikins in fire-impacted soils could elucidate drivers that influence post-fire revegetation. Additionally, characterizing the metabolomic content of post-fire soils could identify metabolites that influence microbial recolonization and soil recovery, which are also important factors for revegetation[132]. Further mass spectrometry analysis is also required to identify the pathways and controls on the formation of N-dense aromatic compounds during wildfire, which according to the results of bacterial bioassays could contribute to post-fire toxicity[52]. An improved understanding of N speciation will elucidate the

biogeochemical roles of organic N in post-fire soils (as a toxin or bioavailable source of nitrogen) and improve estimates of N cycling in post-fire soils, including gaseous emissions, leaching, and bioavailability.

Fire-induced changes in the chemistry of metal particulates must be better understood to predict the risk to human health from wildfires. Laboratory simulations, such as furnace burning, allow for controlled burning at set temperatures and duration to mimic natural fires. But the intensity of thermal reactions in a furnace can be exaggerated relative to natural soil conditions during wildfires, because many laboratory experiments include only a few grams of solids (for example synthetic minerals, soil or plant litter) that are heated for minutes to hours (typically <2 h). Further, sample cooling in furnace experiments could be substantially different from that observed under field conditions. To account for this limitation, both laboratory and field observations of metal speciation changes during and after fire are needed to provide greater insight into how fires catalyse these reactions.

High-resolution electron microscopy (scanning and transmission), along with electron and X-ray spectroscopic techniques, could be used to probe particle morphology, chemistry, and fine-size distribution to provide insight on metal hazards in fire-impacted soils. A predictive framework using these measures for fine particulate metal chemistry following wildfire, including changes in particle size and surface area, is needed. Additionally, it is important to determine whether surface-deposited and airborne metal toxins are derived from biomass burning or altered soil minerals during wildfires because fire management decisions could vary depending on potential toxin release or exposure. However, post-fire observations of surface ash and soil are likely to overlook a large fraction of biomass-derived inorganic products that are released as particulate matter in wildfire smoke or post-fire dust emissions. Therefore, further work coupling soil and biomass

contributions is needed to identify the sources and environmental drivers of toxic metals in particulate matter.

Future research must expand the range of landscapes, geographical locations, and post-fire timescales covered. Existing research is largely focused on North American and European ecosystems, and most of this research was conducted 1–5 years post fire. Given that toxicity, vegetation, microbiome composition, and water quality remain distinct from pre-fire conditions during this timeframe, longer-term studies are needed to provide more insight into the recovery of burned ecosystems. Global increases in fire severity and frequency demand that these persisting knowledge gaps are addressed to help manage wildfire risks to human health, soil health, and ecosystem services.

2.6 AUTHOR CONTRIBUTIONS

According to CRediT criteria, my contributions to this work included conceptualization, formal analysis, investigation, writing – original draft, writing – review & editing, and visualization. Contributions by Alandra Marie Lopez include conceptualization, software development, formal analysis, investigation, data curation, writing – original draft, writing – review & editing, visualization, and supervision. Contributions by Claudia Christine E. Avila include conceptualization, formal analysis, investigation, data curation, writing – original draft, writing – review & editing, visualization, and supervision. Contributions by Holly K. Roth include conceptualization, formal analysis, investigation, writing – original draft, writing – review & editing, and visualization. Contributions by Scott Fendorf include conceptualization, writing – review & editing, supervision, and project administration. Contributions by Thomas Borch include conceptualization, writing – review & editing, supervision, project administration, and funding acquisition.

Alandra Marie Lopez and Claudia Christine E. Avila contributed to the following specific sections of this publication: introduction, factors influencing fire-induced reactions, inorganic minerals in ash and soil, formation of metal(loid) toxins, hydration and dehydration, redox cycling of metal toxins, water quality, and summary and future perspectives. Holly K. Roth contributed to the following specific sections of this publication: introduction, organic matter transformations, water quality, smoke and post-fire dust, and summary and future perspectives. I contributed to the following specific sections of this publication: introduction, organic matter transformations, organo-mineral interactions, microbial degradation of PyOM, revegetation, water quality, and summary and future perspectives. I helped conceptualize the content by determining what topics would be included in this publication. I conducted formal analysis and investigation by reading relevant literature and using that information to guide the content of the publication. For visualization, I was responsible for producing **Figures 2.2** and **2.4**.

2.7 ACKNOWLEDGEMENTS

The authors acknowledge support from the Center for Innovation in Global Health at Stanford University and the London School of Hygiene and Tropical Medicine under the Planetary Health Postdoctoral Fellowship (Alandra Marie Lopez), Stanford Doerr School of Sustainability under the Stanford Earth Postdoctoral Fellowship (Claudia Christine E. Avila), Stanford Woods Institute for the Environment (Scott Fendorf), the National Science Foundation under grant number 2114868 (Holly K. Roth, Jacob P. VanderRoest, Thomas Borch), and USDA National Institute of Food and Agriculture through AFRI grant number 2021-67019-34608 (Holly K. Roth, Jacob P. VanderRoest, Thomas Borch).

CHAPTER 2 REFERENCES

(1) Jones, M. W. et al. Global and regional trends and drivers of fire under climate change. *Rev. Geophys.* **2022**, *60*, e2020RG000726.

(2) Certini, G. Fire as a soil-forming factor. *AMBIO.* **2014**, *43*, 191–195.

(3) McLauchlan, K. K. et al. Fire as a fundamental ecological process: research advances and frontiers. *J. Ecol.* **2020**, *108*, 2047–2069.

(4) Pausas, J. G. & Keeley, J. E. Wildfires as an ecosystem service. *Front. Ecol. Environ*. **2019**, *17*, 289–295.

(5) van der Werf, G. R. et al. Global fire emissions estimates during 1997–2016. *Earth Syst. Sci. Data*. **2017**, *9*, 697–720.

(6) Senande-Rivera, M., Insua-Costa, D. & Miguez-Macho, G. Spatial and temporal expansion of global wildland fire activity in response to climate change. *Nat. Commun*. **2022**, *13*, 1208.

(7) Martin, D. A. Linking fire and the United Nations Sustainable Development Goals. *Sci. Total Environ.* **2019**, 662, 547–558.

(8) Yu, Y. & Ginoux, P. Enhanced dust emission following large wildfires due to vegetation disturbance. *Nat. Geosci.* **2022**, *15*, 878–884.

(9) De la Rosa, J. M. et al. Characterization of wildfire effects on soil organic matter using analytical pyrolysis. *Geoderma*. **2012**, *191*, 24–30.

(10) Barron, S. M., Mladenov, N., Sant, K. E. & Kinoshita, A. M. Surface water quality after the Woolsey fire in Southern California. *Water Air Soil Pollut.* **2022**, *233*, 377.

(11) Giardina, C. P., Sanford, R. L. & Døckersmith, I. C. Changes in soil phosphorus and nitrogen during slash-and-burn clearing of a dry tropical forest. *Soil Sci. Soc. Am. J.* **2000**, *64*, 399–405.

(12) Merino, A. et al. Soil organic matter and phosphorus dynamics after low intensity prescribed burning in forests and shrubland. *J. Environ. Manage*. **2019**, *234*, 214–225.

(13) Schaller, J. et al. Fire enhances phosphorus availability in topsoils depending on binding properties. *Ecology*. **2015**, *96*, 1598–1606.

(14) Nelson, D. C., Flematti, G. R., Ghisalberti, E. L., Dixon, K. W. & Smith, S. M. Regulation of seed germination and seedling growth by chemical signals from burning vegetation. *Annu. Rev. Plant Biol.* **2012**, *63*, 107–130.

(15) Hickenbottom, K., Pagilla, K. & Hanigan, D. Wildfire impact on disinfection byproduct precursor loading in mountain streams and rivers. *Water Res.* **2023**, *244*, 120474.

(16) Panichev, N., Mabasa, W., Ngobeni, P., Mandiwana, K. & Panicheva, S. The oxidation of Cr(III) to Cr(VI) in the environment by atmospheric oxygen during the bush fires. *J. Hazard. Mater.* **2008**, *153*, 937–941.

(17) Gonzalez-Perez, J. A., Gonzalez-Vila, F. J., Almendros, G. & Knicker, H. The effect of fire on soil organic matter — a review. *Environ. Int.* **2004**, *30*, 855–870.

(18) Knicker, H. How does fire affect the nature and stability of soil organic nitrogen and carbon? A review. *Biogeochemistry*. **2007**, *85*, 91–118.

(19) Girona-García, A. et al. Effectiveness of post-fire soil erosion mitigation treatments: a systematic review and meta-analysis. *Earth Sci. Rev.* **2021**, *217*, 103611.

(20) Roshan, A. & Biswas, A. Fire-induced geochemical changes in soil: implication for the element cycling. *Sci. Total Environ*. **2023**, *868*, 161714.

(21) Shakesby, R. A. Post-wildfire soil erosion in the Mediterranean: review and future research directions. *Earth Sci. Rev.* **2011**, *105*, 71–100.

(22) Certini, G. Effects of fire on properties of forest soils: a review. *Oecologia.* **2005**, *143*, 1–10.

(23) Agbeshie, A. A., Abugre, S., Atta-Darkwa, T. & Awuah, R. A review of the effects of forest fire on soil properties. *J. For. Res.* **2022**, *33*, 1419–1441.

(24) Vieira, D. C. S., Fernández, C., Vega, J. A. & Keizer, J. J. Does soil burn severity affect the post-fire runoff and interrill erosion response? A review based on meta-analysis of field rainfall simulation data. *J. Hydrol*. **2015**, *523*, 452–464.

(25) Bladon, K. D., Emelko, M. B., Silins, U. & Stone, M. Wildfire and the future of water supply. *Environ. Sci. Technol.* **2014**, *48*, 8936–8943.

(26) Kotze, D. The effects of fire on wetland structure and functioning. *Afr. J. Aquat. Sci.* **2013**, *38*, 237–247.

(27) Li, X.-Y. et al. Influences of forest fires on the permafrost environment: a review. *Adv. Clim. Change Res.* **2021**, *12*, 48–65.

(28) Galang, M. A., Markewitz, D. & Morris, L. A. Soil phosphorus transformations under forest burning and laboratory heat treatments. *Geoderma*. **2010**, *155*, 401–408.

(29) Pingree, M. R. A. & Kobziar, L. N. The myth of the biological threshold: a review of biological responses to soil heating associated with wildland fire. *For. Ecol. Manag.* **2019**, *432*, 1022–1029.

(30) Doerr, S. H., Santín, C., Merino, A., Belcher, C. M. & Baxter, G. Fire as a removal mechanism of pyrogenic carbon from the environment: effects of fire and pyrogenic carbon characteristics. *Front. Earth Sci.* **2018**. https://doi.org/10.3389/feart.2018.00127.

(31) Doerr, S. H. et al. Effects of heating and post-heating equilibration times on soil water repellency. *Soil Res*. **2005**, *43*, 261–267.

(32) Jordanova, N., Jordanova, D., Mokreva, A., Ishlyamski, D. & Georgieva, B. Temporal changes in magnetic signal of burnt soils — a compelling three years pilot study. *Sci. Total Environ.* **2019**, *669*, 729–738.

(33) Badía, D. et al. Burn effects on soil properties associated to heat transfer under contrasting moisture content. *Sci. Total Environ.* **2017**, *601–602*, 1119–1128.

(34) Honeyman, A. S., Merl, T., Spear, J. R. & Koren, K. Optode-based chemical imaging of laboratory burned soil reveals millimeter-scale heterogeneous biogeochemical responses. *Environ. Res.* **2023**, *224*, 115469.

(35) Caon, L., Vallejo, V. R., Ritsema, C. J. & Geissen, V. Effects of wildfire on soil nutrients in Mediterranean ecosystems. *Earth Sci. Rev.* **2014**, *139*, 47–58.

(36) Bodi, M. B. et al. Wild land fire ash: production, composition and eco-hydro-geomorphic effects. *Earth Sci. Rev.* **2014**, *130*, 103–127.

(37) Santín, C. et al. Towards a global assessment of pyrogenic carbon from vegetation fires. *Glob. Change Biol*. **2016**, *22*, 76–91.

(38) Campos, I. & Abrantes, N. Forest fires as drivers of contamination of polycyclic aromatic hydrocarbons to the terrestrial and aquatic ecosystems. *Curr. Opin. Environ. Sci. Health*. **2021**. https://doi.org/10.1139/er-2022-0055.

(39) Kieta, K. A. et al. Polycyclic aromatic hydrocarbons in terrestrial and aquatic environments following wildfire: a review. *Environ. Rev.* **2023**, *31*, 141–167.

(40) Kim, K.-H., Jahan, S. A., Kabir, E. & Brown, R. J. C. A review of airborne polycyclic aromatic hydrocarbons (PAHs) and their human health effects. *Environ. Int*. **2013**, *60*, 71–80.

(41) Mastrangelo, G., Fadda, E. & Marzia, V. Polycyclic aromatic hydrocarbons and cancer in man. *Environ. Health Perspect*. **1996**, *104*, 1166–1170.

(42) Yang, B. et al. Polycyclic aromatic hydrocarbon occurrence in forest soils in response to fires: a summary across sites. *Environ. Sci. Process. Impacts*. **2022**, *24*, 32–41.

(43) Keiluweit, M., Nico, P. S., Johnson, M. G. & Kleber, M. Dynamic molecular structure of plant biomass-derived black carbon (biochar). *Environ. Sci. Technol*. **2010**, *44*, 1247–1253.

(44) Xu, W., Walpen, N., Keiluweit, M., Kleber, M. & Sander, M. Redox properties of pyrogenic dissolved organic matter (pyDOM) from biomass-derived chars. *Environ. Sci. Technol*. **2021**, *55*, 11434–11444.

(45) Sigmund, G. et al. Environmentally persistent free radicals are ubiquitous in wildfire charcoals and remain stable for years. *Commun. Earth Environ*. **2021**, *2*, 68.

(46) Fang, T. et al. Wildfire particulate matter as a source of environmentally persistent free radicals and reactive oxygen species. *Environ. Sci. Atmos*. **2023**, *3*, 581–594.

(47) Bahureksa, W. et al. Nitrogen enrichment during soil organic matter burning and molecular evidence of Maillard reactions. *Environ. Sci. Technol*. **2022**, *56*, 4597–4609.

(48) Cawley, K. M. et al. Molecular and spectroscopic characterization of water extractable organic matter from thermally altered soils reveal insight into disinfection byproduct precursors. *Environ. Sci. Technol.* **2017**, *51*, 771–779.

(49) Wu, S. et al. Pyridinic- and pyrrolic nitrogen in pyrogenic carbon improves electron shuttling during microbial Fe(III) reduction. *ACS Earth Space Chem*. **2021**, *5*, 900–909.

(50) Roth, H. K. et al. Enhanced speciation of pyrogenic organic matter from wildfires enabled by 21 T FT-ICR mass spectrometry. *Anal. Chem*. **2022**, *94*, 2973–2980.

(51) Torres-Rojas, D. et al. Nitrogen speciation and transformations in fire-derived organic matter. *Geochim. Cosmochim. Acta*. **2020**, *276*, 170–185.

(52) Roth, H. K. et al. Effects of burn severity on organic nitrogen and carbon chemistry in high-elevation forest soils. *Soil Environ. Health.* **2023**, *1*, 100023.

(53) Santos, F., Russell, D. & Berhe, A. A. Thermal alteration of water extractable organic matter in climosequence soils from the Sierra Nevada, California. *J. Geophys. Res. Biogeosci.* **2016**, *121*, 2877–2885.

(54) Sánchez-García, C. et al. Chemical characteristics of wildfire ash across the globe and their environmental and socio-economic implications. *Environ. Int.* **2023**, *178*, 108065.

(55) Vassilev, S. V., Baxter, D. & Vassileva, C. G. An overview of the behaviour of biomass during combustion: part I. Phase-mineral transformations of organic and inorganic matter. *Fuel*. **2013**, *112*, 391–449.

(56) Vassilev, S. V., Baxter, D., Andersen, L. K. & Vassileva, C. G. An overview of the composition and application of biomass ash: part 2. Potential utilisation, technological and ecological advantages and challenges. *Fuel*. **2013**, *105*, 19–39.

(57) Vassilev, S. V., Baxter, D., Andersen, L. K. & Vassileva, C. G. An overview of the composition and application of biomass ash. Part 1. Phase–mineral and chemical composition and classification. *Fuel*, **2013**, *105*, 40–76.

(58) Perrier, N., Gilkes, R. J. & Colin, F. Heating Fe oxide-rich soils increases the dissolution rate of metals. *Clays Clay Min*. **2006**, *54*, 165–175.

(59) Landers, M. & Gilkes, R. J. Dehydroxylation and dissolution of nickeliferous goethite in New Caledonian lateritic Ni ore. *Appl. Clay Sci.* **2007**, *35*, 162–172.

(60) Vassilev, S. V., Baxter, D., Andersen, L. K. & Vassileva, C. G. An overview of the chemical composition of biomass. *Fuel*. **2010**, *89*, 913–933.

(61) Kim, Y. H. et al. Mutagenicity and lung toxicity of smoldering vs. flaming emissions from various biomass fuels: implications for health effects from wildland fires. *Environ. Health Perspect.* **2018**, *126*, 017011.

(62) Jordanova, D., Jordanova, N., Barrón, V. & Petrov, P. The signs of past wildfires encoded in the magnetic properties of forest soils. *Catena*. **2018**, *171*, 265–279.

(63) Pereira, P., Úbeda, X. & Martin, D. A. Fire severity effects on ash chemical composition and water-extractable elements. *Geoderma*. **2012**, *191*, 105–114.

(64) Yan, L., Chen, Q., Yang, Y. & Zhu, R. The significant role of montmorillonite on the formation of hematite nanoparticles from ferrihydrite under heat treatment. *Appl. Clay Sci*. **2021**, *202*, 105962–105962.

(65) Araya, S. N., Fogel, M. L. & Berhe, A. A. Thermal alteration of soil organic matter properties: a systematic study to infer response of Sierra Nevada climosequence soils to forest fires. *SOIL*. **2017**, *3*, 31–44.

(66) Baieta, R., Vieira, A. M. D., Vaňková, M. & Mihaljevič, M. Effects of forest fires on soil lead elemental contents and isotopic ratios. *Geoderma*. **2022**, *414*, 115760.

(67) Oleszek, S., Shiota, K., Chen, M. & Takaoka, M. Effective separation and recovery of manganese and potassium from biomass ash by solvent extraction. *ACS Omega*. **2022**, *7*, 20155–20164.

(68) Clement, B. M., Javier, J., Sah, J. P. & Ross, M. S. The effects of wildfires on the magnetic properties of soils in the Everglades. *Earth Surf. Process. Landf.* **2011**, *36*, 460–466.

(69) Johnston, S. G., Karimian, N. & Burton, E. D. Fire promotes arsenic mobilization and rapid arsenic(III) formation in soil via thermal alteration of arsenic-bearing iron oxides. Front. Earth Sci. **2019**. https://doi.org/10.3389/feart.2019.00139.

(70) Baalousha, M. et al. Discovery and potential ramifications of reduced iron-bearing nanoparticles — magnetite, wustite, and zero-valent iron — in wildland–urban interface fire ashes. *Environ. Sci. Nano*. **2022**, *9*, 4136–4149.

(71) Chen, J. et al. Atmospheric emissions of F, As, Se, Hg, and Sb from coal-fired power and heat generation in China. *Chemosphere*. **2013**, *90*, 1925–1932.

(72) Galbreath, K. C. & Zygarlicke, C. J. Formation and chemical speciation of arsenic-, chromium-, and nickel-bearing coal combustion PM2.5. *Fuel Process. Technol*. **2004**, *85*, 701–726.

(73) Stam, A. F. et al. Chromium speciation in coal and biomass co-combustion products. *Environ. Sci. Technol*. **2011**, *45*, 2450–2456.

(74) Wu, J. et al. Combustion conditions and feed coals regulating the Fe- and Ti-containing nanoparticles in various coal fly ash. *J. Hazard. Mater*. **2023**, *445*, 130482.

(75) Mao, L., Deng, N., Liu, L., Cui, H. & Zhang, W. Effects of Al2O3, Fe2O3, and SiO2 on Cr(VI) formation during heating of solid waste containing Cr(III). *Chem. Eng. J.* **2016**, *304*, 216–222.

(76) Verbinnen, B., Billen, P., Van Coninckxloo, M. & Vandecasteele, C. Heating temperature dependence of Cr(III) oxidation in the presence of alkali and alkaline earth salts and subsequent Cr(VI) leaching behavior. *Environ. Sci. Technol*. **2013**, *47*, 5858–5863.

(77) Yang, Y., Ma, H., Chen, X., Zhu, C. & Li, X. Effect of incineration temperature on chromium speciation in real chromium-rich tannery sludge under air atmosphere. *Environ. Res.* **2020**, *183*, 109159.

(78) Alam, M. et al. Identification and quantification of Cr, Cu, and As incidental nanomaterials derived from CCA-treated wood in wildland-urban interface fire ashes. *J. Hazard. Mater.* **2023**, *445*, 130608.

(79) Wolf, R. E., Morman, S. A., Hageman, P. L., Hoefen, T. M. & Plumlee, G. S. Simultaneous speciation of arsenic, selenium, and chromium: species stability, sample preservation, and analysis of ash and soil leachates. *Anal. Bioanal. Chem*. **2011**, *401*, 2733–2745.

(80) US Environmental Protection Agency Toxicological Review of Hexavalent Chromium (EPA, **1998**).

(81) Johnston, S. G., Burton, E. D. & Moon, E. M. Arsenic mobilization is enhanced by thermal transformation of schwertmannite. *Environ. Sci. Technol*. **2016**, *50*, 8010–8019.

(82) Burton, E. D., Choppala, G., Karimian, N. & Johnston, S. G. A new pathway for hexavalent chromium formation in soil: fire-induced alteration of iron oxides. *Environ. Pollut.* **2019**, *247*, 618–625.

(83) Burton, E. D. et al. Chromium(VI) formation via heating of Cr(III)-Fe(III)-(oxy)hydroxides: a pathway for fire-induced soil pollution. *Chemosphere*. **2019**, *222*, 440–444.

(84) Zhou, Y., Chen, Z., Gong, H. & Yang, Z. Chromium speciation in tannery sludge residues after different thermal decomposition processes. *J. Clean. Prod*. **2021**, *314*, 128071–128071.

(85) Wolf, R. E., Morman, S. A., Plumlee, G. S., Hageman, P. L. & Adams, M. Release of Hexavalent Chromium by Ash and Soils in Wildfire-Impacted Areas pubs.usgs.gov/publication/ofr20081345 (US Geological Survey, **2008**).

(86) Lopez, A. M., Pacheco, J. L. & Fendorf, S. Metal toxin threat in wildland fires determined by geology and fire severity. *Nat. Commun*. **2023**, *14*, 8007.

(87) Alshehri, T. et al. Wildland-urban interface fire ashes as a major source of incidental nanomaterials. *J. Hazard. Mater*. **2023**, *443*, 130311–130311.

(88) Lin, Y.-C. et al. Enhancements of airborne particulate arsenic over the subtropical free troposphere: impact of southern Asian biomass burning. *Atmos. Chem. Phys*. **2018**, *18*, 13865–13879.

(89) Tuhy, M. et al. Metal(loid)s remobilization and mineralogical transformations in smelterpolluted savanna soils under simulated wildfire conditions. *J. Environ. Manage*. **2021**, *293*, 112899.

(90) Burton, C. A. et al. Trace elements in stormflow, ash, and burned soil following the 2009 station fire in Southern California. *PLoS ONE*. **2016**, *11*, e0153372.

(91) Chrysochoou, M., Theologou, E., Bompoti, N., Dermatas, D. & Panagiotakis, I. Occurrence, origin and transformation processes of geogenic chromium in soils and sediments. *Curr. Pollut. Rep*. **2016**, *2*, 224–235.

(92) Kumar, A., Wu, S., Huang, Y., Liao, H. & Kaplan, J. O. Mercury from wildfires: global emission inventories and sensitivity to 2000–2050 global change. *Atmos. Environ*. **2018**, *173*, 6–15.

(93) Dastoor, A. et al. Arctic mercury cycling. *Nat. Rev. Earth Environ*. **2022**, *3*, 270–286.

(94) Lopez, A. F., Barron, E. G. H. & Bugallo, P. M. B. Contribution to understanding the influence of fires on the mercury cycle: systematic review, dynamic modelling and application to sustainable hypothetical scenarios. *Environ. Monit. Assess*. **2022**, *194*, 707.

(95) Webster, J. P., Kane, T. J., Obrist, D., Ryan, J. N. & Aiken, G. R. Estimating mercury emissions resulting from wildfire in forests of the western United States. *Sci. Total Environ.* **2016**, *568*, 578–586.

(96) Biswas, A., Blum, J. D., Klaue, B. & Keeler, G. J. Release of mercury from Rocky Mountain forest fires. *Glob. Biogeochem. Cycles*. **2007**. https://doi.org/10.1029/2006GB002696.

(97) Campos, I., Vale, C., Abrantes, N., Keizer, J. J. & Pereira, P. Effects of wildfire on mercury mobilisation in eucalypt and pine forests. *Catena*. **2015**, *131*, 149–159.

(98) Homann, P. S., Darbyshire, R. L., Bormann, B. T. & Morrissette, B. A. Forest structure affects soil mercury losses in the presence and absence of wildfire. *Environ. Sci. Technol*. **2015**, *49*, 12714–12722.

(99) Zhou, J., Obrist, D., Dastoor, A., Jiskra, M. & Ryjkov, A. Vegetation uptake of mercury and impacts on global cycling. *Nat. Rev. Earth Environ*. **2021**, *2*, 269–284.

(100) Yan, X.-L. et al. Arsenic transformation and volatilization during incineration of the hyperaccumulator Pteris vittata L. *Environ. Sci. Technol*. **2008**, *42*, 1479–1484.

(101) Hata, T. et al. Electron microscopic study on pyrolysis of CCA (chromium, copper and arsenic oxide)-treated wood. *J. Anal. Appl. Pyrolysis*. **2003**, *68–69*, 635–643.

(102) Nguyen, M. N. et al. Thermal induced changes of rice straw phytolith in relation to arsenic release: a perspective of rice straw arsenic under open burning. *J. Environ. Manage*. **2022**, *304*, 114294.

(103) Nguyen, M. N. et al. Arsenic in rice straw phytoliths: encapsulation and release properties. *Appl. Geochem*. **2021**, *127*, 104907.

(104) Schaller, J., Wang, J., Islam, M. R. & Planer-Friedrich, B. Black carbon yields highest nutrient and lowest arsenic release when using rice residuals in paddy soils. *Sci. Rep*. **2018**, *8*, 17004.

(105) Weninger, T., Filipović, V., Mešić, M., Clothier, B. & Filipović, L. Estimating the extent of fire induced soil water repellency in Mediterranean environment. *Geoderma*. **2019**, *338*, 187–196.

(106) Malkinson, D. & Wittenberg, L. Post fire induced soil water repellency — modeling short and long-term processes. *Geomorphology*. **2011**, *125*, 186–192.

(107) Yusiharni, E. & Gilkes, R. J. Short term effects of heating a lateritic podzolic soil on the availability to plants of native and added phosphate. *Geoderma*, **2012**, *191*, 132–139.

(108) Baranyai, V. Z., Kristály, F. & Szűcs, I. Low temperature rehydration of thermally dehydroxylated Bayer–gibbsite, evolution and transformation of phases. *J. Therm. Anal. Calorim.* **2017**, *129*, 1353–1365.

(109) Yusiharni, E. & Gilkes, R. Rehydration of heated gibbsite, kaolinite and goethite: an assessment of properties and environmental significance. *Appl. Clay Sci*. **2012**, *64*, 61–74.

(110) Solomon, D. et al. Micro-and nano-environments of C sequestration in soil: a multielemental STXM–NEXAFS assessment of black C and organomineral associations. *Sci. Total Environ.* **2012**, *438*, 372–388.

(111) Lin, Y., Munroe, P., Joseph, S., Kimber, S. & Van Zwieten, L. Nanoscale organo-mineral reactions of biochars in ferrosol: an investigation using microscopy. *Plant Soil*. **2012**, *357*, 369–380.

(112) Yang, F. et al. Stabilization of dissolvable biochar by soil minerals: release reduction and organo-mineral complexes formation. *J. Hazard. Mater*. **2021**, *412*, 125213.

(113) Yang, F. et al. Kaolinite enhances the stability of the dissolvable and undissolvable fractions of biochar via different mechanisms. *Environ. Sci. Technol*. **2018**, *52*, 8321–8329.

(114) Eckmeier, E. et al. Preservation of fire-derived carbon compounds and sorptive stabilisation promote the accumulation of organic matter in black soils of the Southern Alps. *Geoderma*. **2010**, *159*, 147–155.

(115) Glaser, B., Haumaier, L., Guggenberger, G. & Zech, W. Black carbon in soils: the use of benzenecarboxylic acids as specific markers. *Org. Geochem*. **1998**, *29*, 811–819.

(116) Wiedemeier, D. B., Hilf, M. D., Smittenberg, R. H., Haberle, S. G. & Schmidt, M. W. I. Improved assessment of pyrogenic carbon quantity and quality in environmental samples by high-performance liquid chromatography. *J. Chromatogr. A*. **2013**, *1304*, 246–250.

(117) Chen, X. et al. Rapid simulation of decade-scale charcoal aging in soil: changes in physicochemical properties and their environmental implications. *Environ. Sci. Technol*. **2023**, *57*, 128–138.

(118) Sun, T. et al. Rapid electron transfer by the carbon matrix in natural pyrogenic carbon. *Nat. Commun*. **2017**, *8*, 14873.

(119) Klüpfel, L., Keiluweit, M., Kleber, M. & Sander, M. Redox properties of plant biomassderived black carbon (biochar). *Environ. Sci. Technol*. **2014**, *48*, 5601–5611.

(120) Sun, T. et al. Simultaneous quantification of electron transfer by carbon matrices and functional groups in pyrogenic carbon. *Environ. Sci. Technol*. **2018**, *52*, 8538–8547.

(121) Kappler, A. et al. Biochar as an electron shuttle between bacteria and Fe(III) minerals. *Environ. Sci. Technol. Lett*. **2014**, *1*, 339–344.

(122) Lutfalla, S. et al. Pyrogenic carbon lacks long-term persistence in temperate arable soils. *Front. Earth Sci*. **2017**. https://doi.org/10.3389/feart.2017.00096.

(123) Bostick, K. W. et al. Biolability of fresh and photodegraded pyrogenic dissolved organic matter from laboratory-prepared chars. *J. Geophys. Res. Biogeosci*. **2021**, *126*, e2020JG005981.

(124) Goranov, A. I. et al. Microbial labilization and diversification of pyrogenic dissolved organic matter. *Biogeosciences*. **2022**, *19*, 1491–1514.

(125) Fischer, M. S. et al. Pyrolyzed substrates induce aromatic compound metabolism in the post-fire fungus, Pyronema domesticum. *Front. Microbiol.* **2021**. https://doi.org/10.3389/fmicb.2021.729289.

(126) De la Rosa, J. M., Miller, A. Z. & Knicker, H. Soil-borne fungi challenge the concept of long-term biochemical recalcitrance of pyrochar. *Sci. Rep*. **2018**, *8*, 2896.

(127) Graham, E. B. et al. Potential bioavailability of representative pyrogenic organic matter compounds in comparison to natural dissolved organic matter pools. *Biogeosciences*. **2023**, *20*, 3449–3457.

(128) Liang, B. et al. Stability of biomass-derived black carbon in soils. *Geochim. Cosmochim. Acta.* **2008**, *72*, 6069–6078.

(129) Nelson, A. R. et al. Wildfire-dependent changes in soil microbiome diversity and function. *Nat. Microbiol*. **2022**, *7*, 1419–1430.

(130) Schmidt, M. W. et al. Persistence of soil organic matter as an ecosystem property. *Nature*. **2011**, *478*, 49–56.

(131) Zimmerman, A. R. Abiotic and microbial oxidation of laboratory-produced black carbon (biochar). *Environ. Sci. Technol*. **2010**, *44*, 1295–1301.

(132) VanderRoest, J. P. et al. Fire impacts on the soil metabolome and organic matter biodegradability. *Environ. Sci. Technol*. **2024**, *8*, 4167-4180.

(133) de la Rosa, J. M. & Knicker, H. Bioavailability of N released from N-rich pyrogenic organic matter: an incubation study. *Soil Biol. Biochem*. **2011**, *43*, 2368–2373.

(134) Si, D. et al. Linking pyrogenic carbon redox property to arsenite oxidation: impact of N-doping and pyrolysis temperature. *J. Hazard. Mater*. **2023**, *445*, 130477.

(135) Pennino, M. J., Leibowitz, S. G., Compton, J. E., Beyene, M. T. & LeDuc, S. D. Wildfires can increase regulated nitrate, arsenic, and disinfection byproduct violations and concentrations in public drinking water supplies. *Sci. Total Environ*. **2022**, *804*, 149890.

(136) Thery, G. et al. Wildfires on Cr-rich ferralsols can cause freshwater Cr(VI) pollution: a pilot study in new Caledonia. *Appl. Geochem*. **2023**, *148*, 105513.

(137) Eary, L. E. & Rai, D. Chromate removal from aqueous wastes by reduction with ferrous ion. *Environ. Sci. Technol*. **1988**, *22*, 972–977.

(138) Sass, B. M. & Rai, D. Solubility of amorphous chromium(III)–iron(III) hydroxide solid solutions. *Inorg. Chem*. **1987**, *26*, 14.

(139) Zhong, D. et al. Mechanistic insights into adsorption and reduction of hexavalent chromium from water using magnetic biochar composite: key roles of Fe3O4 and persistent free radicals. *Environ. Pollut*. **2018**, *243*, 1302–1309.

(140) Xu, X., Huang, H., Zhang, Y., Xu, Z. & Cao, X. Biochar as both electron donor and electron shuttle for the reduction transformation of Cr(VI) during its sorption. *Environ. Pollut.* **2019**, *244*, 423–430.

(141) Xu, Z. et al. Participation of soil active components in the reduction of Cr(VI) by biochar: differing effects of iron mineral alone and its combination with organic acid. *J. Hazard. Mater*. **2020**, *384*, 121455.

(142) Borch, T. et al. Biogeochemical redox processes and their impact on contaminant dynamics. *Environ. Sci. Technol*. **2010**, *44*, 15–23.

(143) Fendorf, S. E. Surface reactions of chromium in soils and waters. *Geoderma*. **1995**, *67*, 55–71.

(144) Ku, P. J. et al. Origin, reactivity, and bioavailability of mercury in wildfire ash. *Environ. Sci. Technol*. **2018**, *52*, 14149–14157.

(145) Melendez-Perez, J. J. et al. Soil and biomass mercury emissions during a prescribed fire in the Amazonian rain forest. *Atmos. Environ*. **2014**, *96*, 415–422.

(146) Li, H.-H. et al. Impacts of forest fire ash on aquatic mercury cycling. *Environ. Sci. Technol*. **2022**, *56*, 11835–11844.

(147) Leng, L. et al. An overview of sulfur-functional groups in biochar from pyrolysis of biomass. *J. Environ. Chem. Eng*. **2022**, *10*, 107185.

(148) Nelson, D. C. et al. Karrikins discovered in smoke trigger arabidopsis seed germination by a mechanism requiring gibberellic acid synthesis and light. *Plant Physiol*. **2009**, *149*, 863–873.

(149) Soós, V., Badics, E., Incze, N. & Balázs, E. Fire-borne life: a brief review of smoke-induced germination. *Nat. Prod. Commun*. **2019**. https://doi.org/10.1177/1934578X19872925.

(150) Kochanek, J., Long, R. L., Lisle, A. T. & Flematti, G. R. Karrikins identified in biochars indicate post-fire chemical cues can influence community diversity and plant development. *PLoS ONE*. **2016**, *11*, e0161234.

(151) Moody, J. A., Shakesby, R. A., Robichaud, P. R., Cannon, S. H. & Martin, D. A. Current research issues related to post-wildfire runoff and erosion processes. *Earth Sci. Rev*. **2013**, *122*, 10–37.

(152) Kieta, K. A., Owens, P. N. & Petticrew, E. L. Determination of sediment sources following a major wildfire and evaluation of the use of color properties and polycyclic aromatic hydrocarbons (PAHs) as tracers. *J. Soils Sediment*. **2023**, *23*, 4187–4207.

(153) Barton, R. et al. Hydrology, rather than wildfire burn extent, determines post-fire organic and black carbon export from mountain rivers in central coastal California. *Limnol. Oceanogr. Lett.* **2023**, *9*, 70–80.

(154) Silins, U. et al. Five-year legacy of wildfire and salvage logging impacts on nutrient runoff and aquatic plant, invertebrate, and fish productivity. *Ecohydrology*. **2014**, *7*, 1508–1523.

(155) Emelko, M. B., Silins, U., Bladon, K. D. & Stone, M. Implications of land disturbance on drinking water treatability in a changing climate: demonstrating the need for 'source water supply and protection' strategies. *Water Res*. **2011**, *45*, 461–472.

(156) Bladon, K. D. Rethinking wildfires and forest watersheds. *Science*. **2018**, *359*, 1001–1002.

(157) Nunes, J. P. et al. Assessing water contamination risk from vegetation fires: Challenges, opportunities and a framework for progress. *Hydrol. Process*. **2018**, *32*, 687–694.

(158) Silins, U., Stone, M., Emelko, M. B. & Bladon, K. D. Sediment production following severe wildfire and post-fire salvage logging in the Rocky Mountain headwaters of the Oldman River Basin, Alberta. *Catena*. **2009**, *79*, 189–197.

(159) Emmerton, C. A. et al. Severe western Canadian wildfire affects water quality even at large basin scales. *Water Res*. **2020**, *183*, 116071.

(160) Writer, J. H. et al. Water treatment implications after the High Park Wildfire, Colorado. *J. AWWA*. **2014**, *106*, E189–E199.

(161) Hohner, A. K., Cawley, K., Oropeza, J., Summers, R. S. & Rosario-Ortiz, F. L. Drinking water treatment response following a Colorado wildfire. *Water Res*. **2016**, *105*, 187–198.

(162) Robinne, F. N. et al. Regional-scale index for assessing the exposure of drinking-water sources to wildfires. *Forests*. **2019**, *10*, 1–21.

(163) Robinne, F. N. et al. Global index for mapping the exposure of water resources to wildfire. *Forests*, **2016**, *7*, 1–16.

(164) Martin, D. A. At the nexus of fire, water and society. *Philos. Trans. R. Soc. B*. **2016**, *371*, 20150172.

(165) Rhoades, C. C. et al. The influence of wildfire extent and severity on streamwater chemistry, sediment and temperature following the Hayman fire, Colorado. *Int. J. Wildland Fire.* **2011**, *20*, 430–442.

(166) Rhoades, C. C. et al. The legacy of a severe wildfire on stream nitrogen and carbon in headwater catchments. *Ecosystems*. **2019**, *22*, 643–657.

(167) Burke, M. P. et al. Pre- and post-fire pollutant loads in an urban fringe watershed in southern California. *Environ. Monit. Assess*. **2013**, *185*, 10131–10145.

(168) Gustine, R. N., Hanan, E. J., Robichaud, P. R. & Elliot, W. J. From burned slopes to streams: how wildfire affects nitrogen cycling and retention in forests and fire-prone watersheds. *Biogeochemistry*. **2022**, *157*, 51–68.

(169) Paul, M. J. et al. Wildfire induces changes in receiving waters: a review with considerations for water quality management. *Water Resour. Res*. **2022**, *58*, e2021WR030699.

(170) Rozendaal, D. M. A. et al. Demographic drivers of aboveground biomass dynamics during secondary succession in neotropical dry and wet forests. *Ecosystems*. **2017**, *20*, 340–353.

(171) Turner, M. G., Smithwick, E. A. H., Metzger, K. L., Tinker, D. B. & Romme, W. H. Inorganic nitrogen availability after severe stand-replacing fire in the Greater Yellowstone ecosystem. *Proc. Natl Acad. Sci. USA*. **2007**, *104*, 4782–4789.

(172) Minshall, G. W. Responses of stream benthic macroinvertebrates to fire. *For. Ecol. Manag.* **2003**, *178*, 155–161.

(173) Kronvang, B., Laubel, A. & Grant, R. Suspended sediment and particulate phosphorus transport and delivery pathways in an arable catchment, Gelbæk stream, Denmark. *Hydrol. Process.* **1997**, *11*, 627–642.

(174) House, W. A. Geochemical cycling of phosphorus in rivers. *Appl. Geochem*. **2003**,*18*, 739–748.

(175) Emelko, M. B. et al. Sediment-phosphorus dynamics can shift aquatic ecology and cause downstream legacy effects after wildfire in large river systems. *Glob. Change Biol*. **2016**, *22*, 1168–1184.

(176) Riedel, T., Biester, H. & Dittmar, T. Molecular fractionation of dissolved organic matter with metal salts. *Environ. Sci. Technol*. **2012**, *46*, 4419–4426.

(177) Harper, A. R. et al. Chemical composition of wildfire ash produced in contrasting ecosystems and its toxicity to Daphnia magna. *Int. J. Wildland Fire*. **2019**, *28*, 726–737.

(178) Ré, A. et al. Cytotoxic effects of wildfire ashes: in-vitro responses of skin cells. *Environ. Pollut.* **2021**, *285*, 117279.

(179) Afonso, M. et al. Effects of pine and eucalypt ashes on bacterial isolates from the skin microbiome of the fire salamander (Salamandra salamandra). *Sci. Total Environ*. **2022**, *841*, 156677.

(180) Coelho, L. et al. Effects of eucalypt ashes from moderate and high severity wildfires on the skin microbiome of the Iberian frog (Rana iberica). *Environ. Pollut*. **2022**, *313*, 120065.

(181) Priya, P. S. et al. Syringol, a wildfire residual methoxyphenol causes cytotoxicity and teratogenicity in zebrafish model. *Sci. Total Environ*. **2023**, *864*, 160968.

(182) Campos, I. et al. Assessment of the toxicity of ash-loaded runoff from a recently burnt eucalypt plantation. *Eur. J. For. Res*. **2012**, *131*, 1889–1903.

(183) Brown, D. J. et al. Comparison of short term low, moderate, and high severity fire impacts to aquatic and terrestrial ecosystem components of a southern USA mixed pine/ hardwood forest. *For. Ecol. Manag.* **2014**, *312*, 179–192.

(184) Munro, N. T., Kovac, K.-J., Niejalke, D. & Cunningham, R. B. The effect of a single burn event on the aquatic invertebrates in artesian springs. *Austral Ecol*. **2009**, *34*, 837–847.

(185) Martens, A. M. et al. Long-term impact of severe wildfire and post-wildfire salvage logging on macroinvertebrate assemblage structure in Alberta's Rocky Mountains. *Int. J. Wildland Fire*. **2019**, *28*, 738–749.

(186) Wang, J.-J., Dahlgren, R. A., Erşan, M. S., Karanfil, T. & Chow, A. T. Wildfire altering terrestrial precursors of disinfection byproducts in forest detritus. *Environ. Sci. Technol.* **2015**, *49*, 5921–5929.

(187) Wang, J.-J., Dahlgren, R. A. & Chow, A. T. Controlled burning of forest detritus altering spectroscopic characteristics and chlorine reactivity of dissolved organic matter: effects of temperature and oxygen availability. *Environ. Sci. Technol*. **2015**, *49*, 14019–14027.

(188) Muellner, M. G. et al. Haloacetonitriles vs. regulated haloacetic acids: are nitrogencontaining DBPs more toxic? *Environ. Sci. Technol*. **2007**, *41*, 645–651.

(189) Chow, A. T., Tsai, K.-P., Fegel, T. S., Pierson, D. N. & Rhoades, C. C. Lasting effects of wildfire on disinfection by-product formation in forest catchments. *J. Environ. Qual*. **2019**, *48*, 1826–1834.

(190) Whicker, J. J., Pinder, J. E., Breshears, D. D. & Eberhart, C. F. From dust to dose: effects of forest disturbance on increased inhalation exposure. *Sci. Total Environ*. **2006**, *368*, 519–530.

(191) Grant, E. & Runkle, J. D. Long-term health effects of wildfire exposure: a scoping review. *J. Clim. Change Health*. **2022**, *6*, 100110.

(192) Fann, N. et al. The health impacts and economic value of wildland fire episodes in the U.S.: 2008–2012. *Sci. Total. Env.* **2018**, *610–611*, 802–809.

(193) Haikerwal, A., Doyle, L. W., Wark, J. D., Irving, L. & Cheong, J. L. Y. Wildfire smoke exposure and respiratory health outcomes in young adults born extremely preterm or extremely low birthweight. *Environ. Res*. **2021**, *197*, 111159.

(194) Gould, C. F. et al. Health effects of wildfire smoke exposure. *Annu. Rev. Med*. **2024**, *75*, 277–292.

(195) National Academies of Sciences, Engineering, and Medicine. The Chemistry of Fires at the Wildland–Urban Interface https://doi.org/10.17226/26460 (National Academies Press, **2022**).

(196) Bucheli, T. D., Blum, F., Desaules, A. & Gustafsson, Ö. Polycyclic aromatic hydrocarbons, black carbon, and molecular markers in soils of Switzerland. *Chemosphere*. **2004**, *56*, 1061–1076.

(197) Choi, S.-D. Time trends in the levels and patterns of polycyclic aromatic hydrocarbons (PAHs) in pine bark, litter, and soil after a forest fire. *Sci. Total Environ*. **2014**, *470–471*, 1441–1449.

(198) Santín, C. et al. Carbon sequestration potential and physicochemical properties differ between wildfire charcoals and slow-pyrolysis biochars. *Sci. Rep*. **2017**, *7*, 11233.

(199) Kim, E.-J., Oh, J.-E. & Chang, Y.-S. Effects of forest fire on the level and distribution of PCDD/Fs and PAHs in soil. *Sci. Total Environ*. **2003**, *311*, 177–189.

(200) Chen, H., Uzun, H., Chow, A. T. & Karanfil, T. Low water treatability efficiency of wildfire-induced dissolved organic matter and disinfection by-product precursors. *Water Res.* **2020**, *184*, 116111.

(201) Fernandez-Garcia, V. MOSEV: A global burn severity database from MODIS (2000-2020). *Earth Syst. Sci. Data*. **2021**, *13*, 1925–1938.

(202) Waters, M. T., Scaffidi, A., Flematti, G. R. & Smith, S. M. The origins and mechanisms of karrikin signalling. Curr. Opin. *Plant Biol*. **2013**, *16*, 667–673.

(203) Keeley, J. E. Fire intensity, fire severity and burn severity: a brief review and suggested usage. *Int. J. Wildland Fire*. **2009**, *18*, 11.

(204) Parsons, A., Robichaud, P. R., Lewis, S. A., Napper, C. & Clark, J. T. Field Guide for Mapping Post-Fire Soil Burn Severity, 243 (Citeseer, **2010**).

(205) Schwertmann, U. in Soil Color, 51–69 (Wiley, **1993**).

CHAPTER 3: FIRE IMPACTS ON THE SOIL METABOLOME AND ORGANIC MATTER BIODEGRADABILITY[2]

3.1 INTRODUCTION

Wildfires are widespread ecosystem disturbances that burn millions of hectares each year and are beneficial within fire-adapted environments.[1–4] However, over the past five decades, wildfires have become more frequent, severe (i.e., more vegetation and organic matter are consumed during burning), intense (i.e., higher temperatures and energy output), and are projected to increase in size.[5–8] Thus, understanding how wildfires impact terrestrial ecosystems and the soils that support them is essential.

Wildfires change the composition of both soil organic matter (SOM) (a heterogeneous mixture of organic molecules ranging from low-molecular weight metabolites to lignin-like, proteinaceous, and humic-like substrates) and the soil microbiome (an assemblage of archaea, bacteria, fungi, and viruses).[9] SOM serves as carbon and energy sources for microbes, and microbial metabolism of SOM depends on SOM composition.[10] Wildfires disrupt the interplay between SOM and microbial communities by reducing soil microbial biomass,[11] decreasing microbial Shannon's diversity,[12] shifting microbial community composition (e.g., enrichment in Actinobacteria and loss of ectomycorrhizal fungi)[12,13] and function (e.g., increased thermotolerance and aromatic organic matter degradation),[12,14–17] altering soil mycorrhizal-plant associations,[13] and changing SOM composition.[9,12,18–21] Therefore, studying linkages between

---

[2]Reproduced with permissions from VanderRoest, J. P.; Fowler, J. A.; Rhoades, C. C.; Roth, H. K.; Broeckling, C. D.; Fegel, T. S.; McKenna, A. M.; Bechtold, E. K.; Boot, C. M.; Wilkins, M. J.; Borch, T. Fire Impacts on the Soil Metabolome and Organic Matter Biodegradability. Environmental Science and Technology. 2024, 58, 4167-4180. https://doi.org/10.1021/acs.est.3c09797. Copyright 2024, American Chemical Society.

postfire SOM composition and microbial community structure is essential to understand the extent that microbes metabolize SOM in burned soils to fuel postfire microbial recolonization and soil recovery.

Extensive work has evaluated the impact of wildfires on SOM and the formation, composition, and reactivity of pyrogenic organic matter (PyOM), which is thermochemically altered organic matter.[9,18,21–36] PyOM can be highly resistant to biological degradation compared to unburned OM, with half-lives ranging over millennial time scales (~500 to 8000 years).[23,37] However, recent review papers and laboratory studies indicate that PyOM can exhibit varying degrees of biodegradability with certain carbon pools featuring half-lives of a few weeks to months.[22,33,38] Fischer et al. observed PyOM metabolism by incubating fungi with ^{13}C-labeled burned pine wood for 57 days and detected the release of respired ^{13}C-labeled CO_2.[39] Goranov et al. and Bostick et al. conducted incubations of aqueous extracts of burned oak wood with soil-extracted microbes and, respectively, observed a 16% decrease in C content and a 25 to 67% decrease in aromatic content after only 10 days.[40,41] These studies demonstrate rapid PyOM metabolism that includes aromatic substrates previously considered highly resistant to biodegradation.[39,41] However, laboratory studies have not historically accounted for the polyfunctionality, polydispersity, and molecular complexity of soils, soil carbon, and environmental factors that influence SOM biodegradation (e.g., organo-mineral interactions, soil redox conditions).[42–44] Therefore, it is necessary to evaluate 1) if the biodegradability of laboratory-produced PyOM accurately represents SOM biodegradability in wildfire-burned soils and 2) what biochemical mechanisms drive PyOM degradation.

Prior studies propose mechanisms for aromatic SOM biodegradation in burned soils, but those mechanisms have not been confirmed with chemical analyses such as mass spectrometry.[12,39]

Fischer et al. and Nelson et al. observed the expression of genes associated with the degradation of aromatic molecules within microbial communities that were either incubated with pyrogenic carbon or collected from wildfire-burned soils.[12,39] Both studies independently proposed pathways that generate two key intermediate compounds: catechol and protocatechuate.[12,39] The proposed end products of the degradation are the coenzymes succinyl-CoA and acetyl-CoA, which feed into the citric acid cycle: a central metabolic pathway that releases stored energy from carbohydrates, fats, and proteins, fueling microbial activity.[12,39] These proposed pathways suggest that PyOM, which can remain stable for centuries, can also be metabolized and transformed into metabolites that funnel into key metabolic pathways. However, the proposed pathways were inferred based only on the presence and expression of genes associated with aromatic compound degradation. With the exception of catechol, no other intermediates in these pathways have been detected in burned soils.[45] Moreover, detailed metabolomics analysis of SOM from burned soils has not yet been conducted, so the relative abundance of low-molecular weight metabolites (e.g., saccharides, organic acids, and amino acids) in burned soils remains unknown.

Mass spectrometry can address these knowledge gaps by detecting metabolites and determining broader SOM composition. Pyrolysis gas chromatography−mass spectrometry (GC-MS) has been used to detect low molecular weight molecules in burned soils to examine general changes in postfire SOM composition rather than determining shifts in metabolite content related to microbial metabolism.[46–51] Therefore, GC-MS, which can target specific molecules (targeted analysis) and annotate detected peaks (nontargeted analysis), could be used to elucidate the unknown pools of metabolites in burned soils that likely interact with active microbial assemblages.[52,53] While ideal for detecting specific metabolites, GC-MS features relatively low mass resolution and mass accuracy, limiting its ability to evaluate SOM composition broadly.

Fourier transform ion cyclotron resonance mass spectrometry (FT-ICR MS) has high mass resolving power (up to 3,000,000 at m/z 200), high accuracy (subppm mass measurement error), and assigns molecular formulas across a wide mass range (175−1200 Da).[54] Due to the complexity of SOM, FT-ICR MS is an ideal technique for elucidating SOM composition broadly to compensate for the resolution limitations of GC-MS.[12,18,19,24,55,56]

We simulated a wildfire using a controlled pyrocosm approach[57] to elucidate SOM composition changes associated with microbial activity in burned soil. The objectives were to 1) characterize SOM and microbial community composition throughout the first month following fire, 2) identify postfire shifts in the soil metabolome and metabolite abundances, and 3) determine how changes in SOM composition correspond to microbial community structure. We hypothesized that 1) soil microbes present immediately after burning would mineralize SOM and release CO_2 and that 2) intermediate metabolites in aromatic degradation pathways - namely, catechol, protocatechuate, and citric acid cycle metabolites - would be enriched in burned soil.[12,39] We addressed these objectives and hypotheses by characterizing SOM composition at the molecular level with GC-MS and FT-ICR MS and by characterizing soil microbiome composition using16S rRNA gene and ITS amplicon sequencing.

3.2 MATERIALS AND METHODS

3.2.1 PYROCOSM PREPARATION AND BURNING

Mineral soil and forest litter were collected in August 2022 from an unburned portion of a lodgepole-pine-dominated (Pinus contorta) forest located along Long Draw Road near Cameron Pass, Colorado (40° 30’ 55.4400” N and 105° 46’ 4.9080” W) with an approximate elevation of 3050 m.[58] Total annual precipitation averages 783 mm, and mean annual temperature is 1.1 °C with average annual minima and maxima of −6.4 °C and 8.8 °C, respectively.[58] This location is

representative of a subalpine forest that is burned by wildfires. After removing the litter layer and O-horizon, mineral soil was collected at a depth of 0−10 cm, sieved to 4 mm sieve, homogenized by mixing, and added into pyrocosms.

Pyrocosms simulate a wildfire burn and provide control over experimental variables (e.g., soil type, fuel type, burn duration).[57] The pyrocosms were 53 L galvanized steel buckets (56 cm in length, 25 cm in height, and 38 cm in width) with holes (0.56 cm diameter) drilled into the sides of the pyrocosm (**Figure 3.1**). K-type thermocouples (Extech Instruments) were inserted at depths of 1, 5, 8, and 12 cm below the mineral soil surface for three pyrocosms that were going to be burned labeled "B1," "B2," and "B3" ("B" representing burned). The tips of the thermocouples reached the central area of the B1, B2, and B3 pyrocosms. Three control pyrocosms were labeled "UB1," "UB2," and "UB3" ("UB" representing unburned).

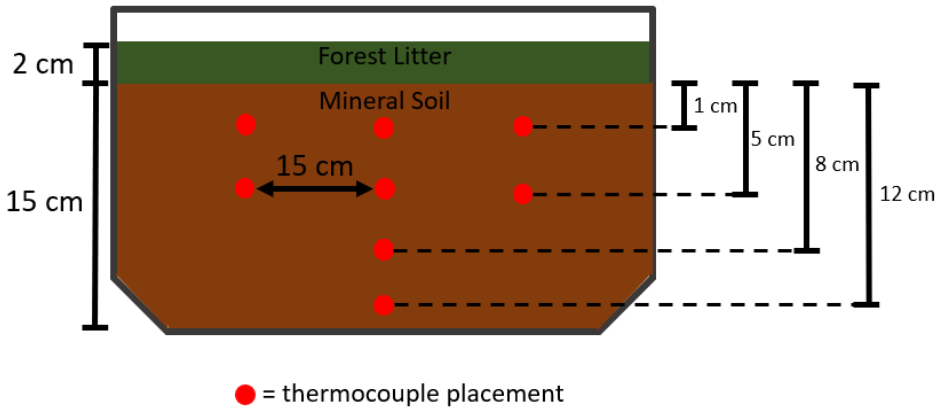

Figure 3.1. Schematic of pyrocosm and thermocouple placement. The dimensions of the pyrocosm were 56 cm in length, 25 cm in height, and 38 cm in width. Figure was produced using images from Microsoft Powerpoint.

The pyrocosms were transported to the Colorado State University Agricultural Research, Development, and Education Center (ARDEC). The B1, B2, and B3 pyrocosms were dug 4.5 m apart to a depth at which the mineral soil inside the pyrocosms was level with the surrounding soil. The UB1, UB2, and UB3 pyrocosms were positioned approximately 30 m away from the B1, B2, and B3 pyrocosms. The collected forest litter was added on top of all six pyrocosms to a depth of

approximately 2 cm. The average gravimetric water content of the six pyrocosms prior to burning was 8.6 ± 1.1%.

Approximately 21 kg of lodgepole pine wood was burned on each of the B1, B2, and B3 pyrocosms (**Figure 3.2**), and soil temperature was monitored during burning (**Figure 3.3**). The measured temperatures were representative of a high intensity wildfire.[59] No wood was burned on top of the UB1, UB2, or UB3 pyrocosms. The morning after the burns (referred to as "Day 0"), a soil density core (6 cm diameter, 10 cm height) was inserted into each of the six pyrocosms. The ash layer in the core was discarded for B1, B2, and B3, and the forest litter layer in the core was discarded for UB1, UB2, and UB3. Mineral soil was sampled from the core to a depth of 0−5 cm. Next, 2 L of Milli-Q water (18 MΩ cm) was added to all pyrocosms to simulate a 1.27 cm precipitation event which falls within the range of precipitation events occurring within Cameron Pass.[58] No additional water was deliberately added to the pyrocosms. Limited natural precipitation events did occur during the soil sampling period (**Figure 3.4**).[60]

Figure 3.2. Pyrocosm assembly and ignition. (A) Mineral soil samples that were packed into the pyrocosms. (B) Pyrocosm being dug into a barren agricultural field with thermocouples inserted into the pyrocosm. (C) Igniting the pyrocosms. (D) Three replicates of burned pyrocosms.

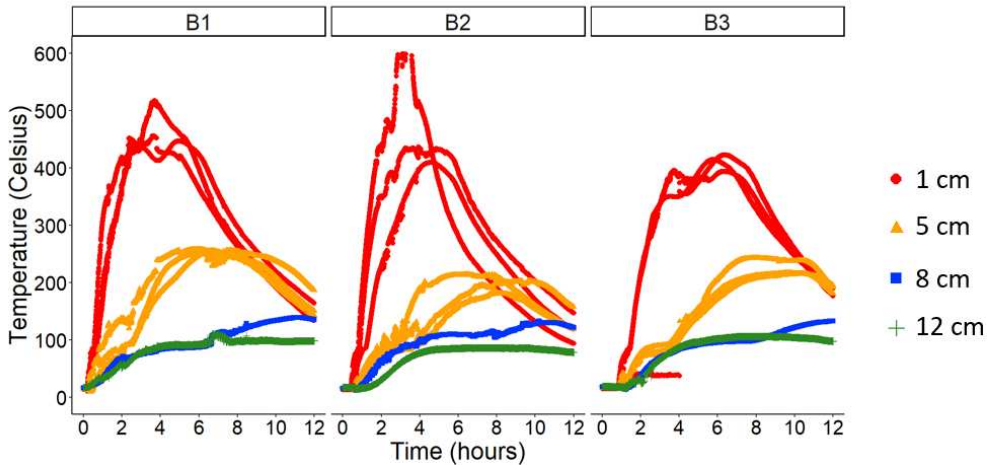

Figure 3.3. Soil temperatures at various depths of the three burned pyrocosms (B1, B2, and B3) measured with thermocouples. Note: the 1 cm thermocouple in B3 featuring lower initial temperature measurements compared to the other 1 cm thermocouples in B3 was unplugged and re-plugged into its datalogger at approximately the four-hour mark of the burn event. After this adjustment, the temperature measurements of that seemingly faulty thermocouple were comparable to the other 1 cm thermocouples in B3.

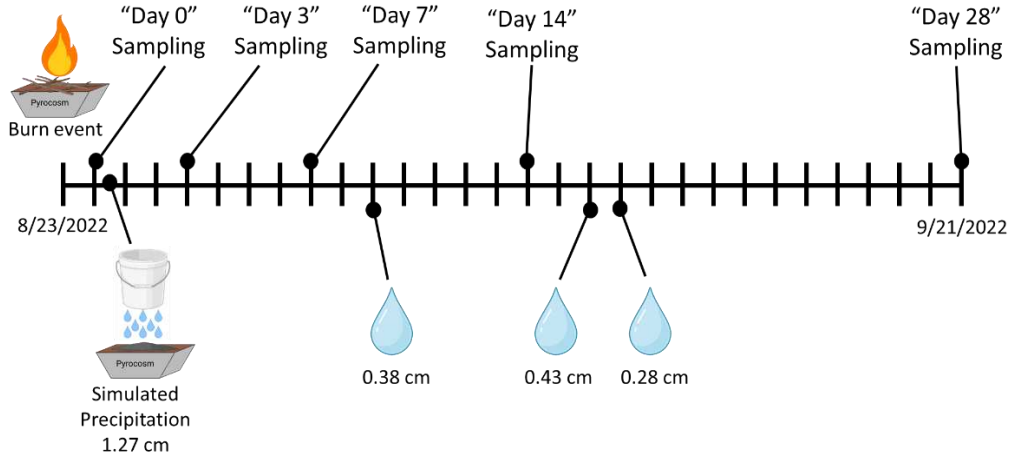

Figure 3.4. Schematic for soil sampling dates. Each tick mark represents one day. Raindrop icon indicates a precipitation event. Precipitation data was acquired from Colorado State University's CoAgMET agricultural weather station database.[60] The figure was created with BioRender.com and Microsoft Powerpoint. See **Table 3.1** for a description of what analytical techniques for soils collected on each sampling day.

Mineral soil samples (0−5 cm) were collected 3 days (”Day 3”), 7 days (”Day 7”), 14 days (”Day 14”), and 28 days (”Day 28”) after the burn event, generating a total of 30 mineral soil samples for the entire study that were stored in zip-top bags in a fridge at 4 °C (**Figure 3.4**). Subsamples of all 30 soil samples were stored in sterile Whirlpak bags (Uline, Pleasant Prairie, WI, USA) in a −80 °C freezer for later microbial analyses. During this 28-day sampling period, the pyrocosms were left at ARDEC and were not disturbed or covered. This 28-day sampling period was selected due to the paucity of studies examining immediate postfire alterations to SOM and soil microbes whereas studies sampling soil multiple months and years postfire are comparatively common.[12,13,18,24,55,61,62] Pyrocosms were used in this experiment for the following reasons. Inserting thermocouples into the pyrocosms allowed for soil temperature monitoring which is essential for evaluating the intensity of the burns. Within this experiment, high intensity burn conditions were observed. Sampling soils immediately after burning is convenient with pyrocosms which is often unachievable with naturally burned areas. Pyrocosms feature burned soils which model the complex, heterogenous soil systems found in naturally burned areas which is not present in laboratory studies. Additionally, post-fire areas are affected by environmental conditions such as wind deposition of microbes, diurnal fluctuations in temperature, and precipitation events. Using pyrocosms incorporates this variability of environmental conditions into the experimental design, making the results more representative of a naturally burned system compared to laboratory studies. See **Table 3.1** for a summary of the analytical techniques employed for each soil sample.

Table 3.1. Analytical techniques employed for each soil sample. "X" indicates that the technique was used while "-" indicates that the technique was not used.

Technique:	Sampling Day				
	Day 0	**Day 3**	**Day 7**	**Day 14**	**Day 28**
Total Soil Carbon and Nitrogen	X	X	X	X	X
pH	X	X	X	X	X
Water Extractable Organic Carbon	X	X	X	X	X
Water Extractable Total Nitrogen	X	X	X	X	X
Ammonium	X	X	X	X	X
Gas Chromatography-Mass Spectrometry	X	X	X	X	X
Fourier Transform Ion Cyclotron Resonance Mass Spectrometry	X	-	-	-	X
Soil CO_2 Respiration Incubation	X	-	X	-	X
Microbial Analyses	X	X	X	X	X

3.2.2 SOIL CARBON AND NITROGEN

Air-dried, 2-mm sieved mineral soil was ground and sieved through a 125-μm sieve. Total carbon and total nitrogen were measured using a Carbon Nitrogen Analyzer (VELP Scientifica CN 802, Deer Park, NY, USA).

3.2.3 SOIL PH

For each soil sample, 20 g of air-dried (24 h at room temperature), 2-mm sieved mineral soil was shaken with 40 mL of Milli-Q water for 1 h. A Thermo Scientific Orion Star A215 pH/conductivity meter and a Thermo Scientific Orion Double Junction pH probe were calibrated

with VWR pH reference standards, and the pH electrode was inserted into the soil-water slurry after shaking the soil slurry by hand to resuspend the soil. Then, 2 mL of a 0.21 M solution of $CaCl_2$ (Fisher Chemical) was added to each sample to produce a final concentration of 0.01 M $CaCl_2$. These soil-water slurries were shaken by hand, and pH was measured.

3.2.4 WATER-EXTRACTABLE ORGANIC CARBON AND WATER-EXTRACTABLE TOTAL NITROGEN

For each soil sample, 20 g of air-dried (24 h at room temperature), 2-mm sieved soil, and 100 mL of Milli-Q water was shaken for 1 h at 200 rpm. The supernatant from each sample was then filtered through 0.45 μm glass fiber filter (Advantec MFS, Inc.). Dissolved organic carbon and dissolved total nitrogen for each sample were measured using a TOC-L Shimadzu analyzer (Shimadzu Corporation, Columbia, MD, USA). The measured dissolved organic carbon and dissolved total nitrogen mass were then normalized to the mass of soil to calculate water-extractable organic carbon and water-extractable total nitrogen, respectively.

3.2.5 AMMONIUM

For each soil sample, 10 g of air-dried, 2-mm sieved mineral soil was shaken with 50 mL of 2 M KCl for 1 h followed by filtration through alpha cotton cellulose filter paper (Whatman plc). Ammonium concentrations were measured using a flow injection analyzer (Lachat QuikChem, 8500, Hach Scientific, Loveland, CO).

3.2.6 GAS CHROMATOGRAPHY-MASS SPECTROMETRY (GC-MS)

Soil-water extracts were filtered, derivatized via methoximation and silylation, and analyzed with an electron impact, Thermo Trace 1310 GC coupled with ISQ single quadruple MS with liquid autosampler. For each soil sample, 2 g of air-dried, 2-mm sieved soil, 4 mL of Milli-Q water, and 4 mL of 1 μg/mL ^{13}C-glucose solution were added to a 15 mL centrifuge tube which

was shaken for 210 rpm for 1 hour followed by centrifugation. This process was repeated for a 15-mL centrifuge tube without soil to act as an experimental blank. The supernatant was filtered through a nylon 0.45 µm pore size, 13 mm diameter filter (Celltreat Scientific Products) into a 20 mL scintillation vial. From each sample, 0.5 mL of filtrate was pooled into a 20 mL scintillation vial to generate a pooled quality control sample. For each sample, 1 mL of filtrate was transferred to a 1.5 mL Eppendorf tube. Five 1 mL aliquots of the pooled quality control sample were transferred to separate 1.5 mL Eppendorf tubes. All Eppendorf tubes were then lyophilized followed by the addition of 75 µL of Milli-Q water and 175 µL of methanol (HPLC grade, Sigma-Aldrich Chemical Co.) to each Eppendorf tube which were then vortexed and stored in a -20˚C freezer for 15 h. After centrifugation, 200 µL of supernatant from each Eppendorf tube were transferred to separate Thermo Scientific 12 x 32 mm Amber Target DP vials which were then dried under nitrogen gas.

The blank, five pooled quality control samples, and soil extracts were derivatized via the following procedure. Fifty milliliters of 25 mg/mL methoxyamine hydrochloride (Sigma Aldrich, >98% purity) in pyridine (Sigma Aldrich, >99% purity) was added to each vial followed by vortexing for 20 s and an incubation at 60˚C for 45 min. The vials were vortexed for 20 s, sonicated for 10 min, and then incubated again at 60˚C for 45 min. After centrifugation, 50 µL of *N*-methyl-*N*-(trimethylsilyl)trifluoroacetamide (MSTFA) + 1% trimethylchlorosilane (TMCS) (Thermo-Scientific) was added to each vial followed by vortexing for 30 s and a 30 min incubation at 60˚C. After centrifugation, the contents of the vials were transferred to glass inserts which were placed back in the vials. For samples that had precipitates in the bottom of the glass inserts, 80 µL of the supernatant was transferred to a new glass insert. The samples were then analyzed through GC-MS (Thermo Trace 1310 GC coupled with ISQ single quadruple MS with liquid autosampler).

Samples (1 μL) were injected at a 10:1 split ratio to a 30 m DB-5ms column (Agilent, 0.25 mm i.d., 0.25 μm film thickness; P/N# 122-5532) with a 1.2 mL/min helium gas flow rate. GC inlet was held at 285°C. The oven program starts at 80°C for 1 min, followed by a ramp of 15°C/min to 330°C and a 7 min hold. Masses between 50-650 m/z were scanned at 5 scans/s under electron impact ionization. Transfer line and ion source were held at 300 and 260°C, respectively.

Chromatogram peaks were integrated using Chromeleon 7 software (Thermo Fisher). Non-targeted analysis was conducted using ADAP-BIG (Java Version: 19.0.1, Du-Lab) software and ADAP-KDB (Beta Version, Du-Lab, accessed 2/8/2023) website. The following databases were used for peak annotation: ADAP-KDB Consensus Spectra, MS-DIAL GCMS Library with Kovats RI, and MassBank 2022.06 (GC-MS). Experimental spectra were compared to library spectra using NIST MS Search (Version 2.3). Peak areas were normalized via total ion current normalization. Zero values for each metabolite were replaced with 10% of the minimum abundance value of the corresponding metabolite. These normalized peak areas with the replaced zero values were Pareto-scaled prior to principal component analysis and nonparametric permutational multivariate analysis of variance (PERMANOVA) analysis. For PERMANOVA analysis, the pareto-scaled peak areas were transformed into a Euclidean distance matrix within the "adonis2" function in the R-programming vegan package.[63] Euclidean distance matrices were used for PERMANOVA analysis because they are commonly used distance matrices that work especially well for compact and isolated clusters which were evident in the PCA plots of Figure 2 and Figure S12 figure.[64,65] R programming code for PERMANOVA analysis for the PCA plots and raw GC-MS data files can be found at this public data repository: https://github.com/jacobvanderroest/Pyrocosm_Project_JPV.

Additionally, the data in Figure 2 are of considerable quality based on two lines of evidence: 1). The quality control samples (which are a mixture of burned and unburned soil water extracts) plotted in between the burned and unburned samples in Figure 2A. 2). The unnormalized and total ion current normalized coefficient of variation values for the ^{13}C-labelled glucose internal standard peak areas in the quality controls were 6.0% and 6.5% respectively (see **Equation 3.1**).

Equation 3.1. Coefficient of variation=

$$\frac{\text{Standard deviation of } ^{13}\text{C-labelled glucose internal standard peak values in quality control samples}}{\text{Average } ^{13}\text{C-labelled glucose internal standard peak values in quality control samples}} * 100\%$$

Peaks that were annotated as a saccharide molecule were referred to simply as “saccharide” and arbitrarily assigned a corresponding number to distinguish them. This was conducted because annotating specific saccharides and assigning chemical identities can be unclear. For example, galactose, glucose, and mannose all have the same molecular weight (180.2 g/mol) and only differ by the stereochemistry of hydroxyl groups, resulting in similar fragmentation patterns. Thus, we have low confidence in assigning specific saccharide identities. Therefore, a more conservative annotation approach was used by referring to annotated saccharides as “saccharide” rather than assigning specific chemical identities (e.g., glucose or galactose).

Catechol and protocatechuate were detected by running catechol (Sigma Aldrich, >99 % purity) and protocatechuate (Sigma Aldrich, >97 % purity) standards on the GC-MS instrument and extracting ion chromatograms to detect these specific molecules. For ion chromatogram analysis, a 254 MS quantitation peak was used for catechol, and a 193 MS quantitation peak was used for protocatechuate.

3.2.7 TWENTY-ONE TESLA FOURIER TRANSFORM ION CYCLOTRON RESONANCE MASS SPECTROMETRY (FT-ICR MS)

For each sample, 50 g of air-dried, 2-mm sieved soil sample and 100 mL of Milli-Q water were shaken for 19 hr at 170 rpm. After centrifugation, the supernatant was filtered through a 0.22 µm polyethersulfone membrane (Merck Millipore Ltd.) using a vacuum flask-based filtration manifold. The extract was acidified to a pH of 2 using a 37 % HCl solution (Fisher Chemical) and concentrated via solid phase extraction according to Dittmar et al. (2008).[66] Agilent Bond Elut PPL (Priority Pollutant) styrene-divinylbenzene polymer cartridges (3 mL, 200 mg) were first rinsed with 15 mL of methanol (HPLC grade, Sigma-Aldrich Chemical Co.) and then rinsed with 15 mL of pH 2 water. Each extract sample was passed through its own PPL cartridge followed by another rinse of 15 mL of pH 2 water to remove any salts. Each sample was eluted from its cartridge by passing 2 mL of grade methanol HPLC grade, Sigma-Aldrich Chemical Co.) through the cartridge and collecting the eluent in a clean glass test tube (combusted at 400˚C). The eluent was transferred to Thermo Scientific 12 x 32 mm Amber Target DP vials, and those vials were then sent to the High Magnetic Field Laboratory at Florida State University for FT-ICR MS analysis.

Sample solution was infused via a microelectrospray source (50 µm i.d. fused silica emitter) at 500 nL/min by a syringe pump.[67] For negative-ion electrospray ionization formation, the emitter voltage ranged from -2.4 to -2.9 kV, the S-lens retention factor level was 45 %, and the temperature of the heated metal capillary was 350°C. For positive-ion electrospray ionization formation, the emitter voltage ranged from 2.4 to 2.9 kV, the S-lens retention factor level was 45 %, and the temperature of the heated metal capillary was 350°C. Extracts were analyzed with a custom-built hybrid linear ion trap FT-ICR mass spectrometer equipped with a 21 T superconducting solenoid magnet.[68,69] Ions were initially accumulated in an external multipole ion

guide (1-5 ms) and released *m/z*-dependently by decrease of an auxiliary radio frequency potential between the multipole rods and the end-cap electrode.[70] Ions were excited to *m/z*-dependent radius to maximize the dynamic range and number of observed mass spectral peaks (32-64 %), and excitation and detection were performed on the same pair of electrodes.[71] The dynamically harmonized ICR cell in the 21 T FT-ICR is operated with 6 V trapping potential.[70,72] Time-domain transients of 3.1 s were conditionally co-added and acquired with the Predator data station that handled excitation and detection only, initiated by a TTL trigger from the commercial Thermo data station, with 100 time-domain acquisitions summed for all experiments.[73] Mass spectra were phase-corrected[74] and internally calibrated with 10-15 highly abundant homologous series that span the entire molecular weight distribution based on the "walking" calibration method.[75] Experimentally measured masses were converted from the International Union of Pure and Applied Chemistry (IUPAC) mass scale to the Kendrick mass scale[76] for rapid identification of homologous series for each heteroatom class (i.e., species with the same $C_cH_hN_nO_oS_s$ content, differing only by degree of alkylation).[77] Peaks with signal magnitude greater than six times the baseline root-mean-square (rms) noise at *m/z* 500 were exported to peak lists.

Molecular formula assignments and data visualization were performed with PetroOrg © software.[78] Molecular formulas containing carbon (C), hydrogen (H), oxygen (O), nitrogen (N), and sulfur (S) were assigned using the experimentally measured masses.[78–81] Singly charged ions (170-1200 Da) were assigned molecular formulae within the bounds of $C_{1\text{-}150}H_{1\text{-}200}O_{1\text{-}40}N_{0\text{-}4}S_{0\text{-}2}$ for negative ESI samples and $C_{2\text{-}150}H_{2\text{-}200}O_{1\text{-}35}N_{0\text{-}4}S_{0\text{-}2}$ $Na_{0\text{-}1}$ for positive ESI samples.[78] Molecular formulae assignments with an error > 0.35 parts-per-million were discarded. Modified aromaticity index (AI_{mod}) and nominal oxidation state of carbon (NOSC) were calculated for each formula, as described by Koch and Dittmar (2006, 2016) and Riedel et al. (2012), respectively.[82–84] Molecular

formulae were classified by heteroatomic content (CHO, CHON, CHOS or CHONS) and categorized based on their elemental ratios and AI_{mod}. For all mass spectra presented herein, between 9,891 and 21,150 peaks were assigned elemental compositions with root-mean-square mass measurement accuracy of 26 to 36 ppb with an average achieved resolving power of 3,400,000 at m/z 200. **Tables 3.2** and **3.3** show the number of assignments and average root-mean-square (RMS) error for all assigned species present in this publication. All 21 T FT-ICR MS files and elemental composition assignments are publicly available via the Open Science Framework at DOI 10.17605/OSF.IO/PB8QU (https://osf.io/pb8qu/).

Table 3.2: Additional data from negative-mode FT-ICR MS analysis. No Na-adducts were assigned in negative-mode.

	Unburned Day 0	Burned Day 0	Unburned Day 28	Burned Day 28
Total detected peaks	35152	24818	56039	35205
Number of assigned molecular formulae (including isotopes)	16526	12515	21150	13944
Average root-mean-square mass error (including isotopes) (ppb)	35	29	36	28
Number of assigned molecular formulae (excluding isotopes)	9362	8364	12892	9033
Average root-mean-square mass error (excluding isotopes) (ppb)	32	29	35	27
Number of nitrogen-containing molecular formulae	1792	3920	3174	4035
Maximum m/z ratio	1015.2	799.2	1043.2	719.2
Minimum m/z ratio	187.2	175.0	187.0	175.0
Mass resolving power at 200 m/z	3312204	3555659	3460896	3474171

3.2.8 SOIL CO_2 RESPRIATION INCUBATIONS

Soil CO_2 respiration measurements were conducted with burned and unburned soil collected on Day 0, Day 14, and Day 28. The five replicates of Day 0, Day 14, and Day 28 burned and unburned soil samples were air-dried overnight, generating a total of 30 subsamples. For each subsample, approximately 20 g of air-dried soil and 6.7 mL of Milli-Q water were added to 120 mL plastic beakers. The beakers were placed individually in half-gallon jars with an airtight lid

featuring a rubber septum and stored in the dark in a constant temperature room (25 °C).[85] CO_2 accumulation in the jar headspace was measured using an infrared gas analyzer (IRGA, model LI-6252, LICOR). After flushing the jars with CO_2-free air (prepared by passing compressed air through soda lime), a subsample of the jar headspace (1 to 10 mL) was extracted using a syringe

Table 3.3: Additional data from positive-mode FT-ICR MS analysis

	Unburned Day 0	Burned Day 0	Unburned Day 28	Burned Day 28
Total detected peaks	24545	14482	26624	26063
Number of assigned molecular formulae (including Na adducts and isotopes)	13888	9891	15101	14086
Average root-mean-square mass error (including and Na adducts and isotopes) (ppb)	31	26	30	32
Number of assigned molecular formulae (including Na adducts, excluding isotopes)	8914	7485	10245	10322
Average root-mean-square mass error (including Na adducts, excluding adducts) (ppb)	29	26	29	32
Number of assigned molecular formulae (excluding Na adducts and isotopes)	6674	7030	8698	9476
Average root-mean-square mass error (excluding Na adducts and isotopes) (ppm)	28	26	29	31
Number of nitrogen-containing molecular formulae	2262	5412	3275	7233
Maximum m/z ratio	899.3	705.3	955.3	705.4
Minimum m/z ratio	175.1	175.1	186.1	175.1
Mass resolving power at 200 m/z	3349013	3367886	3150174	3283490

and injected into the gas analyzer, generating a baseline CO_2 measurement. During the next measurement, the measured CO_2 quantity in the jar headspace was subtracted by the prior CO_2 quantity to quantify CO_2 emitted between sampling points. The jars were then flushed with CO_2-free air to prevent the jars from becoming too concentrated with CO_2, and the baseline CO_2

quantity was measured. This was repeated each time a CO_2 measurement was made, and the accumulated CO_2 values were summed to calculate the total CO_2 emitted.

3.2.9 MICROBIAL ANALYSES - DNA EXTRACTION AND 16S rRNA GENE AND ITS AMPLICON SEQUENCING

Genomic DNA was extracted from each soil sample using the DNeasy PowerMax Soil Kit followed by concentration using a vacuum centrifuge for the burned samples and the DNeasy PowerLyzer PowerSoil Kit (Qiagen) for unburned soils following the manufacturer's protocol. Each kit utilizes the same fundamental chemistry, but the PowerLyzer Kit uses only 0.25 g of input compared to 10 g used in the PowerMax kit providing detectable DNA extraction from low biomass samples. Amplicon libraries were prepared using a single step PCR. Soil bacterial and archaeal communities were amplified using the V4 region of the 16S rRNA gene with the primers 515F[86] (5′-AATGATACGGCGACCACCGAGATCTACACGCT XXXXXXXXXXXX TATGGTAATT GT GTGYCAGCMGCCGCGGTAA-3′, where this sequence includes the 5′ Illumina adapter, the Golay barcode, the forward primer pad, the forward primer linker, and the forward primer, respectively) and 806R (5′- CAAGCAGAAGACGGCATACGAGAT AGTCAGCCAG CC GGACTACNVGGGTWTCTAAT-3′, where this sequence includes the reverse compliment of the 3′ Illumina adapter, the reverse primer pad, the reverse primer linker, and the reverse primer, respectively).[87] Soil fungal communities were amplified using the first internal transcribed spacer (ITS1) of the rDNA with the primers ITS 1f (5′-AATGATACGGCGACCACCGAGATCTACAC GG CTTGGTCATTTAGAGGAAGTAA −3′, where this sequence includes the Illumina adapter, the forward primer linker, and the forward primer, respectively) and ITS2(5′- CAAGCAGAAGACGGCATACGAGAT NNNNNNNNNN CG GCTGCGTTCTTCATCGATGC-3′, where this sequence includes the reverse compliment of

the 3′ Illumina adapter, the Golay barcode, the reverse primer linker, and the reverse primer, respectively).[88] All primers were modified to include Illumina adaptors and unique barcodes as done in the Earth Microbiome Project (EMP) (https://earthmicrobiome.org/).[89] The EMP PCR protocol was modified to use Platinum II Hot Start PCR Master Mix (Invitrogen). PCR products were normalized using SequalPrep Normalization Plate Kit (Applied Biosystems). Pooled DNA products were sequenced on the Illumina MiSeq Platform using 251 bp paired-end sequencing chemistry at the Microbial Community Sequencing Lab (University of Colorado Boulder).

QIIME2 (release 2021.2) was utilized to process resulting reads.[90] First, ITS reverse reads were discarded owing to low quality. After demultiplexing, DADA2 was utilized by QIIME2 on remaining reads to merge (pair-end read joining), quality filter (including denoising), check for chimeras, and bin to create amplicon sequence variants (ASVs).[91] As part of the denoising step, 16S forward reads were trimmed to 245 bp and reverse reads to 225 bp. For ITS data, forward reads were trimmed to 230 bp. Bacterial and archaeal (16S) ASVs were then assigned taxonomy using scikit-learn pretrained SILVA classifiers (version 138)[92–94] while fungal (ITS) ASVs were assigned taxonomy using self-trained UNITE database classifiers.[95,96] Resulting 16S rRNA gene read counts ranged from 586 to 26,221, and ITS amplicon sequencing read counts ranged from 901 to 23,527. Samples with low read counts (**Figure 3.5**). Finally, fungal ASVs were assigned to ecological guilds through FUNGuild if provided a single guild assignment with “highly probable” or “probable” confidence, per creator recommendations.[12,97] Resulting reads were deposited and are available at NCBI within BioProject PRJNA682830, and details are available in **Table B1**.

3.2.10 MICROBIAL COMMUNITY STATISTICS

To assess the impacts of high severity burning of pyrocosms on the soil microbiome, statistical analyses were performed using R version 4.1.2 with significance accepted at $p < 0.05$.[98]

Differences in species richness (alpha diversity) between the burned and unburned pyrocosms across the time series (Days 0 through 28) were tested using pairwise Wilcoxon signed-rank tests

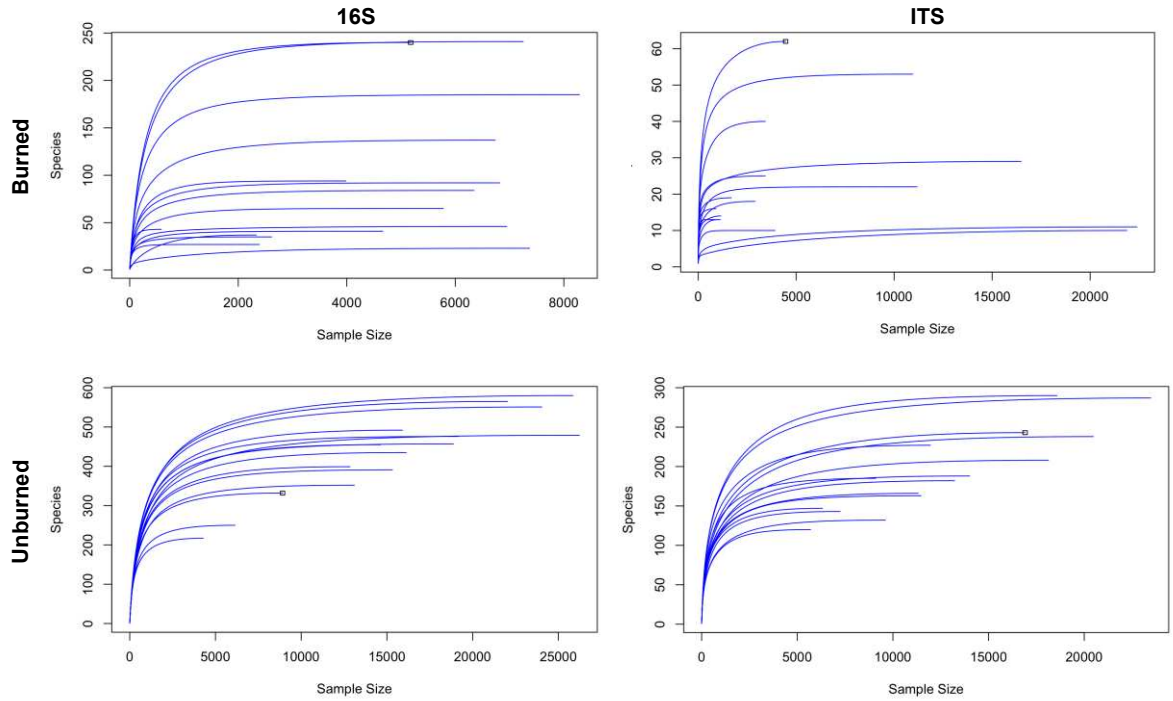

Figure 3.5. Rarefaction curves calculated for all burned (top) and unburned (bottom) samples for both 16S (left) and ITS (right) sequencing data showed that the observed diversity of the communities was equal to their predicted diversity.

with a Bonferroni p-value adjustment for multiple tests using the function "stat_compare_means" in the package ggpubr[99] and the function "pairwise.wilcox.test" in the stats package.[98] Differences in bacterial/archaeal and fungal community composition were similarly assessed using nonparametric permutational multivariate analysis of variance (PERMANOVA)[100] using Bray−Curtis dissimilarity matrices and the "adonis2" function in the vegan package,[63] and these differences were subsequently visualized using Non-Metric Multidimensional Scaling (NMDS). Soil chemistry variables (carbon, nitrogen, and pH) and FUNGuild assignments were correlated with the resulting ordination space in the NMDSs using the "envfit" function in the vegan package with a Bonferroni p-value correction for multiple tests. Differences in beta dispersion between the

burned and unburned microbial communities were assessed using the function "betadisper" in the vegan package and "anova" in the stats package. Next, coupled linear discriminant analysis effect size (LEfSe) and linear discriminant analysis (LDA) analyses were utilized to find taxa at the phyla, genera (bacterial/archaeal), and species (fungal) levels discriminant for either the burned or unburned pyrocosm conditions using the MicrobiomeAnalyst 2.0 server.[101] All visualizations were produced with the ggplot2 package,[102] except for combined LEfSe/LDA visualizations which came from MicrobiomeAnalyst 2.0[101] and formatted in Adobe Illustrator 2023 (v27.2). All statistical codes are available at https://github.com/julieafowler/Pyrocosm_Study_1Month.

3.2.11 TERMINOLOGY

The organic matter collected from the burned soils is referred to as "SOM from burned soils." We cannot conclude with certainty that all the remaining organic matter in the burned soil was thermochemically altered by the fire nor are we using techniques that specifically target PyOM molecules such as polyaromatic hydrocarbons through the benzene polycarboxylic acids (BPCA) method[103,104] or levoglucosan biomarkers.[30,31] Therefore, it would be inaccurate to refer to all the organic matter collected from burned soils as PyOM. Consequently, we employ more conservative terminology ("SOM from burned soils") to describe the organic matter collected from burned soils which likely includes a mixture of PyOM, remaining SOM that was unaltered by fire, and molecules formed from the lysis and breakdown of microbes and plant material. We operationally use the term "biodegradable" to describe SOM that can be metabolized by microbes across the time frame of this study, meaning that the SOM can be both physically accessed by microbes[42] and thermodynamically oxidized.[10]

Furthermore, we operationally use the term "metabolite" to refer to low-molecular weight, biodegradable molecules detected via nontargeted or targeted GC-MS analysis using authentic

standards or curated spectral databases including saccharides, amino acids, and organic acids. The assemblage of these metabolites is referred to as the "metabolome." Our terminology is based on a methods paper published by Swenson et al. in which GC-MS is used to evaluate soil metabolomics.[53] Here, low molecular weight soil molecules such as carbohydrates, alcohols, sterols, and amino acids were referred to as metabolites and were detected with GC-MS.[53]

3.3 RESULTS AND DISCUSSION

3.3.1 MICROBIAL COMMUNITY ASSEMBLAGE IN BURNED SOILS IS ALTERED AND CONTAINS HETEROTROPHIC MICROBES

Microbial amplicon (16S/ITS) sequencing was utilized to assess postfire changes in microbial richness and community composition. Fire impacted the soil microbiome species richness (**Figure 3.6A,B**) and community composition (**Figure 3.6C,D**) while selecting for specific bacterial, archaeal, and fungal taxa and fungal guilds with potentially important roles in the postfire ecosystem. The immediate and persistent decrease in microbial richness in burned soils, in addition to the associated loss of ectomycorrhizal symbionts (**Figure 3.6F**), mirrors trends observed in prior high severity wildfire studies.[12,13,17,62,105] However, pairwise Wilcoxon signed-rank tests revealed no statistically significant differences in richness between burned and unburned samples at any given day postburn likely due to the low sampling size (n = 3) (**Figure 3.6A,B**). Nevertheless, multivariate analyses (nonmetric multidimensional scaling [NMDS] plots) revealed that burning led to distinct microbial communities and increased stochasticity compared to unburned conditions in both bacterial/archaeal and fungal soil communities (beta dispersion: $p = 2.317 \times 10^{-11}$ and $p = 2.2 \times 10^{-16}$, respectively) (**Figure 3.6C,D** and **Figure 3.7**).

Heterotrophic microbes were detected in the burned soil samples with the phyla *Actinobacteria*, *Firmicutes*, and *Protobacteria* notably being enriched postfire (**Figure 3.6E** and

Figure 3.8A). These phyla contain heterotrophic species that could likely metabolize SOM in burned soils.[12,17,106] Other bacterial genera known to possess putative beneficial traits for the

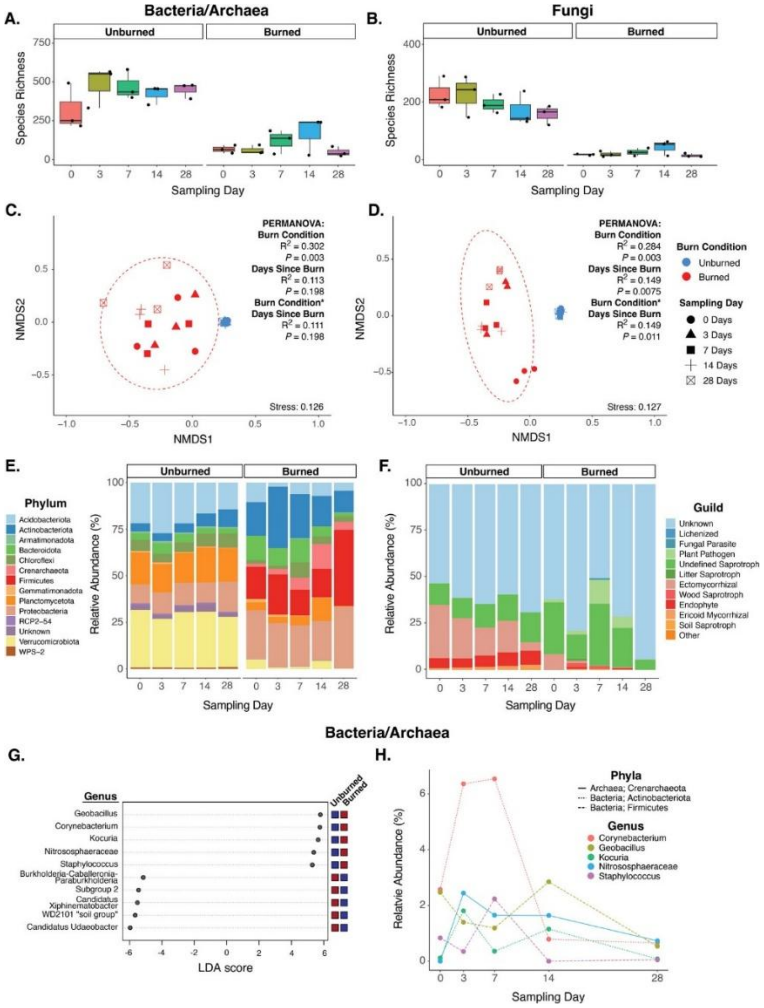

Figure 3.6. (**A** and **B**) Bacterial/archaeal (16S; **A**) and fungal (ITS; **B**) species richness box plots for burned and unburned pyrocosms. (**C** and **D**) Nonmetric multidimensional scaling (NMDS) ordination plots showing Bray−Curtis ASV microbial community composition dissimilarities for bacteria/archaea (16S; **C**) and fungi (ITS; **D**) including NMDS stress metrics and PERMANOVA test results. (**E**) Bar plot showing bacterial/ archaeal phyla relative abundances between the unburned and burned pyrocosms averaged across replicates. (**F**) Bar chart showing the average relative abundances of samples within a given combination of burn condition and sampling day for fungal functional guilds as reported by FUNGuild (Nguyen et al., 2016).[97] The "other" category contains dung saprotroph, animal pathogen, orchid mycorrhizal, and lichen parasite guilds. (**G**) Dot plot showing the top ten results of Kruskal−Wallis rank sum tests followed by LDA analyses for biomarker discovery at the bacterial/archaeal genus level (16S). (**H**) Scatter plot of the average relative abundances of samples from burned pyrocosms of the top five genera from the combined LEfSe/LDA analysis on bacterial/archaeal genera in plot **G**.

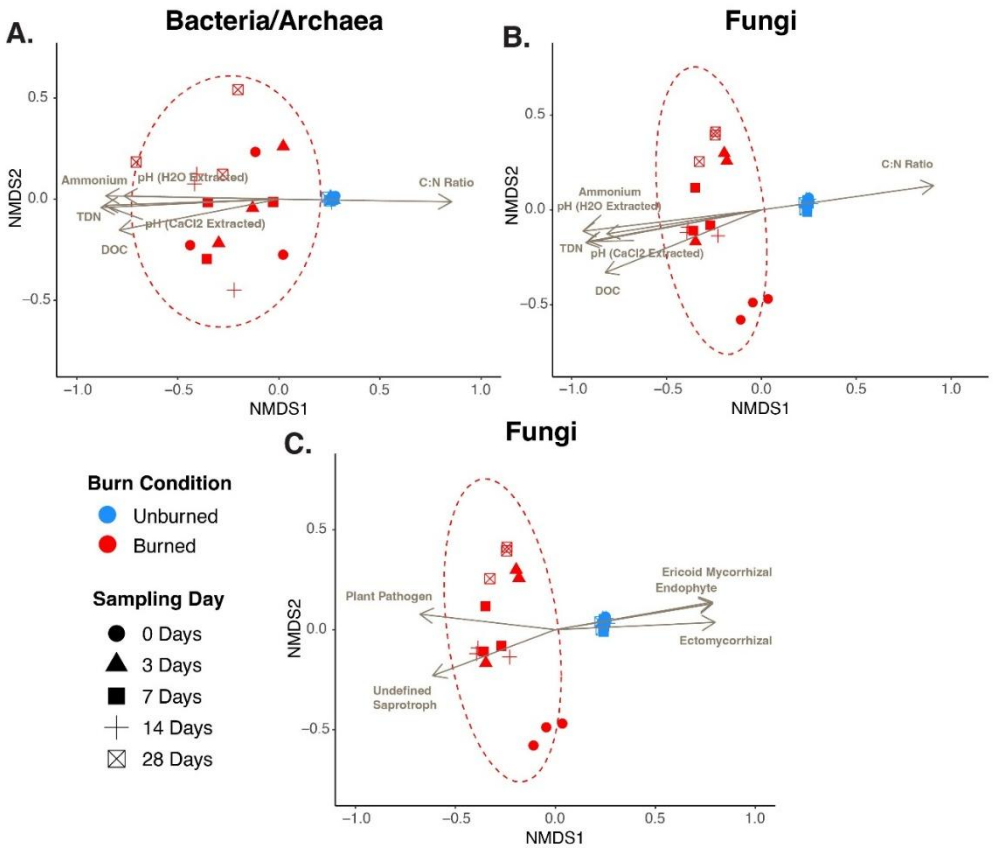

Figure 3.7. Non-metric multidimensional scaling (NMDS) ordination plots showing Bray-Curtis ASV microbial community composition dissimilarities for bacterial/archaeal (16S; **A**) and fungal (ITS; **B** & **C**). Plots A and B include overlaid significant soil chemistry vectors and plot C includes overlaid significant fungal function guild vectors as reported by FUNGuild (Nguyen et al., 2016)[97] denoting significant drivers of community composition dissimilarity for the bacterial/archaeal (**A**) and fungal (**B** & **C**) soil microbial communities.

postfire ecosystem such as *Geobacillus* (spore formation)[107] and *Kocuria* (distribution via dust or smoke)[108] were also identified as discriminant taxa for burned soils (**Figure 3.6G**).

3.3.2 BURNED SOILS HAD HIGHER CONCENTRATIONS OF WATER EXTRACTABLE ORGANIC CARBON

Water extractable organic carbon (WEOC) concentrations were measured to quantify carbon availability for microbial metabolism (**Figure 3.9** and **Table B2**). The burned soil had statistically greater WEOC concentrations (t test, $p < 0.05$) across all sampling dates except for Day 28 despite there being no significant differences between the total carbon values of the burned

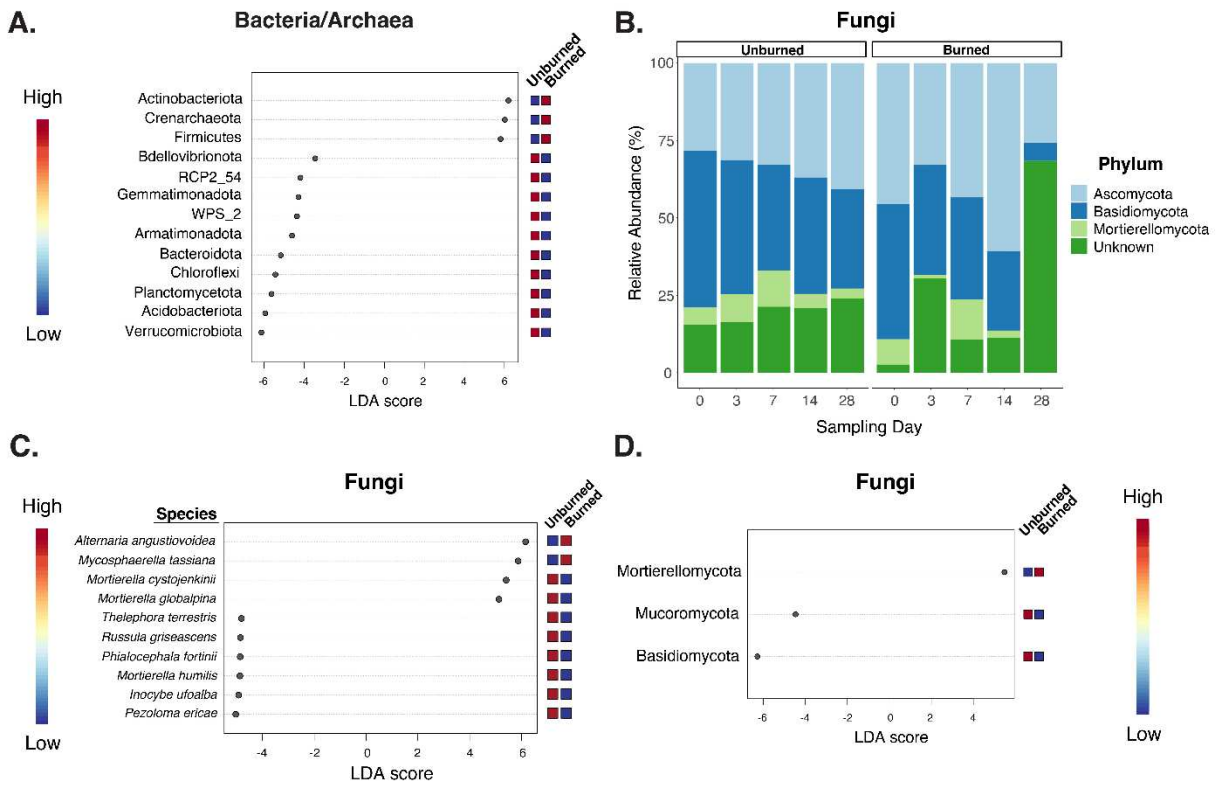

Figure 3.8. (**A**) Dot plot showing the results of Kruskal-Wallis rank sum tests followed by LDA analyses for biomarker discovery at the phyla level for bacterial/archaeal microbial communities between the burned and unburned pyrocosms with all dates included. (**B**) Bar plot showing changes in fungal relative abundance at the phyla level between the unburned and burned pyrocosms across the time series averaged across replicates. (**C** and **D**) Dot plots showing the results of Kruskal-Wallis rank sum tests followed by LDA analyses for biomarker discovery at the fungal species (**C**) and phyla (**D**) level between the burned and unburned pyrocosms with all dates included. Results were calculated using a significance cutoff of $p < 0.05$ after FDR adjustment and a log LDA score = 2.0. Scale colors represent comparative abundance.

and unburned soil for any sampling day (t test, $p < 0.05$) (**Table B3**). The WEOC results align with laboratory-based studies reporting increased WEOC in soils that were heated to approximately 250 °C.[19,20,109,110] The elevated WEOC content could be due to soil aggregate disruption, release of soluble organic compounds from cell lysis, and SOM oxidation during combustion.[12,57,110] WEOC is considered one of the most accessible fractions of carbon because WEOC can be transported through soil pores in water, bringing carbon that may not have been accessible otherwise to

microbes.[79] Therefore, there is simply more WEOC in the burned soil that heterotrophic microbes may metabolize. However, WEOC measurements do not assess molecular SOM composition which influences biodegradability.[10] Thus, two complementary mass spectrometry techniques were used to evaluate SOM composition.

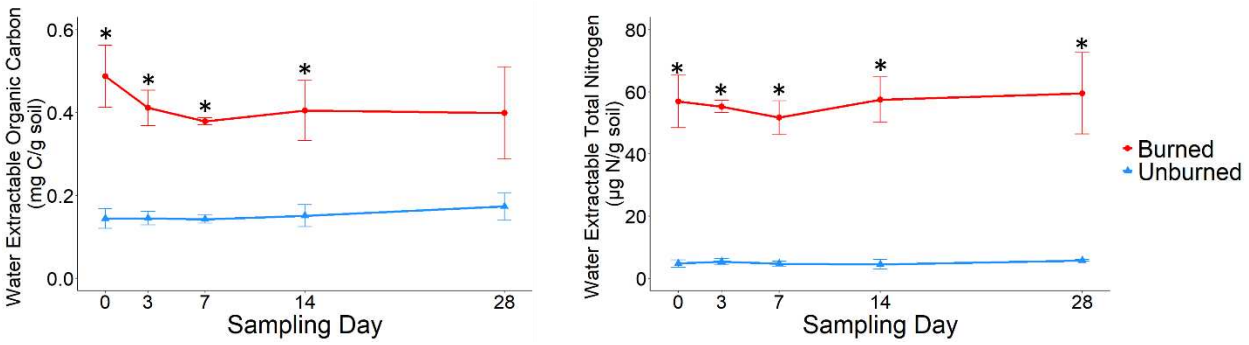

Figure 3.9. Water extractable organic carbon (WEOC) and water extractable total nitrogen (WETN) results for burned and unburned soil samples. Asterisk indicates a statistically significant difference (t-test, $p<0.05$) between burned and unburned values within a given sampling day (n=3, error=standard deviation).

3.3.3 METABOLITES ARE PRESENT IN BURNED SOILS THAT MAY SUPPORT MICROBIAL ACTIVITY

Normalized, scaled peak areas detected in nontargeted GC-MS analysis were plotted in principal component analysis (PCA) score plots to compare the metabolomic profiles of unburned and burned soils (**Figure 3.10**). A comparison of all detected peaks revealed statistically significant separate clustering of burned and unburned samples (**Figure 3.10A**) (PERMANOVA, $p \leq 0.001$), indicating that fire considerably altered the soil metabolite content. To explain differences in the burned and unburned metabolome, specific metabolite ontologies were examined.

Six amino acids were annotated in the samples via nontargeted analysis, and amino acid profiles were significantly different between burned and unburned samples (**Figure 3.10B**) (PERMANOVA, $p \leq 0.001$), likely contributing to the differences observed in the overall metabolome (**Figure 3.10A**). The unburned samples clustered closely among themselves in

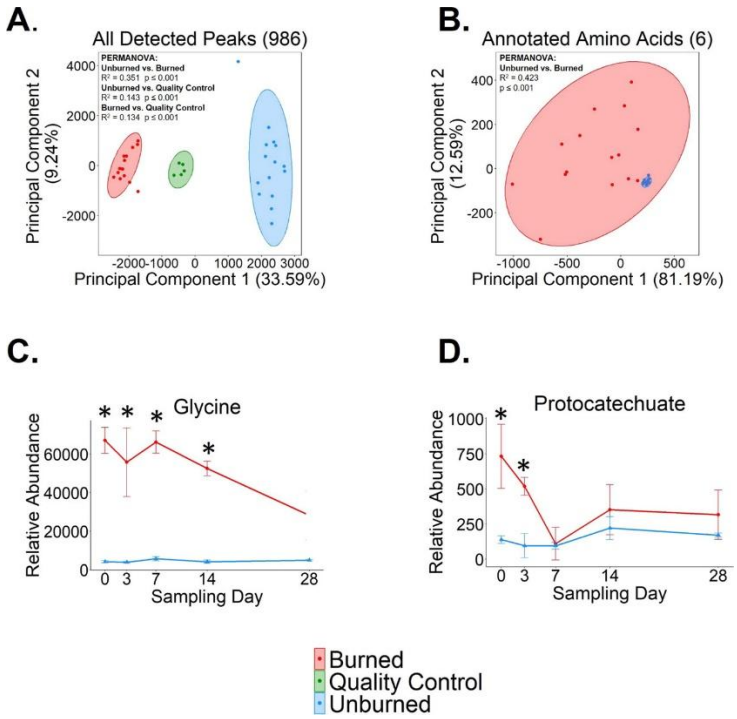

Figure 3.10. (**A** and **B**) Principal component analysis (PCA) score plots of a nontargeted GC-MS data set of water extracts from all 15 burned soil samples (three replicates for five sampling time points), all 15 unburned soil samples (three replicates for five sampling time points), and five quality control samples (prepared by mixing all the burned and unburned soil extracts and running five replicates of that mixture on the GC-MS instrument). The peak areas of detected peaks in the samples were normalized with total ion current normalization, scaled with Pareto scaling, and then used as the input data for the PCA scores plots. These normalized, scaled peak areas are indicative of metabolite relative abundance. (**A**) PCA score plot of peak areas for all 986 detected peaks. (**B**) PCA score plot of peak areas for six annotated amino acid peaks. PERMANOVA analysis was conducted to determine if the burned, unburned, and quality control groups were significantly different from each other for plots **A** and **B**. (**C** and **D**) Normalized abundances of annotated glycine peaks (**C**) and annotated protocatechuate peaks (**D**). Asterisk indicates a statistically significant difference between burned and unburned values within a given sampling day (t test, $p < 0.05$) (n = 3, error = standard deviation).

contrast to the more dispersed burned samples (**Figure 3.10B**). This suggests that fire considerably alters the soil amino acid abundances and/or amino acids abundances in burned soils are more susceptible to short-term (≤28 days) postfire changes.

The abundances of the annotated amino acids were either statistically similar between the burned and unburned samples or higher in the burned samples (**Figures 3.10C** and **Figure 3.11**). Specifically, glycine was ~16 times more abundant in the burned soil than the unburned soil for

Day 0 (**Figure 3.10C**), potentially linked to the bacterial synthesis of glycine betaine which is a known thermoprotectant.[111,112] The higher amino acid abundances in burned soils may be due to protein denaturation or heat-induced microbial lysis which releases intracellular amino acids into the soil,[12] contributing to the "necromass zone" (an area of burned soil where remnants of dead microbes serve as biodegradable sources of carbon and nitrogen)[57] which may fuel postfire microbial metabolism.[56,113]

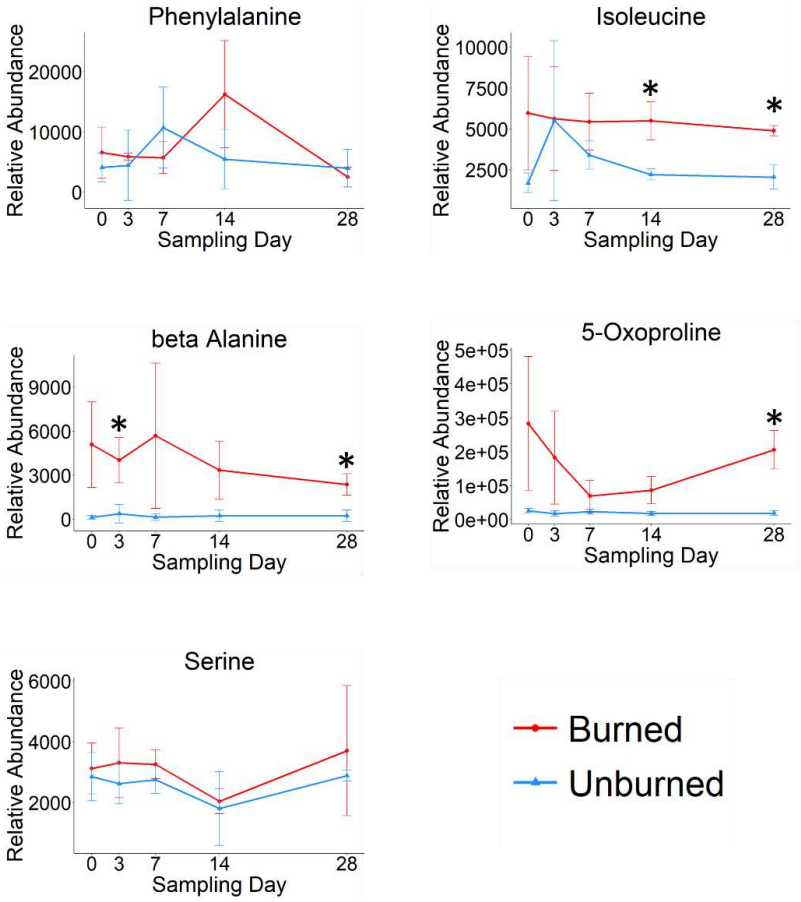

Figure 3.11. Plotting normalized abundances of annotated amino acids. Asterisk indicates a statistically significant difference between burned and unburned values within a given sampling day (t-test, $p < 0.05$) (n=3, error = standard deviation).

Microbes that could consume amino acids were detected in burned soil. *Crenarchaeota*, a thermophilic archaeal phyla, increased in relative abundance from less than 0.07% across the unburned soils to between 1.7% and 13.3% in the burned soils (**Figure 3.6E**).[114] One genera within

this phyla, *Nitrososphaeraceae*, was identified as discriminant for burned samples using combined LEfSe/LDA analysis (**Figures 3.6G,H**). *Nitrososphaeraceae* are chemolithoautotrophic ammonia oxidizing archaea (AOA) and were potentially enriched by the elevated soil ammonium concentrations in the burned soil (**Figure 3.12** and **Table B4**).[115–117] Additionally, *Nitrososphaeraceae* have been shown to uptake amino acids[118] and may have the potential for heterotrophic carbon utilization.[118–120] Therefore, AOA could utilize the enriched amino acids in the burned soil to fuel microbial metabolism.

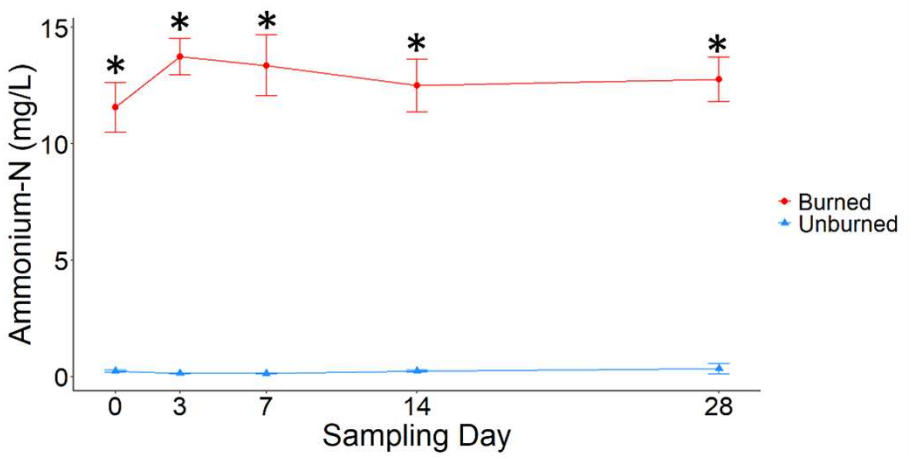

Figure 3.12. Ammonium results for burned and unburned soil samples. Asterisk indicates a statistically significant difference (t-test, $p < 0.05$) between burned and unburned values within a given sampling day. (n=3, error = standard deviation).

Organic acids associated with citric acid cycle and saccharides were also annotated via nontargeted analysis in burned soil. Lactic acid, which is oxidized to pyruvic acid to enter the citric acid cycle, was statistically more abundant in burned soil for three sampling time points (t test, $p < 0.05$) (**Figure 3.13A**). Additionally, fumaric acid, succinic acid, and citric acid were all annotated in the burned and unburned soil samples (**Figure 3.13**). The annotated saccharide profiles of the burned and unburned soil samples were significantly different (**Figure 3.14**) (PERMANOVA, $p \leq 0.001$) with burned samples clustering tightly in contrast to highly dispersed unburned samples. Despite these differences in overall saccharide pool composition, there were

no consistent patterns of saccharide enrichment in burned soils (**Figures 3.15**). Similarly to amino acids, organic acids and saccharides in burned soils were likely derived from heat-induced microbial lysis. The presence of organic acids and saccharides in burned soil further suggests that postfire soils contain biodegradable metabolites that could fuel microbial metabolism.

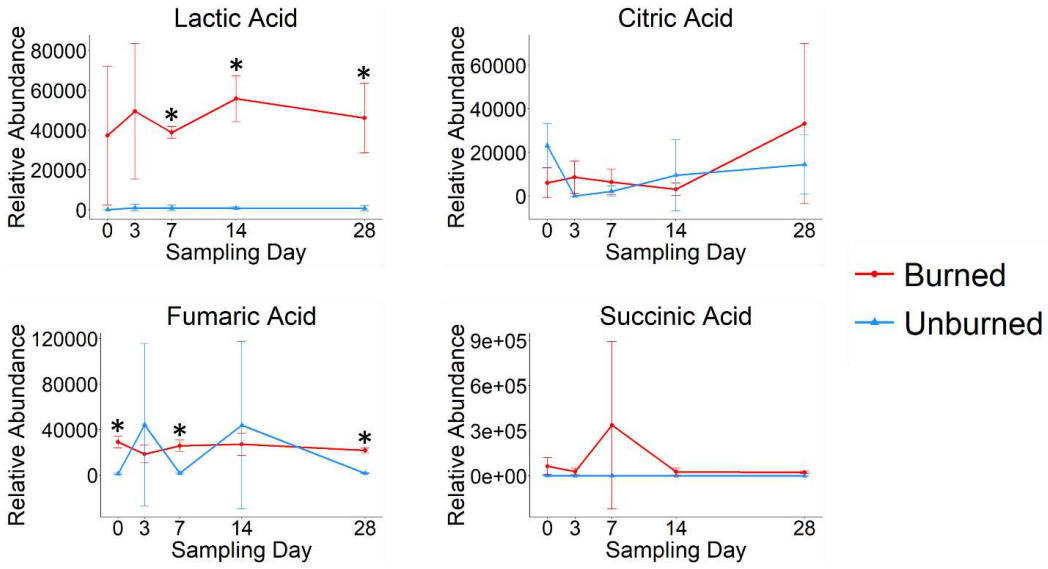

Figure 3.13. Comparing relative abundances of annotated organic acids that are associated with the citric acid cycle. Asterisk indicates that there is a significant difference between burned and unburned values within a given sampling day (t-test, $p<0.05$) (n=3, error = standard deviation).

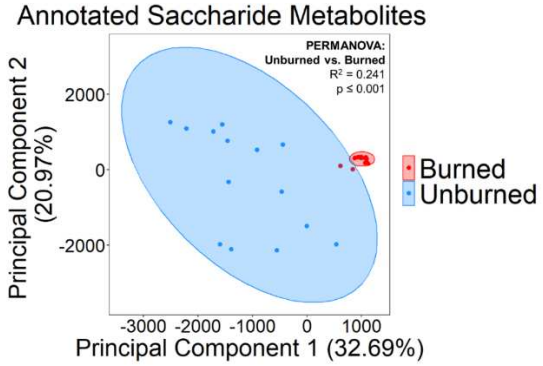

Figure 3.14. Principal component analysis (PCA) scores plot of a nontargeted GC-MS saccharide dataset of water-extracts from all 15 burned soil samples (three replicates for five sampling timepoints) and all 15 unburned soil samples (three replicates for five sampling timepoints). The peak areas of 38 annotated saccharide peaks in the samples were normalized with total ion current normalization, scaled with Pareto scaling, and then used as the input data for this PCA scores plot. These normalized, scaled peak areas are indicative of saccharide relative abundance. PERMANOVA analysis was conducted to determine if the burned and unburned groups were significantly different from each other.

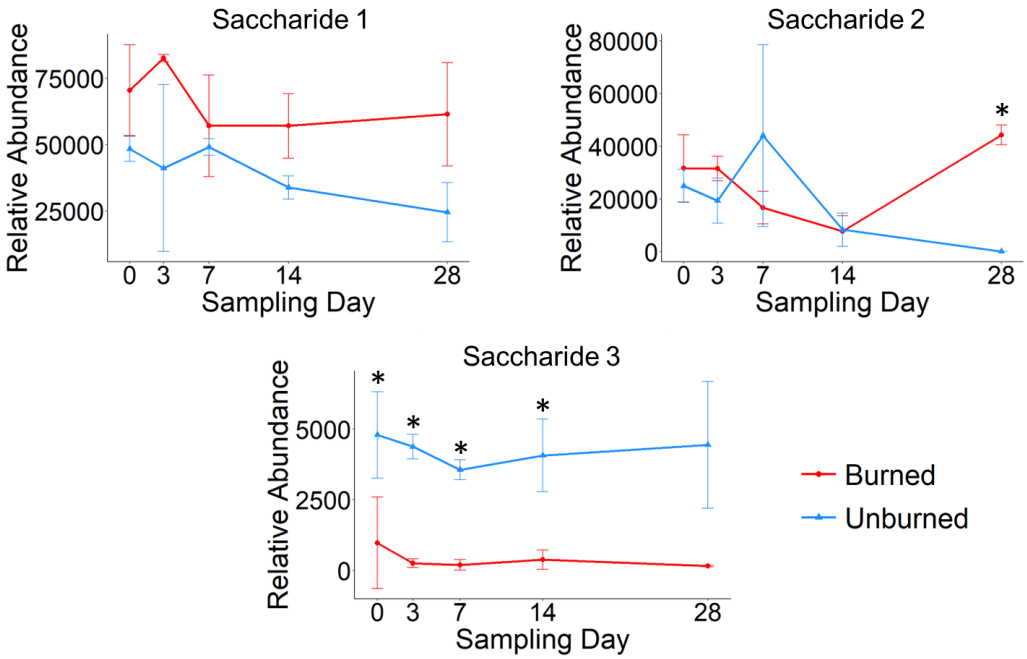

Figure 3.15. Comparing relative abundances of three representative annotated saccharides. Asterisk indicates that there is a significant difference between burned and unburned values within a given sampling day (t-test, $p<0.05$) (n=3, error = standard deviation).

3.3.4 DETECTION OF CATECHOL, PROTOCATECHUATE, AND CITRIC ACID CYCLE METABOLITES SUPPORTS AROMATIC DEGRADATION PATHWAYS

Catechol and protocatechuate were also detected in the burned and unburned soil via targeted metabolomics. Catechol abundances were not statistically different between burned and unburned soil whereas protocatechuate abundances were statistically greater in the burned soil for Day 0 and Day 3 (**Figure 3.10D** and **Figure 3.16**). The targeted detection of catechol and protocatechuate supports proposed pathways of aromatic SOM degradation in burned soil in which catechol and protocatechuate are key intermediates.[12,39] Furthermore, the annotation of citric acid cycle intermediates further supports these pathways in which succinyl-CoA and acetyl-CoA (which feed into the citric acid cycle) are end products of aromatic degradation (**Figure 3.13**). These results support the second hypothesis of this study: while proposed intermediates in aromatic degradation pathways - namely, catechol, protocatechuate, and citric acid cycle metabolites - are

detectable in both burned and unburned soils, the enrichment of specific metabolites (e.g., protocatechuate and lactic acid) in burned samples suggests that aromatic SOM may be degraded one month after fire. Overall, we recommend that burned soil metabolomics be explored in both mesocosm and field studies to further elucidate the biogeochemical pathways governing postfire microbial and vegetative recovery.[121,122]

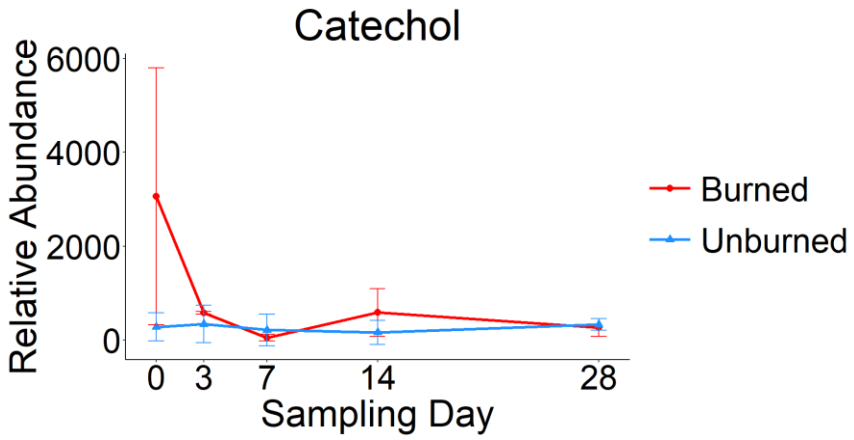

Figure 3.16. Plotting normalized abundances of annotated catechol peaks. There were no statistically significant differences between burned and unburned relative abundances within a given sampling day (t-test, $p<0.05$). (n=3, error = standard deviation).

3.3.5 SOM FROM BURNED SOILS WAS ENRICHED IN NITROGEN-CONTAINING COMPOUNDS AND FEATURED LOWER MOLECULAR WEIGHTS

FT-ICR MS analysis assigned thousands of molecular formulas with masses ranging from 175 to 1043 Da (**Tables 3.2** and **3.3**). The molecular formulas assigned in burned soil featured lower m/z ratios compared to unburned soil (**Figures 3.17** and **3.18**), potentially caused by the depolymerization of lignin-like, protein, and complex carbohydrate molecules.[31] This depolymerized organic matter may be more biodegradable because lower molecular-weight compounds are more easily accessible in the soluble pool, transported through cellular membranes, and subjected to microbial metabolism.[123]

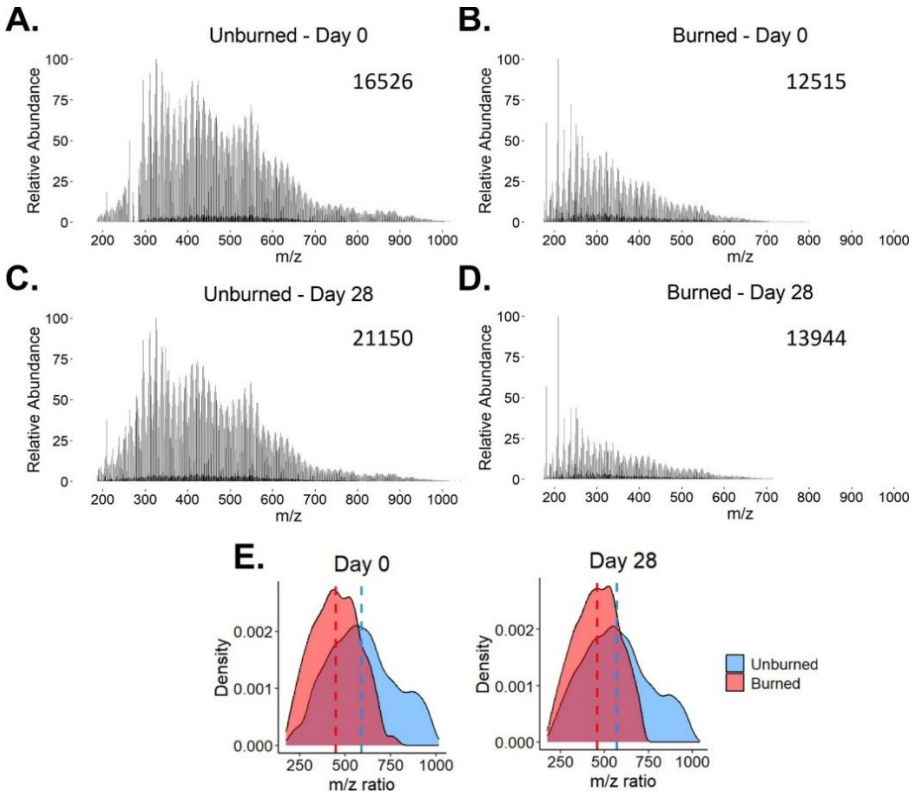

Figure 3.17. (**A**−**D**) FT ICR-MS mass spectra of peaks that were assigned molecular formulas from negative-mode electrospray ionization samples. The number in the upper-right corner of each spectrum is the total number of peaks that were assigned molecular formulas (including isotopes). (**E**) These m/z ratios were compiled into density plots. The y-axis indicates the relative probability of an ion featuring a given m/z ratio. The greater the density value for a given m/z ratio, the more ions that feature that m/z ratio. Dashed lines are mean values.

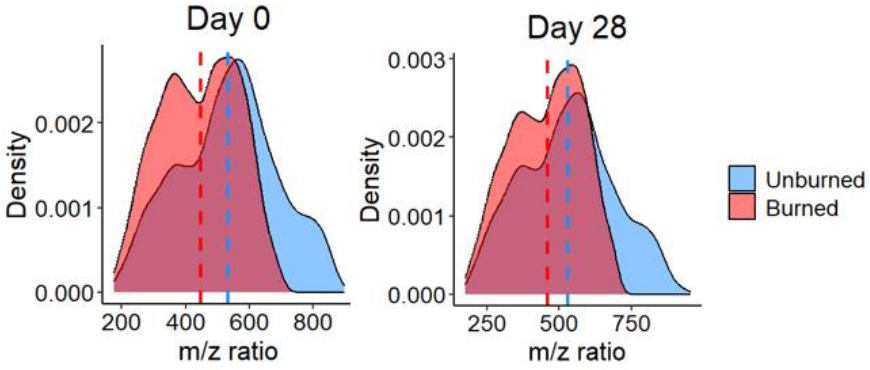

Figure 3.18. Density plots of m/z ratios of assigned molecular formulae from positive-electrospray ionization mode. Dashed lines are mean values. The y-axis indicates the relative probability of an ion featuring a given m/z ratio. The greater the density value for a given m/z ratio, the more ions that feature that m/z ratio.

There were also 20.1% to 43.1% more nitrogen-containing molecular formulas in burned soil compared to unburned soil (**Figure 3.19**), mirroring the increased water extractable total nitrogen values of burned soil (**Figure 3.9**, **Table B5**). Nitrogen enrichment in assigned molecular formulas was also observed in previous laboratory studies and may be due to the Maillard reaction pathway.[18,19,24] Nitrogen is often a limiting nutrient in soil systems;[124] thus, SOM enriched in nitrogen could serve as a nitrogen source for microbes in postfire environments, especially considering that the nitrogen-containing molecules in burned soils likely contain amino sugars and peptides according to van Krevelen analysis (**Figures 3.20** and **3.21**).[125]

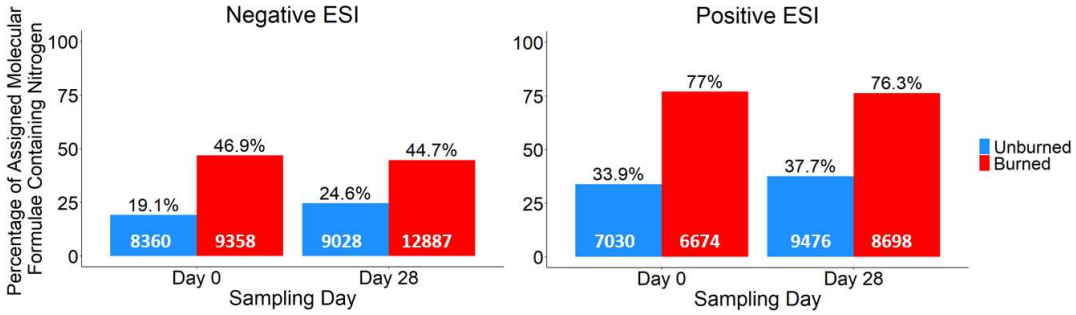

Figure 3.19. Percentage of nitrogen-containing molecular formulae assignments of burned and unburned SOM determined with both negative and positive-mode electrospray ionization FT-ICR MS analysis. The number of total assigned molecular formulae are shown in white. Each bar represents one soil-water extract sample.

3.3.6 MICROBIAL RESPIRATION IS STIMULATED IN THE IMMEDIATE AFTERMATH OF BURNING

Cumulative CO_2 emissions from Day 0, Day 14, and Day 28 soil were measured during 50-day incubations to determine if the burned soil microbiome was metabolically active and could mineralize SOM (**Figure 3.22** and **Table B6**). Day 0, Day 14, and Day 28 burned soil released significantly more CO_2 than the corresponding unburned soil for the first 12, 22, and 6 days of the incubations, respectively. Approximately 3.3 ± 1.1% and 3.7 ± 0.7% of the total soil carbon were released as CO_2–C from the burned and unburned soils, respectively, during the 50-day incubations. Overall, more CO_2 was initially released from the burned soil compared to the

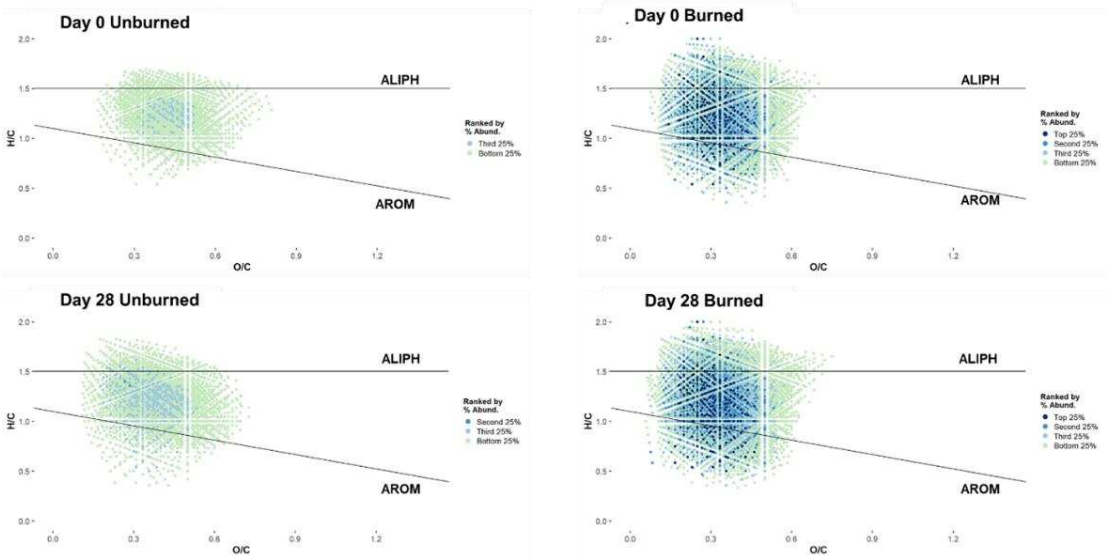

Figure 3.20. Van Krevelen diagrams plotting nitrogen-containing molecular formulae detected using positive-mode electrospray ionization. Molecular formulae plotting below the "AROM" line feature notable aromatic content (modified aromaticity index value ≥0.5).[19] Molecular formulae plotting above "ALIPH" line feature notable aliphatic content.[54] The plotted molecular formulae were categorized based on their abundances in which the "top 25%" data points, for example, are molecular formulae that have greater relative abundances than 75% of the total molecular formulae. "Second 25%" are molecular formulae that have greater relative abundances than 50% of the total molecular formulae and so on. The burned samples featured nitrogen-containing molecular formulae plotting above an H/C ratio of 1.5, suggesting the presence of amino sugars and peptides.[125]

unburned soil, suggesting that heterotrophic microbes were consuming SOM in a complex burned soil environment. The CO_2−C emissions were also normalized to total soil carbon values (**Figure 3.23** and **Table B7**) and featured the same differences between unburned and burned samples. When normalized to WEOC values, the ratio of CO_2−C to WEOC was generally greater in the unburned soil (**Figure 3.24** and **Table B8**). Additionally, the rates of CO_2−C emissions were initially greater in the burned soil (**Figure 3.25** and **Table B9**).

CO_2 emissions were likely due to both physical and biotic factors. When water was added to the soil during incubation preparation, CO_2 in the soil pore spaces may have been physically

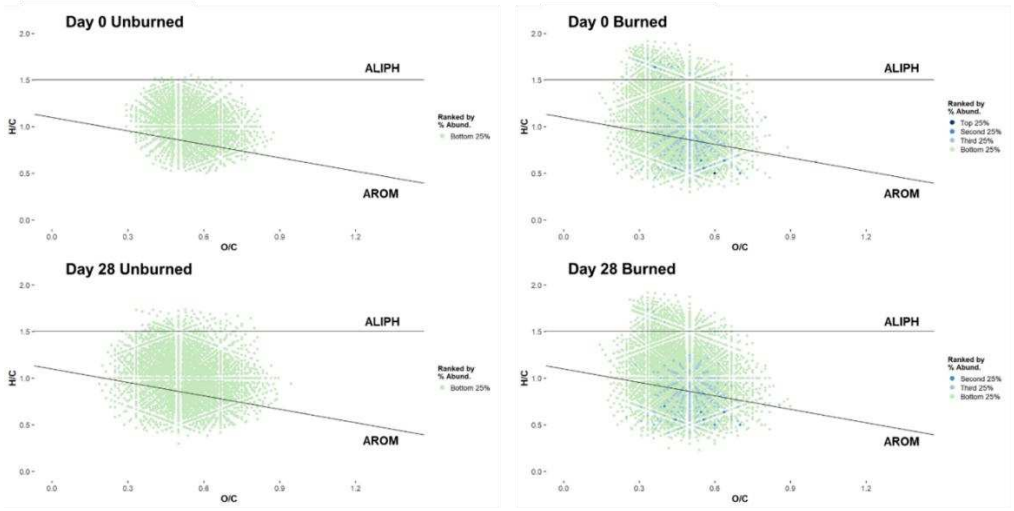

Figure 3.21. Van Krevelen diagrams plotting nitrogen-containing molecular formulae detected using negative-mode electrospray ionization. Molecular formulae plotting below the "AROM" line feature notable aromatic content (modified aromaticity index value ≥0.5).[19] Molecular formulae plotting above "ALIPH" line feature notable aliphatic content.[54] The plotted molecular formulae were categorized based on their abundances in which the "top 25%" data points, for example, are molecular formulae that have greater relative abundances than 75% of the total molecular formulae. "Second 25%" are molecular formulae that have greater relative abundances than 50% of the total molecular formulae and so on. The burned samples featured nitrogen-containing molecular formulae plotting above an H/C ratio of 1.5, suggesting the presence of amino sugars and peptides.[125]

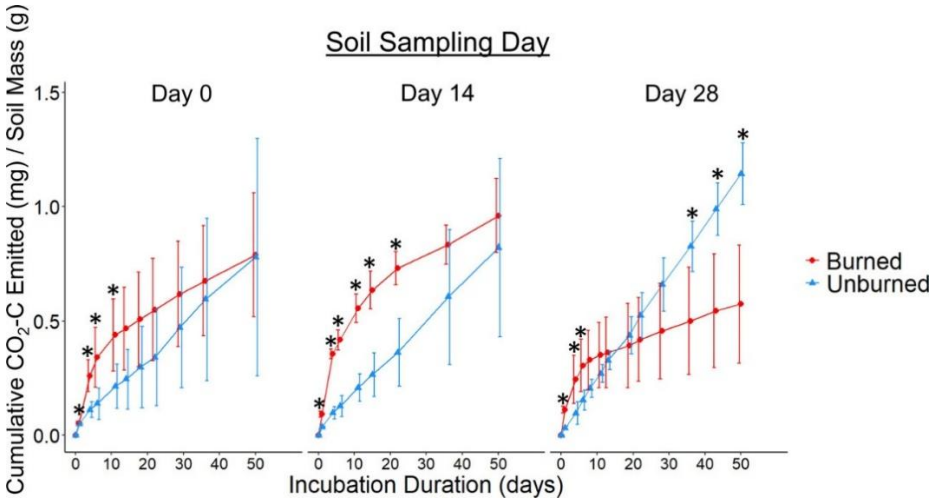

Figure 3.22. Cumulative CO2−C emissions normalized to soil mass from burned and unburned soil incubations. Asterisk indicates a statistically significant difference (t test, $p < 0.05$) between burned and unburned values within a given incubation day (n = 5, error = standard deviation). Error bars were jittered to avoid overlap.

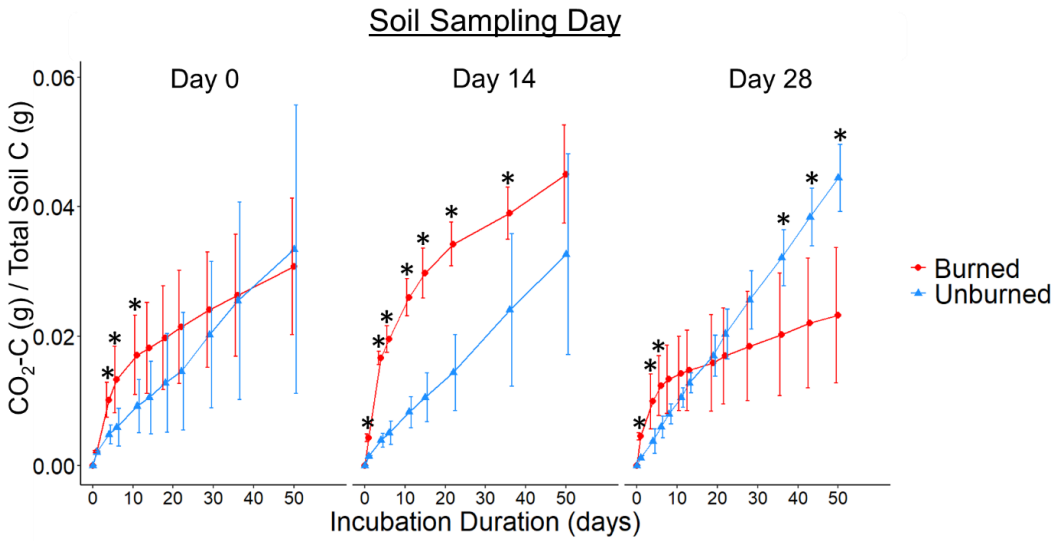

Figure 3.23. Cumulative CO_2-C emissions from burned and unburned soil incubations normalized to total soil carbon content. Total soil carbon data from **Table B3** were used to normalize the carbon dioxide emission data. Asterisk indicates a statistically significant difference (t-test, $p < 0.05$) between burned and unburned values within a given incubation day (n=5, error = standard deviation). Error bars were jittered to avoid overlap.

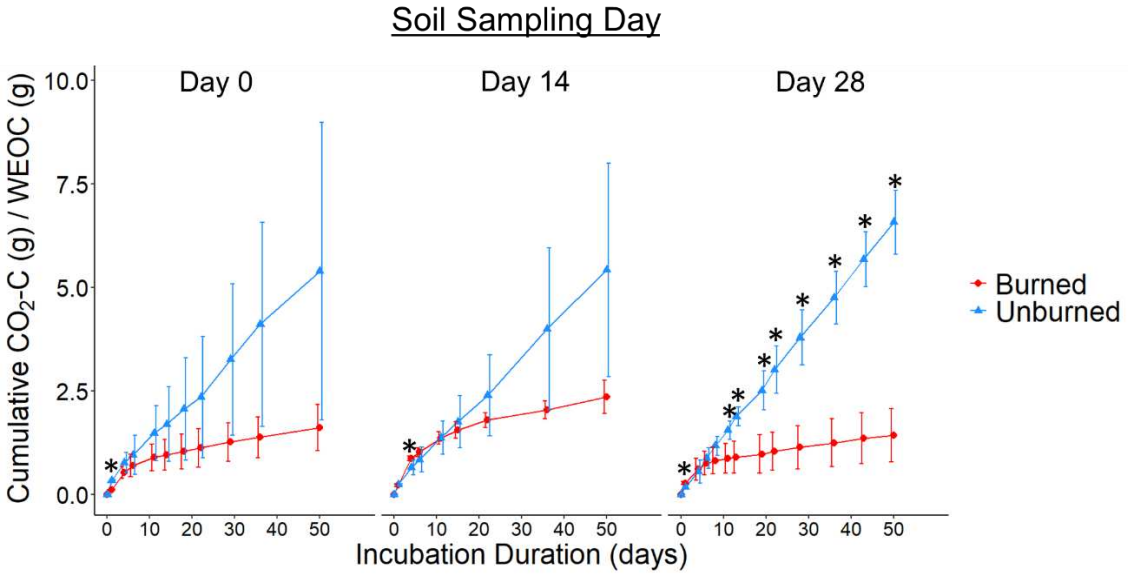

Figure 3.24. Cumulative CO_2-C emissions from burned and unburned soil incubations normalized to water extractable organic carbon (WEOC) content. WEOC data from **Table B2** were used to normalize the carbon dioxide emission data. Asterisk indicates a statistically significant difference (t-test, $p < 0.05$) between burned and unburned values within a given incubation day (n=5, error = standard deviation). Error bars were jittered to avoid overlap.

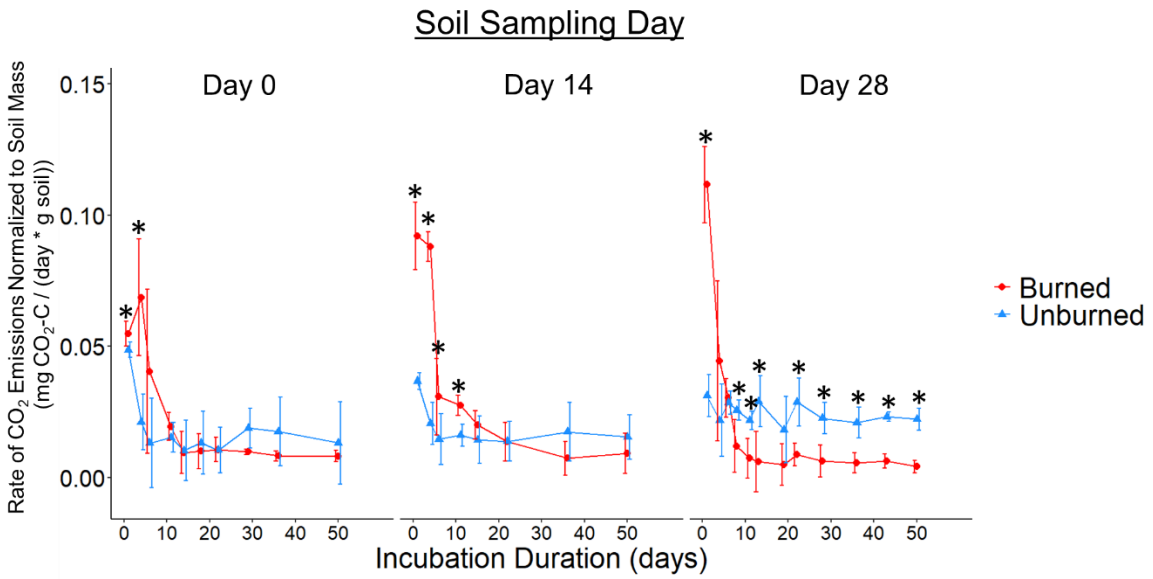

Figure 3.25. Rate of CO_2-C emissions from burned and unburned soil incubations normalized to soil mass. Rates were calculated by dividing the total CO_2-C emitted between two measurement timepoints by the elapsed time between those two measurement timepoints. Asterisk indicates a statistically significant difference (t-test, $p < 0.05$) between burned and unburned values within a given incubation day (n=5, error = standard deviation). Error bars were jittered to avoid overlap.

displaced into the jar headspace; however, this process was likely restricted to the first few hours of incubation as evidenced by Marañón-Jiménez et al. who measured CO2 respiration from burned soils in the Sierra Nevada Natural and National Parks.[126] After comparing decay rates of CO_2 flux after water was added to burned soil, they concluded that approximately 64% of soil CO_2 emissions during the first 2 h could be attributed to the release of CO_2 trapped in soil pores with the rest likely related to biological processes.[126] Thus, we anticipate that the physical displacement of CO_2 in our study was most likely restricted to the first few hours of incubation whereas the remaining CO_2 emissions were due to microbial respiration which can persist over weeks. For example, the biological mineralization of PyOM has been observed over the course of 57, 14, and 35 days in laboratory studies which are comparable time periods to the incubations conducted here.[23,39,127] Overall, the elevated WEOC content, enrichment of amino acids and organic acids, presence of

saccharides, and detection of heterotrophic microbes in burned soil suggest that microbial mineralization of SOM contributed to the CO_2 emissions observed in these incubations.

Soil aggregate disruption may have contributed to the elevated CO_2 emissions in the burned soil. Soil aggregate stability can decrease after high intensity fires due to microbial biomass loss, SOM combustion, and dehydroxylation of clay minerals.[128–131] This aggregate disruption could make SOM more accessible by exposing physically protected SOM to microbial biodegradation, contributing to mineralization and CO_2 soil emissions.[110,132]

Considering that only ~3.3% of total carbon in burned soil was released as CO_2 during the 50-day incubations, the readily biodegradable SOM pool in burned soil likely represents a relatively small fraction of the total SOM content.[127] Nevertheless, the soil CO_2 emission results support our first hypothesis that immediately after fire (i.e., the first 28 days), SOM in burned soil can be mineralized by microbes in a complex, burned soil environment.

Overall, this study demonstrated that readily biodegradable SOM is present and accessible by microbes within mineral soils immediately after a simulated high intensity burn. Burned soil had more WEOC which likely fueled CO_2 emissions despite lower microbial richness. Concurrently, the detection of putative, heterotrophic microbes in the burned soil represents a mechanism via which SOM in burned soil is mineralized.[40,41] The identification of enriched metabolites (i.e., glycine and other amino acids, some saccharides, protocatechuate) in burned soil offers insight into the SOM pools that may be available for microbial metabolism postfire. Finally, this study demonstrated that pyrocosms can be used to evaluate postfire soil dynamics beyond analyzing shifts in fungal community composition as pioneered by Bruns et al.[57]

3.4 ENVIRONMENTAL IMPLICATIONS

The metabolism of SOM in complex burned soils observed in this study supports the laboratory-based studies that reported rapid biodegradation of PyOM,38−41,117[38–41,127] and our findings provide further evidence for the degradation pathways of aromatic compounds in burned soils.[12,39] Our characterization of organic acids, amino acids, and saccharides advances our collective understanding of what substrates are available for microbial metabolism in burned soils that can fuel postfire soil recovery. The loss of ectomycorrhizal fungi after burning (**Figure 3.6F**) - which may have been impacted by soil disturbance and separation from plant hosts during soil sampling and pyrocosm assembly - and decreases in fungal diversity after burning (**Figure 3.6B**) have implications for nutrient transport through fungal networks and may constrain the recovery of ectomycorrhizal-obligate species such as lodgepole pine. However, the detection of heterotrophic microbes, presence of biodegradable SOM, and observed postfire metabolism highlight the resilience of soil systems in response to high severity burns which are projected to increase due to climate change.[6]

Wildfires are well-known to be fatal to many soil microbial taxa and to generate persistent forms of SOM.[12,13,37,133] However, our study highlights that both biodegradable forms of SOM and heterotrophic microbes are present after extreme soil heating. The variety of detected SOM in this study suggests that SOM in burned soil is comprised of a diverse array of chemical compounds (e.g., PyOM, SOM that was not thermochemically altered, and intracellular metabolites released from cell lysis) that feature varying degrees of biodegradability. Thus, severely burned environments are not dominated solely by PyOM and are not sterile. Rather, our experimental burns demonstrated that the surviving soil microbiome was active and able to metabolize the heterogeneous SOM in the burned soil.

3.5 AUTHOR CONTRIBUTIONS

According to CRediT criteria, my contribution to the work included conceptualization, methodology, formal analysis, investigation, data curation, writing – original draft, writing – review and editing, and visualization. Contributions by Julie A. Fowler include conceptualization, methodology, formal analysis, investigation, data curation, writing – original draft, writing – review and editing, and visualization. Contributions by Charles C. Rhoades include conceptualization, methodology, resources, writing – review and editing, and supervision. Contributions by Holly K. Roth include conceptualization, methodology, investigation, and writing – review and editing. Contributions by Corey D. Broeckling include methodology, formal analysis, resources, and writing – review and editing. Contributions by Timothy S. Fegel include investigation, resources, data curation, and writing – review and editing. Contributions by Amy M. McKenna include formal analysis, investigation, resources, data curation, and writing – review and editing. Contributions by Emily K. Bechtold include formal analysis, investigation, data curation, writing – review and editing, and visualization. Contributions by Claudia M. Boot include resources, and writing – review and editing. Contributions by Michael J. Wilkins include conceptualization, resources, writing – review and editing, supervision, project administration, and funding acquisition. Contributions by Thomas Borch include conceptualization, resources, writing – review and editing, supervision, project administration, and funding acquisition.

More specifically, Julie A. Fowler and Emily K. Bechtold were responsible for the microbial analyses. Charles C. Rhoades collected soil and lodgepole pine wood for this chapter. Timothy S. Fegel was responsible for collecting dissolved organic carbon and dissolved total nitrogen values that were used to calculate water-extractable organic carbon and water-extractable total nitrogen as well as generating the ammonium results. Amy M. McKenna operated the Fourier

transform ion cyclotron resonance mass spectrometer and calibrated the resultant data. I designed the pyrocosms used in this study, conducted the pyrocosm burnings, measured total soil carbon and nitrogen, measured soil pH, led the gas chromatography-mass spectrometry analysis, analyzed the Fourier transform ion cyclotron resonance mass spectrometry data, and conducted the soil CO_2 respiration incubations, contributing to my conceptualization, methodology, formal analysis, investigation and data curation. For visualization, I was produced all figures except for **Figures 3.5**, **3.6**, **3.7**, and **3.8** (which were produced by Emily Bechtold and Julie Fowler).

3.6 ACKNOWLEDGEMENTS

This research was funded by M.J.W. and T.B. from the National Science Foundation under grant number 2114868 and the United States Department of Agriculture (USDA) National Institute of Food and Agriculture through AFRI grant number 2021-67019-34608. The Table of Contents artwork was created with BioRender.com. We thank Troy Bauder, Karl Whitman, and the Poudre Fire Authority for providing a safe location for the pyrocosm burns. We thank Daniel Reuss and the EcoCore facility at Colorado State University for assisting with soil CO2 measurements and total soil C and N measurements. GC-MS was performed at the CSU ARC-BIO facility (RRID: SCR_021758). Thanks to Dr. Prithwiraj De for helping with GC-MS derivatization and sample preparation. Thanks to Dr. Robert Young for providing code for the FTICR MS data analysis. Thanks to researchers at the Rocky Mountain Research Station biogeochemistry lab, owned by the USDA Forest Service, for conducting dissolved organic carbon, dissolved total nitrogen, and ammonium measurements. Thanks to researchers at the National High Magnetic Field Laboratory ICR User Facility which is supported by the National Science Foundation Division of Chemistry and Division of Material Research through DMR-1644779 and DMR-2128556. Data for this research were provided by the Niwot Ridge LTER program (NWT VII: NSF DEB-1637686, NWT

VIII: NSF DEB-2224439). Use of firm, trade, or product names is for descriptive purposes only and does not imply indorsement by the U.S. government.

CHAPTER 3 REFERENCES

(1) NIFC. National Large Incident Year-to-Date Report. **2020**.

(2) Hoover, K.; Hanson, L. A. Wildfire Statistics. *Congr. Res. Serv.* **2021**, 1-3. https://crsreports.congress.gov.

(3) Nolan, R. H.; Boer, M. M.; Collins, L.; Resco De Dios, V.; Clarke, H.; Jenkins, M.; Kenny, B.; Bradstock, R. A. Causes and Consequences of Eastern Australia's 2019–20 Season of Mega-fires. *Glob. Change Biol.* **2020**, *26* (3), 1039–1041. https://doi.org/10.1111/gcb.14987.

(4) Pausas, J. G.; Keeley, J. E. Wildfires as an Ecosystem Service. *Front. Ecol. Environ.* **2019**, *17* (5), 289–295. https://doi.org/10.1002/fee.2044.

(5) Keeley, J. E. Fire Intensity, Fire Severity and Burn Severity: A Brief Review and Suggested Usage. *Int. J. Wildland Fire* **2009**, *18* (1), 116–126. https://doi.org/10.1071/wf07049.

(6) Jones, M. W.; Abatzoglou, J. T.; Veraverbeke, S.; Andela, N.; Lasslop, G.; Forkel, M.; Smith, A. J. P.; Burton, C.; Betts, R. A.; Van Der Werf, G. R.; Sitch, S.; Canadell, J. G.; Santín, C.; Kolden, C.; Doerr, S. H.; Le Quéré, C. Global and Regional Trends and Drivers of Fire Under Climate Change. *Rev. Geophys.* **2022**, *60* (3), 1–76. https://doi.org/10.1029/2020rg000726.

(7) Brucker, C. P.; Livneh, B.; Minear, J. T.; Rosario-Ortiz, F. L. A Review of Simulation Experiment Techniques Used to Analyze Wildfire Effects on Water Quality and Supply. *Environ. Sci. Process. Impacts* **2022**, *24* (8), 1110–1132. https://doi.org/10.1039/d2em00045h.

(8) Higuera, P. E.; Cook, M. C.; Balch, J. K.; Stavros, E. N.; Mahood, A. L.; St. Denis, L. A. Shifting Social-Ecological Fire Regimes Explain Increasing Structure Loss from Western Wildfires. *PNAS Nexus* **2023**, *2*, 1–11. https://doi.org/10.1093/pnasnexus/pgad005.

(9) González-Pérez, J. A.; González-Vila, F. J.; Almendros, G.; Knicker, H. The Effect of Fire on Soil Organic Matter—a Review. *Environ. Int.* **2004**, *30* (6), 855–870. https://doi.org/10.1016/j.envint.2004.02.003.

(10) LaRowe, D. E.; Van Cappellen, P. Degradation of Natural Organic Matter: A Thermodynamic Analysis. *Geochim. Cosmochim. Acta* **2011**, *75* (8), 2030–2042. https://doi.org/10.1016/j.gca.2011.01.020.

(11) Pressler, Y.; Moore, J. C.; Cotrufo, M. F. Belowground Community Responses to Fire: Meta-Analysis Reveals Contrasting Responses of Soil Microorganisms and Mesofauna. *Oikos* **2019**, *128* (3), 309–327. https://doi.org/10.1111/oik.05738.

(12) Nelson, A. R.; Narrowe, A. B.; Rhoades, C. C.; Fegel, T. S.; Daly, R. A.; Roth, H. K.; Chu, R. K.; Amundson, K. K.; Young, R. B.; Steindorff, A. S.; Mondo, S. J.; Grigoriev, I. V.; Salamov, A.; Borch, T.; Wilkins, M. J. Wildfire-Dependent Changes in Soil Microbiome Diversity and Function. *Nat. Microbiol.* **2022**, *7* (9), 1419–1430. https://doi.org/10.1038/s41564-022-01203-y.

(13) Caifa, M. V.; Nelson, A. R.; Borch, T.; Roth, H. K.; Fegel, T.; Rhoades, C. C.; Wilkins, M. J.; Glassman, S. I. Distinct Fungal and Bacterial Responses to Fire Severity and Soil Depth across a Ten-Year Wildfire Chronosequence in Bettle-Killed Lodgepole Pine Forests. *For. Ecol. Manag.* **2023**, *544*, 121160.

(14) Woolet, J.; Whitman, T. Pyrogenic Organic Matter Effects on Soil Bacterial Community Composition. *Soil Biol. Biochem.* **2020**, *141*, 107678. https://doi.org/10.1016/j.soilbio.2019.107678.

(15) Whitman, T.; Whitman, E.; Woolet, J.; Flannigan, M. D.; Thompson, D. K.; Parisien, M.-A. Soil Bacterial and Fungal Response to Wildfires in the Canadian Boreal Forest across a Burn

Severity Gradient. *Soil Biol. Biochem.* **2019**, *138*, 107571. https://doi.org/10.1016/j.soilbio.2019.107571.

(16) Whitman, T.; Pepe-Ranney, C.; Enders, A.; Koechli, C.; Campbell, A.; Buckley, D. H.; Lehmann, J. Dynamics of Microbial Community Composition and Soil Organic Carbon Mineralization in Soil Following Addition of Pyrogenic and Fresh Organic Matter. *ISME J.* **2016**, *10* (12), 2918–2930. https://doi.org/10.1038/ismej.2016.68.

(17) Enright, D. J.; Frangioso, K. M.; Isobe, K.; Rizzo, D. M.; Glassman, S. I. Mega-fire in Redwood Tanoak Forest Reduces Bacterial and Fungal Richness and Selects for Pyrophilous Taxa That Are Phylogenetically Conserved. *Mol. Ecol.* **2022**, *31* (8), 2475–2493. https://doi.org/10.1111/mec.16399.

(18) Roth, H. K.; McKenna, A. M.; Simpson, M. J.; Chen, H.; Srikanthan, N.; Fegel, T.; Nelson, A. R.; Rhoades, C. C.; Wilkins, M. J.; Borch, T. Effects of Burn Severity on Organic Nitrogen and Carbon Chemistry in High-Elevation Forest Soils. *Soil Environ. Health* **2023**, 100023.

(19) Bahureksa, W.; Young, R. B.; McKenna, A. M.; Chen, H.; Thorn, K. A.; Rosario-Ortiz, F. L.; Borch, T. Nitrogen Enrichment during Soil Organic Matter Burning and Molecular Evidence of Maillard Reactions. *Environ. Sci. Technol.* **2022**, *56* (7), 4597–4609. https://doi.org/10.1021/acs.est.1c06745.

(20) Cawley, K. M.; Hohner, A. K.; Podgorski, D. C.; Cooper, W. T.; Korak, J. A.; Rosario-Ortiz, F. L. Molecular and Spectroscopic Characterization of Water Extractable Organic Matter from Thermally Altered Soils Reveal Insight into Disinfection Byproduct Precursors. *Environ. Sci. Technol.* **2017**, *51* (2), 771–779. https://doi.org/10.1021/acs.est.6b05126.

(21) Knicker, H. How Does Fire Affect the Nature and Stability of Soil Organic Nitrogen and Carbon? A Review. *Biogeochemistry* **2007**, *85* (1), 91–118. https://doi.org/10.1007/s10533-007-9104-4.

(22) Bird, M. I.; Wynn, J. G.; Saiz, G.; Wurster, C. M.; McBeath, A. The Pyrogenic Carbon Cycle. *Annu. Rev. Earth Planet. Sci.* **2015**, *43* (1), 273–298. https://doi.org/10.1146/annurev-earth-060614-105038.

(23) Zimmerman, A. R. Abiotic and Microbial Oxidation of Laboratory-Produced Black Carbon (Biochar). *Environ. Sci. Technol.* **2010**, *44* (4), 1295–1301. https://doi.org/10.1021/es903140c.

(24) Roth, H. K.; Borch, T.; Young, R. B.; Bahureksa, W.; Blakney, G. T.; Nelson, A. R.; Wilkins, M. J.; McKenna, A. M. Enhanced Speciation of Pyrogenic Organic Matter from Wildfires Enabled by 21 T FT-ICR Mass Spectrometry. *Anal. Chem.* **2022**, *94* (6), 2973–2980. https://doi.org/10.1021/acs.analchem.1c05018.

(25) Zhang, Y.; Biswas, A. The Effects of Forest Fire on Soil Organic Matter and Nutrients in Boreal Forests of North America: A Review; Springer Singapore, 2017; pp 465–476.

(26) Torres-Rojas, D.; Hestrin, R.; Solomon, D.; Gillespie, A. W.; Dynes, J. J.; Regier, T. Z.; Lehmann, J. Nitrogen Speciation and Transformations in Fire-Derived Organic Matter. *Geochim. Cosmochim. Acta* **2020**, *276*, 170–185. https://doi.org/10.1016/j.gca.2020.02.034.

(27) Pellegrini, A. F. A.; Harden, J.; Georgiou, K.; Hemes, K. S.; Malhotra, A.; Nolan, C. J.; Jackson, R. B. Fire Effects on the Persistence of Soil Organic Matter and Long-Term Carbon Storage. *Nat. Geosci.* **2021**, *15*, 5–13. https://doi.org/10.1038/s41561-021-00867-1.

(28) Pellegrini, A. F. A.; Ahlström, A.; Hobbie, S. E.; Reich, P. B.; Nieradzik, L. P.; Staver, A. C.; Scharenbroch, B. C.; Jumpponen, A.; Anderegg, W. R. L.; Randerson, J. T.; Jackson, R.

B. Fire Frequency Drives Decadal Changes in Soil Carbon and Nitrogen and Ecosystem Productivity. *Nature* **2018**, *553* (7687), 194–198. https://doi.org/10.1038/nature24668.

(29) Wagner, S.; Coppola, A. I.; Stubbins, A.; Dittmar, T.; Niggemann, J.; Drake, T. W.; Seidel, M.; Spencer, R. G. M.; Bao, H. Questions Remain about the Biolability of Dissolved Black Carbon along the Combustion Continuum. *Nat. Commun.* **2021**, *12*. https://doi.org/10.1038/s41467-021-24477-y.

(30) Myers-Pigg, A. N.; Louchouarn, P.; Amon, R. M. W.; Prokushkin, A.; Pierce, K.; Rubtsov, A. Labile Pyrogenic Dissolved Organic Carbon in Major Siberian Arctic Rivers: Implications for Wildfire-Stream Metabolic Linkages. *Geophys. Res. Lett.* **2015**, *42* (2), 377–385. https://doi.org/10.1002/2014gl062762.

(31) Norwood, M. J.; Louchouarn, P.; Kuo, L.-J.; Harvey, O. R. Characterization and Biodegradation of Water-Soluble Biomarkers and Organic Carbon Extracted from Low Temperature Chars. *Org. Geochem.* **2013**, *56*, 111–119.

(32) Hestrin, R.; Torres-Rojas, D.; Dynes, J. J.; Hook, J. M.; Regier, T. Z.; Gillespie, A. W.; Smernik, R. J.; Lehmann, J. Fire-Derived Organic Matter Retains Ammonia through Covalent Bond Formation. *Nat. Commun.* **2019**, *10*, 1. https://doi.org/10.1038/s41467-019-08401-z.

(33) Lutfalla, S.; Abiven, S.; Barre, P.; Wiedemeier, D. B.; Christensen, B. T.; Houot, S.; Katterer, T.; Macdonald, A. J.; van Oort, F.; Chenu, C. Pyrogenic Carbon Lacks Long-Term Persistence in Temperate Arable Soils. *Front. Earth Sci.* **2017**, *5*, 1–10.

(34) Bowring, S. P. K.; Jones, M. W.; Ciais, P.; Guenet, B.; Abiven, S. Pyrogenic Carbon Decomposition Critical to Resolving Fire's Role in the Earth System. *Nat. Geosci.* **2022**, *15* (2), 135–142. https://doi.org/10.1038/s41561-021-00892-0.

(35) Coppola, A. I.; Wagner, S.; Lennartz, S. T.; Seidel, M.; Ward, N. D.; Dittmar, T.; Santín, C.; Jones, M. W. The Black Carbon Cycle and Its Role in the Earth System. *Nat. Rev. Earth Environ.* **2022**, *3* (8), 516–532. https://doi.org/10.1038/s43017-022-00316-6.

(36) Santín, C.; Doerr, S. H.; Kane, E. S.; Masiello, C. A.; Ohlson, M.; De La Rosa, J. M.; Preston, C. M.; Dittmar, T. Towards a Global Assessment of Pyrogenic Carbon from Vegetation Fires. *Glob. Change Biol.* **2016**, *22* (1), 76–91. https://doi.org/10.1111/gcb.12985.

(37) Liang, B.; Lehmann, J.; Solomon, D.; Sohi, S.; Thies, J. E.; Skjemstad, J. O.; Luizao, F. J.; Engelhard, M. H.; Neves, E. G.; Wirick, S. Stability of Biomass-Derived Black Carbon in Soils. *Geochim. Cosmochim. Acta* **2008**, *72*, 6069–6078.

(38) De La Rosa, J. M.; Miller, A. Z.; Knicker, H. Soil-Borne Fungi Challenge the Concept of Long-Term Biochemical Recalcitrance of Pyrochar. *Sci. Rep.* **2018**, *8*. https://doi.org/10.1038/s41598-018-21257-5.

(39) Fischer, M. S.; Stark, Frances G.; Berry, T. D.; Zeba, N.; Whitman, T.; Traxler, M. F. Pyrolyzed Substrates Induce Aromatic Compound Metabolism in the Post-Fire Fungus, Pyronema Domesticum. *Front. Microbiol.* **2021**, *12*, 1–12.

(40) Goranov, A. I.; Wozniak, A. S.; Bostick, K. W.; Zimmerman, A. R.; Mitra, S.; Hatcher, P. G. Microbial Labilization and Diversification of Pyrogenic Dissolved Organic Matter. *Biogeosciences* **2022**, *19* (5), 1491–1514. https://doi.org/10.5194/bg-19-1491-2022.

(41) Bostick, K. W.; Zimmerman, A. R.; Goranov, A. I.; Mitra, S.; Hatcher, P. G.; Wozniak, A. S. Biolability of Fresh and Photodegraded Pyrogenic Dissolved Organic Matter From Laboratory-Prepared Chars. *J. Geophys. Res. Biogeosciences* **2021**, *126* (5), 1–17. https://doi.org/10.1029/2020jg005981.

(42) Schmidt, M. W. I.; Torn, M. S.; Abiven, S.; Dittmar, T.; Guggenberger, G.; Janssens, I. A.; Kleber, M.; Kögel-Knabner, I.; Lehmann, J.; Manning, D. A. C.; Nannipieri, P.; Rasse, D. P.; Weiner, S.; Trumbore, S. E. Persistence of Soil Organic Matter as an Ecosystem Property. *Nature* **2011**, *478* (7367), 49–56. https://doi.org/10.1038/nature10386.

(43) Yang, F.; Xu, Z.; Yu, L.; Gao, B.; Xu, X.; Zhao, L.; Cao, X. Kaolinite Enhances the Stability of the Dissolvable and Undissolvable Fractions of Biochar via Different Mechanisms. *Environ. Sci. Technol.* **2018**, *52* (15), 8321–8329. https://doi.org/10.1021/acs.est.8b00306.

(44) Yang, F.; Xu, Z.; Huang, Y.; Tsang, D. C. W.; Sik Ok, Y.; Zhao, L.; Qui, H.; Xu, X.; Cao, X. Stabilization of Dissolvable Biochar by Soil Minerals: Release Reduction and Organo-Mineral Complexes Formation. *J. Hazard. Mater.* **2021**, *412*, 125213.

(45) Wang, M.; Schoettner, M.; Xu, S.; Paetz, C.; Wilde, J.; Baldwin, I. T.; Groten, K. Catechol, a Major Component of Smoke, Influences Primary Root Growth and Root Hair Elongation through Reactive Oxygen Species-mediated Redox Signaling. *New Phytol.* **2017**, *213* (4), 1755–1770. https://doi.org/10.1111/nph.14317.

(46) De La Rosa, J. M.; González-Pérez, J. A.; González-Vázquez, R.; Knicker, H.; López-Capel, E.; Manning, D. A. C.; González-Vila, F. J. Use of Pyrolysis/GC–MS Combined with Thermal Analysis to Monitor C and N Changes in Soil Organic Matter from a Mediterranean Fire Affected Forest. *CATENA* **2008**, *74* (3), 296–303. https://doi.org/10.1016/j.catena.2008.03.004.

(47) Jiménez-González, M. A.; De La Rosa, J. M.; Jiménez-Morillo, N. T.; Almendros, G.; González-Pérez, J. A.; Knicker, H. Post-Fire Recovery of Soil Organic Matter in a Cambisol from Typical Mediterranean Forest in Southwestern Spain. *Sci. Total Environ.* **2016**, *572*, 1414–1421. https://doi.org/10.1016/j.scitotenv.2016.02.134.

(48) Faria, S. R.; De La Rosa, J. M.; Knicker, H.; González-Pérez, J. A.; Keizer, J. J. Molecular Characterization of Wildfire Impacts on Organic Matter in Eroded Sediments and Topsoil in Mediterranean Eucalypt Stands. *CATENA* **2015**, *135*, 29–37. https://doi.org/10.1016/j.catena.2015.07.007.

(49) Jiménez-Morillo, N. T.; de la Rosa, J. M.; Waggoner, D.; Almendros, G.; González-Vila, F. J.; González-Pérez, J. A. Fire Effects in the Molecular Structure of Soil Organic Matter Fractions under Quercus Suber Cover. *CATENA* **2016**, *145*, 266–273.

(50) Jiménez-Morillo, N. T.; Almendros, G.; De la Rosa, J. M.; Jordán, A.; Zavala, L. M.; Granged, A. J. P.; González-Pérez, J. A. Effect of a Wildfire and of Post-Fire Restoration Actions in the Organic Matter Structure in Soil Fractions. *Sci. Total Environ.* **2020**, *728*, 138715. https://doi.org/10.1016/j.scitotenv.2020.138715.

(51) Chen, H.; Wang, J.-J.; Ku, P.-J.; Tsui, M. T.-K.; Abney, R. B.; Berhe, A. A.; Zhang, Q.; Burton, S. D.; Dahlgren, R. A.; Chow, A. T. Burn Intensity Drives the Alteration of Phenolic Lignin to (Poly) Aromatic Hydrocarbons as Revealed by Pyrolysis Gas Chromatography–Mass Spectrometry (Py-GC/MS). *Environ. Sci. Technol.* **2022**, *56* (17), 12678–12687. https://doi.org/10.1021/acs.est.2c00426.

(52) Seitz, V. A.; McGivern, B. B.; Daly, R. A.; Chaparro, J. M.; Borton, M. A.; Sheflin, A. M.; Kresovich, S.; Shields, L.; Schipanski, M. E.; Wrighton, K. C.; Prenni, J. E. Variation in Root Exudate Composition Influences Soil Microbiome Membership and Function. *Appl. Environ. Microbiol.* **2022**, *88* (11), 1.

(53) Swenson, T. L. Untargeted Soil Metabolomics Methods for Analysis of Extractable Organic Matter. *Soil Biol. Biochem.* **2015**, *80*, 189–198. https://doi.org/doi:10.1016/j.soilbio.2014.10.007.

(54) Bahureksa, W.; Borch, T.; Young, R. B.; Weisbrod, C. R.; Blakney, G. T.; McKenna, A. M. Improved Dynamic Range, Resolving Power, and Sensitivity Achievable with FT-ICR Mass Spectrometry at 21 T Reveals the Hidden Complexity of Natural Organic Matter. *Anal. Chem.* **2022**, *94* (6), 2973–2980. https://doi.org/10.1021/acs.analchem.2c02377.

(55) Jimenez-Morillo, N. T.; Gonzalez-Perez, J. A.; Almendros, G.; De la Rosa, J. M.; Waggoner, D. C. J.; Zavala, L. M.; Gonzalez-Vila, F. J. H. Ultra-High Resolution Mass Spectrometry of Physical Speciation Patterns of Organic Matter in Fire-Affected Soils. *J. Environ. Manage.* **2018**, *225*, 139–147.

(56) Zhang, Q.; Wang, Y.; Guan, P.; Zhang, P.; Mo, X.; Yin, G.; Qu, B.; Xu, S.; He, C.; Shi, Q.; Zhang, G.; Dittmar, T.; Wang, J. Temperature Thresholds of Pyrogenic Dissolved Organic Matter in Heating Experiments Simulating Forest Fires. *Environ. Sci. Technol.* **2023**, *57*, 17291–17301.

(57) Bruns, T. D.; Chung, J. A.; Carver, A. A.; Glassman, S. I. A Simple Pyrocosm for Studying Soil Microbial Response to Fire Reveals a Rapid, Massive Response by Pyronema Species. *PLoS ONE* **2020**, *15* (3), 1–20.

(58) Long Draw Reservoir SNOTEL Site 1123 Database. United States Department of Agriculture Natural Resources Convservation Service National Water and Climate Center. Https://Wcc.Sc.Egov.Usda.Gov/Nwcc/Site?Sitenum=1123. (Accessed 2023-09-18).

(59) Roshan, A.; Biswas, A. Fire-Induced Geochemical Changes in Soil: Implication for the Element Cycling. *Sci. Total Environ.* **2023**, *868*, 161714.

(60) CoAgMet Daily Summary Access Database. Colorado State University. Https://Coagmet.Colostate.Edu/Cgi-Bin/Dailysum_form.Pl (Accessed 2023-09-18).

(61) Novara, A.; Gristina, L.; Bodì, M. B.; Cerdà, A. The Impact of Fire on Redistribution of Soil Organic Matter on a Mediterranean Hillslope under Maquia Vegetation Type. *Land Degrad. Dev.* **2011**, *22* (6), 530–536. https://doi.org/10.1002/ldr.1027.

(62) Dove, N. C.; Taş, N.; Hart, S. C. Ecological and Genomic Responses of Soil Microbiomes to High-Severity Wildfire: Linking Community Assembly to Functional Potential. *ISME J.* **2022**, *16* (7), 1853–1863. https://doi.org/10.1038/s41396-022-01232-9.

(63) Oksanen, J.; Simpson, G. L.; Blanchet, F. G.; Kindt, R.; Legendre, P.; Minchin, P. R.; O'Hara, R. B.; Solymos, P.; Stevens, M. H. H.; Szoecs, E.; Wagner, H.; Barbour, M.; Bedward, M.; Bolker, B.; Borcard, D.; Carvalho, G.; Chirico, M.; De Caceres, M.; Durand, S.; Evangelista, H. B. A.; FitzJohn, R.; Friendly, M.; Furneaux, B.; Hannigan, G.; Hill, M. O.; Lahti, L.; McGlinn, D.; Ouellette, M.-H.; Cunha, E. R.; Smith, T.; Stier, A.; Ter Braak, C. J. F.; Weedon, J. Vegan: Community Ecology Package. R Package Version 2.5-7. 2020. **2022**.

(64) Jain, A. K.; Murty, M. N.; Flynn, P. J. Data Clustering: A Review. *ACM Comput. Surv.* **1999**, *31* (3), 264–323.

(65) Ren, S.; Hinzman, A. A.; Kang, E. L.; Szczesniak, R. D.; Lu, L. J. Computational and Statistical Analysis of Metabolomics Data. *Metabolomics* **2015**, *11* (6), 1492–1513. https://doi.org/10.1007/s11306-015-0823-6.

(66) Dittmar, T.; Koch, B.; Hertkorn, N.; Kattner, G. A Simple and Efficient Method for the Solid-Phase Extraction of Dissolved Organic Matter (SPE-DOM) from Seawater. *Limnol. Oceanogr. Methods* **2008**, *6* (6), 230–235. https://doi.org/10.4319/lom.2008.6.230.

(67) Emmett, M. R.; White, F. M.; Hendrickson, C. L.; Shi, S. D.-H.; Marshall, A. G. Application of Micro-Electrospray Liquid Chromatography Techniques to FT-ICR MS to Enable

High-Sensitivity Biological Analysis. *J. Am. Soc. Mass Spectrom.* **1998**, *9* (4), 333–340. https://doi.org/10.1016/S1044-0305(97)00287-0.

(68) Hendrickson, C. L.; Quinn, J. P.; Kaiser, N. K.; Smith, D. F.; Blakney, G. T.; Chen, T.; Marshall, A. G.; Weisbrod, C. R.; Beu, S. C. 21 Tesla Fourier Transform Ion Cyclotron Resonance Mass Spectrometer: A National Resource for Ultrahigh Resolution Mass Analysis. *J. Am. Soc. Mass Spectrom.* **2015**, *26* (9), 1626–1632. https://doi.org/10.1007/s13361-015-1182-2.

(69) Smith, D. F.; Podgorski, D. C.; Rodgers, R. P.; Blakney, G. T.; Hendrickson, C. L. 21 Tesla FT-ICR Mass Spectrometer for Ultrahigh-Resolution Analysis of Complex Organic Mixtures. *Anal. Chem.* **2018**, *90* (3), 2041–2047. https://doi.org/10.1021/acs.analchem.7b04159.

(70) Kaiser, N. K.; McKenna, A. M.; Savory, J. J.; Hendrickson, C. L.; Marshall, A. G. Tailored Ion Radius Distribution for Increased Dynamic Range in FT-ICR Mass Analysis of Complex Mixtures. *Anal. Chem.* **2013**, *85* (1), 265–272. https://doi.org/10.1021/ac302678v.

(71) Chen, T.; Beu, S. C.; Kaiser, N. K.; Hendrickson, C. L. Note: Optimized Circuit for Excitation and Detection with One Pair of Electrodes for Improved Fourier Transform Ion Cyclotron Resonance Mass Spectrometry. *Rev. Sci. Instrum.* **2014**, *85* (6), 066107. https://doi.org/10.1063/1.4883179.

(72) Boldin, I. A.; Nikolaev, E. N. Fourier Transform Ion Cyclotron Resonance Cell with Dynamic Harmonization of the Electric Field in the Whole Volume by Shaping of the Excitation and Detection Electrode Assembly. *Rapid Commun. Mass Spectrom.* **2011**, *25* (1), 122–126. https://doi.org/10.1002/rcm.4838.

(73) Blakney, G. T.; Hendrickson, C. L.; Marshall, A. G. Predator Data Station: A Fast Data Acquisition System for Advanced FT-ICR MS Experiments. *Int. J. Mass Spectrom.* **2011**, *306*, 246–252.

(74) Xian, F.; Hendrickson, C. L.; Blakney, G. T.; Beu, S. C.; Marshall, A. G. Automated Broadband Phase Correction of Fourier Transform Ion Cyclotron Resonance Mass Spectra. *Anal. Chem.* **2010**, *82* (21), 8807–8812. https://doi.org/10.1021/ac101091w.

(75) Savory, J. J.; Kaiser, N. K.; McKenna, A. M.; Xian, F.; Blakney, G. T.; Rodgers, R. P.; Hendrickson, C. L.; Marshall, A. G. Parts-Per-Billion Fourier Transform Ion Cyclotron Resonance Mass Measurement Accuracy with a "Walking" Calibration Equation. *Anal. Chem.* **2011**, *83* (5), 1732–1736. https://doi.org/10.1021/ac102943z.

(76) Kendrick, E. A Mass Scale Based on CH_2 = 14.0000 for High Resolution Mass Spectrometry of Organic Compounds. *Anal. Chem.* **1963**, *35* (13), 2146–2154. https://doi.org/10.1021/ac60206a048.

(77) Hughey, C. A.; Hendrickson, C. L.; Rodgers, R. P.; Marshall, A. G.; Qian, K. Kendrick Mass Defect Spectrum: A Compact Visual Analysis for Ultrahigh-Resolution Broadband Mass Spectra. *Anal. Chem.* **2001**, *73*, 4676–4681. https://doi.org/10.1021/ac010560.

(78) Corilo, Y. E. *PetroOrg Softw.* **2014**, *Florida State University, Omics LLC: Tallahassee, FL*.

(79) Bahureksa, W.; Tfaily, M. M.; Boiteau, R. M.; Young, R. B.; Logan, M. N.; McKenna, A. M.; Borch, T. Soil Organic Matter Characterization by Fourier Transform Ion Cyclotron Resonance Mass Spectrometry (FTICR MS): A Critical Review of Sample Preparation, Analysis, and Data Interpretation. *Environ. Sci. Technol.* **2021**, *55* (14), 9637–9656. https://doi.org/10.1021/acs.est.1c01135.

(80) Vetter, W. F. W.; McLafferty, F. T. Interpretation of Mass Spectra. Fourth Edition (1993). University Science Books, Mill Valley, California. *Biol Mass Spectrom* **1994**, *23* (6), 379.

(81) Kind, T.; Fiehn, O. Seven Golden Rules for Heuristic Filtering of Molecular Formulas Obtained by Accurate Mass Spectrometry. *BMC Bioinformatics* **2007**, *8* (1), 105. https://doi.org/10.1186/1471-2105-8-105.

(82) Koch, B. P.; Dittmar, T. From Mass to Structure: An Aromaticity Index for High-Resolution Mass Data of Natural Organic Matter. *Rapid Commun. Mass Spectrom.* **2006**, *20* (5), 926–932. https://doi.org/10.1002/rcm.2386.

(83) Koch, B. P.; Dittmar, T. From Mass to Structure: An Aromaticity Index for High-Resolution Mass Data of Natural Organic Matter. *Rapid Commun. Mass Spectrom.* **2016**, *30* (1), 250–250. https://doi.org/10.1002/rcm.7433.

(84) Riedel, T.; Biester, H.; Dittmar, T. Molecular Fractionation of Dissolved Organic Matter with Metal Salts. *Environ. Sci. Technol.* **2012**, *46* (8), 4419–4426. https://doi.org/10.1021/es203901u.

(85) Cotrufo, M. F.; Soong, J. L.; Horton, A. J.; Campbell, E. E.; Michelle; Wall, D. H.; Parton, W. J. Formation of Soil Organic Matter via Biochemical and Physical Pathways of Litter Mass Loss. *Nat. Geosci.* **2015**, *8* (10), 776–779. https://doi.org/10.1038/ngeo2520.

(86) Parada, A. E.; Needham, D. M.; Fuhrman, J. A. Every Base Matters: Assessing Small Subunit rRNA Primers for Marine Microbiomes with Mock Communities, Time Series and Global Field Samples. *Environ. Microbiol.* **2016**, *18* (5), 1403–1414. https://doi.org/10.1111/1462-2920.13023.

(87) Apprill, A.; McNally, S.; Parsons, R.; Weber, L. Minor Revision to V4 Region SSU rRNA 806R Gene Primer Greatly Increases Detection of SAR11 Bacterioplankton. *Aquat. Microb. Ecol.* **2015**, *75* (2), 129–137.

(88) White, T. J.; Bruns, T.; Lee, S.; Taylor, J. Amplification and Direct Sequencing of Fungal Ribosomal RNA Genes for Phylogenetics. In PCR Protocols: A Guide to Methods and Applications (Pp. 315–322). New York: Academic Press. **1990**.

(89) Thompson, L. R.; Sanders, J. G.; McDonald, D.; Amir, A.; Ladau, J.; Locey, K. J.; Prill, R. J.; Tripathi, A.; Gibbons, S. M.; Ackermann, G.; Navas-Molina, J. A.; Janssen, S.; Kopylova, E.; Vázquez-Baeza, Y.; González, A.; Morton, J. T.; Mirarab, S.; Zech Xu, Z.; Jiang, L.; Haroon, M. F.; Kanbar, J.; Zhu, Q.; Jin Song, S.; Kosciolek, T.; Bokulich, N. A.; Lefler, J.; Brislawn, C. J.; Humphrey, G.; Owens, S. M.; Hampton-Marcell, J.; Berg-Lyons, D.; McKenzie, V.; Fierer, N.; Fuhrman, J. A.; Clauset, A.; Stevens, R. L.; Shade, A.; Pollard, K. S.; Goodwin, K. D.; Jansson, J. K.; Gilbert, J. A.; Knight, R.; Rivera, J. L. A.; Al-Moosawi, L.; Alverdy, J.; Amato, K. R.; Andras, J.; Angenent, L. T.; Antonopoulos, D. A.; Apprill, A.; Armitage, D.; Ballantine, K.; Bárta, J.; Baum, J. K.; Berry, A.; Bhatnagar, A.; Bhatnagar, M.; Biddle, J. F.; Bittner, L.; Boldgiv, B.; Bottos, E.; Boyer, D. M.; Braun, J.; Brazelton, W.; Brearley, F. Q.; Campbell, A. H.; Caporaso, J. G.; Cardona, C.; Carroll, J.; Cary, S. C.; Casper, B. B.; Charles, T. C.; Chu, H.; Claar, D. C.; Clark, R. G.; Clayton, J. B.; Clemente, J. C.; Cochran, A.; Coleman, M. L.; Collins, G.; Colwell, R. R.; Contreras, M.; Crary, B. B.; Creer, S.; Cristol, D. A.; Crump, B. C.; Cui, D.; Daly, S. E.; Davalos, L.; Dawson, R. D.; Defazio, J.; Delsuc, F.; Dionisi, H. M.; Dominguez-Bello, M. G.; Dowell, R.; Dubinsky, E. A.; Dunn, P. O.; Ercolini, D.; Espinoza, R. E.; Ezenwa, V.; Fenner, N.; Findlay, H. S.; Fleming, I. D.; Fogliano, V.; Forsman, A.; Freeman, C.; Friedman, E. S.; Galindo, G.; Garcia, L.; Garcia-Amado, M. A.; Garshelis, D.; Gasser, R. B.; Gerdts, G.; Gibson, M. K.; Gifford, I.; Gill, R. T.; Giray, T.; Gittel, A.; Golyshin, P.; Gong, D.; Grossart, H.-P.; Guyton, K.; Haig, S.-J.; Hale, V.; Hall, R. S.; Hallam, S. J.; Handley, K. M.; Hasan, N. A.; Haydon, S. R.; Hickman, J. E.; Hidalgo, G.; Hofmockel, K. S.; Hooker, J.; Hulth,

S.; Hultman, J.; Hyde, E.; Ibáñez-Álamo, J. D.; Jastrow, J. D.; Jex, A. R.; Johnson, L. S.; Johnston, E. R.; Joseph, S.; Jurburg, S. D.; Jurelevicius, D.; Karlsson, A.; Karlsson, R.; Kauppinen, S.; Kellogg, C. T. E.; Kennedy, S. J.; Kerkhof, L. J.; King, G. M.; Kling, G. W.; Koehler, A. V.; Krezalek, M.; Kueneman, J.; Lamendella, R.; Landon, E. M.; Lane-Degraaf, K.; Laroche, J.; Larsen, P.; Laverock, B.; Lax, S.; Lentino, M.; Levin, I. I.; Liancourt, P.; Liang, W.; Linz, A. M.; Lipson, D. A.; Liu, Y.; Lladser, M. E.; Lozada, M.; Spirito, C. M.; Maccormack, W. P.; Macrae-Crerar, A.; Magris, M.; Martín-Platero, A. M.; Martín-Vivaldi, M.; Martínez, L. M.; Martínez-Bueno, M.; Marzinelli, E. M.; Mason, O. U.; Mayer, G. D.; McDevitt-Irwin, J. M.; McDonald, J. E.; McGuire, K. L.; McMahon, K. D.; McMinds, R.; Medina, M.; Mendelson, J. R.; Metcalf, J. L.; Meyer, F.; Michelangeli, F.; Miller, K.; Mills, D. A.; Minich, J.; Mocali, S.; Moitinho-Silva, L.; Moore, A.; Morgan-Kiss, R. M.; Munroe, P.; Myrold, D.; Neufeld, J. D.; Ni, Y.; Nicol, G. W.; Nielsen, S.; Nissimov, J. I.; Niu, K.; Nolan, M. J.; Noyce, K.; O'Brien, S. L.; Okamoto, N.; Orlando, L.; Castellano, Y. O.; Osuolale, O.; Oswald, W.; Parnell, J.; Peralta-Sánchez, J. M.; Petraitis, P.; Pfister, C.; Pilon-Smits, E.; Piombino, P.; Pointing, S. B.; Pollock, F. J.; Potter, C.; Prithiviraj, B.; Quince, C.; Rani, A.; Ranjan, R.; Rao, S.; Rees, A. P.; Richardson, M.; Riebesell, U.; Robinson, C.; Rockne, K. J.; Rodriguezl, S. M.; Rohwer, F.; Roundstone, W.; Safran, R. J.; Sangwan, N.; Sanz, V.; Schrenk, M.; Schrenzel, M. D.; Scott, N. M.; Seger, R. L.; Seguin-Orlando, A.; Seldin, L.; Seyler, L. M.; Shakhsheer, B.; Sheets, G. M.; Shen, C.; Shi, Y.; Shin, H.; Shogan, B. D.; Shutler, D.; Siegel, J.; Simmons, S.; Sjöling, S.; Smith, D. P.; Soler, J. J.; Sperling, M.; Steinberg, P. D.; Stephens, B.; Stevens, M. A.; Taghavi, S.; Tai, V.; Tait, K.; Tan, C. L.; Tas¸, N.; Taylor, D. L.; Thomas, T.; Timling, I.; Turner, B. L.; Urich, T.; Ursell, L. K.; Van Der Lelie, D.; Van Treuren, W.; Van Zwieten, L.; Vargas-Robles, D.; Thurber, R. V.; Vitaglione, P.; Walker, D. A.; Walters, W. A.; Wang, S.; Wang, T.; Weaver,

T.; Webster, N. S.; Wehrle, B.; Weisenhorn, P.; Weiss, S.; Werner, J. J.; West, K.; Whitehead, A.; Whitehead, S. R.; Whittingham, L. A.; Willerslev, E.; Williams, A. E.; Wood, S. A.; Woodhams, D. C.; Yang, Y.; Zaneveld, J.; Zarraonaindia, I.; Zhang, Q.; Zhao, H. A Communal Catalogue Reveals Earth's Multiscale Microbial Diversity. *Nature* **2017**, *551* (7681), 457–463. https://doi.org/10.1038/nature24621.

(90) Bolyen, E.; Rideout, J. R.; Dillon, M. R.; Bokulich, N. A.; Abnet, C. C.; Al-Ghalith, G. A.; Alexander, H.; Alm, E. J.; Arumugam, M.; Asnicar, F.; Bai, Y.; Bisanz, J. E.; Bittinger, K.; Brejnrod, A.; Brislawn, C. J.; Brown, C. T.; Callahan, B. J.; Caraballo-Rodríguez, A. M.; Chase, J.; Cope, E. K.; Da Silva, R.; Diener, C.; Dorrestein, P. C.; Douglas, G. M.; Durall, D. M.; Duvallet, C.; Edwardson, C. F.; Ernst, M.; Estaki, M.; Fouquier, J.; Gauglitz, J. M.; Gibbons, S. M.; Gibson, D. L.; Gonzalez, A.; Gorlick, K.; Guo, J.; Hillmann, B.; Holmes, S.; Holste, H.; Huttenhower, C.; Huttley, G. A.; Janssen, S.; Jarmusch, A. K.; Jiang, L.; Kaehler, B. D.; Kang, K. B.; Keefe, C. R.; Keim, P.; Kelley, S. T.; Knights, D.; Koester, I.; Kosciolek, T.; Kreps, J.; Langille, M. G. I.; Lee, J.; Ley, R.; Liu, Y.-X.; Loftfield, E.; Lozupone, C.; Maher, M.; Marotz, C.; Martin, B. D.; McDonald, D.; McIver, L. J.; Melnik, A. V.; Metcalf, J. L.; Morgan, S. C.; Morton, J. T.; Naimey, A. T.; Navas-Molina, J. A.; Nothias, L. F.; Orchanian, S. B.; Pearson, T.; Peoples, S. L.; Petras, D.; Preuss, M. L.; Pruesse, E.; Rasmussen, L. B.; Rivers, A.; Robeson, M. S.; Rosenthal, P.; Segata, N.; Shaffer, M.; Shiffer, A.; Sinha, R.; Song, S. J.; Spear, J. R.; Swafford, A. D.; Thompson, L. R.; Torres, P. J.; Trinh, P.; Tripathi, A.; Turnbaugh, P. J.; Ul-Hasan, S.; Van Der Hooft, J. J. J.; Vargas, F.; Vázquez-Baeza, Y.; Vogtmann, E.; Von Hippel, M.; Walters, W.; Wan, Y.; Wang, M.; Warren, J.; Weber, K. C.; Williamson, C. H. D.; Willis, A. D.; Xu, Z. Z.; Zaneveld, J. R.; Zhang, Y.; Zhu, Q.; Knight, R.; Caporaso, J. G. Reproducible,

Interactive, Scalable and Extensible Microbiome Data Science Using QIIME 2. *Nat. Biotechnol.* **2019**, *37* (8), 852–857. https://doi.org/10.1038/s41587-019-0209-9.

(91) Callahan, B. J.; McMurdie, P. J.; Rosen, M. J.; Han, A. W.; Johnson, A. J. A.; Holmes, S. P. DADA2: High-Resolution Sample Inference from Illumina Amplicon Data. *Nat. Methods* **2016**, *13* (7), 581–583. https://doi.org/10.1038/nmeth.3869.

(92) Quast, C.; Pruesse, E.; Yilmaz, P.; Gerken, J.; Schweer, T.; Yarza, P.; Peplies, J.; Glöckner, F. O. The SILVA Ribosomal RNA Gene Database Project: Improved Data Processing and Web-Based Tools. *Nucleic Acids Res.* **2013**, *41*, 590–596.

(93) Bokulich, N. A.; Kaehler, B. D.; Rideout, J. R.; Dillon, M.; Bolyen, E.; Knight, R.; Huttley, G. A.; Gregory Caporaso, J. Optimizing Taxonomic Classification of Marker-Gene Amplicon Sequences with QIIME 2's Q2-Feature-Classifier Plugin. *Microbiome* **2018**, *6* (1), 1–17. https://doi.org/10.1186/s40168-018-0470-z.

(94) Robeson, M. S.; O'Rourke, D. R.; Kaehler, B. D.; Ziemski, M.; Dillon, M. R.; Foster, J. T.; Bokulich, N. A. RESCRIPt: Reproducible Sequence Taxonomy Reference Database Management. *PLOS Comput. Biol.* **2021**, *17* (11), 1–37. https://doi.org/10.1371/journal.pcbi.1009581.

(95) Nilsson, R. H.; Larsson, K.-H.; Taylor, A. F. S. B.-P.; Jeppesen, T. S.; Schigel, D.; Kennedy, P.; Picard, K.; Glöckner, F. O.; Tedersoo, L.; Saar, I.; Kõljalg, U.; Abarenkov, K. The UNITE Database for Molecular Identification of Fungi: Handling Dark Taxa and Parallel Taxonomic Classifications. *Nucleic Acids Res.* **2019**, *47*, D259–D264.

(96) Kõljalg, U.; Nilsson, H. R.; Schigel, D.; Tedersoo, L.; Larsson, K.-H.; May, T. W.; Taylor, A. F. S.; Jeppesen, T. S.; Frøslev, T. G.; Lindahl, B. D.; Põldmaa, K.; Saar, I.; Suija, A.; Savchenko, A.; Yatsiuk, I.; Adojaan, K.; Ivanov, F.; Piirmann, T.; Pöhönen, R.; Zirk, A.;

Abarenkov, K. The Taxon Hypothesis Paradigm—On the Unambiguous Detection and Communication of Taxa. *Microorganisms* **2020**, *8* (12), 1910. https://doi.org/10.3390/microorganisms8121910.

(97) Nguyen, N. H.; Song, Z.; Bates, S. T.; Branco, S.; Tedersoo, L.; Menke, J.; Schilling, J. S.; Kennedy, P. G. FUNGuild: An Open Annotation Tool for Parsing Fungal Community Datasets by Ecological Guild. *Fungal Ecol.* **2016**, *20*, 241–248.

(98) R Core Team. R: A Language and Environment for Statistical Computing. R Foundation for Statistical Computing, Vienna, Austria. Https://Www.R-Project.Org/. **2021**.

(99) Kassambara, A. Ggpubr: "ggplot2" Based Publication Ready Plots. R Package Version 0.6.0, Https://Rpkgs.Datanovia.Com/Ggpubr/. **2023**.

(100) Anderson, M. J. A New Method for Non-Parametric Multivariate Analysis of Variance. *Austral Ecol.* **2001**, *26* (1), 32–46. https://doi.org/10.1111/j.1442-9993.2001.01070.pp.x.

(101) Lu, Y.; Zhou, G.; Ewald, J.; Pang, Z.; Shiri, T.; Xia, J. MicrobiomeAnalyst 2.0: Comprehensive Statistical, Functional and Integrative Analysis of Microbiome Data. *Nucleic Acids Res.* **2023**.

(102) Wickham, H. Ggplot2: Elegant Graphics for Data Analysis (2nd Ed.) [PDF]. Springer International Publishing. **2016**.

(103) Glaser, B.; Haumaier, L.; Guggenberger, G.; Zech, W. Black Carbon in Soils: The Use of Benzenecarboxylic Acids as Specific Markers. *Org. Geochem.* **1998**, *29*, 811–819.

(104) Wiedemeier, D. B.; Hilf, M. D.; Smittenberg, R. H.; Haberle, S. G.; Schmidt, M. W. I. Improved Assessment of Pyrogenic Carbon Quantity and Quality in Environmental Samples by High-Performance Liquid Chromatography. *J. Chromatogr. A* **2013**, *1304*, 246–250. https://doi.org/10.1016/j.chroma.2013.06.012.

(105) Pulido-Chavez, M. F.; Alvarado, E. C.; DeLuca, T. H.; Edmonds, R. L.; Glassman, S. I. High-Severity Wildfire Reduces Richness and Alters Composition of Ectomycorrhizal Fungi in Low-Severity Adapted Ponderosa Pine Forests. *For. Ecol. Manag.* **2021**, *485*, 118923.

(106) Ferrenberg, S.; O'Neill, S. P.; Knelman, J. E.; Todd, B.; Duggan, S.; Bradley, D.; Robinson, T.; Schmidt, S. K.; Townsend, A. R.; Williams, M. W.; Cleveland, C. C.; Melbourne, B. A.; Jiang, L.; Nemergut, D. R. Changes in Assembly Processes in Soil Bacterial Communities Following a Wildfire Disturbance. *ISME J.* **2013**, *7* (6), 1102–1111. https://doi.org/10.1038/ismej.2013.11.

(107) Najar, I. N.; Thakur, N. A Systematic Review of the Genera Geobacillus and Parageobacillus: Their Evolution, Current Taxonomic Status and Major Applications. *Microbiology* **2020**, *166* (9), 800–816. https://doi.org/10.1099/mic.0.000945.

(108) Tong, D. Q.; Gill, T. E.; Sprigg, W. A.; Van Pelt, R. S.; Baklanov, A. A.; Barker, B. M.; Bell, J. E.; Castillo, J.; Gassó, S.; Gaston, C. J.; Griffin, D. W.; Huneeus, N.; Kahn, R. A.; Kuciauskas, A. P.; Ladino, L. A.; Li, J.; Mayol-Bracero, O. L.; McCotter, O. Z.; Méndez-Lázaro, P. A.; Mudu, P.; Nickovic, S.; Oyarzun, D.; Prospero, J.; Raga, G. B.; Raysoni, A. U.; Ren, L.; Sarafoglou, N.; Sealy, A.; Sun, Z.; Vimic, A. V. Health and Safety Effects of Airborne Soil Dust in the Americas and Beyond. *Rev. Geophys.* **2023**, *61* (2), 1–52. https://doi.org/10.1029/2021rg000763.

(109) Santos, F.; Russell, D.; Berhe, A. A. Thermal Alteration of Water Extractable Organic Matter in Climosequence Soils from the Sierra Nevada, California. *J. Geophys. Res. Biogeosciences* **2016**, *121* (11), 2877–2885. https://doi.org/10.1002/2016jg003597.

(110) Jian, M.; Berhe, A. A.; Berli, M.; Ghezzehei, T. A. Vulnerability of Physically Protected Soil Organic Carbon to Loss Under Low Severity Fires. *Front. Environ. Sci.* **2018**, *6*, 66.

(111) Ferreira, E. A.; Pacheco, C. C.; Rodrigues, J. S.; Pinto, F.; Lamosa, P.; Fuente, D.; Urchueguía, J.; Tamagnini, P. Heterologous Production of Glycine Betaine Using Synechocystis Sp. PCC 6803-Based Chassis Lacking Native Compatible Solutes. *Front. Bioeng. Biotechnol.* **2022**, *9*, 1–19.

(112) Caldas, T.; Demont-Caulet, N.; Ghazi, A.; Richarme, G. Thermoprotection by Glycine Betaine and Choline. *Microbiology* **1999**, *145* (9), 2543–2548. https://doi.org/10.1099/00221287-145-9-2543.

(113) Donhauser, J.; Qi, W.; Bergk-Pinto, B.; Frey, B. High Temperatures Enhance the Microbial Genetic Potential to Recycle C and N from Necromass in High-Mountain Soils. *Glob. Change Biol.* **2021**, *27* (7), 1365–1386. https://doi.org/10.1111/gcb.15492.

(114) Brochier-Armanet, C.; Boussau, B.; Gribaldo, S.; Forterre, P. Mesophilic Crenarchaeota: Proposal for a Third Archaeal Phylum, the Thaumarchaeota. *Nat. Rev. Microbiol.* **2008**, *6* (3), 245–252. https://doi.org/10.1038/nrmicro1852.

(115) Kerou, M.; Schleper, C. Nitrososphaeraceae. In W. B. Whitman, F. Rainey, P. Kämpfer, M. Trujillo, J. Chun, P. DeVos, B. Hedlund, & S. Dedysh (Eds.), Bergey's Manual of Systematics of Archaea and Bacteria (1st Ed., Pp. 1–2). Wiley. Https://Doi.Org/10.1002/9781118960608.Fbm00265. **2016**.

(116) Yeager, C. M.; Northup, D. E.; Grow, C. C.; Barns, S. M.; Kuske, C. R. Changes in Nitrogen-Fixing and Ammonia-Oxidizing Bacterial Communities in Soil of a Mixed Conifer Forest after Wildfire. *Appl. Environ. Microbiol.* **2005**, *71* (5), 2713–2722. https://doi.org/10.1128/aem.71.5.2713-2722.2005.

(117) Baldrian, P. Forest Microbiome: Diversity, Complexity and Dynamics. *FEMS Microbiol. Rev.* **2017**, *41*, 109–130.

(118) Teira, E.; Van Aken, H.; Veth, C.; Herndl, G. J. Archaeal Uptake of Enantiomeric Amino Acids in the Meso- and Bathypelagic Waters of the North Atlantic. *Limnol. Oceanogr.* **2006**, *51* (1), 60–69. https://doi.org/10.4319/lo.2006.51.1.0060.

(119) Hallam, S. J.; Mincer, T. J.; Schleper, C.; Preston, C. M.; Roberts, K.; Richardson, P. M.; DeLong, E. F. Pathways of Carbon Assimilation and Ammonia Oxidation Suggested by Environmental Genomic Analyses of Marine Crenarchaeota. *PLOS Biol.* **2006**, *4* (4), e95. https://doi.org/10.1371/journal.pbio.0040095.

(120) Tourna, M.; Stieglmeier, M.; Spang, A.; Könneke, M.; Schintlmeister, A.; Urich, T.; Engel, M.; Schloter, M.; Wagner, M.; Richter, A.; Schleper, C. *Nitrososphaera Viennensis* , an Ammonia Oxidizing Archaeon from Soil. *Proc. Natl. Acad. Sci.* **2011**, *108* (20), 8420–8425. https://doi.org/10.1073/pnas.1013488108.

(121) Nelson, D. C.; Flematti, G. R.; Ghisalberti, E. L.; Dixon, K. W.; Smith, S. M. Regulation of Seed Germination and Seedling Growth by Chemical Signals from Burning Vegetation. *Annu. Rev. Plant Biol.* **2012**, *63* (1), 107–130. https://doi.org/10.1146/annurev-arplant-042811-105545.

(122) Nelson, D. C.; Riseborough, J.-A. M.; Flematti, G. R.; Stevens, J. C.; Ghisalberti, E. L.; Dixon, K. W.; Smith, S. M. Karrikins Discovered in Smoke Trigger Arabidopsis Seed Germination by a Mechanism Requiring Gibberellic Acid Synthesis and Light. *Plant Physiol.* **2009**, *149* (2), 863–873.

(123) Battin, T. J.; Kaplan, L. A.; Findlay, S.; Hopkinson, C. S.; Marti, E.; Packman, A. I.; Newbold, J. D.; Sabater, F. Biophysical Controls on Organic Carbon Fluxes in Fluvial Networks. *Nat. Geosci.* **2008**, *1* (2), 95–100. https://doi.org/10.1038/ngeo101.

(124) Averill, C.; Waring, B. Nitrogen Limitation of Decomposition and Decay: How Can It Occur? *Glob. Change Biol.* **2018**, *24* (4), 1417–1427. https://doi.org/10.1111/gcb.13980.

(125) Laszakovits, J. R.; Mackay, A. A. Data-Based Chemical Class Regions for Van Krevelen Diagrams. *J. Am. Soc. Mass Spectrom.* **2022**, *33*, 198–202. https://doi.org/10.1021/jasms.1c00230.

(126) Maranon-Jimenez, S.; Castro, J.; Kowalski, A. S.; Serrano-Ortiz, P.; Reverter, B. R.; Sanchez-Canete, E. P.; Zamora, R. Post-Fire Soil Respiration in Relation to Burnt Wood Management in a Mediterranean Mountain Ecosystem. *For. Ecol. Manag.* **2011**, *291* (8), 1436–1447.

(127) Johnson, D. B.; Woolet, J.; Yedinak, K. M.; Whitman, T. Experimentally Determined Traits Shape Bacterial Community Composition One and Five Years Following Wildfire. *Nat. Ecol. Amp Evol.* **2023**, *7* (9), 1419–1431. https://doi.org/10.1038/s41559-023-02135-4.

(128) Mataix-Solera, J.; Cerda, A.; Arcenegui, V.; Jordan, A.; Zavala, L. M. Fire Effects on Soil Aggregation: A Review. *Earth-Sci. Rev.* **2011**, *109*, 44–60.

(129) Soto, B.; Benito, E.; Diaz-Fierros, F. Heat-Induced Degradation Processes in Forest Soils. *Int. J. Wildland Fire* **1991**, *3*, 147–152.

(130) Kemper, W. D.; Rosenau, R. C. Aggregate Stability and Size Distribution. *Klute E Methods Soil Anal. Part 1 Am. Soc. Agron. Madison Wis.* **1986**, 425–442.

(131) García-Corona, R.; Benito, E.; de Blas, E.; Varela, M. E. Effects of Heating on Some Soil Physical Properties Related to Its Hydrological Behaviour in Two North-Western Spanish Soils. *Int. J. Wildland Fire* **2004**, *13*, 195–199.

(132) Jian, M.; Berli, M.; Ghezzehei, T. A. Soil Structural Degradation During Low-Severity Burns. *Geophys. Res. Lett.* **2018**, *45* (11), 5553–5561. https://doi.org/10.1029/2018gl078053.

(133) Pulido-Chavez, M. F.; Randolph, J. W. J.; Zalman, C.; Larios, L.; Homyak, P. M.; Glassman, S. I. Rapid Bacterial and Fungal Successional Dynamics in First Year after Chaparral Wildfire. *Mol. Ecol.* **2023**, *32* (7), 1685–1707. https://doi.org/10.1111/mec.16835.

CHAPTER 4: HEATING SOIL INCREASES METABOLITE ABUNDANCES: IMPLICATIONS FOR WILDFIRES

4.1 INTRODUCTION

Wildfires naturally disturb ecosystems and can be beneficial to ecosystems that have adapted to wildfire activity.[1] Wildfire activity, however, is changing. Fire weather across ~20 % of global burnable land area has deviated from historical patterns,[2] and wildfire intensity (i.e. energy released during burning) has increased globally since the beginning of the 21st century.[3,4] Specifically, extreme wildfire events representing high intensity fires have more than doubled in frequency from 2003 to 2023.[4] Due to these changing wildfire intensity levels, studying the impacts of wildfires across varying intensity conditions is essential, for these wildfires can alter water quality, greenhouse gas emissions, and soil quality.

Wildfires alter various soil parameters including soil hydrophobicity, pH, carbon content, and soil organic matter (SOM) composition.[5–27] SOM is a highly complex mixture of organic molecules ranging in size from metabolites (e.g. amino acids and organic acids) to larger, humic-like substances. SOM increases water retention, maintains soil structure, and provides nutrients for microbial activity, contributing to productive, resilient soils. SOM composition can be drastically altered by wildfire activity.[28] Wildfires generally cause SOM to become more aromatic with increased fire intensity, enriched in nitrogen, and more soluble (i.e. water extractable organic carbon content often increases when soil is heated up to ~250 °C).[29–33] However, wildfire impacts on small metabolites are relatively unknown.

Metabolites are low-molecular weight molecules including small aromatic compounds, organic acids, and saccharides often detected with gas chromatography-mass spectrometry (GC-

MS) and/or liquid chromatography-mass spectrometry (LC-MS).[34–36] Metabolites play critical roles in microbial protein biosynthesis, cellular energy production (e.g. the citric acid cycle), and nutrient cycling. Metabolite identification is often categorized using the Schymanski index which ranges from Level 5 (lowest confidence) to Level 1 (highest confidence): Level 5 (only the mass of detected metabolite is known), Level 4 (molecular formula is known), Level 3 (chemical category [e.g. saccharide-like, organic acid] is known), Level 2 (probable structure and identity determined with library database comparison), and Level 1 (probable structure and identity determined with authentic reference standard).[37] Metabolites identified at Level 2 or 3 confidence can also be referred to as "annotated" metabolites.[38] The study of metabolites is called metabolomics, and the terms "metabolite profile" or "metabolome" refer to the metabolite content of a given sample. Metabolomics research has grown exponentially from 1998 to 2023 with over 80,000 metabolomics-related studies being published during that timeframe.[39] As of 2022, 8 % of all published metabolomics studies examine soil metabolomics because metabolites influence soil carbon dynamics, nutrient cycling, and microbial metabolism, positioning metabolites as a keystone component of a healthy soil system.[35,36,40–46]

Despite the exponential growth in metabolomics-based studies, wildfire impacts on soil metabolomics are understudied. Low molecular weight molecules in burned soils (Level 2 or 3 on the Schymanski index) have been detected with pyrolysis GC-MS, but such analysis offered no insight into how individual metabolite abundances were affected.[47–52] Individual metabolites have been detected in soil after pyrogenic organic matter addition in a laboratory-based experiment, but the metabolites were unidentified (Level 4 and Level 5 on the Schymanski Index).[37,53] Thus, there is a paucity of wildfire studies featuring high metabolite identification confidence (Level 3 or higher) coupled with abundance quantification. Individual metabolites in experimentally burned

soil have been annotated and quantified on a relative basis via total ion current normalization, showcasing higher relative abundances of amino acids and organic acids in burned soil compared to unburned soil.[54] Such results imply that burned soil may contain an enriched, more abundant metabolome compared to unburned soil. However, this study only tested one soil type under one fire intensity condition (e.g. high intensity), so pertinent research questions remain: how do metabolite profiles of soil change under different fire intensity conditions, and are fire-induced changes to soil metabolites consistent across different forested ecosystems?

We conducted the first laboratory-based, soil heating experiment that evaluates how soil metabolomes change under different fire intensity conditions across disparate forested ecosystems. Specifically, we heated O-horizon and mineral soil from three forested ecosystems in Colorado at discrete temperatures (150 °C, 250 °C, and 450 °C) using a muffle furnace and identified and quantified individual metabolites using GC-MS and LC-MS analyses. While other modes of soil heating may be more representative of wildfire conditions,[55] we used a muffle furnace for soil heating because it provides heightened control over heating temperature, can be used to identify temperature-dependent transformations of metabolites, and is an established method for simulating wildfire conditions.[17,30–33,56–58] Our overarching objective was to identify and quantify changes in soil metabolomes at different fire intensities (represented by differing heating temperatures) across three forested ecosystems. We hypothesized that 1) soil metabolomic profiles will be distinct across different heating temperatures, 2) abundances of amino acids, peptides, and organic acids will peak at ~250 °C (mirroring observed increases in water extractable organic carbon concentrations at 250 °C)[29–33] and 3) abundances of aromatic metabolites will increase as heating temperature increases.

4.2 METHODS

4.2.1 SOIL SAMPLING

O-horizon and mineral soil were collected from a total of four unburned ecosystems as a part of the Adaptive Silviculture for Climate Change Network[59]: 1). mineral soil from a lodgepole pine-dominated forest (*Pinus contorta*) with a minor component of Engelmann spruce (*Picea engelmannii*) and subalpine fir (*Abies lasiocarpa*) in Taylor Park, Colorado (GPS coordinates: 38.89753° N, -106.61034° W) (referred to hereafter as "lodgepole pine forest") on September 6th, 2023, 2). O-horizon from a lodgepole pine-dominated forest (*Pinus contorta*) near Cameron Pass, Colorado (40.50693° N, -105.77093° W) collected in August 2022, 3). O-horizon and mineral soil from a mixed conifer forest comprised of ponderosa pine (*Pinus ponderosa*), Douglas-fir (*Pseudotsuga menziesii*), white fir (*Abies concolor*), aspen (*Populus tremuloides)*, and Gambel oak (*Quercus gambelii)* in San Juan National Forest, Colorado (GPS coordinates: 37.35112° N, -106.94901° W) (referred to hereafter as "mixed conifer forest") collected on September 26th, 2023, and 4). O-horizon and mineral soil from a spruce-fir (*Picea engelmannii* and *Abies lasiocarpa*) dominated forest featuring minor components of lodgepole pine (*Pinus contorta*) and aspen (*Populus tremuloides*) in State Forest State Park, Colorado (37.35042° N, -106.95082° W) (referred to hereafter as "spruce-fir forest") collected on August 23rd, 2023. Note: O-horizon was not collected from the lodegepole pine-dominated forest in Taylor Park, so O-horizon from lodgepole pine-dominated forest near Cameron Pass was used for the "lodgepole pine forest" O-horizon. All four ecosystems are representative of subalpine forests that are exposed to wildfires. During sampling, O-horizon was collected using a hand rake, and a bulb corer was used to take 0-15 cm samples of mineral soil. The mineral soil samples were sieved to 4 mm, homogenized via mixing, and stored in a 4 °C fridge. O-horizon samples were stored at 25 °C in a dry storage room.

Overall, this procedure generated O-horizon and mineral soil samples representing three forested ecosystems: “lodgepole pine forest,” “mixed conifer forest,” and “spruce-fir forest.”

4.2.2 SOIL HEATING

For each of the three forested ecosystems, the O-horizon and mineral soil were heated at 150 °C, 250 °C, and 450 °C in a muffle furnace (Thermolyne 30400 Furnace). For a given forested ecosystem and temperature, 15 260-mL ceramic crucibles were filled with 50 g of mineral soil each (**Figure 4.1**). In each crucible, 3.1 to 3.6 g of O-horizon were added to cover the mineral soil (**Figure 4.1**). The 15 crucibles were heated in the muffle furnace for 2 h with the muffle furnace door slightly cracked open to prevent pyrolysis conditions (**Figure 4.1**). After heating, ~10 mL of Milli-Q water (18 MΩ·cm) were added to each crucible to simulate a 15-minute intensity, 1 year return interval precipitation event.[60] O-horizon and mineral soil were dried overnight and sieved to 2 mm. Any large O-horizon debris that passed through the sieve (such as pine needles) were removed with tweezers. The 15 dried, 2-mm sieved samples were combined into five replicates (content of three crucibles per replicate) (**Figure 4.2**). Fifteen crucibles of 50 g of mineral soil were used rather than five crucibles of 150 grams of mineral soil to ensure uniform soil heating.[30] “Control” samples underwent the same procedure except these samples were not heated in the muffle furnace.

4.2.3 WATER-EXTRACTABLE ORGANIC CARBON AND WATER-EXTRACTABLE TOTAL NITROGEN

For each sample replicate, 20 g of soil was shaken in 100 mL of Milli-Q water at 200 rpm for 1 h. The supernatant was filtered through a 0.5 µm glass fiber filter (Advantec MSF, Inc.). Dissolved organic carbon and dissolved total nitrogen of the filtrate were measured with a TOC-L Shimadzu analyzer (Shimadzu Corporation, Columbia, MD, USA). Water-extractable organic

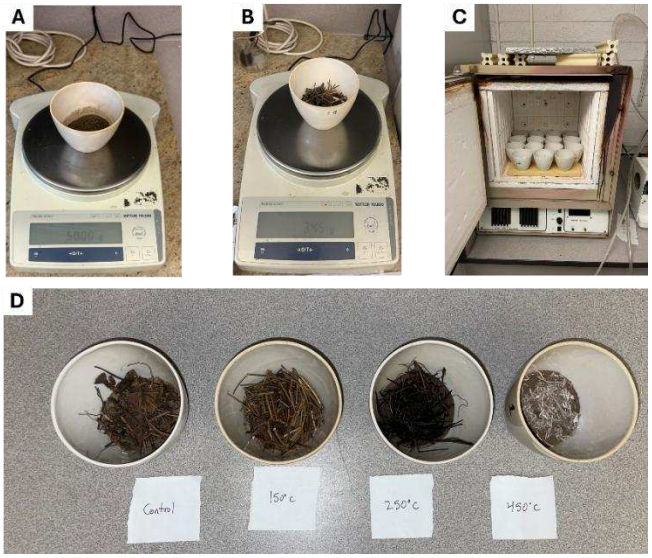

Figure 4.1. Heated soil preparation. **A**). Adding mineral soil to crucible. **B**). Adding O-horizon to crucible. **C**). Placing 15 crucibles in muffle furnace. Note: during heating, the muffle furnace door was slightly cracked open to prevent pyrolysis conditions. The muffle furnace door was **not** ajar during heating like it is in this figure. **D**). Control, 150 °C, 250 °C, and 450 °C soil samples after heating. Note the distinct change in color of O-horizon across the temperature gradient.

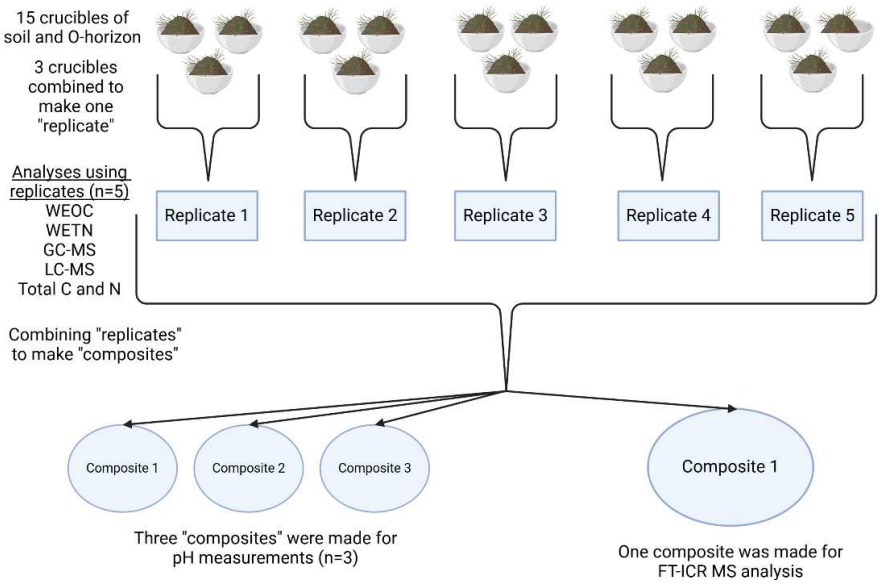

Figure 4.2. Flow diagram illustrating how "replicates" and "composites" were prepared for various analyses. This flow diagram represents one soil temperature from one forested ecosystem (e.g. 250 °C soil from mixed conifer forest). Contents of crucibles were air-dried and sieved (2 mm) prior to combining to produce replicates. Please refer to the methods section for more details regarding how much soil was used to make each "replicate" and "composite." WEOC = water extractable organic carbon. WETN = water extractable total nitrogen. GC-MS = gas chromatography-mass spectrometry. LC-MS = liquid chromatography-mass spectrometry. FT-ICR MS = Fourier Transform Ion Cyclotron Resonance Mass Spectrometry.

carbon and water-extractable total nitrogen were respectively determined by normalizing the dissolved organic carbon and dissolved total nitrogen masses to the sample soil mass.

4.2.4 SOIL PH

For each ecosystem and heating temperature, 2 g of soil from each of the five replicates were combined to make a composite sample (10 grams total) (**Figure 4.2**). This was repeated two additional times to generate three composite samples. Each composite sample was shaken in 20 mL of Milli-Q water for 1 h at 200 rpm. A Thermo Scientific Orion Star A215 pH/conductivity meter and Thermo Scientific Orion Double Junction pH probe were calibrated with pH reference standards (VWR International). After shaking the soil-water slurry by hand to resuspend the soil, the pH electrode was inserted into the slurry, and pH was measured.

4.2.5 TOTAL SOIL C AND N

For each sample replicate, ~2 g of soil were ground to a fine powder. Total carbon and total nitrogen were measured using a VELP 802 elemental analyzer (VELP Scientific, Inc.).

4.2.6 GAS CHROMATOGRAPHY-MASS SPECTROMETRY (GC-MS)

For each replicate, 2 g of mineral soil were shaken for 1 h at 210 rpm in 8 mL of Milli-Q water rpm followed by centrifugation, and supernatants were filtered (nylon 0.45 µm pore size, 13 mm diameter filters, Celltreat Scientific Products). A pooled quality control sample was prepared by mixing 500 µL of each filtered extract. Seven 1-mL aliquots of the pooled quality control and 1-mL aliquots of each filtered replicate were lyophilized overnight, suspended in 75 µL of Milli-Q water and 175 µL of methanol (LC-MS grade, Supelco, Inc.), and stored at -20 °C for ~3 h. After centrifugation, 200 µL of the water-methanol supernatant were transferred to 1.8 mL borosilicate, 12 x 32 mm GC-MS autosampler vials (Avantor, Inc.), and 40 µL of a 0.100 mg ^{13}C-glucose (99 % purity, Cambridge Isotope Laboratories, Inc.)/mL Milli-Q H_2O solution were added

to each vial to assess derivatization and sample injection variability and to account for potential matrix effects. This entire process was also repeated for two experimental blank which both did not feature any soil and only one blank received the ^{13}C-glucose internal standard solution. The lodgepole pine forest samples, mixed conifer forest samples, and spruce-fir forest samples were prepared separately in batches. Therefore, the pooled quality control sample for the lodgepole pine forest samples, for example, only contains filtered extracts from lodgepole pine forest samples and no filtered extracts from mixed conifer forest and spruce-fir forest samples.

Samples were derivatized via methoximation and trimethylsilylation. All vials were dried under N_2 gas, and 50 µL of 25 mg methoxylamine hydrochloride (98 % purity, Beantown Chemical Corporation) per mL of anhydrous pyridine (99.5 % purity, Thermo Fisher Scientific Inc.) solution were added to each vial. The vials were vortexed for 30 s, incubated for 45 min at 65 °C, vortexed for an additional 30 s, sonicated for 10 min, incubated again for 45 min at 65 °C, and centrifuged to 2000 rpm after which 50 µL of N-methyl-N-(trimethylsilyl)trifluoroacetamide (MSTFA) + 1 % trimethylchlorosilane (TCMS) (Thermo Fisher Scientific, Inc.) were added to each vial. The vials were vortexed for 30 s, incubated at 65 °C for 30 min, and centrifuged to 2000 rpm. The vial contents were pipetted to 250 µL glass inserts which were placed back in the vials followed by centrifugation at 2000 rpm for 5 min. The batches of lodgepole pine forest, mixed conifer forest, and spruce-fir forest samples were derivatized and then analyzed with a Thermo GC-TSQ8000 Evo Triple Quad GC mass spectrometer with liquid autosampler on different days (lodgepole pine forest samples on July 5th, 2024 with 20 soil samples, 7 pooled quality control samples and 2 blanks; mixed conifer forest samples on July 19th, 2024 with 20 soil samples, 7 pooled quality control samples and 2 blanks; spruce-fir forest samples on July 25th, 2024 with 20 soil samples, 7 pooled quality control samples and 2 blanks).

Samples (1 µL) were injected through a splitless liner (SSL liner 4 mm ID, 78.5 mm, Thermo P/N 453A1925) to a column (Zebron ZB-5HT Inferno, 30 m x 0.25 mm i.d. x 25 film thickness, Phenomenex P/N 7HG-G015-11) featuring a 1.2 mL/min helium gas flow rate. The GC inlet temperature was set at 285 °C. The oven temperature was held at 80 °C for 1 min, increased to 330 °C via a rate of 15 °C increase/min, and held at 330 °C for 7 min. Electron impact ionization was used. Only the first quadrupole mass analyzer was used to replicate experimental conditions of a prior publication.[54] Masses (50-650 m/z) were scanned at 5 scans/s. Ion source and transfer line temperatures were held at 260 °C and 300 °C, respectively.

Chromatogram peak integration of the ^{13}C-glucose internal standard was performed with Chromeleon 7 software (Thermo Fisher) using extracted ion chromatogram mz value of 323. The coefficient of variation values of the internal standard extracted ion chromatogram peak areas across the pooled quality control samples were 7.5 %, 10.8 %, and 9.7% for the lodgepole pine forest sample run, the mixed conifer forest sample run, and the spruce-fir forest sample run, respectively. For non-targeted analysis, ADAP-BIG software (Java Version: 19.0.1, Du-Lab) performed peak detection, spectral deconvolution, and peak alignment while feature annotation was conducted with the ADAP-KDB website (Version 1.8.4, accessed 7/26/2024). The following three databases were used for feature annotation: MS-DIAL GC-MS Library with Kovats RI | 2022-02-18, MassBank Release 2022.06 | 2022-07-18 (GC-MS), and HMDB (v5) Experimental GC-MS Spectra. Feature annotations were determined by fragmentation score (>700). Annotation assignments with fragmentation scores between 600 and 700 were supported with retention index matching using NIST MS Search 3.0. ADAP-BIG and ADAP-KDB analyses were conducted separately for the lodgepole pine forest samples, mixed conifer forest samples, and the spruce-fir forest samples. Consequently, some metabolites may be annotated in one sample set but not in

another (e.g. levoglucosan being annotated in lodgepole pine forest and spruce-fir forest samples and not in mixed conifer forest samples). Out of 212, 268, and 232 detected features, 43, 52, and 54 features were annotated in lodgepole pine forest samples, mixed conifer forest samples, and spruce-fir forest samples, respectively. Detected peak areas in a given sample were normalized to the internal standard peak area of that same sample to account for analytical variation and matrix effects. For a given metabolite, zero and n/a values normalized peak area values were replaced with 10 % of the minimum abundance value of the metabolite. All normalized peak area values were multiplied by a factor of 100,000, 10,000, and 10,000 for lodgepole pine forest samples, mixed conifer forest samples, and spruce-fir forest samples, respectively, to transform the data into values greater than 1 for easier comparisons as opposed to values comprised of only decimals. Normalized peak areas were used to quantify individual metabolites and are reported as "abundance" values. Normalized peak area values were then Pareto-scaled prior to principal component analysis.

Other than N-acetyl-D-glucosamine and levoglucosan, features that were annotated as a saccharide-like molecule were designated as either an "inositol," "sugar alcohol," "monosaccharide," "disaccharide," or "trisaccharide" and were assigned an arbitrary number to distinguish them. This was performed because achieving level 2 confidence on the Schymanski index could not be achieved with this annotation approach.[37] For example, sucrose, trehalulose, and maltose all feature the same molecular weight (342.3 g/mol) and only differ by hydroxyl group stereochemistry. When these three isomers are fragmented during electron impact ionization, similar fragmentation patterns will be generated, preventing the isomers from being distinguished from each other. Thus, these saccharide-like compounds were annotated to level 3 of the Schymanksi index (i.e. "disaccharide 1" or "trisaccharide 1") rather than level 2 (i.e. "sucrose" or

"maltotriose"). Because the lodgepole pine forest samples, mixed conifer forest samples, and spruce-fir forest samples were analyzed with ADAP-KDB software separately, the labels of Level 3 saccharide-like compounds are not necessarily the same saccharide. For example, "Disaccharide 1" for lodgepole pine forest samples (which is an arbitrary label for a disaccharide) does not mean that it has the same molecular identity as "Disaccharide 1" for mixed conifer forest samples. Rather, those were dissacharide compounds identified in lodgepole pine forest samples and mixed conifer forest samples that received the same label since they were both the first disaccharide annotated in those separate batches.

4.2.7 LIQUID CHROMATOGRAPHY-MASS SPECTROMETRY (LC-MS)

For each replicate, 2 g of soil were shaken for 1 h at 210 rpm in 8 mL of Milli-Q water, and the supernatant was filtered (nylon 0.45 μm pore size, 13 mm diameter filter, Celltreat Scientific Products). A pooled quality control (QC) sample was produced by mixing 200 μL of filtered extract from each sample replicate. Ten 1 mL aliquots of the pooled quality control sample and 1 mL aliquots of each filtered replicate were lyophilized and resuspended in 125 μL of Milli-Q water followed by vortexing and centrifugation. After transferring all samples to 1.8 mL borosilicate, 12 x 32 mm GC-MS autosampler vials (Avantor, Inc.), 10 μL of a 10.125 μg/mL solution of DL-tryptophan-2,3,3-d3 (98 % purity, CDN Isotopes) solution in Milli-Q water was added to each vial as an internal standard assessing ionization efficiency and sample injection variability. This process was repeated for two experimental blank samples in which one received the internal standard while the other did not. All samples from lodgepole pine forest soil, mixed conifer forest soil, and spruce-fir forest soil were prepared at the same time in one batch on November 14th, 2024. Thus, the pooled quality control for liquid chromatography-mass spectrometry features aliquots of

filtered extract from the lodgepole pine forest soils, mixed conifer forest soils, and spruce-fir forest soils.

All 72 samples (60 soil extracts, 10 pooled QC samples, 2 blanks) were analyzed with a Waters Xevo G2-XS quadrupole time of flight mass spectrometer coupled with ultra-performance liquid chromatography (Waters™). For each sample, 50 µL were injected using a Waters Acquity UPLC system and ACQUITY Flow-thru-needle sample handler, using a 50 µL sample loop and 15 µL flow-thru needle. Separation was achieved using a Waters ACQUITY UPLC Premier T3 1.7 µm Column (1.7 µM, 2.1 x 100 mm), using a gradient from solvent A (water + 0.1 % formic acid) to solvent B (acetonitrile with 0.1 % formic acid) and a flow rate of 0.5 mL/min. The 20 min gradient is shown in **Table 4.1**. The column and samples were held at 45 °C and 6 °C, respectively.

Table 4.1. Solvent gradient for buffer B.

Time (min)	**Buffer B %**
0 – 1 Hold	1 %
1 – 13 Linear Gradient	1 % to 98 %
13—16 Hold	98 %
16—16.05 Step Gradient	98 % to 1 %
16.05—20 Hold	1 %

Data was acquired with electrospray ionization in positive sensitivity mode with fast-data dependent acquisition MS/MS. The mass range for survey scans was 50-1200 m/z, with a 0.13 s scan time. The threshold for switching from survey scan to MS/MS was 10,000 counts, and a maximum of one MS/MS scan was performed per survey scan. Collision energy for MS/MS was 25 V, and scan time was 0.3 s. Iterative exclusion was performed via Auto_CatV1 script, with exclusion list reset after every 10 samples, and an exclusion window of 0.5 Da and 6 s.

Mass calibration was performed using sodium formate with <1 ppm mass accuracy. The capillary voltage was held at 700 V. The source temperature was held at 150 °C and the nitrogen desolvation temperature at 450 °C with a desolvation flow rate of 1000 L/hr. WATERS Lockspray

reference was used to correct for mass drift during runs, with 40 s interval between scans, 0.1 s/scan and signal averaging over 3 scans. LeuEnk was used for mass correction, with reference mass of +556.2771 m/z. RAW data was converted to mzML for further analysis using WATERS DataConnect version 2.1.0. For non-targeted analysis, MZmine software (Version 4.5.0) performed peak detection, spectral deconvolution, and peak alignment while feature annotation was conducted with SIRIUS software (Version 6.2.2).[61] The following databases were used in SIRIUS for feature annotation: PubChem, Biocyc, Blood Exposome, CHEBI, COCONUT, DSSTox, FooDB, GNPS, HMDB, HSDB, KEGG, KNApSAcK, LOTUS, LipidMaps, Maconda, MeSH, MiMeDB, NORMAN, Plantcyc, PubChem: bio and metabolites, PubChem: drug, PubChem: food, PubChem: safety and toxic, PubMed, SuperNatural, TeroMOL, and YMDB. Feature annotations were determined with confidence threshold values (>0.650). Out of 25,844 detected features, 48 features were annotated. Detected peak areas in a given sample were normalized to the internal standard peak area of that same sample to account for analytical variation and matrix effects. For a given metabolite, zero and n/a normalized peak area values were replaced with 10 % of the minimum abundance value of the metabolite similarly to GC-MS analysis. All normalized peak area values were then multiplied by a factor of 10,000 to transform the data into values greater than 1 for easier comparisons as opposed to values comprised of only decimals. These normalized peak areas were used to quantify individual metabolites across soils heated at different temperatures. These normalized peak areas were reported as “abundance” values. Normalized peak area values of the top 16,383 most abundant features were then Pareto-scaled prior to principal component analysis. While top 16,383 most abundant features were selected due to data size constraints in Microsoft Excel sheets, this fraction of the features

represented 97.8 % of the total feature abundances, resulting in this subset of features being representative of all features.

4.2.8 FOURIER TRANSFOM ION CYCLOTRON RESONANCE-MASS SPECTROMETRY (FT ICR-MS)

For each forested ecosystem and heating temperature, 10 g of soil from each of the five replicates were combined to make a single composite sample (50 g total) which was shaken for 1 h at 200 rpm in 100 mL of Milli-Q water to generate 12 total composite samples: lodgepole pine forest control, 150 °C, 250 °C, 450 °C; mixed conifer forest control, 150 °C, 250 °C, 450 °C; and spruce-fir forest control, 150 °C, 250 °C, and 450 °C. After vacuum filtration (0.22 μm poly(ether sulfone) membrane, Merck Millipore Ltd.), the filtrates were acidified to approximately a pH of 2 using a 37 % HCl solution (Fisher Chemical) and concentrated via solid phase extraction according to Dittmar et al. (2008).[62] Agilent Bond Elut PPL (Priority Pollutant) styrene-divinylbenzene polymer cartridges (3 mL, 200 mg) were rinsed with 15 mL of methanol (LC-MS grade, Supelco, Inc.) followed by 15 mL of pH 2 water. The filtered, acidified extracts were passed through an individual PPL cartridge (12 cartridges total) followed by 15 mL of pH 2 water. After the cartridges dried, 2 mL of methanol (LC-MS grade, Supelco, Inc.) were passed through each cartridge collected in a combusted (400 °C) glass test tube. For each sample, 1 mL of eluent was transferred to a 1.8 mL borosilicate autosampler vial (VWR International) and were stored at -20 °C until being shipped to the High Magnetic Field Laboratory at Florida State University for FT-ICR MS analysis. A blank was prepared by conducting the aforementioned process but without any mineral soil.

At the High Magnetic Field Laboratory, an aliquot of each sample was diluted with an equal volume of methanol, centrifuged for 10 min at 3,000 rpm, and the supernatant was

transferred to an HPLC vial immediately prior to analysis. Briefly, 25 µL of the sample was pumped to the source at 3 µL/min with a 0.5 µm inline filter (MAC-MOD Analytical) with methanol (LC-MS grade, Honeywell) as the carrier solvent. Following each sample injection, the lines were rinsed with ~300 µL of methanol to prevent sample carryover. A heated electrospray ionization source was operated in negative mode with a voltage of -3,500 V. The auxiliary gas was three and sheath gas was eight (arbitrary units). The ion transfer tube and vaporizer temperatures were set to 300 °C and 35 °C, respectively. Ultrahigh resolution data were acquired using the Eclipse/FT-ICR MS at 21 T housed at the National High Magnetic Field Laboratory (Tallahassee, FL, USA). A transient length of 3 s was used, with 5 fills of 400,000 ions each. For each sample, 100 scans were co-added, then the resultant spectrum was phase corrected.[63] Mass spectra were calibrated with 10-15 highly abundant homologous series spanning the molecular weight distribution according to the "walking" calibration method.[64]

Experimentally determined masses were converted from the International Union of Pure and Applied Chemistry (IUPAC) mass scale to the Kendrick mass scale[65] for homologous series identification for each heteroatom class (i.e. molecular formulae with the same $C_cH_hN_nO_oS_s$ content but differ only by the number of methylene subunits).[66] Peaks with signal magnitudes exceeding six times the baseline root-mean-square (rms) noise at m/z 500 were included in the peak lists. Molecular formulae assignments were conducted using PetroOrg © software.[67] Molecular formulae were assigned to singly-charged ions (170-12—Da) within the bounds of $C_{4\text{-}75}H_{4\text{-}150}O_{1\text{-}30}N_{0\text{-}4}S_{0\text{-}2}$ and were discarded if the error was greater than 0.35 parts-per-million.[67] Modified aromaticity index (AI_{mod}) and nominal oxidation state of carbon (NOSC) values were calculated for each assigned molecular formula.[68–70]

4.2.9 STATISTICS

For comparing the mean values within a forested ecosystem (e.g. control, 150 °C, 250 °C, and 450 °C replicates across lodgepole pine forest samples) for WEOC, WETN, GC-MS annotated metabolite abundances, LC-MS annotated metabolite abundances, total C and N, and pH analyses, data normality was assessed using the Shapiro-Wilk test, and homogeneity of variances was evaluated using Levene's test. If the data were parametric and the variances were equal, ANOVA and Tukey's tests were used. If the data were parametric but the variances were not equal, Welch's ANOVA and Games-Howell tests were used. If the data were not parametric (irrespective of variance homogeneity), the Kruskal-Wallis and Dunn's tests were used. These tests were conducted with the "rstatix" R package using RStudio (version 4.2.2).

4.3 RESULTS AND DISCUSSION

4.3.1 METABOLITE CONTENTS OF SOIL HEATED AT DIFFERENT TEMPERATURES WERE DISTINCT

For all forested ecosystems, the metabolomic profiles of the control, 150 °C, 250 °C, and 450 °C were distinct (**Figure 4.3**). Within **Figure 4.3**, data points that cluster closely feature similar metabolomic profiles comparatively to data points that cluster separately. The abundances of all detected metabolites were used to generate the plots in **Figure 4.3**; thus, **Figure 4.3** illustrates changes in the entire metabolome at different heating temperatures. Metabolomic profiles detected via GC-MS featured distinct clustering with minimal overlap amongst heating temperatures (**Figure 1A, B, C**). GC-MS analysis detects lower molecular weight, volatile metabolites. As soil temperature increases, these volatile metabolites would steadily volatilize out of the soil, contributing to distinct GC-MS-detected metabolomes at each soil heating temperature.

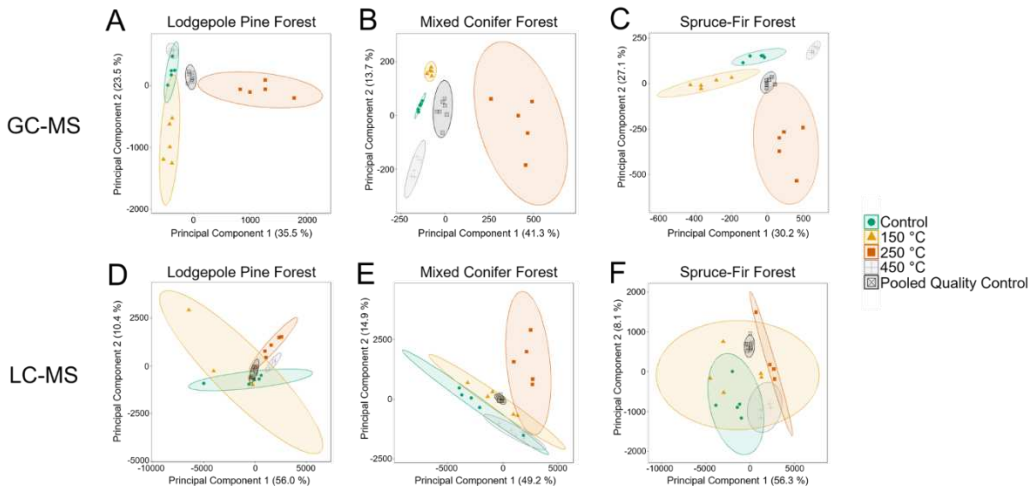

Figure 4.3. Principal component analysis (PCA) scores plots. **A**, **B**, and **C**: PCA scores plots of gas chromatography-mass spectrometry data (GC-MS). **D**, **E**, and **F**: PCA scores plots of liquid chromatography-mass spectrometry data (LC-MS). n = 5 for Control, 150 °C, 250 °C, and 450 °C. n = 7 for Pooled Quality Control. For all PCA plots, the peak areas of detected features in the samples were normalized to the internal standard peak areas, scaled with Pareto scaling, and then used as the input data for the PCA scores plots. Ellipses represent 95 % confidence levels of the treatment groups. Pooled Quality Control samples were an even mixture of Control, 150 °C, 250 °C, and 450 °C samples and should plot in the middle of the Control, 150 °C, 250 °C, and 450 °C samples in a PCA plot.

Comparatively, metabolomic profiles detected by LC-MS were distinct for 250 °C and 450 °C samples, but more overlap was observed between control and 150 °C samples (**Figure 4.3D, E, F**). LC-MS analysis detects higher molecular weight, less volatile metabolites than GC-MS. These less volatile metabolites likely require higher temperatures (>150 °C) to volatilize and/or thermochemically degrade, contributing to minimal changes in soil metabolomic profiles between control and 150 °C soils. Nevertheless, the overall metabolomic profile of the soils distinctly shifted at different temperatures, supporting hypothesis 1 (soil metabolomic profiles will be distinct across different heating temperatures). These results suggest that soils impacted by wildfires of varying intensities would feature unique post-fire metabolomic profiles.

While **Figure 4.3** examined alterations to soil metabolomes as a whole, the *types* and *abundances* of specific metabolites that are changing at different heating temperatures remain

unknown. Consequently, the abundances of specific chemical categories and individual metabolites need to be explored.

4.3.2 SOILS HEATED TO 150 °C WERE ENRICHED IN AMINO ACIDS AND PEPTIDES

150 °C samples generally featured higher amino acid abundances compared to control, 250 °C, and 450 °C samples (**Figure 4.4**). Specifically, lodgepole pine forest serine and allothreonine were significantly more abundant in 150 °C samples compared to 250 °C and 450 °C samples (**Figure 4.5**). Mixed conifer forest serine, allothreonine, and alanine were significantly more abundant in 150 °C samples compared to control and 450 °C samples (**Figure 4.6**). Spruce-fir forest serine was significantly more abundant in 150 °C samples compared to control, 250 °C, and 450 °C samples (**Figure 4.7**).

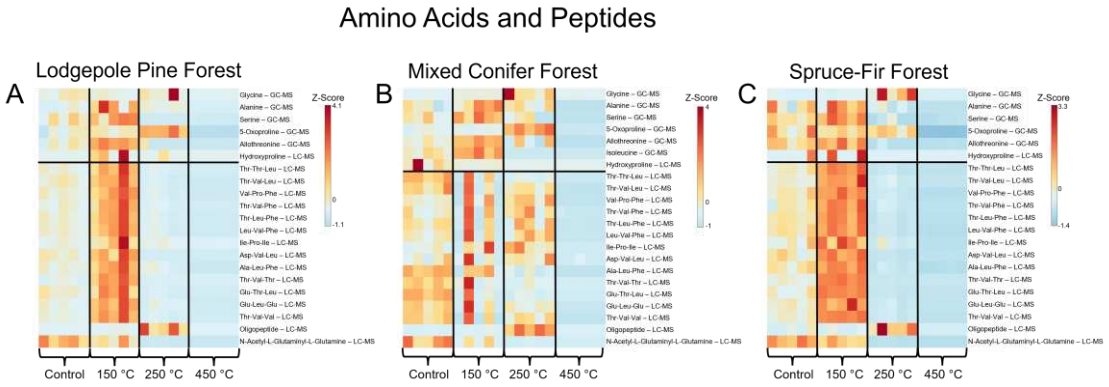

Figure 4.4. Heatmaps for annotated amino acids and peptides from **A**) lodgepole pine forest, **B**) mixed conifer forest, and **C**) spruce-fir forest soils**.** For quantification, the internal-standardized normalized peak areas for each metabolite were autoscaled and plotted using MetaboAnalyst (Version 6.0) software. Horizontal black lines separate amino acids (above line) from peptides (below line). "GC-MS" and "LC-MS" denotes whether the annotated metabolites were detected via GC-MS or LC-MS analyses, respectively. Yellow and red colors indicate above-average abundance values while blue color indicates below-average abundance values. n=5 for Control, 150 °C, 250 °C, and 450 °C samples. Amino acids and peptides were identified with Level 2 identification confidence.[37]

Excluding mixed conifer forest soil, 150 °C samples also featured higher peptide abundances compared to control, 250 °C, and 450 °C samples. Eight lodgepole pine forest peptides were significantly more abundant in 150 °C samples compared to control, 250 °C, and

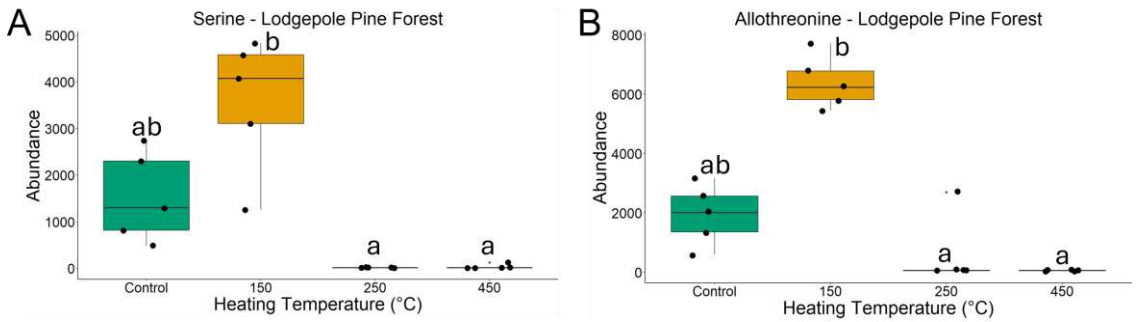

Figure 4.5. Quantification of **A**) serine and **B**) allothreonine from lodgepole pine forest soil visualized with box plots. Abundance values were calculated by dividing the peak area of the metabolites by the peak area of the internal standard to account for matrix effects and analytical variation. Therefore, abundance values themselves are arbitrary and cannot be compared across metabolites, but the abundance values can be compared across treatments for a given metabolite. Letters above boxes indicate significant differences between treatments determined by either ANOVA and Tukey HSD tests, Welch's ANOVA and Games-Howell tests, or Kruskal-Wallis and Dunn's tests (see Statistics section 4.2.9 within Methods). The statistical tests of serine and allothreonine were conducted independently of each other. n = 5 for control, 150 °C, 250 °C, and 450 °C samples. Box plots show the median (central line), first and third quartiles (box edges), and whiskers extending to minimum and maximum values within 1.5 times the interquartile range. Data beyond the end of the whiskers are "outlying" points and are plotted individually. Both metabolites were detected with gas chromatography-mass spectrometry.

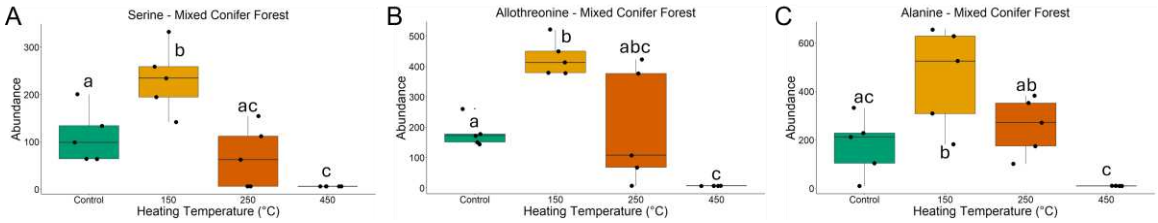

Figure 4.6. Quantification of **A**) serine, **B**) allothreonine, and **C**) alanine from mixed conifer forest soil visualized with box plots. Abundance values were calculated by dividing the peak area of the metabolites by the peak area of the internal standard to account for matrix effects and analytical variation. Therefore, abundance values themselves are arbitrary and cannot be compared across metabolites, but the abundance values can be compared across treatments for a given metabolite. Letters above boxes indicate significant differences between treatments determined by either ANOVA and Tukey HSD tests, Welch's ANOVA and Games-Howell tests, or Kruskal-Wallis and Dunn's tests (see Statistics section 4.2.9 within Methods). The statistical tests of serine, allothreonine, and alanine were conducted independently of each other. n = 5 for control, 150 °C, 250 °C, and 450 °C samples. Box plots show the median (central line), first and third quartiles (box edges), and whiskers extending to minimum and maximum values within 1.5 times the interquartile range. Data beyond the end of the whiskers are "outlying" points and are plotted individually. All metabolites were detected with gas chromatography-mass spectrometry.

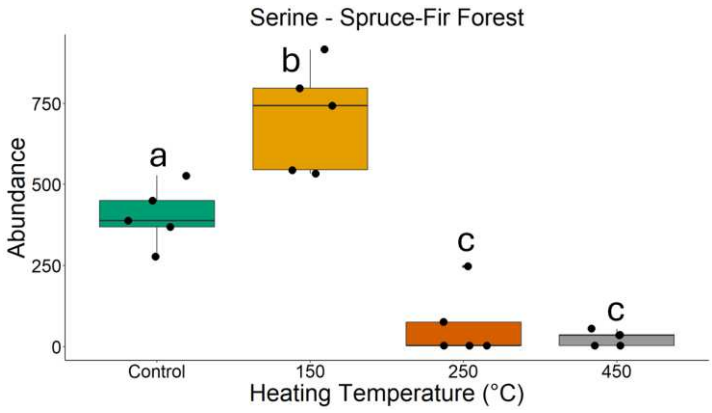

Figure 4.7. Quantification of serine from spruce-fir forest soil visualized with box plots. Abundance values were calculated by dividing the peak area of the metabolites by the peak area of the internal standard to account for matrix effects and analytical variation. Therefore, abundance values themselves are arbitrary and cannot be compared across metabolites, but the abundance values can be compared across treatments for a given metabolite. Letters above boxes indicate significant differences between treatments determined by either ANOVA and Tukey HSD tests, Welch's ANOVA and Games-Howell tests, or Kruskal-Wallis and Dunn's tests (see Statistics section 4.2.9 within Methods). n = 5 for control, 150 °C, 250 °C, and 450 °C samples. Box plots show the median (central line), first and third quartiles (box edges), and whiskers extending to minimum and maximum values within 1.5 times the interquartile range. Data beyond the end of the whiskers are "outlying" points and are plotted individually. Serine detected with gas chromatography-mass spectrometry.

450 °C samples (**Figure 4.8**). Ten spruce-fir forest peptides were also significantly more abundant in 150 °C samples compared to control, 250 °C, and 450 °C samples (**Figure 4.9**). Mixed conifer forest soil did not exhibit peptide enrichment in 150 °C samples to the degree in lodgepole pine forest and spruce-fir forest soils but rather featured greater peptide content in the control samples compared to the other two forest types (**Figure 4.4B**). This discrepancy may be due to the deciduous content of the mixed conifer forest which featured aspen and Gambel oak trees compared to the other two forests which were predominantly coniferous. Deciduous trees annually shed their leaves which are comprised of proteins, likely differentiating the composition of the underlying O-horizon and mineral soil by increasing peptide content. Overall, due to the increase in amino acid and peptide abundance in 150 °C lodgepole pine and spruce-fir soils, we reject the amino acid- and peptide-related components of our second hypothesis (abundances of amino acids,

peptides, and organic acids will peak at ~250 °C). Soils burned to low intensity conditions (~150 °C) likely feature increased amino acid and peptide abundances which could facilitate protein biosynthesis and microbial biomass accumulation, enhancing post-fire microbial activity and repopulation.

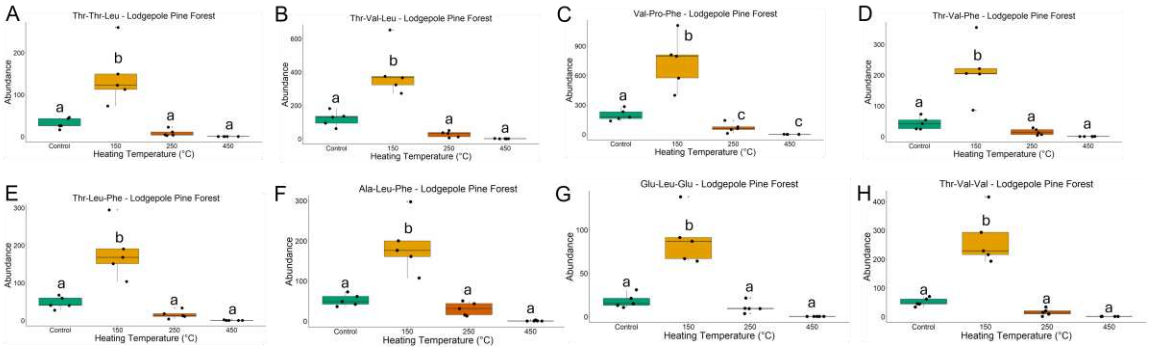

Figure 4.8. Quantification of **A**) Thr-Thr-Leu, **B**) Thr-Val-Leu, **C**) Val-Pro-Phe, **D**) Thr-Val-Phe, **E**) Thr-Leu-Phe, **F**) Ala-Leu-Phe, **G**) Glu-Leu-Glu, and **H**) Thr-Val-Val peptides from lodgepole pine forest soil visualized with box plots. Abundance values were calculated by dividing the peak area of the metabolites by the peak area of the internal standard to account for matrix effects and analytical variation. Therefore, abundance values themselves are arbitrary and cannot be compared across metabolites, but the abundance values can be compared across treatments for a given metabolite. Letters above boxes indicate significant differences between treatments determined by either ANOVA and Tukey HSD tests, Welch's ANOVA and Games-Howell tests, or Kruskal-Wallis and Dunn's tests (see Statistics section 4.2.9 within Methods). The statistical tests of the peptides were conducted independently of each other. n = 5 for control, 150 °C, 250 °C, and 450 °C samples. Box plots show the median (central line), first and third quartiles (box edges), and whiskers extending to minimum and maximum values within 1.5 times the interquartile range. Data beyond the end of the whiskers are "outlying" points and are plotted individually. All peptides were detected with liquid chromatography-mass spectrometry. Thr = threonine. Leu = leucine. Val = Val. Pro = proline. Phe = phenylalanine. Ala = Alanine. Glu = glutamic acid.

4.3.3 SOILS HEATED TO 250 °C WERE ENRICHED IN AROMATIC METABOLITES, ORGANIC ACIDS, AND NITROGEN-CONTAINING SACCHARIDES

250 °C soils featured greater aromatic metabolite abundances compared to control, 150 °C and 450 °C soils (**Figure 4.9**). Seven aromatic metabolites from lodgepole pine forest soils were significantly more abundant in the 250 °C soils compared to control, 150 °C, and 450 °C samples (**Figure 4.10**). Six aromatic metabolites from mixed conifer forest soils were significantly more

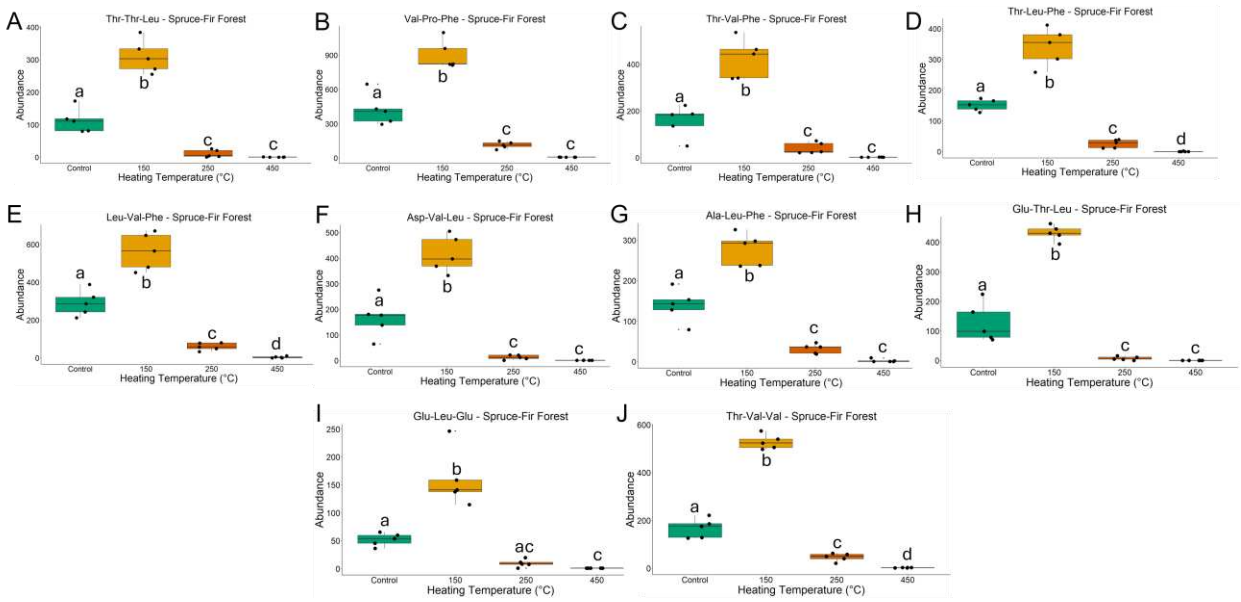

Figure 4.9. Quantification of A) Thr-Thr-Leu, B) Val-Pro-Phe, C) Thr-Val-Phe, D) Thr-Leu-Phe, E) Leu-Val-Phe, F) Asp-Val-Leu, G) Ala-Leu-Phe, H) Glu-Thr-Leu, I) Glu-Leu-Glu, and J) Thr-Val-Val peptides from spruce-fir forest soil visualized with box plots. Abundance values were calculated by dividing the peak area of the metabolites by the peak area of the internal standard to account for matrix effects and analytical variation. Therefore, abundance values themselves are arbitrary and cannot be compared across metabolites, but the abundance values can be compared across treatments for a given metabolite. Letters above boxes indicate significant differences between treatments determined by either ANOVA and Tukey HSD tests, Welch's ANOVA and Games-Howell tests, or Kruskal-Wallis and Dunn's tests (see Statistics section 4.2.9 within Methods). The statistical tests of the peptides were conducted independently of each other. n = 5 for control, 150 °C, 250 °C, and 450 °C samples. Box plots show the median (central line), first and third quartiles (box edges), and whiskers extending to minimum and maximum values within 1.5 times the interquartile range. Data beyond the end of the whiskers are "outlying" points and are plotted individually. All peptides were detected with liquid chromatography-mass spectrometry. Thr = threonine. Leu = leucine. Val = Val. Pro = proline. Phe = phenylalanine. Asp = aspartic acid. Ala = Alanine. Glu = glutamic acid.

abundant in the 250 °C soils compared to control, 150 °C, and 450 °C soils (**Figure 4.11**). Four aromatic metabolites from spruce-fir forest soils were significantly more abundant in the 250 °C soils compared to control, 150 °C, and 450 °C soils (**Figure 4.12**). This increase in aromatic content within 250 °C soils was also observed in the FT-ICR MS analysis where 250 °C soils featured greater modified aromaticity index values compared to control soils (**Figure 4.13**). Overall, we reject hypothesis 3 (abundances of aromatic metabolites will increase as heating

temperature increases) because aromatic metabolite abundances peaked in 250 °C soils and then generally decreased in 450 °C soils.

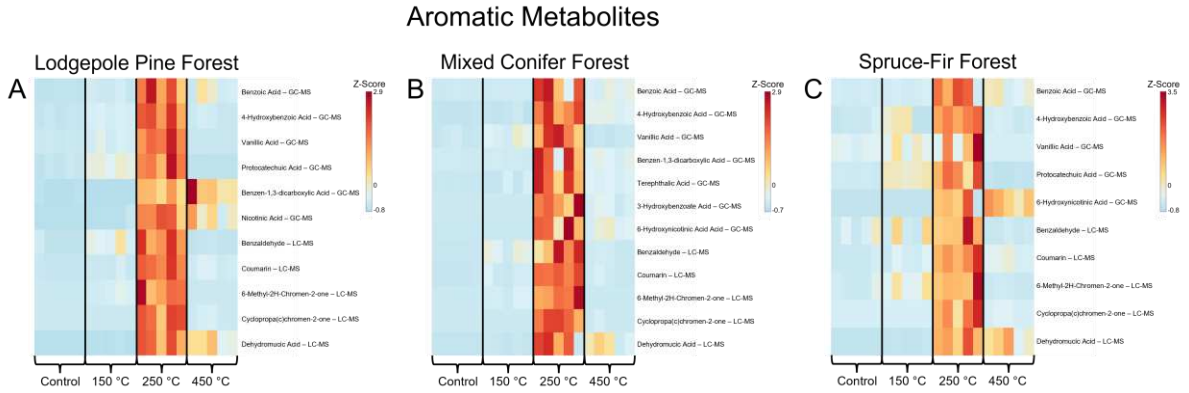

Figure 4.9. Heatmaps for annotated aromatic metabolites from A) lodgepole pine forest, B) mixed conifer forest, and C) spruce-fir forest soils. For quantification, the internal-standardized normalized peak areas for each metabolite were autoscaled and plotted using MetaboAnalyst (Version 6.0) software. Horizontal black lines separate amino acids (above line) from peptides (below line). "GC-MS" and "LC-MS" denotes whether the annotated metabolites were detected via GC-MS or LC-MS analyses. Yellow and red colors indicate above-average abundance values while blue color indicates below-average abundance values. n=5 for Control, 150 °C, 250 °C, and 450 °C samples. Aromatic metabolites were identified with Level 2 identification confidence.[37]

Previous studies have observed soil organic matter from burned soils featuring heightened aromatic content.[5,28,30,32,49,50,52,71–74] Such conclusions were drawn predominantly from spectroscopy, pyrolysis GC-MS, and FT-ICR MS analyses. However, to the authors' knowledge, our study is the first to discover that increased aromatic content in burned soils extends to the lower molecular weight aromatic metabolites as well. These aromatic metabolites are involved in various microbial metabolic pathways. For example, benzoic acid, 4-hydroxybenzoic acid, and protocatechuic acid can be degraded into intermediates that feed into the citric acid cycle, producing adenosine triphosphate (ATP) for cellular energy.[71,75] Benzaldehyde, vanillic acid, and terephthalic acid participate in aminobenzoate degradation while nicotinic acid and 6-hydroxynicotinic acid are involved in nicotinate and nicotinamide metabolism, producing essential coenzymes NAD^+ and $NADP^+$.[76–78] So, these aromatic metabolites enriched in 250 °C soils can be

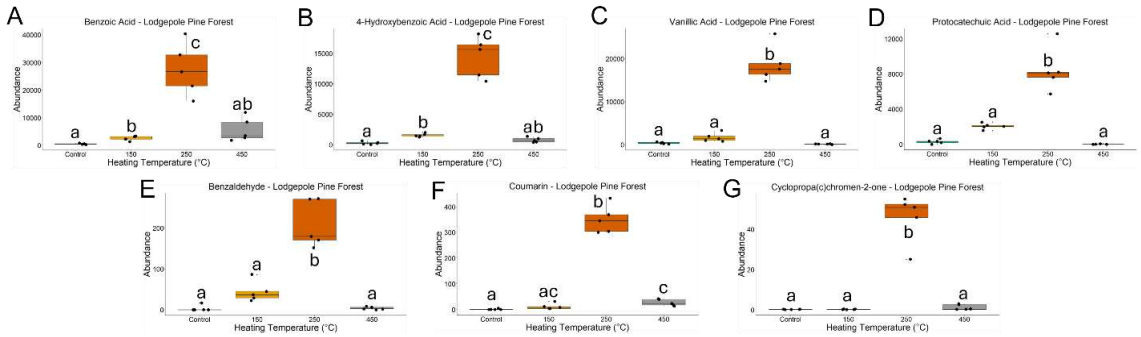

Figure 4.10. Quantification of **A**) benzoic acid, **B**) 4-hydroxybenzoic acid, **C**) vanillic acid, **D**) protocatechuic acid, **E**) benzaldehyde, **F**) coumarin, and **G**) cyclopropa(c)chromen-2-one from lodgepole pine forest soil visualized with box plots. Abundance values were calculated by dividing the peak area of the metabolites by the peak area of the internal standard to account for matrix effects and analytical variation. Therefore, abundance values themselves are arbitrary and cannot be compared across metabolites, but the abundance values can be compared across treatments for a given metabolite. Letters above boxes indicate significant differences between treatments determined by either ANOVA and Tukey HSD tests, Welch's ANOVA and Games-Howell tests, or Kruskal-Wallis and Dunn's tests (see Statistics section 4.2.9 within Methods). The statistical tests of plots **A**, **B**, **C**, **D**, **E**, **F**, and **G** were conducted independently of each other. n = 5 for control, 150 °C, 250 °C, and 450 °C samples. Box plots show the median (central line), first and third quartiles (box edges), and whiskers extending to minimum and maximum values within 1.5 times the interquartile range. Data beyond the end of the whiskers are "outlying" points and are plotted individually. Benzoic acid, 4-hydroxybenzoic acid, vanillic acid, and protocatechuic acid were detected with gas chromatography-mass spectrometry. Benzaldehyde, coumarin, and cyclopropa(c)chromen-2-one were detected with liquid chromatography-mass spectrometry.

involved in key metabolic pathways, providing biologically-relevant metabolites for post-fire microbial activity.

Organic acids were generally most abundant in the 250 °C soils (**Figure 4.14A, B, C**). Three lodgepole pine forest organic acids (succinic acid, 2-furoic acid, and glyceric acid) were significantly more abundant in 250 °C soils compared to control soils (**Figure 4.15**). Two mixed conifer forest organic acids (succinic acid and 2-hydroxybutyric acid) were significantly more abundant in 250 °C soils compared to control soils (**Figure 4.16**). Four spruce-fir forest amino acids (succinic acid, 2-furoic acid, 2-hydroxybutyric acid, and oxoadipic acid) were significantly more abundant in 250 °C soils compared to control soils (**Figure 4.17**). Thus, we accept the organic acid-related component of hypothesis 2: abundances of amino acids, peptides, and organic acids

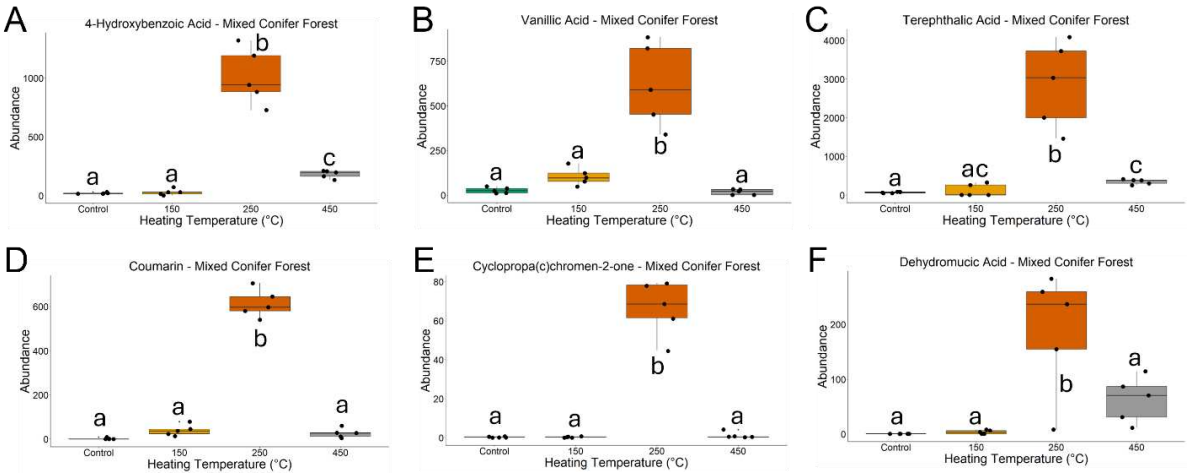

Figure 4.11. Quantification of **A**) 4-hydroxybenzoic acid, **B**) vanillic acid, **C**) terephthalic acid, **D**) coumarin, **E**) cyclopropa(c)chromen-2-one, and **F**) dehydromucic acid from mixed conifer forest soil visualized with box plots. Abundance values were calculated by dividing the peak area of the metabolites by the peak area of the internal standard to account for matrix effects and analytical variation. Therefore, abundance values themselves are arbitrary and cannot be compared across metabolites, but the abundance values can be compared across treatments for a given metabolite. Letters above boxes indicate significant differences between treatments determined by either ANOVA and Tukey HSD tests, Welch's ANOVA and Games-Howell tests, or Kruskal-Wallis and Dunn's tests (see Statistics section 4.2.9 within Methods). The statistical tests of plots **A**, **B**, **C**, **D**, **E** and **F** were conducted independently of each other. n = 5 for control, 150 °C, 250 °C, and 450 °C samples. Box plots show the median (central line), first and third quartiles (box edges), and whiskers extending to minimum and maximum values within 1.5 times the interquartile range. Data beyond the end of the whiskers are "outlying" points and are plotted individually. 4-Hydroxybenzoic acid, vanillic acid, and terephthalic acid were detected with gas chromatography-mass spectrometry. Coumarin, cyclopropa(c)chromen-2-one, and dehydromucic acid were detected with liquid chromatography-mass spectrometry.

will peak at ~250 °C. Similarly to the aromatic metabolites, these organic acids are involved in metabolic pathways. Succinic acid and fumaric acid are intermediates in the citric acid cycle producing ATP,[79,80] 2-furoic acid can be the sole source of carbon and energy for *Pseudomonas putida* (a saprophytic soil bacterium),[81,82] glyceric acid is involved in glycine, serine, and threonine metabolism,[83] and 2-hydroxybutyric acid is involved in propanoate metabolism.[84] Therefore, soils burned to ~250 °C by wildfires likely feature enriched abundances of biologically-relevant organic acids.

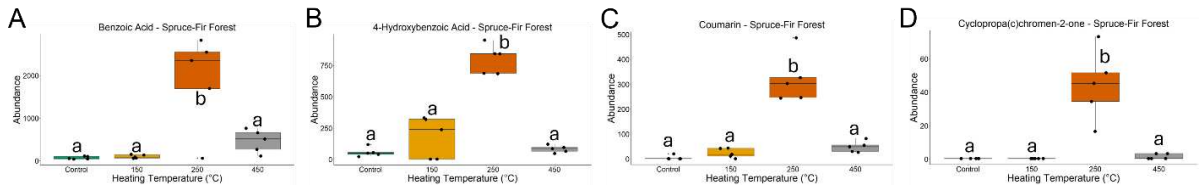

Figure 4.12. Quantification of **A**) benzoic acid, **B**) 4-hydroxybenzoic acid, **C**) coumarin, and **D**) cyclopropa(c)chromen-2-one from spruce-fir forest soil visualized with box plots. Abundance values were calculated by dividing the peak area of the metabolites by the peak area of the internal standard to account for matrix effects and analytical variation. Therefore, abundance values themselves are arbitrary and cannot be compared across metabolites, but the abundance values can be compared across treatments for a given metabolite. Letters above boxes indicate significant differences between treatments determined by either ANOVA and Tukey HSD tests, Welch's ANOVA and Games-Howell tests, or Kruskal-Wallis and Dunn's tests (see Statistics section 4.2.9 within Methods). The statistical tests of plots **A**, **B**, **C**, and **D** were conducted independently of each other. n = 5 for control, 150 °C, 250 °C, and 450 °C samples. Box plots show the median (central line), first and third quartiles (box edges), and whiskers extending to minimum and maximum values within 1.5 times the interquartile range. Data beyond the end of the whiskers are "outlying" points and are plotted individually. Benzoic acid and 4-hydroxybenzoic acid were detected with gas chromatography-mass spectrometry. Coumarin and cyclopropa(c)chromen-2-one were detected with liquid chromatography-mass spectrometry.

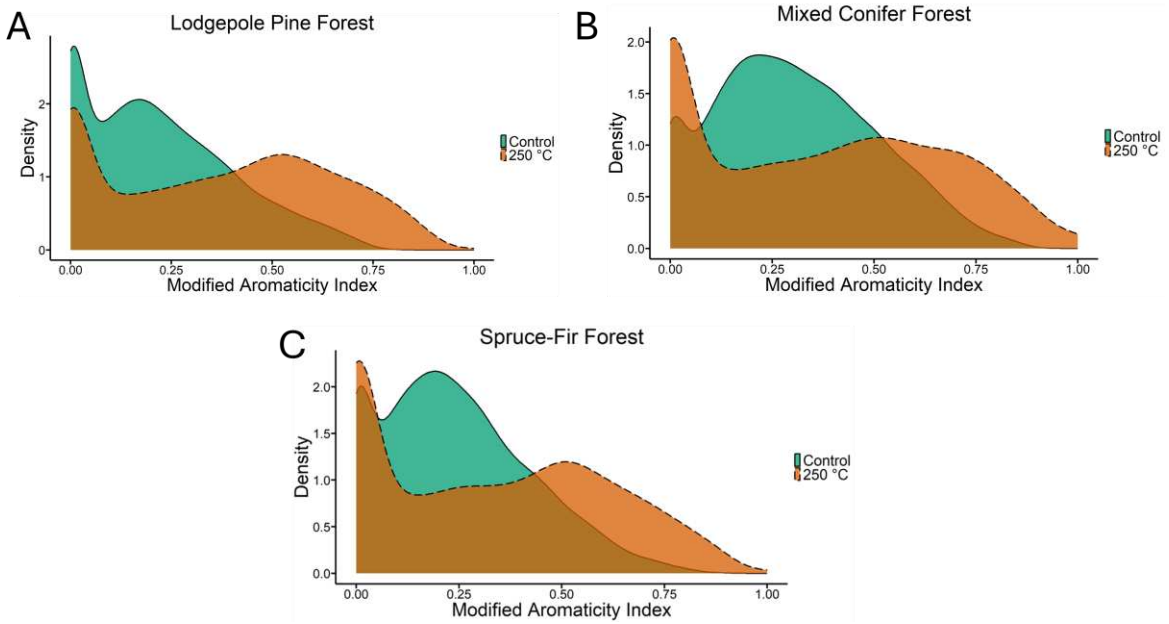

Figure 4.13. Density plots showcasing Fourier transform ion cyclotron resonance-mass spectrometry results that illustrate differences in modified aromaticity index values of unique molecular formulae between control and 250 °C samples with **A**) lodgepole pine forest soil, **B**) mixed conifer forest soil, and **C**) spruce-fir forest soil. A unique molecular formula, for example, is a molecular formula assigned in Sample X but not assigned in Sample Y. In that case, that assigned molecular formulae is unique to sample X.

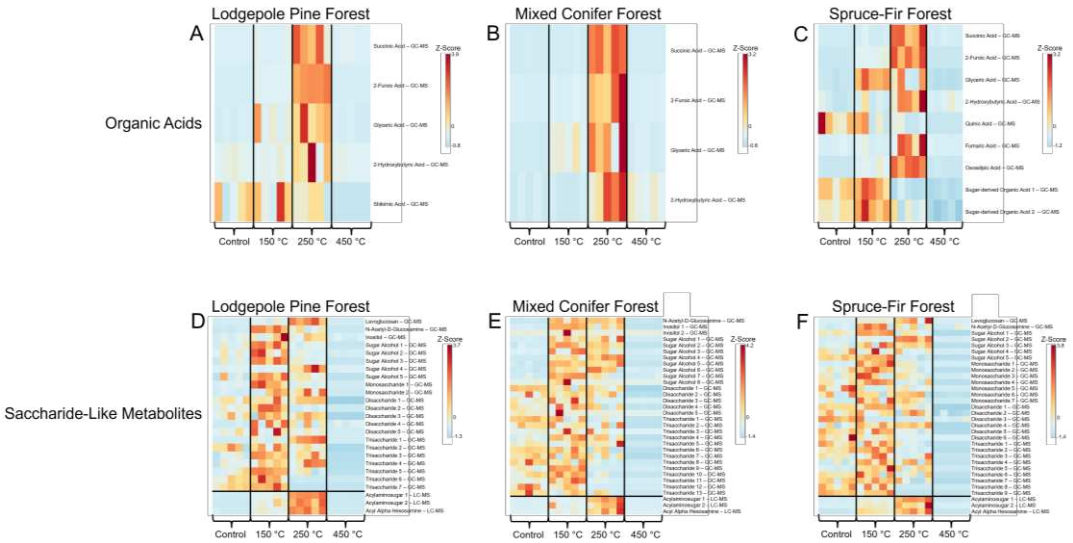

Figure 4.14. Heatmaps for annotated organic acids (**A, B, C**) and saccharide-like metabolites (**D, E, F**) from lodgepole pine forest (**A, D**), mixed conifer forest (**B, E**), spruce-fir forest (**C, E**) soils. For quantification, the internal-standardized normalized peak areas for each metabolite were autoscaled and plotted using MetaboAnalyst (Version 6.0) software. For D, E, and F, horizontal black line separates saccharide-like compounds detected with gas chromatography-mass spectrometry (above-line) from nitrogen-containing saccharides detected with liquid chromatography-mass spectrometry (below line). "GC-MS" and "LC-MS" denotes whether the annotated metabolites were detected via GC-MS or LC-MS analyses. Yellow and red colors indicate above-average abundance values while blue color indicates below-average abundance values. n=5 for Control, 150 °C, 250 °C, and 450 °C samples. Succinic acid, 2-furoic acid, glyceric acid, 2-hydroxybutyric acid, fumaric acid, oxoadipic acid, levoglucosan, and N-acetyl-D-glucosamine, acylaminosugar 1, acylaminosugar 2, and acyl alpha hexosamine were identified with Level 2 identification confidence.[37] The sugar-derived organic acids, sugar alcohols, monosaccharides, disaccharides, and trisaccharides were identified with Level 3 identification confidence.[37]

Soils heated to 250 °C were enriched in nitrogen-containing saccharides (**Figure 4.14D, E, F**). Nitrogen-enriched organic matter often forms following soil heating and burning, presumably due to the Maillard reaction pathway (i.e. condensation of reducing sugars and amino acids).[30,72] The increased abundances of nitrogen-containing saccharides in the 250 °C soils provide further evidence of post-fire nitrogen enrichment in SOM and contribute to burned soils featuring biologically-relevant saccharides for microbial activity. The results of saccharide-like metabolites detected by GC-MS were less consistent compared to previous chemical categories (**Figure 4.14D,**

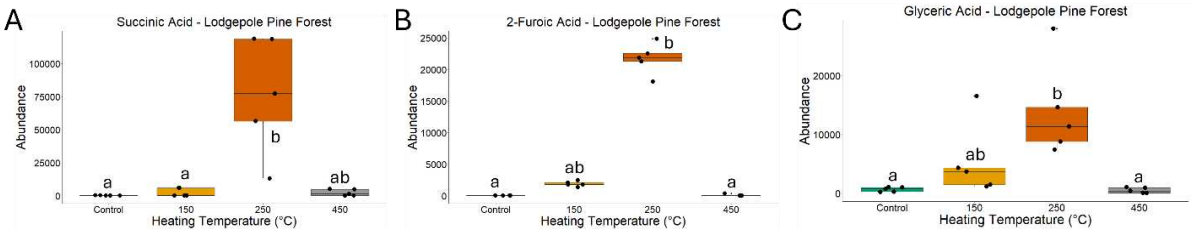

Figure 4.15. Quantification of **A**) succinic acid, **B**) 2-furoic acid, and **C**) glyceric acid from lodgepole pine forest soil visualized with box plots. Abundance values were calculated by dividing the peak area of the metabolites by the peak area of the internal standard to account for matrix effects and analytical variation. Therefore, abundance values themselves are arbitrary and cannot be compared across metabolites, but the abundance values can be compared across treatments for a given metabolite. Letters above boxes indicate significant differences between treatments determined by either ANOVA and Tukey HSD tests, Welch's ANOVA and Games-Howell tests, or Kruskal-Wallis and Dunn's tests (see Statistics section 4.2.9 within Methods). The statistical tests of plots **A**, **B**, and **C**, were conducted independently of each other. n = 5 for control, 150 °C, 250 °C, and 450 °C samples. Box plots show the median (central line), first and third quartiles (box edges), and whiskers extending to minimum and maximum values within 1.5 times the interquartile range. Data beyond the end of the whiskers are "outlying" points and are plotted individually. All metabolites in this figure were detected via gas chromatography-mass spectrometry.

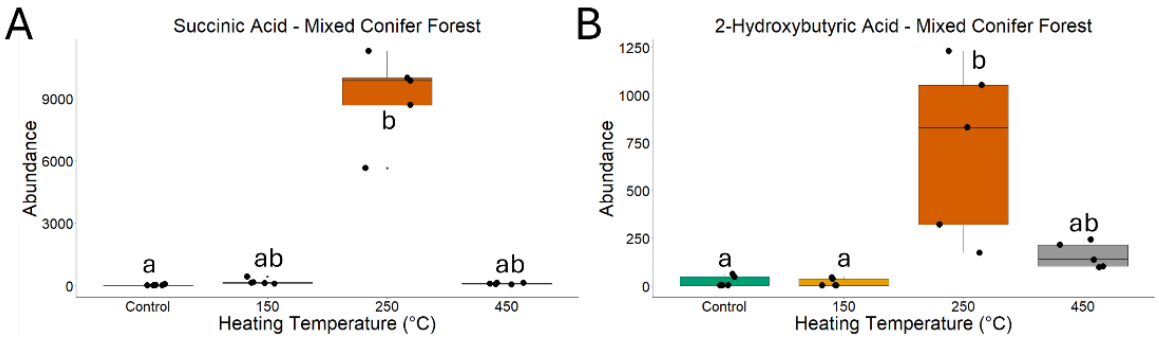

Figure 4.16. Quantification of **A**) succinic acid and **B**) 2-hydroxybutyric acid from mixed conifer forest soil visualized with box plots. Abundance values were calculated by dividing the peak area of the metabolites by the peak area of the internal standard to account for matrix effects and analytical variation. Therefore, abundance values themselves are arbitrary and cannot be compared across metabolites, but the abundance values can be compared across treatments for a given metabolite. Letters above boxes indicate significant differences between treatments determined by either ANOVA and Tukey HSD tests, Welch's ANOVA and Games-Howell tests, or Kruskal-Wallis and Dunn's tests (see Statistics section 4.2.9 within Methods). The statistical tests of plots **A** and **B** were conducted independently of each other. n = 5 for control, 150 °C, 250 °C, and 450 °C samples. Box plots show the median (central line), first and third quartiles (box edges), and whiskers extending to minimum and maximum values within 1.5 times the interquartile range. Data beyond the end of the whiskers are "outlying" points and are plotted individually. Both metabolites in this figure were detected via gas chromatography-mass spectrometry.

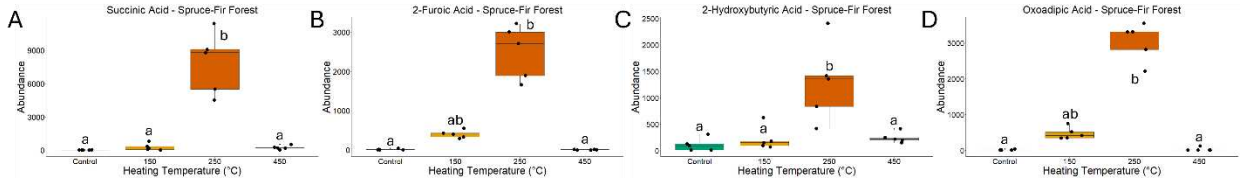

Figure 4.17. Quantification of A) succinic acid, B) 2-furoic acid, C) 2-hydroxybutyric acid, and D) oxoadipic acid from spruce-fir forest soil visualized with box plots. Abundance values were calculated by dividing the peak area of the metabolites by the peak area of the internal standard to account for matrix effects and analytical variation. Therefore, abundance values themselves are arbitrary and cannot be compared across metabolites, but the abundance values can be compared across treatments for a given metabolite. Letters above boxes indicate significant differences between treatments determined by either ANOVA and Tukey HSD tests, Welch's ANOVA and Games-Howell tests, or Kruskal-Wallis and Dunn's tests (see Statistics section 4.2.9 within Methods). The statistical tests of plots **A**, **B**, **C**, and **D** were conducted independently of each other. n = 5 for control, 150 °C, 250 °C, and 450 °C samples. Box plots show the median (central line), first and third quartiles (box edges), and whiskers extending to minimum and maximum values within 1.5 times the interquartile range. Data beyond the end of the whiskers are "outlying" points and are plotted individually. Both metabolites in this figure were detected via gas chromatography-mass spectrometry.

E, and F). Nevertheless, 150 °C and 250 °C soils both featured saccharide-like metabolites that could provide carbon and energy sources for post-fire microbes.

4.3.4 SOILS HEATED TO 150 °C AND 250 °C WERE ENRICHED IN METABOLITES COMPARED TO CONTROL SOIL

For lodgepole pine forest, mixed conifer forest, and spruce-fir forest soils, 91 metabolites were annotated (43 from GC-MS and 48 from LC-MS), 100 metabolites were annotated (52 from GC-MS, 48 from LC-MS), and 102 metabolites were annotated (54 from GC-MS, 48 from LC-MS), respectively, to Level 2 or 3 confidence.[37] 150 °C and 250 °C soils featured more significantly abundant metabolites compared to the control soils. For example, for lodgepole pine forest, mixed conifer forest, and spruce-fir forest samples, 24.2 %, 20 %, and 25.5 % of annotated metabolites, respectively, were significantly more abundant in 150 °C compared to control soil while only 3.3 %, 4 %, and 2 % of annotated metabolites, respectively, were more abundant in control compared to 150 °C soil. Similar results were observed for 250 °C soils. For lodgepole pine forest, mixed

conifer forest, and spruce-fir forest soils, 30.8 %, 30 %, and 18.6 % of annotated metabolites, respectively, were significantly more abundant in 250 °C compared to control soil while only 12.1 %, 15 %, and 22.5 % of annotated metabolites, respectively, were more abundant in control compared to 250 °C soil. Thus, the majority of 150 °C and 250 °C soils featured significantly greater annotated metabolite abundances compared to control soils. Such increased metabolite abundances could have contributed to greater water extractable organic carbon values in 150 °C and 250 °C soils (**Figure 4.18** and **Figure 4.19**) which has been previously observed in other studies.[29–33] Additional bulk soil parameters can be found in Appendix C (**Figure C1-C4**).

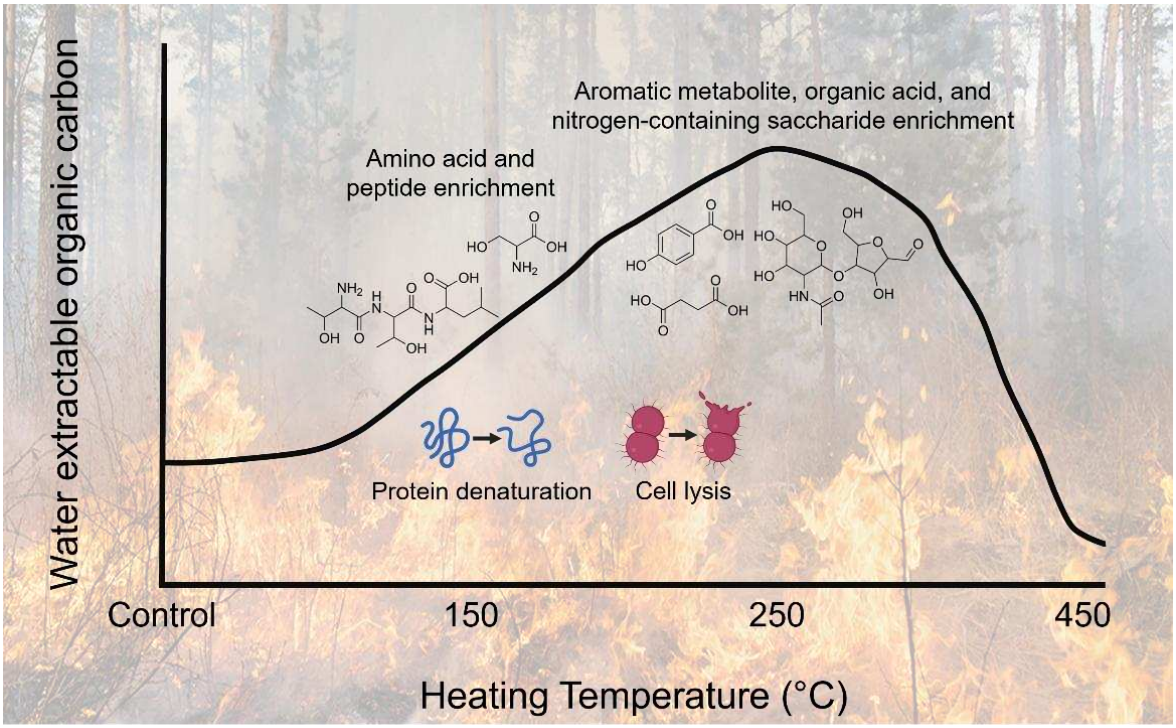

Figure 4.18. Conceptual diagram summarizing key conclusions from this study. As the soil heating temperature initially increases, water extractable organic carbon values (indicated by the black line streaking across the plot) increase to 250 °C and then decrease to 450 °C (**Figure 4.19**). This pattern may be due to the increased metabolite abundances at 150 °C and 250 °C. At ~150 °C, the soils are enriched in amino acids and peptides as proteins in the soil denature. Cell lysis likely contributes to the enrichment of aromatic metabolites, organic acids, and nitrogen-containing saccharides observed in the soils heated to ~250 °C. This figure was made using BioRender.com. Background image of wildfire was from www.iii.org.

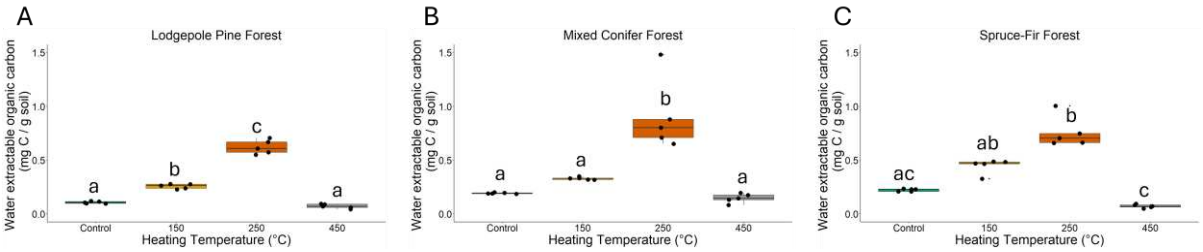

Figure 4.19. Water extractable organic carbon (WEOC) concentrations visualized with box plots for **A**) lodgepole pine forest soil, **B**) mixed conifer forest soil, and **C**) spruce-fir forest soil. Letters above boxes indicate significant differences between treatments determined by either ANOVA and Tukey HSD tests, Welch's ANOVA and Games-Howell tests, or Kruskal-Wallis and Dunn's tests (see Statistics section 4.2.9 within Methods). The statistical tests within each forest type were conducted independently of each other. n = 5 for control, 150 °C, 250 °C, and 450 °C samples. Box plots show the median (central line), first and third quartiles (box edges), and whiskers extending to minimum and maximum values within 1.5 times the interquartile range. Data beyond the end of the whiskers are "outlying" points and are plotted individually.

During wildfires, soil is often heated heterogeneously, contributing to a range of soil heating temperatures.[8,54,75,85–87] To account for heterogeneous heating conditions, all heated soils (150 °C, 250 °C, and 450 °C) vs control soil comparisons were made. For lodgepole pine forest, mixed conifer forest, and spruce-fir forest soils, 51.6 %, 43 %, and 44.1 % of annotated metabolites, respectively, were significantly more abundant in heated soils compared to control soils whereas only 1.1 %, 4 %, and 1 % of annotated metabolites, respectively, were more abundant in control soil compared to all heated soils. Thus, soil burned by wildfires could feature augmented abundances of biologically-relevant metabolites.

Overall, the 150 °C samples were enriched in peptides and amino acids (**Figure 4.4**) while the 250 °C samples were enriched in aromatic metabolites, organic acids, and nitrogen-containing saccharides (**Figures 4.9** and **4.14**). This discrepancy between the temperatures suggests that at 150 °C, proteins in the soil began to denature and tripeptides were detected via LC-MS.[88] Then at 250 °C, sufficient temperatures were met to form aromatic metabolites and nitrogen-containing saccharides and to broadly cause cell lysis, releasing organic acids into the soil. Cell lysis occurs during wildfires when high soil temperatures cause microbial cells to break open, producing

necromass (i.e. organic matter from dead microbes)[89] and releasing intracellular metabolites into the soil.[71,90–92] This idea is further supported by the increased abundance of thymine in the heated soils, especially in the 250 °C soils (**Figure 4.20**). Thymine is a nucleobase and is one of the four building blocks of DNA. Thymine is housed within the nucleoid of prokaryotic cells (like archaea and bacteria) and within the nucleus of eukaryotic cells (like fungi). When microbial cells lyse open during soil heating, intracellular nucleobases like thymine would likely enter the soil, increasing thymine abundances. Mortality thresholds of soil microbes can range between 35 °C and 800 °C.[93] Thus, having cell lysis peak at ~250 °C is plausible. Within 450 °C samples, many of the metabolites that lysed out of cells, including thymine, either volatilized or combusted into CO_2.[7,94,95] Therefore, 150 °C and 250 °C may be the "Goldilocks" zone for metabolite release in soil during wildfires: hot enough to denature proteins, form aromatic metabolites and nitrogen-containing saccharides, lyse cells open, and release intracellular metabolites into the soil but not too hot to volatilize or combust those released metabolites (**Figure 4.18**).

The observed metabolomic results were largely consistent across the three forested ecosystems. Despite collecting soils from three distinct forest types across Colorado, the following parameters exhibited consistent results: metabolomic profiles of metabolites detected with GC-MS changing at different heating temperatures (**Figure 4.1A, B, C**), amino acid abundances (**Figure 4.2**), aromatic metabolite abundances (**Figure 4.9**), organic acid abundances (**Figure 4.14A, B, C**), and nitrogen-containing saccharide abundances (**Figure 4.14D, E, F**). Therefore, the results observed within this study could potentially be extrapolated to soils of other forested ecosystems.

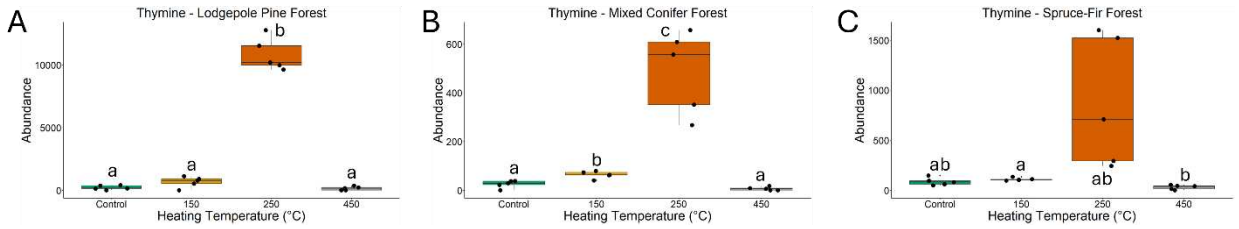

Figure 4.20. Quantification of thymine from **A**) lodgepole pine forest soil, **B**) mixed conifer forest soil, and **C**) spruce-fir forest visualized with box plots. Abundance values were calculated by dividing the peak area of the metabolites by the peak area of the internal standard to account for matrix effects and analytical variation. Therefore, abundance values themselves are arbitrary and cannot be compared across metabolites, but the abundance values can be compared across treatments for a given metabolite. Letters above boxes indicate significant differences between treatments determined by either ANOVA and Tukey HSD tests, Welch's ANOVA and Games-Howell tests, or Kruskal-Wallis and Dunn's tests (see Statistics section 4.2.9 within Methods). The statistical tests of lodgepole pine forest, mixed conifer forest, and spruce-fir forest were conducted independently of each other. n = 5 for control, 150 °C, 250 °C, and 450 °C samples. Box plots show the median (central line), first and third quartiles (box edges), and whiskers extending to minimum and maximum values within 1.5 times the interquartile range. Data beyond the end of the whiskers are "outlying" points and are plotted individually. Thymine was detected with gas chromatography-mass spectrometry.

4.4 ENVIRONMENTAL IMPLICATIONS

Overall, heating soil to distinct temperatures drastically changed the soil metabolome (**Figure 4.1**). Soils heated to 150 °C were enriched in amino acids and peptides (**Figure 4.2**). Soils heated to 250 °C were enriched in aromatic metabolites, organic acids, and nitrogen-containing saccharides (**Figures 4.9** and **4.14**). Lastly, soils heated to 150 °C and 250 °C were enriched in metabolites compared to the control soils, and these results were largely consistent across the three forested ecosystems. This study provides an initial description of expected changes to soil metabolomes when exposed to wildfires of varying intensities, establishing boundary conditions that can guide future investigations on wildfire impacts on SOM.

These results imply that soils burned by wildfires are likely not devoid of biologically-relevant organic matter; rather, burned soils may be enriched in metabolites (especially by wildfires of low to moderate intensity) and may feature an abundant, diverse metabolome compared to unburned soils. These post-fire metabolites could then be utilized by microbes to

accumulate biomass, generate cellular energy, and drive post-fire activity. Therefore, this flush of metabolites may serve as a key component supporting microbial pioneer species that initiate post-fire soil and forest recovery processes. On the other hand, increased metabolite abundances in post-fire soils may lead to increased microbial CO_2 respiration rates, potentially increasing post-fire soil greenhouse gas emissions.

4.5 ACKNOWLEDGEMENTS

This research was funded by Dr. Mike Wilkins and Dr. Thomas Borch from the National Science Foundation under grant number 2114868 and the United States Department of Agriculture (USDA) National Institute of Food and Agriculture through AFRI grant number 2021-67019-34608. We thank Dr. Charles Rhoades of the United States Forest Service for providing soil samples for this investigation. We thank Dr. Nathan Montgomery from the Bioanalysis and Omics Center within the Analytical Resources Core at Colorado State University for operating the LC-MS instrument (RRID: SCR_021758). We thank Paul Mathews and Dr. Claudia Boot from the Analytical Resources Core at Colorado State University who assisted in GC-MS operation and provided guidance for the LC-MS data analysis process, respectively. We thank Daniel Reuss and Rodney Simpson from the EcoCore Analytical Facility at Colorado State University who provided access to a soil grinder and the instrumentation for measuring total carbon and total carbon. We thank Dr. Robert Young for establishing FT-ICR MS analysis within the Borch lab at Colorado State University and for providing helpful code for FT-ICR MS data processing. We also thank Isabel McPherson from the United State Forest Service Rocky Mountain Research Laboratory for operating the TOC-L Shimadzu analyzer. The TOC art was made using BioRender.com.

4.6 AUTHOR CONTRIBUTIONS

Jacob VanderRoest contributed to conceptualization, data curation, formal analysis, investigation, project administration, software, visualization, writing – original draft preparation, and writing – review and editing. Corey Broeckling contributed to methodology, resources, writing – review and editing. Tim Fegel contributed to methodology, formal analysis, resources, supervision and writing – review and editing. Lydia Babcock-Adams contributed to data curation, investigation, resources, and writing – review and editing. Martin Kurek contributed to formal analysis, software, and writing – review and editing. Thomas Borch contributed to conceptualization, supervision, funding acquisition, project administration, resources, and writing – review and editing.

Specifically, Timothy S. Fegel collected and provided the soil and litter samples and generated dissolved organic carbon and dissolved total nitrogen values that were used to calculate water-extractable organic carbon and water-extractable total nitrogen. Lydia C. Babcock-Adams operated the Fourier transform ion cyclotron resonance mass spectrometry instrument. Martin R. Kurek calibrated the data from the Fourier transform ion cyclotron resonance mass spectrometry instrument and assigned molecular formulae to the detected peaks. I conducted the soil heating experiments, measured soil pH, measured total soil C and N, led the gas chromatography-mass spectrometry analysis, led the liquid chromatography-mass spectrometry analysis, and analyzed the molecular formula assignment data from the Fourier transform ion cyclotron resonance mass spectrometry instrument, contributing to my conceptualization, data curation, formal analysis, investigation, project administration, and software contributions. For visualization, I produced all of the figures in this chapter.

CHAPTER 4 REFERENCES

(1) Pausas, J. G.; Keeley, J. E. Wildfires as an Ecosystem Service. *Front. Ecol. Environ.* **2019**, *17* (5), 289–295. https://doi.org/10.1002/fee.2044.

(2) Abatzoglou, J. T.; Williams, A. P.; Barbero, R. Global Emergence of Anthropogenic Climate Change in Fire Weather Indices. *Geophys. Res. Lett.* **2019**, *46* (1), 326–336. https://doi.org/10.1029/2018gl080959.

(3) Keeley, J. E. Fire Intensity, Fire Severity and Burn Severity: A Brief Review and Suggested Usage. *Int. J. Wildland Fire* **2009**, *18* (1), 116–126. https://doi.org/10.1071/wf07049.

(4) Cunningham, C. X.; Williamson, G. J.; Bowman, D. M. J. S. Increasing Frequency and Intensity of the Most Extreme Wildfires on Earth. *Nat. Ecol. Evol.* **2024**, *8*, 1420–1425. https://doi.org/10.1038/s41559-024-02452-2.

(5) Jiménez-Morillo, N. T.; Almendros, G.; Miller, A. Z.; Hatcher, P. G.; González-Pérez, J. A. Hydrophobicity of Soils Affected by Fires: An Assessment Using Molecular Markers from Ultra-High Resolution Mass Spectrometry. *Sci. Total Environ.* **2022**, 152957. https://doi.org/10.1016/j.scitotenv.2022.152957.

(6) Knicker, H. How Does Fire Affect the Nature and Stability of Soil Organic Nitrogen and Carbon? A Review. *Biogeochemistry* **2007**, *85* (1), 91–118. https://doi.org/10.1007/s10533-007-9104-4.

(7) Alcañiz, M.; Outeiro, L.; Francos, M.; Farguell, J.; Úbeda, X. Long-Term Dynamics of Soil Chemical Properties after a Prescribed Fire in a Mediterranean Forest (Montgrí Massif, Catalonia, Spain). *Sci. Total Environ.* **2016**, *572*, 1329–1335. https://doi.org/10.1016/j.scitotenv.2016.01.115.

(8) Roshan, A.; Biswas, A. Fire-Induced Geochemical Changes in Soil: Implication for the Element Cycling. *Sci. Total Environ.* **2023**, *868*, 161714.

(9) Sánchez-García, C.; Santín, C.; Doerr, S. H.; Strydom, T.; Urbanek, E. Wildland Fire Ash Enhances Short-Term CO2 Flux from Soil in a Southern African Savannah. *Soil Biol. Biochem.* **2021**, *160*, 108334. https://doi.org/10.1016/j.soilbio.2021.108334.

(10) Memoli, V.; Panico, S. C.; Santorufo, L.; Barile, R.; Di Natale, G.; Di Nunzio, A.; Toscanesi, M.; Trifuoggi, M.; De Marco, A.; Maisto, G. Do Wildfires Cause Changes in Soil Quality in the Short Term? *Int. J. Environ. Res. Public. Health* **2020**, *17* (15), 5343. https://doi.org/10.3390/ijerph17155343.

(11) Marfella, L.; Mairota, P.; Marzaioli, R.; Glanville, H. C.; Pazienza, G.; Rutigliano, F. A. Long-Term Impact of Wildfire on Soil Physical, Chemical and Biological Properties within a Pine Forest. *Eur. J. For. Res.* **2024**. https://doi.org/10.1007/s10342-024-01696-8.

(12) Su, W.-Q.; Yu, M.; Lin, J.; Tang, C.; Xu, J. Fire Decreases Gross Mineralization Rate but Does Not Alter Gross Nitrification Rate in Boreal Forest Soils. *Soil Biol. Biochem.* **2022**, *175*, 108838. https://doi.org/10.1016/j.soilbio.2022.108838.

(13) Fowler, J. A.; Nelson, A. R.; Bechtold, E. K.; Paul, R.; Wettengel, A. M.; McNorvell, M. A.; Stevens-Rumann, C. S.; Fegel, T. S.; Anderson, E.; Rhoades, C. C.; Wilkins, M. J. Pile Burns as a Proxy for High Severity Wildfire Impacts on Soil Microbiomes. *Geoderma* **2024**, *448*, 116982. https://doi.org/10.1016/j.geoderma.2024.116982.

(14) Zhu, S.; Yang, P.; Yin, Y.; Zhang, S.; Lv, J.; Tian, S.; Jiang, T.; Wang, D. Influences of Wildfire on the Soil Dissolved Organic Matter Characteristics and Its Electron-Donating Capacity. *Water Res.* **2024**, *266*, 122382. https://doi.org/10.1016/j.watres.2024.122382.

(15) Zheng, X.; Zhang, Y.; Deng, Y.; Cui, X. Effects of Wildfire on the Adsorption-Desorption of Soil Free Amino Acids in a Dahurian Larch Forest in Northeast China. *J. Soil Sci. Plant Nutr.* **2024**. https://doi.org/10.1007/s42729-024-02027-x.

(16) Johnson, D. B.; Yedinak, K. M.; Sulman, B. N.; Berry, T. D.; Kruger, K.; Whitman, T. Effects of Fire and Fire-Induced Changes in Soil Properties on Post-Burn Soil Respiration. *Fire Ecol.* **2024**, *20* (1). https://doi.org/10.1186/s42408-024-00328-1.

(17) Araya, S. N.; Meding, M.; Berhe, A. A. Thermal Alteration of Soil Physico-Chemical Properties: A Systematic Study to Infer Response of Sierra Nevada Climosequence Soils to Forest Fires. *SOIL* **2016**, *2* (3), 351–366. https://doi.org/10.5194/soil-2-351-2016.

(18) Rhoades, C. C.; Fegel, T. S.; Fowler, J. A.; Starr, B.; Wilkins, M. J. Rapid Changes in the Chemistry of Ash and Underlying Soil Layers after Pile Burning in a Subalpine Forest. *Trees For. People* **2025**, *22*, 101035. https://doi.org/10.1016/j.tfp.2025.101035.

(19) Cheng, Y.; Luo, P.; Yang, H.; Li, H.; Luo, C.; Jia, H.; Huang, Y. Fire Effects on Soil Carbon Cycling Pools in Forest Ecosystems: A Global Meta-Analysis. *Sci. Total Environ.* **2023**, *895*, 165001.

(20) Köster, K.; Kohli, J.; Lindberg, H.; Pumpanen, J. Post-Fire Soil Greenhouse Gas Fluxes in Boreal Scots Pine Forests–Are They Affected by Surface Fires with Different Severities? *Agric. For. Meteorol.* **2024**, *349*, 109954.

(21) Hudiburg, T.; Mathias, J.; Bartowitz, K.; Berardi, D. M.; Bryant, K.; Graham, E.; Kolden, C. A.; Betts, R. A.; Lynch, L. Terrestrial Carbon Dynamics in an Era of Increasing Wildfire. *Nat. Clim. Change* **2023**, *13*, 1306–1316.

(22) Xu, S.; Eisenhauer, N.; Pellegrini, A.; Wang, J.; Certini, G.; Guerra, C.; Lai, D. Fire Frequency and Type Regulate the Response of Soil Carbon Cycling and Storage to Fire across Soil Depths and Ecosystems: A Meta-Analysis. *Sci. Total Environ.* **2022**, *825*, 153921.

(23) Strydom, T.; Smit, I. P. J.; van Tol, J. J. Short and Long-Term Fire Effects on Soil C and N in an African Savanna. *Geoderma Reg.* **2024**, *37*, 1–8.

(24) Krichels, A. H.; Stephens, E. Z.; Reid, C.; Barriga, M. F. P.; Ordoñez, M. E.; McLaren, J. R.; Kargul, M.; Larios, L.; Glassman, S. I.; Homyak, P. M. Wildfire-Induced Losses of Soil Particulate and Mineral-Associated Organic Carbon Persist for Over 4 Years in a Chaparral Ecosystem. *Glob. Change Biol.* **2025**, *31* (8), e70404. https://doi.org/10.1111/gcb.70404.

(25) Lopez, A. M.; Avila, C. C. E.; VanderRoest, J. P.; Roth, H. K.; Fendorf, S.; Borch, T. Molecular Insights and Impacts of Wildfire-Induced Soil Chemical Changes. *Nat. Rev. Earth Environ.* **2024**, *5*, 431–446. https://doi.org/10.1038/s43017-024-00548-8.

(26) Roth, H. K.; Nelson, A. R.; McKenna, A. M.; Fegel, T. S.; Young, R. B.; Rhoades, C. C.; Wilkins, M. J.; Borch, T. Impact of Beaver Ponds on Biogeochemistry of Organic Carbon and Nitrogen along a Fire-Impacted Stream. *Environ. Sci. Process. Amp Impacts* **2022**. https://doi.org/10.1039/d2em00184e.

(27) Roth, H. K.; McKenna, A. M.; Simpson, M. J.; Chen, H.; Srikanthan, N.; Fegel, T.; Nelson, A. R.; Rhoades, C. C.; Wilkins, M. J.; Borch, T. Effects of Burn Severity on Organic Nitrogen and Carbon Chemistry in High-Elevation Forest Soils. *Soil Environ. Health* **2023**, 100023.

(28) González-Pérez, J. A.; González-Vila, F. J.; Almendros, G.; Knicker, H. The Effect of Fire on Soil Organic Matter—a Review. *Environ. Int.* **2004**, *30* (6), 855–870. https://doi.org/10.1016/j.envint.2004.02.003.

(29) Santos, F.; Russell, D.; Berhe, A. A. Thermal Alteration of Water Extractable Organic Matter in Climosequence Soils from the Sierra Nevada, California. *J. Geophys. Res. Biogeosciences* **2016**, *121* (11), 2877–2885. https://doi.org/10.1002/2016jg003597.

(30) Bahureksa, W.; Young, R. B.; McKenna, A. M.; Chen, H.; Thorn, K. A.; Rosario-Ortiz, F. L.; Borch, T. Nitrogen Enrichment during Soil Organic Matter Burning and Molecular Evidence of Maillard Reactions. *Environ. Sci. Technol.* **2022**, *56* (7), 4597–4609. https://doi.org/10.1021/acs.est.1c06745.

(31) Cawley, K. M.; Hohner, A. K.; Podgorski, D. C.; Cooper, W. T.; Korak, J. A.; Rosario-Ortiz, F. L. Molecular and Spectroscopic Characterization of Water Extractable Organic Matter from Thermally Altered Soils Reveal Insight into Disinfection Byproduct Precursors. *Environ. Sci. Technol.* **2017**, *51* (2), 771–779. https://doi.org/10.1021/acs.est.6b05126.

(32) Zhang, Q.; Wang, Y.; Guan, P.; Zhang, P.; Mo, X.; Yin, G.; Qu, B.; Xu, S.; He, C.; Shi, Q.; Zhang, G.; Dittmar, T.; Wang, J. Temperature Thresholds of Pyrogenic Dissolved Organic Matter in Heating Experiments Simulating Forest Fires. *Environ. Sci. Technol.* **2023**, *57*, 17291–17301.

(33) Hohner, A. K.; Rhoades, C. C.; Wilkerson, P.; Rosario-Ortiz, F. L. Wildfires Alter Forest Watersheds and Threaten Drinking Water Quality. *Acc. Chem. Res.* **2019**, *52* (5), 1234–1244. https://doi.org/10.1021/acs.accounts.8b00670.

(34) Cochran, D.; Powers, R. Fourier Transform Ion Cyclotron Resonance Mass Spectrometry Applications for Metabolomics. *Biomedicines* **2024**, *12* (8), 1786. https://doi.org/10.3390/biomedicines12081786.

(35) Baran, R.; Brodie, E. L.; Mayberry-Lewis, J.; Hummel, E.; Da Rocha, U. N.; Chakraborty, R.; Bowen, B. P.; Karaoz, U.; Cadillo-Quiroz, H.; Garcia-Pichel, F.; Northen, T. R.

Exometabolite Niche Partitioning among Sympatric Soil Bacteria. *Nat. Commun.* **2015**, *6* (1), 8289. https://doi.org/10.1038/ncomms9289.

(36) Swenson, T. L.; Karaoz, U.; Swenson, J. M.; Bowen, B. P.; Northen, T. R. Linking Soil Biology and Chemistry in Biological Soil Crust Using Isolate Exometabolomics. *Nat. Commun.* **2018**, *9* (1). https://doi.org/10.1038/s41467-017-02356-9.

(37) Schymanski, E. L.; Jeon, J.; Gulde, R.; Fenner, K.; Ruff, M.; Singer, H. P.; Hollender, J. Identifying Small Molecules via High Resolution Mass Spectrometry: Communicating Confidence. *Environ. Sci. Technol.* **2014**, *48* (4), 2097–2098. https://doi.org/10.1021/es5002105.

(38) Zweigle, J.; Tisler, S.; Bevilacqua, M.; Tomasi, G.; Nielsen, N. J.; Gawlitta, N.; Lübeck, J. S.; Smilde, A. K.; Christensen, J. H. Prioritization Strategies for Non-Target Screening in Environmental Samples by Chromatography – High-Resolution Mass Spectrometry: A Tutorial. *J. Chromatogr. A* **2025**, *1751*, 465944. https://doi.org/10.1016/j.chroma.2025.465944.

(39) Bifarin, O. O.; Yelluru, V. S.; Simhadri, A.; Fernández, F. M. A Large Language Model–Powered Map of Metabolomics Research. *Anal. Chem. 97* (27), 14088–14096. https://doi.org/10.1021/acs.analchem.5c01672.

(40) McGivern, B. B.; Tfaily, M. M.; Borton, M. A.; Kosina, S. M.; Daly, R. A.; Nicora, C. D.; Purvine, S. O.; Wong, A. R.; Lipton, M. S.; Hoyt, D. W.; Northen, T. R.; Hagerman, A. E.; Wrighton, K. C. Decrypting Bacterial Polyphenol Metabolism in an Anoxic Wetland Soil. *Nat. Commun.* **2021**, *12* (1). https://doi.org/10.1038/s41467-021-22765-1.

(41) Swenson, T. L. Untargeted Soil Metabolomics Methods for Analysis of Extractable Organic Matter. *Soil Biol. Biochem.* **2015**, *80*, 189–198. https://doi.org/doi:10.1016/j.soilbio.2014.10.007.

(42) Bhattacharjya, S.; Ghosh, A.; Sahu, A.; Agnihotri, R.; Pal, N.; Sharma, P.; Manna, M. C.; Sharma, M. P.; Singh, A. B. Utilizing Soil Metabolomics to Investigate the Untapped Metabolic Potential of Soil Microbial Communities and Their Role in Driving Soil Ecosystem Processes: A Review. *Appl. Soil Ecol.* **2024**, *195*, 105238.

(43) Withers, E.; Hill, P. W.; Chadwick, D. R.; Jones, D. L. Use of Untargeted Metabolomics for Assessing Soil Quality and Microbial Function. *Soil Biol. Biochem.* **2020**, *143*, 107758. https://doi.org/10.1016/j.soilbio.2020.107758.

(44) Li, W.; Liu, X.; Xia, Q.; Gao, Z.; Zheng, W.; Zhai, B.; Yang, Z. Untargeted Metabolomics to Study Changes in Soil Microbial Community in Response to Tillage Practices. *Appl. Soil Ecol.* **2024**, *199*, 105409.

(45) Brown, R. W.; Chadwick, D. R.; Zang, H.; Jones, D. L. Use of Metabolomics to Quantify Changes in Soil Microbial Function in Response to Fertiliser Nitrogen Supply and Extreme Drought. *Soil Biol. Biochem.* **2021**, *160*, 108351. https://doi.org/10.1016/j.soilbio.2021.108351.

(46) Lai, X.; Duan, W.; Zhang, W.; Peng, Z.; Wang, X.; Wang, H.; Qi, X.; Pi, H.; Chen, K.; Yan, L. Integrative Analysis of Microbiome and Metabolome Revealed the Effect of Microbial Inoculant on Microbial Community Diversity and Function in Rhizospheric Soil under Tobacco Monoculture. *Microbiol. Spectr.* **2024**, *12* (8). https://doi.org/10.1128/spectrum.04046-23.

(47) Chen, H.; Wang, J.-J.; Ku, P.-J.; Tsui, M. T.-K.; Abney, R. B.; Berhe, A. A.; Zhang, Q.; Burton, S. D.; Dahlgren, R. A.; Chow, A. T. Burn Intensity Drives the Alteration of Phenolic Lignin to (Poly) Aromatic Hydrocarbons as Revealed by Pyrolysis Gas Chromatography–Mass Spectrometry (Py-GC/MS). *Environ. Sci. Technol.* **2022**, *56* (17), 12678–12687. https://doi.org/10.1021/acs.est.2c00426.

(48) De La Rosa, J. M.; González-Pérez, J. A.; González-Vázquez, R.; Knicker, H.; López-Capel, E.; Manning, D. A. C.; González-Vila, F. J. Use of Pyrolysis/GC–MS Combined with Thermal Analysis to Monitor C and N Changes in Soil Organic Matter from a Mediterranean Fire Affected Forest. *CATENA* **2008**, *74* (3), 296–303. https://doi.org/10.1016/j.catena.2008.03.004.

(49) Jiménez-González, M. A.; De La Rosa, J. M.; Jiménez-Morillo, N. T.; Almendros, G.; González-Pérez, J. A.; Knicker, H. Post-Fire Recovery of Soil Organic Matter in a Cambisol from Typical Mediterranean Forest in Southwestern Spain. *Sci. Total Environ.* **2016**, *572*, 1414–1421. https://doi.org/10.1016/j.scitotenv.2016.02.134.

(50) Faria, S. R.; De La Rosa, J. M.; Knicker, H.; González-Pérez, J. A.; Keizer, J. J. Molecular Characterization of Wildfire Impacts on Organic Matter in Eroded Sediments and Topsoil in Mediterranean Eucalypt Stands. *CATENA* **2015**, *135*, 29–37. https://doi.org/10.1016/j.catena.2015.07.007.

(51) Jiménez-Morillo, N. T.; de la Rosa, J. M.; Waggoner, D.; Almendros, G.; González-Vila, F. J.; González-Pérez, J. A. Fire Effects in the Molecular Structure of Soil Organic Matter Fractions under Quercus Suber Cover. *CATENA* **2016**, *145*, 266–273.

(52) Jiménez-Morillo, N. T.; Almendros, G.; De la Rosa, J. M.; Jordán, A.; Zavala, L. M.; Granged, A. J. P.; González-Pérez, J. A. Effect of a Wildfire and of Post-Fire Restoration Actions in the Organic Matter Structure in Soil Fractions. *Sci. Total Environ.* **2020**, *728*, 138715. https://doi.org/10.1016/j.scitotenv.2020.138715.

(53) Zeba, N.; Berry, T. D.; Fischer, M. S.; Traxler, M. F.; Whitman, T. Soil Carbon Mineralization and Microbial Community Dynamics in Response to Pyrogenic Organic Matter Addition. *Soil Biol. Biochem.* **2024**, *191*, 109328.

(54) VanderRoest, J. P.; Fowler, J. A.; Rhoades, C. C.; Roth, H. K.; Broeckling, C. D.; Fegel, T. S.; McKenna, A. M.; Bechtold, E. K.; Boot, C. M.; Wilkins, M. J.; Borch, T. Fire Impacts on the Soil Metabolome and Organic Matter Biodegradability. *Environ. Sci. Technol.* **2024**, *58*, 4167–4180. https://doi.org/10.1021/acs.est.3c09797.

(55) Myers-Pigg, A. N.; Grieger, S.; Roebuck Jr., J. A.; Barnes, M. E.; Bladon, K. D.; Bailey, J. D.; Barton, R.; Chu, R. K.; Graham, E. B.; Homolka, K. K.; Kew, W.; Lipton, A. S.; Scheibe, T.; Toyoda, J. G.; Wagner, S. Experimental Open Air Burning of Vegetation Enhances Organic Matter Chemical Heterogeneity Compared to Laboratory Burns. *Environ. Sci. Technol.* **2024**, *58*, 9679−9688.

(56) Promi, S. I.; Gardner, C. M.; Hohner, A. K. Biodegradability of Unheated and Laboratory Heated Dissolved Organic Matter. *Environ. Sci. Process. Impacts* **2024**. https://doi.org/10.1039/d3em00383c.

(57) Namayandeh, A.; Lamb, C.; Sarabia, J. L.; Shakouri, M.; Lopes, E.; Lezama Pacheco, J.; Honeyman, A.; Coker, A.; Stewart, B.; Tikoo, S.; Peak, D.; Fendorf, S. Nonlinear Redox Transformations of Chromium in Soil during Wildfire Heating: The Critical Role of Iron Mineralogy. *Environ. Sci. Technol.* **2025**, *59* (50), 27623–27634. https://doi.org/10.1021/acs.est.5c10407.

(58) Brucker, C. P.; Livneh, B.; Minear, J. T.; Rosario-Ortiz, F. L. A Review of Simulation Experiment Techniques Used to Analyze Wildfire Effects on Water Quality and Supply. *Environ. Sci. Process. Impacts* **2022**, *24* (8), 1110–1132. https://doi.org/10.1039/d2em00045h.

(59) Nagel, L. M.; Palik, B. J.; Battaglia, M. A.; D'Amato, A. W.; Guldin, J. M.; Swanston, C. W.; Janowiak, M. K.; Powers, M. P.; Joyce, L. A.; Millar, C. I.; Peterson, D. L.; Ganio, L. M.; Kirschbaum, C.; Roske, M. R. Adaptive Silviculture for Climate Change: A National Experiment

in Manager-Scientist Partnerships to Apply an Adaptation Framework. *J. For.* **2017**, *115*, 167–178. https://doi.org/10.5849/jof.16-039.

(60) NOAA ATLAS 14 POINT PRECIPITATION FREQUENCY ESTIMATES: CO. National Oceanic and Atmospheric Administration. Https://Hdsc.Nws.Noaa.Gov/Pfds/Pfds_map_cont.Html?Bkmrk=co (Accessed 4/16/2024).

(61) Schmid, R.; Heuckeroth, S.; Korf, A.; Smirnov, A.; Myers, O.; Dyrlund, T. S.; Bushuiev, R.; Murray, K. J.; Hoffmann, N.; Lu, M.; Sarvepalli, A.; Zhang, Z.; Fleischauer, M.; Dührkop, K.; Wesner, M.; Hoogstra, S. J.; Rudt, E.; Mokshyna, O.; Brungs, C.; Ponomarov, K.; Mutabdžija, L.; Damiani, T.; Pudney, C. J.; Earll, M.; Helmer, P. O.; Fallon, T. R.; Schulze, T.; Rivas-Ubach, A.; Bilbao, A.; Richter, H.; Nothias, L.-F.; Wang, M.; Orešič, M.; Weng, J.-K.; Böcker, S.; Jeibmann, A.; Hayen, H.; Karst, U.; Dorrestein, P. C.; Petras, D.; Du, X.; Pluskal, T. Integrative Analysis of Multimodal Mass Spectrometry Data in MZmine 3. *Nat. Biotechnol.* **2023**, *41* (4), 447–449. https://doi.org/10.1038/s41587-023-01690-2.

(62) Dittmar, T.; Koch, B.; Hertkorn, N.; Kattner, G. A Simple and Efficient Method for the Solid-Phase Extraction of Dissolved Organic Matter (SPE-DOM) from Seawater. *Limnol. Oceanogr. Methods* **2008**, *6* (6), 230–235. https://doi.org/10.4319/lom.2008.6.230.

(63) Xian, F.; Hendrickson, C. L.; Blakney, G. T.; Beu, S. C.; Marshall, A. G. Automated Broadband Phase Correction of Fourier Transform Ion Cyclotron Resonance Mass Spectra. *Anal. Chem.* **2010**, *82* (21), 8807–8812. https://doi.org/10.1021/ac101091w.

(64) Savory, J. J.; Kaiser, N. K.; McKenna, A. M.; Xian, F.; Blakney, G. T.; Rodgers, R. P.; Hendrickson, C. L.; Marshall, A. G. Parts-Per-Billion Fourier Transform Ion Cyclotron Resonance Mass Measurement Accuracy with a “Walking” Calibration Equation. *Anal. Chem.* **2011**, *83* (5), 1732–1736. https://doi.org/10.1021/ac102943z.

(65) Kendrick, E. A Mass Scale Based on CH_2 = 14.0000 for High Resolution Mass Spectrometry of Organic Compounds. *Anal. Chem.* **1963**, *35* (13), 2146–2154. https://doi.org/10.1021/ac60206a048.

(66) Hughey, C. A.; Hendrickson, C. L.; Rodgers, R. P.; Marshall, A. G.; Qian, K. Kendrick Mass Defect Spectrum: A Compact Visual Analysis for Ultrahigh-Resolution Broadband Mass Spectra. *Anal. Chem.* **2001**, *73*, 4676–4681. https://doi.org/10.1021/ac010560.

(67) Corilo, Y. E. *PetroOrg Softw.* **2014**, *Florida State University, Omics LLC: Tallahassee, FL*.

(68) Koch, B. P.; Dittmar, T. From Mass to Structure: An Aromaticity Index for High-Resolution Mass Data of Natural Organic Matter. *Rapid Commun. Mass Spectrom.* **2006**, *20* (5), 926–932. https://doi.org/10.1002/rcm.2386.

(69) Koch, B. P.; Dittmar, T. From Mass to Structure: An Aromaticity Index for High-Resolution Mass Data of Natural Organic Matter. *Rapid Commun. Mass Spectrom.* **2016**, *30* (1), 250–250. https://doi.org/10.1002/rcm.7433.

(70) Riedel, T.; Biester, H.; Dittmar, T. Molecular Fractionation of Dissolved Organic Matter with Metal Salts. *Environ. Sci. Technol.* **2012**, *46* (8), 4419–4426. https://doi.org/10.1021/es203901u.

(71) Nelson, A. R.; Narrowe, A. B.; Rhoades, C. C.; Fegel, T. S.; Daly, R. A.; Roth, H. K.; Chu, R. K.; Amundson, K. K.; Young, R. B.; Steindorff, A. S.; Mondo, S. J.; Grigoriev, I. V.; Salamov, A.; Borch, T.; Wilkins, M. J. Wildfire-Dependent Changes in Soil Microbiome Diversity and Function. *Nat. Microbiol.* **2022**, *7* (9), 1419–1430. https://doi.org/10.1038/s41564-022-01203-y.

(72) Roth, H. K.; Borch, T.; Young, R. B.; Bahureksa, W.; Blakney, G. T.; Nelson, A. R.; Wilkins, M. J.; McKenna, A. M. Enhanced Speciation of Pyrogenic Organic Matter from Wildfires Enabled by 21 T FT-ICR Mass Spectrometry. *Anal. Chem.* **2022**, *94* (6), 2973–2980. https://doi.org/10.1021/acs.analchem.1c05018.

(73) Yin, G.; Guan, P.; Wang, Y.-H.; Zhang, P.; Qu, B.; Xu, S.; Zhang, G.; He, C.; Shi, Q.; Wang, J. Temporal Variations in Fire Impacts on Characteristics and Composition of Soil-Derived Dissolved Organic Matter at Qipan Mountain, China. *Environ. Sci. Technol.* **2024**. https://doi.org/10.1021/acs.est.4c00446.

(74) Cao, X.; Ma, H.; Li, S.-A.; Huang, H.; Cui, F.; Tanentzap, A. J. Enhanced Release and Reactivity of Soil Water-Extractable Organic Matter Following Wildfire in a Subtropical Forest. *Environ. Sci. Technol.* **2025**, *59* (8), 3992–4002. https://doi.org/10.1021/acs.est.4c13557.

(75) Monika S. Fischer; Frances G. Stark; Timothy D. Berry; Nayela Zeba; Thea Whitman; Matthew F. Traxler. Pyrolyzed Substrates Induce Aromatic Compound Metabolism in the Post-Fire Fungus, Pyronema Domesticum. *Front. Microbiol.* **2021**, *12*, 1–12.

(76) Kyoto Encyclopedia of Genes and Genomes (KEGG) Database. *KEGG COMPOUND: C00261*. https://www.kegg.jp/entry/C00261 (accessed 2026-01-13).

(77) Kyoto Encyclopedia of Genes and Genomes (KEGG) Database. *KEGG COMPOUND: C06672*. https://www.kegg.jp/entry/C06672 (accessed 2025-12-04).

(78) Kyoto Encyclopedia of Genes and Genomes (KEGG) Database. *KEGG COMPOUND: C06337*. https://www.kegg.jp/entry/C06337 (accessed 2026-01-13).

(79) Kyoto Encyclopedia of Genes and Genomes (KEGG) Database. *KEGG COMPOUND: C00042*. https://www.kegg.jp/entry/C00042 (accessed 2026-01-12).

(80) Kyoto Encyclopedia of Genes and Genomes (KEGG) Database. *KEGG COMPOUND: C00122*. https://www.kegg.jp/entry/C00122 (accessed 2026-01-12).

(81) Koenig, K.; Andreesen, J. R. Molybdenum Involvement in Aerobic Degradation of 2-Furoic Acid by Pseudomonas Putida Fu1. *Appl. Environ. Microbiol.* **1989**, *55* (7), 1829–1834. https://doi.org/10.1128/aem.55.7.1829-1834.1989.

(82) Palleroni, N. J. Pseudomonas. In *Bergey's Manual of Systematics of Archaea and Bacteria*; John Wiley & Sons, Ltd, 2015; pp 1–1. https://doi.org/10.1002/9781118960608.gbm01210.

(83) Kyoto Encyclopedia of Genes and Genomes (KEGG) Database. *KEGG COMPOUND: C00258*. https://www.kegg.jp/entry/C00258 (accessed 2026-01-13).

(84) Kyoto Encyclopedia of Genes and Genomes (KEGG) Database. *KEGG COMPOUND: C05984*. https://www.kegg.jp/entry/C05984 (accessed 2025-12-04).

(85) Massman, W. J.; Frank, J. M.; Reisch, N. B. Long-Term Impacts of Prescribed Burns on Soil Thermal Conductivity and Soil Heating at a Colorado Rocky Mountain Site: A Data/Model Fusion Study. *Int. J. Wildland Fire* **2008**, *17*, 131–146.

(86) Busse, M. D.; Hubbert, K. R.; Fiddler, G. O.; Shestak, C. J.; Powers, R. F. Lethal Soil Temperatures during Burning of Masticated Forest Residues. *Int. J. Wildland Fire* **2005**, *14*, 267–276.

(87) Smith, J. E.; Cowan, A. D.; Fitzgerald, S. A. Soil Heating during the Complete Combustion of Mega-Logs and Broadcast Burning in Central Oregon USA Pumice Soils. *Int. J. Wildland Fire 2511 1202-1207* **2016**, *25*, 1202–1207. https://doi.org/10.1071/WF16016.

(88) Matsuura, Y.; Takehira, M.; Joti, Y.; Ogasahara, K.; Tanaka, T.; Ono, N.; Kunishima, N.; Yutani, K. Thermodynamics of Protein Denaturation at Temperatures over 100 °C: CutA1

Mutant Proteins Substituted with Hydrophobic and Charged Residues. *Sci. Rep.* **2015**, *5* (1), 15545. https://doi.org/10.1038/srep15545.

(89) Finley, B. K.; Enalls, B. C.; de Raad, M.; Al Said, M.; Chen, M.; Joyner, D. C.; Hazen, T. C.; Northen, T. R.; Chakraborty, R. Unraveling the Influence of Microbial Necromass on Subsurface Microbiomes: Metabolite Utilization and Community Dynamics. *ISME Commun.* **2025**, *5* (1), ycaf006. https://doi.org/10.1093/ismeco/ycaf006.

(90) Schill, M. L. Severe Wildfires Reduce Soil Microbial Exoenzyme Production and Fungal Abundances in the Southern Appalachian Mountains. M.S., The University of Texas at San Antonio, United States -- Texas, 2022. https://www.proquest.com/docview/2754032717/abstract/AB501B1EC2A54BF5PQ/1 (accessed 2026-01-15).

(91) Nelson, A. R.; Rhoades, C. C.; Fegel, T. S.; Roth, H. K.; Caiafa, M. V.; Glassman, S. I.; Borch, T.; Wilkins, M. J. Wildfire Impact on Soil Microbiome Life History Traits and Roles in Ecosystem Carbon Cycling. *ISME Commun.* **2024**. https://doi.org/10.1093/ismeco/ycae108.

(92) Johnson, D. B.; Woolet, J.; Yedinak, K. M.; Whitman, T. Experimentally Determined Traits Shape Bacterial Community Composition One and Five Years Following Wildfire. *Nat. Ecol. Amp Evol.* **2023**, *7* (9), 1419–1431. https://doi.org/10.1038/s41559-023-02135-4.

(93) Pingree, M. R. A.; Kobziar, L. N. The Myth of the Biological Threshold: A Review of Biological Responses to Soil Heating Associated with Wildland Fire. *For. Ecol. Manag.* **2019**, *432*, 1022–1029. https://doi.org/10.1016/j.foreco.2018.10.032.

(94) Salehi, M. H.; Beni, O. H.; Harchegani, H. B.; Borujeni, I. E.; Motaghian, H. R. Refining Soil Organic Matter Determination by Loss-on-Ignition. *Pedosphere* **2011**, *21* (4), 473–482. https://doi.org/10.1016/S1002-0160(11)60149-5.

(95) *Methods of Soil Analysis Part 3 - Chemical Methods* -; Soil Science Society of America. 1996. Pages 1-1390. ISBN-13: 978-0-89118-825-4.

CHAPTER 5: WILDFIRE ENHANCES SOIL ORGANIC MATTER BIODEGRADABILITY, METABOLOME, AND SOIL CO_2 EMISSIONS

5.1. INTRODUCTION

Wildfires have become more prevalent during the past few decades. While global burn area has declined since 2001 largely due to reductions in African savannah burning, every other wildfire-prone continent has experienced increasing burn area and extreme wildfire events with ~367,000,000 ha burning globally in 2024.[1] Within the United States, the average wildfire size and frequency have increased by 4-fold and 3-fold respectively in the 2000s compared to the 1980s through the 1990s.[2] These wildfires can drastically impact forested ecosystems, watersheds, and underlying soil.

Wildfires can change the composition of soil organic matter (SOM): a heterogenous assemblage of organic molecules featuring small metabolites like saccharides and organic acids to larger lignin-like compounds. SOM serves as key substrates driving microbial metabolism, fueling microbial activity, influencing soil greenhouse gas emissions, and contributing to overall soil health. Wildfires change SOM composition, often making the SOM more condensed and increasing aromaticity.[3–10] However, the effects of wildfires on the abundances of soil metabolites (a specific pool of SOM) is understudied, preventing further discoveries related to post-fire nutrient cycling, SOM biodegradability, and microbial activity.

Metabolites are small, biodegradable compounds such as amino acids and saccharides typically detected using gas chromatography-mass spectrometry (GC-MS) and liquid chromatography-mass spectrometry (LC-MS).[11–13] Metabolites in a sample are often referred to as the metabolome or metabolite profile, and metabolomics refers to the investigation of metabolites,

providing valuable insight into microbial metabolism and carbon cycling.[12–21] Nevertheless, the effects of wildfires on soil metabolite profiles remain relatively unknown. Pyrolysis GC-MS has been utilized to putatively identify small, volatile metabolites in burned soils but the abundances of the individual metabolites and how changes to those metabolites impact microbial metabolism were not examined.[8,22–26] In a study examining SOM in soil featuring pyrogenic organic matter, individual metabolites were observed using LC-MS, but the metabolite identities were not determined since only Level 4 and Level 5 on the Schymanski Index were achieved.[27,28] Metabolites in soils that were burned in pyrocosms have been putatively identified and relatively quantified.[29] However, metabolites and their abundances have yet to be studied within soils impacted by a natural wildfire. Therefore, we do not know the extent to which wildfires change the presence and abundance of key metabolites that can directly influence post-fire microbial activity, reforestation, greenhouse gas emissions, and soil recovery. Understanding the post-fire metabolome will also provide critical insight into the biodegradability of SOM from burned soils.

A direct assessment of SOM biodegradability from wildfire-impacted soils has yet to be conducted. Herein, we operationally employ the term "biodegradable" to describe SOM that can be accessed and mineralized to CO_2 by microbes. The biodegradability of post-fire SOM will influence post-fire microbial metabolism, soil recovery, and the degree to which burned environments behave more as carbon sources or carbon sinks, warranting investigations of post-fire SOM biodegradability. Historically, pyrogenic organic matter (thermochemically altered organic matter produced from incomplete combustion often present in burned soils)[30] has been considered minimally biodegradable with half-lives ranging over millennial timescales.[31–33] However, recent laboratory experiments conducted since 2018 have observed 1) the degradation of pyrogenic organic matter within as few as 10 days,[3,34–37] 2) that pyrogenic organic matter can

induce a positive priming effect for SOM degradation,[27] and 3) that pyrogenic organic matter can feature faster decay rates compared to non-pyrogenic organic matter.[38,39] While studying just the pyrogenic content of soil is valuable to determine specifically how thermochemically altered organic matter influences post-fire soil dynamics, examining the entire SOM pool within burned soils provides a more holistic evaluation of wildfire impacts on SOM biodegradability. SOM from wildfire-impacted soils have exhibited heightened reactivity based on mass spectrometry-driven reactomics analyses compared to unburned soils.[10,40] A recent incubation-based experiment observed significantly more biodegradation of organic matter from experimentally heated soil and litter compared to unheated soil and litter.[41] These reactomics- and incubation-based studies provide a more holistic assessment of wildfire impacts on SOM biodegradability; however, a direct assessment (i.e. an incubation) of SOM from soils *burned by a natural wildfire* has yet to be conducted.

Herein, we determined how wildfires impact the soil metabolome and SOM biodegradability. We specifically conducted a field study sampling soil from unburned, low severity, and high severity areas within the 2024 Alexander Mountain Fire burn scar in which "severity" refers to the degree of surface organic matter consumption from fire and is qualitatively determined.[42,43] This study addresses these pertinent research questions: 1) In burned soil, what metabolites are enriched and how biodegradable is the SOM compared to unburned soil? 2) How would those chemical differences, in conjunction with changes to microbiology, influence short-term soil carbon mineralization and CO_2 emissions? 3) Do recently burned soils act more as carbon sinks or carbon sources? We hypothesized that 1). abundances of metabolites will be significantly greater in low severity soil compared to unburned and high severity soils due to the release of intracellular metabolites during fire-induced cell lysis and 2). low severity SOM will be

significantly more biodegradable than unburned and high severity SOM because of augmented metabolite abundances in low severity soil. We answered these questions and tested these hypotheses by utilizing three state of the art mass spectrometry techniques, spectroscopy analyses, 16S rRNA gene and ITS amplicon sequencing for microbial community composition assessment, laboratory incubations, and *in-situ* soil CO_2 flux measurements.

5.2 METHODS

5.2.1 FIELD SITE AND SOIL SAMPLING

The Alexander Mountain Fire began on July 28, 2024 and was 100 % contained on August 17th, 2024.[44] In total, 9,668 acres were burned within the Roosevelt National Forest featuring areas of low, moderate, and high burn severity within the burn scar.[44]

In a ponderosa pine-dominated (*Pinus ponderosa*) forest within the Alexander Mountain Fire burn scar, soil was collected from October 2nd, 2024 through October 4th, 2024, and soil gas flux was measured on October 8th, 2024. No precipitation events occurred during this sampling period (October 2nd, 2024 through October 8th, 2024).[45] Sampling occurred approximately 1.5 months after the fire was 100 % contained, providing an opportunity for more immediate post-fire sampling compared to other studies.[4,5,9,46–48] Approximately 2.7 cm of precipitation fell during the period between the fire being 100% contained (August 17th, 2024) and when sampling began (October 8th, 2024).[45] The most prevalent soil types were within the Cypher-Wetmore-Ratake families complex: loamy-skeletal Lithic Haplustepts, loamy-skeletal Lithic Haplustalfs, and loamy-skeletal Typic Haplustolls.[49] The dominant vegetation types in the sampling area were *Pinus ponderosa, Ribes aureum, cercocarpus montanus, Koeleria macrantha, Leymus cinereus, Artemisia ludoviciana, Solidago nemoralis, Artemisia frigida, and Schizachyrium scoparium*. The total annual precipitation in the sample area averages 402.3 mm.[50] The mean annual temperature

is 9 °C, and the average annual minimum and maximum temperatures are -26°C and 37 °C, respectively.[50] The sample locations ranged in elevation from 2110 m to 2145 m (Bad Elf GNSS Surveyor, Model: Be-GPS-3300).

Soil samples were collected from unburned, low burn severity, and high burn severity locations within the Alexander Mountain Fire Burn Scar (**Figures 5.1-5.10**). GPS coordinates for these locations were collected using a Bad Elf GNSS Surveyor (Model: Be-GPS-3300). Burn severity conditions were classified based on surficial organic matter cover following US Forest Service guidelines.[43] Low severity and high severity conditions featured greater than 50 % and less than 20 % of surficial organic matter cover, respectively (**Figure 5.9** and **5.10**). At each sampling location, ten 0.5 m x 0.5 m sampling grids were placed on the ground along the edge of separate ponderosa pine (*Pinus ponderosa*) canopies. Within each grid, the O-horizon within unburned and low severity samples was removed using a soil knife (sterilized with 70:30 reagent alcohol [90 % ethyl alcohol, 5 % methyl alcohol, 5 % isopropyl alcohol, Fisher Scientific International, Inc]:Milli-Q water [18 MΩ cm]), and the ash layer was scraped away with a sterilized soil knife for the high severity samples. Mineral soil (0-5 cm and 5-10 cm depths) was collected with a sterilized soil knife for all samples. Mineral soil samples for chemical analyses and DNA extractions were collected in plastic zip-top bags and sterile centrifuge tubes (15 mL, Falcon®), respectively. All collected samples were stored in coolers with blue ice in the field and transported to Colorado State University on the same day. Mineral soil samples for chemical analysis were air-dried, sieved to 2 mm, and then stored in a 4 °C fridge, and mineral soil samples for DNA extractions were stored in a -20 °C freezer. A total of 60 mineral soil samples for both chemical and microbial analysis were collected: 10 replicates for unburned 0-5 cm, unburned 5-

10 cm, low severity 0-5 cm, low severity 5-10 cm, high severity 0-5 cm, and high severity 5-10 cm, respectively.

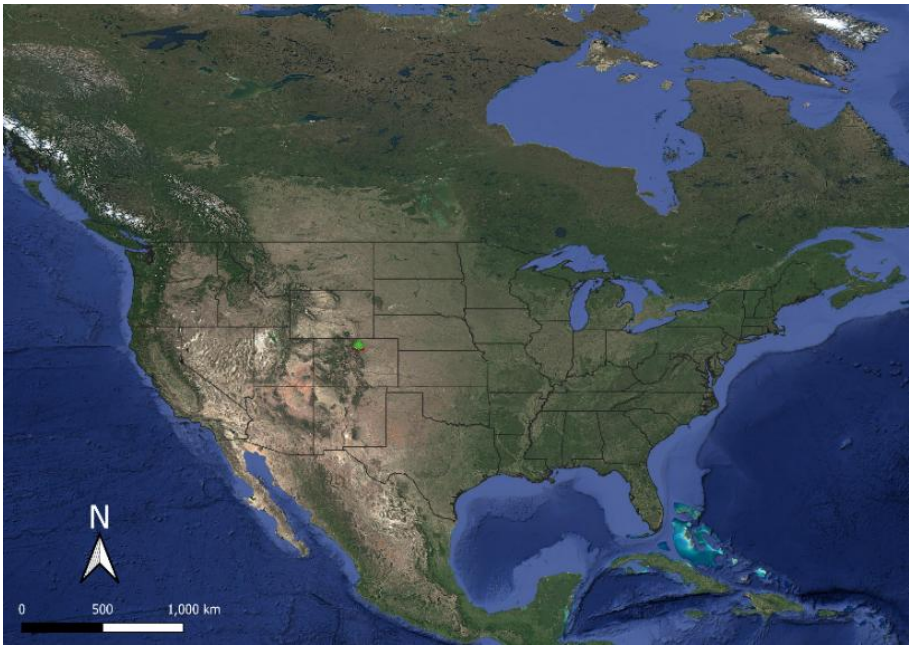

Figure 5.1. Map of sampling area. The green dot within Colorado, USA indicates the sampling area. Map made with QGIS Desktop 3.40.8.

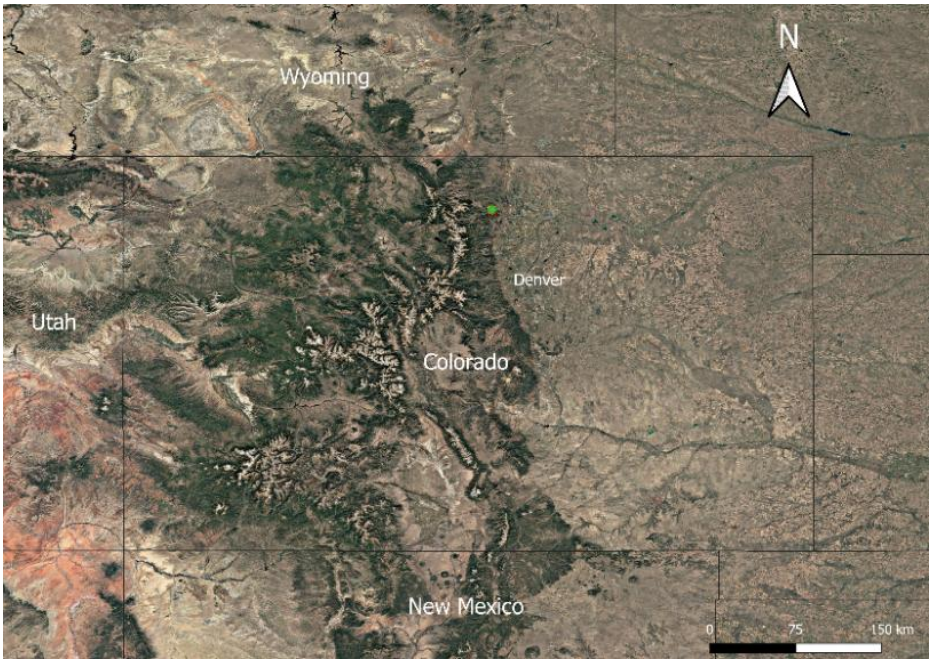

Figure 5.2. Map of sampling area. The green dot northwest of Denver, CO indicates the sampling area. Map made with QGIS Desktop 3.40.8.

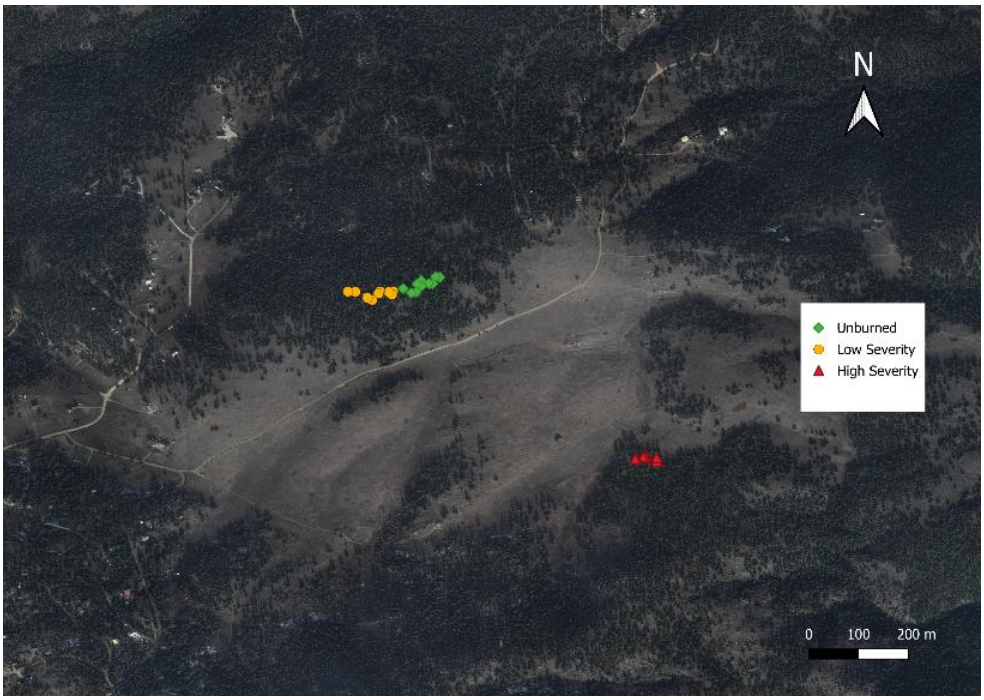

Figure 5.3. Map of sampling area. Map made with QGIS Desktop 3.40.8.

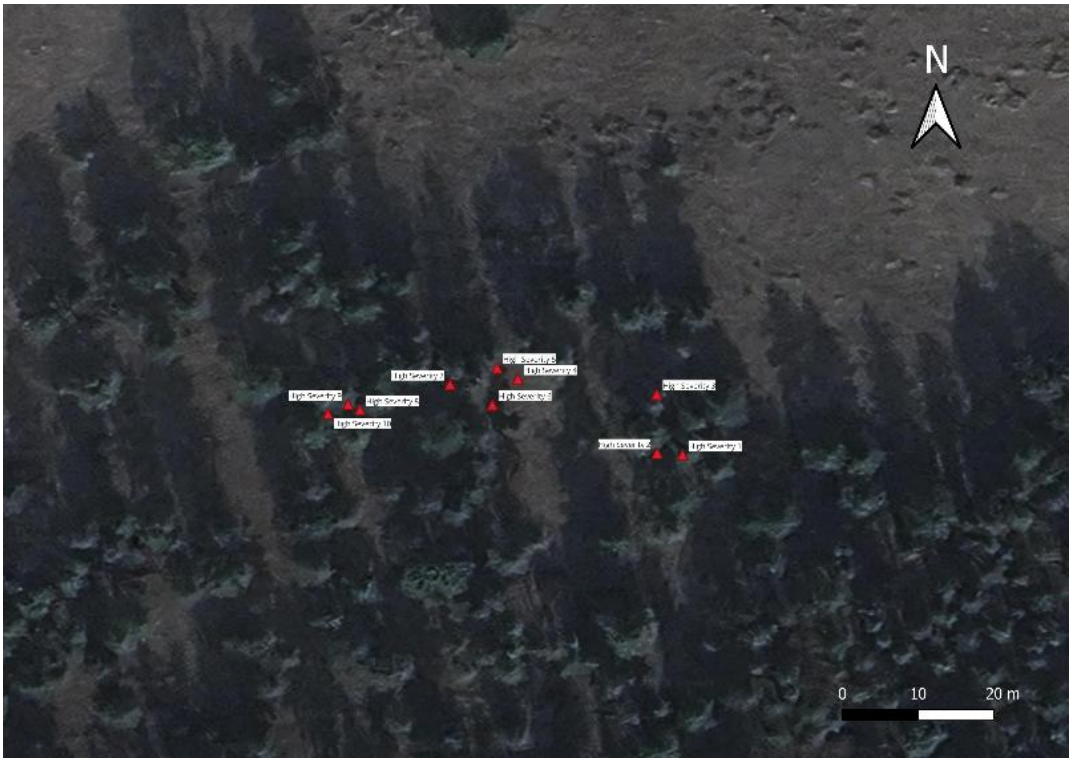

Figure 5.4. Map of sampling area zoomed into high severity samples. Map made with QGIS Desktop 3.40.8.

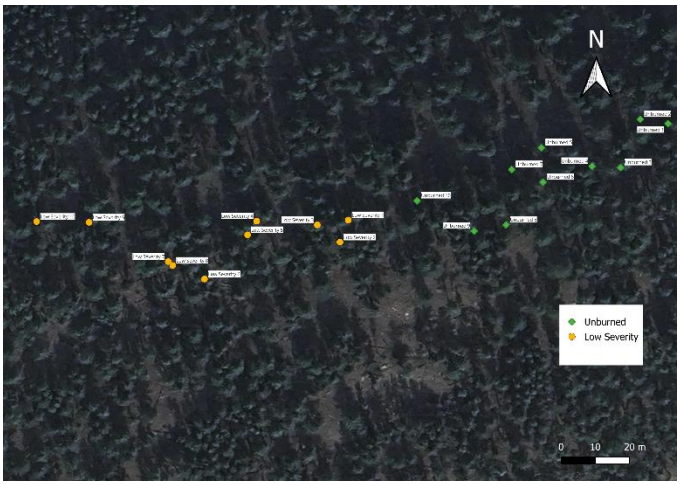

Figure 5.5. Map of sampling area zoomed into unburned and low severity samples. Map made with QGIS Desktop 3.40.8.

Figure 5.6. Image of firebreak. This manmade firebreak was likely constructed right before the Alexander Mountain Fire. The left side of the firebreak is the unburned area while the right side is the low severity area. Photo credit: Jacob VanderRoest

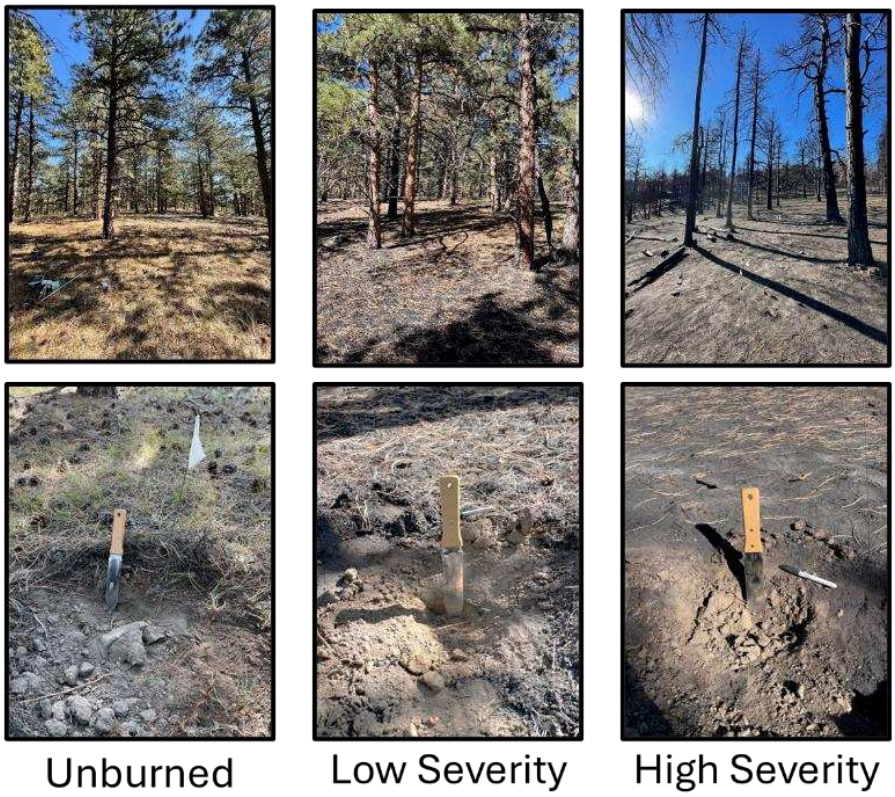

Figure 5.7. Photos of unburned, low severity, and high severity sampling locations. The unburned location featured minimal understory vegetation. The high severity location had substantially less remaining surface organic matter compared to the low severity location. Photo credit: Jacob VanderRoest

Figure 5.8. Photos of unburned sampling location. Note the minimal understory vegetation. Flags were placed in ground to designate sampling positions. Photo credit: Jacob VanderRoest

Figure 5.9 Photos of low severity sampling location. Recognizable charred organic matter (e.g. charred pine needles) was present on the surface, contributing to the "low severity" classification of this area. Photo credit: Jacob VanderRoest

Figure 5.10. Photos of high severity sampling location. Recognizable charred organic matter (e.g. charred pine needles) was not present on the surface, contributing to the "high severity" classification of this area. Photo credit: Jacob VanderRoest

5.2.2 FOURIER TRANSFORM ION CYCLOTRON RESONANCE-MASS SPECTROMETRY (FT ICR-MS)

For each sampling location (e.g., unburned 0-5 cm), a composite sample was prepared by mixing 5 g from each of the 10 replicates (50 grams total of dry, sieved soil). This generated six composite samples: unburned 0-5 cm, unburned 5-10 cm, low severity 0-5 cm, low severity 5-10 cm, high severity 0-5 cm, and high severity 5-10 cm. Each of the six composite samples were

shaken with 100 mL of Milli-Q water for 1 h at 210 rpm. Extracts were centrifuged and filtered through 0.22-micron polyethersulfone membranes (Merck Millipore Ltd.). The filtrates were acidified to a pH of ~2 with a 37 % HCl solution (Fisher Chemical). The acidified filtrates were then concentrated via solid phase extraction according to Dittmar et al. (2008) to concentrate the carbon content and remove salts.[51] For solid phase extraction, styrene-divinylbenzene polymer cartridges (Agilent Bond Elut PPL [Priority Pollutant], 3 mL, 200 mg) were rinsed first with 15 mL of methanol (LC-MS grade, Supelco, Inc.) and then rinsed with 15 mL of pH 2 water. The extracts that were filtered and acidified were then rinsed through separate PPL cartridges (six cartridges total) after which 15 mL of pH 2 water were rinsed through each cartridge. The cartridges were then dried by pulling vacuum through the cartridges followed by 2 mL of methanol (LC-MS grade, Supelco, Inc.) being rinsed through each cartridge. The methanol eluents were collected in separate glass test tubes that were combusted at 400 °C. One milliliter of each eluent was pipetted into separate 1.8 mL borosilicate autosampler vials (VWR International) which were stored in a -20 °C freezer. The vials were transported to the National High Magnetic Field Laboratory at Florida State University. A blank sample was also generated by performing the entire procedure from this paragraph but without any mineral soil.

Ultrahigh resolution data were generated with the Eclipse/FT-ICR MS at 21 T located at the National High Magnetic Field Laboratory in Tallahassee, FL. Each sample was diluted with an equal volume of methanol. After centrifugation at 3,000 rpm for 10 min, the supernatant was transferred to an HPLC vial. For each sample, 25 µL was pumped to the source at 3 µL/min with methanol (LC-MS grade, Honeywell) with a 0.5 µm inline filter (MAC-MOD Analytical). The lines were flushed with ~300 µL of methanol after each sample injection to minimize the likelihood of sample carryover contaminating the next sample. A heated electrospray ionization source

featured a voltage of -3,500 V and was operated in negative mode The auxiliary gas and sheath gas were set at arbitrary units of 3 and 8, respectively. The vaporizer temperature was set to 35 °C. The ion transfer tube temperature was set to 300 °C. The transient length was set to 3 s featuring 5 fills of 400,000 ions each. For an individual sample, 100 scans were co-added and the subsequent spectrum was phase corrected.[52] Individual mass spectrum were calibrated using the "walking calibration method" with 10 to 15 abundant homologous series covering the mass spectrum.[53]

Masses, which were generated in the International Union of Pure and Applied Chemistry (IUPAC) mass scale, were converted to the Kendrick mass scale[54] to identify homologous series within heteroatom classes. Here, heteroatom classes refer to molecular formulae with the same carbon, hydrogen, nitrogen, oxygen, and sulfur content but feature different numbers of methylene subunits.[55] Peaks were included in the peak lists only if the peak signal magnitudes surpassed six times the baseline root-mean-square (rms) noise at m/z 500. PetroOrg © software was used to assign molecular formulae to the peaks in the peak list.[56] Singly-charged ions were assigned molecular formulae within the bounds of $C_{4\text{-}75}H_{4\text{-}150}O_{1\text{-}30}N_{0\text{-}4}S_{0\text{-}2}$ with molecular weights ranging from 170 to 1200 Da. Assigned molecular formulae were discarded if the error exceeded 0.35 ppm.[56] The molecular composition for each assigned molecular formula were used to calculate nominal oxidation state of carbon (NOSC) and modified aromaticity index (AI_{mod}) values.[57–59]

5.2.3 GAS CHROMATOGRAPHY-MASS SPECTROMETRY

Two grams of mineral soil were shaken in 8 mL of Milli-Q water for 1 h at 210 rpm. After centrifugation, supernatants were filtered through nylon 0.45 μm pore size, 13 mm diameter filters (Celltreat Scientific Products). To generate a pooled quality control sample, 200 μL of each filtered extract were mixed together. Seven 1-mL aliquots of the pooled quality control mixture and 1-mL aliquots of each sample were freeze dried overnight. The remaining contents of the samples and

pooled quality control aliquots were suspended in 175 µL of methanol (LC-MS grade, Supelco, Inc.) and 75 µL of Milli-Q water and stored at -20 °C for approximately 2 h. Following centrifugation, 200 µL of the supernatant were pipetted to individual 1.8 mL borosilicate, 12 x 32 mm GC-MS autosampler vials (Avantor, Inc.). To introduce an internal standard to assess derivatization and sample injection variability, 40 µL of a 0.100 mg ^{13}C-glucose (99 % purity, Cambridge Isotope Laboratories, Inc.)/mL Milli-Q H_2O solution were pipetted into each. Experimental blanks were generated by performing the procedure from this paragraph but without the addition of mineral soil.

Methoximation and trimethylsilylation derivatization was performed. The vials were dried with N_2 gas after which 50 µL of 25 mg methoxylamine hydrochloride (98 % purity, Beantown Chemical Corporation) per mL of anhydrous pyridine (99.5 % purity, Thermo Fisher Scientific Inc.) solution were added to each vial. The vials were vortexed for 30 s. After incubating the vortexed samples for 45 min at 65 °C, the vials were vortexed for an additional 30 s followed by 10 minutes of sonication. After sonication, the vials were incubated at 65 °C for 45 min. After centrifuging the vials up to 2000 rpm, 50 µL of N-methyl-N-(trimethylsilyl)trifluoroacetamide (MSTFA) + 1 % trimethylchlorosilane (TCMS) (Thermo Fisher Scientific, Inc.) were pipetted into each vial. The vials were then vortexed for 30 s and incubated at 65 °C for 30 min. After centrifugation up to 2000 rpm, the vial contents were transferred into 250 µL glass inserts which were put in the vials. The vials were centrifuged at 2000 rpm for 5 min.

The derivatized contents of the vials were analyzed with a Thermo GC-TSQ8000 Evo Triple Quad GC mass spectrometer equipped with a liquid autosampler. For an individual vial, 1 µL was injected through a splitless liner (SSL liner 4 mm ID, 78.5 mm, Thermo P/N 453A1925) to a gas chromatography column (Zebron ZB-5HT Inferno, 30 m x 0.25 mm i.d. x 25 film

thickness, Phenomenex P/N 7HG-G015-11). A 1.2 mL/min flow rate of helium gas was used. The gas chromatography inlet temperature was 285 °C. The oven temperature was initially set to 80 °C for 1 min after sample injection which was increased to 330 °C with a ramp-up rate of 15 °C increase/min. The oven temperature was then maintained at 330 °C for 7 min. Electron impact ionization was used to fragment analytes. Only the first quadrupole mass analyzer was utilized to reproduce the methods of a prior publication examining metabolites in experimentally burned soils.[29] Masses ranging from 50 m/z to 650 m/z were scanned at a scan rate of 5 scans/s. Ion source temperature was set to 260 °C. Transfer line temperature was set to 300 °C.

Chromeleon 7 software (Thermo Fisher) was utilized to integrate the ^{13}C-glucose internal standard chromatogram peak using extracted ion chromatogram m/z value of 323. The coefficient of variation value of the internal standard extracted ion chromatogram peak areas within the pooled quality control samples was 4.5 %. The detected features were analyzed using non-targeted analysis. Peak detection, spectral deconvolution, and peak alignment were conducted with ADAP-BIG software (Java Version: 19.0.1, Du-Lab). Feature annotation was performed with the ADAP-KDB website (Version 1.8.8, accessed 11/5/2024) utilizing the following databases: MS-DIAL GC-MS Library with Kovats RI | 2022-02-18, HMDB (v5) Experimental GC-MS Spectra, and MassBank Release 2022.06 | 2022-07-18 (GC-MS). The fragmentation score threshold for annotation was >700. Retention index matching using NIST MS Search 3.0 was used for annotating features with fragmentation scores between 600 and 700. Out of 233 features, 29 of them were annotated to Level 2 or Level 3 of the Schymanski index.[28] For a given sample, peak areas of features were normalized to the peak area of the internal standard within that given sample. This internal standard normalization helps account for matrix effects and analytical variation associated with the gas chromatography-mass spectrometer. Zero and n/a values normalized peak

area values for a given feature were replaced with 10 % of the minimum abundance value of that given feature across all samples and pooled quality control replicates. The normalized peak area values for all features were multiplied by 10,000 to transform the data into values greater than 1. This allows for easier comparison of whole number values as opposed to comparing values comprised of only decimals. Normalized peak areas multiplied by 10,000 were reported as "abundance" values. These abundance values were used to quantify individual metabolites in box plots. Prior to principal component analysis, these abundance values were Pareto-scaled.

Features that were annotated as a saccharide-like molecules (except for levoglucosan and N-acetyl-D-glucosamine) were putatively identified as either an "inositol," "disaccharide," or "trisaccharide." The "inositols," "disaccharides," and "trisaccharides" were designated an arbitrary number to distinguish different features (e.g. "disaccharide 2" or "trisaccharide 1"). This was conducted because reaching level 2 confidence on the Schymanski index could not be achieved with our annotation process.[28] For instance, maltose, trehalulose, and sucrose are isomers that all have the same molecular weight of 342.3 g/mol. The only distinguishing component across these saccharides is the stereochemistry of their hydroxyl groups. Similar fragmentation patterns will be generated during electron impact ionization of these saccharides, and the gas chromatography-mass spectrometry instrument cannot differentiate the hydroxyl group stereochemistry of the fragments. Therefore, these saccharide isomers cannot be distinguished from each other with this method. Consequently, Level 3 of the Schymanksi index (i.e. "disaccharide 2" or "trisaccharide 1") rather than Level 2 (i.e. "sucrose" or "maltotriose") were achieved for all saccharides other than levoglucosan and N-acetyl-D-glucosamine.

5.2.4 LIQUID CHROMATOGRAPHY-MASS SPECTROMETRY

Two grams of mineral soil were added to a 15 mL centrifuge tube. The soil was shaken with 8 mL of Milli-Q water for 1 h at 210 rpm. After centrifuging, the supernatant was filtered through a nylon 0.45 µm pore size, 13 mm diameter filter (Celltreat Scientific Products), and a pooled quality control (QC) sample was produced by mixing 200 µL of filtered extract from sample. One milliliter aliquots of each sample and ten 1-mL aliquots of the pooled quality control mixture were freeze-dried overnight followed by the addition of 125 µL of Milli-Q water, vortexing, and centrifugation. All samples were pipetted into 1.8 mL borosilicate, 12 x 32 mm GC-MS autosampler vials (Avantor, Inc.) followed by the addition 10 µL of a 10.125 µg/mL solution of DL-tryptophan-2,3,3-d3 (98 % purity, CDN Isotopes) solution in Milli-Q water in each vial. The DL-tryptophan-2,3,3-d3 served as an internal standard to assess sample injection variability and ionization efficiency while also accounting for matrix effects. The procedure in this paragraph was repeated for two experimental blank samples that didn't feature any mineral soil. One of these blanks received the internal standard while the other blank did not.

All 72 vials (60 soil samples, 10 pooled quality control samples, and 2 blanks) were ran on a Waters Xevo G2-XS quadrupole time of flight mass spectrometer coupled with ultra-performance liquid chromatography (Waters^{TM}). For each soil sample, pooled quality control sample, and blank, 50 µL were injected using a Waters Acquity UPLC system and ACQUITY Flow-thru-needle sample handler featuring a 15 µL flow-thru needle and a 50 µL sample loop. A Waters ACQUITY UPLC Premier T3 1.7 µm Column (1.7 µM, 2.1 x 100 mm) was used to separate analytes. A 20 min gradient from solvent A (water + 0.1 % formic acid) to solvent B (acetonitrile with 0.1 % formic acid) was used with a 0.5 mL/min flow rate (**Table 5.1**). The samples were held at 6 °C. The column was held at 45 °C.

Table 5.1. Solvent gradient for buffer B.

Time (min)	Buffer B %
0 – 1 Hold	1 %
1 – 13 Linear Gradient	1 % to 98 %
13—16 Hold	98 %
16—16.05 Step Gradient	98 % to 1 %
16.05—20 Hold	1 %

Electrospray ionization in positive sensitivity mode was used along with Fast-DDA MS/MS. A mass range of 50-1200 m/z was used. The time for each scan was 0.13 s. For switching from survey scan to MS/MS, a threshold of 10,000 counts needed to be exceeded. One MS/MS scan with a scan time of 0.3 s was allowed per survey scan. The collision energy for MS/MS scans was set to 25 V. Auto_CatV1 script was used for iterative exclusion. The exclusion list was reset every 10 samples with an exclusion window of 0.5 Da and 6 s.

Sodium formate with <1 ppm mass accuracy was used for mass calibration. The capillary voltage was set at 700 V. The source temperature was set at 150 °C. The nitrogen desolvation temperature was set at 450 °C. The desolvation flow rate was set at 1000 L/hr. Mass drift was corrected with WATERS Lockspray reference featuring 40 s interval between scans, 0.1 seconds/scan, and signal averaging over 3 scans. Mass correction with a reference mass of +556.2771 m/z was performed with LeuEnk. WATERS DataConnect version 2.1.0 was used to convert RAW data to mzML files for non-targeted analysis with MZmine software (Version 4.7.27) which conducted peak detection, spectral deconvolution, and peak alignment. SIRIUS software (Version 6.2.2) was used for annotating features that were detected with MZmine software by utilizing the following databases: PubChem, Biocyc, Blood Exposome, CHEBI, COCONUT, DSSTox, FooDB, GNPS, HMDB, HSDB, KEGG, KNApSAcK, LOTUS, LipidMaps, Maconda, MeSH, MiMeDB, NORMAN, Plantcyc, PubChem: bio and metabolites, PubChem: drug, PubChem: food, PubChem: safety and toxic, PubMed, SuperNatural, TeroMOL, and YMDB.[60]

Features with confidence threshold values exceeding 0.650 were annotated. For the 12729 detected features, 48 features were annotated. Internal standard normalization was conducted to account for matrix effects and analytical variation. Specifically, for a given sample, peak areas of all features were normalized to the peak area of the internal standard of that given. For a given metabolite across samples, zero and n/a normalized peak area values were changed to 10 % of the minimum abundance value of that given metabolite. All normalized peak area values were then multiplied by 10,000 and reported as “abundance” values. These “abundance” values were used to quantify individual metabolites. Prior to analysis via principal comment analysis, the normalized peak areas that were multiplied by 10,000 were scaled with Pareto scaling.

5.2.5 PH AND ELECTRICAL CONDUCTIVITY

For each sample, 10 g of mineral soil were shaken in 20 mL of Milli-Q water at 210 rpm for 1 h. An Orion Double Junction pH probe (Thermo Scientific) and an Orion COND 4 Cell Lab & Field conductivity probe (Thermo Scientific), which were both connected to a Thermo Scientific Orion Star A215 pH/conductivity meter, were calibrated with pH reference standards (VWR International) and a 1413 µS/cm standard solution (Hach), respectively. The soil-water slurry was shaken by hand to resuspend the soil. Then, the pH electrode was inserted into the soil-water slurry to measure pH followed by insertion of the conductivity probe to measure electrical conductivity.

5.2.6 TOTAL SOIL C AND N

For each sample, ~ 20 g of air-dried, 2-mm sieved mineral soil were ground using a soil grinder table. A VELP 802 elemental analyzer (VELP Scientific, Inc.) was then utilized to measure total carbon and total nitrogen in the ground soil samples.

5.2.7 NITRATE AND AMMONIUM

For each soil sample, 20 g of air-dried, 2-mm sieved mineral soil was shaken with 100 mL of 2 M KCl for 1 h. The extract was filtered through alpha cotton cellulose filter paper (Whatman plc). Ammonium and nitrate concentrations were quantified with a flow injection analyzer (Lachat QuikChem, 8500, Hach Scientific, Loveland, CO).

5.2.8 GRAVIMETRIC WATER CONTENT

Mineral soil samples collected using a soil bulk density ring (6.1 cm diameter, 2.5 cm height) were heated at 105 °C for 44 hrs. Gravimetric water content was calculated with the following **Equation 5.1**:

Equation 5.1. $\text{Gravimetric water content} = \left(\frac{(\text{Mass of wet soil (g)} - \text{Mass of dry soil (g)})}{\text{Mass of dry soil (g)}}\right) * 100\ \%$

5.2.9 WATER EXTRACTABLE ORGANIC CARBON, WATER EXTRACTABLE TOTAL NITROGEN, AND SPECTROSCOPIC MEASUREMENTS

For each sample, 1 g of soil was shaken in 5 mL of Milli-Q water for 24 hr at 200 rpm. Following filtration through polytetrafluoroethylene (PTFE) 0.45 μm filters (Cole-Parmer®), 1 mL of the filtrate was diluted with 18 mL of Milli-Q water, and dissolved organic carbon and dissolved total nitrogen values were measured using a Shimadzu TOC-L instrument (Shimadzu Scientific Instruments, Inc.). The dissolved organic carbon and dissolved total nitrogen masses were normalized to the extracted soil mass (1 g) to calculate water-extractable organic carbon and water-extractable total nitrogen, respectively.

Fluorescent dissolved organic matter (DOM) composition was characterized with excitation-emission matrix (EEMs) fluorescence spectroscopy. For each sample, 0.2 mL of the filtrate and 2.5 mL of Milli-Q water were added to a quartz cuvette which was analyzed with a HORIBA Scientific Aqualog 800 instrument (HORIBA Instruments Inc.). The instrument was

calibrated using deionized water blanks, and subsequent fluorescent intensities were normalized to the instrument's Raman Area. Wavelengths between 230 nm and 700 nm were measured with 2 nm intervals and a 1 s integration time. Fluorescence peak indices (i.e., Coble Peaks A, C, B, and T) were calculated and normalized to the previously-described dissolved organic carbon concentrations.[61] Fluorescent index (FI), humification index (HIX), and biological index (BIX) were calculated[62–64]These peaks and indices were calculated using published equations, and the chemical properties that the indices represent were inferred based on previous studies (**Table 5.2**).[61–64]

5.2.10 BIOLOGICAL OXYGEN DEMAND INCUBATIONS

Biological oxygen demand incubations were performed to assess the biodegradability of the water-extractable organic matter from the unburned, low severity, and high severity soils. Composite samples of 200 g, 100 g, and 100 g of mineral soil for unburned 0-5 cm, low severity 0-5 cm, and high severity 0-5 cm, respectively, were shaken in 1000 mL of Milli-Q water in separate HDPE bottles at 200 rpm for 24 h. Water extracts were then filtered through autoclaved 0.1 μm polyethersulfone filters (Sterlitech Corporation) to remove microbial biomass. Water from the Big Thompson River (adjacent to sampling location), which was collected on Sept. 26, 2024 (GPS coordinates: 40.422034 N, -105.5220541 W) and filtered through 1.2 μm glass microfiber filters (Whatman plc), served as the microbial inoculum for these incubations. The following solutions were prepared in autoclaved 310 mL biological oxygen demand assay bottles (Flinn Scientific Inc.) featuring autoclavable oxygen sensor spots (PreSens, Precision Sensing GmbH). Ten milliliters of the filtered Big Thompson River water was mixed with filtered, unburned soil extracts and Milli-Q water so that the dissolved organic carbon (DOC) concentration of the incubation solution was ~10 mg/L (measured with Shimadzu TOC-L instrument [Shimadzu

Table 5.2. Excitation-emission matrix indices, calculations, and corresponding chemical properties.

Indices	Calculation	Representative chemical properties	Source
Coble A	Excitation 260 nm / Emission 450 nm	Terrestrial-like source, soil-humics	(Coble 1996)[61]
Coble C	Excitation 340 nm / Emission 450 nm	Terrestrial-like source, soil-humics	(Coble 1996)[61]
Coble B	Excitation 275 nm / Emission 305 nm	Tyrosine-like ($C_9H_{11}NO_3$), protein-like	(Coble 1996)[61]
Coble T	Excitation 275 nm / Emission 340 nm	Tryptophan-like ($C_{11}H_{12}N_2O_2$), protein-like	(Coble 1996)[61]
HIX	$HIX = \frac{\sum_{435\ nm}^{480\ nm} emission}{\sum_{300\ nm}^{345\ nm} emission}\ at\ 254\ nm\ excitation$	Higher values indicate increased humic substance content (i.e. higher degree of humification)	(Ohno 2002)[62]
BIX	$BIX = \frac{emission\ 380\ nm}{emission\ 430\ nm}\ at\ 310\ nm\ excitation$	Higher values correspond to recently produced microbially-derived DOM	(Huguet et al. 2009)[63]
FI	$FI = \frac{emission\ 470\ nm}{emission\ 520\ nm}\ at\ 370\ nm\ excitation$	Approximates DOM source. Higher values indicate microbially-derived DOM while lower values indicate terrestrially-derived DOM.	(Cory and McKnight 2005)[64]

Scientific Instruments, Inc.]). This process was repeated for three total unburned replicates, three low severity extract replicates, and three high severity extract replicates so that all incubation solutions started at ~10 mg/L DOC (**Table 5.3**). A 10 mg/L DOC mixture sample was prepared by mixing unburned extract, low severity extract, high severity extract, and Milli-Q water so that a

third of the DOC content was contributed by the unburned, low severity, and high severity extracts, respectively, and no Big Thompson River water was added. Milli-Q water and Big Thompson River water were also added to individual incubation bottles, generating 12 total solutions for these incubations. The 12 solutions were stored in the dark at 20 °C for the duration of the 8.25-day incubations, and dissolved oxygen concentrations in the bottles were monitored using oxy-4 probes (PreSens, Precision Sensing GmbH) and PreSens Measurement Studio 2 software (Version 4.0.0.2353, PreSens, Precision Sensing GmbH). Dissolved oxygen concentrations were used to calculate cumulative oxygen consumption during the incubations. DOC for each solution was measured after the incubations (**Table 5.3**).

5.2.11 SOIL CO2 FLUX ANALYSIS

Soil CO_2 gas fluxes were measured on October 8th, 2024 to determine how soil burn severity alters soil-atmosphere gas flux. Gas fluxes were measured using a transparent, dome chamber connected to a closed-loop chamber system attached to an FTIR gas analyzer (LI-7810, LiCor). Gas fluxes were measured within the unburned, low severity, and high severity locations directly beside each 0.5 m x 0.5 m grid used for soil sampling. Both "light" (i.e., transparent chamber) and "dark" (i.e., tarp over transparent chamber) measurements were collected at the unburned and low severity locations, and only "light" measurements were collected at the high severity location because there was no living vegetation, resulting in minimal photosynthetic activity which negated the need for "dark" measurements. Fifty gas flux measurements were taken in total: 10 unburned "light," 10 unburned "dark," 10 low severity "light," 10 low severity "dark," and 10 high severity "light". For each of the 50 measurements, gas CO_2 concentrations (ppm) were

Table 5.3. Dissolved organic carbon concentration (DOC) changes during biological oxygen demand incubations.

Sample	Initial [DOC] (mg/L)	Final [DOC] (mg/L)	Final – Initial [DOC] (mg/L)
Unburned extract + river water inoculum replicate 1	9.873	9.378	-0.495
Unburned extract + river water inoculum replicate 2	9.847	9.446	-0.401
Unburned extract + river water inoculum replicate 3	9.933	9.503	-0.430
Low severity extract + river water inoculum replicate 1	10.26	8.916	-1.344
Low severity extract + river water inoculum replicate 2	10.15	8.609	-1.541
Low severity extract + river water inoculum replicate 3	10.32	8.785	-1.535
High severity extract + river water inoculum replicate 1	9.749	8.592	-1.157
High severity extract + river water inoculum replicate 2	9.877	8.616	-1.261
High severity extract + river water inoculum replicate 3	9.826	8.635	-1.191
River water inoculum only	2.613	2.679	+0.066
Mixture of filtered unburned, low severity, and high severity extract only (no river water inoculum)	9.830	9.764	-0.066
Milli-Q water control	0.057	0.134	+0.077

recorded every 1 s for approximately 3 min. Gas fluxes were calculated using the following **Equation 5.2**:

Equation 5.2. $Soil\ Gas\ Flux = \frac{\Delta c}{\Delta t}\frac{V}{S}\frac{Pa}{RT}$

where c is the mole fraction of CO_2 or CH_4 in μmol mol^{-1}, t is the observation time (3 min), V is the total volume of the closed system, S is the surface area of the soil chamber, Pa is the atmospheric pressure, R is the universal gas constant, and T is the surface soil temperature measured with a K-type thermocouple (Extech Instruments). A linear fit was applied to calculate

$\Delta c/\Delta t$ using code previously developed in MatLab.[65] Average R^2 values for CO_2 fits were 0.87 indicating that linear fits were applied when the atmospheric conditions inside the chamber were stable. “Light” and “dark” measurements were used to calculate Net Ecosystem Exchange (NEE) and Ecosystem Respiration (R_{eco}).

5.2.12 SOIL BULK DENSITY

Soil bulk density was measured on November 10th, 2024 from the following samples: unburned replicate 1, unburned replicate 3, unburned replicate 5, unburned replicate 7, unburned replicate 9, low severity replicate 1, low severity replicate 3, low severity replicate 5, low severity replicate 7, low severity replicate 9, high severity replicate 1, high severity replicate 3, high severity replicate 5, high severity replicate 7, and high severity replicate 9. Litter and ash were brushed off the soil surface, and a soil bulk density core (2.5 cm height, 6.1 cm diameter) was inserted into the soil. A soil knife was used to remove the core from the soil. Soil samples were then dried at 105 °C for 24 h.[66] The mass of the dried soil was then divided by the volume of the core to calculate soil bulk density.

5.2.13 ION CHROMATOGRAPHY

Composite samples were prepared by combining two consecutive replicates (1 and 2, 3 and 4, 5 and 6, 7 and 8, 9 and 10) from the ten replicates in of the unburned, low severity, and high severity soil samples. Approximately 10 g of sieved soil were added from each replicate (~20 g for each composite samples). The ~20 g composite samples were shaken in 100 mL of Milli-Q water for 1 h at 2000 rpm. The samples were filterd with Q5 quantitative grade filter paper (Fisher Scientific™). A Dionex Inuvion instrument using a Dionex IonPac™ AG28-Fast-4µm RFIC ™ 4 X 150 mm analytical column was used to identify and quantify fluoride, chloride, nitrite, nitrate,

bromide, sulfate, and phosphate in the samples based on a standard solution of those seven anions (Thermo Scientific Dionex seven anion standard II, Sunnyvale, CA).

5.2.14 MICROBIAL ANALYSES METHODS

Genomic DNA was extracted from soil subsamples using the Zymo Quick-DNA Fecal/Soil Microbe Miniprep Kit according to the manufacturer's instructions. Amplicon libraries were generated via a single-step PCR approach using barcoded primer sets specific to each sample. For soil bacterial communities, the V4 region of the 16S rRNA gene was amplified using the primers 515F (5'-GTGYCAGCMGCCGCGGTAA-3') and 806R (5'-GGACTACNVGGGTWTCTAAT-3').[67,68] Soil fungal communities were amplified using primers targeting the first internal transcribed spacer (ITS1) region of the ribosomal DNA, ITS1f (5′-CTTGGTCATTTAGAGGAAGTAA-3′) and ITS2 (5′-GCTGCGTTCTTCATCGATGC-3′) (White et al., 2012).[69] For each sample, duplicate PCR reactions were conducted using 1 μL of template DNA, after which amplicons were pooled prior to purification and normalization using the SequalPrep normalization kit (Invitrogen, CA). Multiplexed libraries were sequenced on the Illumina MiSeq Platform using 251 bp paired-end sequencing at the Next Generation Sequencing Core at Colorado State University. Raw reads were deposited on NCBI under BioProject PRJNA1403077.

Raw sequencing reads were analyzed in QIIME2 (release 2021.2).[70] Reverse reads from the ITS dataset were excluded due to low quality. Amplicon sequence variants (ASVs) were inferred from demultiplexed 16S and ITS reads using the DADA2 pipeline, including merging, denoising, and binning.[71] Forward and reverse reads were truncated at 200 bp during denoising, with no trimming applied to the 5′ ends. Counts for 16S rRNA genes ranged between 1,071 – 91,049, and ITS gene counts ranged from 1,047 – 116,306. Bacterial and archaeal ASVs were

assigned taxonomy using the pre-trained SILVA classifier (version 138),[72–74] while fungal ASVs were assigned taxonomy using a self-trained UNITE database classifier (version 9.0).[75,76] Non-fungal ITS sequences and bacterial ASVs classified as chloroplasts or mitochondria were removed prior to downstream analyses. To standardize sequencing depth, samples were rarefied to 2,900 reads.

To evaluate variation in soil microbial community diversity and composition across sites and soil layers, statistical analyses were conducted in R version 4.1.2 (R Core Team, 2021) with significance defined at $p \leq 0.05$. Alpha diversity of bacterial/archaeal (16S) and fungal (ITS) communities was assessed using Shannon diversity and observed ASV richness, calculated from ASV count tables using the "diversity" and "specnumber" functions in the vegan package in R.[77] Differences in bacterial and fungal community composition across sites and depths were examined using permutational multivariate analysis of variance (PERMANOVA)[78] based on Bray-Curtis dissimilarity matrices and implemented with the "adonis2" function in the vegan package.[77] Community patterns were visualized using Non-Metric Multidimensional Scaling (NMDS) ordination. Soil chemical variables were fitted to NMDS ordinations using the "envfit" function in the vegan package (999 permutations), and variables with significant fits ($p \leq 0.05$) were overlaid. All figures for microbial data were generated using ggplot2.[79]

Fungal guilds were assigned using the FUNGuildR v0.3.0 package in R, which annotates ASVs based on the FUNGuild database.[80] Only ASVs with "Probable" or "Highly Probable" confidence rankings were retained, while ASVs annotated as "Possible" or "NA" were classified as Unassigned. To reduce annotation uncertainty, only taxa resolved to at least the genus level were considered. For ASVs annotated with multiple potential guilds, only the primary guild (first-listed assignment) was retained. Multi-guild assignments were further resolved using a functional

priority hierarchy relevant to forest ecosystems: mycorrhizal > saprotroph > plant pathogen > endophyte/epiphyte/lichenized > undefined. Saprotrophic subcategories (e.g., wood-, soil-, and litter-associated saprotrophs) were consolidated into a single Saprotroph category, while mycorrhizal subtypes (e.g., ectomycorrhizal, arbuscular) were retained and analyzed separately. Taxa annotated as non-plant pathogens or parasites (e.g., animal or fungal parasites) were grouped as Other Parasites/Pathogens, and taxa lacking guild assignment or with ambiguous multi-guild assignments were classified as Unassigned.

5.2.15 STATISTICS

When determining significant differences across mean values from three samples (e.g. unburned 0-5 cm soils, low severity 0-5 cm soils, and high severity 0-5 cm soils), data normality and equality of variances were first determined using the Shapiro-Wilk test and Levene's test, respectively. If the data were not normally distributed (P<0.05 for Shapiro-Wilk test), Kruskal-Wallis and Dunn's tests were used (P<0.05 indicates significant differences) regardless of whether the variances were equal or not. If the data were normally distributed (P>0.05 for Shapiro-Wilk test) but the variances of the data were not equal (P<0.05 for Levene's test), Welch's ANOVA and Games-Howell tests were used (P<0.05 indicates significant differences). If the data were normally distributed and the variances of the data were equal (P>0.05 for Levene's test), ANOVA and Tukey HSD tests were used (P<0.05 indicates significant differences).

When determining significant differences between mean values from two samples (e.g. unburned 0-5 cm soils and unburned 5-10 cm soils). If the data were not normally distributed (P<0.05 for Shapiro-Wilk test), Mann-Whitney U test (also known as the Wilcoxon rank-sum test) was used (P<0.05 indicates significant differences). If the data were normally distributed (P>0.05 for Shapiro-Wilk test) but the variances of the data were not equal (P<0.05 for Levene's test),

Welch's t-test was used (P<0.05 indicates significant differences). If the data were normally distributed and the variances of the data were equal (P>0.05 for Levene's test), Student's t-test were used.

5.3 RESULTS AND DISCUSSION

5.3.1 LOW AND HIGH SEVERITY SOILS LIKELY EXPERIENCED COMPARABLE SOIL BURN TEMPERATURES

Soil from unburned, low fire severity, and high fire severity areas within the Alexander Mountain Fire burn scar were collected for this investigation (**Figures 5.1-5.10**). Fire severity refers to the degree of surface organic matter consumption from fire and is qualitatively determined.[42,43] Here, unburned soil featured no evidence of surface burning (**Figures 5.7** and **5.8**), low severity soils exhibited charred yet recognizable surface organic matter (**Figures 5.7** and **5.9**), and high severity soils featured complete consumption of recognizable surface organic matter (**Figures 5.7** and **5.10**). Despite qualitative differences between low and high severity soils, the soils likely experienced comparable heating temperature during burning due to minimal forest understory and similar water-extractable organic carbon concentrations. The Alexander Mountain Fire burned in a ponderosa pine (*Pinus ponderosa*)-dominated forest with relatively minimal understory (i.e. grasses and fallen pine needles) contributing to less vegetative fuel for burning compared to other forested ecosystems such as lodgepole pine (*Pinus contorta*)-dominated forests and boreal forests. The presence of less vegetative fuel during the Alexander Mountain Fire likely generated cooler soil burn temperatures compared to the other aforementioned forested ecosystems, resulting in similar soil burn temperatures for low and high severity soils. Comparable soil burn temperatures were also supported by the water extractable organic carbon results (**Figure 5.11**). Water-extractable organic carbon and dissolved organic carbon concentrations generally

increase with soil burn temperature to ~250 °C (representing low to moderate severity conditions) and then decrease at temperatures higher than ~250 °C which often occur during high severity conditions.[81–89] Here, low severity and high severity 0-5 cm soil water-extractable organic carbon concentrations were not significantly different (**Figure 5.11a**), suggesting comparable soil burn temperatures. Overall, while the low severity and high severity soils are qualitatively different on the surface, they likely experienced similar burn temperatures within the soil. Thus, we will be focusing primarily on unburned vs. burned comparisons within this manuscript. Nevertheless, this is a key ecosystem to investigate, for ponderosa pine forests cover ~15 million hectares in North America, ranging from southern Canada to central Mexico and including 16 states within the United States.[90] Additional soil physical and chemistry parameters have been included in **Figures D1-D12**.

5.3.2 FIRE ALTERS SOIL METABOLITE PROFILES AND AUGMENTS SOIL METABOLITE ABUNDANCES

The metabolite profiles of the burned soils were distinct from that of the unburned soils based on principal component analysis (PCA) scores plots (**Figure 5.12a,b**). In these plots, data points that cluster closely (or separately) feature similar (or disparate) metabolite profiles. In both **Figures 5.12a** and **5.12b**, the unburned data points cluster separately from the burned data points. **Figure 5.12a** shows GC-MS data featuring lower molecular weight, volatile metabolites while **Fig. 5.12b** features LC-MS data which contains nonvolatile metabolites with higher molecular weights compared to GC-MS. Despite these two methods detecting separate pools of SOM, their results converge on the same conclusion: burned soil features distinctive metabolite contents compared to unburned soil. While previous studies have observed similar results within laboratory-

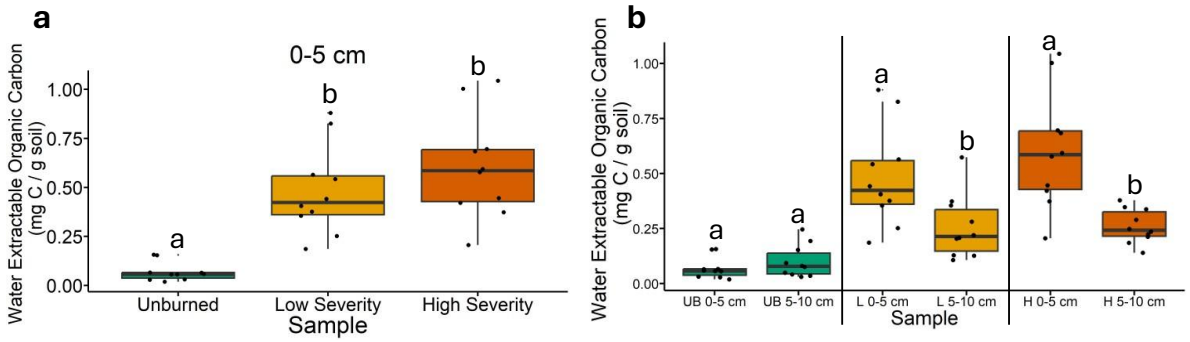

Figure 5.11. Water extractable organic carbon (WEOC) concentrations visualized with box plots. **a,** Comparing WEOC concentrations amongst soil samples collected at 0-5 cm depth. Letters above boxes indicate significant differences between treatments determined by either ANOVA and Tukey HSD tests, Welch's ANOVA and Games-Howell tests, or Kruskal-Wallis and Dunn's tests (see Statistics section 5.2.15 within Methods). n = 10 for unburned, low severity, and high severity samples. **b,** Comparing WEOC concentrations between depths of each sample type. The statistical tests within sample types (i.e. unburned, low severity, and high severity) were conducted independently of each other. Letters above the boxes indicate significant differences between depths and were determined with either Student's t-test, Welch's t-test, or Mann-Whitney U tests (see Statistics section 5.2.15 within Methods). n=10 for unburned 0-5 cm, unburned 5-10 cm, low severity 0-5 cm, low severity 5-10 cm, high severity 0-5 cm, and high severity 5-10 cm samples. UB = unburned. L = low severity. H = high severity. Box plots show the median (central line), first and third quartiles (box edges), and whiskers extending to minimum and maximum values within 1.5 times the interquartile range. Data beyond the end of the whiskers are "outlying" points and are plotted individually.

or mesocosm-scaled experiments,[27,29] this study is the first to apply the field of metabolomics within the context of a wildfire.

The impact of wildfires on metabolite contents diminished with depth (**Figures 5.13** and **5.14**). The principal component analysis scores plot in **Figure 5.13** demonstrates this result more clearly: the deeper burned soils (5-10 cm) plot in between the unburned soils and shallow burned soils (0-5 cm). This implies that the wildfire changed the metabolite contents of the deeper soils but less drastically compared to the shallower soils. This diminishing impact of wildfires on soil chemistry with soil depth has also been observed in soil microbial communities.[4] While **Figure 5.12** indicated that the overall soil metabolite profiles shifted due to wildfire, no information is

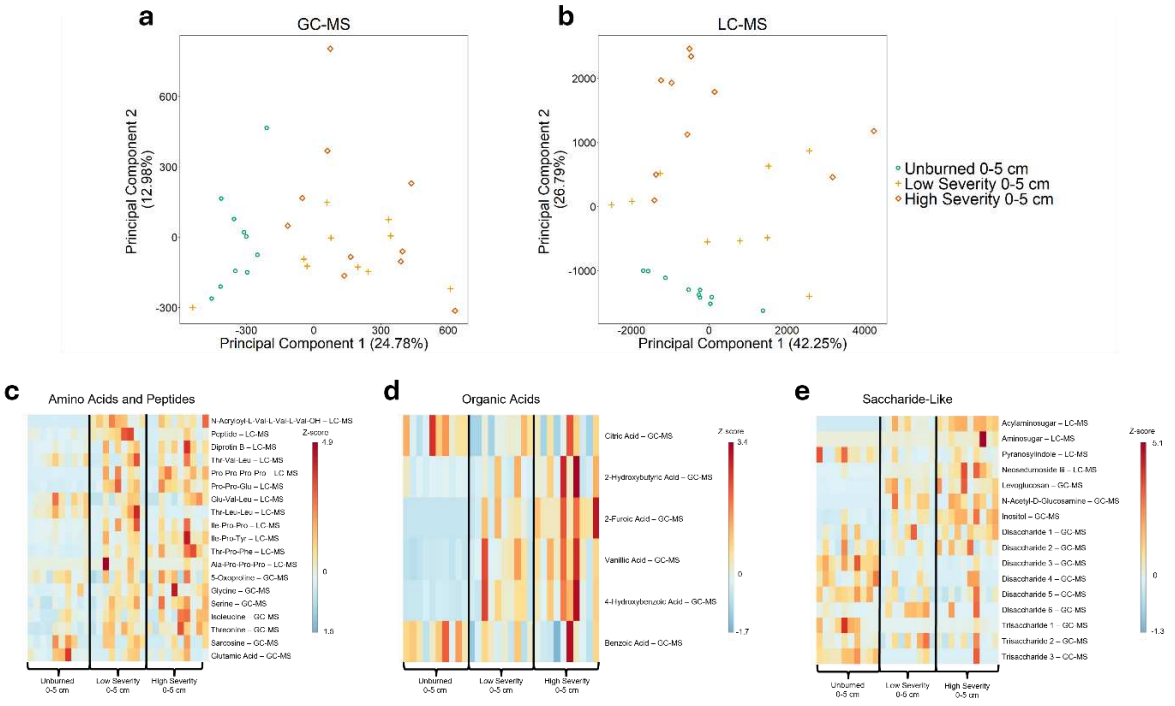

Figure 5.12. Principal component analysis (PCA) scores plots and heat maps of metabolomics data. **a,** PCA scores plot of GC-MS data. n=10 for Unburned 0-5 cm, Low Severity 0-5 cm, and High Severity 0-5 cm samples. **b,** PCA scores plot of LC-MS data. n=10, n=9, and n=10 for Unburned 0-5 cm, Low Severity 0-5 cm, and High Severity 0-5 samples, respectively. For both Fig 2a and Fig 2b, the peak areas of detected features in the samples were normalized to the internal standard peak areas, scaled with Pareto scaling, and then used as the input data for the PCA scores plots. **c,** Heat map of annotated amino acids and peptides. **d,** Heat map of annotated organic acids. **e,** Heat map of annotated saccharide-like metabolites. For all heat maps, "GC-MS" and "LC-MS" denote whether the annotated metabolites derived from GC-MS or LC-MS analyses. For quantification, the internal-standard normalized peak areas for each metabolite were autoscaled and plotted using MetaboAnalyst (Version 6.0) software. Yellow and red colors above-average abundance values while blue color indicates below-average abundance values. For all heat maps, n=10 for unburned 0-5 cm, n=9 for low severity 0-5 cm, and n=10 for high severity 0-5 cm.

revealed regarding what *types* of metabolites are changing and whether their abundances are increasing or decreasing. Thus, exploring specific molecular categories and individual metabolites is essential to more thoroughly understand how wildfires may impact the soil metabolome.

Burned soils were enriched in amino acids and peptides (**Figure 5.12c**). **Figure 5.12c** features amino acids and peptides whose abundance z-scores were generally greater in the burned soils compared to unburned soils. Such enrichment in protein-like metabolites in burned soil was

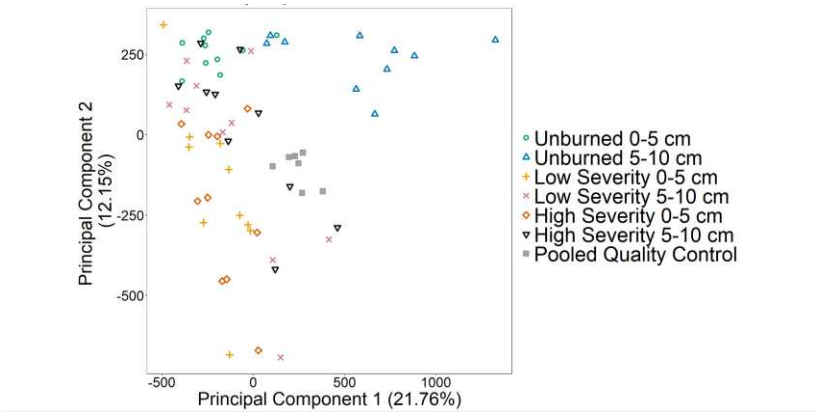

Figure 5.13. PCA scores plots of GC-MS data for soils sampled at 0-5 cm and 5-10 cm depths. The peak areas of detected features in the samples were normalized to the internal standard peak area, scaled with Pareto scaling, and then used as the input data for the PCA scores plots. "Pooled Quality Control" samples were prepared by mixing aliquots of all the samples together, producing a mixture that should plot in the middle of the samples in a PCA scores plot.

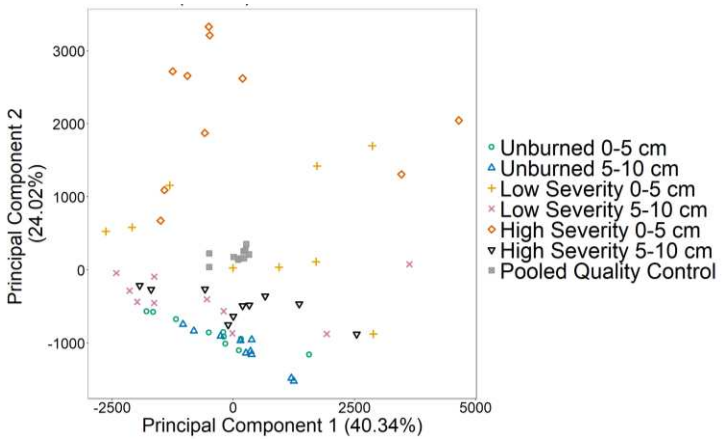

Figure 5.14. PCA scores plots of LC-MS data for soils sampled at 0-5 cm and 5-10 cm depths. The peak areas of detected features in the samples were normalized to the internal standard peak area, scaled with Pareto scaling, and then used as the input data for the PCA scores plots. "Pooled Quality Control" samples were prepared by mixing aliquots of all the samples together, producing a mixture that should plot in the middle of the samples in a PCA scores plot.

also observed in the excitation-emission matrix fluorescence spectroscopy results where tryptophan-like and protein-like fluorescent compounds were significantly more abundant in burned soils (**Figure 5.15**). Augmented amino acid and peptide abundances in burned soils could

help facilitate protein biosynthesis and microbial biomass accumulation while enhancing the biodegradability of the SOM, contributing to post-fire microbial activity.

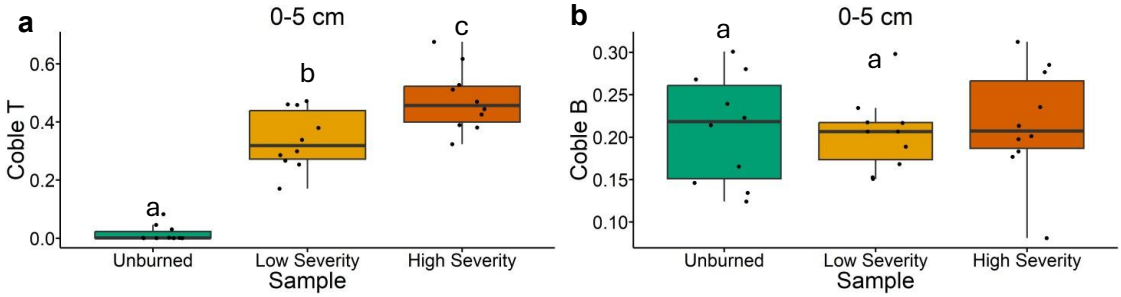

Figure 5.15. Excitation-emission matrix spectroscopy results for soil collected at 0-5 cm depth visualized with box plots. **a,** Coble T values correspond to abundances of tryptophan-like and protein-like fluorescent compounds.[61] **b,** Coble B values correspond to abundances of tyrosine-like and protein-like fluorescent compounds.[61] Letters above boxes indicate significant differences between treatments determined by either ANOVA and Tukey HSD tests, Welch's ANOVA and Games-Howell tests, or Kruskal-Wallis and Dunn's tests (see Statistics section 5.2.15 within Methods). The Coble B and Coble T statistical tests were conducted independently of each other. n = 10 for unburned, low severity, and high severity samples. Box plots show the median (central line), first and third quartiles (box edges), and whiskers extending to minimum and maximum values within 1.5 times the interquartile range. Data beyond the end of the whiskers are "outlying" points and are plotted individually.

Burned soils were also enriched in organic acids (**Figure 5.12d**). Such organic acids play key roles in biochemical pathways and metabolism. For example, 2-hydroxybutyric acid is involved in propanoate metabolism,[91] vanillic acid influences aminobenzoate degradation,[92] and 2-furoic acid can be the sole source of carbon and energy for *Pseudomonas putida* (a saprophytic soil bacterium).[93,94] Consequently, these are very biologically relevant organic acids whose abundances were greater in the burned soils.

Comparatively to amino acids, peptides, and organic acids, saccharide-like compounds were not consistently more abundant in burned soils (**Figure 5.12e**). Interestingly, lower molecular weight saccharide-like compounds detected via GC-MS were generally less abundant in burned soils, perhaps due to disaccharides and trisaccharides volatizing during burning. Conversely, the larger molecular weight saccharide-like compounds detected by LC-MS were generally more

abundant in burned soils. These larger saccharides may have been less likely to volatilize during burning due to their larger molecular weights. Three of the LC-MS-detected saccharides ("acylaminosugar," "aminosugar," and "pyranosylindole") are amino sugars containing nitrogen. The increased abundances of these nitrogen-containing amino sugars in the burned soil provides further evidence for fire-induced nitrogen incorporation into SOM.[6,82] Overall, saccharide-like compounds where detected and, in some cases, more abundant in the burned soils, providing biodegradable organic matter for post-fire soil microbes. For the first time, this study successfully evaluated the abundances of individual metabolite categories in post-wildfire soils, providing an essential baseline for future investigations.

Figures 5.12c-e demonstrated that burned soils can be enriched with biologically-relevant metabolite categories such as amino acids, peptides, organic acids, and saccharide-like compounds that provide biodegradable organic matter for post-fire microbial communities. Such analyses can be interpreted further to examine individual metabolites and how their abundances respond to wildfires (**Figure 5.16**).

Individual metabolites were significantly more abundant in burned soils compared to unburned soils (**Figure 5.16**). Specifically, levoglucosan was significantly more abundant in the burned soils (**Figure 5.16a**). Levoglucosan is an anhydrosugar involved in bacterial metabolism, is produced during the burning of carbohydrates such as cellulose, and is one of the most well-studied fire biomarkers.[95,96] Thus, levoglucosan's augmented abundances in the burned soils were expected, providing confidence in our approach for identifying and quantifying individual metabolites (**Figure 5.16a**). Serine was significantly more abundant in the burned soils and is an amino acid involved in amino acid metabolism and protein biosynthesis (**Figure 5.16b**).[97,98] Thus, microbes in burned soil have greater access to this key amino acid to fuel metabolism and biomass

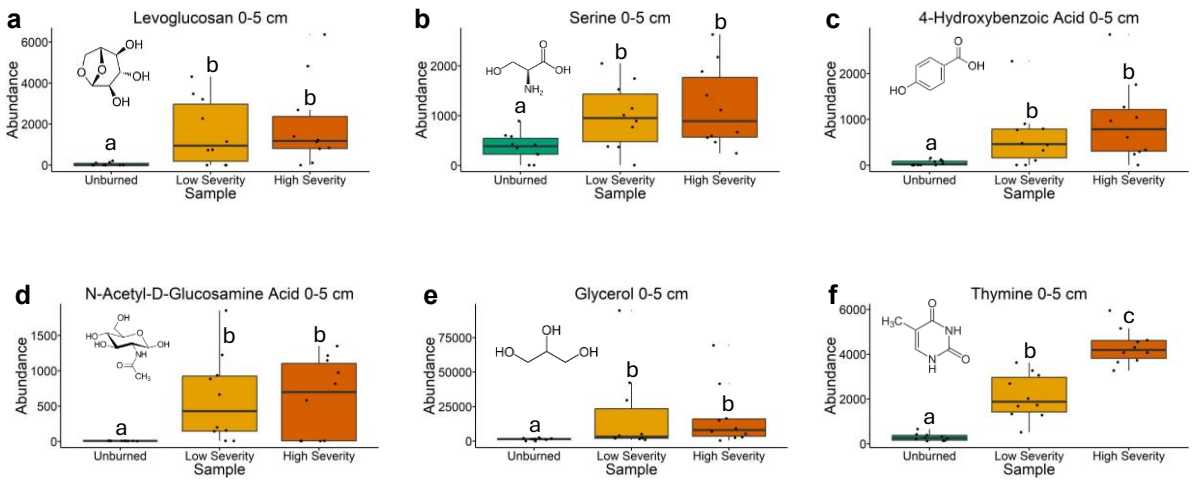

Figure 5.16. Quantification of annotated metabolites abundances from GC-MS analysis from soil collected at 0-5 cm depth visualized with box plots. Abundance values were calculated by dividing the peak area of the metabolites by the peak area of the internal standard to account for matrix effects and analytical variation. Therefore, abundance values themselves are arbitrary and cannot be compared across metabolites, but the abundance values can be compared across treatments for a given metabolite. Letters above boxes indicate significant differences between treatments determined by either ANOVA and Tukey HSD tests, Welch's ANOVA and Games-Howell tests, or Kruskal-Wallis and Dunn's tests (see Statistics section 5.2.15 within Methods). The statistical tests of each individual metabolite (**a** through **f**) were conducted independently of each other. n = 10 for unburned, low severity, and high severity samples. Box plots show the median (central line), first and third quartiles (box edges), and whiskers extending to minimum and maximum values within 1.5 times the interquartile range. Data beyond the end of the whiskers are "outlying" points and are plotted individually.

accumulation. 4-hydroxybenzoic acid was significantly more abundant in the burned soils and is involved in the degradation of aromatic compounds and can be transformed into protocatechuate (a key aromatic intermediate that can be further degraded into metabolites that feed directly into the citric acid cycle producing adenosine triphosphate [ATP]) (**Figure 5.16c**).[4,34,99,100] The increased abundances of 4-hydroxybenzoic acid in the burned soils implies that microbes may be metabolizing aromatic compounds, producing 4-hydroxybenzoic acid which can eventually propagate the citric acid cycle. Post-fire microbes may be adapted to specifically consume aromatic compounds in burned soils based on microbial genetic-based studies.[4,34] Herein, we provide further evidence of this emerging phenomenon of post-fire microbial consumption of

aromatic compounds but from a novel chemistry perspective. N-acetyl-D-glucosamine and glycerol significantly increased in abundance in the burned soils (**Figures 5.16d** and **5.16e**). N-acetyl-D-glucosamine is a saccharide-like compound and bacterial metabolite while glycerol serves as the backbone of fatty acids and is involved in galactose and glycerolipid metabolism.[101–103]

The increased metabolite abundances in burned soil likely come from microbial cell lysis. Cell lysis occurs during wildfires when high soil temperatures cause microbial cells to break open, releasing their intracellular metabolites into the soil. This idea is further supported by the increased abundance of thymine in the burned soils (**Figure 5.16f**). Thymine is a nucleobase, one of the four building blocks of DNA, and stored within the nucleus of eukaryotic cells (like fungi) and within the nucleoid of prokaryotic cells (like bacteria and archaea). When microbial cells lyse open, intracellular nucleobases would likely enter the soil matrix and increase thymine soil abundances. Thus, the increased thymine abundance observed herein support this cell lysis premise. Abundances of recently produced microbial derived organic matter were significantly greater in the burned soils and the degree of SOM decomposition into stable humus was significantly lower in burned soils based on excitation-emission matrix fluorescence spectroscopy (**Figure 5.17**), implying that burned soils contained fresh, recently introduced organic matter likely from microbes. Thus, this study provides further evidence supporting the notion of cell lysis contributing to increased metabolite abundances in burned soils.

Herein we demonstrate that metabolite abundances were significantly greater in the burned soils compared to unburned soils. These metabolites represent a broad suite of metabolite categories such as amino acids, aromatic organic acids, anhydrosugars, and nucleobases. In total, 77 metabolites were putatively identified in this study at either levels 2 or 3 of the Schymanski

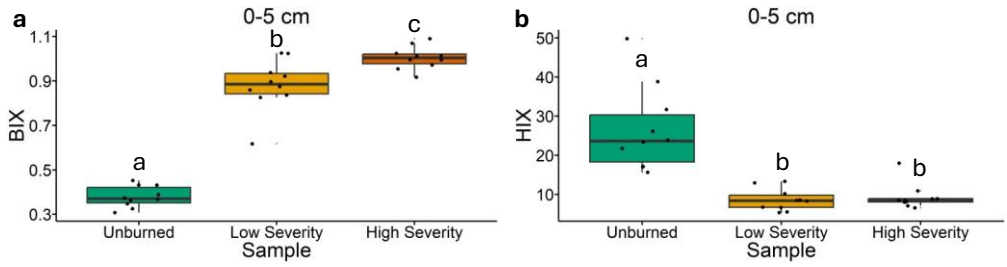

Figure 5.17. Excitation-emission matrix spectroscopy results for soil collected at 0-5 cm depth visualized with box plots. **a,** Biological Index (BIX) values correspond to abundances of recently produced microbial derived organic matter.[63] **b,** Humification Index (HIX) values correspond to abundances of humic substances and greater degrees of humification.[62] Letters above boxes indicate significant differences between treatments determined by either ANOVA and Tukey HSD tests, Welch's ANOVA and Games-Howell tests, or Kruskal-Wallis and Dunn's tests (see Statistics section 5.2.15 within Methods). The BIX and HIX statistical tests were conducted independently of each other. n = 10 for unburned, low severity, and high severity samples. Box plots show the median (central line), first and third quartiles (box edges), and whiskers extending to minimum and maximum values within 1.5 times the interquartile range. Data beyond the end of the whiskers are "outlying" points and are plotted individually.

index.[28] Only 4 % of the putatively identified metabolites were significantly more abundant in unburned soils compared to both burned soil types (i.e. low and high severity) (**Table 5.4**). 51 % of the putatively identified metabolites featured no significant differences in abundance between unburned and burned soils (**Table 5.4**). Conversely, 45 % of the putatively identified metabolites were significantly more abundant in at least one of the two *burned* soil types compared to the unburned soils (**Table 5.4**). In other words, 96 % of the putatively identified metabolites were either statistically similar or significantly greater in abundance in the *burned* soils compared to the unburned soils. Thus, burned soils were enriched in biologically relevant metabolites compared to unburned soils, potentially providing microbes with key substrates for metabolism to promote microbial activity and broader post-fire soil recovery. Consequently, we reject our first hypothesis due to the surprising lack of differences in metabolite abundances between low and high severity soils likely resulting from similar soil burn temperatures. Overall, this is the first investigation to

reveal that soils impacted by a natural wildfire can be enriched with biologically-relevant metabolites.

Table 5.4. Comparing significant differences between unburned and burned samples at a depth of 0-5 cm. For the left-hand column, an annotated metabolite is in the column if either the low severity or high severity samples feature significantly greater abundances compared to the unburned samples. For the middle column, an annotated metabolite is in the column if the unburned sample features significantly greater abundances compared to both the low severity and high severity samples. For the right-hand column, an annotated metabolite is in the column if the unburned sample does not feature significantly greater abundances compared to both the low severity and high severity samples

Significantly greater abundances in burned soils compared to unburned soils.	**Significantly greater abundances in unburned soils compared to burned soils.**	**No significant differences between unburned and burned soils**
Glycerol	Disaccharide 3	Citric acid
Levoglucosan	Trisaccharide 1	Glutamic acid
Vanillic acid	Trisaccharide 3	5-Oxoproline
Thymine		2-Hydroxybutyric acid
4-Hydroxybenzoic acid		Glycine
2-Furoic acid		Sarcosine
Serine		Palmitic acid
Threonine		Isoleucine
N-Acetyl-D-glucosamine		Stearic acid
Inositol		Benzoic acid
N-Acryloyl-L-Val-L-Val-L-Val-OH		Disaccharide 1
Peptide		Disaccharide 2
Pro-Pro-Pro-Pro		Disaccharide 4
Pro-Pro-Glu		Disaccharide 5
Thr-Pro-Phe		Disaccharide 6
Acylaminosugar		Trisaccharide 2
Amino sugar		Diprotin B
Neosedumoside Iii		Thr-Val-Leu
Diterpenoid 1		Glu-Val-Leu
Diterpenoid 2		Thr-Leu-Leu
Diterpenoid 3		Ile-Pro-Pro
Diterpenoid 4		Ile-Pro-Tyr
Diterpenoid 5		Ala-Pro-Pro-Pro
Alkaloid 2		Pyranosylindole
Alkaloid 6		Alkaloid 1
Alpha amino acid 1		Alkaloid 3
Dehp		Alkaloid 4
Furan-2,5-dicarbaldehyde		Alkaloid 5

Cgmp		Amino acid derivative alkaloid 1
Clindamycin		Amino acid derivative alkaloid 2
Aureine		Alpha amino acid 2
Purine nucleotide		Alpha amino acid 3
Fatty acid ester		Benzoic acid ester
Azole		Ampelopsin
Triphenyl phosphate		Dechlorogriseofulvin
		Dialkyl ether
		Polyethylene glycol
		Lipid-like
		Napelline

5.3.3 SOM FROM BURNED SOILS WAS MORE BIODEGRADABLE THAN SOM FROM UNBURNED SOIL

The burned soils contained more biodegradable molecules at lower molecular weights compared to unburned soils. **Figures 5.18a** and **5.18c** compare unique molecular formulae between unburned and low severity soils and between unburned and high severity soils detected using 21 tesla Fourier transform ion cyclotron resonance-mass spectrometry (21 T FT ICR-MS). 21 T FT ICR-MS features the highest mass resolving power and mass accuracy in the world, providing sufficient analytical power to analyze complex soil matrices.[82,104,105] In both comparisons, the burned soils feature more unique molecular formulae that have higher H/C ratios. Molecular formulae with higher H/C ratios are generally considered more biodegradable.[106] These more biodegradable molecular formulae can be quantified with the molecular lability boundary (MLB_L) value which divides the number of molecular formula with H/C ratio greater than 1.5 by the total number of molecular formulae; the higher the MLB_L value, the more biodegradable the molecular formulae. The MLB_L values for the low severity and high severity unique molecular formulae (30.6 % and 28.9 % respectively) were substantially greater when individually compared to the unburned unique molecular formulae (5.5 % and 5.6 % respectively), indicating that the

burned soil contained more biodegradable SOM. Additionally, the burned unique molecular formulae were considerably lower in molecular weight compared to the unburned unique molecular formulae (**Figures 5.18b** and **5.18d**). Specifically, the average molecular weight of the low and high severity unique molecular formulae were 271 and 259 Daltons less than that of the unburned unique molecular formulae. This may contribute to more biodegradable SOM in burned soils due to lower molecular weight compounds being more easily carried through cellular membranes and metabolized.[107] Additional FT-ICR MS results can be found in **Figure D13**. In conclusion, the FT ICR-MS results indicated that SOM from the burned soils were more biodegradable than that from the unburned soils, complementing the metabolomics results. For further evidence, laboratory incubations were conducted to provide a more direct assessment of SOM biodegradability.

Biological oxygen demand incubations revealed that SOM from burned soil was more biodegradable compared to unburned soil (**Figure 5.19**). For these incubations, SOM was extracted with water, the extract was filtered to 0.1 μm, and a river water microbial inoculum was added to the extract to start the incubation. Dissolved oxygen concentrations in the incubation solutions were monitored to calculate oxygen consumption as a proxy for SOM biodegradability; the more oxygen consumption, the more biodegradable the SOM. Therefore, this established method can provide a direct, holistic assessment of SOM biodegradability.[109–111] Over the course of the incubations, significantly more oxygen was consumed in the burned samples compared to the unburned samples (**Figures 5.19** and **5.20**, **Table D1**). This pattern was also observed in dissolved organic carbon consumption during the incubation (**Figure 5.21**, **Table D2**). The three samples (unburned, low severity, and high severity) all started at the same initial dissolved organic carbon concentrations (~10 mg/L). Thus, differences in oxygen consumption are due to differences

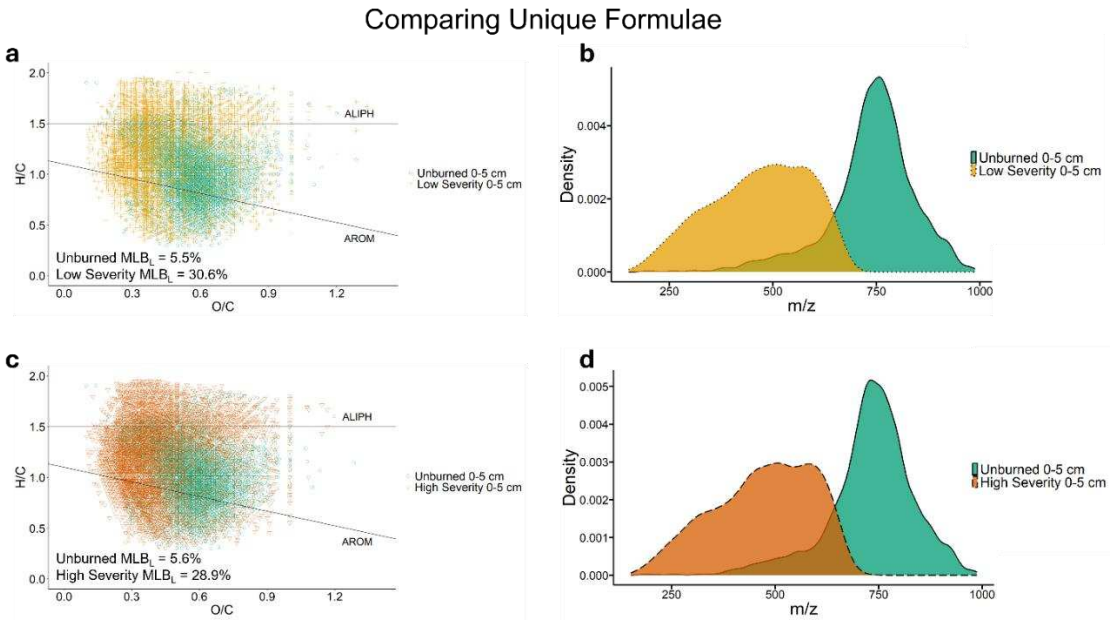

Figure 5.18. Fourier transform ion cyclotron resonance-mass spectrometry results illustrating key differences in unique assigned molecular formulae for unburned, low severity, and high severity soils collected at 0-5 cm depth. A unique molecular formula, for example, is a molecular formula assigned in Sample X but not assigned in Sample Y. In that case, that assigned molecular formula is unique to sample X. **a,** Van Krevelen diagram plotting assigned molecular formula unique to unburned and low severity samples.[108] **b,** Density plot plotting m/z values of assigned molecular formula unique to unburned and low severity samples. m/z values are representative of the molecular weights of the assigned molecular formulae. **c,** Van Krevelen diagram plotting assigned molecular formula unique to unburned and high severity samples.[108] **d,** Density plot plotting m/z values of assigned molecular formula unique to unburned and high severity samples. m/z values are representative of the molecular weights of the assigned molecular formulae. UB = unburned. L = low severity. H = high severity. MLB_L is the molecular lability boundary value indicates the percentage of assigned molecular formulae featuring H/C ratios greater than 1.5 and is a metric for quantifying more chemical constituents.[106]

in SOM composition, not SOM quantity. The greater oxygen consumption in the low severity samples compared to the high severity samples could be explained by the lower severity soils featuring SOM with slightly higher nominal oxidation state of carbon values and slightly lower modified aromaticity index values compared to the high severity soil samples (**Figures 5.22** and **5.23**).[57–59] Conversely, the nuanced differences between the low severity and high severity samples may simply lie outside of the analytical techniques that we employed (GC-MS, LC-MS, FT ICR-MS). Nuclear magnetic resonance spectroscopy, for example, could have been used to account for

other pools of SOM not detected by our instrumentation. Nevertheless, SOM from the burned soils were more biodegradable than that of the unburned soils, likely due to the increased metabolite abundances observed within the burned soils.

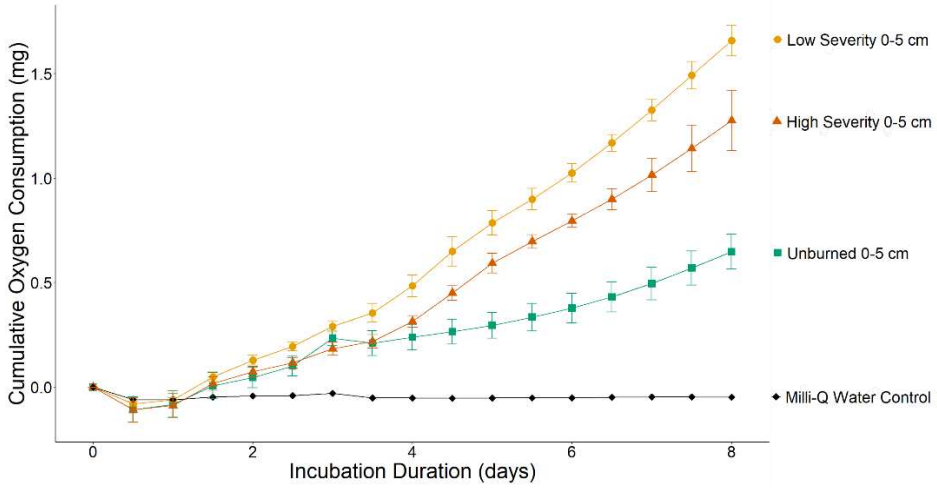

Figure 5.19. Biological oxygen demand incubation results. n = 3 for unburned, low severity, and high severity samples. n = 1 for Milli-Q water control. Data points are average values, and error bars are standard deviation values. "0-5 cm" indicates that the soils used in these incubations were sampled at a depth of 0-5 cm.

5.3.4 BURNED SOILS WERE ENRICHED IN MICROBIAL COMMUNITIES THAT CAN CONTAIN HETEROTROPHS AND COPIOTROPHS

Bacterial, archaeal, and fungal community compositions were assessed to determine if there are any congruences between fire impacts on SOM and microbiology. 16S rRNA and ITS amplicon sequencing were specifically conducted (**Figure 5.24**).

Microbial communities from unburned and burned soils were distinct based on nonmetric multidimensional scaling (NMDS) ordination analysis (**Figures 5.24a** and **5.24b**). In NMDS plots, data points that cluster closely (or separately) have similar (or distinct) microbial communities which is very similar to the interpretation of metabolomics PCA plots (**Figures 5.12a,b**). For both bacterial/archaeal (**Figure 5.24a**) and fungal communities (Figure **5.24b**), unburned and burned soils plotted separately and to a significant extent based on PERMANOVA analysis. Thus, burning

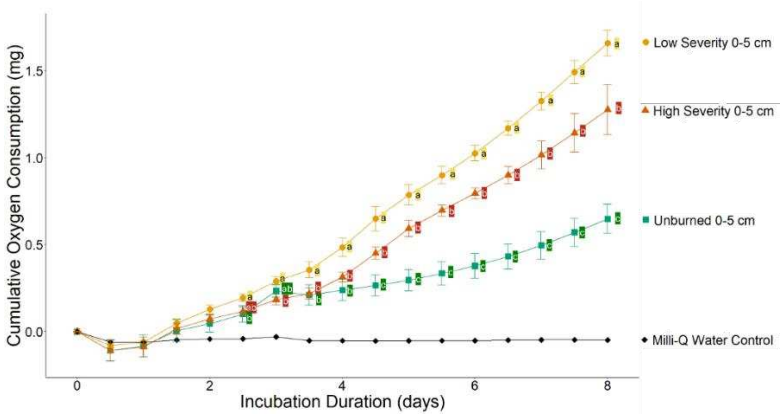

Figure 5.20. Biological oxygen demand incubation results with statistical comparisons. Within each measurement period (e.g. Day 1 and Day 2), the values of the unburned, low severity, and high severity samples were statistically compared amongst each other. For Day 0 (start of incubation), Day 0.5, Day 1, Day 1.5, and Day 2, there were no significant differences amongst unburned, low severity, and high severity samples. The letters next to data points in Day 2.5 and beyond indicate significant differences amongst the amongst unburned, low severity, and high severity samples determined by either ANOVA and Tukey HSD tests, Welch's ANOVA and Games-Howell tests, or Kruskal-Wallis and Dunn's tests (see Statistics section 5.2.15 within Methods). For example, at Day 4, the unburned and high severity samples were not significantly different whereas the low severity sample was significantly different compared to both unburned and high severity samples. n = 3 for unburned, low severity, and high severity samples. n = 1 for Milli-Q water control. Data points are average values, and error bars are standard deviation values. "0-5 cm" indicates that the soils used in these incubations were sampled at a depth of 0-5 cm.

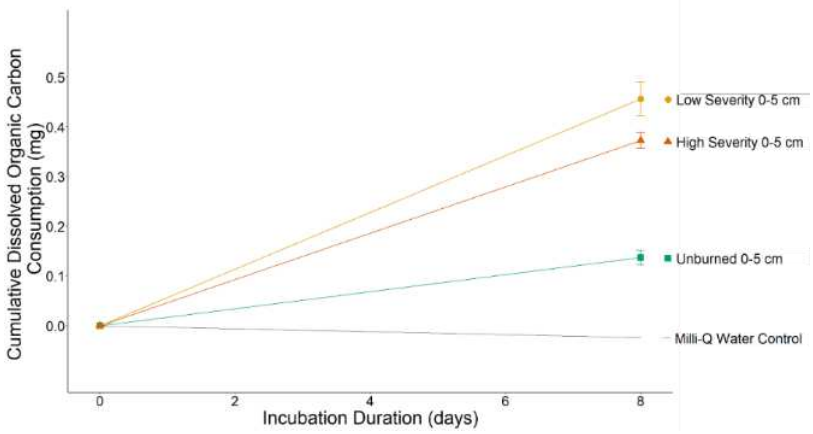

Figure 5.21. Dissolved organic carbon consumption during biological oxygen demand incubations. Dissolved organic carbon concentrations were only measured at the beginning (Day 0) and end (Day 8) of the incubation. n = 3 for unburned, low severity, and high severity samples. n = 1 for Milli-Q water control. Data points are average values, and error bars are standard deviation values. "0-5 cm" indicates that the soils used in these incubations were sampled at a depth of 0-5 cm. The Day 8 values for unburned, low severity, and high severity samples were all significantly different from each other (ANOVA and Tukey tests, $p<0.05$).

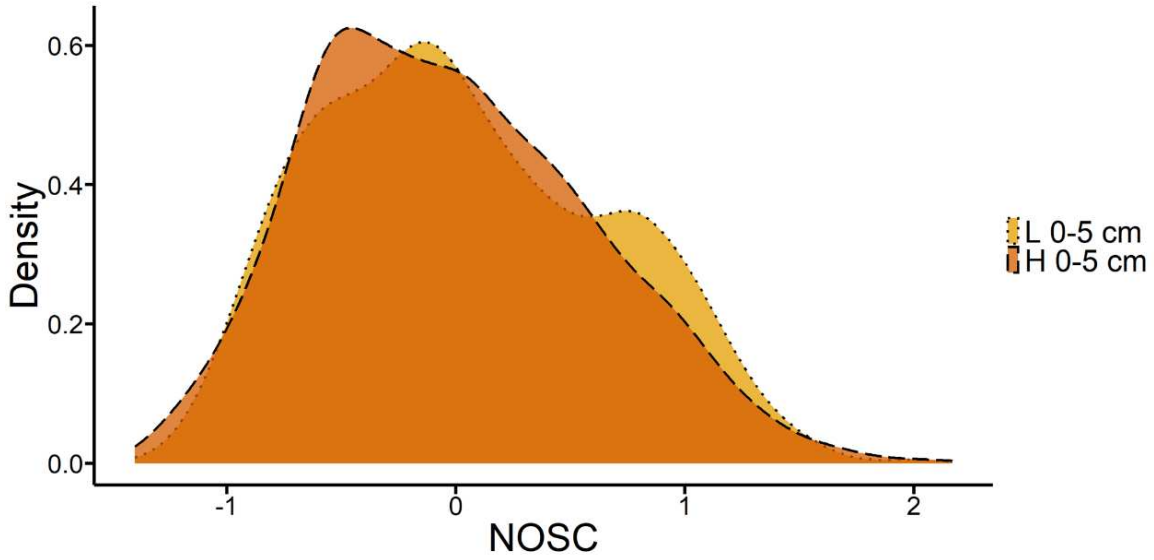

Figure 5.22. Density plot comparing the nominal oxidation state of carbon (NOSC) values of unique molecular formulae assigned with Fourier transform ion cyclotron resonance-mass spectrometry within low (L) severity and high (H) severity soils collected at a depth of 0-5 cm.[59] Molecular formulae with high NOSC values require less energy to oxidize, resulting in those formulae being more biodegradable from a purely thermodynamic perspective.[112] Note the slight shoulder near 1 on the x-axis for the low severity sample.

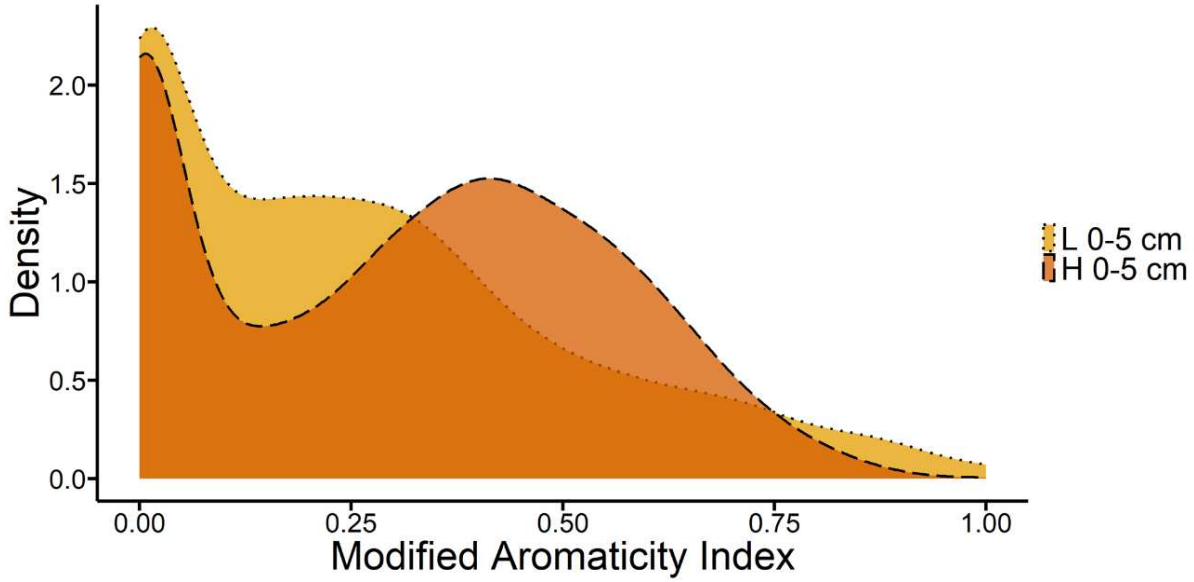

Figure 5.23. Density plot comparing the modified aromaticity index values of unique molecular formulae assigned with Fourier transform ion cyclotron resonance-mass spectrometry within low (L) severity and high (H) severity soils collected at a depth of 0-5 cm.[57,58]

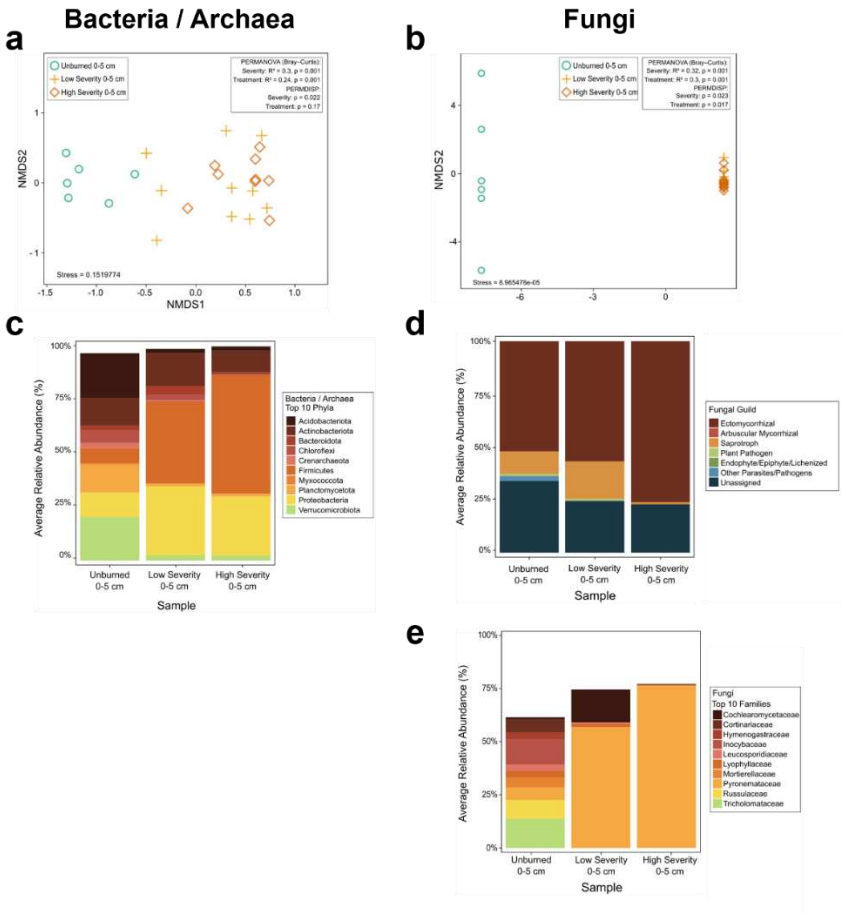

Figure 5.24. 16S rRNA and ITS amplicon sequencing results. Bacteria and archaea results are in the left column while fungal results are in the right column. **a** and **b,** Nonmetric multidimensional scaling (NMDS) ordination plots including Bray-Curtis ASV microbial community composition dissimilarities for bacterial/archaeal communities (**a**) and fungal communities (**b**). n =10 for unburned, low severity, and high severity soils. **c,** Bar plot showing relative abundance values averaged across replicates for the top ten most abundant bacterial and archaeal phyla. **d,** Average relative abundance values for notable fungal guilds. **e,** Average relative abundance values for the top ten most abundant fungal families.

drastically alters soil microbial community composition as previously observed.[4,29,39,48,113–117] However, the distinct separations between unburned and burned soils within both the microbial NMDS plots (**Figures 5.24a,b**) *and* the metabolite PCA plots (**Figures 5.12a,b**) are novel, suggesting that alterations to the soil metabolite profiles and microbial communities go hand in hand.

Burned soils were enriched in copiotroph-containing and heterotroph-containing phyla (e.g. *Firmicutes* and *Proteobacteria*) and featured losses of oligotrophic-containing phyla (e.g. *Verrucomicrobiota*, *Acidobacteriota*, *Planctomycetota*). *Firmicutes* (and *Proteobacteria)* increased in relative abundance by 31.4 % (and 20.7 %) in low severity soils and by 48.5 % (and 16.1 %) in high severity soils compared to unburned soils (**Figure 5.24c** and **Table D3**). These two phyla can contain heterotrophic microbes that may consume the enriched metabolites within the burned soils.[4,118] *Firmicutes* feature endospore-forming taxa that can survive the initial heat pulse during fire and capitalize on the post-fire biodegradable organic matter. The *Firmicutes* were dominated by genera *Bacillus* and *Paenibacillus* which are known plant growth-promoting rhizobacteria. Thus, these post-fire *Firmicutes* may not just be post-fire pioneer microbes but may actively support early plant recovery. The *Proteobacteria* phylum specifically featured copiotrophs which thrive in soils rich in organic matter and nutrients. The enrichment of this copiotrophic-containing phyla further indicates that post-fire soils are rich in biodegradable SOM. While *Firmicutes* and *Proteobacteria* increased in relative abundance in burned soils, *Verrucomicrobiota*, *Acidobacteriota*, and *Planctomycetota* decreased in average relative abundance by 17.9 % and 18.0 % for *Verrucomicrobiota*, 18.8 % and 18.8 % for *Acidobacteriota*, and 11.7 % and 11.9 % for *Planctomycetota* in low severity and high severity soils, respectively, compared to unburned soils (**Figure 5.24c** and **Table D3**). *Verrucomicrobiota*, *Acidobacteriota*, and *Planctomycetota* can contain oligotrophs which populate nutrient-poor environments and exhibit slow growth and slow rates of metabolism. The loss of oligotrophic-containing phyla here implies that the burned soils are not nutrient-depleted environments; rather, in the burned soils, these oligotrophs are replaced by spore-forming, copiotrophic *Firmicutes* and *Proteobacteria* that are better suited for the post-fire soils rich in biodegradable SOM.

Post-fire fungal communities were dominated by a singular ectomycorrhizal fungal species: *Wilcoxina rehmii*. *Wilxocina rehmii* was the dominant species within ectomycorrhizal fungal guild which increased in average relative abundance by 4.7 % and 24.0 % for low severity and high severity soils, respectively, compared to unburned soils (**Figure 5.24d** and **Table D4**). Furthermore, the *Pyronemataceae* fungal family (which increased in average relative abundance by 51.0 % and 70.3 % within low severity and high severity soils respectively compared to unburned soils [**Figure 5.24e** and **Table D5**]) was also dominated by *Wilcoxina rehmii*. Thus, rather than a broad bloom of post-fire pyrophilous fungi, we observed ectomycorrhizal fungal dominance by this one species. Generally, ectomycorrhizal fungal communities decrease in abundance after fires and rarely collapse into a single taxon as observed here.[4,29,48,117] This fungal homogenization may constrain the diversity of post-fire vegetation.

5.3.5 BURNED SOIL EMITTED SIGNIFICANTLY MORE CARBON DIOXIDE THAN UNBURNED SOIL

Soil CO_2 respiration was measured to determine how the enrichment of metabolites, more biodegradable SOM, and heterotrophic-containing bacterial/archaeal phyla in the burned soils may impact soil activity and post-fire carbon emissions. Soil CO_2 respiration fluxes were greater in burned soils than in unburned soils (**Figure 5.25**). Specifically, the high severity soils respired significantly more CO_2 at the time of measurement compared to the low severity and unburned soils (**Figure 5.25**). While there was no statistically significant difference between the soil CO_2 respiration fluxes between unburned and low severity soils, the average value of the soil CO_2 respiration fluxes for low severity soils was 41 % greater than that of the unburned soils. Soil CO_2 net ecosystem exchange (i.e. the balance between CO_2 uptake from photosynthesis and CO_2 release from respiration), was also measured (**Figure 5.26**), but there were no significant differences

between respiration and net ecosystem exchange fluxes (**Figure 5.27**), suggesting that there was minimal photosynthetic activity from the underlying vegetation. Overall, burned soils exhibited augmented CO_2 respiration compared to unburned soils, likely due to burned soils featuring greater abundances of metabolites, enriched heterotrophic-containing bacterial/archaeal communities, and SOM with heightened biodegradability.

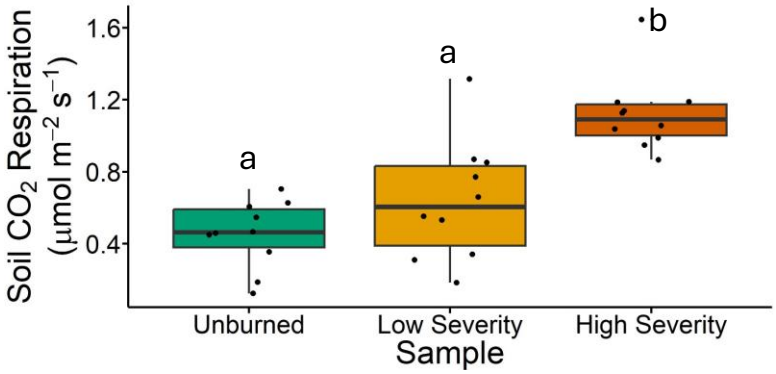

Figure 5.25. Soil CO_2 respiration results visualized with a box plot. The gas analyzer chamber was covered with a tarp during measurements to minimize photosynthetic activity, providing a more direct assessment of soil respiration. The measurements were conducted 52 days after the Alexander Mountain Fire was 100 % contained. Letters above boxes indicate significant differences between treatments determined by either ANOVA and Tukey HSD tests, Welch's ANOVA and Games-Howell tests, or Kruskal-Wallis and Dunn's tests (see Statistics section 5.2.15 within Methods). n = 10 for unburned, low severity, and high severity samples. Box plots show the median (central line), first and third quartiles (box edges), and whiskers extending to minimum and maximum values within 1.5 times the interquartile range. Data beyond the end of the whiskers are "outlying" points and are plotted individually.

5.4 IMPLICATIONS

This study, leveraging metabolomic, mass spectrometry, microbial, and gas flux analyses, revealed the presence of enriched metabolites and enhanced biodegradable SOM within burned soils. Specifically, 96 % of the putatively identified metabolites were either statistically similar or significantly greater in abundance in burned soils compared to unburned soils, and over 2.0x more microbial metabolism of SOM occurred during incubations with burned soil extracts compared to unburned soil extracts. Burned soils can certainly feature augmented aromatic SOM content,[4–10]

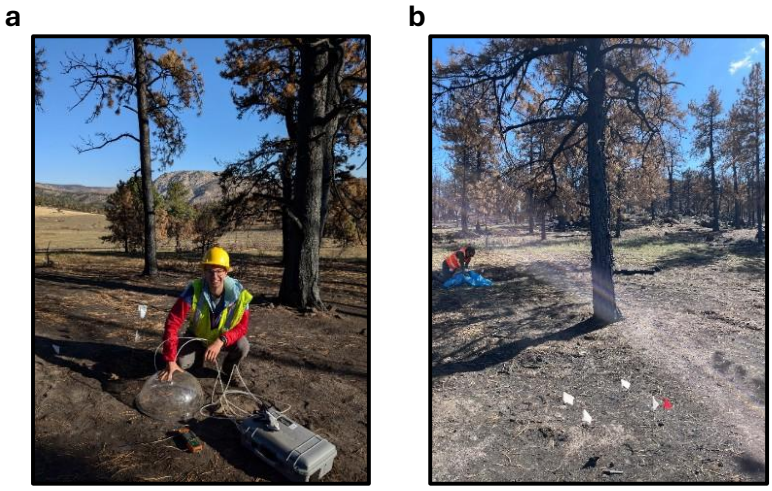

Figure 5.26. Photos of soil CO_2 gas flux measurements. **a,** Jacob VanderRoest measuring soil CO_2 net ecosystem exchange with the gas chamber not covered by a tarp. Photo credit: Dr. Sean Fettrow. **b,** Dr. Sean Fettrow measuring soil CO_2 respiration by covering the gas chamber with a tarp during measurements. Photo credit: Jacob VanderRoest

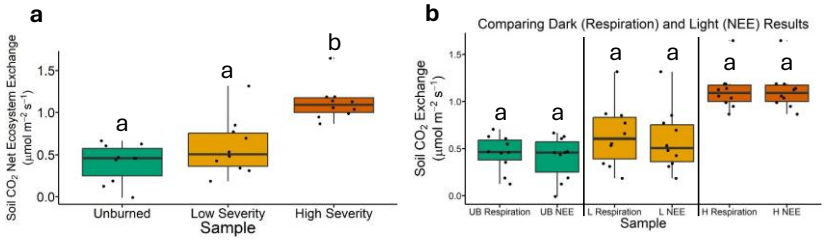

Figure 5.27. Additional soil CO_2 exchange results visualized with box plots. **a,** Soil CO_2 net ecosystem exchange results measured by not covering gas analyzer chamber with a tarp during measurement, allowing for photosynthetic activity. Letters above boxes indicate significant differences between treatments determined by either ANOVA and Tukey HSD tests, Welch's ANOVA and Games-Howell tests, or Kruskal-Wallis and Dunn's tests (see Statistics section 5.2.15 within Methods). n = 10 for unburned, low severity, and high severity samples. **b,** Comparison between respiration and net ecosystem exchange (NEE) results. UB = unburned. L = low severity. H = high severity. The statistical tests within sample types (i.e. unburned, low severity, and high severity) were conducted independently of each other. Letters above the boxes indicate significant differences between depths and were determined with either Student's t-test, Welch's t-test, or Mann-Whitney U tests (see Statistics section 5.2.15 within Methods). n = 10 for unburned, low severity, and high severity samples. "Dark" refers to respiration measurements conducted with the gas chamber being covered with a tarp. "Light" refers to NEE measurements in which the gas chamber was not covered with a tarp. The lack of significant differences between respiration and NEE indicates that the vegetation within the gas chamber during measurement was relatively photosynthetically inactive. Box plots show the median (central line), first and third quartiles (box edges), and whiskers extending to minimum and maximum values within 1.5 times the interquartile range. Data beyond the end of the whiskers are "outlying" points and are plotted individually.

contributing to SOM being more resistant to microbial degradation. However, conceptual models describing SOM content in burned soils now need to include a biodegradable pool that features the metabolites and biodegradable SOM observed in this study (**Figure 5.28**). The inclusion of this biodegradable pool would complement previous studies that have identified a "slow cycling pool" as well as a "fast cycling pool" in pyrogenic organic matter.[38,39] The "slow cycling pool" is likely comprised of more persistent, aromatic organic matter while the "fast cycling pool" likely contains metabolites derived from cell-lysis and more biodegradable SOM which was observed in this study. Thus, this study has laid the groundwork for a new fundamental understanding of SOM from burned soil that includes the presence of metabolites and biodegradable SOM contributing to a "fast cycling pool" of organic matter.

This fast-cycling pool could impact post-fire microbial activity, forest management strategies, and soil greenhouse gas emissions. The increased biodegradable organic matter content could provide heterotrophic microbes with key substrates for metabolism, initiating and fueling post-fire microbial activity and broader soil recovery. Such soil recovery could aid in post-fire reforestation,[3] contributing to habitat redevelopment and carbon sequestration. The flush of metabolites in burned soils would provide microbes with more nutrients compared to unburned soil. This increase in nutrient content is additional evidence supporting low severity, prescribed burning in forests as a forest management strategy. Not only will prescribed burning prevent the buildup of vegetation that could fuel intense wildfires, but prescribed burning may also introduce biodegradable nutrients into the soil, contributing to a more active, healthy soil microbiome.

However, more biodegradable SOM and more metabolites in burned soils could contribute to post-fire soil greenhouse gas emissions via microbial respiration as observed in this study (**Figure 5.25**). Thus, post-fire soils may behave more so as carbon sources rather than carbon sinks

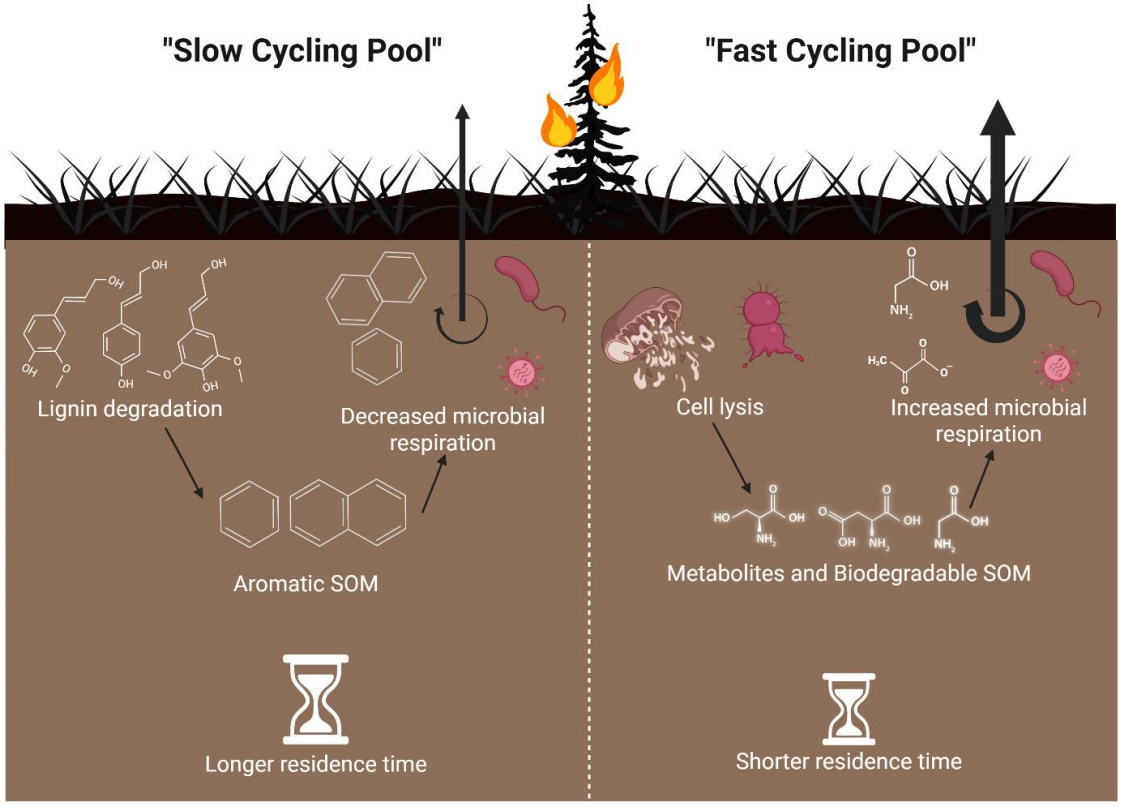

Figure 5.28. Conceptual diagram illustrating "slow cycling" and "fast cycling" organic matter pools within burned soils. The organic matter content of the "slow cycling" pool was already known due to extensive research examining aromatic organic matter in burned soils.[5–10,82,119] This study revealed the likely content of the "fast cycling" pool: biodegradable metabolites. Figure created with BioRender.com.

in the immediate aftermath of a wildfire. Longer-term studies are necessary to determine the extent of this post-fire greenhouse gas pulse. Overall, this study demonstrates that burned soils are not sterile matrices devoid of biodegradable organic matter. Conversely, burned soils can feature heightened metabolite abundances and organic matter that is more biodegradable compared to nearby unburned soils.

5.5 ACKNOWLEDGEMENTS

This research was funded by Dr. Mike Wilkins and Thomas Borch from the National Science Foundation under grant number 2114868 and the United States Department of Agriculture (USDA) National Institute of Food and Agriculture through AFRI grant number

2021-67019-34608. We sincerely thank Angela Stanford, Silas Binkely, and Laura Armstrong from the Heart-J-Center in Loveland, CO for providing access to the Alexander Mountain Fire burn scar. This research would not have been possible without them. We thank the Heart-J Center Junior Rangers (Avi Strauss, Samarah Strauss, and Lincoln Porter) who helped measure soil CO_2 gas flux. They are off to an exceptional start in their scientific careers. We thank Dr. Jeffrey L. Collett, Jr. for providing us with the FTIR gas analyzer (LI-7810, LiCor). We thank Dr. Nathan Montgomery from the Bioanalysis and Omics Center within the Analytical Resources Core at Colorado State University for operating the LC-MS instrument (RRID: SCR_021758). We thank Dr. Claudia Boot from the Analytical Resources Core at Colorado State University who provided guidance in the LC-MS data analysis process. We thank Daniel Reuss from the EcoCore Analytical Facility at Colorado State University who provided the instrumentation for measuring dissolved organic carbon, dissolved total nitrogen, total carbon, and total carbon. Thanks to researchers at the National High Magnetic Field Laboratory ICR User Facility which is supported by the National Science Foundation Division of Chemistry and Division of Material Research through DMR-1644779 and DMR-2128556. We thank Dr. Robert Young for paving the way for FT-ICR MS analysis within the Borch lab at Colorado State University and for providing helpful code for FT-ICR MS data processing. We thank the United States Forest Service Rocky Mountain Research Laboratory (specifically Isabel McPherson, Timothy Fegel, and Dr. Charles Rhoades) for providing guidance on our field sampling campaign, providing the equipment for the biological oxygen demand incubations, providing the equipment and instrumentation for KCl extractions followed by NH_4^+ and NO_3^- quantification. The Table of Contents artwork was created with BioRender.com. Use of firm, trade, or product names is for descriptive purposes only and does not imply endorsement by the U.S. government. The TOC art was made using

BioRender.com, and the background of the TOC art came from the following URL: https://www.iii.org/article/background-on-wildfires.

5.6 AUTHOR CONTRIBUTIONS

Jacob P. VanderRoest contributed to conceptualization, data curation, formal analysis, investigation, project administration, software, visualization, writing – original draft preparation, and writing – review and editing. Dr. Sean Fettrow contributed to conceptualization, data curation, formal analysis, investigation, software, writing – review and editing. Kya Sparks contributed to data curation, formal analysis, investigation, software, visualization, and writing – review and editing. Dr. Lydia C. Babcock-Adams contributed to data curation, investigation, resources, and writing – review and editing. Dr. Martin R. Kurek contributed to formal analysis, software, and writing – review and editing. Amelia M. Skinner contributed to data curation, form analysis, investigation, and writing – review and editing. Dr. Corey D. Broeckling contributed to resources and writing – review and editing. Dr. Mike J. Wilkins contributed to funding acquisition, resources, and writing – review and editing. Dr. Thomas Borch contributed to conceptualization, funding acquisition, supervision, project administration, resources, and writing – review and editing.

Specifically, Sean Fettrow measured water-extractable organic carbon and water-extractable total nitrogen, conducted excitation-emission matrix fluorescence spectroscopy, and led the soil CO_2 flux measurements. Kya Sparks conducted the microbial analyses. Lydia C. Babcock-Adams operated the Fourier transform ion cyclotron resonance mass spectrometry instrument. Martin R. Kurek calibrated the data from the Fourier transform ion cyclotron resonance mass spectrometry instrument and assigned molecular formulae to the detected peaks. Amelia Skinner conducted ion chromatography. I led the field campaign and soil sampling, led

the gas chromatography-mass spectrometry analysis, led the liquid chromatography-mass spectrometry analysis, analyzed the molecular formula assignment data from the Fourier transform ion cyclotron resonance mass spectrometry instrument, measured soil pH and electrical conductivity, measured total soil C and N, calculated gravimetric water content and soil bulk density, and conducted the biological oxygen demand incubations, contributing to my conceptualization, data curation, formal analysis, investigation, project administration, and software contributions. For visualization, I produced all figures in this chapter except for **Figure 5.24** (which was produced by Kya Sparks).

CHAPTER 5 REFERENCES

(1) Kolden, C. A.; Abatzoglou, J. T.; Jones, M. W.; Jain, P. Wildfires in 2024. *Nat. Rev. Earth Environ.* **2025**, *6* (4), 237–239. https://doi.org/10.1038/s43017-025-00663-0.

(2) Iglesias, V.; Balch, J. K.; Travis, W. R. U.S. Fires Became Larger, More Frequent, and More Widespread in the 2000s. *Sci. Adv.* **2022**, *8* (11), eabc0020. https://doi.org/10.1126/sciadv.abc0020.

(3) Lopez, A. M.; Avila, C. C. E.; VanderRoest, J. P.; Roth, H. K.; Fendorf, S.; Borch, T. Molecular Insights and Impacts of Wildfire-Induced Soil Chemical Changes. *Nat. Rev. Earth Environ.* **2024**, *5*, 431–446. https://doi.org/10.1038/s43017-024-00548-8.

(4) Nelson, A. R.; Narrowe, A. B.; Rhoades, C. C.; Fegel, T. S.; Daly, R. A.; Roth, H. K.; Chu, R. K.; Amundson, K. K.; Young, R. B.; Steindorff, A. S.; Mondo, S. J.; Grigoriev, I. V.; Salamov, A.; Borch, T.; Wilkins, M. J. Wildfire-Dependent Changes in Soil Microbiome Diversity and Function. *Nat. Microbiol.* **2022**, *7* (9), 1419–1430. https://doi.org/10.1038/s41564-022-01203-y.

(5) Roth, H. K.; McKenna, A. M.; Simpson, M. J.; Chen, H.; Srikanthan, N.; Fegel, T.; Nelson, A. R.; Rhoades, C. C.; Wilkins, M. J.; Borch, T. Effects of Burn Severity on Organic Nitrogen and Carbon Chemistry in High-Elevation Forest Soils. *Soil Environ. Health* **2023**, 100023.

(6) Roth, H. K.; Borch, T.; Young, R. B.; Bahureksa, W.; Blakney, G. T.; Nelson, A. R.; Wilkins, M. J.; McKenna, A. M. Enhanced Speciation of Pyrogenic Organic Matter from Wildfires Enabled by 21 T FT-ICR Mass Spectrometry. *Anal. Chem.* **2022**, *94* (6), 2973–2980. https://doi.org/10.1021/acs.analchem.1c05018.

(7) González-Pérez, J. A.; González-Vila, F. J.; Almendros, G.; Knicker, H. The Effect of Fire on Soil Organic Matter—a Review. *Environ. Int.* **2004**, *30* (6), 855–870. https://doi.org/10.1016/j.envint.2004.02.003.

(8) Chen, H.; Wang, J.-J.; Ku, P.-J.; Tsui, M. T.-K.; Abney, R. B.; Berhe, A. A.; Zhang, Q.; Burton, S. D.; Dahlgren, R. A.; Chow, A. T. Burn Intensity Drives the Alteration of Phenolic Lignin to (Poly) Aromatic Hydrocarbons as Revealed by Pyrolysis Gas Chromatography–Mass Spectrometry (Py-GC/MS). *Environ. Sci. Technol.* **2022**, *56* (17), 12678–12687. https://doi.org/10.1021/acs.est.2c00426.

(9) Yin, G.; Guan, P.; Wang, Y.-H.; Zhang, P.; Qu, B.; Xu, S.; Zhang, G.; He, C.; Shi, Q.; Wang, J. Temporal Variations in Fire Impacts on Characteristics and Composition of Soil-Derived Dissolved Organic Matter at Qipan Mountain, China. *Environ. Sci. Technol.* **2024**. https://doi.org/10.1021/acs.est.4c00446.

(10) Cao, X.; Ma, H.; Li, S.-A.; Huang, H.; Cui, F.; Tanentzap, A. J. Enhanced Release and Reactivity of Soil Water-Extractable Organic Matter Following Wildfire in a Subtropical Forest. *Environ. Sci. Technol.* **2025**, *59* (8), 3992–4002. https://doi.org/10.1021/acs.est.4c13557.

(11) Cochran, D.; Powers, R. Fourier Transform Ion Cyclotron Resonance Mass Spectrometry Applications for Metabolomics. *Biomedicines* **2024**, *12* (8), 1786. https://doi.org/10.3390/biomedicines12081786.

(12) Baran, R.; Brodie, E. L.; Mayberry-Lewis, J.; Hummel, E.; Da Rocha, U. N.; Chakraborty, R.; Bowen, B. P.; Karaoz, U.; Cadillo-Quiroz, H.; Garcia-Pichel, F.; Northen, T. R. Exometabolite Niche Partitioning among Sympatric Soil Bacteria. *Nat. Commun.* **2015**, *6* (1), 8289. https://doi.org/10.1038/ncomms9289.

(13) Swenson, T. L.; Karaoz, U.; Swenson, J. M.; Bowen, B. P.; Northen, T. R. Linking Soil Biology and Chemistry in Biological Soil Crust Using Isolate Exometabolomics. *Nat. Commun.* **2018**, *9* (1). https://doi.org/10.1038/s41467-017-02356-9.

(14) Bifarin, O. O.; Yelluru, V. S.; Simhadri, A.; Fernández, F. M. A Large Language Model–Powered Map of Metabolomics Research. *Anal. Chem. 97* (27), 14088–14096. https://doi.org/10.1021/acs.analchem.5c01672.

(15) McGivern, B. B.; Tfaily, M. M.; Borton, M. A.; Kosina, S. M.; Daly, R. A.; Nicora, C. D.; Purvine, S. O.; Wong, A. R.; Lipton, M. S.; Hoyt, D. W.; Northen, T. R.; Hagerman, A. E.; Wrighton, K. C. Decrypting Bacterial Polyphenol Metabolism in an Anoxic Wetland Soil. *Nat. Commun.* **2021**, *12* (1). https://doi.org/10.1038/s41467-021-22765-1.

(16) Swenson, T. L. Untargeted Soil Metabolomics Methods for Analysis of Extractable Organic Matter. *Soil Biol. Biochem.* **2015**, *80*, 189–198. https://doi.org/doi:10.1016/j.soilbio.2014.10.007.

(17) Bhattacharjya, S.; Ghosh, A.; Sahu, A.; Agnihotri, R.; Pal, N.; Sharma, P.; Manna, M. C.; Sharma, M. P.; Singh, A. B. Utilizing Soil Metabolomics to Investigate the Untapped Metabolic Potential of Soil Microbial Communities and Their Role in Driving Soil Ecosystem Processes: A Review. *Appl. Soil Ecol.* **2024**, *195*, 105238.

(18) Withers, E.; Hill, P. W.; Chadwick, D. R.; Jones, D. L. Use of Untargeted Metabolomics for Assessing Soil Quality and Microbial Function. *Soil Biol. Biochem.* **2020**, *143*, 107758. https://doi.org/10.1016/j.soilbio.2020.107758.

(19) Li, W.; Liu, X.; Xia, Q.; Gao, Z.; Zheng, W.; Zhai, B.; Yang, Z. Untargeted Metabolomics to Study Changes in Soil Microbial Community in Response to Tillage Practices. *Appl. Soil Ecol.* **2024**, *199*, 105409.

(20) Brown, R. W.; Chadwick, D. R.; Zang, H.; Jones, D. L. Use of Metabolomics to Quantify Changes in Soil Microbial Function in Response to Fertiliser Nitrogen Supply and Extreme Drought. *Soil Biol. Biochem.* **2021**, *160*, 108351. https://doi.org/10.1016/j.soilbio.2021.108351.

(21) Lai, X.; Duan, W.; Zhang, W.; Peng, Z.; Wang, X.; Wang, H.; Qi, X.; Pi, H.; Chen, K.; Yan, L. Integrative Analysis of Microbiome and Metabolome Revealed the Effect of Microbial Inoculant on Microbial Community Diversity and Function in Rhizospheric Soil under Tobacco Monoculture. *Microbiol. Spectr.* **2024**, *12* (8). https://doi.org/10.1128/spectrum.04046-23.

(22) De La Rosa, J. M.; González-Pérez, J. A.; González-Vázquez, R.; Knicker, H.; López-Capel, E.; Manning, D. A. C.; González-Vila, F. J. Use of Pyrolysis/GC–MS Combined with Thermal Analysis to Monitor C and N Changes in Soil Organic Matter from a Mediterranean Fire Affected Forest. *CATENA* **2008**, *74* (3), 296–303. https://doi.org/10.1016/j.catena.2008.03.004.

(23) Jiménez-González, M. A.; De La Rosa, J. M.; Jiménez-Morillo, N. T.; Almendros, G.; González-Pérez, J. A.; Knicker, H. Post-Fire Recovery of Soil Organic Matter in a Cambisol from Typical Mediterranean Forest in Southwestern Spain. *Sci. Total Environ.* **2016**, *572*, 1414–1421. https://doi.org/10.1016/j.scitotenv.2016.02.134.

(24) Faria, S. R.; De La Rosa, J. M.; Knicker, H.; González-Pérez, J. A.; Keizer, J. J. Molecular Characterization of Wildfire Impacts on Organic Matter in Eroded Sediments and Topsoil in Mediterranean Eucalypt Stands. *CATENA* **2015**, *135*, 29–37. https://doi.org/10.1016/j.catena.2015.07.007.

(25) Jiménez-Morillo, N. T.; de la Rosa, J. M.; Waggoner, D.; Almendros, G.; González-Vila, F. J.; González-Pérez, J. A. Fire Effects in the Molecular Structure of Soil Organic Matter Fractions under Quercus Suber Cover. *CATENA* **2016**, *145*, 266–273.

(26) Jiménez-Morillo, N. T.; Almendros, G.; De la Rosa, J. M.; Jordán, A.; Zavala, L. M.; Granged, A. J. P.; González-Pérez, J. A. Effect of a Wildfire and of Post-Fire Restoration Actions in the Organic Matter Structure in Soil Fractions. *Sci. Total Environ.* **2020**, *728*, 138715. https://doi.org/10.1016/j.scitotenv.2020.138715.

(27) Zeba, N.; Berry, T. D.; Fischer, M. S.; Traxler, M. F.; Whitman, T. Soil Carbon Mineralization and Microbial Community Dynamics in Response to Pyrogenic Organic Matter Addition. *Soil Biol. Biochem.* **2024**, *191*, 109328.

(28) Schymanski, E. L.; Jeon, J.; Gulde, R.; Fenner, K.; Ruff, M.; Singer, H. P.; Hollender, J. Identifying Small Molecules via High Resolution Mass Spectrometry: Communicating Confidence. *Environ. Sci. Technol.* **2014**, *48* (4), 2097–2098. https://doi.org/10.1021/es5002105.

(29) VanderRoest, J. P.; Fowler, J. A.; Rhoades, C. C.; Roth, H. K.; Broeckling, C. D.; Fegel, T. S.; McKenna, A. M.; Bechtold, E. K.; Boot, C. M.; Wilkins, M. J.; Borch, T. Fire Impacts on the Soil Metabolome and Organic Matter Biodegradability. *Environ. Sci. Technol.* **2024**, *58*, 4167–4180. https://doi.org/10.1021/acs.est.3c09797.

(30) Woolet, J.; Whitman, T. Pyrogenic Organic Matter Effects on Soil Bacterial Community Composition. *Soil Biol. Biochem.* **2020**, *141*, 107678. https://doi.org/10.1016/j.soilbio.2019.107678.

(31) Liang, B.; Lehmann, J.; Solomon, D.; Sohi, S.; Thies, J. E.; Skjemstad, J. O.; Luizao, F. J.; Engelhard, M. H.; Neves, E. G.; Wirick, S. Stability of Biomass-Derived Black Carbon in Soils. *Geochim. Cosmochim. Acta* **2008**, *72*, 6069–6078.

(32) Zimmerman, A. R. Abiotic and Microbial Oxidation of Laboratory-Produced Black Carbon (Biochar). *Environ. Sci. Technol.* **2010**, *44* (4), 1295–1301. https://doi.org/10.1021/es903140c.

(33) Kuzyakov, Y.; Subbotina, I.; Chen, H.; Bogomolova, I.; Xu, X. Black Carbon Decomposition and Incorporation into Soil Microbial Biomass Estimated by 14C Labeling. *Soil Biol. Biochem.* **2009**, *41*, 210–219.

(34) Monika S. Fischer; Frances G. Stark; Timothy D. Berry; Nayela Zeba; Thea Whitman; Matthew F. Traxler. Pyrolyzed Substrates Induce Aromatic Compound Metabolism in the Post-Fire Fungus, Pyronema Domesticum. *Front. Microbiol.* **2021**, *12*, 1–12.

(35) De La Rosa, J. M.; Miller, A. Z.; Knicker, H. Soil-Borne Fungi Challenge the Concept of Long-Term Biochemical Recalcitrance of Pyrochar. *Sci. Rep.* **2018**, *8*. https://doi.org/10.1038/s41598-018-21257-5.

(36) Goranov, A. I.; Wozniak, A. S.; Bostick, K. W.; Zimmerman, A. R.; Mitra, S.; Hatcher, P. G. Microbial Labilization and Diversification of Pyrogenic Dissolved Organic Matter. *Biogeosciences* **2022**, *19* (5), 1491–1514. https://doi.org/10.5194/bg-19-1491-2022.

(37) Bostick, K. W.; Zimmerman, A. R.; Goranov, A. I.; Mitra, S.; Hatcher, P. G.; Wozniak, A. S. Biolability of Fresh and Photodegraded Pyrogenic Dissolved Organic Matter From Laboratory-Prepared Chars. *J. Geophys. Res. Biogeosciences* **2021**, *126* (5), 1–17. https://doi.org/10.1029/2020jg005981.

(38) Johnson, D. B.; Yedinak, K. M.; Sulman, B. N.; Berry, T. D.; Kruger, K.; Whitman, T. Effects of Fire and Fire-Induced Changes in Soil Properties on Post-Burn Soil Respiration. *Fire Ecol.* **2024**, *20* (1). https://doi.org/10.1186/s42408-024-00328-1.

(39) Johnson, D. B.; Woolet, J.; Yedinak, K. M.; Whitman, T. Experimentally Determined Traits Shape Bacterial Community Composition One and Five Years Following Wildfire. *Nat. Ecol. Amp Evol.* **2023**, *7* (9), 1419–1431. https://doi.org/10.1038/s41559-023-02135-4.

(40) Cao, M.; Ma, H.; Ye, Y.; Li, S.-A.; Cao, X.; Huang, H.; Li, Z.; Cui, F. Wildfire-Derived Pyrogenic Dissolved Organic Matter (pyDOM) Enhances Riverine DOM Reactivities and Nitrogen Metabolisms. *Environ. Sci. Technol.* **2025**, *59* (23), 11597–11606. https://doi.org/10.1021/acs.est.5c01794.

(41) Promi, S. I.; Gardner, C. M.; Hohner, A. K. Biodegradability of Unheated and Laboratory Heated Dissolved Organic Matter. *Environ. Sci. Process. Impacts* **2024**. https://doi.org/10.1039/d3em00383c.

(42) Keeley, J. E. Fire Intensity, Fire Severity and Burn Severity: A Brief Review and Suggested Usage. *Int. J. Wildland Fire* **2009**, *18* (1), 116–126. https://doi.org/10.1071/wf07049.

(43) Parson, A.; Robichaud, P. R.; Lewis, S. A.; Napper, C.; Clark, J. T. Field Guide for Mapping Post-Fire Soil Burn Severity. *Gen Tech Rep RMRS-GTR-243 Fort Collins CO US Dep. Agric. For. Serv. Rocky Mt. Res. Stn. 49 P* **2010**. https://doi.org/10.2737/RMRS-GTR-243.

(44) Alexander Mountain Fire Burned Area Summary Burned Area Report. **2024**.

(45) Ambient Weather Network - 33 Mountain Peak Ln, Drake Station (Accessed 10/15/2024).

(46) Whitman, T.; Whitman, E.; Woolet, J.; Flannigan, M. D.; Thompson, D. K.; Parisien, M.-A. Soil Bacterial and Fungal Response to Wildfires in the Canadian Boreal Forest across a Burn Severity Gradient. *Soil Biol. Biochem.* **2019**, *138*, 107571. https://doi.org/10.1016/j.soilbio.2019.107571.

(47) Pulido-Chavez, M. F.; Alvarado, E. C.; DeLuca, T. H.; Edmonds, R. L.; Glassman, S. I. High-Severity Wildfire Reduces Richness and Alters Composition of Ectomycorrhizal Fungi in Low-Severity Adapted Ponderosa Pine Forests. *For. Ecol. Manag.* **2021**, *485*, 118923.

(48) Caifa, M. V.; Nelson, A. R.; Borch, T.; Roth, H. K.; Fegel, T.; Rhoades, C. C.; Wilkins, M. J.; Glassman, S. I. Distinct Fungal and Bacterial Responses to Fire Severity and Soil Depth across a Ten-Year Wildfire Chronosequence in Bettle-Killed Lodgepole Pine Forests. *For. Ecol. Manag.* **2023**, *544*, 121160.

(49) SoilWeb - Https://Casoilresource.Lawr.Ucdavis.Edu/Gmap/ - Accessed 10/21/2024.

(50) Colorado Climate Center - Colorado State University - WATERDALE Station - Accessed 10/18/2024 - Https://Climate.Colostate.Edu/Data_access_new.Html.

(51) Dittmar, T.; Koch, B.; Hertkorn, N.; Kattner, G. A Simple and Efficient Method for the Solid-Phase Extraction of Dissolved Organic Matter (SPE-DOM) from Seawater. *Limnol. Oceanogr. Methods* **2008**, *6* (6), 230–235. https://doi.org/10.4319/lom.2008.6.230.

(52) Xian, F.; Hendrickson, C. L.; Blakney, G. T.; Beu, S. C.; Marshall, A. G. Automated Broadband Phase Correction of Fourier Transform Ion Cyclotron Resonance Mass Spectra. *Anal. Chem.* **2010**, *82* (21), 8807–8812. https://doi.org/10.1021/ac101091w.

(53) Savory, J. J.; Kaiser, N. K.; McKenna, A. M.; Xian, F.; Blakney, G. T.; Rodgers, R. P.; Hendrickson, C. L.; Marshall, A. G. Parts-Per-Billion Fourier Transform Ion Cyclotron Resonance Mass Measurement Accuracy with a “Walking” Calibration Equation. *Anal. Chem.* **2011**, *83* (5), 1732–1736. https://doi.org/10.1021/ac102943z.

(54) Kendrick, E. A Mass Scale Based on CH_2 = 14.0000 for High Resolution Mass Spectrometry of Organic Compounds. *Anal. Chem.* **1963**, *35* (13), 2146–2154. https://doi.org/10.1021/ac60206a048.

(55) Hughey, C. A.; Hendrickson, C. L.; Rodgers, R. P.; Marshall, A. G.; Qian, K. Kendrick Mass Defect Spectrum: A Compact Visual Analysis for Ultrahigh-Resolution Broadband Mass Spectra. *Anal. Chem.* **2001**, *73*, 4676–4681. https://doi.org/10.1021/ac010560.

(56) Corilo, Y. E. *PetroOrg Softw.* **2014**, *Florida State University, Omics LLC: Tallahassee, FL*.

(57) Koch, B. P.; Dittmar, T. From Mass to Structure: An Aromaticity Index for High-Resolution Mass Data of Natural Organic Matter. *Rapid Commun. Mass Spectrom.* **2006**, *20* (5), 926–932. https://doi.org/10.1002/rcm.2386.

(58) Koch, B. P.; Dittmar, T. From Mass to Structure: An Aromaticity Index for High-Resolution Mass Data of Natural Organic Matter. *Rapid Commun. Mass Spectrom.* **2016**, *30* (1), 250–250. https://doi.org/10.1002/rcm.7433.

(59) Riedel, T.; Biester, H.; Dittmar, T. Molecular Fractionation of Dissolved Organic Matter with Metal Salts. *Environ. Sci. Technol.* **2012**, *46* (8), 4419–4426. https://doi.org/10.1021/es203901u.

(60) Schmid, R.; Heuckeroth, S.; Korf, A.; Smirnov, A.; Myers, O.; Dyrlund, T. S.; Bushuiev, R.; Murray, K. J.; Hoffmann, N.; Lu, M.; Sarvepalli, A.; Zhang, Z.; Fleischauer, M.; Dührkop, K.; Wesner, M.; Hoogstra, S. J.; Rudt, E.; Mokshyna, O.; Brungs, C.; Ponomarov, K.; Mutabdžija, L.; Damiani, T.; Pudney, C. J.; Earll, M.; Helmer, P. O.; Fallon, T. R.; Schulze, T.; Rivas-Ubach, A.; Bilbao, A.; Richter, H.; Nothias, L.-F.; Wang, M.; Orešič, M.; Weng, J.-K.; Böcker, S.; Jeibmann, A.; Hayen, H.; Karst, U.; Dorrestein, P. C.; Petras, D.; Du, X.; Pluskal, T. Integrative Analysis of Multimodal Mass Spectrometry Data in MZmine 3. *Nat. Biotechnol.* **2023**, *41* (4), 447–449. https://doi.org/10.1038/s41587-023-01690-2.

(61) Coble, P. G. Characterization of Marine and Terrestrial DOM in Seawater Using Excitation-Emission Matrix Spectroscopy. *Mar. Chem.* **1996**, *51* (4), 325–346. https://doi.org/10.1016/0304-4203(95)00062-3.

(62) Ohno, T. Fluorescence Inner-Filtering Correction for Determining the Humification Index of Dissolved Organic Matter. *Environ. Sci. Technol.* **2002**, *36* (4), 742–746. https://doi.org/10.1021/es0155276.

(63) Huguet, A.; Vacher, L.; Relexans, S.; Saubusse, S.; Froidefond, J. M.; Parlanti, E. Properties of Fluorescent Dissolved Organic Matter in the Gironde Estuary. *Org. Geochem.* **2009**, *40* (6), 706–719. https://doi.org/10.1016/j.orggeochem.2009.03.002.

(64) Cory, R. M.; McKnight, D. M. Fluorescence Spectroscopy Reveals Ubiquitous Presence of Oxidized and Reduced Quinones in Dissolved Organic Matter. *Environ. Sci. Technol.* **2005**, *39* (21), 8142–8149. https://doi.org/10.1021/es0506962.

(65) Limmer, M. A.; Mann, J.; Amaral, D. C.; Vargas, R.; Seyfferth, A. L. Silicon-Rich Amendments in Rice Paddies: Effects on Arsenic Uptake and Biogeochemistry. *Sci. Total Environ.* **2018**, *624*, 1360–1368. https://doi.org/10.1016/j.scitotenv.2017.12.207.

(66) *Methods of Soil Analysis Part 1 - Physical and Mineralogical Methods.*; Soil Science Society of America. 1986. Pages 1-1188. ISBN-13: 978-0-89118-811-7.

(67) Parada, A. E.; Needham, D. M.; Fuhrman, J. A. Every Base Matters: Assessing Small Subunit rRNA Primers for Marine Microbiomes with Mock Communities, Time Series and Global Field Samples. *Environ. Microbiol.* **2016**, *18* (5), 1403–1414. https://doi.org/10.1111/1462-2920.13023.

(68) Apprill, A.; McNally, S.; Parsons, R.; Weber, L. Minor Revision to V4 Region SSU rRNA 806R Gene Primer Greatly Increases Detection of SAR11 Bacterioplankton. *Aquat. Microb. Ecol.* **2015**, *75* (2), 129–137.

(69) White, David; Drummond, James; Fuqua, Clay. *The Physiology and Biochemistry of Prokaryotes*; Oxford University Press, 2012.

(70) Bolyen, E.; Rideout, J. R.; Dillon, M. R.; Bokulich, N. A.; Abnet, C. C.; Al-Ghalith, G. A.; Alexander, H.; Alm, E. J.; Arumugam, M.; Asnicar, F.; Bai, Y.; Bisanz, J. E.; Bittinger, K.; Brejnrod, A.; Brislawn, C. J.; Brown, C. T.; Callahan, B. J.; Caraballo-Rodríguez, A. M.; Chase, J.; Cope, E. K.; Da Silva, R.; Diener, C.; Dorrestein, P. C.; Douglas, G. M.; Durall, D. M.; Duvallet, C.; Edwardson, C. F.; Ernst, M.; Estaki, M.; Fouquier, J.; Gauglitz, J. M.; Gibbons, S. M.; Gibson, D. L.; Gonzalez, A.; Gorlick, K.; Guo, J.; Hillmann, B.; Holmes, S.; Holste, H.; Huttenhower, C.; Huttley, G. A.; Janssen, S.; Jarmusch, A. K.; Jiang, L.; Kaehler, B. D.; Kang, K. B.; Keefe, C. R.; Keim, P.; Kelley, S. T.; Knights, D.; Koester, I.; Kosciolek, T.; Kreps, J.; Langille, M. G. I.; Lee, J.; Ley, R.; Liu, Y.-X.; Loftfield, E.; Lozupone, C.; Maher, M.; Marotz, C.; Martin, B. D.; McDonald, D.; McIver, L. J.; Melnik, A. V.; Metcalf, J. L.; Morgan, S. C.; Morton, J. T.; Naimey, A. T.; Navas-Molina, J. A.; Nothias, L. F.; Orchanian, S. B.; Pearson, T.; Peoples, S. L.; Petras, D.; Preuss, M. L.; Pruesse, E.; Rasmussen, L. B.; Rivers, A.; Robeson, M. S.; Rosenthal, P.; Segata, N.; Shaffer, M.; Shiffer, A.; Sinha, R.; Song, S. J.; Spear, J. R.; Swafford, A. D.; Thompson, L. R.; Torres, P. J.; Trinh, P.; Tripathi, A.; Turnbaugh, P. J.; Ul-Hasan, S.; Van Der Hooft, J. J. J.; Vargas, F.; Vázquez-Baeza, Y.; Vogtmann, E.; Von Hippel, M.; Walters, W.; Wan, Y.; Wang, M.; Warren, J.; Weber, K. C.; Williamson, C. H. D.; Willis, A. D.; Xu, Z. Z.; Zaneveld, J. R.; Zhang, Y.; Zhu, Q.; Knight, R.; Caporaso, J. G. Reproducible, Interactive, Scalable and Extensible Microbiome Data Science Using QIIME 2. *Nat. Biotechnol.* **2019**, *37* (8), 852–857. https://doi.org/10.1038/s41587-019-0209-9.

(71) Callahan, B. J.; McMurdie, P. J.; Rosen, M. J.; Han, A. W.; Johnson, A. J. A.; Holmes, S. P. DADA2: High-Resolution Sample Inference from Illumina Amplicon Data. *Nat. Methods* **2016**, *13* (7), 581–583. https://doi.org/10.1038/nmeth.3869.

(72) Bokulich, N. A.; Kaehler, B. D.; Rideout, J. R.; Dillon, M.; Bolyen, E.; Knight, R.; Huttley, G. A.; Gregory Caporaso, J. Optimizing Taxonomic Classification of Marker-Gene Amplicon Sequences with QIIME 2's Q2-Feature-Classifier Plugin. *Microbiome* **2018**, *6* (1), 1–17. https://doi.org/10.1186/s40168-018-0470-z.

(73) Quast, C.; Pruesse, E.; Yilmaz, P.; Gerken, J.; Schweer, T.; Yarza, P.; Peplies, J.; Glöckner, F. O. The SILVA Ribosomal RNA Gene Database Project: Improved Data Processing and Web-Based Tools. *Nucleic Acids Res.* **2013**, *41*, 590–596.

(74) Robeson, M. S.; O'Rourke, D. R.; Kaehler, B. D.; Ziemski, M.; Dillon, M. R.; Foster, J. T.; Bokulich, N. A. RESCRIPt: Reproducible Sequence Taxonomy Reference Database Management. *PLOS Comput. Biol.* **2021**, *17* (11), 1–37. https://doi.org/10.1371/journal.pcbi.1009581.

(75) Kõljalg, U.; Nilsson, H. R.; Schigel, D.; Tedersoo, L.; Larsson, K.-H.; May, T. W.; Taylor, A. F. S.; Jeppesen, T. S.; Frøslev, T. G.; Lindahl, B. D.; Põldmaa, K.; Saar, I.; Suija, A.; Savchenko, A.; Yatsiuk, I.; Adojaan, K.; Ivanov, F.; Piirmann, T.; Pöhönen, R.; Zirk, A.; Abarenkov, K. The Taxon Hypothesis Paradigm—On the Unambiguous Detection and Communication of Taxa. *Microorganisms* **2020**, *8* (12), 1910. https://doi.org/10.3390/microorganisms8121910.

(76) Nilsson, R. H.; Anslan, S.; Bahram, M.; Wurzbacher, C.; Baldrian, P.; Tedersoo, L. Mycobiome Diversity: High-Throughput Sequencing and Identification of Fungi. *Nat. Rev. Microbiol.* **2019**, *17* (2), 95–109. https://doi.org/10.1038/s41579-018-0116-y.

(77) Oksanen, J.; Simpson, G.; Blanchet, F. G.; Kindt, R.; Legendre, P.; Minchin, P.; hara, R.; Solymos, P.; STEVENS, H.; Szöcs, E.; Wagner, H.; Barbour, M.; Bedward, M.; Bolker, B.;

Borcard, D.; Carvalho, G.; Chirico, M.; De Cáceres, M.; Durand, S.; Weedon, J. *Vegan Community Ecology Package Version 2.6-2 April 2022*; 2022.

(78) Anderson, M. J. Distance-Based Tests for Homogeneity of Multivariate Dispersions. *Biometrics* **2006**, *62* (1), 245–253. https://doi.org/10.1111/j.1541-0420.2005.00440.x.

(79) Wickham, H. *Ggplot2*; 2016. https://doi.org/10.1007/978-3-319-24277-4.

(80) Nguyen, N. H.; Song, Z.; Bates, S. T.; Branco, S.; Tedersoo, L.; Menke, J.; Schilling, J. S.; Kennedy, P. G. FUNGuild: An Open Annotation Tool for Parsing Fungal Community Datasets by Ecological Guild. *Fungal Ecol.* **2016**, *20*, 241–248.

(81) Santos, F.; Russell, D.; Berhe, A. A. Thermal Alteration of Water Extractable Organic Matter in Climosequence Soils from the Sierra Nevada, California. *J. Geophys. Res. Biogeosciences* **2016**, *121* (11), 2877–2885. https://doi.org/10.1002/2016jg003597.

(82) Bahureksa, W.; Young, R. B.; McKenna, A. M.; Chen, H.; Thorn, K. A.; Rosario-Ortiz, F. L.; Borch, T. Nitrogen Enrichment during Soil Organic Matter Burning and Molecular Evidence of Maillard Reactions. *Environ. Sci. Technol.* **2022**, *56* (7), 4597–4609. https://doi.org/10.1021/acs.est.1c06745.

(83) Cawley, K. M.; Hohner, A. K.; Podgorski, D. C.; Cooper, W. T.; Korak, J. A.; Rosario-Ortiz, F. L. Molecular and Spectroscopic Characterization of Water Extractable Organic Matter from Thermally Altered Soils Reveal Insight into Disinfection Byproduct Precursors. *Environ. Sci. Technol.* **2017**, *51* (2), 771–779. https://doi.org/10.1021/acs.est.6b05126.

(84) Zhang, Q.; Wang, Y.; Guan, P.; Zhang, P.; Mo, X.; Yin, G.; Qu, B.; Xu, S.; He, C.; Shi, Q.; Zhang, G.; Dittmar, T.; Wang, J. Temperature Thresholds of Pyrogenic Dissolved Organic Matter in Heating Experiments Simulating Forest Fires. *Environ. Sci. Technol.* **2023**, *57*, 17291–17301.

(85) Hohner, A. K.; Rhoades, C. C.; Wilkerson, P.; Rosario-Ortiz, F. L. Wildfires Alter Forest Watersheds and Threaten Drinking Water Quality. *Acc. Chem. Res.* **2019**, *52* (5), 1234–1244. https://doi.org/10.1021/acs.accounts.8b00670.

(86) Knicker, H. How Does Fire Affect the Nature and Stability of Soil Organic Nitrogen and Carbon? A Review. *Biogeochemistry* **2007**, *85* (1), 91–118. https://doi.org/10.1007/s10533-007-9104-4.

(87) Jian, M.; Berli, M.; Ghezzehei, T. A. Soil Structural Degradation During Low-Severity Burns. *Geophys. Res. Lett.* **2018**, *45* (11), 5553–5561. https://doi.org/10.1029/2018GL078053.

(88) Jian, M.; Berhe, A. A.; Berli, M.; Ghezzehei, T. A. Vulnerability of Physically Protected Soil Organic Carbon to Loss Under Low Severity Fires. *Front. Environ. Sci.* **2018**, *6*. https://doi.org/10.3389/fenvs.2018.00066.

(89) Smith, J. E.; Cowan, A. D.; Fitzgerald, S. A. Soil Heating during the Complete Combustion of Mega-Logs and Broadcast Burning in Central Oregon USA Pumice Soils. *Int. J. Wildland Fire 2511 1202-1207* **2016**, *25*, 1202–1207. https://doi.org/10.1071/WF16016.

(90) McKinney, S. T. Systematic Review and Meta-Analysis of Fire Regime Research in Ponderosa Pine (Pinus Ponderosa) Ecosystems, Colorado, USA. *Fire Ecol.* **2019**, *15* (1), 38. https://doi.org/10.1186/s42408-019-0056-6.

(91) Kyoto Encyclopedia of Genes and Genomes (KEGG) Database. *KEGG COMPOUND: C05984*. https://www.kegg.jp/entry/C05984 (accessed 2025-12-04).

(92) Kyoto Encyclopedia of Genes and Genomes (KEGG) Database. *KEGG COMPOUND: C06672*. https://www.kegg.jp/entry/C06672 (accessed 2025-12-04).

(93) Koenig, K.; Andreesen, J. R. Molybdenum Involvement in Aerobic Degradation of 2-Furoic Acid by Pseudomonas Putida Fu1. *Appl. Environ. Microbiol.* **1989**, *55* (7), 1829–1834. https://doi.org/10.1128/aem.55.7.1829-1834.1989.

(94) Palleroni, N. J. Pseudomonas. In *Bergey's Manual of Systematics of Archaea and Bacteria*; John Wiley & Sons, Ltd, 2015; pp 1–1. https://doi.org/10.1002/9781118960608.gbm01210.

(95) Myers-Pigg, A. N.; Louchouarn, P.; Amon, R. M. W.; Prokushkin, A.; Pierce, K.; Rubtsov, A. Labile Pyrogenic Dissolved Organic Carbon in Major Siberian Arctic Rivers: Implications for Wildfire-Stream Metabolic Linkages. *Geophys. Res. Lett.* **2015**, *42* (2), 377–385. https://doi.org/10.1002/2014gl062762.

(96) You, C.; Wang, J.; Dong, X.; Xu, C. Geochemistry of Vegetation Fires Using Levoglucosan: A Review. *Environ. Chem. Lett.* **2025**. https://doi.org/10.1007/s10311-025-01826-7.

(97) Kyoto Encyclopedia of Genes and Genomes (KEGG) Database. *KEGG COMPOUND: C00065*. https://www.kegg.jp/entry/C00065 (accessed 2025-12-04).

(98) The Human Metabolome Database. *Showing metabocard for Serine (HMDB0000187)*. https://www.hmdb.ca/metabolites/HMDB0000187 (accessed 2025-12-04).

(99) Kyoto Encyclopedia of Genes and Genomes (KEGG) Database. *KEGG COMPOUND: C00156*. https://www.kegg.jp/entry/C00156 (accessed 2025-12-04).

(100) Karegoudar, T. B.; Chae, J. C.; Kim, C. K. Catabolism of 4-Hydroxybenzoic Acid by Pseudomonas Sp. DJ-12. *J. Microbiol.* **1999**, *37* (3), 123–127.

(101) National Library of Medicine - National Center for Biotechnology Information. *N-Acetyl-D-Glucosamine*. https://pubchem.ncbi.nlm.nih.gov/compound/N-Acetyl-D-Glucosamine (accessed 2025-12-04).

(102) The Human Metabolome Database. *Showing metabocard for Glycerol (HMDB0000131)*. https://www.hmdb.ca/metabolites/HMDB0000131 (accessed 2025-12-04).

(103) Kyoto Encyclopedia of Genes and Genomes (KEGG) Database. *KEGG COMPOUND: C00116*. https://www.kegg.jp/entry/C00116 (accessed 2025-12-04).

(104) Bowman, A. P.; Blakney, G. T.; Hendrickson, C. L.; Ellis, S. R.; Heeren, R. M. A.; Smith, D. F. Ultra-High Mass Resolving Power, Mass Accuracy, and Dynamic Range MALDI Mass Spectrometry Imaging by 21-T FT-ICR MS. *Anal. Chem.* **2020**, *92* (4), 3133–3142. https://doi.org/10.1021/acs.analchem.9b04768.

(105) Bahureksa, W.; Borch, T.; Young, R. B.; Weisbrod, C. R.; Blakney, G. T.; McKenna, A. M. Improved Dynamic Range, Resolving Power, and Sensitivity Achievable with FT-ICR Mass Spectrometry at 21 T Reveals the Hidden Complexity of Natural Organic Matter. *Anal. Chem.* **2022**, *94* (6), 2973–2980. https://doi.org/10.1021/acs.analchem.2c02377.

(106) D'Andrilli, J.; Cooper, W. T.; Foreman, C. M.; Marshall, A. G. An Ultrahigh-resolution Mass Spectrometry Index to Estimate Natural Organic Matter Lability. *Rapid Commun. Mass Spectrom.* **2015**, *29* (24), 2385–2401. https://doi.org/10.1002/rcm.7400.

(107) Battin, T. J.; Kaplan, L. A.; Findlay, S.; Hopkinson, C. S.; Marti, E.; Packman, A. I.; Newbold, J. D.; Sabater, F. Biophysical Controls on Organic Carbon Fluxes in Fluvial Networks. *Nat. Geosci.* **2008**, *1* (2), 95–100. https://doi.org/10.1038/ngeo101.

(108) van Krevelen, D. W. Graphical-Statistical Method for the Study of Structure and Reaction Processes of Coal. *Fuel* **1950**, *29*, 269–284.

(109) Fegel, T.; Boot, C. M.; Broeckling, C. D.; Baron, J. S.; Hall, E. K. Assessing the Chemistry and Bioavailability of Dissolved Organic Matter From Glaciers and Rock Glaciers. *J. Geophys. Res. Biogeosciences* **2019**, *124* (7), 1988–2004. https://doi.org/10.1029/2018jg004874.

(110) Fegel, T. S.; Boot, C. M.; Covino, T. P.; Elder, K.; Hall, E. K.; Starr, B.; Stegen, J.; Rhoades, C. C. Amount and Reactivity of Dissolved Organic Matter Export Are Affected by Land Cover Change from Old-growth to Second-growth Forests in Headwater Ecosystems. *Hydrol. Process.* **2021**, *35* (8). https://doi.org/10.1002/hyp.14343.

(111) Worrall, F.; Howden, N. J. K.; Burt, T. P. BOD as a Measure of Fluvial Organic Matter Lability—The Decoupling of O_2 Consumption From CO_2 Production. *J. Geophys. Res. Biogeosciences* **2021**, *126* (12). https://doi.org/10.1029/2021jg006401.

(112) LaRowe, D. E.; Van Cappellen, P. Degradation of Natural Organic Matter: A Thermodynamic Analysis. *Geochim. Cosmochim. Acta* **2011**, *75* (8), 2030–2042. https://doi.org/10.1016/j.gca.2011.01.020.

(113) Pulido-Chavez, M. F.; Randolph, J. W. J.; Zalman, C.; Larios, L.; Homyak, P. M.; Glassman, S. I. Rapid Bacterial and Fungal Successional Dynamics in First Year after Chaparral Wildfire. *Mol. Ecol.* **2023**, *32* (7), 1685–1707. https://doi.org/10.1111/mec.16835.

(114) Fowler, J. A.; Nelson, A. R.; Bechtold, E. K.; Paul, R.; Wettengel, A. M.; McNorvell, M. A.; Stevens-Rumann, C. S.; Fegel, T. S.; Anderson, E.; Rhoades, C. C.; Wilkins, M. J. Pile Burns as a Proxy for High Severity Wildfire Impacts on Soil Microbiomes. *Geoderma* **2024**, *448*, 116982. https://doi.org/10.1016/j.geoderma.2024.116982.

(115) Nelson, A. R.; Rhoades, C. C.; Fegel, T. S.; Roth, H. K.; Caiafa, M. V.; Glassman, S. I.; Borch, T.; Wilkins, M. J. Wildfire Impact on Soil Microbiome Life History Traits and Roles in Ecosystem Carbon Cycling. *ISME Commun.* **2024**. https://doi.org/10.1093/ismeco/ycae108.

(116) Fischer, M. S.; Patel, N. J.; de Lorimier, P. J.; Traxler, M. F. Prescribed Fire Selects for a Pyrophilous Soil Sub-Community in a Northern California Mixed Conifer Forest. *Environ. Microbiol.* **2023**, *25* (11), 2498–2515. https://doi.org/10.1111/1462-2920.16475.

(117) Krichels, A. H.; Stephens, E. Z.; Reid, C.; Barriga, M. F. P.; Ordoñez, M. E.; McLaren, J. R.; Kargul, M.; Larios, L.; Glassman, S. I.; Homyak, P. M. Wildfire-Induced Losses of Soil Particulate and Mineral-Associated Organic Carbon Persist for Over 4 Years in a Chaparral Ecosystem. *Glob. Change Biol.* **2025**, *31* (8), e70404. https://doi.org/10.1111/gcb.70404.

(118) Enright, D. J.; Frangioso, K. M.; Isobe, K.; Rizzo, D. M.; Glassman, S. I. Mega-fire in Redwood Tanoak Forest Reduces Bacterial and Fungal Richness and Selects for Pyrophilous Taxa That Are Phylogenetically Conserved. *Mol. Ecol.* **2022**, *31* (8), 2475–2493. https://doi.org/10.1111/mec.16399.

(119) Nelson, A. R.; Rhoades, C. C.; Fegel, T. S.; Roth, H. K.; Caiafa, M. V.; Glassman, S. I.; Borch, T.; Wilkins, M. J. Wildfire Impact on Soil Microbiome Life History Traits and Roles in Ecosystem Carbon Cycling. *ISME Commun.* **2024**, *4* (1), ycae108. https://doi.org/10.1093/ismeco/ycae108.

CHAPTER 6: SUMMARY, CONCLUSIONS, IMPLICATIONS, AND FUTURE DIRECTIONS

6.1 SUMMARY

Chapter 2 indicated that non-targeted mass spectrometry methods are needed to analyze low-molecular weight organic molecules in burned soils. Chapter 3 discovered that soils burned in pyrocosms were enriched in heterotrophic microbes, featured increased relative abundances of glycine, protocatechuate, and other metabolites, and respired more CO_2 in laboratory incubations compared to unburned soils. Chapter 4 featured soils from three different forested ecosystems heated in a muffle furnace and observed greater abundances of amino acids and peptides in 150 °C soils and greater abundances of aromatic metabolites, organic acids, and nitrogen-containing saccharides in 250 °C soils. In fact, 43 to 52 % of the detected metabolites across the tested forested ecosystems were significantly more abundant in the heated soils compared to the control soils. Chapter 5 examined SOM from unburned, low severity, and high severity soils within the 2024 Alexander Mountain Fire burn scar and reported that 96 % of the detected metabolites were either statistically similar or significantly greater in abundance in burned soils compared unburned soils. Additionally, burned soils exhibited on average 2.0 to 2.6x greater microbial metabolism of SOM and 1.4 to 2.5x greater CO_2 fluxes, respectively, compared to unburned soils.

6.2 CONCLUSIONS

Chapter 1 posed the following research questions: How do wildfires impact the soil metabolome, and how do abundances of soil metabolites change post-fire? Does SOM become more or less biodegradable after wildfires? How do these changes in soil metabolite content and SOM biodegradability influence biogeochemical carbon cycling and the propensity of burned soils to act more as carbon sources rather than as carbon sinks? These questions were answered by the following discoveries outlined in this dissertation: burned soils are enriched in metabolites

(Chapters 3-5), SOM from burned soils immediately post-fire can be more biodegradable than corresponding unburned soils (Chapters 3 and 5), and burned soils may act as carbon sources immediately after fire due to the metabolite enrichment and biodegradability enhancement (Chapters 3 and 5) (**Figure 6.1**). As Chapter 5 outlined (**Figure 5.28**), conceptual diagrams of SOM from burned soils now ought to feature a "fast cycling pool" comprised of enriched metabolites and more biodegradable SOM.

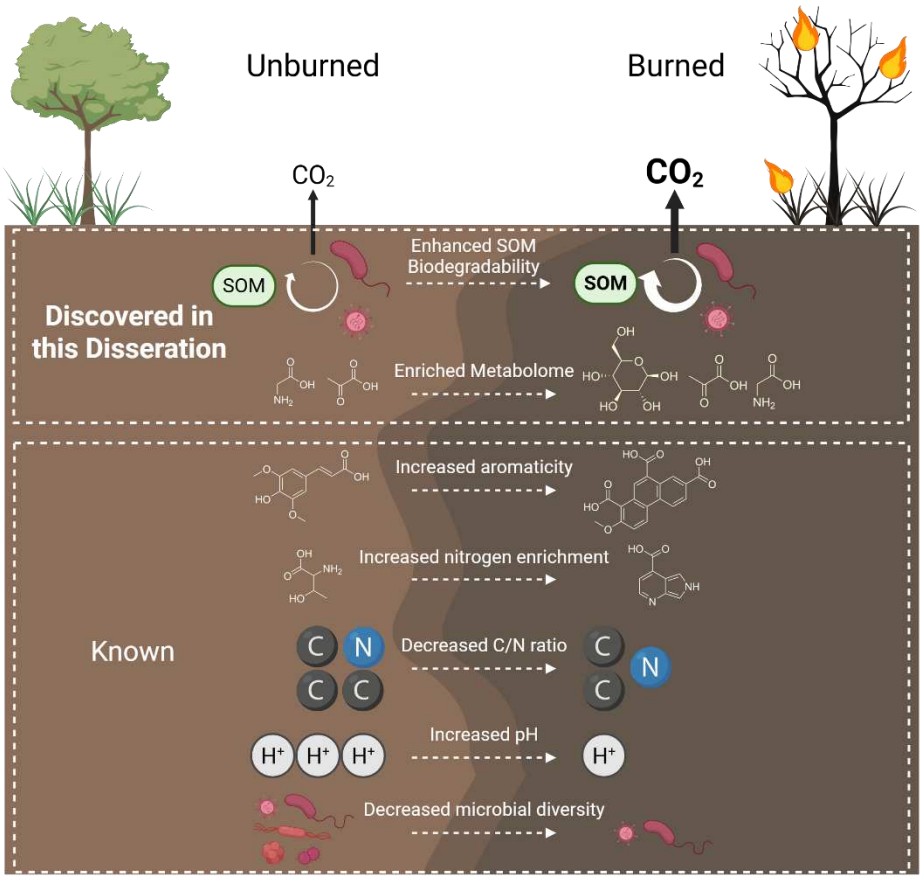

Figure 6.1. Conceptual diagram outlining major discoveries of this dissertation in conjunction with known phenomena related to wildfire impacts on soil chemistry and microbiology.

These major discoveries were largely consistent across experimental scales. Metabolomic profiles were distinct between unburned/control and burned/heated soils as exhibited by principal component analysis (PCA) scores plots in Chapters 3-5. Metabolite abundances and water extractable organic carbon values were generally greater in burned/heated soils compared to

unburned/control soils in Chapters 3-5. SOM from burned soils was more biodegradable than SOM from unburned soils based on soil CO_2 respiration incubations in Chapter 3 and biological oxygen demand incubations in Chapter 5. Such consistency was also observed in the microbial results in which burned soils were enriched in heterotrophic bacteria and archaea in Chapters 3 and 5. These consistent results bolster our confidence in our conclusions that burned soils feature increased metabolite abundances and enhanced SOM biodegradability shortly after fire.

6.3 IMPLICATIONS

The major implications of this dissertation relate to prescribed burning as a forest management strategy, post-fire microbial activity, and post-fire soil behaving as a carbon source vs. carbon sink. Prescribed burning (i.e. any supervised burn conducted to meet specific land management objectives) is a potential alternative to fire suppression as a forest management strategy.[1] Deliberately burning vegetation can prevent the buildup of hazardous vegetative fuel quantities that contribute to massive, high severity wildfires if ignited.[1] Additionally, if these prescribed burns are conducted at lower severity conditions, the resultant soil may be enriched in nutrients like metabolites and biodegradable SOM based on the results in this dissertation. Thus, not only will prescribed burning help prevent larger, devastating wildfires, it may also contribute to a healthy soil system with richer, more diverse SOM. This enriched SOM content could then drive soil microbial activity which is an essential first step in post-fire soil recovery. For example, providing metabolites and nutrients for ectomycorrhizal fungi (which form symbiotic relationships with trees such as lodgepole pine) could help re-establish those beneficial relationships, aiding post-fire forest recovery processes.[2,3] This increased microbial activity, while beneficial for producing a healthy soil system, may increase post-fire soil CO_2 emissions through microbial metabolism. In this dissertation, burned soils respired more CO_2 than unburned soils, both in

controlled experiments (Chapter 3) and in a burned forest (Chapter 5). Considering that soils contain the largest dynamic carbon stock on Earth (3,500 to 4,800 Pg) and that around 70% of the total global topsoil C is exposed to fire,[4,5] wildfire-burned soils may act as a substantial source of CO_2 emissions. Therefore, post-fire soils may act more as a carbon source than sink in the immediate aftermath of a wildfire which agrees with recent projections indicating that wildfires weaken the effectiveness of land carbon sinks.[6]

6.4 FUTURE DIRECTIONS

Future post-fire soil metabolomics studies can further elucidate wildfire impacts on soil chemistry and soil CO_2 emissions. While providing novel discoveries, this dissertation only focuses on the immediate aftermath of wildfires and soil heating across a monthly post-fire timeframe. While burned soils are enriched in metabolites and biodegradable SOM immediately following burning, the persistence of that metabolite enrichment and SOM biodegradability enhancement is unknown. Are metabolites enriched in post-fire soil one year, multiple years, or even decades after a wildfire? What about the enhanced biodegradable SOM content? I surmise that the flush of post-fire metabolites and biodegradable SOM persists for a few months post-fire but decreases with time due to microbes consuming and respiring that reactive SOM pool. Multiple years after a fire, I'd suspect that the metabolite profile and SOM biodegradability of once burned soil are similar to that of nearby unburned soil. However, that remains entirely unknown. Beyond temporal considerations, investigating changes in soil metabolomics and biodegradable SOM across varying ecosystems is required. This dissertation focused on coniferous forests in Colorado. While this is a relevant area to study wildfires, it represents one of the myriad of ecosystem types affected by wildfires. Would the conclusions from this dissertation be observed in post-fire chapparal forests in northern California, deciduous forests in southeast United States, boreal

forests of Canada, savannah grasslands in Africa, rainforests of South America, or broadleaf forests in China? Investigating the geographic extent of these results would provide a more accurate assessment of how post-fire soil metabolomics and biodegradable SOM influence soil CO_2 emissions on a global scale.

The metabolomics techniques in this dissertation are predominantly non-targeted analysis. Thus, extensive targeted metabolomics work has yet to be conducted within post-fire soils. Specific molecules should be targeted within burned soils to better understand post-fire soil biogeochemistry and forest recovery. For example, karrakins – a family of carboxylate esters – can promote seed germination.[7] Targeting for karrakins in post-fire soils could unlock a key mechanism driving post-fire reforestation. For example, forests that didn't recover well after a wildfire may be deficient in soil karrakin concentrations. Beyond karrakins, more aromatic intermediates produced during the degradation of aromatic SOM could be targeted to determine the extent to which post-fire microbes harness aromatic, condensed pyrogenic organic matter as a nutrient source.[8,9] Additionally, intermediates within the citric acid cycle (e.g. isocitrate or malate) could be targeted to assess adenosine triphosphate (ATP) generation in burned soils which may drive microbial activity. Such metabolomics analysis could be coupled with microbial metagenomics and metatranscriptomics analyses to further elucidate soil microbial responses to post-fire metabolite enrichment. Overall, targeted metabolomics would provide a more detailed understanding of how microbes are utilizing the enriched metabolite content while providing insight into mechanisms driving post-fire soil and forest recovery.

Additional instrumentation could be employed to detect more soil metabolites and account of the limitations of the instruments used in this dissertation. Traditional GC-MS only detects volatile, electron-impact ionizable metabolites found in GC-MS library databases. LC-MS only

detects metabolites that are, in this case, ionizable with positive-mode electrospray ionization and found within LC-MS library databases. To expand analytical scope, nuclear magnetic resonance (NMR) spectroscopy could be utilized. While less sensitive than mass spectrometry, NMR spectroscopy does not require ionization and does not preferentially detect molecules within a specific mass range, allowing for the detection of a unique pool of metabolites. NMR spectroscopy has been used to detect metabolites such as acetate, glycine betaine, and monomethylamine in environmental samples and could be utilized within a post-fire soil context to broaden the scope of detectable metabolites.[10,11] Fourier transform ion cyclotron resonance-mass spectrometry (FT ICR-MS)-based metabolomics is an emerging sector of metabolomics analysis with developing library databases that could also be employed.[12,13] Harnessing the mass accuracy and resolving power of FT ICR-MS alongside curated library databases could drastically expand metabolite identification in burned soils.

The increased CO_2 respiration from burned soils implies that burned soils may act more as carbon sources immediately following wildfires. However, to confirm this implication, more extensive soil CO_2 respiration measurements need to be conducted and incorporated into global climate models. Within climate models, these post-fire soil CO_2 respiration quantities can be compared to other CO_2 sources. Such comparisons will contextualize the role that post-fire soils may serve in intensifying climate change. Without this contextualization, the extent and impact that post-fires may have on CO_2 emissions remain unknown.

Overall, the field of post-fire soil metabolomics has been initiated by this dissertation. Further investigation is warranted to elucidate the climatic impacts of post-fire soil metabolite enrichment and SOM biodegradability enhancement.

CHAPTER 6 REFERENCES

(1) Santín, C.; Doerr, S. H. Fire Effects on Soils: The Human Dimension. *Philos. Trans. R. Soc. B Biol. Sci.* **2016**, *371* (1696), 20150171. https://doi.org/10.1098/rstb.2015.0171.

(2) Douglas, R. B.; Parker, V. T.; Cullings, K. W. Belowground Ectomycorrhizal Community Structure of Mature Lodgepole Pine and Mixed Conifer Stands in Yellowstone National Park. *For. Ecol. Manag.* **2005**, *208* (1), 303–317. https://doi.org/10.1016/j.foreco.2004.12.011.

(3) Anthony, M. A.; Crowther, T. W.; van der Linde, S.; Suz, L. M.; Bidartondo, M. I.; Cox, F.; Schaub, M.; Rautio, P.; Ferretti, M.; Vesterdal, L.; De Vos, B.; Dettwiler, M.; Eickenscheidt, N.; Schmitz, A.; Meesenburg, H.; Andreae, H.; Jacob, F.; Dietrich, H.-P.; Waldner, P.; Gessler, A.; Frey, B.; Schramm, O.; van den Bulk, P.; Hensen, A.; Averill, C. Forest Tree Growth Is Linked to Mycorrhizal Fungal Composition and Function across Europe. *ISME J.* **2022**, *16* (5), 1327–1336. https://doi.org/10.1038/s41396-021-01159-7.

(4) Pellegrini, A. F. A.; Harden, J.; Georgiou, K.; Hemes, K. S.; Malhotra, A.; Nolan, C. J.; Jackson, R. B. Fire Effects on the Persistence of Soil Organic Matter and Long-Term Carbon Storage. *Nat. Geosci.* **2021**, *15*, 5–13. https://doi.org/10.1038/s41561-021-00867-1.

(5) Boye, K.; Noël, V.; Tfaily, M. M.; Bone, S. E.; Williams, K. H.; John; Fendorf, S. Thermodynamically Controlled Preservation of Organic Carbon in Floodplains. *Nat. Geosci.* **2017**, *10* (6), 415–419. https://doi.org/10.1038/ngeo2940.

(6) Burton, C. A.; Kelley, D. I.; Burke, E.; Mathison, C.; Jones, C. D.; Betts, R. A.; Robertson, E.; Teixeira, J. C. M.; Cardoso, M.; Anderson, L. O. Fire Weakens Land Carbon Sinks before 1.5 °C. *Nat. Geosci.* **2024**, *17* (11), 1108–1114. https://doi.org/10.1038/s41561-024-01554-7.

(7) Lopez, A. M.; Avila, C. C. E.; VanderRoest, J. P.; Roth, H. K.; Fendorf, S.; Borch, T. Molecular Insights and Impacts of Wildfire-Induced Soil Chemical Changes. *Nat. Rev. Earth Environ.* **2024**, *5*, 431–446. https://doi.org/10.1038/s43017-024-00548-8.

(8) Nelson, A. R.; Narrowe, A. B.; Rhoades, C. C.; Fegel, T. S.; Daly, R. A.; Roth, H. K.; Chu, R. K.; Amundson, K. K.; Young, R. B.; Steindorff, A. S.; Mondo, S. J.; Grigoriev, I. V.; Salamov, A.; Borch, T.; Wilkins, M. J. Wildfire-Dependent Changes in Soil Microbiome Diversity and Function. *Nat. Microbiol.* **2022**, *7* (9), 1419–1430. https://doi.org/10.1038/s41564-022-01203-y.

(9) Fischer, M. S.; Stark, Frances G.; Berry, T. D.; Zeba, N.; Whitman, T.; Traxler, M. F. Pyrolyzed Substrates Induce Aromatic Compound Metabolism in the Post-Fire Fungus, Pyronema Domesticum. *Front. Microbiol.* **2021**, *12*, 1–12.

(10) Daly, R. A.; Borton, M. A.; Wilkins, M. J.; Hoyt, D. W.; Kountz, D. J.; Wolfe, R. A.; Welch, S. A.; Marcus, D. N.; Trexler, R. V.; MacRae, J. D.; Krzycki, J. A.; Cole, D. R.; Mouser, P. J.; Wrighton, K. C. Microbial Metabolisms in a 2.5-Km-Deep Ecosystem Created by Hydraulic Fracturing in Shales. *Nat. Microbiol.* **2016**, *1* (10), 16146. https://doi.org/10.1038/nmicrobiol.2016.146.

(11) Emwas, A.-H.; Roy, R.; McKay, R. T.; Tenori, L.; Saccenti, E.; Gowda, G. A. N.; Raftery, D.; Alahmari, F.; Jaremko, L.; Jaremko, M.; Wishart, D. S. NMR Spectroscopy for Metabolomics Research. *Metabolites* **2019**, *9* (7). https://doi.org/10.3390/metabo9070123.

(12) Cochran, D.; Powers, R. Fourier Transform Ion Cyclotron Resonance Mass Spectrometry Applications for Metabolomics. *Biomedicines* **2024**, *12* (8), 1786. https://doi.org/10.3390/biomedicines12081786.

(13) Coffey, N. R.; Dewey, C.; Manning, K.; Corilo, Y.; Kew, W.; Babcock-Adams, L.; McKenna, A. M.; Stuart, R. K.; Boiteau, R. M. Annotation of DOM Metabolomes with an Ultrahigh Resolution Mass Spectrometry Molecular Formula Library. *Org. Geochem.* **2024**, *197*, 104880. https://doi.org/10.1016/j.orggeochem.2024.104880.

APPENDIX A: SUPPLEMENTARY INFORMATION FOR CHAPTER 2

Table A1. Summary of major organic and inorganic speciation changes in various fire-affected ecosystems and controlled studies, such as laboratory heating simulations.

Topic	Ecosystem	Description	Fire Conditions (Severity/Intensity)	Observations	Reference
PAH	Pine bark, litter, and soil in Pohang, South Korea	Samples collected 1, 3, 5, and 7 months after a forest fire		Control samples showed lowest PAH levels; PAHs decreased over time	Choi, 2014[1]
	Varies	143 sets of published data		Total PAHs in fire-affected soils increased by 205% compared to unburned soils	Yang et al. 2022[2]
Organic Carbon	Computational study	Representative PyOM and DOM molecules from database	N/A	Observed considerable overlap between preicted metabolic rates of PyOM and DOM microbial degradation	Graham et al. 2023[3]
	Old-growth, lodgepole pine-dominated (*P. Contorta*) forest	Collected surface mineral soil (0-5 cm depth)	Unburned control, low severity, and high severity samples	Soil organic matter from high severity burned soils featured higher nominal oxidation state of carbon values, generating lower Gibbs free energy of oxidation values	Nelson et al. 2022[4]
	Laboratory Study	Soil-water extracts from pyrolyzed oak wood were incubated with soil-derived microbial consortium	Oak wood (*Quercus hemisphaerica*) was pyrolyzed at 400°C and 650°C for three hours	25-67% of aromatic content was biomineralized within a 10-day incubation	Bostick et al. 2021[5]
	Laboratory Study	Soil-water extracts from pyrolyzed oak wood were incubated with soil-derived	Oak wood (*Quercus hemisphaerica*) was pyrolyzed at 400°C and 650°C for three hours	Upwards of 25% of carbon content was biomineralized within a 10-day incubation	Goranov et al. 2022[6]

		microbial consortium			
	Laboratory Study	PyOM produced from pylrolzing pine wood was incubated with *Pyronema domesticum* fungi	Eastern white pine wood (*Pinus strobus*) was pyrolyzed at 750°C for 30 minutes	PyOM was biomineralized within the span of 57 days	Fischer et al. 2021[7]
Organic Nitrogen	Laboratory Study	Mineral soil samples were collected from subalpine canyon located in northern Colorado	Soil was burned under oxic conditions at low severity (225°C), moderate severity (350°C), and high severity (500°C) in a muffle furnace.	Number of nitrogen-containing soil organic matter molecules increased by 20% after burning at 225°C	Cawley et al. 2017[8]
	Laboratory Study	Mineral soil samples were collected from coniferous forest located in northern Colorado	Soil was burned under oxic conditions at 150°C, 250°C, 350°C, and 450°C in a muffle furnace.	Number of nitrogen-containing soil organic matter molecules increased by 32% after burning at 250°C	Bahureksa et al. 2022[9]
Karrikins	Laboratory study	Germination assays of *Arabidopsis thaliana* seeds with solutions of karrikins	None	Karrikins promoted the germination of *Arabidopsis thaliana seeds*	Nelson et al. 2009[10]
	Laboratory study	Karrikin quantities in smoke water samples were measured.	None	Developed method for quantifying karrikins in smoke water using ultra-high performance liquid chromatography-tandem mass spectrometry	Hrdlička et al. 2019[11]
Disinfection byproducts (DBP)	Watersheds from ponderosa pine (*Pinus ponderosa*) and Douglas-fir (*Pseudotsuga*	13 first- and second-roder catchments were	Sampled five unburned catchments, six that burned at moderate severity (<50% of catchment area	Linear relationship between watershed burned area and haloacetonitrile formation was observed	Chow et al. 2019[12]

	menziesii) forests located in Colorado	sampled 12 years after the 2002 Hayman fire	burned with <25% at high severity), and two that burned at high severity (75-95% of catchment area was burned with 50-60% at high severity)		
	Laboratory study	Forest detritus (0-5 cm) collected from Stanislaus National Forest was burned, and chlorination-based DBP formation potential tests were conducted on the leachate of the burned samples	Forest detritus samples were burned at 250°C and 400°C under oxic conditions and pyrolyzed at 250°C and 400°C in a muffle furnace	Formation potential of haloacetonitriles increased by 324% in detritus pyrolyzed at 250°C compared to unburned detritus.	Wang et al. 2015[13]
Cr	Laboratory study	Synthetic Cr(III)-substituted ferrihydrite, goethite, and hematite and ferrosol-type soil were heated in a muffle furnace	200, 400, 600, and 800ºC at a duration of 2 h	Cr(VI) detected in all heated samples but extent depended on oxide type. Moderate temperatures (200-600ºC) yielded greater Cr(VI) formation in the ferrihydrite, hematite, and Ferrosol-type soil and decreased considerably at 800ºC. In contrast, Cr(VI) formation within the Cr(III)-substituted goethite increased almost linearly with temperature, approaching 100% of total Cr at 800ºC	Burton et al 2019[14]
	Laboratory study	Grass samples, *Hyperthelia dissolute*, burned in a muffle furnace.	200ºC for 4 h, then heated at specific max temperatures (500, 600, 700, 800, and 900ºC) for 1 h	Natural Cr(VI)/Total Cr concentration of 2.5% increased to 23% when heated at 500ºC and to 58% when heated to 800°C.	Panichev et al. 2008[15]

	Field study	Soils from South Africa were samples before and after bushfires		Unburned soil samples contained <1 % (Cr(VI)/Total Cr and burned topsoil with grass contained 2.7%. Black ash were shown to contain higher proportion (9.3%) of Cr(VI).	Panichev et al 2008[15]
	Field study	Soils and ash collected from 3 natural preserves that burned during the Kincade fire of California were sampled shortly after fire and 10 months post-fire in various geology types	Low, moderate, and high severity fire	High Cr(VI) concentration (222-3,335 µg/kg) observed in surface ash layers in wildfire-affected ultramafic soils. Elevated Cr(VI) in soil and ash from a burned chaparral persisted 10 months after wildfire.	Lopez et al 2023[16]l
	Field study	Collected ash and burned soils from California wildland and residential areas	Multiple fires of varying severities	Dominant form of Cr found was Cr(VI) and greater in the wildland-urban interface.	Wolf et al 2008[17]
As	Field study	Speciation of soils and biological leachates of ashes from California wildfires were assessed (Cr, As, Se)	Multiple fires of varying severities	Unpolluted soil- and ash-bound As concentrations were relatively low after multiple California wildfires but when As was measured, it was typically As(V)	Wolf et al 2011[18]
Hg	Laboratory study	Brake fern plants and mixtures (plant residue, As2O5 (aq), with	Heating temperature of 100 to 800 °C with the heating rate of 25 °C/min for 4 h	Arsenic emissions from As(V) reduction followed by volatilization as arsine gas was observed when burning an As-hyperaccumulating plant,	Yan et al. 2008[19]

		or without charcoal) were heated in a muffle furnace		brake ferns (*Pteris vittata*), even at temperatures less than 400°C. Arsenic(III) volatilization increased as temperatures were increased from 100-800°C	
	Field study	Mercury emissions from 2000-2013 wildfires in the US were measured in various ecosystems	Varied	Hg emissions varied across vegetation types where low biomass ecosystems (desert scrub) are lower emission sources	Webster et al. 2016[20]

Table A2. Effects of fire on toxicity of aqueous ash extracts (AEA) or soils from burned areas.

Reference	Ecosystem(s)	Species tested	Sampling notes	Observations
Harper et al., 2019[21]	Australian eucalypt, USA chaparral, Canadian spruce, Spanish heathland, Spanish pine forest, UK grassland	*Daphnia magna*	Composite ash samples; 1 : 10 ratio of ash to culture medium	Significant acute toxicity observed for 3 of 6 ash types tested
Brito et al., 2017[22]	Brazilian *Cerrado*, pasture, and transition area between palm swamp and savanna	*Ceriodaphnia dubia, Danio rerio, Biomphalaria glabrata*	Ashes collected (five locations) within burned area one day postfire and homogenized; 1 : 10 ratio of ash to culture medium	All ash types caused acute toxicity to *C. dubia*, transition area ashes were toxic to *D. rerio*, all other species and ash types were not affected
Campos et al., 2012[23]	75% eucalypt plantations (Eucalyptus globulus Labill.), 25% Maritime Pine (*Pinus pinaster*), Portugal	*Vibrio fischeri, Pseudokirchneriella subcapitata, Lemna minor, Daphnia magna*	Overland flow collected after first significant rainfall event following fire and about one year later	Significant inhibitory effects on *V. fishceri, P. subcapitata*, and *L. minor*, but not D. magna; runoff immediately after fire was less toxic than water collected one year later
Ré et al., 2021[24]	Mixed Eucalypt (*Eucalyptus globulus*) and pine	Human keratinocytes	Ash from each site mixed for composite AEA	Increasing concentration of aqueous ash extracts decreased cell viability

	(*Pinus pinaster*), Portugal			
Afonso et al., 2022[25]	Maritime Pine (*Pinus Pinaster*), Eucalypt (*Eucalyptus globulus*)	Skin bacteria from *Salamandra salamandra*	1 : 4 v/v in culture medium collected 3 days post-wildfire	Growth inhibition found at low ash concentrations; eucalypt extracts had a higher negative impact than pine
Atwi et al., 2022[26]	Pin oak foliage (*Quercus plustris*), Pignut hickory twigs (*Carya glabra*), Slash pine needles (*Pinus elliottii*)	Immortalized human bronchial epithelial cells	25 g of each fuel smoldered, fresh and aged (2 h photo-oxidation) $PM_{2.5}$ collected	Strongest reduction in microbial activity from PM from hickory combustion; fresh PM induced more reduction in metabolic activity for all fuels; aged PM induced higher apoptosis
Coelho et al., 2022[27]	Eucalypt (*Eucalyptus globulus*)	Iberian frog (*Rana iberica*) skin bacteria	Black ash (moderate severity) and grey-white ash (moderate-high severity) collected 3 days post-fire; AEA	Increasing aqueous ash extract concentrations increased the number of bacteria whose growth was negatively affected; high severity ash had more adverse effects than moderate severity
Priya et al., 2023[28]	Syringol exposure	Human embryonic kidney cell line (HEK-293), Zebrafish (*Danio rerio*)	Varying concentrations of syringol (0.5-2 mg/L)	HEK-293: syringol exposure induced concentration-dependent cytotoxicity; zebrafish: dose-dependent embryo toxic effects and changes in growth metrics
Muñiz Gonzàlez et al., 2023 [29]	Maritime pine (*Pinus pinaster*)	*Chironomus riparius*	High severity and low severity ashes prepared to concentration of 10 g/L and diluted to several concentrations	38 of 42 genes altered from high severity ashes, 22 genes altered from low severity ashes; apoptosis response/endocrine disruption observed
Roth et al., 2023[30]	Lodgepole pine (*Pinus contorta*)	*Aliivibrio fischeri*	Soil burn severity gradient	Increased heterocyclic N as burn severity increased; positive relationship between soil burn severity and toxicity

APPENDIX A REFERENCES

(1) Choi, S.-D. Time trends in the levels and patterns of polycyclic aromatic hydrocarbons (PAHs) in pine bark, litter, and soil after a forest fire. *Sci. Total Environ.* **2014**, *470–471*, 1441–1449.

(2) Yang, B. *et al.* Polycyclic aromatic hydrocarbon occurrence in forest soils in response to fires: a summary across sites. *Environ. Sci. Process. Impacts*. **2022**, *24*, 32–41.

(3) Graham, E. B., Song, H.-S., Grieger, S. & Garayburu, V. A. Inferred molecular bioavailability of pyrogenic organic matter compared to natural organic matter from global sediments and 2 surface waters 3.

(4) Nelson, A. R. *et al.* Wildfire-dependent changes in soil microbiome diversity and function. *Nat. Microbiol.* **2022**, *7*, 1419–1430.

(5) Bostick, K. W. *et al.* Biolability of Fresh and Photodegraded Pyrogenic Dissolved Organic Matter From Laboratory-Prepared Chars. *J. Geophys. Res. Biogeosciences.* **2021**, *126*, e2020JG005981.

(6) Goranov, A. I. *et al.* Microbial labilization and diversification of pyrogenic dissolved organic matter. *Biogeosciences.* **2022**, *19*, 1491–1514.

(7) Fischer, M. S. *et al.* Pyrolyzed Substrates Induce Aromatic Compound Metabolism in the Post-fire Fungus, Pyronema domesticum. *Front. Microbiol.* **2021**, *12*, 3085–3085.

(8) Cawley, K. M. *et al.* Molecular and spectroscopic characterization of water extractable organic matter from thermally altered soils reveal insight into disinfection byproduct precursors. *Environ. Sci. Technol.* **2017**, *51*, 771–779.

(9) Bahureksa, W. *et al.* Nitrogen enrichment during soil organic matter burning and molecular evidence of Maillard reactions. *Environ. Sci. Technol.* **2022**, *56*, 4597–4609.

(10) Nelson, D. C. *et al.* Karrikins Discovered in Smoke Trigger Arabidopsis Seed Germination by a Mechanism Requiring Gibberellic Acid Synthesis and Light. *Plant Physiol.* **2009**, *149*, 863–873.

(11) Hrdlička, J. *et al.* Quantification of karrikins in smoke water using ultra-high performance liquid chromatography–tandem mass spectrometry. *Plant Methods*. **2019**, *15*, 81.

(12) Chow, A. T., Tsai, K.-P., Fegel, T. S., Pierson, D. N. & Rhoades, C. C. Lasting effects of wildfire on disinfection by-product formation in forest catchments. *J. Environ. Qual.* **2019**, *48*, 1826–1834.

(13) Wang, J.-J., Dahlgren, R. A., Erşan, M. S., Karanfil, T. & Chow, A. T. Wildfire Altering Terrestrial Precursors of Disinfection Byproducts in Forest Detritus. *Environ. Sci. Technol.* **2015**, *49*, 5921–5929.

(14) Burton, E. D., Choppala, G., Karimian, N. & Johnston, S. G. A new pathway for hexavalent chromium formation in soil: Fire-induced alteration of iron oxides. *Environ. Pollut.* **2019***, 247*, 618–625.

(15) Panichev, N., Mabasa, W., Ngobeni, P., Mandiwana, K. & Panicheva, S. The oxidation of Cr(III) to Cr(VI) in the environment by atmospheric oxygen during the bush fires. *J. Hazard. Mater.* **2008***, 153*, 937–941.

(16) Lopez, A. M., Pacheco, J. L. & Fendorf, S. Metal toxin threat in wildland fires determined by geology and fire severity. *Nat. Commun.* **2023**, *14*, 8007.

(17) Wolf, R. E., Morman, S. A., Plumlee, G. S., Hageman, P. L. & Adams, M. Release of Hexavalent Chromium by Ash and Soils in Wildfire-Impacted Areas. Open-File Report https://pubs.usgs.gov/publication/ofr20081345 (**2008**) doi:10.3133/ofr20081345.

(18) Wolf, R. E., Morman, S. A., Hageman, P. L., Hoefen, T. M. & Plumlee, G. S. Simultaneous speciation of arsenic, selenium, and chromium: species stability, sample preservation, and analysis of ash and soil leachates. *Anal. Bioanal. Chem.* **2011**, *401*, 2733–2745.

(19) Yan, X.-L. *et al.* Arsenic Transformation and Volatilization during Incineration of the Hyperaccumulator Pteris vittata L. *Environ. Sci. Technol.* **2008***, 42*, 1479–1484.

(20) Webster, J. P., Kane, T. J., Obrist, D., Ryan, J. N. & Aiken, G. R. Estimating mercury emissions resulting from wildfire in forests of the Western United States. *Sci. Total Environ.* **2016***, 568*, 578–586.

(21) Harper, A. R. *et al.* Chemical composition of wildfire ash produced in contrasting ecosystems and its toxicity to Daphnia magna. *Int. J. Wildland Fire*. **2019**, *28*, 726–737.

(22) Brito, D. Q., Passos, C. J. S., Muniz, D. H. F. & Oliveira-Filho, E. C. Aquatic ecotoxicity of ashes from Brazilian savanna wildfires. *Environ. Sci. Pollut. Res.* **2017**, *24*, 19671–19682.

(23) Campos, I. *et al.* Assessment of the toxicity of ash-loaded runoff from a recently burnt eucalypt plantation. *Eur. J. For. Res.* **2012**, *131*, 1889–1903.

(24) Ré, A. *et al.* Cytotoxic effects of wildfire ashes: In-vitro responses of skin cells. *Environ. Pollut.* ***2021***, *285*, 117279.

(25) Afonso, M. *et al.* Effects of Pine and Eucalypt ashes on bacterial isolates from the skin microbiome of the fire salamander (Salamandra salamandra). *Sci. Total Environ.* **2022**, *841*, 156677.

(26) Atwi, K. *et al.* Differential response of human lung epithelial cells to particulate matter in fresh and photochemically aged biomass-burning smoke. *Atmos. Environ.* **2022***, 271*, 118929.

(27) Coelho, L. *et al.* Effects of Eucalypt ashes from moderate and high severity wildfires on the skin microbiome of the Iberian frog (Rana iberica). *Environ. Pollut.* **2022**, *313*, 120065.

(28) Priya, P. S. *et al.* Syringol, a wildfire residual methoxyphenol causes cytotoxicity and teratogenicity in zebrafish model. *Sci. Total Environ.* **2023**, *864*, 160968.

(29) Muñiz González, A.-B., Campos, I., Re, A., Martínez-Guitarte, J.-L. & Abrantes, N. Effects of wildfire ashes on aquatic invertebrates: First molecular approach on Chironomus riparius larvae. *Sci. Total Environ.* **2023***, 858*, 159899.

(30) Roth, H. K. *et al.* Effects of burn severity on organic nitrogen and carbon chemistry in high-elevation forest soils. *Soil Environ. Health*. **2023**, *1*, 100023.

APPENDIX B: SUPPLEMENTARY INFORMATION FOR CHAPTER 3

Table B1. Details for BioProject PRJNA682830

Accession	Sample Name	SPUID	Organism	Tax ID	Strain	Isolate	BioProject	Link
SAMN36416513	JQ1_16S	JQ1_16S	soil metagenome	410658	Not Applicable	Not Applicable	PRJNA682830	36416513: https://www.ncbi.nlm.nih.gov/sra/36416513
SAMN36416514	JQ10_16S	JQ10_16S	soil metagenome	410658	Not Applicable	Not Applicable	PRJNA682830	36416514: https://www.ncbi.nlm.nih.gov/sra/36416514
SAMN36416515	JQ11_16S	JQ11_16S	soil metagenome	410658	Not Applicable	Not Applicable	PRJNA682830	36416515: https://www.ncbi.nlm.nih.gov/sra/36416515
SAMN36416516	JQ12_16S	JQ12_16S	soil metagenome	410658	Not Applicable	Not Applicable	PRJNA682830	36416516: https://www.ncbi.nlm.nih.gov/sra/36416516
SAMN36416517	JQ13_16S	JQ13_16S	soil metagenome	410658	Not Applicable	Not Applicable	PRJNA682830	36416517: https://www.ncbi.nlm.nih.gov/sra/36416517
SAMN36416518	JQ14_16S	JQ14_16S	soil metagenome	410658	Not Applicable	Not Applicable	PRJNA682830	36416518: https://www.ncbi.nlm.nih.gov/sra/36416518
SAMN36416519	JQ15_16S	JQ15_16S	soil metagenome	410658	Not Applicable	Not Applicable	PRJNA682830	36416519: https://www.ncbi.nlm.nih.gov/sra/36416519
SAMN36416520	JQ2_16S	JQ2_16S	soil metagenome	410658	Not Applicable	Not Applicable	PRJNA682830	36416520: https://www.ncbi.nlm.nih.gov/sra/36416520
SAMN36416521	JQ3_16S	JQ3_16S	soil metagenome	410658	Not Applicable	Not Applicable	PRJNA682830	36416521: https://www.ncbi.nlm.nih.gov/sra/36416521
SAMN36416522	JQ4_16S	JQ4_16S	soil metagenome	410658	Not Applicable	Not Applicable	PRJNA682830	36416522: https://www.ncbi.nlm.nih.gov/sra/36416522
SAMN36416523	JQ5_16S	JQ5_16S	soil metagenome	410658	Not Applicable	Not Applicable	PRJNA682830	36416523: https://www.ncbi.nlm.nih.gov/sra/36416523
SAMN36416524	JQ6_16S	JQ6_16S	soil metagenome	410658	Not Applicable	Not Applicable	PRJNA682830	36416524: https://www.ncbi.nlm.nih.gov/sra/36416524
SAMN36416525	JQ7_16S	JQ7_16S	soil metagenome	410658	Not Applicable	Not Applicable	PRJNA682830	36416525: https://www.ncbi.nlm.nih.gov/sra/36416525
SAMN36416526	JQ8_16S	JQ8_16S	soil metagenome	410658	Not Applicable	Not Applicable	PRJNA682830	36416526: https://www.ncbi.nlm.nih.gov/sra/36416526

SAMN36416527	JQ9_16S	JQ9_16S	soil metagenome	410658	Not Applicable	Not Applicable	PRJNA682830	36416527: https://www.ncbi.nlm.nih.gov/sra/36416527
SAMN36416528	PLJ1_16S	PLJ1_16S	soil metagenome	410658	Not Applicable	Not Applicable	PRJNA682830	36416528: https://www.ncbi.nlm.nih.gov/sra/36416528
SAMN36416529	PLJ10_16S	PLJ10_16S	soil metagenome	410658	Not Applicable	Not Applicable	PRJNA682830	36416529: https://www.ncbi.nlm.nih.gov/sra/36416529
SAMN36416530	PLJ11_16S	PLJ11_16S	soil metagenome	410658	Not Applicable	Not Applicable	PRJNA682830	36416530: https://www.ncbi.nlm.nih.gov/sra/36416530
SAMN36416531	PLJ12_16S	PLJ12_16S	soil metagenome	410658	Not Applicable	Not Applicable	PRJNA682830	36416531: https://www.ncbi.nlm.nih.gov/sra/36416531
SAMN36416532	PLJ13_16S	PLJ13_16S	soil metagenome	410658	Not Applicable	Not Applicable	PRJNA682830	36416532: https://www.ncbi.nlm.nih.gov/sra/36416532
SAMN36416533	PLJ14_16S	PLJ14_16S	soil metagenome	410658	Not Applicable	Not Applicable	PRJNA682830	36416533: https://www.ncbi.nlm.nih.gov/sra/36416533
SAMN36416534	PLJ15_16S	PLJ15_16S	soil metagenome	410658	Not Applicable	Not Applicable	PRJNA682830	36416534: https://www.ncbi.nlm.nih.gov/sra/36416534
SAMN36416535	PLJ16_16S	PLJ16_16S	soil metagenome	410658	Not Applicable	Not Applicable	PRJNA682830	36416535: https://www.ncbi.nlm.nih.gov/sra/36416535
SAMN36416536	PLJ17_16S	PLJ17_16S	soil metagenome	410658	Not Applicable	Not Applicable	PRJNA682830	36416536: https://www.ncbi.nlm.nih.gov/sra/36416536
SAMN36416537	PLJ18_16S	PLJ18_16S	soil metagenome	410658	Not Applicable	Not Applicable	PRJNA682830	36416537: https://www.ncbi.nlm.nih.gov/sra/36416537
SAMN36416538	PLJ2_16S	PLJ2_16S	soil metagenome	410658	Not Applicable	Not Applicable	PRJNA682830	36416538: https://www.ncbi.nlm.nih.gov/sra/36416538
SAMN36416539	PLJ3_16S	PLJ3_16S	soil metagenome	410658	Not Applicable	Not Applicable	PRJNA682830	36416539: https://www.ncbi.nlm.nih.gov/sra/36416539
SAMN36416540	PLJ4_16S	PLJ4_16S	soil metagenome	410658	Not Applicable	Not Applicable	PRJNA682830	36416540: https://www.ncbi.nlm.nih.gov/sra/36416540
SAMN36416541	PLJ5_16S	PLJ5_16S	soil metagenome	410658	Not Applicable	Not Applicable	PRJNA682830	36416541: https://www.ncbi.nlm.nih.gov/sra/36416541
SAMN36416542	PLJ6_16S	PLJ6_16S	soil metagenome	410658	Not Applicable	Not Applicable	PRJNA682830	36416542: https://www.ncbi.nlm.nih.gov/sra/36416542

SAMN36416543	PLJ7_16S	PLJ7_16S	soil metagenome	410658	Not Applicable	Not Applicable	PRJNA682830	36416543: https://www.ncbi.nlm.nih.gov/sra/36416543
SAMN36416544	PLJ8_16S	PLJ8_16S	soil metagenome	410658	Not Applicable	Not Applicable	PRJNA682830	36416544: https://www.ncbi.nlm.nih.gov/sra/36416544
SAMN36416545	PLJ9_16S	PLJ9_16S	soil metagenome	410658	Not Applicable	Not Applicable	PRJNA682830	36416545: https://www.ncbi.nlm.nih.gov/sra/36416545
SAMN36416546	JQ1_ITS	JQ1_ITS	soil metagenome	410658	Not Applicable	Not Applicable	PRJNA682830	36416546: https://www.ncbi.nlm.nih.gov/sra/36416546
SAMN36416547	JQ10_ITS	JQ10_ITS	soil metagenome	410658	Not Applicable	Not Applicable	PRJNA682830	36416547: https://www.ncbi.nlm.nih.gov/sra/36416547
SAMN36416548	JQ11_ITS	JQ11_ITS	soil metagenome	410658	Not Applicable	Not Applicable	PRJNA682830	36416548: https://www.ncbi.nlm.nih.gov/sra/36416548
SAMN36416549	JQ12_ITS	JQ12_ITS	soil metagenome	410658	Not Applicable	Not Applicable	PRJNA682830	36416549: https://www.ncbi.nlm.nih.gov/sra/36416549
SAMN36416550	JQ13_ITS	JQ13_ITS	soil metagenome	410658	Not Applicable	Not Applicable	PRJNA682830	36416550: https://www.ncbi.nlm.nih.gov/sra/36416550
SAMN36416551	JQ14_ITS	JQ14_ITS	soil metagenome	410658	Not Applicable	Not Applicable	PRJNA682830	36416551: https://www.ncbi.nlm.nih.gov/sra/36416551
SAMN36416552	JQ15_ITS	JQ15_ITS	soil metagenome	410658	Not Applicable	Not Applicable	PRJNA682830	36416552: https://www.ncbi.nlm.nih.gov/sra/36416552
SAMN36416553	JQ2_ITS	JQ2_ITS	soil metagenome	410658	Not Applicable	Not Applicable	PRJNA682830	36416553: https://www.ncbi.nlm.nih.gov/sra/36416553
SAMN36416554	JQ3_ITS	JQ3_ITS	soil metagenome	410658	Not Applicable	Not Applicable	PRJNA682830	36416554: https://www.ncbi.nlm.nih.gov/sra/36416554
SAMN36416555	JQ4_ITS	JQ4_ITS	soil metagenome	410658	Not Applicable	Not Applicable	PRJNA682830	36416555: https://www.ncbi.nlm.nih.gov/sra/36416555
SAMN36416556	JQ5_ITS	JQ5_ITS	soil metagenome	410658	Not Applicable	Not Applicable	PRJNA682830	36416556: https://www.ncbi.nlm.nih.gov/sra/36416556
SAMN36416557	JQ6_ITS	JQ6_ITS	soil metagenome	410658	Not Applicable	Not Applicable	PRJNA682830	36416557: https://www.ncbi.nlm.nih.gov/sra/36416557
SAMN36416558	JQ7_ITS	JQ7_ITS	soil metagenome	410658	Not Applicable	Not Applicable	PRJNA682830	36416558: https://www.ncbi.nlm.nih.gov/sra/36416558

SAMN36416559	JQ8_ITS	JQ8_ITS	soil metagenome	410658	Not Applicable	Not Applicable	PRJNA682830	36416559: https://www.ncbi.nlm.nih.gov/sra/36416559
SAMN36416560	JQ9_ITS	JQ9_ITS	soil metagenome	410658	Not Applicable	Not Applicable	PRJNA682830	36416560: https://www.ncbi.nlm.nih.gov/sra/36416560
SAMN36416561	PLJ1_ITS	PLJ1_ITS	soil metagenome	410658	Not Applicable	Not Applicable	PRJNA682830	36416561: https://www.ncbi.nlm.nih.gov/sra/36416561
SAMN36416562	PLJ10_ITS	PLJ10_ITS	soil metagenome	410658	Not Applicable	Not Applicable	PRJNA682830	36416562: https://www.ncbi.nlm.nih.gov/sra/36416562
SAMN36416563	PLJ11_ITS	PLJ11_ITS	soil metagenome	410658	Not Applicable	Not Applicable	PRJNA682830	36416563: https://www.ncbi.nlm.nih.gov/sra/36416563
SAMN36416564	PLJ12_ITS	PLJ12_ITS	soil metagenome	410658	Not Applicable	Not Applicable	PRJNA682830	36416564: https://www.ncbi.nlm.nih.gov/sra/36416564
SAMN36416565	PLJ13_ITS	PLJ13_ITS	soil metagenome	410658	Not Applicable	Not Applicable	PRJNA682830	36416565: https://www.ncbi.nlm.nih.gov/sra/36416565
SAMN36416566	PLJ14_ITS	PLJ14_ITS	soil metagenome	410658	Not Applicable	Not Applicable	PRJNA682830	36416566: https://www.ncbi.nlm.nih.gov/sra/36416566
SAMN36416567	PLJ15_ITS	PLJ15_ITS	soil metagenome	410658	Not Applicable	Not Applicable	PRJNA682830	36416567: https://www.ncbi.nlm.nih.gov/sra/36416567
SAMN36416568	PLJ16_ITS	PLJ16_ITS	soil metagenome	410658	Not Applicable	Not Applicable	PRJNA682830	36416568: https://www.ncbi.nlm.nih.gov/sra/36416568
SAMN36416569	PLJ17_ITS	PLJ17_ITS	soil metagenome	410658	Not Applicable	Not Applicable	PRJNA682830	36416569: https://www.ncbi.nlm.nih.gov/sra/36416569
SAMN36416570	PLJ18_ITS	PLJ18_ITS	soil metagenome	410658	Not Applicable	Not Applicable	PRJNA682830	36416570: https://www.ncbi.nlm.nih.gov/sra/36416570
SAMN36416571	PLJ2_ITS	PLJ2_ITS	soil metagenome	410658	Not Applicable	Not Applicable	PRJNA682830	36416571: https://www.ncbi.nlm.nih.gov/sra/36416571
SAMN36416572	PLJ3_ITS	PLJ3_ITS	soil metagenome	410658	Not Applicable	Not Applicable	PRJNA682830	36416572: https://www.ncbi.nlm.nih.gov/sra/36416572
SAMN36416573	PLJ4_ITS	PLJ4_ITS	soil metagenome	410658	Not Applicable	Not Applicable	PRJNA682830	36416573: https://www.ncbi.nlm.nih.gov/sra/36416573
SAMN36416574	PLJ5_ITS	PLJ5_ITS	soil metagenome	410658	Not Applicable	Not Applicable	PRJNA682830	36416574: https://www.ncbi.nlm.nih.gov/sra/36416574

SAMN36416575	PLJ6_ITS	PLJ6_ITS	soil metagenome	410658	Not Applicable	Not Applicable	PRJNA682830	36416575: https://www.ncbi.nlm.nih.gov/sra/36416575
SAMN36416576	PLJ7_ITS	PLJ7_ITS	soil metagenome	410658	Not Applicable	Not Applicable	PRJNA682830	36416576: https://www.ncbi.nlm.nih.gov/sra/36416576
SAMN36416577	PLJ8_ITS	PLJ8_ITS	soil metagenome	410658	Not Applicable	Not Applicable	PRJNA682830	36416577: https://www.ncbi.nlm.nih.gov/sra/36416577
SAMN36416578	PLJ9_ITS	PLJ9_ITS	soil metagenome	410658	Not Applicable	Not Applicable	PRJNA682830	36416578: https://www.ncbi.nlm.nih.gov/sra/36416578

Table B2. Water Extractable Organic Carbon Values (mg C / g soil) (n=3, error = standard deviation)

Treatment	Soil Sampling Day				
	0	3	7	14	28
Unburned	0.14±0.02	0.145±0.016	0.143±0.010	0.15±0.03	0.17±0.03
Burned	0.49±0.08	0.41±0.04	0.379±0.009	0.41±0.07	0.40±0.11

Table B3. Total Carbon Values (% by weight) (n=3, error = standard deviation)

Treatment	Soil Sampling Day				
	0	3	7	14	28
Unburned	2.33±0.02	2.41±0.07	2.36±0.09	2.51±0.03	2.57±0.14
Burned	2.6±0.3	2.5±0.2	2.19±0.05	2.1±0.2	2.5±0.2

Table B4. Ammonium-N Values (mg/L) (n=3, error = standard deviation)

Treatment	Soil Sampling Day				
	0	3	7	14	28
Unburned	0.23±0.04	0.14±0.01	0.13±0.02	0.24±0.04	0.34±0.22
Burned	11.57±1.07	13.73±0.78	13.37±1.31	12.50±1.13	12.77±0.95

Table B5. Water Extractable Total Nitrogen Values (µg N / g soil) (n=3, error = standard deviation)

Treatment	Soil Sampling Day				
	0	3	7	14	28
Unburned	4.8±1.2	5.40±1.0	4.7±0.8	4.5±1.5	5.7±0.3
Burned	56.9±8.4	55.3±2.0	51.7±5.5	57.5±7.3	59.5±13.1

Table B6. Cumulative CO_2-C Emitted (mg) / Soil Mass (g) (n=5, error = standard deviation)

Sample	Incubation Day															
	1	4	6	8	11	13	14	15	18	19	22	28	29	36	43	50
Day 0 Unburned	0.04±0.003	0.11±0.03	0.14±0.07	-	0.21±0.10	-	0.25±0.13	-	0.30±0.18	-	0.3±0.2	-	0.5±0.3	0.6±0.4	-	0.8±0.5
Day 0 Burned	0.05±0.005	0.267±0.07	0.34±0.13	-	0.44±0.16	-	0.47±0.18	-	0.5±0.2	-	0.5±0.2	-	0.6±0.2	0.7±0.2	-	0.8±0.3
Day 14 Unburned	0.037±0.003	0.10±0.03	0.13±0.05	-	0.21±0.06	-	-	0.27±0.10	-	-	0.36±0.15	-	-	0.6±0.3	-	0.8±0.4

Day14 Burned	0.092± 0.013	0.36± 0.02	0.42± 0.04	-	0.56± 0.06	-	-	0.64± 0.08	-	-	0.73± 0.07	-	-	0.83± 0.09	-	0.96 ± 0.16
Day 28 Unburned	0.031± 0.008	0.10± 0.05	0.15± 0.04	0.21 ± 0.04	0.27± 0.04	0.33± 0.04	-	-	-	0.44± 0.08	0.52± 0.10	0.66 ± 0.11	-	0.83± 0.11	0.99 ± 0.11	1.14 ± 0.13
Day 28 Burned	0.112± 0.015	0.24± 0.11	0.31± 0.11	0.33 ± 0.13	0.35± 0.14	0.36± 0.15	-	-	-	0.39± 0.18	0.42± 0.18	0.5± 0.2	-	0.5±0 .2	0.5± 0.2	0.6± 0.3

Table B7. Cumulative CO_2-C emitted divided by total soil carbon (g/g) (n=5, error = standard deviation)

Sample	Incubation Day															
	1	**4**	**6**	**8**	**11**	**13**	**14**	**15**	**18**	**19**	**22**	**28**	**29**	**36**	**43**	**50**
Day 0 Unburned	0.00209 ±0.00013	0.00478 ±0.0015	0.006 ±0.003	-	0.009 ±0.004	-	0.011 ±0.006	-	0.013 ±0.008	-	0.015 ±0.009	-	0.020 ±0.011	0.025 ±0.015	-	0.03 ±0.02
Day 0 Burned	0.00213 ±0.00018	0.010 ±0.003	0.013 ±0.005	-	0.017 ±0.006	-	0.018 ±0.007	-	0.020 ±0.008	-	0.021 ±0.009	-	0.024 ±0.009	0.026 ±0.009	-	0.031 ±0.011
Day 14 Unburned	0.00146 ±0.00012	0.0039 ±0.0011	0.0051 ±0.0018	-	0.008 ±0.002	-	-	0.011 ±0.004	-	-	0.014 ±0.006	-	-	0.024 ±0.012	-	0.033 ±0.015
Day14 Burned	0.0043 ±0.0006	0.0167 ±0.010	0.020 ±0.002	-	0.026 ±0.003	-	-	0.030 ±0.004	-	-	0.034 ±0.003	-	-	0.039 ±0.004	-	0.045 ±0.008
Day 28 Unburned	0.0012 ±0.0003	0.0038 ±0.019	0.0060 ±0.0017	0.0080 ±0.015	0.0105 ±0.0015	0.0128 ±0.0016	-	-	-	0.017 ±0.003	0.020 ±0.004	0.026 ±0.005	-	0.032 ±0.004	0.0384 ±0.004	0.044 ±0.005
Day 28 Burned	0.0045 ±0.0006	0.010 ±0.004	0.0124 ±0.004	0.013 ±0.005	0.014 ±0.006	0.015 ±0.006	-	-	-	0.016 ±0.007	0.017 ±0.007	0.018 ±0.008	-	0.020 ±0.009	0.022 ±0.010	0.023 ±0.010

Table B8. Cumulative CO_2-C emitted divided by water-extractable organic carbon (g/g) (n=5, error = standard deviation)

Sample	Incubation Day															
	1	**4**	**6**	**8**	**11**	**13**	**14**	**15**	**18**	**19**	**22**	**28**	**29**	**36**	**43**	**50**
Day 0 Unburned	0.34 ± 0.02	0.8± 0.2	1.0± 0.5	-	1.5±0.7	-	1.7± 0.9	-	2.1± 1.2	-	2.4±1.5	-	3.3± 1.8	4.1±2.5	-	5.4±3.6
Day 0 Burned	0.112± 0.010	0.53 ± 0.14	0.7± 0.3	-	0.9±0.3	-	1.0± 0.4	-	1.0± 0.4	-	1.1±0.5	-	1.3± 0.5	1.4±0.5	-	1.6±0.6
Day 14 Unburned	0.24 ± 0.02	0.65 ± 0.18	0.8± 0.3	-	1.4± 0.4	-	-	1.8± 0.6	-	-	2.4±1.0	-	-	4.0±2.0	-	5.4±2.6
Day14 Burned	0.23 ± 0.03	0.87 ± 0.05	1.03 ± 0.11	-	1.36± 0.15	-	-	1.6± 0.2	-	-	1.80± 0.18	-	-	2.0±0.2	-	2.4±0.4
Day 28 Unburned	0.18 ± 0.05	0.6± 0.3	0.9± 0.3	1.2± 0.2	1.6±0.2	1.9± 0.2	-	-	-	2.5±0.5	3.0±0.6	3.8±0.7	-	4.8±0.6	5.7± 0.7	6.6±0.8
Day 28 Burned	0.28 ± 0.04	0.6± 0.3	0.8± 0.3	0.8± 0.3	0.9±0.4	0.9± 0.4	-	-	-	1.0±0.5	1.0±0.5	1.1±0.5	-	1.3±0.6	1.4 ±0.6	1.4±0.6

Table B9. Rate of CO_2 emissions normalized to soil mass (mg CO_2-C / (day * g soil)) (n=5, error = standard deviation)

Sample	Incubation Day															
	1	4	6	8	11	13	14	15	18	19	22	28	29	36	43	50
Day 0 Unburned	0.049 ± 0.003	0.021± 0.011	0.013 ± 0.017	-	0.015± 0.006	-	0.010 ± 0.011	-	0.013 ± 0.012	-	0.010 ± 0.009	-	0.019± 0.008	0.018 ± 0.013	-	0.013± 0.016
Day 0 Burned	0.055 ± 0.005	0.07 ± 0.02	0.04± 0.03	-	0.019± 0.005	-	0.010 ± 0.008	-	0.010 ± 0.007	-	0.011 ± 0.005	-	0.0098± 0.0010	0.0082±0.0019	-	0.008± 0.002
Day 14 Unburned	0.037 ± 0.003	0.021± 0.008	0.015 ± 0.010	-	0.016± 0.004	-	-	0.014 ± 0.009	-	-	0.014 ± 0.007	-	-	0.017 ± 0.011	-	0.015± 0.008
Day14 Burned	0.092 ± 0.013	0.088± 0.006	0.031 ± 0.015	-	0.028± 0.004	-	-	0.020 ± 0.005	-	-	0.014 ± 0.007	-	-	0.007 ± 0.006	-	0.009± 0.008
Day 28 Unburned	0.031 ± 0.008	0.022± 0.014	0.029 ± 0.004	0.026± 0.004	0.022± 0.004	0.029± 0.010	-	-	-	0.018 ± 0.013	0.029 ± 0.009	0.023 ± 0.006	-	0.021 ± 0.006	0.0231±0.017	0.022± 0.004
Day 28 Burned	0.112 ± 0.014	0.04 ± 0.03	0.030 ± 0.007	0.012± 0.010	0.007± 0.008	0.006± 0.012	-	-	-	0.005 ± 0.008	0.009 ± 0.004	0.006 ± 0.006	-	0.006 ± 0.004	0.006 ± 0.003	0.004± 0.002

Table B10. Total Nitrogen Values (% by weight) (n=3, error = standard deviation)

Treatment	Soil Sampling Day				
	0	3	7	14	28
Unburned	0.108±0.013	0.099±0.007	0.112±0.010	0.101±0.008	0.111±0.019
Burned	0.144±0.010	0.136±0.011	0.121±0.009	0.134±0.015	0.19±0.10

Table B11. Soil pH Values (Water Extracted) (n=3, error = standard deviation)

Treatment	Soil Sampling Day				
	0	3	7	14	28
Unburned	5.12±0.05	5.17±0.05	5.22±0.03	5.13±0.08	5.19±0.05
Burned	5.6±0.3	5.37±0.08	6.0±0.4	6.7±0.2	6.0±0.2

Table B12. Soil pH Values ($CaCl_2$ Extracted) (n=3, error = standard deviation)

Treatment	Soil Sampling Day				
	0	3	7	14	28
Unburned	4.27±0.04	4.31±0.03	4.327±0.015	4.343±0.006	4.36±0.03
Burned	5.4±0.4	5.14±0.13	5.8±0.3	6.68±0.18	5.76±0.17

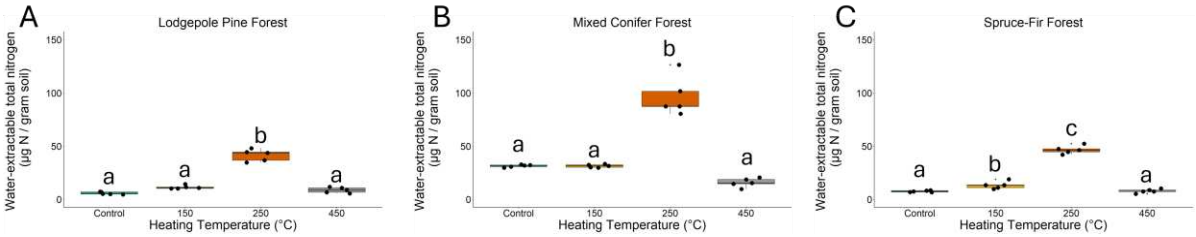

Figure C1. Water extractable total nitrogen carbon (WETN) concentrations visualized with box plots for **A**) lodgepole pine forest soil, **B**) mixed conifer forest soil, and **C**) spruce-fir forest soil. Letters above boxes indicate significant differences between treatments determined by either ANOVA and Tukey HSD tests, Welch's ANOVA and Games-Howell tests, or Kruskal-Wallis and Dunn's tests (see Statistics section 4.2.9 within Methods). The statistical tests within each forest type were conducted independently of each other. n = 5 for control, 150 °C, 250 °C, and 450 °C samples. Box plots show the median (central line), first and third quartiles (box edges), and whiskers extending to minimum and maximum values within 1.5 times the interquartile range. Data beyond the end of the whiskers are "outlying" points and are plotted individually.

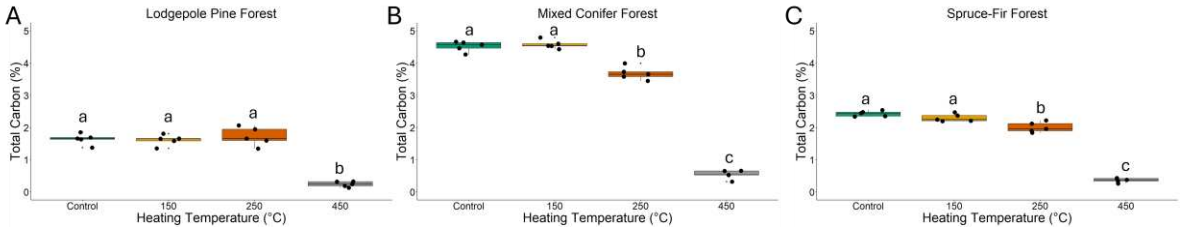

Figure C2. Total carbon concentrations visualized with box plots for **A**) lodgepole pine forest soil, **B**) mixed conifer forest soil, and **C**) spruce-fir forest soil. Letters above boxes indicate significant differences between treatments determined by either ANOVA and Tukey HSD tests, Welch's ANOVA and Games-Howell tests, or Kruskal-Wallis and Dunn's tests (see Statistics section 4.2.9 within Methods). The statistical tests within each forest type were conducted independently of each other. n = 5 for control, 150 °C, 250 °C, and 450 °C samples. Box plots show the median (central line), first and third quartiles (box edges), and whiskers extending to minimum and maximum values within 1.5 times the interquartile range. Data beyond the end of the whiskers are "outlying" points and are plotted individually.

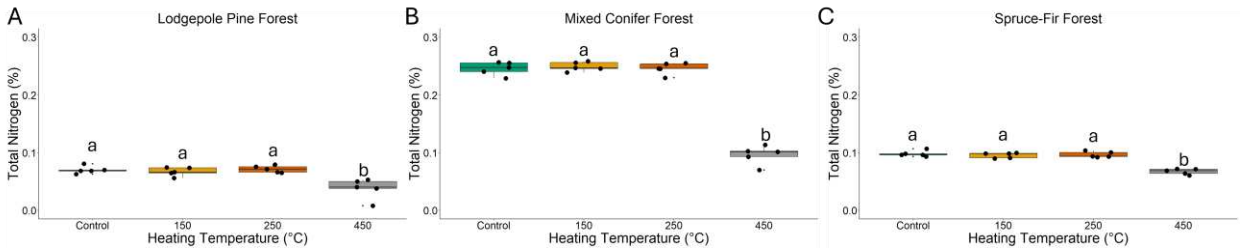

Figure C3. Total nitrogen concentrations visualized with box plots for **A**) lodgepole pine forest soil, **B**) mixed conifer forest soil, and **C**) spruce-fir forest soil. Letters above boxes indicate significant differences between treatments determined by either ANOVA and Tukey HSD tests, Welch's ANOVA and Games-Howell tests, or Kruskal-Wallis and Dunn's tests (see Statistics section 4.2.9 within Methods). The statistical tests within each forest type were conducted independently of each other. n = 5 for control, 150 °C, 250 °C, and 450 °C samples. Box plots show the median (central line), first and third quartiles (box edges), and whiskers extending to minimum and maximum values within 1.5 times the interquartile range. Data beyond the end of the whiskers are "outlying" points and are plotted individually.

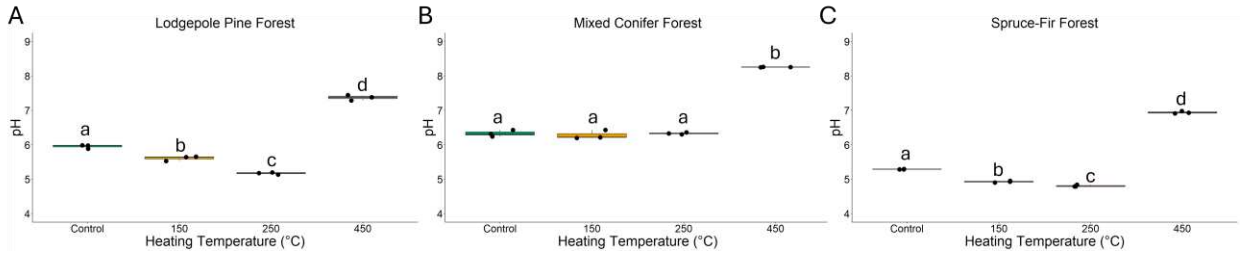

Figure C4. Soil pH values visualized with box plots for **A**) lodgepole pine forest soil, **B**) mixed conifer forest soil, and **C**) spruce-fir forest soil. Letters above boxes indicate significant differences between treatments determined by either ANOVA and Tukey HSD tests, Welch's ANOVA and Games-Howell tests, or Kruskal-Wallis and Dunn's tests (see Statistics section 4.2.9 within Methods). The statistical tests within each forest type were conducted independently of each other. n = 5 for control, 150 °C, 250 °C, and 450 °C samples. Box plots show the median (central line), first and third quartiles (box edges), and whiskers extending to minimum and maximum values within 1.5 times the interquartile range. Data beyond the end of the whiskers are "outlying" points and are plotted individually.

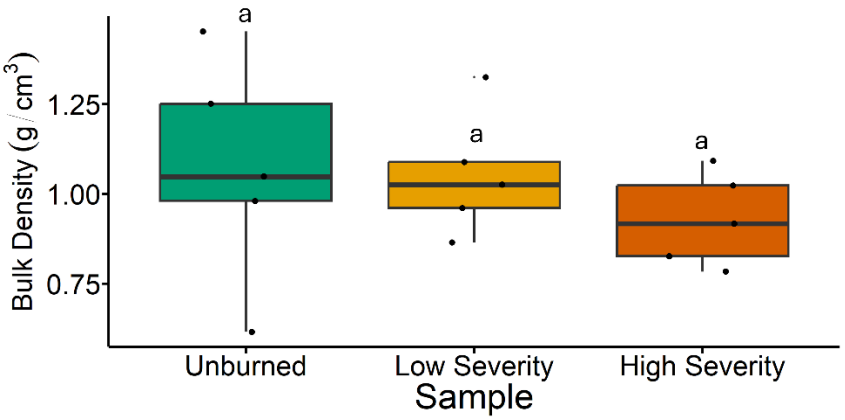

Figure D1. Bulk density values visualized with box plots. Letters above boxes indicate significant differences between treatments determined by either ANOVA and Tukey HSD tests, Welch's ANOVA and Games-Howell tests, or Kruskal-Wallis and Dunn's tests (see Statistics section 5.2.15 within Methods). n = 5 for unburned, low severity, and high severity samples. Box plots show the median (central line), first and third quartiles (box edges), and whiskers extending to minimum and maximum values within 1.5 times the interquartile range. Data beyond the end of the whiskers are "outlying" points and are plotted individually.

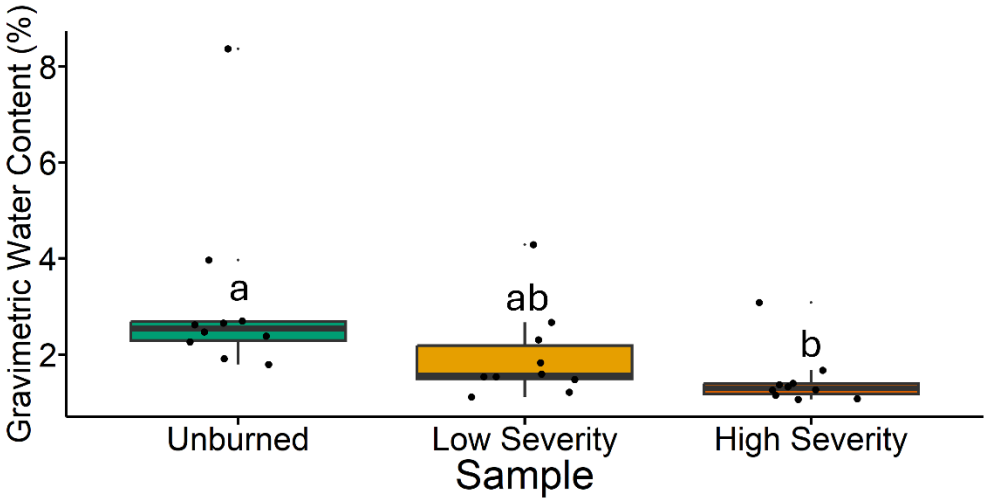

Figure D2. Gravimetric water content values visualized with box plots. Letters above boxes indicate significant differences between treatments determined by either ANOVA and Tukey HSD tests, Welch's ANOVA and Games-Howell tests, or Kruskal-Wallis and Dunn's tests (see Statistics section 5.2.15 within Methods). n = 5 for unburned, low severity, and high severity samples. Box plots show the median (central line), first and third quartiles (box edges), and whiskers extending to minimum and maximum values within 1.5 times the interquartile range. Data beyond the end of the whiskers are "outlying" points and are plotted individually.

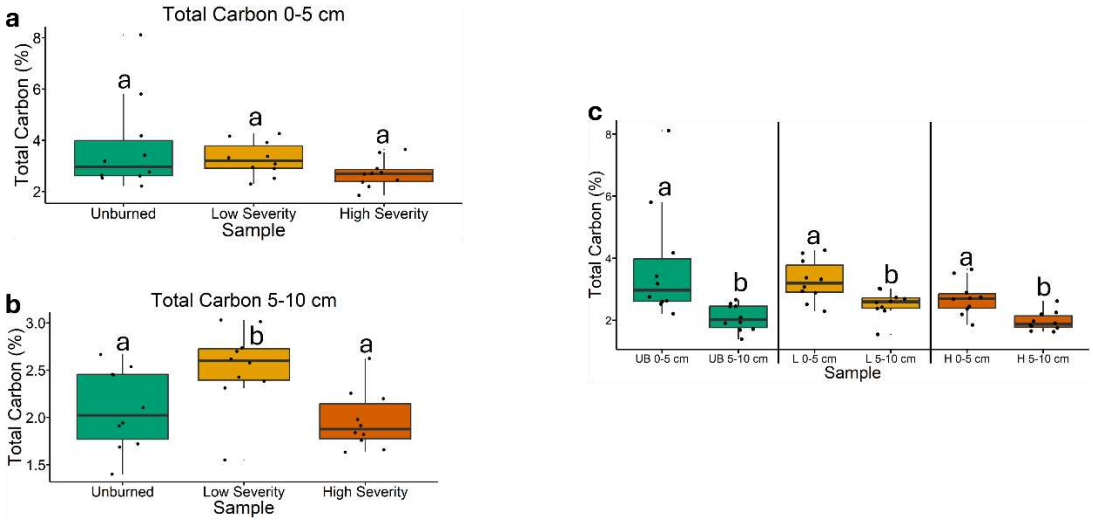

Figure D3. Soil total carbon values visualized with box plots. Comparing soil total carbon values amongst soil samples collected at 0-5 cm depth (**a)** and 5-10 cm depth (**b**). Letters above boxes indicate significant differences between treatments determined by either ANOVA and Tukey HSD tests, Welch's ANOVA and Games-Howell tests, or Kruskal-Wallis and Dunn's tests (see Statistics section 5.2.15 within Methods). n = 10 for unburned, low severity, and high severity samples. **c,** Comparing soil total carbon values between depths of each sample type. The statistical tests within sample types (i.e. unburned, low severity, and high severity) were conducted independently of each other. Letters above the boxes indicate significant differences between depths and were determined with either Student's t-test, Welch's t-test, or Mann-Whitney U tests (see Statistics section 5.2.15 within Methods). n=10 for unburned 0-5 cm, unburned 5-10 cm, low severity 0-5 cm, low severity 5-10 cm, high severity 0-5 cm, and high severity 5-10 cm samples. UB = unburned. L = low severity. H = high severity. Box plots show the median (central line), first and third quartiles (box edges), and whiskers extending to minimum and maximum values within 1.5 times the interquartile range. Data beyond the end of the whiskers are "outlying" points and are plotted individually.

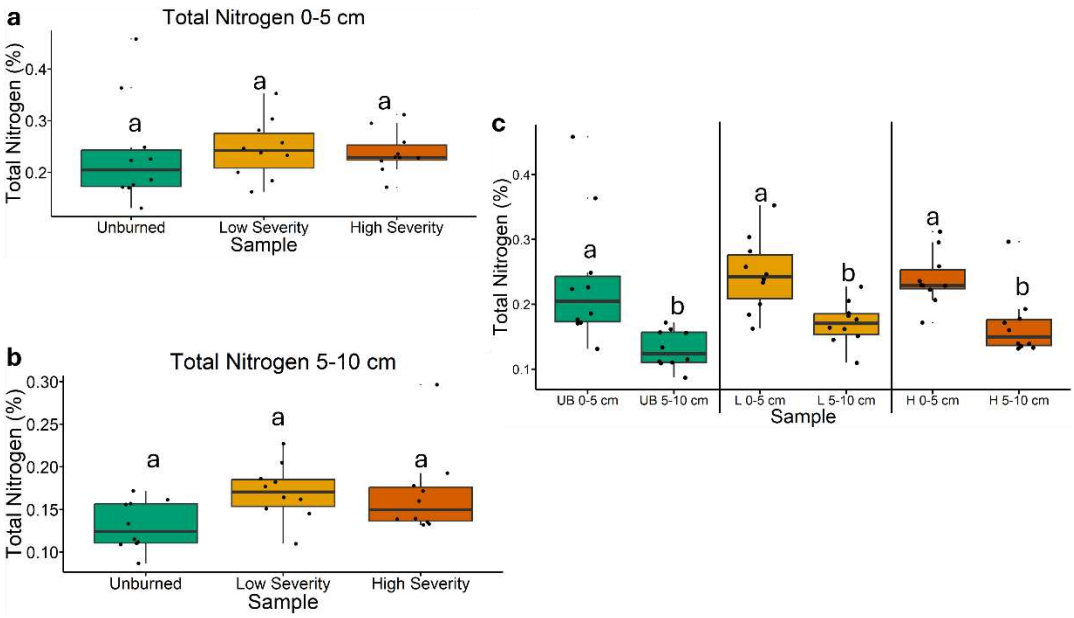

Figure D4. Soil total nitrogen values visualized with box plots. Comparing soil total nitrogen values amongst soil samples collected at 0-5 cm depth (**a)** and 5-10 cm depth (**b**). Letters above boxes indicate significant differences between treatments determined by either ANOVA and Tukey HSD tests, Welch's ANOVA and Games-Howell tests, or Kruskal-Wallis and Dunn's tests (see Statistics section 5.2.15 within Methods). n = 10 for unburned, low severity, and high severity samples. **c,** Comparing soil total nitrogen values between depths of each sample type. The statistical tests within sample types (i.e. unburned, low severity, and high severity) were conducted independently of each other. Letters above the boxes indicate significant differences between depths and were determined with either Student's t-test, Welch's t-test, or Mann-Whitney U tests (see Statistics section 5.2.15 within Methods). n=10 for unburned 0-5 cm, unburned 5-10 cm, low severity 0-5 cm, low severity 5-10 cm, high severity 0-5 cm, and high severity 5-10 cm samples. UB = unburned. L = low severity. H = high severity. Box plots show the median (central line), first and third quartiles (box edges), and whiskers extending to minimum and maximum values within 1.5 times the interquartile range. Data beyond the end of the whiskers are "outlying" points and are plotted individually.

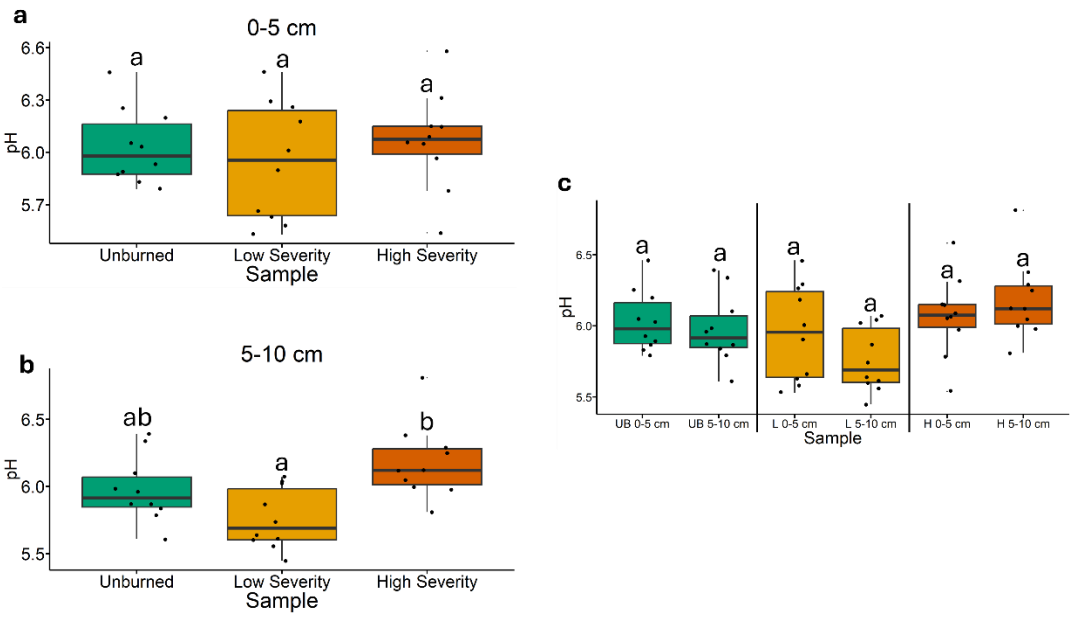

Figure D5. Soil pH values visualized with box plots. Comparing soil total carbon values amongst soil samples collected at 0-5 cm depth (**a)** and 5-10 cm depth (**b**). Letters above boxes indicate significant differences between treatments determined by either ANOVA and Tukey HSD tests, Welch's ANOVA and Games-Howell tests, or Kruskal-Wallis and Dunn's tests (see Statistics section 5.2.15 within Methods). n = 10 for unburned, low severity, and high severity samples. **c,** Comparing soil pH values between depths of each sample type. The statistical tests within sample types (i.e. unburned, low severity, and high severity) were conducted independently of each other. Letters above the boxes indicate significant differences between depths and were determined with either Student's t-test, Welch's t-test, or Mann-Whitney U tests (see Statistics section 5.2.15 within Methods). n=10 for unburned 0-5 cm, unburned 5-10 cm, low severity 0-5 cm, low severity 5-10 cm, high severity 0-5 cm, and high severity 5-10 cm samples. UB = unburned. L = low severity. H = high severity. Box plots show the median (central line), first and third quartiles (box edges), and whiskers extending to minimum and maximum values within 1.5 times the interquartile range. Data beyond the end of the whiskers are "outlying" points and are plotted individually.

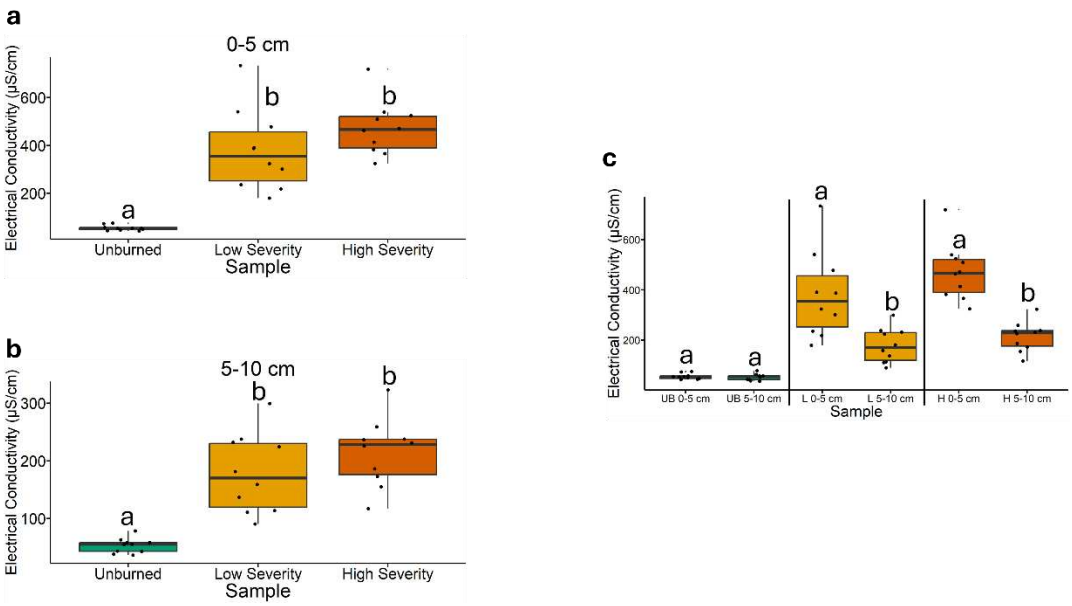

Figure D6. Soil electrical conductivity values visualized with box plots. Comparing soil total carbon values amongst soil samples collected at 0-5 cm depth (**a)** and 5-10 cm depth (**b**). Letters above boxes indicate significant differences between treatments determined by either ANOVA and Tukey HSD tests, Welch's ANOVA and Games-Howell tests, or Kruskal-Wallis and Dunn's tests (see Statistics section 5.2.15 within Methods). n = 10 for unburned, low severity, and high severity samples. **c,** Comparing soil electrical conductivity values between depths of each sample type. The statistical tests within sample types (i.e. unburned, low severity, and high severity) were conducted independently of each other. Letters above the boxes indicate significant differences between depths and were determined with either Student's t-test, Welch's t-test, or Mann-Whitney U tests (see Statistics section 5.2.15 within Methods). n=10 for unburned 0-5 cm, unburned 5-10 cm, low severity 0-5 cm, low severity 5-10 cm, high severity 0-5 cm, and high severity 5-10 cm samples. UB = unburned. L = low severity. H = high severity. Box plots show the median (central line), first and third quartiles (box edges), and whiskers extending to minimum and maximum values within 1.5 times the interquartile range. Data beyond the end of the whiskers are "outlying" points and are plotted individually.

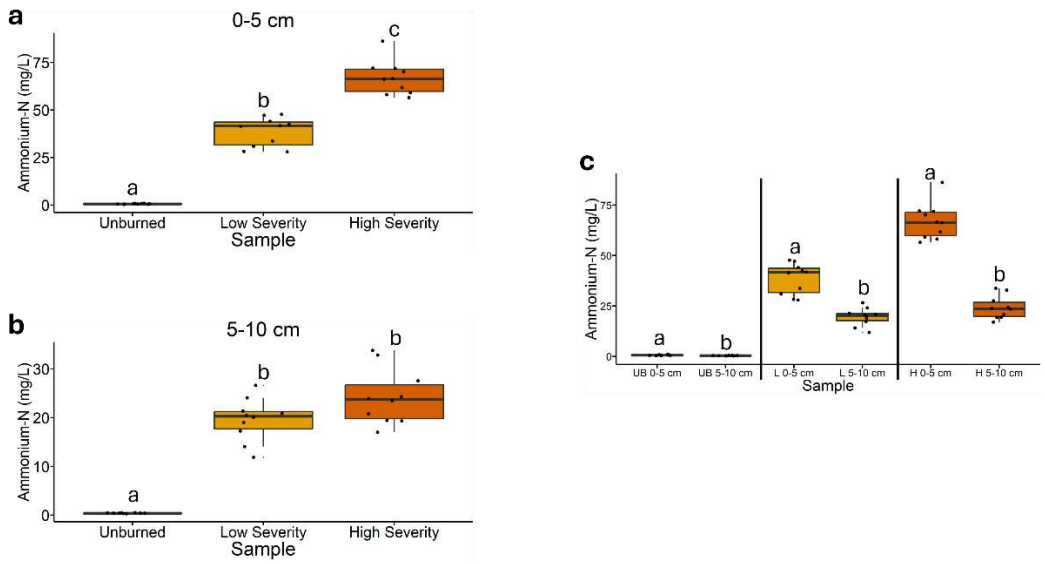

Figure D7. Ammonium-N concentrations in soil-water extracts visualized with box plots. Comparing soil total carbon values amongst soil samples collected at 0-5 cm depth (**a)** and 5-10 cm depth (**b**). Letters above boxes indicate significant differences between treatments determined by either ANOVA and Tukey HSD tests, Welch's ANOVA and Games-Howell tests, or Kruskal-Wallis and Dunn's tests (see Statistics section 5.2.15 within Methods). n = 10 for unburned, low severity, and high severity samples. **c,** Comparing ammonium-N concentrations in soil-water extracts between depths of each sample type. The statistical tests within sample types (i.e. unburned, low severity, and high severity) were conducted independently of each other. Letters above the boxes indicate significant differences between depths and were determined with either Student's t-test, Welch's t-test, or Mann-Whitney U tests (see Statistics section 5.2.15 within Methods). n=10 for unburned 0-5 cm, unburned 5-10 cm, low severity 0-5 cm, low severity 5-10 cm, high severity 0-5 cm, and high severity 5-10 cm samples. UB = unburned. L = low severity. H = high severity. Box plots show the median (central line), first and third quartiles (box edges), and whiskers extending to minimum and maximum values within 1.5 times the interquartile range. Data beyond the end of the whiskers are "outlying" points and are plotted individually.

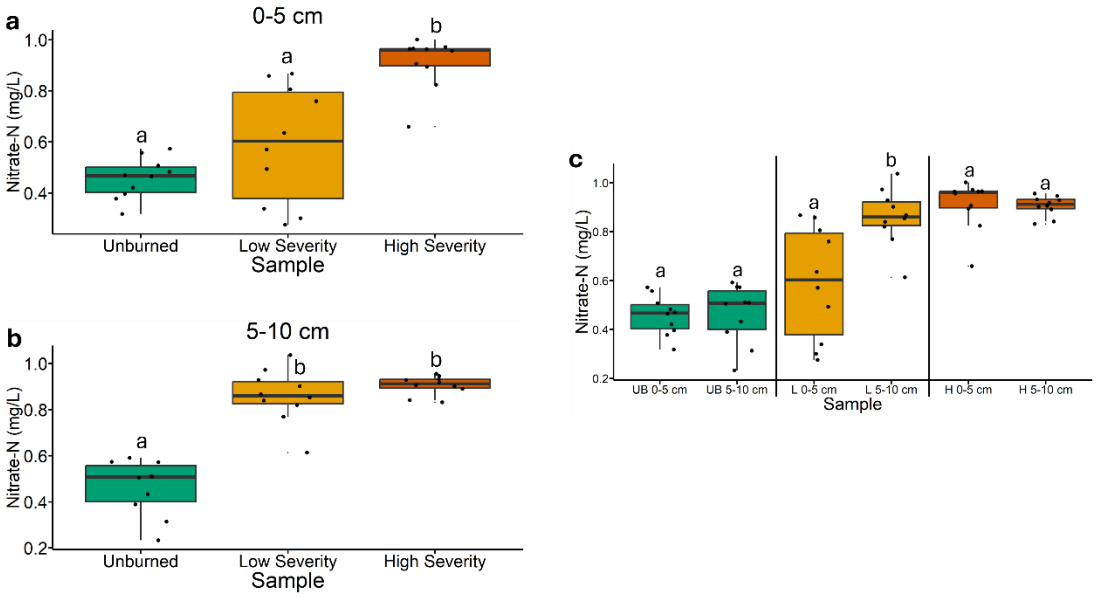

Figure D8. Nitrate-N concentrations in soil-water extracts visualized with box plots. Comparing soil total carbon values amongst soil samples collected at 0-5 cm depth (**a)** and 5-10 cm depth (**b**). Letters above boxes indicate significant differences between treatments determined by either ANOVA and Tukey HSD tests, Welch's ANOVA and Games-Howell tests, or Kruskal-Wallis and Dunn's tests (see Statistics section 5.2.15 within Methods). n = 10 for unburned, low severity, and high severity samples. **c,** Comparing nitrate-N concentrations in soil-water extracts between depths of each sample type. The statistical tests within sample types (i.e. unburned, low severity, and high severity) were conducted independently of each other. Letters above the boxes indicate significant differences between depths and were determined with either Student's t-test, Welch's t-test, or Mann-Whitney U tests (see Statistics section 5.2.15 within Methods). n=10 for unburned 0-5 cm, unburned 5-10 cm, low severity 0-5 cm, low severity 5-10 cm, high severity 0-5 cm, and high severity 5-10 cm samples. UB = unburned. L = low severity. H = high severity. Box plots show the median (central line), first and third quartiles (box edges), and whiskers extending to minimum and maximum values within 1.5 times the interquartile range. Data beyond the end of the whiskers are "outlying" points and are plotted individually.

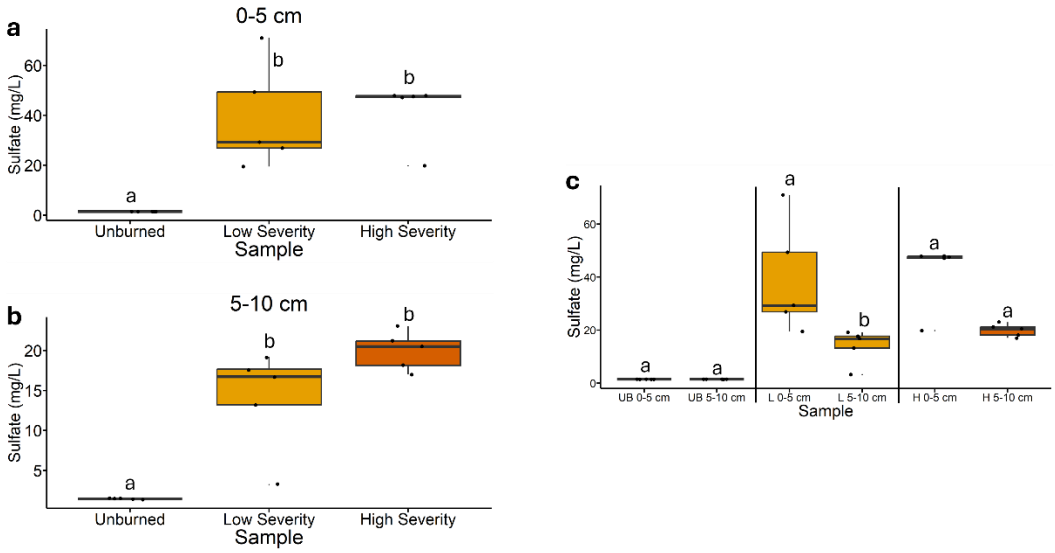

Figure D9. Sulfate concentrations in soil-water extracts visualized with box plots. Comparing soil total carbon values amongst soil samples collected at 0-5 cm depth (**a)** and 5-10 cm depth (**b**). Letters above boxes indicate significant differences between treatments determined by either ANOVA and Tukey HSD tests, Welch's ANOVA and Games-Howell tests, or Kruskal-Wallis and Dunn's tests (see Statistics section 5.2.15 within Methods). n = 10 for unburned, low severity, and high severity samples. **c,** Comparing sulfate concentrations in soil-water extracts between depths of each sample type. The statistical tests within sample types (i.e. unburned, low severity, and high severity) were conducted independently of each other. Letters above the boxes indicate significant differences between depths and were determined with either Student's t-test, Welch's t-test, or Mann-Whitney U tests (see Statistics section 5.2.15 within Methods). n=10 for unburned 0-5 cm, unburned 5-10 cm, low severity 0-5 cm, low severity 5-10 cm, high severity 0-5 cm, and high severity 5-10 cm samples. UB = unburned. L = low severity. H = high severity. Box plots show the median (central line), first and third quartiles (box edges), and whiskers extending to minimum and maximum values within 1.5 times the interquartile range. Data beyond the end of the whiskers are "outlying" points and are plotted individually.

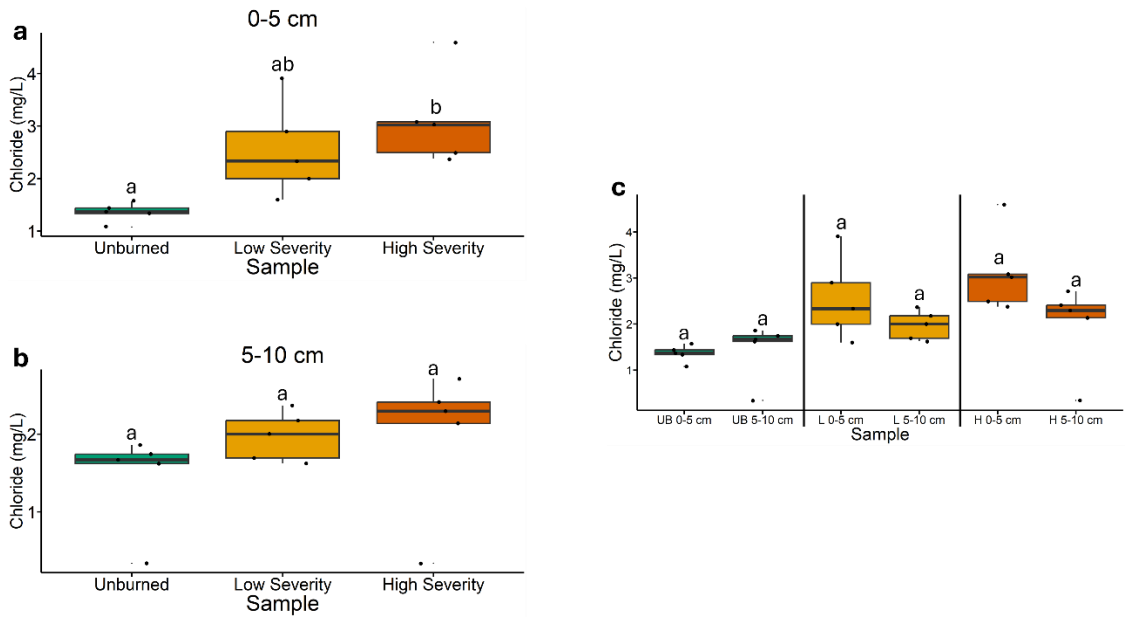

Figure D10. Chloride concentrations in soil-water extracts visualized with box plots. Comparing soil total carbon values amongst soil samples collected at 0-5 cm depth (**a)** and 5-10 cm depth (**b**). Letters above boxes indicate significant differences between treatments determined by either ANOVA and Tukey HSD tests, Welch's ANOVA and Games-Howell tests, or Kruskal-Wallis and Dunn's tests (see Statistics section 5.2.15 within Methods). n = 10 for unburned, low severity, and high severity samples. **c,** Comparing chloride concentrations in soil-water extracts between depths of each sample type. The statistical tests within sample types (i.e. unburned, low severity, and high severity) were conducted independently of each other. Letters above the boxes indicate significant differences between depths and were determined with either Student's t-test, Welch's t-test, or Mann-Whitney U tests (see Statistics section 5.2.15 within Methods). n=10 for unburned 0-5 cm, unburned 5-10 cm, low severity 0-5 cm, low severity 5-10 cm, high severity 0-5 cm, and high severity 5-10 cm samples. UB = unburned. L = low severity. H = high severity. Box plots show the median (central line), first and third quartiles (box edges), and whiskers extending to minimum and maximum values within 1.5 times the interquartile range. Data beyond the end of the whiskers are "outlying" points and are plotted individually.

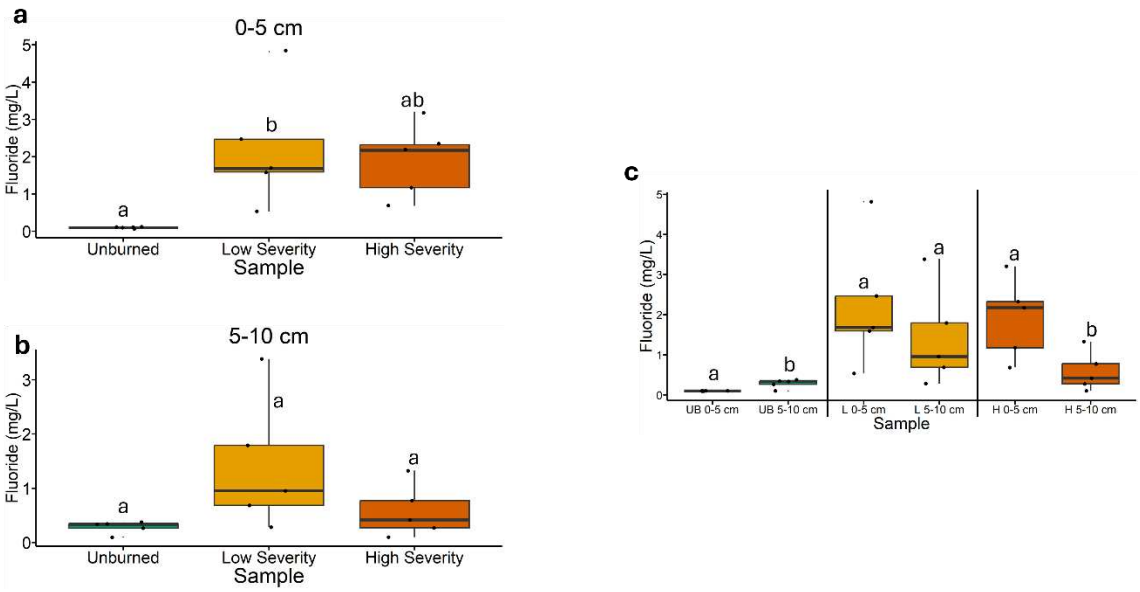

Figure D11. Fluoride concentrations in soil-water extracts visualized with box plots. Comparing soil total carbon values amongst soil samples collected at 0-5 cm depth (**a)** and 5-10 cm depth (**b**). Letters above boxes indicate significant differences between treatments determined by either ANOVA and Tukey HSD tests, Welch's ANOVA and Games-Howell tests, or Kruskal-Wallis and Dunn's tests (see Statistics section 5.2.15 within Methods). n = 10 for unburned, low severity, and high severity samples. **c,** Comparing fluoride concentrations in soil-water extracts between depths of each sample type. The statistical tests within sample types (i.e. unburned, low severity, and high severity) were conducted independently of each other. Letters above the boxes indicate significant differences between depths and were determined with either Student's t-test, Welch's t-test, or Mann-Whitney U tests (see Statistics section 5.2.15 within Methods). n=10 for unburned 0-5 cm, unburned 5-10 cm, low severity 0-5 cm, low severity 5-10 cm, high severity 0-5 cm, and high severity 5-10 cm samples. UB = unburned. L = low severity. H = high severity. Box plots show the median (central line), first and third quartiles (box edges), and whiskers extending to minimum and maximum values within 1.5 times the interquartile range. Data beyond the end of the whiskers are "outlying" points and are plotted individually.

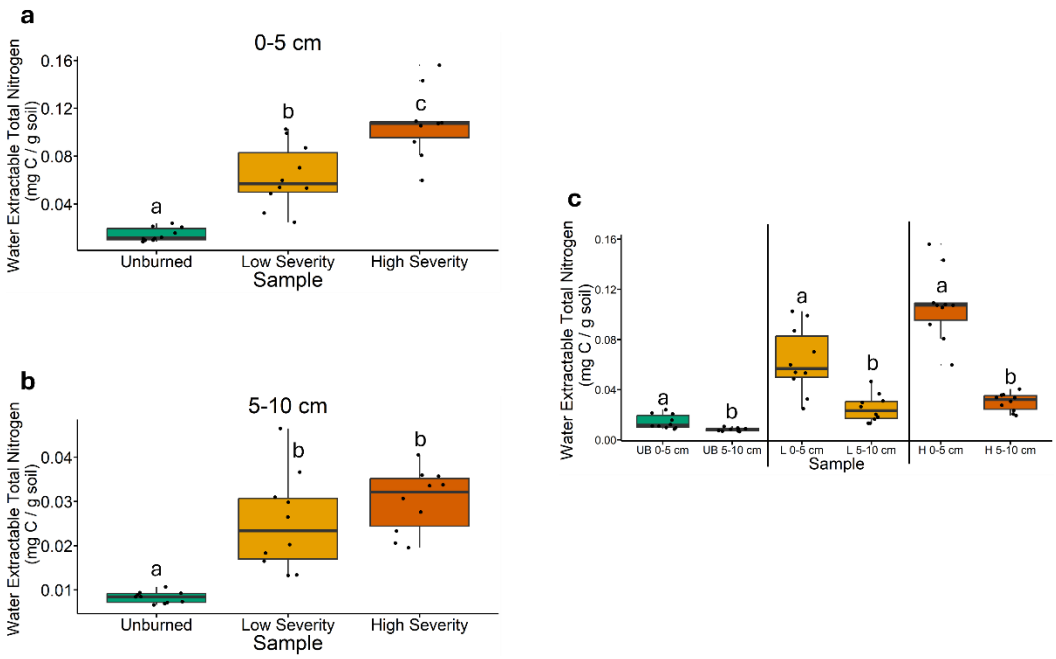

Figure D12. Water extractable total nitrogen concentrations visualized with box plots. Comparing soil total carbon values amongst soil samples collected at 0-5 cm depth (**a)** and 5-10 cm depth (**b**). Letters above boxes indicate significant differences between treatments determined by either ANOVA and Tukey HSD tests, Welch's ANOVA and Games-Howell tests, or Kruskal-Wallis and Dunn's tests (see Statistics section 5.2.15 within Methods). n = 10 for unburned, low severity, and high severity samples. **c,** Comparing Water extractable total nitrogen concentrations between depths of each sample type. The statistical tests within sample types (i.e. unburned, low severity, and high severity) were conducted independently of each other. Letters above the boxes indicate significant differences between depths and were determined with either Student's t-test, Welch's t-test, or Mann-Whitney U tests (see Statistics section 5.2.15 within Methods). n=10 for unburned 0-5 cm, unburned 5-10 cm, low severity 0-5 cm, low severity 5-10 cm, high severity 0-5 cm, and high severity 5-10 cm samples. UB = unburned. L = low severity. H = high severity. Box plots show the median (central line), first and third quartiles (box edges), and whiskers extending to minimum and maximum values within 1.5 times the interquartile range. Data beyond the end of the whiskers are "outlying" points and are plotted individually.

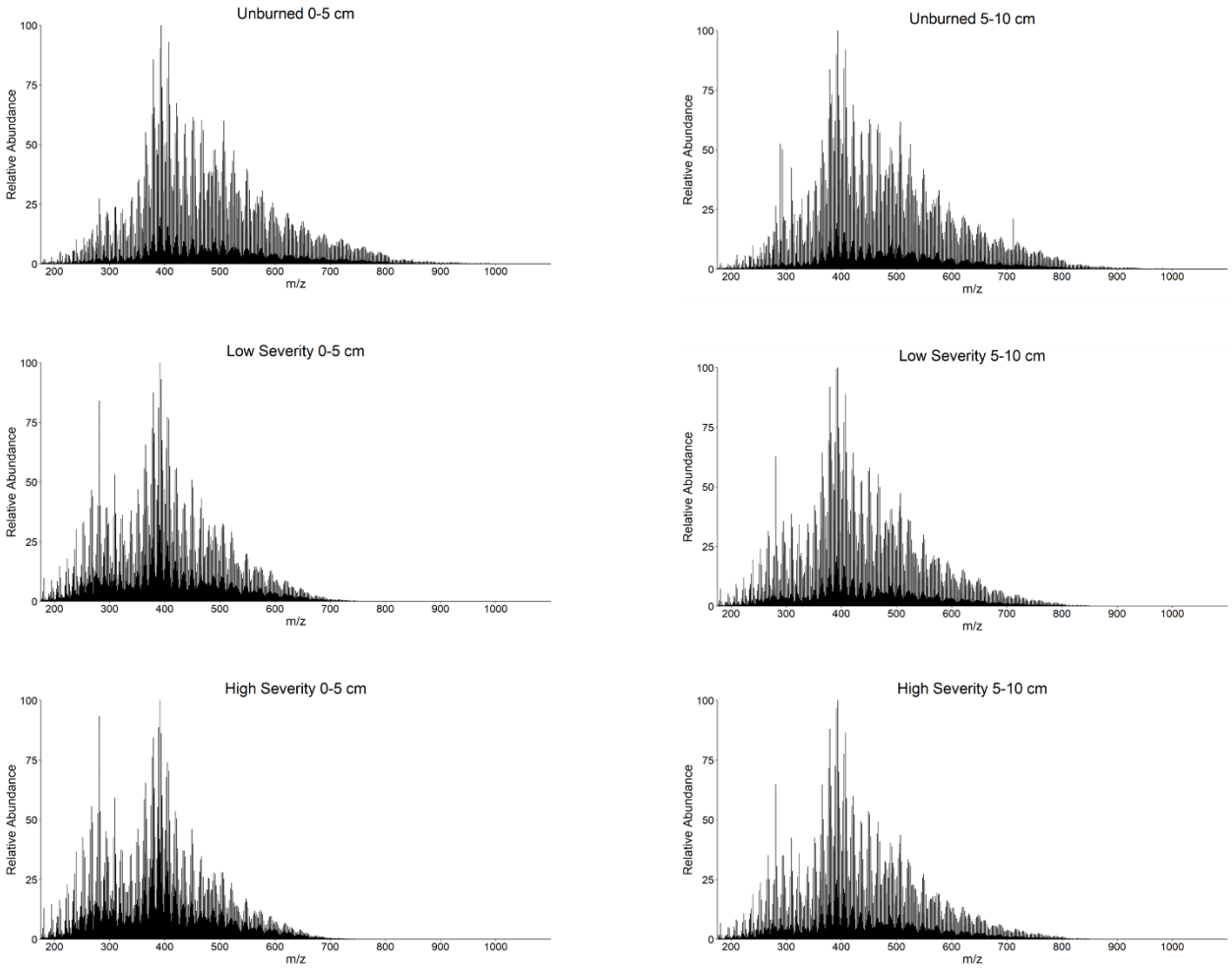

Figure D13. Fourier transform ion cyclotron resonance-mass spectrometry mass spectra.

Table D1. Total oxygen consumption during biological oxygen demand incubations.

Sample	Total Oxygen Consumption (mg)
Unburned extract + river water inoculum replicate 1	0.751
Unburned extract + river water inoculum replicate 2	0.726
Unburned extract + river water inoculum replicate 3	0.595
Low severity extract + river water inoculum replicate 1	1.731
Low severity extract + river water inoculum replicate 2	1.813
Low severity extract + river water inoculum replicate 3	1.673
High severity extract + river water inoculum replicate 1	1.494
High severity extract + river water inoculum replicate 2	1.370
High severity extract + river water inoculum replicate 3	1.179
River water inoculum only (no soil extract)	0.013
Mixture of filtered unburned, low severity, and high severity extract only (no river water inoculum)	0.399
Milli-Q water control	-0.047

Table D2. Dissolved organic carbon concentration (DOC) changes during biological oxygen demand incubations.

Sample	Initial [DOC] (mg/L)	Final [DOC] (mg/L)	Final – Initial [DOC] (mg/L)
Unburned extract + river water inoculum replicate 1	9.873	9.378	-0.495
Unburned extract + river water inoculum replicate 2	9.847	9.446	-0.401
Unburned extract + river water inoculum replicate 3	9.933	9.503	-0.430
Low severity extract + river water inoculum replicate 1	10.26	8.916	-1.344
Low severity extract + river water inoculum replicate 2	10.15	8.609	-1.541
Low severity extract + river water inoculum replicate 3	10.32	8.785	-1.535
High severity extract + river water inoculum replicate 1	9.749	8.592	-1.157
High severity extract + river water inoculum replicate 2	9.877	8.616	-1.261
High severity extract + river water inoculum replicate 3	9.826	8.635	-1.191
River water inoculum only	2.613	2.679	+0.066
Mixture of filtered unburned, low severity, and high severity extract only (no river water inoculum)	9.830	9.764	-0.066
Milli-Q water control	0.057	0.134	+0.077

Table D3. Average relative abundance values of the top 10 most abundant bacteria/archaea phyla.

Phyla	Unburned 0-5 cm average relative abundance (%)	Low Severity 0-5 cm average relative abundance (%)	High Severity 0-5 cm average relative abundance (%)
Acidobacteriota	20.8	2.0	2.0
Actinobacteriota	13.0	15.3	10.1
Bacteroidota	2.2	4.3	0.8
Chloroflexi	5.8	2.5	0.4
Crenarchaeota	2.6	0.4	0.1
Firmicutes	6.7	38.1	55.2
Myxococcota	0.8	0.2	0.1
Planctomycetota	13.0	1.3	1.1
Proteobacteria	11.4	32.1	27.5
Verrucomicrobiota	20.3	2.4	2.3

Table D4. Average relative abundance values of fungal guilds.

Fungal guilds	Unburned 0-5 cm average relative abundance (%)	Low Severity 0-5 cm average relative abundance (%)	High Severity 0-5 cm average relative abundance (%)
Ectomycorrhizal	52.2	56.9	76.2
Arbuscular Mycorrhizal	0.0	0.0	0.0
Saprotroph	10.3	17.7	0.9
Plant Pathogen	1.1	1.0	0.0
Endophyte/Epiphyte/Lichenized	0.0	0.0	0.0
Other Parasites/Pathogens	2.4	0.0	0.0
Unassigned	33.9	24.5	22.9

Table D5. Average relative abundance values of the top 10 most abundant fungal families.

Families	Unburned 0-5 cm average relative abundance (%)	Low Severity 0-5 cm average relative abundance (%)	High Severity 0-5 cm average relative abundance (%)
Cochlearomycetaceae	1.0	15.6	0.3
Cortinariaceae	6.1	0.0	0.0
Hymenogastraceae	3.22	0.0	0.0
Inocybacaea	11.9	0.0	0.0
Leucosporidiaceae	3.0	0.6	0.0
Lyophyllaceaea	3.1	1.6	0.4
Mortierellaceae	4.8	0.1	0.3
Pyronemataceae	5.8	56.8	76.1
Russulaceae	8.9	0.0	0.0
Tricholomataceae	13.8	0.0	0.0

APPENDIX E: CO-AUTHOR CONTRIBUTIONS TO "CHARACTERIZATION OF BURNED SOIL ORGANIC MATTER VIA SEQUENTIAL SOLVENT EXTRACTIONS AND 21 T FT-ICR MASS SPECTROMETRY WITH ELECTROSPRAY AND ATMOSPHERIC PRESSURE PHOTOIONIZATION"

Reprinted from Roth, H. K.; McKenna, A. M.; Aguilera, M. L.; VanderRoest, J. P.; Chen, H.; Borch, T. Characterization of Burned Soil Organic Matter via Sequential Solvent Extractions and 21 T FT-ICR Mass Spectrometry with Electrospray and Atmospheric Pressure Photoionization. *Anal. Chem.* **2025**, *97* (43), 24040–24049. https://doi.org/10.1021/acs.analchem.5c04154.

According to CRediT criteria, my contributions include conceptualization, methodology, resources, and writing – review & editing. I introduced the use of pyrocosms within the Borch lab which was used as the method of soil burning in this publication, resulting in my conceptualization, methodology, and resources contributions. Content of this publication was also featured in the appendix of Holly Roth's dissertation.

analytical chemistry

pubs.acs.org/ac Article

Characterization of Burned Soil Organic Matter via Sequential Solvent Extractions and 21 T FT-ICR Mass Spectrometry with Electrospray and Atmospheric Pressure Photoionization

Holly K. Roth, Amy M. McKenna, Martha L. Aguilera, Jacob P. VanderRoest, Huan Chen, and Thomas Borch*

Cite This: Anal. Chem. 2025, 97, 24040−24049 Read Online

ACCESS | Metrics & More | Article Recommendations | Supporting Information

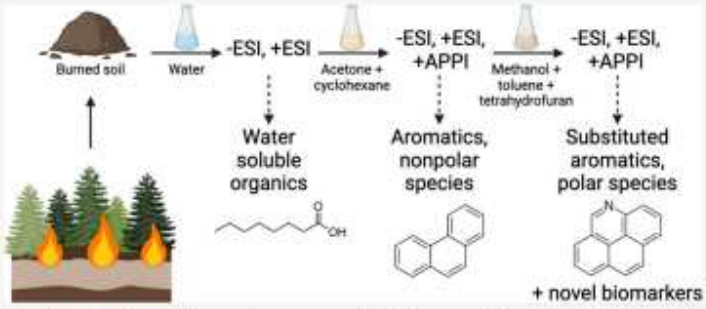

ABSTRACT: Wildfires significantly alter soil organic matter (SOM) composition, generating complex mixtures of polar and nonpolar compounds which are difficult to analyze. This study combines sequential extractions with electrospray ionization (ESI) and atmospheric pressure photoionization (APPI) followed by 21 T Fourier transform ion cyclotron resonance mass spectrometry (FT-ICR MS) to improve the molecular characterization of SOM from burned soils. Soils were extracted first with water and then Soxhlet extracted with organic solvents (acetone/cyclohexane and methanol/toluene/tetrahydrofuran). The compositional range of species identified by positive and negative ESI was expanded by 8−62%, and APPI enabled the detection of hydrocarbons and nitrogen-containing species that were largely undetected by ESI alone. Among the identified compounds, molecular formulas consistent with biomarkers such as stigmasta-3,5-diene, a plant-derived sterol degradation product, were present only in the organic solvents. Stigmasta-3,5-diene and similar compounds have been observed after fire events across various vegetation types, including forest ecosystems. Highly abundant compounds detected at four double bond equivalents (e.g., 25-azacoprostane) may represent sterol interrupters or cholesterol metabolism inhibitors, potentially serving as additional biomarkers for fire conditions. The calculated nominal oxidation state of carbon (NOSC) revealed distinct groupings based on solvent type and ionization mode, emphasizing the selective extraction of less labile organic matter by organic solvents compared to water. These results highlight the critical role of sequential solvent extraction and diverse data analysis strategies in advancing the understanding of fire-impacted SOM chemistry and provide a framework for biomarker discovery in environmental monitoring and biogeochemical studies.

INTRODUCTION

Wildfires are natural environmental disturbances that have been increasing in both frequency and severity since the 1970s.[1,2] High-severity wildfires, characterized by significant organic matter loss from the soil surface, directly alter physical and chemical soil properties, potentially degrading water quality and other ecosystem services.[3,4] Fires also modify soil organic matter (SOM) composition and concentration, alter soil minerals, and influence SOM redox properties.[5]

Soil organic matter in burned soils often exhibits higher aromaticity and hydrophobicity, along with altered elemental stoichiometries, which can alter biogeochemical processes.[6,7] Among the aromatic species generated are polycyclic aromatic hydrocarbons (PAHs), a class of low-polarity carcinogenic compounds produced by incomplete combustion.[8,9] In oxygen-rich conditions, fires can also catalyze the formation of polar carboxylic acid-rich compounds,[5] highlighting the system's complexity and the potential limitations of single extraction methods in capturing all analytes of interest.

Received: July 11, 2025
Revised: October 3, 2025
Accepted: October 9, 2025
Published: October 22, 2025

https://doi.org/10.1021/acs.analchem.5c04154
Anal. Chem. 2025, 97, 24040−24049

Molecular speciation of SOM in burned soil is inherently challenging due to the low water solubility of many fire-derived species and their complex composition, which can hinder mass spectrometry analyses[10,11] Aqueous extraction effectively isolates the mobile fraction while organic solvents enhance recovery of organic matter, particularly in systems where gas chromatography (GC)-based techniques are used; however, these are restricted to compounds within the GC volatility window. In contrast, Fourier transform ion cyclotron resonance mass spectrometry (FT-ICR MS), assisted by atmospheric pressure photoionization and electrospray ionization, offers unparalleled capability to resolve nonvolatile molecular species with mass differences as small as the mass of an electron, enabling detailed characterization of the ultracomplex organic matter.[12]

Before analysis, SOM must be extracted from the soil matrix. Aqueous and solid-phase extractions (SPE) are commonly used during FT-ICR MS analysis to isolate water-soluble organics (WSO) and detect highly polar, oxygen-enriched species across a broad carbon range. However, aqueous extractions alone are insufficient for recovering hydrophobic molecules or those adsorbed onto mineral surfaces.[13,14] Consequently, incorporating organic solvent fractionation into the extraction process extends the analytical window and enables the detection of less polar species.[15,16]

Organic solvent fractionation via Soxhlet extraction has been widely used for heavy oil characterization[17] and has high recovery yields for the 16 US Environmental Protection Agency (EPA) priority pollutant PAHs in biochar.[18,19] Soxhlet extraction can be used to isolate specific chemical functional groups such as nonpolar hydrocarbons, abundant O_1 species, and weakly acidic or neutral N_{1-3} compounds that are not identified in the water-soluble fraction.[20,21] Specifically, acetone selectively removes small/pericondensed rings capable of dipole−dipole interactions.[22,23] Methanol routinely isolates polar species from a wide range of carbon matrices,[24] and mixing methanol with toluene and tetrahydrofuran further facilitates the extraction of polar, aromatic species that can form hydrogen bonds with the silanol groups in soils and mineral surfaces.[25,26] Therefore, solvent fractionation methods could be applied to burned soil systems to expand the detection of SOM molecules.

While FT-ICR MS provides valuable insights into SOM composition, analyses are further limited by the ability of ion sources to volatilize and ionize compounds within the samples.[27] The complementarity of electrospray ionization (ESI) and atmospheric pressure photoionization (APPI) has been reported for petroleum,[28,29] lake and marine dissolved organic matter,[30,31] and biochar-derived OM,[16] but has not been routinely applied to fire-impacted soils. Negative ESI is well-suited to ionize highly polar lignin derivatives, lipids, and pyrolytic sugars with varying degrees of oxygenation,[32] while positive-ion mode (+ESI) is more specific to sugar derivatives and nitrogenated species.[11,28] APPI extends the dynamic range and molecular coverage to less polar molecules, especially complex and low-volatility PAHs.[33] Because burned soils are ultracomplex mixtures that are subject to selective ionization,[34] coupling solvent extractions, extrography, and targeted ionization methods in FT-ICR MS analyses provides a more comprehensive molecular investigation.[25]

In this study, we investigate burned SOM as a highly complex, polyfunctional mixture of organic molecules and introduce a solvent fractionation method aimed at dissociating aggregated species for enhanced molecular characterization. First, we compare the chemical properties of SOM from burned soil after sequential extraction with water and organic solvents ionized by ESI. Second, we leverage APPI to target nonpolar aromatic species isolated by organic solvents, complementing ESI for broader compositional coverage. ESI results reveal that Soxhlet fractionation increases the number of assigned molecular species by 8−62%, capturing compounds undetected in the water-soluble fraction alone. APPI further enabled the identification of 981 additional hydrocarbons and 136 nitrogen-containing hydrocarbons (N-hydrocarbons), demonstrating its efficacy in detecting low-polarity compounds beyond ESI's capabilities. These findings advance our understanding of fire-impacted soil chemistry and extend the potential application of these methods to other environmental matrices. Furthermore, the fractionation approach developed here provides a robust framework for sample preparation in complementary analytical techniques, such as nuclear magnetic resonance (NMR) spectroscopy, facilitating comprehensive analyses of complex organic mixtures.

METHODS

Soil Sampling. Mineral soil and forest litter were collected from unburned lodgepole pine (*Pinus contorta*)-dominated forest in Roosevelt National Forest, Colorado, USA. The forest type is representative of subalpine forests that frequently burn in Colorado.[35] The O horizon was removed to expose the mineral soil, which was then sampled from a depth of 0−10 cm. Before buring, the soil was sieved to a particle size of 12.7 mm (0.5 in.).

Pyrocosm Experimental Design. Pyrocosms were constructed to simulate wildfire conditions while maintaining control over key experimental variables, including soil type, fuel type, fuel load, and burn duration.[36,37] Briefly, 12-quart galvanized steel buckets were methanol-washed and marked at 0.5, 5, and 10 cm depths, and holes were drilled to accommodate thermocouple leads (two holes at 0.5 cm, one hole each at 5 and 10 cm) to measure soil temperature (Figure S1; T_{max} = 455 °C). Soil was added to 5 cm from the rim of the bucket, and a stainless-steel screen (20 mesh, Valchoose), precleaned with HPLC-grade toluene, was placed at the 5 cm mark to ensure consistent sampling depth. Additional soil was then added to fill the bucket for a final bulk density of 1 g cm^{-1}.

Pyrocosm Burning. After assembly, the pyrocosms were transported to the Colorado State University Agricultural Research, Development, and Education Center (CSU ARDEC) in field 100A, where all vegetation had been cleared. To insulate the system, each bucket was placed into a dug hole. Before the burn, a layer of pine litter (~2.54 cm or 1 in.) was added to the soil surface, along with small twigs to serve as kindling. During the burn, approximately 9 kg of pine wood was gradually added to the soil surface to sustain combustion. After 24 h, large debris was removed and ash and mineral soil up to 5 cm depth were collected with a small trowel (cleaned with HPLC-grade methanol) in a gallon bag and transported to CSU. The soil was then air-dried and sieved to 2 mm before storage at 4 °C.

Soil Extractions. All glassware was solvent-washed with toluene and combusted in a muffle furnace (400 °C for 6 h). All solvents were purchased from Sigma-Aldrich Chemical Co., St. Louis, MO, USA.

https://doi.org/10.1021/acs.analchem.5c04154
Anal. Chem. 2025, 97, 24040−24049

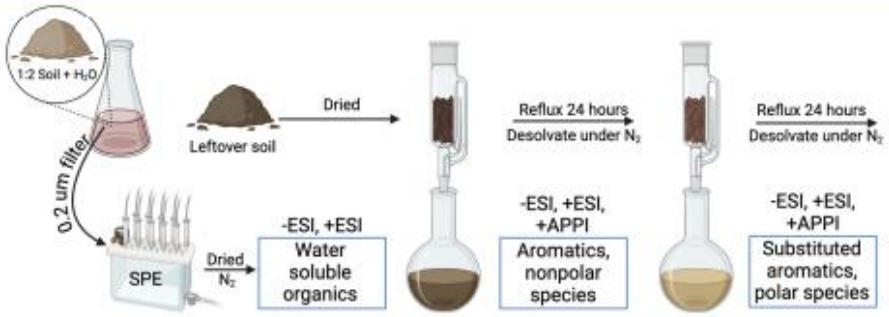

Figure 1. Sample preparation schematic illustrating the serial solvent extractions ($n = 1$). The burned soil was first extracted with water, and the extract was filtered prior to solid phase extraction (SPE). The final extract was eluted with methanol and dried for analysis by positive and negative ion electrospray ionization (ESI). The remaining soil was dried prior to Soxhlet extraction with a 1:1 ratio of acetone and cyclohexane, which was refluxed for 24 h and desolvated under nitrogen gas (N_2). The soil was then dried again and refluxed for 24 h with 1:1:1 ratio of methanol, toluene, and tetrahydrofuran and desolvated under N_2. The extracts from the solvent extractions were analyzed by ESI and atmospheric pressure photoionization (APPI).

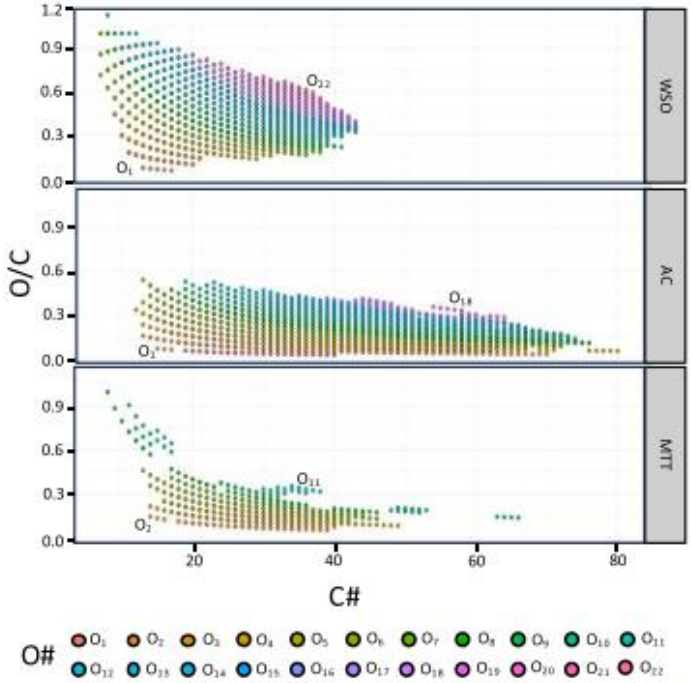

Figure 2. Carbon number (C#) vs O/C ratio plots for formulas containing only carbon, hydrogen, and oxygen (CHO-only) derived from -ESI FT-ICR MS for water-soluble species isolated by SPE-PPL (top; WSO), and solvent extraction with acetone + cyclohexane (center; AC) and methanol + toluene + tetrahydrofuran (bottom; MTT). Colors represent the number of oxygens per formula.

Water-Soluble Organics (WSO). 100 g of soil and 200 mL Milli-Q water were combined in precombusted Erlenmeyer flasks and shaken for 10 h at 170 rpm. The resulting soil slurry was transferred to 50 mL centrifuge tubes and centrifuged at 7500 rpm for 20 min. The supernatant was filtered through 0.2 μm polyether sulfone (PES) filters prior to acidification to pH 2 using trace-metal grade hydrochloric acid. A styrene-divinylbenzene (SDVB) polymer modified with a proprietary nonpolar surface (Bond Elut Priority Pollutant, Agilent Technologies) cartridge was prepared by sequentially rinsing with HPLC-grade methanol and pH 2 water. Following the sample introduction, the cartridge was rinsed again with pH 2 water to remove salts, and then the water-soluble organics (WSO) were eluted with 2 mL HPLC-grade methanol.[58]

Soxhlet Extractions. After the water extraction, the remaining soil was dried and prepared for Soxhlet extractions, as illustrated in Figure 1. 40 g of dried soil was placed in a glass fiber thimble and positioned in a toluene-washed Soxhlet extractor, with a layer of glass wool added on top. Two sequential extractions were conducted: for the first extraction,

https://doi.org/10.1021/acs.analchem.5c04154
Anal. Chem. 2025, 97, 24040−24049

250 mL of 1:1 acetone and cyclohexane (AC) was added to a round-bottom flask containing a stir bar and heated on a mantle. The solvent was brought to a boil and refluxed for 24 h or until it became clear. The solvent was then evaporated, and the extract was resuspended in 2 mL of solvent and transferred to a glass amber vial and stored at 4 °C. The soil-packed thimble was subsequently air-dried, and the process was repeated with a 1:1:1 mixture of methanol, toluene, and tetrahydrofuran (MTT).

Ionization: +APPI and −ESI. For negative-ion micro-ESI, widely applied to dissolved organic matter to target acidic species, soil extracts were analyzed at 250 μg/mL (in 50:50 toluene: methanol), and WSO extracts were analyzed in 100% methanol at a flow rate of 0.5 μL/min. Positive-ion APPI was selected to ionize aromatics,[39,40] and solvent extracts were resuspended in toluene to yield a final concentration of 125 μg/mL for dopant-assisted ionization at a 50 μL/min flow rate. Ions were generated at atmospheric pressure via an APPI source (Ion Max APPI source, Thermo-Fisher Scientific, Inc., San Jose, CA, U.S.A.) or microelectrospray. Due to the requirement of a high ratio of dopant to analyte for APPI, samples were redissolved to yield a final solvent composition of 70/30 (v/v), MeOH/Toluene before APPI analysis. Complete experimental details on ionization can be found in the Supporting Information. The WSO samples were analyzed by FT-ICR MS in positive- and negative-ion mode electrospray ionization (±ESI). The solvent extracts (AC and MTT) were analyzed by ±ESI and positive-ion atmospheric pressure photoionization (+APPI).

21 T FT-ICR MS and Data Analysis. Soil extracts were analyzed with a custom-built hybrid linear ion trap FT-ICR mass spectrometer equipped with a 21 T superconducting solenoid magnet.[41,42] The dynamically harmonized ICR cell in the 21 T FT-ICR is operated with 6 V trapping potential.[43,44] Mass spectra were phase-corrected[45] and internally calibrated with 10−15 highly abundant homologous series that span the entire molecular weight distribution based on the "walking" calibration method.[46] Additional information can be found in the Supporting Information.

RESULTS AND DISCUSSION

Solvent Partitioning Affects Formula Assignments. Three distinct fractions of a burned soil sample were generated using sequential extractions: water isolated the water-soluble organics (WSO), acetone/cyclohexane (AC) isolated targeted aromatic species, and methanol/toluene/tetrahydrofuran (MTT) extracted polar-substituted compounds. All three extracts were analyzed in negative and positive-ion electrospray ionization at 21 T FT-ICR MS. In negative-ion ESI, the number of assigned peaks ranged from 1,408 to 15,755, while positive-ion ESI produced 560 to 15,107 peaks. Regardless of ionization mode, WSO yielded the highest number of assigned species (>15,000 for both modes). The number of formulas assigned followed the order: WSO > AC > MTT for positive- and negative-ESI.

Solvent fractionation expands the compositional diversity of analytes, particularly within the CHO elemental class. This effect is best illustrated in the density plot of CHO species across sequential extractions analyzed by positive and negative ESI (Figure S2), highlighting a shift toward lower oxygen content (O) in organic solvent extracts compared to WSO extracts. To further analyze solvent partitioning effects on detected species, we plotted C# vs O/C of the CHO species observed in ESI (Figure 2) and noted a clear distinction in C# and O/C when comparing WSO to AC and MTT, in agreement with the C# data in Table 1 and O/C data in Table S2. The C range of WSO was much smaller compared to the organic solvent extracts, and the average C per molecule decreased by 2 to 26 (Table S1). The O/C range was also substantially impacted by the extractant, with the average O/C of WSO nearly double that of the organic solvent extracts. The observed differences in O/C and C# can be attributed to WSO selectively extracting smaller molecules,[47] which must have enough oxygen to be water-soluble. In contrast, organic solvent-extracted species displayed a pronounced shift toward higher hydrophobicity, indicated by lower O/C ratios and higher C# values.

Table 1. Elemental Assignment Ranges for Carbon (C), Hydrogen (H), Oxygen (O), Nitrogen (N), and Sulfur (S) from Positive-Ion and Negative-Ion ESI Spectra FT-ICR MS for Water-Soluble Species (WSO) Isolated by SPE-PPL and Organic Solvent Extraction with Acetone + Cyclohexane (AC) and Methanol + Toluene + Tetrahydrofuran (MTT)[a]

Sample	C	H	O	N	S
−ESI WSO	6−43	3−58	1−22	0−4	0−1
−ESI AC	12−80	4−154	1−19	0−2	0−1
−ESI MTT	6−78	10−96	2−22	0−1	0−2
+ESI WSO	6−42	4−66	1−18	0−4	N.a.
+ESI AC	22−89	32−116	0−12	0−1	0−1
+ESI MTT	19−90	26−124	0−16	0−1	0−2

[a]N.a. = not assigned.

Oxygen-containing heteroatoms were consistently observed across all extractions, with data overlaps trending toward lower oxygen in organic solvent extracts and higher oxygen in WSO fractions. The results reported here are consistent with biochar studies that showed that across the same heteroatom class, water-soluble species correspond to lower C# compounds compared to organic solvent extracts.[16] The C# vs O/C plots in Figure 2 reveal common homologous series across all extractions, with distinct molecules detected within each series. WSO are enriched in molecules with lower carbon numbers (C#) and higher oxygen content (O), whereas molecules with higher carbon numbers and lower oxygen content dominate AC and MTT extracts.

Species Composition Differs among Solvents. To evaluate compositional differences in the spectra from the sequential extractions, elemental assignments of carbon (C), hydrogen (H), nitrogen (N) oxygen (O), and sulfur (S) were compared (Table 1). In general, WSO exhibited a higher heteroatom content and lower carbon content than the organic solvent extracts, reflecting the detection of smaller molecular species in the spectra. Hydrocarbons were exclusively observed in + ESI AC and MTT spectra, as -ESI predominantly targets highly acidic species.[11,48]

Van Krevelen diagrams are widely applied to rapidly visualize compositional differences between samples analyzed by FT-ICR MS by plotting the H/C ratio versus O/C ratio of neutral species.[49] Figure S3 displays van Krevelen diagrams of the WSO, AC, and MTT samples analyzed by ± ESI. WSO species (Figure S3a,d) are centered around O/C ~0.3−0.5 and span H/C ratios of ~0.5 to 1.8. Compared to the WSO assignments, AC is shifted toward higher H/C and lower O/C ratios (Figure S3b,f), highlighting the relationship between the

https://doi.org/10.1021/acs.analchem.5c04154
Anal. Chem. 2025, 97, 24040−24049

solvent and the composition of the assigned species. The species assigned in MTT were similar in O/C and H/C ratios to AC (Figure S3c,g), although fewer species were assigned. Overall, we observed lower O/C ratios and higher H/C ratios for organic solvent extracts than WSO, which is consistent with previous reports.[16,25]

To further explore the differences in elemental composition between samples, heteroatom classes of the assigned species were plotted in a bar chart (Figure S4). WSO samples exhibited the highest proportions of CHNO species, accounting for over 50% of the formulas assigned in both ionization modes. The proportion of CHO increased across the extractions for the −ESI spectra, as the organic solvents targeted species with lower polarity than those extracted by water. In +ESI, we noted a substantial contribution from CHOS, attributed to alkylbenzenesulfonic acids or other man-made contaminants.[50] These contaminants could be introduced during sample preparation steps or may represent ubiquitous chemical noise commonly observed in mass spectrometry.

Solvent Extraction Identifies Unique Species in ±ESI 21 T FT-ICR MS. To assess the uniqueness of species detected in each spectrum, we made Venn diagrams illustrating the overlap of assigned formulas among extractions and the species unique to each extract. In the +ESI spectra (Figure 3, top), the organic solvent extractions identified an additional 837 unique formulas, representing a 5.24% increase compared to WSO alone. Interestingly, there was no overlap in formulas assigned between the WSO fraction and the two organic solvents due to the prevalence of sulfonated species in the solvent spectra. However, a substantial overlap was observed between the two organic solvent extractions, suggesting shared compositional features.

In −ESI, sequential extractions resulted in a substantially higher number of elemental composition assignments compared to +ESI. Organic solvent extractions resulted in 9,821 new assignments that were not present in the WSO, a 62% increase in total assigned elemental compositions. There was limited overlap in the proportion of assigned species between WSO and the organic solvent extracts, although substantial overlap was observed between MTT and AC (Figure 3, bottom). We attribute these observations to ion suppression in −ESI of complex organic mixtures, which is dominated by low molecular weight carboxylic acids readily soluble in water. Since solvent extraction was performed sequentially, the most polar species were isolated during the initial water extraction and were less prevalent in the solvent extracts due to their reduced polar functional group content.

Positive APPI FT-ICR MS Expands the Analytical Window. Figure S5 illustrates a broadband positive-ion APPI 21 T FT-ICR mass spectrum for the acetone/cyclohexane fraction of burned soil. The spectrum contains more than 4,000 distinct peaks, each with a signal magnitude at least 4σ above baseline noise and within the mass range of 175−1000 Da. The resolving power ($m/\Delta m_{50}\%$)—defined as the full mass spectral peak width at half-maximum peak height—is greater than 1,800,000 at m/z 400 (bottom left) The mass-scale expanded segment at m/z 411 (bottom right) highlights the spectral density with peaks resolved within a 4.476 mDa mass window (top right) that is necessary to accurately assign element compositions.

Previous studies have demonstrated that ESI and APPI are highly complementary in their ionization capabilities.[31] APPI broadens the analytical window by detecting less polar and more aromatic species and is effective for analyzing environmentally relevant molecules such as polycyclic aromatic hydrocarbons (PAHs) which ionize poorly via electrospray.[51] The results presented here are consistent with the aforementioned findings, as shown in Figure S3, which highlights species with relatively low O/C and high H/C ratios in the organic solvent extractions compared to WSO.

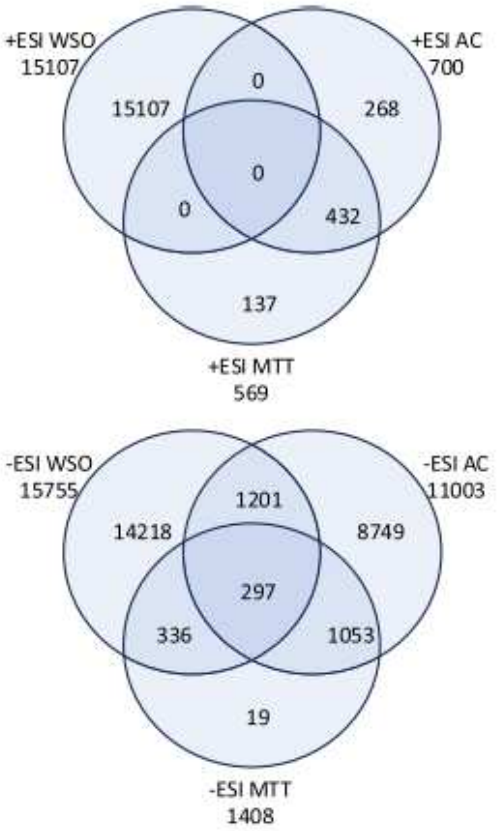

Figure 3. Venn diagrams comparing assigned formulas across the sequential extractions in +ESI (top) and −ESI (bottom). Formulas are derived from -ESI FT-ICR MS for water-soluble species isolated by SPE-PPL (WSO), and solvent extraction with acetone + cyclohexane (AC) and methanol + toluene + tetrahydrofuran (MTT). Numbers outside of the circles represent the total number of formulas assigned.

Hydrocarbon Analysis Is Enabled by +APPI. Although a small number of hydrocarbons (HCs) were identified in +ESI, +APPI significantly improved the ionization of HCs. Previous studies have also reported improved analysis of HCs with APPI, which are not as efficiently ionized by ESI due to their low polarity.[16] Double bond equivalents (DBE) distributions for HCs detected in the AC and MTT +APPI spectra are presented in Figure 4. The AC-soluble fraction exhibited a relatively even distribution between ionization mechanisms (Figure 4a), with a maximum relative abundance at DBE of 6 for radical species and 8 for protonated species. The data reflected selective ionization by the two mechanisms; protonated species were shifted toward lower DBE values,

https://doi.org/10.1021/acs.analchem.5c04154
Anal. Chem. 2025, 97, 24040−24049

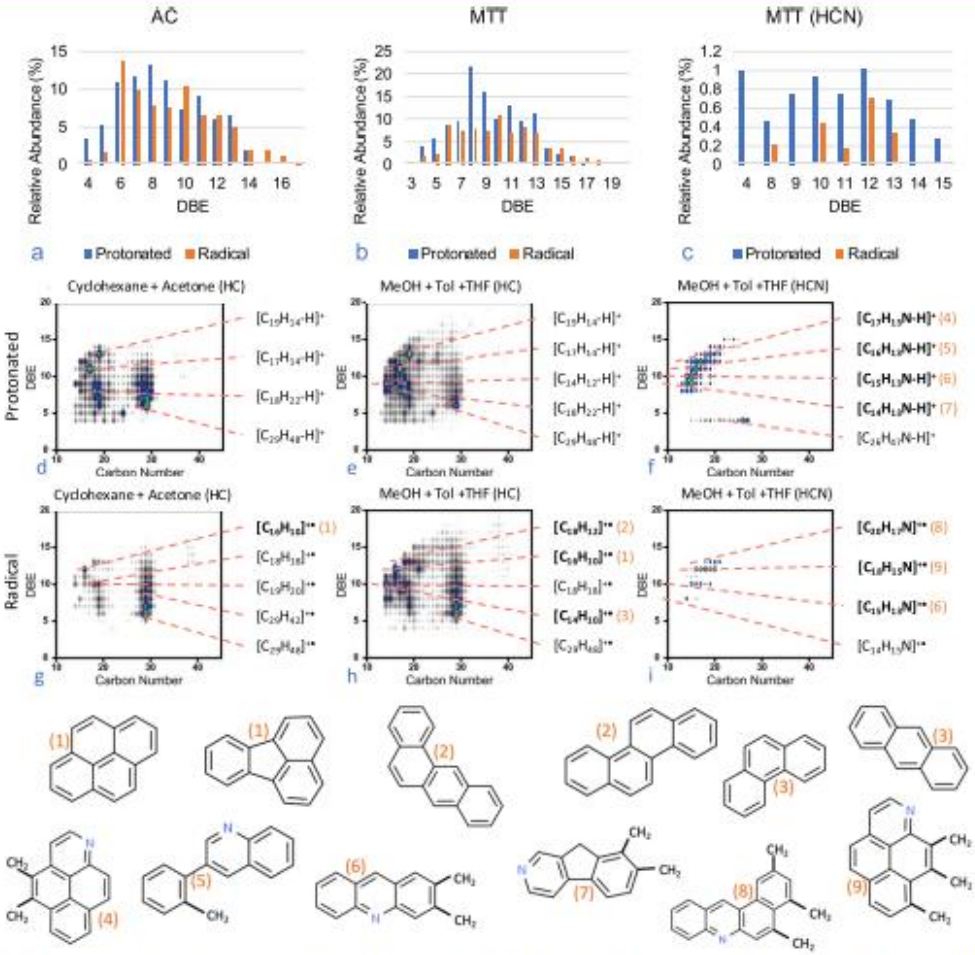

Figure 4. (a–c). Double bond equivalents (DBE, number of rings plus double bonds to carbon) distributions for hydrocarbon (HC) and nitrogenated hydrocarbon (HCN) species isolated by Soxhlet extraction with acetone + cyclohexane (AC) and methanol + toluene + tetrahydrofuran (MTT) derived from positive-ion APPI FT-ICR MS. (d–i). Isoabundance color-coded contour plots for HC and HCN species plotted according to DBE versus carbon number for HC and HCN. Dotted lines and formulas represent species of high relative abundance. Formulas matching polycyclic aromatic hydrocarbons (PAH) and nitrogenated polycyclic aromatic hydrocarbons (N-PAH) are in bold. Orange numbers denote the representative core structures of PAH (1–3) and N-PAH (4–9) species with corresponding elemental compositions detected in the burned soil extracts.

while radical species were shifted toward higher DBE values. The MTT HC spectrum had a higher proportion of protonated species than radical species (Figure 4b), as did the MTT nitrogenated hydrocarbon (HCN) series (Figure 4c). This trend can be attributed to the MTT extract isolating more polar species with higher proton affinities in the gas phase. Similar behavior has been reported for asphaltenes, where protonated ions typically dominate the signal in APPI. For samples extracted using MTT, the enhanced ionization efficiency of polar species preferentially leads to the formation of protonated ions due to the higher polarity and favorable proton affinity of the extracted compounds.[25,27]

Contour plots of DBE vs C# (Figure 4d–i) allow visualization of the most abundant core structures and highlight specific structural trends. APPI produces two ion types, and both the protonated and radical cation species are plotted separately.[39] Here, DBE vs C# plots are used to highlight the pericondensed molecular structures identified in the HC and HCN elemental classes. Identified species correspond to DBE values between 1 and 20 and C# values between 10 and 45, which indicate the prevalence of aromatic molecules with limited alkyl substitution. Such species are similar to highly pericondensed structures reported in previous wildfire studies.[52,53]

Across both the AC and MTT +APPI spectra, we identified three elemental compositions that match the molecular formulas of known PAHs (Structures 1–3 in Figure 4; Table S5), which have routinely been identified in burned soils.[54,55] Potential PAHs were more likely to be present in a radical form due to the presence of aromatic rings in the structure. No PAH formulas were assigned in the corresponding ±ESI spectra due to their low polarity and low abundance, whereas

https://doi.org/10.1021/acs.analchem.5c04154
Anal. Chem. 2025, 97, 24040−24049

APPI more efficiently ionizes PAHs. The putative identification of PAHs in both AC and MTT spectra reinforces the need for prior separations to observe fractions that are difficult to ionize.

+APPI MTT Allows Putative Identification of Diverse Azaarenes. Heterocyclic PAHs are formed by the incomplete combustion of a number of substances and are ubiquitous in environmental matrices.[56−58] Nitrogenated PAHs (N-PAHs), or azaarenes, frequently co-occur with PAHs in contaminated soils. Emerging evidence suggests that N-PAHs may pose ecotoxicity and human health risks.[59,60] Despite being recognized as combustion byproducts, a Web of Science search for "azaarenes" and "soil" yielded only 11 results, none of which referenced fire or wildfires.

Within the +APPI MTT spectrum, 136 HCNs were assigned. All species were plotted in Figure 4, and the most abundant species were identified in Table S5. Among the HCN class, eight homologous azaarene series (DBE 9−16) were investigated, based on prior reports that identified these species using high-performance liquid chromatography-quadrupole time-of-flight mass spectrometry (HPLC-qTOF MS) in PAH-contaminated soils.[61] Eighteen potential azaarene congeners were tentatively identified (Table S6), including seven highly abundant congeners (Structures 4−9 in Figure 4) that have not been previously reported in wildfire-affected soils. Azaarenes are toxic species that are more water-soluble, and therefore more mobile, than PAHs;[61] thus, the putative identification of such structures here illuminates the need to understand their occurrence and fate in environmental systems.

Potential Biomarkers Identified by Organic Solvent Extractions and FT-ICR MS. A highly abundant peak corresponding to $C_{29}H_{48}$ was conserved across all four HC plots (AC and MTT, protonated and radical; Figure 4d,e,g,h). Although exact structures cannot be determined from +APPI FT-ICR MS alone, a ChemSpider search revealed that $C_{29}H_{48}$ matches the formula for the terpene stigmasta-3,5-diene, a known plant biomarker. Terpenes, including stigmasta-3,5-diene, are aromatic compounds commonly found in plants where they serve various biological functions such as acting as antioxidants. Stigmasta-3,5-diene is a sterol degradation product, and its formation can be promoted by elevated temperatures.[62] It has been previously identified in smoke from shrub-dominated forests[62] and in extracts from charred jack pine (*Pinus banksiana*) wood and soil.[63] The high abundance of $C_{29}H_{48}$ in all four hydrocarbon spectra, and its previous identification in other fire-affected systems, suggests that it could be a possible indicator of combustion across forested ecosystems. However, further analysis (e.g., collision-induced dissociation) is required to positively identify the isomer(s) that contribute to this highly abundant peak.

Within the HCN class, we noted the presence of abundant species at DBE 4 (Figure 4f,i), the most abundant of which was $C_{26}H_{47}N$. Although FT-ICR MS data does not allow for the definitive assignment of structural isomers, $C_{26}H_{47}N$ matches the chemical formula of 25-azacoprostane, a cholesterol metabolism inhibitor in nematodes[64] and insects.[65] Other compounds detected at DBE 4 may represent sterol interrupters or aliphatic amines,[66] potentially serving as additional biomarkers in soil that could provide insights into ecosystem recovery in future studies. Given the effects of sterol interrupters on physiological development and larval viability, such compound classes could represent important indicators for revegetation and succession in burned soils.

APPI Increases the Compositional Range of Formula Assignments. To visualize broad compositional differences between extracts and ionization modes, we determined compound classes based on the elemental stoichiometry and aromaticity index (Table S7) of the assigned formulas in each spectrum (Figure 5).[67] Although the classifications are an

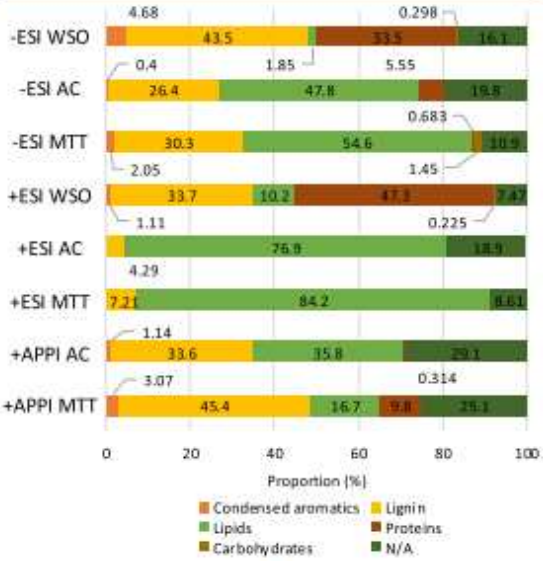

Figure 5. Molecular composition for water-soluble species (WSO) isolated by SPE-PPL and organic solvent extraction with acetone + cyclohexane (AC) and methanol + toluene + tetrahydrofuran (MTT) as observed by ESI and APPI FT-ICR MS. Biochemical categories were determined according to Hockaday et al.[31]

oversimplification of the data, they facilitate rapid comparisons between the samples. Each formula was assigned to one of six categories: condensed aromatics, lipids, carbohydrates, lignin, proteins, and not assigned (N/A).[31] Across all solvents and ionization modes, Figure 5 demonstrates that selectivity is highly variable between samples. Specifically, WSO contains the highest proportion of protein-like assignments, and +ESI WSO contains more protein-like species than -ESI WSO which agrees with previous research.[11,68] Additionally, carbohydrate-like species were only identified in −ESI MTT. APPI shifted the assigned formulas toward higher proportions of condensed aromatics and a much lower proportion of lipids than either ESI ionization mode for the corresponding solvent. Collectively, these results show that a combination of ESI and APPI represents a more comprehensive view of the compounds present in SOM.

There is a myriad of ways to demonstrate shifts in compositional classes, but another method commonly used to describe FT-ICR MS data is the nominal oxidation state of carbon (NOSC). NOSC describes the degradability of a molecule through its relationship to the Gibbs free energy of the reduction half-reaction between organic matter as the electron donor and the available terminal electron acceptor (oxygen in aerobic systems).[69] Box and whisker plots of the assigned formulas demonstrate that both the extractant used

https://doi.org/10.1021/acs.analchem.5c04154
Anal. Chem. 2025, 97, 24040−24049

and the ionization mechanism influenced the NOSC distribution of each sample (Figure S6). Distinct groupings were observed between spectra, where + ESI AC and MTT displayed the lowest variability in NOSC. −ESI AC and MTT and APPI AC displayed intermediate variability and low median NOSC, representative of less degradable OM.[70] −ESI WSO, +ESI WSO, and +APPI MTT displayed the highest variation in calculated NOSC values, although the median NOSC for both WSO samples was higher than for +APPI MTT. Taken together, the data presented in Figure 5 and Figure S6 demonstrate that solvents are selective for compounds with differing characteristics and both ionization mode and solvent choice influence calculated classes and chemical properties. Such differences emphasize the selective extraction of less degradable SOM by organic solvents compared to water. Collectively, the elemental stoichiometry and NOSC results indicate that solvent extractions and ionization are selective toward specific compound classes and must be carefully chosen to highlight the analytes of interest.

CONCLUSIONS

This study demonstrates the efficacy of sequential solvent extractions combined with advanced ionization techniques in expanding the compositional range of analytes from burned SOM. The choice of solvents significantly influenced the extraction of molecular species, with water selectively extracting more polar, oxygen-rich compounds while organic solvents selectively isolated more hydrophobic, aromatic, and nitrogen-containing species. Similarly, the choice of ionization method played a critical role in detecting and characterizing distinct compound classes. Negative electrospray ionization (−ESI) was particularly effective at identifying highly polar, acidic molecules, whereas positive atmospheric pressure photoionization (+APPI) expanded the analytical window to include less polar and highly aromatic compounds, such as polycyclic aromatic hydrocarbons (PAHs) and nitrogenated PAHs (N-PAHs).

The combined use of ESI and APPI demonstrated their complementarity, enabling a more comprehensive molecular characterization of SOM. This integrative approach uncovered unique molecular species, including stigmasta-3,5-diene and azaarenes, which would otherwise remain undetected in single-mode extractions or ionization methods. These compounds serve as potential biomarkers for fire conditions, providing valuable insights into the complex chemical nature of fire-impacted soils. Moreover, the study underscores the importance of molecular markers, such as sterol degradation products and aliphatic amines, in understanding fire-affected SOM and their potential applications in tracking fire severity and soil recovery. The findings emphasize the importance of tailoring both extraction methods and ionization techniques to specific research objectives, as each step selectively shapes the detected molecular composition.

The enhanced understanding of SOM composition following wildfires establishes a foundation for assessing its role in biogeochemical cycles, ecosystem recovery, and global change. Future studies should build upon this framework by integrating diverse analytical approaches to further elucidate the ecological and chemical impacts of wildfires on soil systems. This includes identifying additional biomarkers and evaluating long-term soil transformations across varying environmental conditions.

ASSOCIATED CONTENT

Supporting Information

The Supporting Information is available free of charge at https://pubs.acs.org/doi/10.1021/acs.analchem.5c04154.

Double bond equivalence calculation, nominal oxidation state of carbon calculation, mass-to-charge ratio (m/z) and elemental assignment averages for carbon (C), hydrogen (H), oxygen (O), nitrogen (N), and sulfur (S) for all spectra, range of oxygen to carbon (O/C) and hydrogen to carbon (H/C) ratios calculated from ESI spectra, selected m/z, mass error, and elemental composition for DBE values derived from positive-ion APPI hydrocarbon species extracted from burned soils with acetone and cyclohexane, selected m/z, mass error, and elemental composition for DBE values derived from positive-ion APPI hydrocarbon species extracted from burned soils with methanol, toluene, and tetrahydrofuran, selected m/z, mass error, and elemental composition for DBE values derived from positive-ion APPI nitrogenated hydrocarbon (i.e., CHN) species extracted from burned soils with methanol, toluene, and tetrahydrofuran, potential polycyclic aromatic hydrocarbons (PAHs) and nitrogenated (N)-PAHs identified in the mass spectra, compound class criteria, schematic of pyrocosm setup, density plot of carbon, hydrogen, and oxygen-containing species (CHO) detected in the ESI spectra, Van Krevelen diagrams of the H/C versus O/C ratio for the molecular formulas derived from all spectra, elemental composition assignments derived from ESI spectra, broadband positive-ion atmospheric pressure photoionization (APPI) 21 T Fourier transform ion cyclotron resonance mass spectrum of the acetone/cyclohexane fraction of a burned soil, and nominal oxidation state of carbon (NOSC) distribution for the assigned species in each spectrum (PDF)

AUTHOR INFORMATION

Corresponding Author

Thomas Borch − *Department of Soil and Crop Sciences, Colorado State University, Fort Collins, Colorado 80523-1170, United States; Department of Chemistry, Colorado State University, Fort Collins, Colorado 80523, United States;* orcid.org/0000-0002-4251-1613; Email: Thomas.Borch@colostate.edu

Authors

Holly K. Roth − *Department of Soil and Crop Sciences, Colorado State University, Fort Collins, Colorado 80523-1170, United States;* Present Address: Environmental Sciences Division, Oak Ridge National Laboratory, Oak Ridge, Tennessee, 37831, United States; orcid.org/0000-0003-2733-517X

Amy M. McKenna − *Department of Soil and Crop Sciences, Colorado State University, Fort Collins, Colorado 80523-1170, United States; National High Magnetic Field Laboratory, Ion Cyclotron Resonance User Facility, Florida State University, Tallahassee, Florida 32310-4005, United States;* orcid.org/0000-0001-7213-521X

Martha L. Aguilera − *National High Magnetic Field Laboratory, Ion Cyclotron Resonance User Facility, Florida State University, Tallahassee, Florida 32310-4005, United States;* orcid.org/0000-0002-7273-5343

Jacob P. VanderRoest – *Department of Chemistry, Colorado State University, Fort Collins, Colorado 80523, United States*

Huan Chen – *National High Magnetic Field Laboratory, Ion Cyclotron Resonance User Facility, Florida State University, Tallahassee, Florida 32310-4005, United States;* orcid.org/0000-0002-6032-6569

Complete contact information is available at: https://pubs.acs.org/10.1021/acs.analchem.5c04154

Author Contributions

The manuscript was written through contributions of all authors.

Notes

Notice: This manuscript has been authored by UT-Battelle, LLC, under contract DE-AC05–00OR22725 with the US Department of Energy (DOE). The US government retains and the publisher, by accepting the article for publication, acknowledges that the US government retains a nonexclusive, paid-up, irrevocable, worldwide license to publish or reproduce the published form of this manuscript, or allow others to do so, for US government purposes. DOE will provide public access to these results of federally sponsored research in accordance with the DOE Public Access Plan (https://www.energy.gov/doe-public-access-plan).

The authors declare no competing financial interest.

■ ACKNOWLEDGMENTS

This research was funded by the National Science Foundation 2114868 and the USDA National Institute of Food Agriculture through AFRI grant no. 2021-67019-34608. A portion of the work was performed at the National High Magnetic Field Laboratory ICR User Facility, which is supported by the National Science Foundation Division of Chemistry and Division of Material Research through DMR-1644779 and the State of Florida. The authors thank Chuck Rhoades and Tim Fegel from the Rocky Mountain Research Station for providing soil for the pyrocosm burns and the Poudre Fire Authority for their support during the burns. Figure 1 and Figure S1 were created with BioRender.com.

■ REFERENCES

(1) Abatzoglou, J. T.; Kolden, C. A.; Williams, A. P.; Lutz, J. A.; Smith, A. M. S. *International Journal of Wildland Fire* **2017**, *26* (4), 269–279.

(2) Williams, A. P.; Abatzoglou, J. T. *Current Climate Change Reports* **2016**, *2* (1), 1–14.

(3) Rhoades, C. C.; Chow, A. T.; Covino, T. P.; Fegel, T. S.; Pierson, D. N.; Rhea, A. E. *Ecosystems* **2019**, *22* (3), 643–657.

(4) Bladon, K. D.; Emelko, M. B.; Silins, U.; Stone, M. *Environ. Sci. Technol.* **2014**, *48* (16), 8936–8943.

(5) Lopez, A. M.; Avila, C. C. E.; VanderRoest, J. P.; Roth, H. K.; Fendorf, S.; Borch, T. *Nature Reviews Earth & Environment* **2024**, *5* (6), 431–446.

(6) Viedma, O.; Quesada, J.; Torres, I.; De Santis, A.; Moreno, J. M. *Ecosystems* **2015**, *18* (2), 237–250.

(7) Doerr, S. H.; Santin, C. *Philos. Trans R Soc. Lond B Biol. Sci.* **2016**, *371*, 20150345.

(8) Campos, I.; Abrantes, N. *Current Opinion in Environmental Science & Health* **2021**, *24*, 100293.

(9) Kieta, K. A.; Owens, P. N.; Petticrew, E. L.; French, T. D.; Koiter, A. J.; Rutherford, P. M. *Environmental Reviews* **2023**, *31* (1), 141–167.

(10) McKenna, A. M.; Williams, J. T.; Putman, J. C.; Aeppli, C.; Reddy, C. M.; Valentine, D. L.; Lemkau, K. L.; Kellermann, M. Y.; Savory, J. J.; Kaiser, N. K.; et al. *Energy Fuels* **2014**, *28* (4), 2454–2464.

(11) Roth, H. K.; Borch, T.; Young, R. B.; Bahureksa, W.; Blakney, G. T.; Nelson, A. R.; Wilkins, M. J.; McKenna, A. M. *Anal. Chem.* **2022**, *94* (6), 2973–2980.

(12) Bahureksa, W.; Borch, T.; Young, R. B.; Weisbrod, C. R.; Blakney, G. T.; McKenna, A. M. *Anal. Chem.* **2022**, *94* (32), 11382–11389.

(13) Fox, P. M.; Nico, P. S.; Tfaily, M. M.; Heckman, K.; Davis, J. A. *Org. Geochem.* **2017**, *114*, 12–22.

(14) Lopez-Sangil, L.; Rovira, P. *Soil Biology and Biochemistry* **2013**, *62*, 57–67.

(15) Otto, A.; Simpson, M. J. *Biogeochemistry* **2006**, *80* (2), 121–142.

(16) McKenna, A. M.; Chacon-Patino, M. L.; Chen, H.; Blakney, G. T.; Mentink-Vigier, F.; Young, R. B.; Ippolito, J. A.; Borch, T. *Anal. Chem.* **2021**, *93* (46), 15365–15372.

(17) Wang, C.; Wang, Y.; Herath, H. M. S. K. *Org. Geochem.* **2017**, *114*, 1–11.

(18) Hilber, I.; Blum, F.; Leifeld, J.; Schmidt, H. P.; Bucheli, T. D. *J. Agric. Food Chem.* **2012**, *60* (12), 3042–3050.

(19) Fabbri, D.; Rombolà, A. G.; Torri, C.; Spokas, K. A. *Journal of Analytical and Applied Pyrolysis* **2013**, *103*, 60–67.

(20) Shi, Q.; Zhao, S.; Xu, Z.; Chung, K. H.; Zhang, Y.; Xu, C. *Energy Fuels* **2010**, *24* (7), 4005–4011.

(21) Zhang, Y.; Xu, C.; Shi, Q.; Zhao, S.; Chung, K. H.; Hou, D. *Energy Fuels* **2010**, *24* (12), 6321–6326.

(22) Chacón, F. J.; Cayuela, M. L.; Roig, A.; Sánchez-Monedero, M. A. *Reviews in Environmental Science and Bio/Technology* **2017**, *16* (4), 695–715.

(23) Giraldo-Dávila, D.; Chacón-Patiño, M. L.; Orrego-Ruiz, J. A.; Blanco-Tirado, C.; Combariza, M. Y. *Fuel* **2016**, *185*, 45–58.

(24) Jonker, M. T.; Koelmans, A. A. *Environ. Sci. Technol.* **2002**, *36*, 4107–4113.

(25) Chacón-Patiño, M. L.; Heshka, N.; Alvarez-Majmutov, A.; Hendrickson, C. L.; Rodgers, R. P. *Energy Fuels* **2022**, *36* (14), 7542–7557.

(26) Niles, S. F.; Chacón-Patiño, M. L.; Smith, D. F.; Rodgers, R. P.; Marshall, A. G. *Energy Fuels* **2020**, *34* (2), 1492–1505.

(27) Chacón-Patiño, M. L.; Gray, M. R.; Rüger, C.; Smith, D. F.; Glattke, T. J.; Niles, S. F.; Neumann, A.; Weisbrod, C. R.; Yen, A.; McKenna, A. M.; et al. *Energy Fuels* **2021**, *35* (20), 16335–16376.

(28) Hertzog, J.; Carre, V.; Le Brech, Y.; Mackay, C. L.; Dufour, A.; Masek, O.; Aubriet, F. *Anal. Chim. Acta* **2017**, *969*, 26–34.

(29) Ventura, G. T.; Rossel, P. E.; Simoneit, B. R. T.; Dittmar, T. *Org. Geochem.* **2020**, *149*, 104085.

(30) D'Andrilli, J.; Dittmar, T.; Koch, B. P.; Purcell, J. M.; Marshall, A. G.; Cooper, W. T. *Rapid Commun. Mass Spectrom.* **2010**, *24* (5), 643–650.

(31) Hockaday, W. C.; Purcell, J. M.; Marshall, A. G.; Baldock, J. A.; Hatcher, P. G. *Limnology and Oceanography: Methods* **2009**, *7* (1), 81–95.

(32) Chacón-Patiño, M. L.; Mase, C.; Maillard, J. F.; Barrère-Mangote, C.; Dayton, D. C.; Afonso, C.; Giusti, P.; Rodgers, R. P. *Energy Fuels* **2023**, *37* (21), 16612–16628.

(33) Jiang, B.; Liang, Y.; Xu, C.; Zhang, J.; Hu, M.; Shi, Q. *Environ. Sci. Technol.* **2014**, *48* (9), 4716–4723.

(34) Bahureksa, W.; Tfaily, M. M.; Boiteau, R. M.; Young, R. B.; Logan, M. N.; McKenna, A. M.; Borch, T. *Environ. Sci. Technol.* **2021**, *55* (14), 9637–9656.

(35) Wright, J. L.; Roy, S. S. *Remote Sensing Applications: Society and Environment* **2022**, *28*, 100872.

(36) Bruns, T. D.; Chung, J. A.; Carver, A. A.; Glassman, S. I. *PLoS One* **2020**, *15* (3), No. e0222691.

(37) VanderRoest, J. P.; Fowler, J. A.; Rhoades, C. C.; Roth, H. K.; Broeckling, C. D.; Fegel, T. S.; McKenna, A. M.; Bechtold, E. K.; Boot, C. M.; Wilkins, M. J.; et al. *Environ. Sci. Technol.* **2024**, *58* (9), 4167–4180.

(38) Dittmar, T.; Koch, B.; Hertkorn, N.; Kattner, G. *Limnology and Oceanography: Methods* **2008**, *6*, 230−235.
(39) Purcell, J. M.; Hendrickson, C. L.; Rodgers, R. P.; Marshall, A. G. *J. Am. Soc. Mass Spectrom.* **2007**, *18* (9), 1682−1689.
(40) Chacón-Patiño, M. L.; Rowland, S. M.; Rodgers, R. P. *Energy Fuels* **2017**, *31* (12), 13509−13518.
(41) Hendrickson, C. L.; Quinn, J. P.; Kaiser, N. K.; Smith, D. F.; Blakney, G. T.; Chen, T.; Marshall, A. G.; Weisbrod, C. R.; Beu, S. C. *J. Am. Soc. Mass Spectrom.* **2015**, *26* (9), 1626−1632.
(42) Smith, D. F.; Podgorski, D. C.; Rodgers, R. P.; Blakney, G. T.; Hendrickson, C. L. *Anal. Chem.* **2018**, *90* (3), 2041−2047.
(43) Kaiser, N. K.; McKenna, A. M.; Savory, J. J.; Hendrickson, C. L.; Marshall, A. G. *Anal. Chem.* **2013**, *85* (1), 265−272.
(44) Boldin, I. A.; Nikolaev, E. N. *Rapid Commun. Mass Spectrom.* **2011**, *25* (1), 122−126.
(45) Xian, F.; Hendrickson, C. L.; Blakney, G. T.; Beu, S. C.; Marshall, A. G. *Anal. Chem.* **2010**, *82*, 8807−8812.
(46) Savory, J. J.; Kaiser, N. K.; McKenna, A. M.; Xian, F.; Blakney, G. T.; Rodgers, R. P.; Hendrickson, C. L.; Marshall, A. G. *Anal. Chem.* **2011**, *83* (5), 1732−1736.
(47) Ohno, T.; Sleighter, R. L.; Hatcher, P. G. *Anal Bioanal Chem.* **2016**, *408* (10), 2497−2504.
(48) Roth, V. N.; Dittmar, T.; Gaupp, R.; Gleixner, G. *PLoS One* **2015**, *10* (3), No. e0119188.
(49) Kim, S.; Kramer, R. W.; Hatcher, P. G. *Anal. Chem.* **2003**, *75*, 5336−5344.
(50) Zhao, P.; Du, Z.; Fu, Q.; Ai, J.; Hu, A.; Wang, D.; Zhang, W. *Water Res.* **2023**, *232*, 119687.
(51) Purcell, J. M.; Hendrickson, C. L.; Rodgers, R. P.; Marshall, A. G. *Anal. Chem.* **2006**, *78*, 5906−5912.
(52) Chen, H.; Wang, J. J.; Ku, P. J.; Tsui, M. T.; Abney, R. B.; Berhe, A. A.; Zhang, Q.; Burton, S. D.; Dahlgren, R. A.; Chow, A. T. *Environ. Sci. Technol.* **2022**, *56* (17), 12678−12687.
(53) Chen, H.; Chow, A. T.; Li, X.-W.; Ni, H.-G.; Dahlgren, R. A.; Zeng, H.; Wang, J.-J. *ACS Earth and Space Chemistry* **2018**, *2* (12), 1262−1270.
(54) Yang, B.; Shi, Y.; Xu, S.; Wang, Y.; Kong, S.; Cai, Z.; Wang, J. *Environ. Sci. Process Impacts* **2022**, *24* (1), 32−41.
(55) Keiluweit, M.; Nico, P. S.; Johnson, M. G.; Kleber, M. *Environ. Sci. Technol.* **2010**, *44*, 1247−1253.
(56) Krzyszczak, A.; Czech, B. *Sci. Total Environ.* **2021**, *788*, 147738.
(57) Soursou, V.; Campo, J.; Picó, Y. *Trends in Environmental Analytical Chemistry* **2023**, *37*, No. e00195.
(58) Ren, K.; Wei, Y.; Li, J.; Han, C.; Deng, Y.; Su, G. *Chemosphere* **2021**, *283*, 131190.
(59) Brinkmann, M.; Schneider, A. L.; Bluhm, K.; Schiwy, S.; Lehmann, G.; Deutschmann, B.; Muller, A.; Tiehm, A.; Hollert, H. *Environ. Toxicol. Chem.* **2019**, *38* (6), 1343−1355.
(60) Idowu, O.; Semple, K. T.; Ramadass, K.; O'Connor, W.; Hansbro, P.; Thavamani, P. *Sci. Total Environ.* **2020**, *699*, 134303.
(61) Tian, Z.; Vila, J.; Wang, H.; Bodnar, W.; Aitken, M. D. *Environ. Sci. Technol.* **2017**, *51* (24), 14047−14054.
(62) Alves, C. A.; Gonçalves, C.; Evtyugina, M.; Pio, C. A.; Mirante, F.; Puxbaum, H. *Atmos. Environ.* **2010**, *44* (23), 2750−2759.
(63) Otto, A.; Gondokusumo, R.; Simpson, M. J. *Appl. Geochem.* **2006**, *21* (1), 166−183.
(64) Choi, B. K.; Chitwood, D. J.; Paik, Y. K. *Mol. Cell Proteomics* **2003**, *2* (10), 1086−1095.
(65) Svoboda, J. A.; Herbert, E. W.; Thompson, M. J. *Archives of Insect Biochemistry and Physiology* **1987**, *6* (1), 1−8.
(66) Li, H.; Cuthbertson, A. A.; Alamer, A. A.; Cecon, V. S.; Radhakrishnan, H.; Wu, J.; Curtzwiler, G. W.; Vorst, K. L.; Bai, X.; Landis, C. R.; et al. *Green Chem.* **2024**, *26* (15), 8718−8727.
(67) Kaufman, P. B.; Cseke, L. J.; Warber, S.; Duke, J. A.; Brielmann, H. L. *Natural Products from Plants*; CRC Press: 1999.
(68) Roth, H. K.; Nelson, A. R.; McKenna, A. M.; Fegel, T. S.; Young, R. B.; Rhoades, C. C.; Wilkins, M. J.; Borch, T. *Environ. Sci. Process Impacts* **2022**, *24* (10), 1661−1677.
(69) LaRowe, D. E.; Van Cappellen, P. *Geochim. Cosmochim. Acta* **2011**, *75* (8), 2030−2042.
(70) Boye, K.; Herrmann, A. M.; Schaefer, M. V.; Tfaily, M. M.; Fendorf, S. *Frontiers in Environmental Science* **2018**, *6*, 1−14.

https://doi.org/10.1021/acs.analchem.5c04154
Anal. Chem. 2025, 97, 24040−24049

Supporting Information

Characterization of Burned Soil Organic Matter via Sequential Solvent Extractions and 21 T FT-ICR Mass Spectrometry with Electrospray and Atmospheric Pressure Photoionization

Holly K. Roth[1,†], Amy M. McKenna[1,2], Martha L. Aguilera[2], Jacob P. VanderRoest[3], Huan Chen[2], Thomas Borch[1,3]*

[1] *Department of Soil and Crop Sciences, Colorado State University, Fort Collins, Colorado 80523-1170, United States*

[2] *National High Magnetic Field Laboratory, Ion Cyclotron Resonance User Facility, Florida State University, 1800 East Paul Dirac Dr., Tallahassee, Florida 32310-4005, United States*

[3] *Department of Chemistry, Colorado State University, Fort Collins, Colorado 80523, United States*

Present Addresses

†*Environmental Sciences Division, Oak Ridge National Laboratory, Oak Ridge, Tennessee, 37831, United States*

Table of contents

$$DBE = 1 + \frac{1}{2}(2C - H + N) \qquad \textbf{(EQ S1)}$$

Where DBE conveys hydrogen deficiency as the number of rings plus double bonds to C, which calculate the number of π bonds and rings within the sample.[39]

$$NOSC = 4 - \frac{5C + H - 3N - 2O - 2S}{C} \qquad \textbf{(EQ S2)}$$

In which NOSC is dependent on the number of carbon (C), hydrogen (H), nitrogen (N), oxygen (O), and sulfur (S) atoms. [92]

Table S1. *Mass-to-charge ratio (m/z) and elemental assignment averages for carbon (C), hydrogen (H), oxygen (O), nitrogen (N), and sulfur (S) from positive-ion and negative-ion ESI spectra FT-ICR MS for water-soluble species isolated by SPE-PPL (WSO) and solvent extraction with acetone + cyclohexane (AC) and toluene + tetrahydrofuran + methanol (MTT).*

Sample	m/z	C	H	O	N	S
-ESI WSO	514	24.54	27.22	10.87	1.18	0.0825
-ESI AC	657	40.42	64.12	6.62	0.167	0.0147
-ESI MTT	503	30.03	46.69	5.46	0.0249	0.149
+ESI WSO	482	23.99	31.89	8.47	1.17	n.a.
+ESI AC	798	49.56	75.42	6.31	0.0866	0.744
+ESI MTT	712	41.62	68.47	6.86	0.51	0.995

Table S2. *Range of oxygen to carbon (O/C) and hydrogen to carbon (H/C) ratios calculated from positive-ion and negative-ion ESI spectra FT-ICR MS for water-soluble species isolated by SPE-PPL (WSO) and solvent extraction with acetone + cyclohexane (AC) and toluene + tetrahydrofuran + methanol (MTT).*

Sample	O/C	H/C
-ESI WSO	0.0588-1.17	0.231-1.92
-ESI AC	0.0250-0.538	0.235-2.17
-ESI MTT	0.0441-1.00	0.423-2.17
+ESI WSO	0.0530-0.833	0.364-1.96
+ESI AC	0-0.293	1.05-1.81
+ESI MTT	0-0.294	1.07-1.82

Table S3. *Selected m/z, mass error, and elemental composition for DBE values derived from positive-ion APPI hydrocarbon species extracted from burned soils with acetone and cyclohexane. A complete list of elemental compositions is publicly available via DOI 10.17605/OSF.IO/QZVGD.*

Experimental mass (Da)	Elemental Composition	DBE	Mass error (ppm)
	Protonated		
397.38288	$[C_{29}H_{48}+H]^+$	6	-0.0050545
219.11682	$[C_{17}H_{14}+H]^+$	11	0.03149484
239.17943	$[C_{18}H_{22}+H]^+$	8	-0.0118839
395.36724	$[C_{29}H_{46}+H]^+$	7	-0.0305354

243.11682	$[C_{19}H_{14}+H]^+$	13	0.02838574
381.35159	$[C_{28}H_{44}+H]^+$	7	-0.0318259
253.19508	$[C_{19}H_{24}+H]^+$	8	-0.0109728
393.35159	$[C_{29}H_{44}+H]^+$	8	-0.030855
255.21073	$[C_{19}H_{26}+H]^+$	7	-0.0106348
377.32027	$[C_{28}H_{40}+H]^+$	9	0.02049948
	Radical		
396.37505	$[C_{29}H_{48}]^{+\cdot}$	6	0.00746606
394.3594	$[C_{29}H_{46}]^{+\cdot}$	7	0.00734158
390.32808	$[C_{29}H_{42}]^{+\cdot}$	9	0.0583277
388.31244	$[C_{29}H_{40}]^{+\cdot}$	10	0.03271283
392.34377	$[C_{29}H_{44}]^{+\cdot}$	8	-0.0437599
202.0777	$[C_{16}H_{10}]^{+\cdot}$	12	0.00861401
402.32809	$[C_{30}H_{42}]^{+\cdot}$	10	0.03173266
234.14029	$[C_{18}H_{18}]^{+\cdot}$	10	0.05123962
408.37505	$[C_{30}H_{48}]^{+\cdot}$	7	0.00724667
248.15595	$[C_{19}H_{20}]^{+\cdot}$	10	0.00830687

Table S4. *Selected m/z, mass error, and elemental composition for DBE values derived from positive-ion APPI hydrocarbon species extracted from burned soils with methanol, toluene, and tetrahydrofuran. A complete list of elemental compositions is publicly available via DOI 10.17605/OSF.IO/QZVGD.*

Experimental mass (Da)	Elemental composition	DBE	Mass error (ppm)
	Protonated		
239.17943	$[C_{18}H_{22}+H]^+$	8	-0.0118839
219.11682	$[C_{17}H_{14}+H]^+$	11	0.03149484
243.11682	$[C_{19}H_{14}+H]^+$	13	0.02838574
237.16378	$[C_{18}H_{20}+H]^+$	9	-0.0122554
225.16377	$[C_{17}H_{20}+H]^+$	8	0.0315036
181.10121	$[C_{14}H_{12}+H]^+$	9	-0.1831191
397.38288	$[C_{29}H_{48}+H]^+$	6	-0.0050545
S	$[C_{14}H_{14}+H]^+$	8	-0.1261432
253.19508	$[C_{19}H_{24}+H]^+$	8	-0.0109728
195.11682	$[C_{15}H_{14}+H]^+$	9	0.03536881
	Radical		
396.37505	$[C_{29}H_{48}]^{+\cdot}$	6	0.00746606
202.0777	$[C_{16}H_{10}]^{+\cdot}$	12	0.00861401
394.35939	$[C_{29}H_{46}]^{+\cdot}$	7	0.03269916
178.0777	$[C_{14}H_{10}]^{+\cdot}$	10	0.00977495
234.1403	$[C_{18}H_{18}]^{+\cdot}$	10	0.00853018
228.09335	$[C_{18}H_{12}]^{+\cdot}$	13	0.00791273
204.09335	$[C_{16}H_{12}]^{+\cdot}$	11	0.00884321
390.32808	$[C_{29}H_{42}]^{+\cdot}$	9	0.0583277
254.2029	$[C_{19}H_{26}]^{+\cdot}$	7	0.00886622
222.1403	$[C_{17}H_{18}]^{+\cdot}$	9	0.00899098

***Table S5**. Selected m/z, mass error, and elemental composition for DBE values derived from positive-ion APPI nitrogenated hydrocarbon (i.e., CHN) species extracted from burned soils with methanol, toluene, and tetrahydrofuran. A complete list of elemental compositions is publicly available via DOI 10.17605/OSF.IO/QZVGD.*

Experimental mass (Da)	Elemental composition	DBE	Mass error (ppm)
	Protonated		
208.11208	$[C_{15}H_{13}N+H]^+$	10	-0.01982690
210.12773	$[C_{15}H_{15}N+H]^+$	9	-0.01933150
220.11208	$[C_{16}H_{13}N+H]^+$	11	-0.01874600
194.09642	$[C_{14}H_{11}N+H]^+$	10	0.02993172
232.11207	$[C_{17}H_{13}N+H]^+$	12	0.02530579
374.37812	$[C_{26}H_{47}N+H]^+$	4	0.01860194
196.11207	$[C_{14}H_{13}N+H]^+$	9	0.02995114
246.12772	$[C_{18}H_{15}N+H]^+$	12	0.02412536
218.09643	$[C_{16}H_{11}N+H]^+$	12	-0.01921330
258.12772	$[C_{19}H_{15}N+H]^+$	13	0.02300381
	Radical		
273.15119	$[C_{20}H_{19}N]^{+\cdot}$	12	0.04039569
245.11989	$[C_{18}H_{15}N]^{+\cdot}$	12	0.04449190
217.0886	$[C_{16}H_{11}N]^{+\cdot}$	12	0.003581810
231.10425	$[C_{17}H_{13}N]^{+\cdot}$	12	0.003642120
207.10425	$[C_{15}H_{13}N]^{+\cdot}$	10	0.004064190
259.13555	$[C_{19}H_{17}N]^{+\cdot}$	12	0.003743180
235.13554	$[C_{17}H_{17}N]^{+\cdot}$	10	0.04665390
271.13553	$[C_{20}H_{17}N]^{+\cdot}$	13	0.07734135
197.1199	$[C_{14}H_{15}N]^{+\cdot}$	8	0.004595430
221.11991	$[C_{16}H_{15}N]^{+\cdot}$	10	-0.04112770

***Table S6**. Potential polycyclic aromatic hydrocarbons (PAHs) and nitrogenated (N)-PAHs identified in the mass spectra. C1 = methylated, C2 = dimethylated, C3 = trimethylated. DBE refers to double-bond equivalents.*

Elemental Composition	DBE	Potential (N-)PAH	Solvent
$C_{14}H_{10}$	10	Phenanthrene, anthracene	AC, MTT
$C_{16}H_{10}$	12	Fluoranthene, pyrene	AC, MTT
$C_{18}H_{12}$	13	Benzo[a]anthracene, chrysene	AC, MTT
$C_{20}H_{12}$	15	Benzo[b]fluorene, benzo[k]fluorene, benzo[a]pyrene	MTT
$C_{13}H_{11}N$	9	C1-azafluorene	MTT
$C_{14}H_{13}N$	9	C2-azafluorene	MTT
$C_{14}H_{11}N$	10	C1-acridine	MTT
$C_{15}H_{13}N$	10	C2-acridine	MTT
$C_{16}H_{15}N$	10	C3-acridine	MTT
$C_{15}H_{11}N$	11	Phenylquinoline	MTT
$C_{16}H_{13}N$	11	C1-phenylquinoline	MTT
$C_{17}H_{15}N$	11	C2-phenylquinoline	MTT
$C_{15}H_{9}N$	12	Azapyrene	MTT
$C_{16}H_{11}N$	12	C1-azapyrene	MTT
$C_{17}H_{13}N$	12	C2-azapyrene	MTT
$C_{18}H_{15}N$	12	C3-azapyrene	MTT
$C_{17}H_{11}N$	13	Benzo[a]acridine	MTT
$C_{18}H_{13}N$	13	C1-benzo[a]acridine	MTT
$C_{19}H_{15}N$	13	C2-benzo[a]acridine	MTT
$C_{20}H_{17}N$	13	C3-benzo[a]acridine	MTT
$C_{19}H_{13}N$	14	Phenylacridine	MTT
$C_{20}H_{15}N$	14	C1-phenylacridine	MTT

***Table S7**: Compound class criteria, adapted from Hockaday et. al, 2009.[1] AI refers to "aromaticity index".*

Compound Class	Criteria
Lignin	1.5 > H/C > 0.7; 0.67 > O/C > 0.1
Protein	800 > m/z > 300; N ≥ 1; 2.2 > H/C > 1.0; 0.67 > O/C > 0.1
Carbohydrates	H/C > 1.5; O/C > 0.67
Lipids	2.0 > H/C > 1.5; O/C < 0.3
Condensed aromatics	AI > 0.7

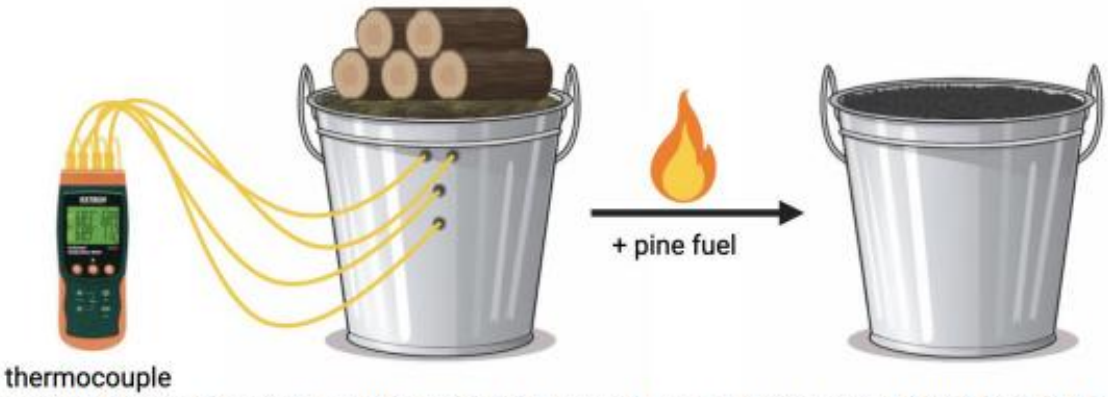

***Figure S1**. Schematic of pyrocosm setup. Holes were drilled to measure temperature at 0.5 cm, 5 cm, and 10 cm depths from the top of the soil.*

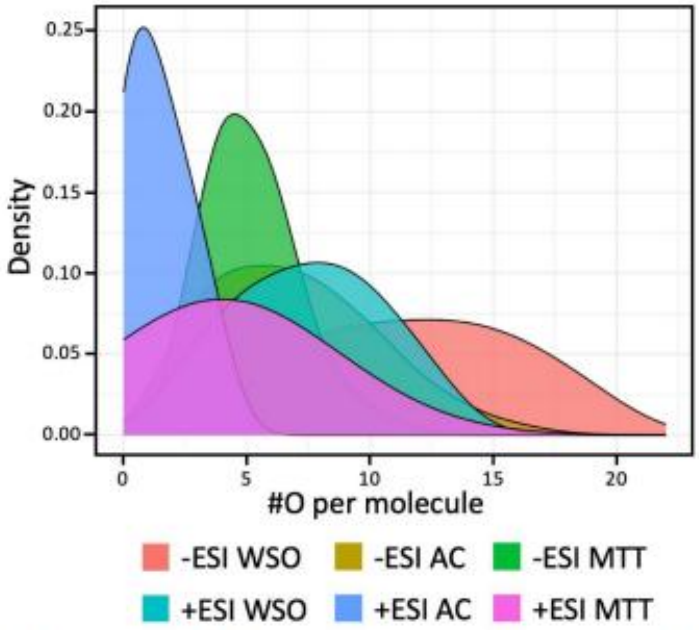

***Figure S2**. Density plot of carbon, hydrogen, and oxygen-containing species (CHO) of negative-ion and positive-ion ESI FT-ICR MS for water-soluble species isolated by SPE-PPL (WSO) and solvent extraction with acetone + cyclohexane (AC) and methanol*

+ toluene + tetrahydrofuran (MTT). Density plots represent the proportion of data that corresponds with the x-axis. The integral over the entire space is 1.

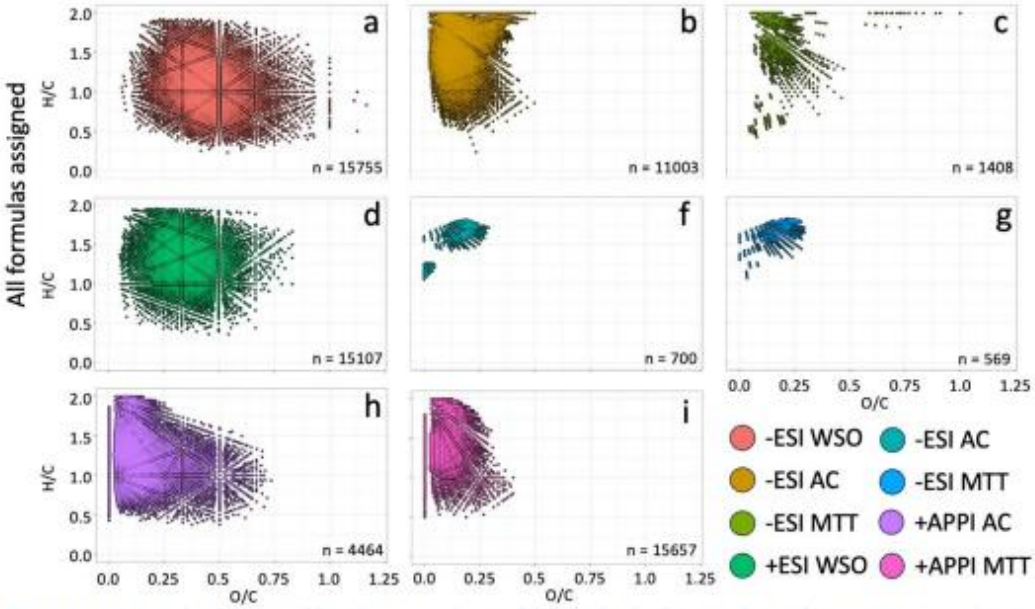

***Figure S3**. Van Krevelen diagrams of the H/C versus O/C ratio for the molecular formulae derived from negative-ion and positive-ion electrospray ionization (ESI) FT-ICR MS for water-soluble species (WSO) isolated by SPE-PPL (a and d) and solvent extraction with acetone + cyclohexane (AC; b and f)) and methanol + toluene + tetrahydrofuran (MTT; c and g). Plots h and i are derived from positive ion atmospheric pressure photoionization (APPI) FT-ICR MS for AC (h) and MTT (i) extracts. Number of assigned formulas (n) is denoted in the bottom right corner of each plot.*

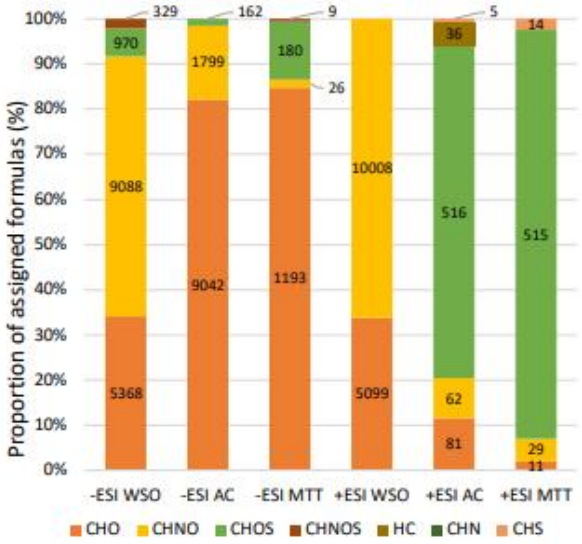

Figure S4. *Elemental composition assignments derived from negative-ion and positive-ion electrospray ionization FT-ICR MS for water-soluble species (WSO) isolated by SPE-PPL and solvent extraction with acetone + cyclohexane (AC) and methanol + toluene + tetrahydrofuran (MTT). Numbers in the bars represent the number of formulas assigned per elemental class, and each bar is scaled to 100%. C = carbon, H = hydrogen, N = nitrogen, O = oxygen, and S = sulfur.*

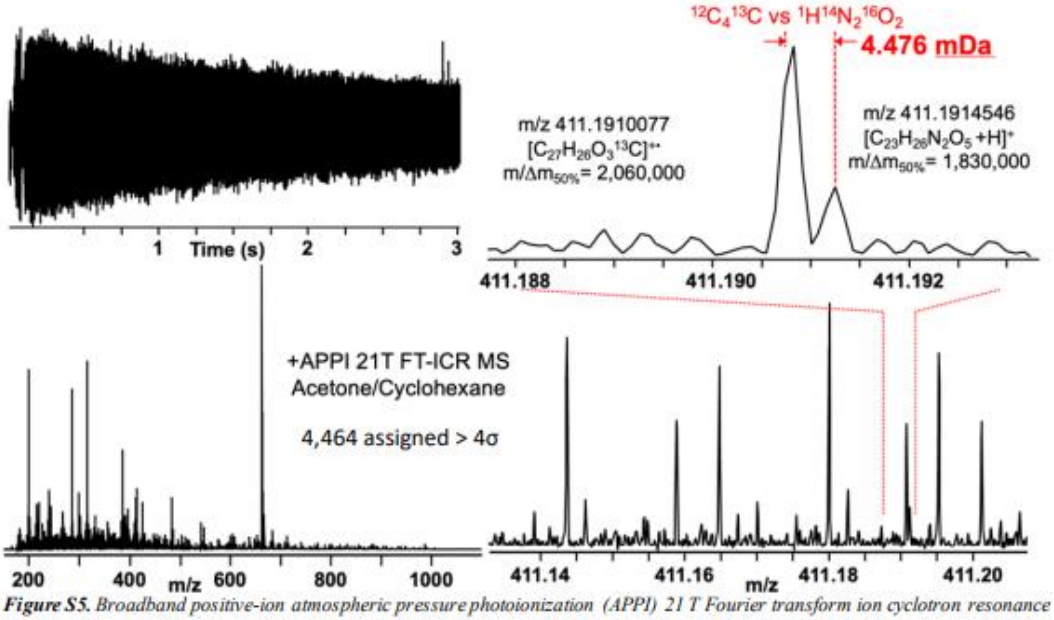

Figure S5. *Broadband positive-ion atmospheric pressure photoionization (APPI) 21 T Fourier transform ion cyclotron resonance mass spectrum of the acetone/cyclohexane fraction of a burned soil. Bottom left: Broadband FT-ICR mass spectrum containing more than 4,000 mass spectral peaks, each with a signal magnitude greater than 4σ of baseline noise. Bottom right: mass-scale expanded segment across m/z 411.14-411.20, demonstrating the high occurrence of isobaric overlaps. Top right: ~0.004 Da mass scale-expanded segment, showing resolution of a 4.476 mDa isobaric overlap.*

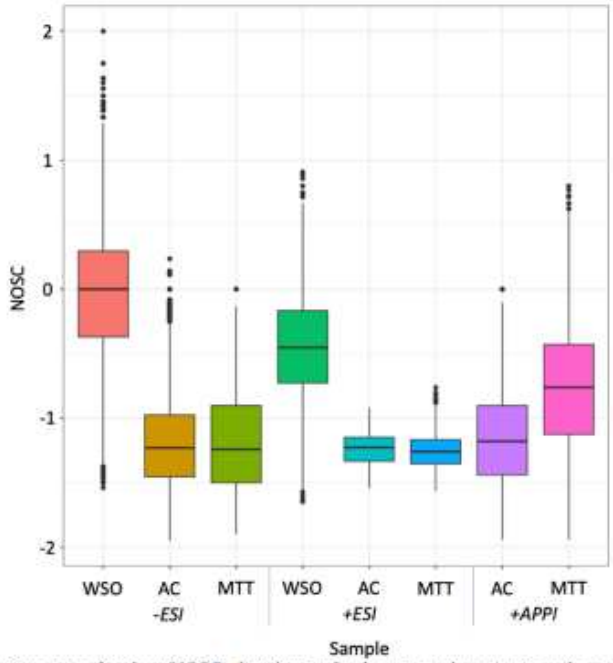

***Figure S6**. Nominal oxidation state of carbon (NOSC) distribution for the assigned species in each spectrum. The lower and upper hinges of the boxplots represent the 25th and 75th percentile and the middle line is the median. The upper whisker extends to the median plus 1.5x interquartile range and the lower whisker extends to the median minus 1.5x interquartile range. NOSC values were calculated according to LaRowe and van Cappellen, 2011.*[2]

References

(1) Hockaday, W. C.; Purcell, J. M.; Marshall, A. G.; Baldock, J. A.; Hatcher, P. G. Electrospray and photoionization mass spectrometry for the characterization of organic matter in natural waters: a qualitative assessment. *Limnology and Oceanography: Methods* **2009**, *7* (1), 81-95. DOI: 10.4319/lom.2009.7.81.
(2) LaRowe, D. E.; Van Cappellen, P. Degradation of natural organic matter: A thermodynamic analysis. *Geochimica et Cosmochimica Acta* **2011**, *75* (8), 2030-2042. DOI: 10.1016/j.gca.2011.01.020.

APPENDIX F: CO-AUTHOR CONTRIBUTIONS TO "DETERMINATION OF SOIL CONTAMINATION AT THE WILDLAND-URBAN INTERFACE AFTER THE 2021 MARSHALL FIRE IN COLORADO, USA"

Reprinted from Jech, S.; Adamchak, C.; Stokes, S. C.; Wiltse, M. E.; Callen, J.; VanderRoest, J.; Kelly, E. F.; Hinckley, E.-L. S.; Stein, H. J.; Borch, T.; Fierer, N. Determination of Soil Contamination at the Wildland-Urban Interface after the 2021 Marshall Fire in Colorado, USA. *Environmental Science & Technology* **2024**, *58* (9), 4326–4333. https://doi.org/10.1021/acs.est.3c08508.

According to CRediT criteria, my contributions include investigation (preparing soil samples for metal and polycyclic aromatic hydrocarbon analyses) formal analysis (reviewing how data were interpreted and presented) and writing – review & editing.

Environmental Science & Technology

pubs.acs.org/est

Article

Determination of Soil Contamination at the Wildland-Urban Interface after the 2021 Marshall Fire in Colorado, USA

Sierra Jech, Clifford Adamchak, Sean C. Stokes, Marin E. Wiltse, Jessica Callen, Jacob VanderRoest, Eugene F. Kelly, Eve-Lyn S. Hinckley, Holly J. Stein, Thomas Borch,* and Noah Fierer*

Cite This: Environ. Sci. Technol. 2024, 58, 4326−4333

Read Online

ACCESS | Metrics & More | Article Recommendations | Supporting Information

ABSTRACT: Wildfires at the wildland-urban interface (WUI) are increasingly common. The impacts of such events are likely distinct from those that occur strictly in wildland areas, as we would expect an elevated likelihood of soil contamination due to the combustion of anthropogenic materials. We evaluated the impacts of a wildfire at the WUI on soil contamination, sampling soils from residential and nonresidential areas located inside and outside the perimeter of the 2021 Marshall Fire in Colorado, USA. We found that fire-affected residential properties had elevated concentrations of some heavy metals (including Zn, Cu, Cr, and Pb), but the concentrations were still below levels of likely concern, and we observed no corresponding increases in concentrations of polycyclic aromatic hydrocarbons (PAHs). The postfire increases in metal concentrations were not generally observed in the nonresidential soils, highlighting the importance of combustion of anthropogenic materials for potential soil contamination from wildfires at the WUI. While soil contamination from the 2021 Marshall Fire was lower than expected, and likely below the threshold of concern for human health, our study highlights some of the challenges that need to be considered when assessing soil contamination after such fires.

KEYWORDS: *soil contamination, wildfire, 2021 Marshall Fire, wildland-urban interface, PAH, heavy metals, mercury*

INTRODUCTION

Wildfire risk at the wildland-urban interface (WUI) is expected to increase in the future due to expansion of the WUI and increased wildfire activity.[1,2] The WUI, defined as the area where houses meet or intermingle with undeveloped wildland vegetation,[3] is expanding in many regions across the globe. This expansion is particularly evident in the United States, where home construction from 1990 to 2010 increased the WUI area from 581,000 km^2 to 770,000 km^2 and increased the number of houses at the WUI from 30.8 million to 43.4 million.[4] The frequency and size of WUI wildfires are expected to increase as many wildland-urban regions become hotter, drier, and experience more frequent drought events due to climate change.[2,5−7] The increased risk of catastrophic WUI wildfire events is exacerbated by the elevated potential for human-driven ignition, barriers to fire prevention and suppression,[8] and the high flammability of structures.[2,9] Compared to wildland fires, WUI fires can be particularly damaging to public health and costly for local economies, with potentially larger societal repercussions. Unfortunately, there are numerous global examples of the devastation wrought by WUI wildfires, including multiple fires in Greece and Portugal in 2023, the 2018 Camp Fire that destroyed Paradise, California, and the 2023 Lahaina fire in Maui, one of the deadliest wildfires in US history.

The impacts of wildland fires on air, water, and soil quality in nonresidential areas have been relatively well-studied.[10−13] In contrast, the environmental impacts of wildfires that occur at the WUI have received far less attention, a point highlighted in a recent U.S. National Academies report.[14] Addressing this knowledge gap is crucial because the impacts of WUI wildfires on soil quality are likely distinct from those of wildland fires, including a greater potential for soil contamination. Whereas wildland fires are typically fueled solely by vegetation combustion, WUI fires can also be fueled by the partial or complete combustion of structures, vehicles, and other components of urban infrastructure. These anthropogenic fuels often contain materials with high concentrations of toxic compounds. These compounds include toxic metals and polycyclic aromatic hydrocarbons (PAHs) that can be released into soil after a fire event.[15−21] In fact, studies that have investigated soil contamination after fires fueled entirely, or in part, by structures have often found evidence for significant postfire soil contamination.[16,22−25] This potential for postwildfire soil contamination could have long-term impacts on the health of people, animals, and plants living in or near burned areas of the WUI.[14]

Received: October 13, 2023
Revised: February 6, 2024
Accepted: February 7, 2024
Published: February 23, 2024

https://doi.org/10.1021/acs.est.3c08508
Environ. Sci. Technol. 2024, 58, 4326−4333

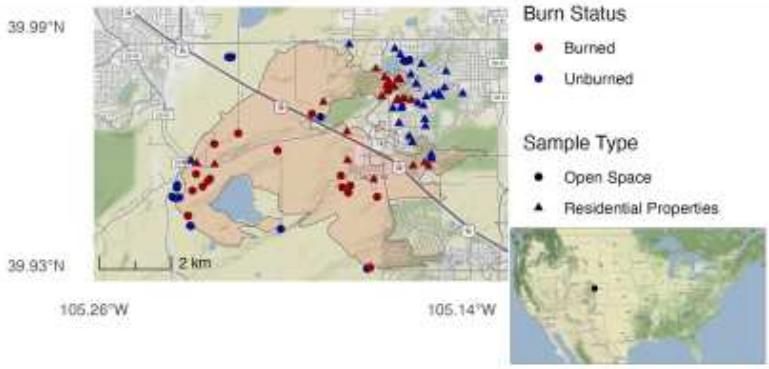

Figure 1. Map of the sampling area. Residential properties (triangles) and nonresidential grassland (circles) sampling locations are plotted with the outline of the Marshall Fire (shaded in light orange). Burn status of sampling locations indicated with red (burned) and blue (unburned) symbols.

The primary objective of this study was to determine the existence and extent of soil contamination following the 2021 Marshall Fire in Colorado, USA, a particularly catastrophic example of the types of wildfire events that can occur at the WUI. The fire started on December 30, 2021, and quickly spread into suburban neighborhoods due to unseasonably warm, dry, and exceptionally windy conditions. This resulted in the most destructive wildfire in terms of structure loss in Colorado history with over 1000 homes being destroyed across a ~2500 ha area. In fact, more homes were destroyed in the Marshall Fire than in the two largest wildfires in recorded Colorado history, both of which were ~80,000 ha in size.[7]

We conducted an extensive and systematic sampling of soils from burned and unburned residential properties that were within or adjacent to the perimeter of the 2021 Marshall Fire. In addition, we collected soils from nonresidential sites (grasslands) inside and outside of the burn perimeter to provide samples representative of a wildland wildfire. We hypothesized that, given the presence of anthropogenic materials in residential areas, burned residential soils would have significantly higher concentrations of metals and PAHs than unburned residential and nonresidential soils. Ultimately, we sought to use this study of the 2021 Marshall Fire to better assess how wildfires at the WUI may uniquely impact soil quality, building the knowledge base needed to safeguard the reestablishment and repopulation of impacted and adjacent residential areas after WUI wildfire events.

■ MATERIALS AND METHODS

Study Area. The Marshall Fire began on 30 December 2021 in the semiarid Colorado Front Range urban corridor situated in the foothills east of the Rocky Mountains at an elevation of ~1650 m (Figure 1). The climate in the region is characterized by mean monthly temperatures typically ranging from 1 to 23 °C (NOAA 2023a) and mean monthly precipitation amounts between 20 and 80 mm (NOAA 2023b). The vegetation in the study area is mainly grasslands interspersed with patches of Ponderosa pine (*Pinus ponderosa*) forests. This land cover is mostly intact at the western to central part of the study area, but an urban landscape dominates the eastern area. Prior to the wildfire event, conditions were unusually dry and warm for that time period, and the fire moved rapidly from west to east with wind speeds often exceeding 160 km h^{-1}. The fire was contained on 31 December 2021 due to fire-fighting activities, a decrease in wind speeds, and a snowfall event that occurred. For additional details on the fire event and associated conditions, see Fovell et al.[26] and the NOAA Boulder Web site[27] which also includes images and videos taken from the area during and after the fire event.

Site Selection. In March 2022, we developed a survey to identify homeowners within the wildfire-affected area who were willing to participate in this project. The survey was distributed by the Cooperative Institute for Research in Environmental Sciences (CIRES, University of Colorado Boulder) and received nearly 300 responses. We selected 58 properties within or adjacent to the fire perimeter for sampling (Figure 1), 29 properties that were completely burned and 29 properties that were completely unburned (noting that these "unburned" properties may have received some wind-deposited ash during the fire event, but were outside the fire perimeter and were not directly damaged by the fire). We selected properties that minimized geographic distances and other potentially confounding landscape characteristics (including topography and vegetation cover). We also did not select properties where there was evidence of substantial postfire debris removal or surface soil scraping. In addition to sampling from these residential locations, we also selected burned and unburned locations distributed across the Marshall Fire footprint in neighboring, undeveloped (nonresidential) grasslands for comparable sampling of wildland conditions (Figure 1).

Field Sampling. Sampling sites were visited over a three-week period in April 2022, four months after the Marshall Fire with multiple rain and snow events occurring during this period between the fire event and the soil sampling. Soil samples were collected from four different locations at each of the 59 residential properties selected for this study. Specifically, lawns and landscaped areas were sampled at these properties, avoiding any structural debris, nonsoil surfaces, or areas where any alteration to the soil surface (including mulching or scraping) was evident. For each soil sample, rocks and loose plant material were scraped off the soil surface, and eight soil cores (0-5 cm depth) were collected from four separate ~1 m^2 areas per property to obtain sufficient material for chemical analyses (total of 32 soil cores from each property). These sampling areas were selected without considering whether they were on the windward or leeward side of the main structure

https://doi.org/10.1021/acs.est.3c08508
Environ. Sci. Technol. 2024, 58, 4326−4333

during the fire event as this was often difficult to determine and many properties did not have soil on all sides of the main structure. In nearly all cases, the sampling areas were within 20 m of the main structure on each property. The eight soil cores collected within each individual ~1 m^2 area were combined, yielding four composited soil samples per residential property. Each composited sample was sieved to ≤2 mm to remove rocks and larger debris and then stored at 4 °C until further analysis. In total, we collected 118 soil samples from the residential properties for chemical analyses: 50% from burned properties and 50% from unburned properties. We note that there was no visible ash on the surface of the sampled soils. We presume that any ash had been transported away from the sampling site via wind or transported deeper into the soil profile via rainfall or melting snow over the four-month period between the fire event and the soil sampling.

Soil cores from 33 nonresidential, grassland locations were also collected inside and outside of the fire perimeter (Figure 1). Soils from these grassland sampling sites were collected in the same manner as described above with eight soil cores (0-5 cm) collected and composited per sampling location. This effort yielded a total of 17 fire-affected nonresidential, grassland soil samples collected from sites within the fire perimeter and a corresponding 16 grassland soil samples collected from neighboring sites outside the fire perimeter. No ash was visible at the surface of these soils but we did note the presence of partially combusted vegetation (shrubs, grass, trees) in close proximity to all of the grassland sampling sites located within the fire perimeter.

Bulk Soil Chemical Analyses. For measuring pH, total nitrogen (TN), total carbon (TC), total inorganic carbon (TIC), and total organic carbon (TOC), soils were air-dried for 1 week and then ground using a roller mill for 24 h. A subsample of each soil (100 ± 0.01 mg) was combusted at >1000 °C within a CN 802 Carbon Nitrogen Elemental Analyzer (VELP Scientific, Deer Park, NY) to determine TC and TN content (LOD = 0.5% TC and 0.001 mg TN). TIC was calculated using a modified pressure-calcimeter method.[28] Total TOC was calculated by subtracting TIC from the TC. Soil pH was measured in a 1:1 soil/water slurry.[29]

Soil Metal Analyses. EPA Method 6200[30] was used for X-ray fluorescence (XRF) measurements of bulk soil concentrations of common metals. Air-dried, ground soil samples were packed tightly into plastic XRF sampling cups (SC-4331-32 mm) and covered with a 4 μm thick plastic film (SpectroMembrane, Chemplex Industries). A hand-held XRF analyzer (Olympus Delta) was used in a secure tabletop setup to maximize accuracy of total metal concentrations with the analyzer calibrated using a certified XRF reference material before conducting analyses on the soil samples. We focused our analyses only on elements that are potentially toxic (Zn, Pb, Cu, Ni, Cr, As) or generally nontoxic elements that are important soil nutrients (Ca, Fe, K, P, S, Mn, Cl).

A subset of the soil samples collected from the burned and unburned residential properties (43 samples in total) were also analyzed via inductively coupled plasma-mass spectrometry (ICP-MS) to provide a better indication of metal bioavailability. This subset was selected from 19 soils for which the XRF results indicated high concentrations of metals of human health concern and an additional 24 soils collected from six properties (4 samples per property) which were heavily impacted by the fire event. The air-dried and ground soil samples were extracted using the Mehlich 3 method: a nondigestion method that is more representative of metal bioavailability than total digestion.[31] The extractant solution utilized trace metal-grade quality chemicals and all clean glassware was thoroughly washed with pH 2 HCl. The extracts were diluted with 2% nitric acid and then analyzed with an ICP-MS instrument (NexION 350D, PerkinElmer, Waltham, MA) following EPA Method 6020[32] with 6 calibration standards and multiple internal standards run alongside the soil samples.

Soil Polycyclic Aromatic Hydrocarbon (PAH) Analyses. We selected a subset of 20 soil samples for PAH analyses with one randomly chosen sample from each of 10 burned and 10 unburned properties. The ten burned samples were selected from residential properties located in the center of neighborhoods with extensive fire damage. The ten unburned samples were selected from nearby residential properties that were unaffected by the fire. PAH extraction was conducted following a cyclohexane/acetone extraction using a Soxhlet distillation extractor following a protocol described previously.[33] A mixture of standards containing 5 ppm of phenanthrene, fluoranthene, anthracene, naphthalene, chrysene, acenaphthylene, pyrene, perylene, benzo[a]pyrene, benzo[a,h]anthracene, 9-methylanthracene, 9,10-dimethylanthracene, 1-phenylnaphthalene, 2-ethylnaphthalene, and 1-methylnaphthalene. and a nitrobenzene-d5 (15 ppm) internal standard was prepared for accurate quantification. This mixture was serially diluted to 2.5, 1, 0.5, 0.1, and 0.05 ppm. Singular standards were also made to confirm retention times. These PAH compounds were selected since they are all known to be toxic and are likely present in the WUI fire-impacted soils.

PAH concentrations in the Soxhlet extracts were quantified using atmospheric pressure gas chromatography (APGC) coupled with Waters Xevo G2 quadrupole time-of-flight (QTOF) mass spectrometer (Milford, MA). One microliter of each sample was injected and compounds separated using an Agilent DB-5MS (30m × 250 μm × 0.25 μm) column. The chromatography temperature gradient was set to 18 °C/min with a final temperature of 330 °C resulting in a run time of 16.89 min. The inlet was split/splitless using a pulsed splitless mode. The pulse time was 0.50 min. The mass spectrometer was run in positive mode with 0.1 s of scan time at a collision energy of 4 V. The analyzer was set to sensitivity mode with an API source. The scan range was 50-1200 Da.

Soil Mercury Analyses. A subset of 31 soil samples from both burned and unburned areas were analyzed for their mercury concentrations on a Milestone Direct Mercury Analyzer (DMA) at AIRIE, Fort Collins, Colorado. The detection limit is about 5 ppb, and the external precision is <5% at one standard deviation. AIRIE routinely verifies external precision through analysis of an in-house organic-rich garden soil and the NIST SRM 1632e. Standard data and analytical details including stepwise temperature tests are available at https://www.airieprogram.org. Whole soil samples (full organic plus clastic components) were used for this study. Sample sizes were between 50 and 200 mg of soil, optimized to yield 3-12 ng total Hg for DMA analysis. Samples were combusted at 650 °C to release all Hg.

Statistical Analyses. All statistical analyses were performed in R (4.2.1). The XRF data and soil chemistry data were based on a hierarchical experimental design with four sampling locations per residential property. Thus, we used linear mixed effects models to determine differences in metal concentrations and soil characteristics between burned and

https://doi.org/10.1021/acs.est.3c08508
Environ. Sci. Technol. 2024, 58, 4326−4333

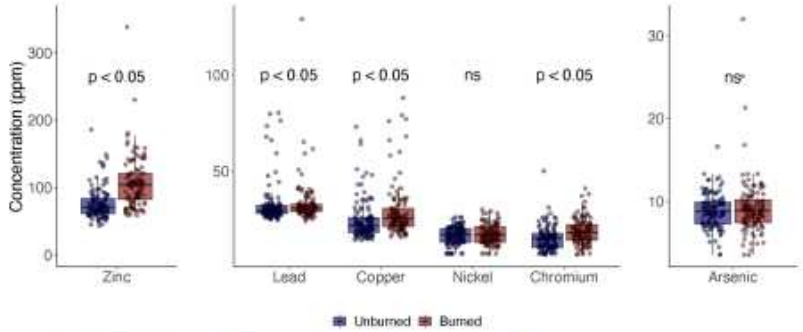

Figure 2. Comparison of metal concentrations in unburned and burned soils from residential properties as measured by XRF, with the statistical significance of the differences indicated for each element (ns = not significant). Note different scales on y-axes. These soil metal concentrations, regardless of burn status, are all well below the concentrations typically considered to pose a risk to human health (see Discussion).

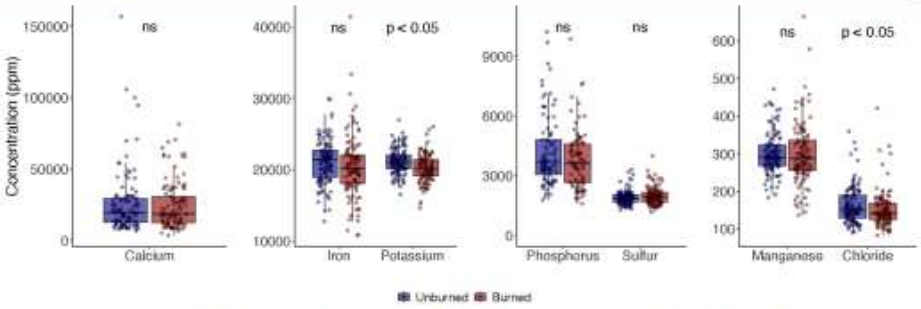

Figure 3. Comparison of the concentrations of generally nontoxic elements in soils from burned and unburned residential properties as measured by XRF with the statistical significance of the differences indicated for each element (ns = not significant). Note different scales on y-axes.

unburned residential soils with property as a random effect in the *lme4* package.[34] For each response variable, we implemented a mixed effects model using the Gaussian error distribution. When necessary, we used a log transformation of the response variable to meet assumptions of the linear model. Values that were beyond three absolute deviations from the median value were considered outliers and were removed.[35,36] Elemental concentrations below detection limits were adjusted to the limit of detection divided by the square root of two. For analyses where a hierarchical experimental design was not used (including soil metal concentrations as determined by ICP-MS, soil Hg and PAH concentrations, and analyses of the nonresidential, grassland soils from burned and unburned locations) we used parametric *t* tests and Wilcoxon rank-based tests, depending on the distribution of the data.

RESULTS

Measured total soil nitrogen (TN), total inorganic carbon (TIC), total organic carbon (TOC), and soil pH were not statistically different between burned and unburned residential properties (linear mixed effects models, p-value >0.05) (Supplementary Table 1). However, TN concentrations in burned nonresidential grassland soils (0.31 ± 0.13%) were significantly lower as compared to unburned grassland soils (0.36 ± 0.19%, linear mixed effect model, t = 2.25, p-value = 0.02) (Supplemental Table 2).

The results of the XRF analyses show that the fire-impacted residential properties had significantly higher concentrations of total soil Cr, Cu, Pb, and Zn (Figure 2, Supplemental Table 3) which are typically considered toxic contaminants.[37,38] Fire-impacted properties had significantly lower concentrations of Cl and K (Figure 3, Supplemental Table 3). For the nonresidential grassland soils, total metal concentrations were not significantly different between burned and unburned soils (Supplemental Figure 1, Supplemental Table 4) with the exception of Cl concentrations which were significantly lower in the fire-impacted nonresidential grassland soils (Supplemental Figure 1, linear mixed effect model, t = 3.017, p-value = 0.003).

ICP-MS analyses of the bioavailable fraction demonstrated that Zn, As, and P concentrations were significantly higher in fire-impacted residential properties (Supplemental Figure 2, Supplemental Table 5). We also measured mercury concentrations in a subset of samples and found that mercury concentrations do not appear to be significantly different between soils from burned and unburned residential properties (Supplemental Figure 3, Supplemental Table 7).

Concentrations of the 12 targeted PAHs were not statistically different between burned and unburned soils from the residential properties (Supplemental Table 6). Importantly, the concentrations of the five PAHs of most concern for human health (anthracene, pyrene, benzo[a]-

https://doi.org/10.1021/acs.est.3c08508
Environ. Sci. Technol. 2024, 58, 4326−4333

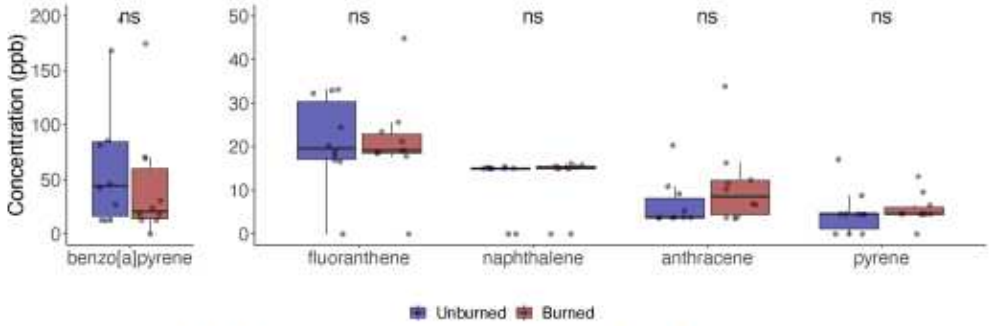

Figure 4. Concentrations of five PAHs of human health concern in residential soils. Note different scales on y-axes. We found no significant differences in PAH concentrations between burned and unburned soil samples from the residential properties (Wilcoxon rank-based test, $p > 0.05$). ns = not significant. For the concentrations of the other measured PAHs, see Supplemental Table 6.

pyrene, fluoranthene, and napthalene, shown in Figure 4) were not different between burned and unburned properties.

DISCUSSION

Some of the toxic metals measured, namely Cr, Cu, Pb, and Zn were more concentrated in soils from burned residential properties compared to soils from unburned properties (Figure 2). However, the concentrations of these metals were not elevated in nonresidential grassland areas (Supplemental Figure 1), highlighting the likely importance of anthropogenic material combustion (including structures and vehicles) to postfire soil contamination. These results are consistent with previous studies which have also documented increases in soil metal concentrations after fire events driven in part by the burning of structures and other urban infrastructure.[15,18,21−23] While other studies of *wildland* fires have observed increases in soil PAH concentrations postfire,[17,20] such increases were not observed in this study (Figure 4, Supplemental Table 6). However, it is difficult to place our PAH results in the context of the broader literature given the lack of studies examining WUI fire-driven soil PAH concentrations.

Given the elevated concentrations of some toxic metals in burned residential properties, we sought to determine if soil contamination from WUI wildfires could pose a threat to human health. To determine the human health risk of the quantified concentrations of the PAHs and metals, we used the threshold concentration for dermal exposure to children in residential soils using a Target Hazard Quotient (THQ) = 0.1, a conservative approach to estimating toxicity/carcinogenicity risk when exposed to multiple contaminants.[39] We determined that dermal exposures were the most plausible exposure pathway for metal contaminants since it is unlikely that residential soil would be ingested or inhaled in amounts of any concern to human health. Although concentrations of toxic metals did increase in fire-impacted residential soils (Figure 2), their concentrations were well below the estimated thresholds of concern. More specifically, we note that the concentrations of Zn, Cr, As, Cu, and Pb measured in the collected soils, even soils from burned residential properties, are all well below thresholds commonly considered to pose a risk to human health through dermal exposure.[39]

We acknowledge there are still unquantified risks associated with these postfire changes in soil metal concentrations since our analysis only quantified elemental concentrations. Thus, we cannot exclude the possibility that the fire event mobilized or transformed metals to increase their bioavailability/toxicity and, perhaps, elevate their risk to human health. For instance, even at low concentrations, methylmercury and hexavalent chromium can threaten human health.[40,41] Finally, we are hesitant to define risk with specific threshold values for soil metal concentrations given that the risk is context dependent. Health risks associated with exposure to metals in wind-blown soil (dust) could be very different from risks associated with growing and consuming crops in fire-impacted soils or risks associated with the movement of metals from soils into aquifers.[42] We need additional studies of soil contamination after WUI wildfires to specifically examine how the bioavailability of metals or other contaminants are affected by wildfires and the potential for the transport of soil contaminants into the atmosphere and water sources.

All wildfire events are unique, and the effects of wildfires on soils will always be context dependent. The specific effects of fire events on soil chemistry will vary depending on the intensity and duration of the fire event, soil properties, and the characteristics of the combusted materials.[18,21] Thus, we need to be careful not to extrapolate the results from this single wildfire event to all wildfire events, including those in other WUIs. The high winds associated with this fire event may have dispersed contaminants away from the fire perimeter, reducing the potential for local soil contamination. Likewise, the dominant grassland vegetation type in the sampled area could lead to distinct fire characteristics (faster moving, lower intensity) than wildfire events that may occur in more forested WUI areas. Also, we sampled soils four months after the fire event, making it possible that contaminants were transported away from surface soils by wind, surface water runoff,[43] postfire debris removal, or movement of contaminants deeper into the soil profile with melting snow or rainfall. Similarly, we note that we only collected soils from a small fraction of the residential properties located within or adjacent to the fire perimeter and we only collected soil from four locations per property. Clearly there is a high degree of spatial variation in soil PAH and metal concentrations (Figures 2−4). This variation, which is likely a product of soil heterogeneity, landscape position, ash transport and deposition, land-use practices, proximity to combusted structures or vehicles, and other factors, needs to be accounted for in future studies, particularly in highly heterogeneous residential areas. Sampling soils from fire-impacted residential areas is not trivial and

https://doi.org/10.1021/acs.est.3c08508
Environ. Sci. Technol. 2024, 58, 4326−4333

careful design of such sampling efforts is essential when trying to quantify postfire soil contamination.

Soil contamination results from wildland fire studies may not necessarily apply to WUI fires. The nature and distribution of the contaminants are likely affected by the unique source of combusted materials. WUI regions can be highly dissimilar, and the wildfire events that may occur in these areas can be highly variable. There is a clear need for more studies specifically investigating the impacts of wildfires at the WUI on potential soil contamination. WUI wildfires are likely to become more common and pose greater risks to human populations in coming years.[2] Thus, additional information is needed on the impacts of WUI fires on soil quality to guide policy and provide informed recommendations for the resettlement of areas affected by WUI wildfires.

■ ASSOCIATED CONTENT

Supporting Information

The Supporting Information is available free of charge at https://pubs.acs.org/doi/10.1021/acs.est.3c08508.

Supplemental Table 1: Summary of basic soil chemical characteristics for soils collected from burned and unburned residential properties. Supplemental Table 2: Summary of basic soil chemical characteristics for soils collected from burned and unburned nonresidential grassland sites. Supplemental Table 3: Summary of soil metal and metalloid concentrations as measured via XRF for the samples collected from the residential properties. Supplemental Table 4: Summary of soil metal and metalloid concentrations as measured via XRF for the samples collected from the nonresidential grassland locations. Supplemental Table 5: Summary of soil metal and metalloid concentrations as measured via ICP-MS for the subset of samples collected from residential properties. Supplemental Table 6: Summary of measured PAH concentrations for the subset of soil samples collected from residential properties. Supplemental Table 7: Subset of samples with measured Hg concentrations in soils from burned and unburned residential sites. Supplemental Figure 1: Comparison of the concentrations of metals (as measured via XRF) in soils collected from the nonresidential grassland locations. Supplemental Figure 2. Comparison of metal and metalloid concentrations in burned and unburned residential properties as measured by ICP-MS. Supplemental Figure 3: Concentrations of mercury in a subset of soils collected from burned and unburned residential properties. (PDF)

■ AUTHOR INFORMATION

Corresponding Authors

Noah Fierer − *Department of Ecology & Evolutionary Biology, University of Colorado Boulder, Boulder, Colorado 80309-0216, United States; Cooperative Institute for Research in Environmental Sciences, University of Colorado Boulder, Boulder, Colorado 80309, United States;* orcid.org/0000-0002-6432-4261; Email: Noah.Fierer@colorado.edu

Thomas Borch − *Department of Soil & Crop Sciences, Colorado State University, Fort Collins, Colorado 80523-1101, United States; Department of Chemistry, Colorado State University, Fort Collins, Colorado 80523-1872, United States;* orcid.org/0000-0002-4251-1613; Email: Thomas.Borch@colostate.edu

Authors

Sierra Jech − *Department of Ecology & Evolutionary Biology, University of Colorado Boulder, Boulder, Colorado 80309-0216, United States*

Clifford Adamchak − *Department of Ecology & Evolutionary Biology, University of Colorado Boulder, Boulder, Colorado 80309-0216, United States; Cooperative Institute for Research in Environmental Sciences, University of Colorado Boulder, Boulder, Colorado 80309, United States*

Sean C. Stokes − *Department of Soil & Crop Sciences, Colorado State University, Fort Collins, Colorado 80523-1101, United States;* orcid.org/0000-0001-9019-3739

Marin E. Wiltse − *Department of Chemistry, Colorado State University, Fort Collins, Colorado 80523-1872, United States*

Jessica Callen − *Department of Soil & Crop Sciences, Colorado State University, Fort Collins, Colorado 80523-1101, United States*

Jacob VanderRoest − *Department of Chemistry, Colorado State University, Fort Collins, Colorado 80523-1872, United States*

Eugene F. Kelly − *Department of Soil & Crop Sciences, Colorado State University, Fort Collins, Colorado 80523-1101, United States*

Eve-Lyn S. Hinckley − *Department of Ecology & Evolutionary Biology, University of Colorado Boulder, Boulder, Colorado 80309-0216, United States; Cooperative Institute for Research in Environmental Sciences, University of Colorado Boulder, Boulder, Colorado 80309, United States*

Holly J. Stein − *AIRIE, Applied Isotope Research for Industry and the Environment, Fort Collins, Colorado 80524-2313, United States; Department of Geosciences, University of Oslo, Oslo NO-0316, Norway*

Complete contact information is available at: https://pubs.acs.org/10.1021/acs.est.3c08508

Notes

The authors declare no competing financial interest.

■ ACKNOWLEDGMENTS

We thank all of the individuals in the Marshall Fire region who kindly offered to let us sample soils from their properties. We also thank Jerry Magloughlin and ARC-Bio at Colorado State University for the use of their analytical instruments. We thank Aaron Zimmerman (AIRIE Program at Innosphere Ventures) for his assistance with the mercury analyses. Funding for this project was provided by the Cooperative Institute for Research in Environmental Sciences at the University of Colorado Boulder and the Colorado State University Agricultural Experiment Station.

■ REFERENCES

(1) Theobald, D. M.; Romme, W. H. Expansion of the US wildland-urban interface. *Landsc. Urban Plan.* **2007**, *83* (4), 340−354.

(2) Peterson, G. C. L.; Prince, S. E.; Rappold, A. G. Trends in fire danger and population exposure along the wildland-urban interface. *Environ. Sci. Technol.* **2021**, *55* (23), 16257−16265.

(3) Carlson, A. R.; Helmers, D. P.; Hawbaker, T. J.; Mockrin, M. H.; Radeloff, V. C. The wildland-urban interface in the United States Based on 125 Million Building Locations. *Ecol. Appl.* **2022**, *32* (5), No. e2597.

(4) Radeloff, V. C.; Helmers, D. P.; Kramer, H. A.; Mockrin, M. H.; Alexandre, P. M.; Bar-Massada, A.; Butsic, V.; Hawbaker, T. J.; Martinuzzi, S.; Syphard, A. D.; Stewart, S. I. Rapid growth of the US wildland-urban interface raises wildfire risk. *Proc. Natl. Acad. Sci. U. S. A.* **2018**, *115* (13), 3314−3319.
(5) Bowman, D. M. J. S.; Kolden, C. A.; Abatzoglou, J. T.; Johnston, F. H.; van der Werf, G. R.; Flannigan, M. Vegetation fires in the Anthropocene. *Nat. Rev. Earth Environ* **2020**, *1* (10), 500−515.
(6) Ellis, T. M.; Bowman, D. M. J. S.; Jain, P.; Flannigan, M. D.; Williamson, G. J. Global Increase in wildfire risk due to climate-driven declines in fuel moisture. *Glob. Chang. Biol.* **2022**, *28* (4), 1544−1559.
(7) Shuman, J. K.; Balch, J. K.; Barnes, R. T.; Higuera, P. E.; Roos, C. I.; Schwilk, D. W.; Stavros, E. N.; Banerjee, T.; Bela, M. M.; Bendix, J.; Bertolino, S.; Bililign, S.; Bladon, K. D.; Brando, P.; Breidenthal, R. E.; Buma, B.; Calhoun, D.; Carvalho, L. M. V.; Cattau, M. E.; Cawley, K. M.; Chandra, S.; Chipman, M. L.; Cobian-Iñiguez, J.; Conlisk, E.; Coop, J. D.; Cullen, A.; Davis, K. T.; Dayalu, A.; De Sales, F.; Dolman, M.; Ellsworth, L. M.; Franklin, S.; Guiterman, C. H.; Hamilton, M.; Hanan, E. J.; Hansen, W. D.; Hantson, S.; Harvey, B. J.; Holz, A.; Huang, T.; Hurteau, M. D.; Ilangakoon, N. T.; Jennings, M.; Jones, C.; Klimaszewski-Patterson, A.; Kobziar, L. N.; Kominoski, J.; Kosovic, B.; Krawchuk, M. A.; Laris, P.; Leonard, J.; Loria-Salazar, S. M.; Lucash, M.; Mahmoud, H.; Margolis, E.; Maxwell, T.; McCarty, J. L.; McWethy, D. B.; Meyer, R. S.; Miesel, J. R.; Moser, W. K.; Nagy, R. C.; Niyogi, D.; Palmer, H. M.; Pellegrini, A.; Poulter, B.; Robertson, K.; Rocha, A. V.; Sadegh, M.; Santos, F.; Scordo, F.; Sexton, J. O.; Sharma, A. S.; Smith, A. M. S.; Soja, A. J.; Still, C.; Swetnam, T.; Syphard, A. D.; Tingley, M. W.; Tohidi, A.; Trugman, A. T.; Turetsky, M.; Varner, J. M.; Wang, Y.; Whitman, T.; Yelenik, S.; Zhang, X. Reimagine fire science for the Anthropocene. *PNAS Nexus* **2022**, *1* (3). DOI: 10.1093/pnasnexus/pgac115.
(8) Mell, W. E.; Manzello, S. L.; Maranghides, A.; Butry, D. T.; Rehm, R. G. The wildland-urban interface fire problem - current approaches and research needs. *Int. J. Wildland Fire* **2010**, *19*, 238−251.
(9) Spyratos, V.; Bourgeron, P. S.; Ghil, M. Development at the wildland-urban interface and the mitigation of forest-fire risk. *Proc. Natl. Acad. Sci. U. S. A.* **2007**, *104* (36), 14272−14276.
(10) Martin, D.; Tomida, M.; Meacham, B. Environmental impact of fire. *Fire Science Reviews* **2016**, *5* (1), 1−21.
(11) Pereira, P.; Francos, M.; Brevik, E. C.; Ubeda, X.; Bogunovic, I. Post-fire soil management. *Curr. Opin. Environ. Sci. Health* **2018**, *5*, 26−32.
(12) Hohner, A. K.; Rhoades, C. C.; Wilkerson, P.; Rosario-Ortiz, F. L. Wildfires alter forest watersheds and threaten drinking water quality. *Acc. Chem. Res.* **2019**, *52* (5), 1234−1244.
(13) Jaffe, D. A.; O'Neill, S. M.; Larkin, N. K.; Holder, A. L.; Peterson, D. L.; Halofsky, J. E.; Rappold, A. G. Wildfire and prescribed burning impacts on air quality in the United States. *J. Air Waste Manag. Assoc.* **2020**, *70* (6), 583−615.
(14) National Academies of Sciences, Engineering, and Medicine. *The Chemistry of Fires at the Wildland-Urban Interface*; The National Academies Press, 2022.
(15) Alexakis, D. E. Suburban areas in flames: dispersion of potentially toxic elements from burned vegetation and buildings. Estimation of the associated ecological and human health risk. *Environ. Res.* **2020**, *183*, 109153.
(16) Alshehri, T.; Wang, J.; Singerling, S. A.; Gigault, J.; Webster, J. P.; Matiasek, S. J.; Alpers, C. N.; Baalousha, M. Wildland-Urban Interface Fire Ashes as a Major Source of Incidental Nanomaterials. *J. Hazard. Mater.* **2023**, *443*, 130311.
(17) Vergnoux, A.; Malleret, L.; Asia, L.; Doumenq, P.; Theraulaz, F. Impact of forest fires on PAH level and distribution in soils. *Environ. Res.* **2011**, *111* (2), 193−198.
(18) Abraham, J.; Dowling, K.; Florentine, S. The unquantified risk of post-fire metal concentration in soil: A review. *Water Air Soil Pollut.* **2017**, *228*, 175.
(19) Terzano, R.; Rascio, I.; Allegretta, I.; Porfido, C.; Spagnuolo, M.; Khanghahi, M. Y.; Crecchio, C.; Sakellariadou, F.; Gattullo, C. E. Fire effects on the distribution and bioavailability of potentially toxic elements (PTEs) in agricultural soils. *Chemosphere* **2021**, *281*, 130752.
(20) Campos, I.; Abrantes, N. Forest fires as drivers of contamination of polycyclic aromatic hydrocarbons to the terrestrial and aquatic ecosystems. *Current Opin. Environ. Sci. Health* **2021**, *24*, 100293.
(21) Fernandez-Marcos, M. L. Potentially toxic substances and associated risks in soils affected by wildfires: A review. *Toxics* **2022**, *10* (1), 31.
(22) Young, S.; Balluz, L.; Malilay, J. Natural and technologic hazardous material releases during and after natural disasters: A review. *Sci. Total Environ.* **2004**, *322* (1−3), 3−20.
(23) Guerra, M. B. B.; Neto, E. L.; Prianti, M. T. A.; Pereira-Filho, E. R.; Schaefer, C. E. G. R. Post-fire study of the Brazilian Scientific Antarctic Station: Toxic element contamination and potential mobility on the surrounding environment. *Microchem. J.* **2013**, *110*, 21−27.
(24) Assessment of Burn Debris - 2015 Wildfires, Lake and Calaveras Counties. California Environmental Protection Agency, 2015. https://calepa.ca.gov/wp-content/uploads/sites/6/2016/10/Disaster-Documents-2015yr-FireSample.pdf.
(25) Stec, A. A.; Dickens, K.; Barnes, J. L. J.; Bedford, C. Environmental contamination following the Grenfell Tower fire. *Chemosphere* **2019**, *226*, 576−586.
(26) Fovell, R. G.; Brewer, M. J.; Garmong, R. J. The December 2021 Marshall Fire: Predictability and gust forecasts from operational models. *Atmosphere* **2022**, *13* (5), 765.
(27) Marshall Fire. *Storymaps*, 2022. https://storymaps.arcgis.com/stories/cd7e211f5d594f9996b061d05670e779.
(28) Sherrod, L. A.; Dunn, G.; Peterson, G. A.; Kolberg, R. L. Inorganic carbon analysis by modified pressure-calcimeter method. *Soil Sci. Soc. Am. J.* **2002**, *66* (1), 299−305.
(29) Thomas, G. W. Soil pH and Soil Acidity. In *Methods of Soil Analysis*; Soil Science Society of America, American Society of Agronomy, 2018; pp 475−490.
(30) SW-846 Test Method 6200: Field Portable X-Ray Fluorescence Spectrometry for the Determination of Elemental Concentrations in Soil and Sediment. *United States Environmental Protection Agency*. https://www.epa.gov/hw-sw846/sw-846-test-method-6200-field-portable-x-ray-fluorescence-spectrometry-determination (accessed 2023-08-23).
(31) Mehlich, A. Mehlich 3 soil test extractant: A modification of Mehlich extractant. *Commun. Soil Sci. Plant Anal.* **1984**, *15*, 1409−1416.
(32) Method 6020B (SW-846): Inductively Coupled Plasma-Mass Spectrometry. *United States Environmental Protection Agency*. https://www.epa.gov/esam/epa-method-6020b-sw-846-inductively-coupled-plasma-mass-spectrometry (accessed 2023-08-23).
(33) McKenna, A. M.; Chacón-Patiño, M. L.; Chen, H.; Blakney, G. T.; Mentink-Vigier, F.; Young, R. B.; Ippolito, J. A.; Borch, T. Expanding the analytical window for biochar speciation: Molecular comparison of solvent extraction and water-soluble fractions of biochar by FT-ICR mass spectrometry. *Anal. Chem.* **2021**, *93* (46), 15365−15372.
(34) Bates, D.; Mächler, M.; Bolker, B.; Walker, S. Fitting linear mixed-effects models using Lme4. *arXiv [stat.CO]*, 2014. http://arxiv.org/abs/1406.5823.
(35) Rock, N. M. S. Summary statistics in geochemistry: A study of the performance of robust estimates. *Mathematical Geol.* **1988**, *20*, 243−275.
(36) Leys, C.; Ley, C.; Klein, O.; Bernard, P.; Licata, L. Detecting outliers: Do not use standard deviation around the mean, use absolute deviation around the median. *J. Exp. Soc. Psychol.* **2013**, *49* (4), 764−766.
(37) Chen, H.; Teng, Y.; Lu, S.; Wang, Y.; Wang, J. Contamination features and health risk of soil heavy metals in China. *Sci. Total Environ.* **2015**, *512*−*513*, 143−153.

(38) Hou, D.; O'Connor, D.; Igalavithana, A. D.; Alessi, D. S.; Luo, J.; Tsang, D. C. W.; Sparks, D. L.; Yamauchi, Y.; Rinklebe, J.; Ok, Y. S. Metal contamination and bioremediation of agricultural soils for food safety and sustainability. *Nature Rev. Earth Environ.* **2020**, *1* (7), 366−381.
(39) *United States Environmental Protection Agency*. Regional Screening Levels (RSLs) - Generic Tables. https://www.epa.gov/risk/regional-screening-levels-rsls-generic-tables.
(40) Gworek, B.; Dmuchowski, W.; Baczewska-Dabrowska, A. H. Mercury in the terrestrial environment: A Review. *Environ. Sci. Eur.* **2020**, *32*, 128.
(41) Mishra, S.; Bharagava, R. N. Toxic and genotoxic effects of hexavalent chromium in environment and its bioremediation strategies. *J. Environ. Sci. Health C Environ. Carcinog. Ecotoxicol. Rev.* **2016**, *34* (1), 1−32.
(42) Jankowski, C.; Isaacson, K.; Larsen, M.; Ley, C.; Cook, M.; Whelton, A. J. Wildfire damage and contamination to private drinking water wells.*AWWA Water Science* **2023** *5* DOI: 10.1002/aws2.1319.
(43) Magliozzi, L.; Mansfeldt, C.; McKnight, D.; Korak, J.A. Water quality in Coal Creek following the 2021 Marshall Fire. *Natural Hazards Center Quick Response Report Series. University of Colorado Boulder*. 2023

https://doi.org/10.1021/acs.est.3c08508
Environ. Sci. Technol. 2024, 58, 4326−4333

Supporting Information

Determination of soil contamination at the wildland-urban interface after the 2021 Marshall Fire in Colorado, USA

Sierra Jech[1], Clifford Adamchak[1,2], Sean C. Stokes[3], Marin E. Wiltse[4], Jessica Callen[3], Jacob VanderRoest[4], Eugene F. Kelly[3], Eve-Lyn S. Hinckley[1,2], Holly J. Stein[5,6], Thomas Borch[3,4*], Noah Fierer[1,2*]

[1] Department of Ecology & Evolutionary Biology, University of Colorado Boulder, Boulder, CO, 80309-0216 USA
[2] Cooperative Institute for Research in Environmental Sciences, University of Colorado Boulder, Boulder, CO, 80309 USA
[3] Department of Soil & Crop Sciences, Colorado State University, Fort Collins, CO, 80523-1101 USA
[4] Department of Chemistry, Colorado State University, Fort Collins, CO, 80523-1872 USA
[5] AIRIE, Applied Isotope Research for Industry and the Environment, Fort Collins, CO, 80524-2313 USA
[6] Department of Geosciences, University of Oslo, Oslo NO-0316 Norway

12 Pages
7 Supplemental Tables
3 Supplemental Figures

Supplemental Table 1: Summary of basic soil chemical characteristics for soils collected from burned and unburned residential properties. SD = standard deviation

	Unburned		Burned		Statistical Comparison of Means
	Range	Median (SD)	Range	Median (SD)	
pH	5.60-8.50	7.69 (0.49)	6.22-8.28	7.63 (0.42)	W = 406.5 p = 0.8337 (Wilcoxon)
Total Nitrogen (%)	0-0.63	0.36 (0.11)	0.11-0.88	0.32 (0.11)	W = 323.5 p = 0.1334 (Wilcoxon)
Total Carbon (%)	1.88-11.24	4.17 (1.28)	1.83-10.73	3.91 (1.53)	W = 355 p = 0.3121 (Wilcoxon)
Total Inorganic Carbon (%)	0-2.10	0.18 (0.36)	0-1.28	0.18 (0.30)	W = 429.5 p = 0.7135 (Wilcoxon)
Total Organic Carbon (%)	1.44-11.24	3.87 (1.32)	1.59-10.72	3.71 (1.54)	W = 327 p = 0.1481 (Wilcoxon)

Supplemental Table 2: Summary of basic soil chemical characteristics for soils collected from burned and unburned nonresidential grassland sites. SD = standard deviation

	Unburned		Burned		Statistical Comparison of Means
	Range	Median (SD)	Range	Median (SD)	
pH	5.15-8.17	6.68 (1.03)	5.63-7.59	6.66 (0.62)	W = 118.5 p = 0.54 (Wilcoxon)
Total Nitrogen (%)	0.25-0.88	0.36 (0.19)	0.15-0.67	0.31 (0.13)	W = 83 p = 0.06 (Wilcoxon)
Total Carbon (%)	3.02-18.22	5.49 (3.69)	1.87-12.31	4.06 (2.54)	W = 90 p = 0.10 (Wilcoxon)
Total Inorganic Carbon (%)	0-0.45	0.09 (0.15)	0-0.01	0.002 (0.003)	W = 4.5 p = 0.006 (Wilcoxon)
Total Organic Carbon (%)	3.02-18.22	5.24 (3.72)	1.86-12.31	4.1 (2.54)	W = 91 p = 0.11 (Wilcoxon)

Supplemental Table 3: Summary of soil metal and metalloid concentrations as measured via XRF for the samples collected from the residential properties. SD = standard deviation.

	Unburned Properties		Burned Properties		Statistical Comparison of Means
Element	Range (ppm)	Median (SD) (ppm)	Range (ppm)	Median (SD) (ppm)	
P	1,784 – 10,238	3,696 (1,750)	1,590 – 9,881	3,641 (1,428)	t = 1.42 p = 0.16
S	1,285 – 3,306	1,854 (352)	1,173 – 11,113	1,948 (960)	t = -1.35 p = 0.18
Cl	90 – 359	151 (48)	83 – 421	141 (48)	t = 2.08 p = 0.04
K	16,543 – 26,983	21,088 (1,759)	14,639 – 26,058	20,164 (1,941)	t = 2.62 p = 0.01
Ca	6,880 – 156,758	19,478 (21,581)	3,587 – 81,575	18,723 (16,252)	t = 0.002 p = 1
Cr	6 – 50	15 (6)	7 – 41	18 (7)	t = -3.59 p = 0.0003
Mn	183 – 472	290 (54)	137 – 664	288 (81)	t = 0.44 p = 0.66
Fe	12,782 – 29,897	21,376 (2,992)	10,814 – 41,430	20,234 (4,359)	t = 1.07 p = 0.29
Ni	7 – 26	17 (5)	7 – 30	17 (5)	t = -0.63 p = 0.53
Cu	14 – 73	22 (11)	16 – 88	25 (14)	t = -2.24 p = 0.03
Zn	43 – 186	71 (23)	59 – 1,030	104 (94)	t = -6.12 p = 9.4e-10
As	4 – 17	9 (2)	4 – 32	9 (4)	t = 0.052 p = 0.96
Pb	24 - 80	30 (11)	24 - 129	31 (11)	t = -2.51 p = 0.01

Supplemental Table 4: Summary of soil metal and metalloid concentrations as measured via XRF for the samples collected from the nonresidential grassland locations. SD = standard deviation.

	Unburned Properties		Burned Properties		Statistical Comparison of Means
Element	Range (ppm)	Median (SD) (ppm)	Range (ppm)	Median (SD) (ppm)	
P	1,879 – 3,788	2,433 (639)	2,340 – 2,972	2,805 (284)	t = -0.26 p = 0.79
S	1,284 – 5,297	1,883 (996)	1,180 - 3,501	1,533 (593)	t = 1.55 p = 0.12
Cl	101 - 238	142 (38)	93 – 150	112 (20)	t = 3.02 p = 0.003
K	10,277 – 25,332	20,429 (4,132)	15,763 – 22,964	18,714 (2,258)	t = 1.32 p = 0.19
Ca	3,748 – 46,630	8,018 (10,813)	2,271 – 12,708	5,387 (2,617)	t = 0.59 p = 0.55
Cr	7 - 25	16 (5)	8 – 48	20 (10)	t = -0.93 p = 0.35
Mn	196 - 440	315 (76)	147 – 457	263 (76)	t = 1.31 p = 0.19
Fe	11,162 – 29,438	21,913 (4,925)	9,384 - 23,988	16,924 (4,130)	t = 1.81 p = 0.07
Ni	7 - 25	15 (6)	7 – 24	13 (6)	t = 0.18 p = 0.85
Cu	11 – 37	21 (7)	11 - 22	16 (3)	t = 1.95 p = 0.05
Zn	36 – 200	70 (39)	44 - 101	67 (18)	t = 0.43 p = 0.67
As	5 – 15	10 (2)	5 - 12	10 (2)	t = -0.13 p = 0.89
Pb	28 - 75	44 (14)	32 - 54	42 (7)	t = 0.47 p = 0.64

Supplemental Table 5: Summary of soil metal and metalloid concentrations as measured via ICP-MS for the subset of samples collected from residential properties and the results of the statistical tests comparing concentrations in burned versus unburned properties.

	Unburned Properties		Burned Properties		Statistical Comparison of Means
Element	Range (ppm)	Median (SD) (ppm)	Range (ppm)	Median (SD) (ppm)	
P	26.48-903.47	98.95 (228.87)	98.04-719.90	172.28 (179.12)	W = 305 p = 0.018 (Wilcoxon)
Mg	244.68-479.50	382.36 (77.56)	187.16-1181.50	479.43 (262.50)	W = 290 p = 0.049 (Wilcoxon)
Cr	0.08-0.21	0.13 (0.05)	0.07-0.76	0.14 (0.16)	W = 250.5 p = 0.336 (Welch's t-test)
Zn	2.9-51.11	16.25 (13.07)	10.83-212.21	33.57 (38.11)	W = 343 p = 0.001 (Wilcoxon)
Fe	123.04-281.99	202.74 (39.44)	122.73-247.31	196.43 (29.89)	t = 0.016 df = 28 p = 0.988 (Welch's t-test)
Co	0.37-1.18	0.75 (0.23)	0.46-1.27	0.91 (0.23)	t = 1.27 df = 34.7 p = 0.214 (Welch's t-test)
Cu	1.16-10.78	3.02 (3.06)	1.23-5.82	2.27 (1.19)	W = 200.5 p = 0.768 (Wilcoxon)
Mn	22.22-73.85	48.46 (13.55)	15.19-79.89	52.34 (16.67)	t = 0.95 df = 38.6 p = 0.348 (Welch's t-test)
Ni	1.21-2.76	1.89 (0.37)	1.27-2.64	1.81 (0.30)	t = 0.20 df = 29.8 p = 0.840 (Welch's t-test)
K	688.19-2593.65	1024.99 (462.62)	424.92-2,946.37	1487.76 (670.92)	W = 288 p = 0.055 (Wilcoxon)
Cd	0.07-0.42	0.13 (0.11)	0.04-0.34	0.12 (0.07)	W = 171 p = 0.292 (Wilcoxon)

Pb	2.07-26.52	6.60 (8.27)	1.7-17.14	3.48 (4.02)	W = 142 p = 0.073 (Wilcoxon)
As	0.10-0.93	0.15 (0.21)	0.20-7.99	0.42 (1.72)	W = 350 p = 0.0005 (Wilcoxon)

Supplemental Table 6: Summary of measured PAH concentrations for the subset of soil samples collected from residential properties and the results of the statistical tests comparing concentrations in burned versus unburned properties.

	Unburned Properties		Burned Properties		Statistical Comparison of Means
PAH	Range (ppb)	Median (SD) (ppb)	Range (ppb)	Median (SD) (ppb)	
anthracene	3.71-20.31	3.78 (5.41)	3.64-33.83	8.57 (9.11)	W = 62 p = 0.39 (Wilcoxon)
pyrene	0-17.09	4.56 (5.12)	0-13.17	4.58 (3.53)	W = 60 p = 0.50 (Wilcoxon)
benzo[a]pyrene	12.41-195.88	43.98 (65.77)	0-174.53	20.83 (51.92)	W = 38 p = 0.39 (Wilcoxon)
fluoranthene	0-33.11	19.59 (10.09)	0-44.83	19.12 (10.88)	W = 51 p = 1 (Wilcoxon)
naphthalene	0-15.43	15.04 (6.37)	0-16.13	15.12 (6.50)	W = 63 p = 0.34 (Wilcoxon)
chrysene	21.41-147.70	65.17 (39.33)	38.74-127.44	57.51 (25.63)	t = -0.17 df = 15.5 p = 0.86 (Welch's t-test)
acenaphthylene	0-10.04	9.68 (3.08)	9.52-10.36	9.75 (0.33)	W = 56 p = 0.71 (Wilcoxon)
perylene	0-29.78	8.21 (9.98)	0-16.09	0 (5.44)	W = 27 p = 0.06 (Wilcoxon)
9-methylanthracene	0-19.59	0 (9.14)	0-23.59	8.92 (10.96)	W = 62 p = 0.35 (Wilcoxon)
9,10-dimethylanthracene	0-28.81	28.34 (11.98)	0-29.20	28.44 (12.08)	W = 60 p = 0.47 (Wilcoxon)
1-phenylnaphthalene	0-4.49	4.44 (1.41)	4.32-4.52	4.44 (0.07)	W = 54 p = 0.79

					(Wilcoxon)
1-methylnaphthalene	8.24-8.67	8.30 (0.15)	8.14-9.27	8.62 (0.41)	t = 1.84 df = 11.5 p = 0.09 (Welch's t-test)

Supplemental Table 7: Subset of samples with measured Hg concentrations in soils from burned and unburned residential sites (designated by first letter B or U in sample name). All concentrations are at the ppb level with replicates (boxed) showing reproducibility.

AIRIE Hg Run Number	Sample Name	Sample Weight [g]	Hg [ng]	Hg Conc [ppb]
Hg-3434	B10.4	0.1373	4.49	32.73
Hg-3435	B10.4 rep1	0.1267	4.50	35.51
Hg-3436	B10.4 rep2	0.1185	3.93	33.17
Hg-3429	B11.3	0.1278	5.58	43.67
Hg-3430	B11.3 rep1	0.1181	4.24	35.88
Hg-3418	B12.2	0.1218	2.79	22.92
Hg-3427	B13.4	0.1326	3.02	22.76
Hg-3407	B21.4	0.1384	3.54	25.55
Hg-3450	B23.1	0.1181	2.94	24.88
Hg-3437	B23.2	0.1247	3.63	29.13
Hg-3428	B23.3	0.1254	5.07	40.44
Hg-3446	B23.4	0.1318	4.21	31.94
Hg-3447	B23.4 rep1	0.1286	4.05	31.51
Hg-3404	B25.4	0.1380	3.01	21.84
Hg-3465	B25.4 rep1	0.1274	3.30	25.94
Hg-3423	B26.3	0.1366	2.52	18.47
Hg-3420	B28.2	0.1286	7.00	54.47
Hg-3421	B28.2 rep1	0.1229	5.89	47.94
Hg-3425	B6.2	0.1229	4.76	38.75
Hg-3426	B6.2 rep1	0.1403	5.63	40.16
Hg-3469	B8.3	0.1303	3.51	26.95
Hg-3433	B9.1	0.1180	2.27	19.24
Hg-3451	B9.1 rep1	0.1947	3.99	20.50
Hg-3452	B9.1 rep2	0.1895	3.76	19.87
Hg-3453	B9.1 rep3	0.1961	3.81	19.45
Hg-3400	BGB.1	0.1181	5.96	50.50
Hg-3401	BGB.1 rep1	0.1268	6.01	47.41
Hg-3402	BGB.1 rep2	0.1242	5.89	47.41
Hg-3405	U1.2	0.1343	7.56	56.26
Hg-3466	U2.1	0.1263	5.73	45.40
Hg-3467	U2.1 rep1	0.1231	5.31	43.14
Hg-3468	U12.2	0.1289	2.92	22.64
Hg-3422	U13.4	0.1273	5.31	41.69

Hg-3406	U14.3	0.1432	19.13	133.60
Hg-3431	U17.2	0.1235	3.04	24.60
Hg-3444	U20.1	0.1397	4.37	31.26
Hg-3424	U20.4	0.1199	2.60	21.71
Hg-3403	U22.2	0.1291	3.85	29.83
Hg-3432	U23.4	0.1237	8.48	68.58
Hg-3470	U28.1	0.1025	13.49	131.57
Hg-3419	U28.2	0.1173	20.15	171.76
Hg-3454	U28.2 rep1	0.0496	7.86	158.44
Hg-3455	U28.2 rep2	0.0487	8.00	164.18
Hg-3456	U28.2 rep3	0.0505	8.42	166.73
Hg-3445	U28.3	0.1226	14.58	118.94
Hg-3448	U28.4	0.1265	11.96	94.51
Hg-3449	U28.4 rep1	0.1267	12.02	94.85
Hg-3441	UBG.1	0.1256	5.12	40.77
Hg-3442	UBG.1 rep1	0.1379	6.53	47.36
Hg-3443	UBG.1 rep2	0.1254	5.55	44.24

Sample Name, first letter: B = Burned Soil, U = Unburned Soil
Analyses by Direct Mercury Analyzer (DMA), AIRIE, Colorado
Instrument external precision <5% (one standard deviation)
rep1, rep2, rep3, rep4 = replicate analyses of same sample
Analyst, Aaron Zimmerman, Research Associate, AIRIE

Supplemental Figure 1: Comparison of the concentrations of metals (as measured via XRF) in soils collected from the nonresidential grassland locations. ns = not statistically significant.

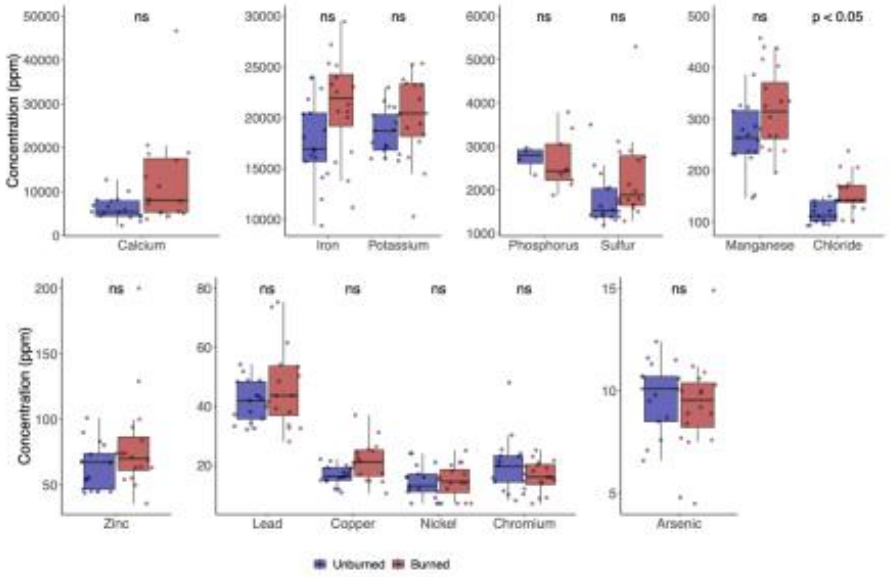

Supplemental Figure 2. Comparison of metal and metalloid concentrations in burned and unburned residential properties as measured by ICP-MS. The statistical results for each element (comparing burned versus unburned) are shown at the top, ns = not significant.

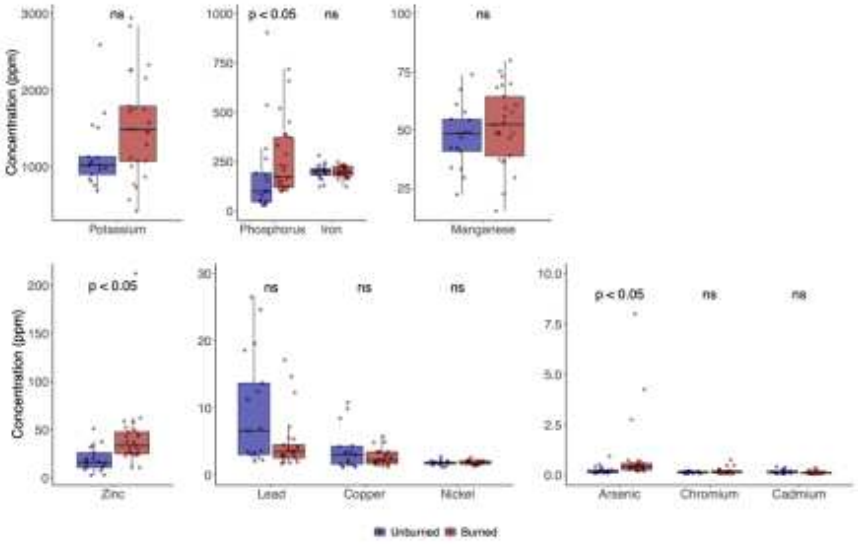

Supplemental Figure 3: Concentrations of mercury in a subset of soils collected from burned and unburned residential properties (see Methods for details). The differences were not statistically significant (ns).

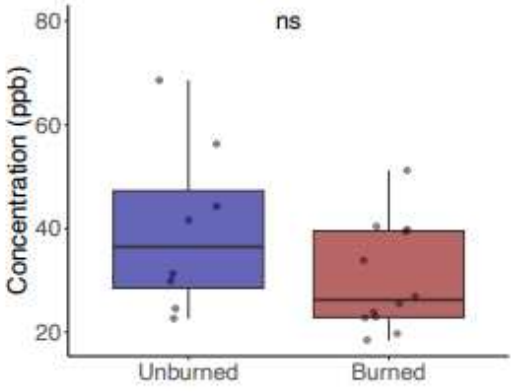

APPENDIX G: CO-AUTHOR CONTRIBUTIONS TO "ROLE OF PERMAFROST THAW TRANSITIONS IN BIOGEOCHEMICAL NITROGEN CYCLING"

Reprinted from Logan, M. N.; Patzner, M. S.; VanderRoest, J. P.; McGivern, B. B.; Srikanthan, N.; Simpson, M. J.; McKenna, A. M.; Wrighton, K. C.; Bryce, C.; Kappler, A.; Borch, T. Role of Permafrost Thaw Transitions in Biogeochemical Nitrogen Cycling. *Soil & Environmental Health* **2025**, *3* (2), 100148. https://doi.org/10.1016/j.seh.2025.100148.

According to CRediT criteria, my contributions include formal analysis (interpreting data and evaluating how the data should be presented in the publication), writing – review & editing, and visualization. As for visualization, I helped produce the TOC art and Figure 3. This publication was included as a chapter in Merritt Logan's dissertation.

Soil & Environmental Health 3 (2025) 100148

Contents lists available at ScienceDirect

Soil & Environmental Health

journal homepage: www.sciencedirect.com/journal/soil-and-environmental-health

Research Paper

Role of permafrost thaw transitions in biogeochemical nitrogen cycling

Merritt N. Logan [a], Monique S. Patzner [b], Jacob P. VanderRoest [a], Bridget B. McGivern [a], Nivetha Srikanthan [c], Myrna J. Simpson [c], Amy M. McKenna [e,a], Kelly C. Wrighton [a], Casey Bryce [d], Andreas Kappler [b,f], Thomas Borch [a,*]

[a] Department of Soil & Crop Sciences and Department of Chemistry, Colorado State University, 307 University Ave, Fort Collins, CO 80523-1170, USA
[b] Geomicrobiology, Department of Geosciences, University of Tuebingen, Schnarrenbergstrasse 94-96, 72076 Tuebingen, Germany
[c] Environmental NMR Centre and Department of Physical & Environmental Sciences, University of Toronto Scarborough, Toronto, Ontario, M1C 1A4, Canada
[d] School of Earth Sciences, University of Bristol, Bristol, BS8 1RL, UK
[e] Ion Cyclotron Resonance Facility, National High Magnetic Field Laboratory, Florida State University, Tallahassee, FL 32310-4005, USA
[f] Cluster of Excellence EXC 2124: Controlling Microbes to Fight Infections, Tübingen, Germany

HIGHLIGHTS

- Permafrost thaw corresponds with a spike in dissolved organic N.
- Permafrost thaw fronts serve as transition zones with distinct dissolved organic N.
- Peptide-like organic N is limited at the point of permafrost collapse.
- Upregulated N-utilizing metabolomic pathways correlated to limited organic N in bog.

GRAPHICAL ABSTRACT

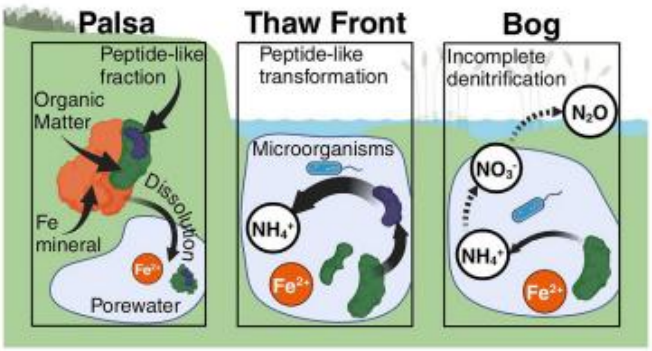

ARTICLE INFO

Handling Editor: Lena Q. Ma
Technical Editor: Lena Q. Ma

Keywords:
N dynamics
Climate change
Metatranscriptomics
Environmental health
Microbial activity changes
NMR and FT-ICR MS
Bog and peatlands

ABSTRACT

Significant organic nitrogen (ON) stocks have accumulated in permafrost peatlands over millennia. Climate change is expected to increase peatland thaw, making this ON more susceptible to biogeochemical degradation. However, the interplay between thaw-released N and N cycling remains poorly understood. To elucidate ON composition across a thaw transition (palsa to thaw front to bog), we employed 21 T electrospray ionization Fourier transform ion cyclotron resonance mass spectrometry (FT-ICR MS) and nuclear magnetic resonance (NMR) spectroscopy. In addition, we performed metatranscriptomic sequencing to evaluate microbial activity changes in N cycling pathways between the palsa and bog. We observed an approximate 10-fold increase in dissolved ON and a significant rise in ammonium concentration between the palsa and thaw front. Additionally, there was a reduction in the peptide-like fraction and an increase in the aromatic fraction of dissolved ON molecules. Dissolved ON concentrations decreased by 73 % between the thaw front and bog, while expression of

* Corresponding author.
E-mail addresses: merritt.logan@colostate.edu (M.N. Logan), thomas.borch@colostate.edu (T. Borch).

https://doi.org/10.1016/j.seh.2025.100148
Received 4 February 2025; Received in revised form 25 March 2025; Accepted 26 March 2025
Available online 28 March 2025

Palsa and thaw front
Dissolved organic N
Transcriptomic gene expression

ammonium-producing genes was significantly higher in the bog compared to the palsa. Our findings highlight the release and rapid compositional shift of ON during thaw transitions. This underscores the need for further studies on thaw-released N to enhance models predicting N cycling and Arctic greenhouse gas emissions.

1. Introduction

Approximately 15 % of land area in the northern hemisphere is underlain by permafrost, serving as a major sink for both carbon and nitrogen (Hugelius et al., 2014; Hugelius et al., 2020; Mishra et al., 2017; Obu, 2021; Schuur et al., 2013; Zhang et al., 2008). The northern circumpolar permafrost region stores an estimated 1600 Pg of carbon and 67 Pg of nitrogen accumulated over thousands of years in frozen or saturated anoxic soils, representing approximately 33 % and 50 % of the total global carbon and nitrogen stocks respectively (Batjes, 1996; Harden et al., 2012; Schuur et al., 2022; Voigt et al., 2017). Climate change is expected to release large quantities of these stocks as greenhouse gas (GHG), and between 1971 and 2019 warming in permafrost regions has increased two to four times faster than global averages, accelerating permafrost loss and environmental disturbances (Abbott et al., 2022; AMAP, 2021).

Permafrost peatlands, a subset of permafrost, cover ~3.7 million km^2 and store ~415 Pg of carbon and ~10 Pg of nitrogen (Harris et al., 1988; Holmes et al., 2022; Hugelius et al., 2020; Wilson et al., 2016). Many permafrost peatlands are especially susceptible to thawing as their average annual near-surface temperatures are within 1 °C of freezing (Jorgenson et al., 2001). Therefore, minimal warming can raise average annual temperatures above 0 °C, inducing thaw and exposing the stored organic carbon and nitrogen to biogeochemical mineralization (McGuire; et al., 2018; Schädel et al., 2014). This increased mineralization is expected to release substantial amounts of GHG, contributing to climate change and further accelerating thawing (Schuur et al., 2015). While many studies focus on carbon cycling and carbonaceous GHG (Cooper et al., 2017; Knoblauch et al., 2018; Schaefer et al., 2014), research on nitrogen cycling and nitrogenous GHG release is comparatively limited. However, the fate of organic nitrogen is drawing increased interest due in part to its potential transformation to N_2O (a greenhouse gas with a warming potential 298 times greater than CO_2 (Butterbach-Bahl et al., 2013; Hugelius et al., 2020; Marushchak et al., 2021; Voigt et al., 2017) and the important role that nitrogen plays in nutrient cycling.

Nitrogen availability and utilization in permafrost peatlands are influenced by seasonal thaw depth and thaw conditions (Fiencke et al., 2022; Harms and Jones, 2012; Norby et al., 2019; Walker et al., 2005). The active layer, which thaws each summer, varies in depth depending on seasonal conditions and temperature. Within this layer, the upper 5–15 cm contains lower nitrogen concentrations than deeper, perennially frozen soils. However, nitrogen bioavailability is limited by either restricted root access within the deeper active layer or by frozen conditions in the permafrost below (Keuper et al., 2012; Salmon et al., 2018). Research has demonstrated that active layer expansion of ~10 cm into permafrost can result in a sevenfold increase in dissolved inorganic nitrogen (DIN) release compared to seasonally thawed regions (Keuper et al., 2012; Salmon et al., 2018). Nitrogen inputs to peatlands through biological fixation and atmospheric deposition are relatively minor compared to stored nitrogen content (Ramm et al., 2022), despite varying with landscape and vegetation type. In permafrost systems, thaw events provide the primary source of nitrogen for biogeochemical cycling (Burke et al., 2022; Chen et al., 2018; Fiencke et al., 2022; Keuper et al., 2012).

Nitrogen cycling in terrestrial ecosystems involves complex interactions between organic and inorganic forms, mediated by microbial processes and environmental conditions (Kuypers et al., 2018). In permafrost systems, these cycles are particularly important as they influence ecosystem productivity and greenhouse gas emissions (Abbott and Jones, 2015; Marushchak et al., 2021; Patzner et al., 2022a). Recently, Ramm et al. (2022) proposed an updated model for nitrogen cycling within permafrost soils suggesting higher nitrogen cycling activity in seasonally thawed surface soils than previously presumed (Ramm et al., 2022). This model illustrates the relationships between organic nitrogen pools and the production of bioavailable nitrogen forms (ammonium, nitrate, and N_2). Their work indicates that while protein depolymerization rates are high, they do not directly control nitrogen turnover. Instead, dissolved organic nitrogen (DON) concentration during seasonal thawing appears to be the primary driver of inorganic nitrogen cycling (Ramm et al., 2022). Furthermore, the composition of the DON can affect ammonification and production of inorganic nitrogen; however, the controls of ammonification in thawing permafrost are still not well-studied (Fiencke et al., 2022; Ramm et al., 2022; Wegner et al., 2022; Wild et al., 2014). Soil conditions during thaw also affect inorganic nitrogen concentrations by influencing the activity of nitrogen cycling pathways (Fiencke et al., 2022; Voigt et al., 2020). For example, thaw transition studies have observed increased nitrate concentrations in thawed soil with moderate moisture (40–80 % water filled pore space) adjacent to existing permafrost. These studies suggest that increased nitrate concentrations could enhance N_2O emissions via denitrification, provided that an active nitrogen reducing microbial community is present (Mao et al., 2019; Wegner et al., 2022). Ultimately, nitrogen demand and fate in permafrost systems are controlled by the interplay of available ammonium, nitrification and denitrification activity, and soil moisture conditions. In permafrost peatlands, thaw creates distinct moisture interfaces that manifest as either thermokarst features or thaw slumps (Mao et al., 2019; Schuur et al., 2007; Wegner et al., 2022). When thaw occurs adjacent to bog areas, soil can collapse and become saturated depending on water table depth. In thaw slumps, rather than exhibiting the peat breakage characteristic of thermokarsts, the peat surface undergoes elevation loss while maintaining structural integrity (Varner et al., 2022). These thaw transitions represent zones of variable water saturation and rapidly shifting microbial communities and have been identified as potential hotspots of GHG release due to their fluctuating oxic and anoxic conditions (Elder et al., 2021; Fiencke et al., 2022; Wegner et al., 2022). However, to our knowledge, previous studies examining nitrogen dynamics across thaw transitions have not investigated fully saturated thawed soil conditions (Mao et al., 2019; Wegner et al., 2022), nor have they characterized the composition of the organic nitrogen pool (AminiTabrizi et al., 2020; Hodgkins et al., 2014; Hodgkins et al., 2016; Mann et al., 2015; Moore et al., 2023). Understanding biogeochemical nitrogen cycling within these dynamic thaw front environments requires detailed characterization of both the released organic nitrogen composition and the expression of microbial genes involved in nitrogen transformation pathways (Grosse et al., 2016; Ramm et al., 2022; Voigt et al., 2017).

Evaluating organic nitrogen composition within complex organic matter requires molecular-level analytical techniques capable of resolving tens of thousands of polyfunctional molecules. Such characterization demands a mass analyzer with high dynamic range, high sensitivity, and ultrahigh resolving power across a wide molecular weight range (m/z 150–1500) (Bahureksa et al., 2022; Smith et al., 2018). Fourier transform ion cyclotron resonance mass spectrometry (FT-ICR MS) uniquely meets these requirements, with the 21 T hybrid linear ion trap/FT-ICR mass analyzer achieving the highest resolving power to date (3,000,000 at m/z 200) (Bahureksa et al., 2022). The ultrahigh resolution of 21T FT-ICR MS enables accurate molecular formula assignments within complex dissolved organic matter (DOM) matrices

(Bahureksa et al., 2021; Hawkes and Kew, 2020; Nebbioso and Piccolo, 2013; Patzner et al., 2022a; Sleighter and Hatcher, 2007). This capability allows for post-analysis isolation of nitrogen-containing formulae, separating them from the larger, total DOM pool. Such isolation enhances our ability to track patterns of selective degradation or preservation of nitrogenous species that would otherwise be obscured in the total DOM pool. While FT-ICR MS has been successfully employed to study OM composition changes between bogs and fens and in laboratory incubation studies, it has not yet been applied to characterize organic nitrogen within a thaw front (Hodgkins et al., 2016; MacDonald et al., 2021; Stücheli et al., 2018; Textor et al., 2019; Wilson et al., 2022; Zherebker et al., 2019).

In this study, we examined the thaw transition from palsa to thaw front to bog, which represents the progressive stages of permafrost thaw. We present a molecular-level characterization of DON and inorganic nitrogen using electrospray ionization FT-ICR MS, NMR spectroscopy, and elemental analysis, allowing us to examine the changes in the composition of both organic and inorganic nitrogen and corroborate shifts in molecular structure. In addition, we complemented our chemical analysis by examining previously collected palsa and bog samples for the expression of genes associated with microbial nitrogen cycling pathways. Although these samples were collected during a separate field campaign than the porewater samples used for molecular and elemental analysis, the site conditions are highly comparable. This allowed us to evaluate the microbiome response in these distinct systems and provide a possible explanation for the biogeochemical shifts we observed. We hypothesized that (i) the thaw front will have elevated ammonium concentrations but not elevated nitrate concentrations due to wet, anoxic conditions, (ii) across the palsa-to-thaw front transition, peptide-like molecules will be depleted while aromatic molecules will be more abundant due to preferential microbial degradation, and (iii) the predominantly anoxic bog will not show increased microbial gene expression associated with denitrification due to nitrate limitations.

2. Materials and methods

2.1. Site description

Field sampling was conducted at Stordalen Mire (68 22′ N, 19 03′E), a subarctic peatland underlain by discontinuous permafrost in northern Sweden with peat depth between 1 and 3 m (Malmer et al., 2005). This site has been studied since the 1970s, with anthropogenic warming driving ecosystem changes through permafrost thaw (Holmes et al., 2022; Rosswall et al., 1975; Rosswall and Granhall, 1980). The site comprises three distinct ecosystems (palsa, bog, and fen), whose characteristics and boundaries have remained stable over time, as demonstrated through DOM and gas flux measurements (AminiTabrizi et al., 2020; Holmes et al., 2022; Lakomiec et al., 2021; Patzner et al., 2022a; Patzner et al., 2022; Varner et al., 2022; Wilson et al., 2022). Although at our sampling site the position of the thaw front has progressed into the palsa, the adjacent palsa and bog have been stable ecosystems since at least 2000 (Olefeldt and Roulet, 2012). Greenhouse gas emissions at Stordalen are primarily controlled by thaw state and saturation conditions rather than interannual variation, and ecosystem differences remain consistent interannually (Lakomiec et al., 2021; Varner et al., 2022). This temporal stability supports the validity of comparing our samples collected at different time points (cores in 2016; porewater in 2019 and 2022).

We selected Stordalen Mire because its palsa-to-bog thaw transition provides a well-defined system where the shift to waterlogged, anoxic conditions coincides with reductive dissolution of Fe(III) minerals and substantial DOC release and oxidation (Patzner et al., 2022a). The sampling location within the mire as well as a photo of the sampling site are shown in Fig. 1. The three dominant vegetation communities of the mire are (1) ericaceous and woody plants in palsa (intact permafrost); (2) *Sphagnum* spp., sedges, and shrubs in ombrotrophic peatland or bog

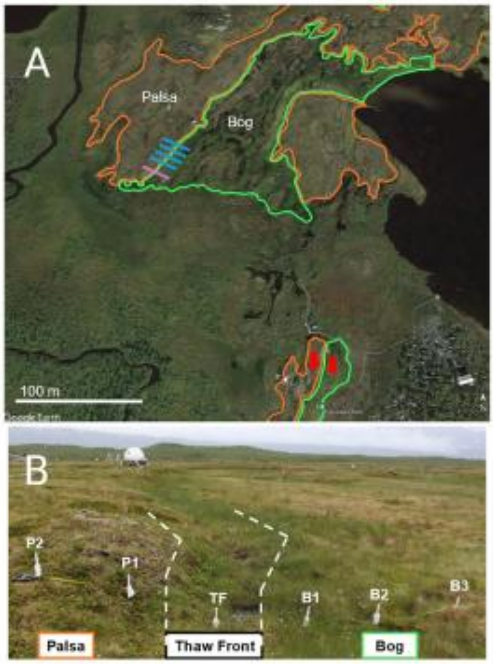

Fig. 1. (A) Stordalen mire, Abisko (Sweden) shown with palsa and bog regions. Transects 1–4 are shown as blue lines, transect 5 is shown as a purple line, and the soil cores used for metatranscriptome analysis are shown as red arrows. Palsa and bog regions are based on reported hydrological data (Holmes et al., 2022; Johansson et al., 2006; Olefeldt et al., 2012) and first hand observation during sampling. Maps data: Google Earth, CNES/Airbus, Lantmateriet/Metria, Maxar Technologies; copyright 2024. (B) Transect one lysimeters shown crossing the thaw transition. Palsa, thaw front, and bog regions in addition to sample points for transect one are shown. Dashed lines show thaw front moving away from the camera. Photo was taken looking north at 68°21′18.70″N, 19° 2′38.00″E.

(intermediate thaw); (3) sedges, mainly *Eriophorum* spp. in minerotrophic peatland or fen (full permafrost thaw) (Bäckstrand et al., 2010; Olefeldt et al., 2012).The palsa is oxic, features pH values of 4.5–5.5, and is elevated by underlying intact permafrost, leading to higher elevation than nearby bogs (Bockheim and Munroe, 2014; Payandi-Rolland et al., 2021). Bogs generally feature pH values of ~3.6, are waterlogged, and contain deep underlying permafrost (Fofana et al., 2022; Hodgkins et al., 2014, 2016; Olefeldt and Roulet, 2012).

2.2. Sample collection

Sampling was conducted along four transects incorporating the thaw transition (Fig. 2A). A fifth transect was collected 3 m adjacent to the initial sampling grid for inorganic and organic nitrogen content analysis. Transects 1–4 were collected in June/July 2019 and transect 5 was collected in September 2022. Transect locations were based on previously sampled palsa and bog locations (Patzner et al., 2020). Thaw front location was determined by measuring rapid reductive dissolution of reactive iron (III) (oxyhydr)oxide minerals due to soil saturation, releasing a pulse of aqueous Fe^{2+} (Patzner et al., 2022a). Therefore, the thaw front position was defined as the point in the transect with the highest $Fe^{2+}_{(aq)}$ concentration, correlating with the point of soil saturation. Due to natural variation in the thaw progression, the thaw front occurred at different points in our sampling transects (Fig. 2A). Based on

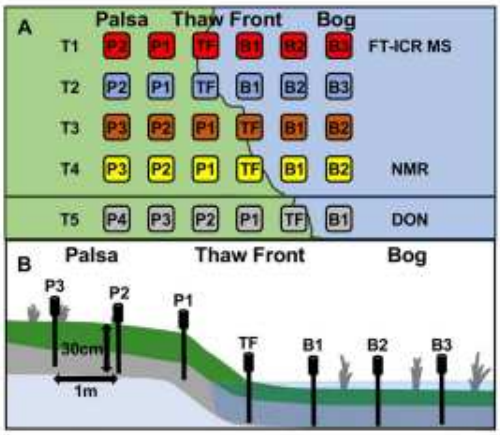

Fig. 2. (A) Top-down view of porewater sampling transects with sample points marked by thaw conditions along the transect. Palsa (P) and bog (B) are numbered according to their distance from the thaw front. The thaw front (TF) is identified as the point with the maximum $Fe^{2+}_{(aq)}$ concentration in each transect. Transects are labeled as T1-4 and are spaced 1 m apart. Transect 5 is located approximately 3 m to the south of T4 and crosses the same thaw transition. Transects 1–4 were used for elemental analysis. FT-ICR MS and NMR analyses were conducted on porewater from T1 and T4, respectively, and dissolved organic nitrogen (DON) was measured for T5. (B) Cross-section of porewater sampling within each transect showing sampling depth at 30 cm, lysimeters spaced every meter, permafrost collapse at the thaw front, and the approximate height of the water table in the bog. Green and gray layers comprise the active layer's primarily organic content and transition between organic and mineral horizons respectively. The light blue region shows permafrost ice.

thaw front location, the palsa (defined as intact permafrost) and the bog (opposing the palsa on the other side of the thaw front) were both labeled according to their respective distances from the thaw front (Fig. 2A). Porewater was collected along each transect at a depth of 30 cm, corresponding to the interface between the seasonally thawed active layer and the underlying perennially frozen permafrost, and consistently located within a transition zone between the organic and mineral horizons (Patzner et al., 2022a). Samples were labeled according to their position in the transect (Fig. 2B). The thawed-frozen interface serves as a lateral flow path, directing water from precipitation and active layer deepening from palsa to bog (Koch et al., 2013). Porewater was collected using lysimeters that were spaced 1 m apart along a given transect. The collected porewater was syringe filtered (0.22 μm) and transferred to dinitrogen-flushed SCHOTT bottles that were wrapped in aluminum foil to prevent photodegradation. The samples were then stored at 4 °C until further analysis, and sample volumes are reported in SI Table S1. Instrument access and sample volume limitations necessitated the use of select transects for FT-ICR MS and NMR, which are shown in Fig. 2A. Further description of porewater sampling can be found in previous work (Patzner et al., 2022a).

2.3. Porewater analysis

Total iron ($Fe_{(s)}$ and $Fe^{2+}_{(aq)}$) was measured by acidifying the porewater using 2 M HCl followed by a ferrozine assay and colorimetric analysis measured at 560 nm with further detail described in previous work (Patzner et al., 2022a; Patzner et al., 2020; Stookey, 1970). To measure DOC concentration, porewater was acidified with 2 M HCl to remove inorganic carbon and analyzed by total carbon analyzer (High TOC II, Elementar, Germany). Dissolved organic nitrogen was determined by measuring total nitrogen alongside DOC and subtracting inorganic nitrogen (Patzner et al., 2022a; Patzner et al., 2020; Treat et al., 2016). $Ammonium_{(aq)}$, $nitrate_{(aq)}$, and $nitrite_{(aq)}$ concentrations were measured with a flow injection analyzer (Seal Analytical, Germany) equipped with a dialysis membrane to remove $Fe^{2+}_{(aq)}$ and prevent side reactions during measurement. Due to sample volume limitations, nitrite and nitrate were analyzed in transects 1–4, DOC, $Fe^{2+}_{(aq)}$, and ammonium were analyzed in transects 1–5, and DON was analyzed in transect 5 (Table S2).

The mean analyte concentrations of the palsa samples (n = 13), thaw front samples (n = 5), and bog samples (n = 11) were statistically compared to each other. First, the normality of the analyte concentrations from each thaw state were evaluated using the Shapiro-Wilk test. If the populations of each thaw state were normally distributed, then the average analyte concentration of two thaw states were compared with the Welch's *t*-test. If one of the populations was not normally distributed, then the Mann-Whitney *U* test was used.

2.4. Nuclear magnetic resonance (NMR) spectroscopy

Nuclear magnetic resonance spectroscopy was utilized to determine the distribution of structural groups in total organic matter. Although ^{1}H NMR does not select for nitrogen containing compounds, it does provide an overview of the DOM chemistry that can be used for sample comparison with the corroborating molecular class abundances identified using FT-ICR MS (Bahureksa et al., 2021; Kim et al., 2022; Zark & Dittmar, 2018). Filtered (0.22 μm) porewater was lyophilized and yielded approximately 1 mg of freeze dried material. The freeze dried extracts were further dried over phosphorus pentoxide in a vacuum desiccator and then re-dissolved into 60 μL of deuterium oxide (D_2O, 99.9 % D) and 5 μL of sodium deuteroxide (NaOD, 99.5 % D, 30 wt % in D_2O). These dissolved samples were then centrifuged (10,000×*g* and 4 °C), and the supernatants were transferred into 1.7 mm NMR tubes (Norell). All samples were analyzed using a Bruker BioSpin Avance III 500 MHz NMR spectrometer (Karlsruhe, Germany) equipped with a ^{1}H-^{15}N-^{13}C TXI 1.7 mm microprobe with an actively shielded Z gradient. One-dimensional ^{1}H NMR spectra were collected using water suppression via pre-saturation utilizing relaxation gradients and, the spectra were collected using 2048 scans per sample with a recycle delay of 2 s and 32K time domain points. The spectra were processed using a zero-filling factor of two and were apodized by multiplication with an exponential decay corresponding to 0.3 Hz line broadening (Mitchell et al., 2018). NMR spectra were integrated based on typical DOM chemical shift regions associated with materials derived from linear terpenoids (MDLT; 0.6–1.6 ppm), carboxyl-rich alicyclic molecules (CRAM; 1.6–3.2 ppm), carbohydrates and peptides (3.2–4.5 ppm), and aromatic and phenolic components (6.5–8.4 ppm) (Mitchell et al., 2018; Woods and Simpson, 2011). The integration was performed using Analysis of Mixtures (AMIX; v. 3.9.15) software and expressed as percentage of the sum of the specific integration regions such that our comparison considered relative changes between these specific regions. It is important to note that some resonances (~1.9 ppm: likely from acetic acid; ~3.3 ppm likely from methanol; and ~8.4 ppm: likely from formic acid) (Mitchell et al., 2018; Tong et al., 2021; Woods and Simpson, 2011) do not align with the typical regions of DOM but were not excluded during integration due to overlapping resonances in some samples.

2.5. Metatranscriptome sequencing

Metatranscriptome sequencing was utilized to evaluate upregulation or downregulation of gene expression of enzymes in nitrogen cycling pathways, including but not limited to ammonification, nitrification, and denitrification. To survey microbial gene expression in Stordalen Mire, we used the genomes recovered in Woodcroft and Singleton et al. (Woodcroft et al., 2018). The 1529 metagenome-assembled genomes (MAGs) were dereplicated at 99 % identity with dRep (v2.6.2) (Olm et al., 2017) into 649 MAGs. The 99 % dereplicated MAGs were annotated with DRAM (v1.4.4)

(Shaffer et al., 2020). To assess the gene expression of these MAGs in the palsa and bog, we used metatranscriptome samples previously published in Ellenbogen et al. (2023). The metatranscriptomes derive from cores taken in July 2016 from defined palsa and bog environmental conditions at an adjacent thaw transition, and the thaw states have been well defined by previous work (Bäckstrand et al., 2010, 2008; Holmes et al., 2022; Johansson et al., 2006; Varner et al., 2022). We recognize the possibility of variability between the porewater transects and metatranscriptome peat cores. However, site restrictions prevented the collection of peat cores at the porewater thaw transition location. Furthermore, both sites represent well-defined thaw transitions in Stordalen Mire (Holmes et al., 2022). Additionally, the conditions of the palsa and bog are consistent at an interannual scale although there are year to year differences, the observed differences between them are consistent (AminiTabrizi et al., 2020; Wilson et al., 2022). Therefore, we are confident that the findings from the metatranscriptome analysis can be applied to the comparable porewater sampled from the palsa to bog transition. Soil cores were sectioned in the field at three depths: "surface" (1–4 cm), "middle" (10–14 cm), and "deep" (20–24 cm) and immediately put into LifeGuard (Qiagen). Metatranscriptome analysis used the deep section of the cores, as the 20–24 cm depth is most comparable to the 30 cm depth of porewater samples. Core sections were stored at −20 °C until analysis. DNA and RNA were co-extracted from 5 to 10 g peat using the Mobio PowerMax Soil DNA/RNA isolation kit (cat# 12966-10). Details on metatranscriptome library preparation, raw reads, gene annotation, and pathway expression comparison are provided in more detail in the SI (SI Section 1 and SI Data 1).

2.6. 21 T FT-ICR MS analysis

Fourier transform ion cyclotron resonance mass spectrometry assigns nitrogen-containing molecular formulae within the dissolved organic matter pool. The ability to segregate formulae according to elemental classes, like those that include nitrogen, enables us to differentiate compositional variations within each class that might otherwise be indiscernible within the total FT-ICR MS identified OM pool. Porewater DOM was analyzed with 21 T FT-ICR MS to identify and monitor DON compositional changes. Porewater was prepared for FT-ICR MS analysis by solid phase extraction (SPE) under N_2 atmosphere (glove bag) following a modified procedure based on Dittmar et al. (2008) and Li et al. (2016), which has been described in previous work (Patzner et al., 2022a; Patzner et al., 2020; Stücheli et al., 2018). The samples were processed under N_2 using degassed solvents to maintain the oxygen concentrations present *in situ*, and Hypersep Retain CX cartridges were selected for SPE due to reported improved nitrogen containing formulae and peptide-like formulae recovery compared to commonly used PPL cartidges (Stücheli et al., 2018). Hypersep Retain CX SPE cartridges (part# 60107-305, Thermo Fisher Scientific, Waltham, MA) were rinsed with 5 mL of HPLC grade methanol (Sigma-Aldrich, Rehovot, Israel) followed by 5 mL of 0.01 M HCl. Each DOM sample was acidified to pH ~2.5 and 0.5 mg C was loaded onto the SPE columns. After sample loading, the SPE cartridges were rinsed with 5 mL of 0.01 M HCl followed by drying with N_2 for 3–5 min. Finally, the samples were eluted with 1 mL of HPLC grade methanol and stored in airtight amber sample vials wrapped in aluminum foil at 4 °C. No additional dilution of the samples was performed prior to FT-ICR MS analysis.

Samples were analyzed as negative ions in a custom-built hybrid linear ion trap FT-ICR mass spectrometer equipped with a 21 T superconducting solenoid magnet (Hendrickson et al., 2015; Smith et al., 2018). Ionization conditions, instrument settings, and molecular formula assignment procedure are described in more detail in the SI (SI Section 2). The molecular formulae were assigned molecular class (condensed aromatic, aromatics/polyphenols, highly unsaturated, unsaturated aliphatic, saturated fatty acids, peptides, and sugars) according to the formula boundaries outlined by Poulin et al. (2017) (Table S3). For all mass spectra presented herein, between 10,024–11,357 mass peaks were assigned elemental compositions with root-mean-square mass measurement accuracy of 55–70 ppb with achieved resolving power of 3, 400,000 at m/z 200. The *m/z* range including all samples was 165.0193–1155.211. Data processing post-formula assignment was performed with RStudio utilizing R software (V4.1.2). Table S4 shows the sample name, RMS error, and number of assignments for all spectra discussed herein. PetroOrg files, calibrated peak lists, and peak assignments are publicly available via the Open Science Framework via DOI 10.17605/OSF.IO/TZKWN.

3. Results

3.1. The thaw front featured the highest aqueous Fe^{2+}, DOC, ammonium, and DON concentrations

Transects 1–4 exhibited a pulse of $Fe^{2+}_{(aq)}$ and DOC at the saturated thaw front (Fig. 3A). Transect 5, which was collected to analyze DON concentrations, showed changes in concentration of $Fe^{2+}_{(aq)}$, ammonium, and DOC consistent with the previously sampled four transects, despite the 3-year gap in sampling time. The palsa, generally dry and oxic (Hodgkins et al., 2014), had the lowest levels of all measured species (Fig. 3 and Table S2). The only exception to this was nitrate, which had no statistically significant change between any of

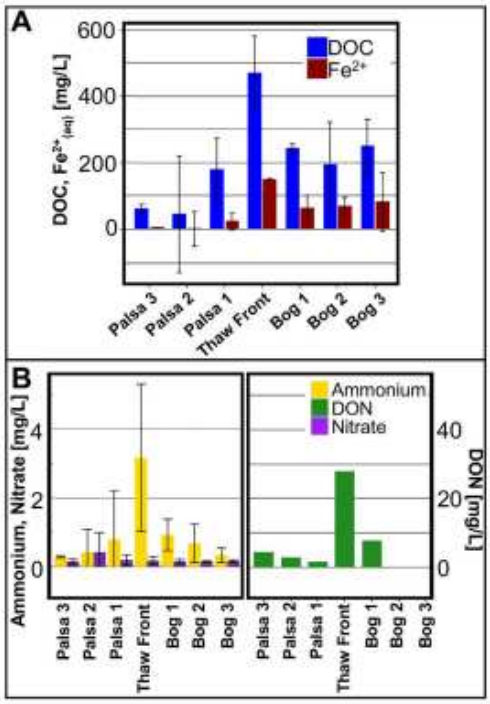

Fig. 3. Porewater composition across the thaw transition. (A) DOC and $Fe^{2+}_{(aq)}$ concentrations across the thaw transition. (B) Ammonium, nitrate, and DON concentrations across the thaw transition. Reported values and error bars represent the average and standard deviation of palsa-to-bog sampling transects. Error bars are not present for DON as only one transect (T5) was analyzed for DON, so n = 1 for all DON values. There were no DON values for Bog 2 and Bog 3 since there were no Bog 2 and Bog 3 sampling points for transect 5 due to the position of the thaw front. N-values for the remaining sample positions varied due to different thaw front positions in the transects (see Table S2 for full transect data).

the thaw states (Welch's *t*-test, $P > 0.05$) ranging between 1.27 and 0.07 mg/L. The thaw front had the highest concentrations of all analyzed species, with significantly higher levels (Welch's *t*-test, $P < 0.05$) of DOC and ammonium compared to the palsa and bog. The bog, which the palsa drains into via the thaw front (Olefeldt and Roulet, 2012), contained concentrations of ammonium that were not significantly different (Welch's *t*-test, $P > 0.05$) from the palsa. Similarly to ammonium, DON concentration decreased by 73 % immediately after the thaw front (Fig. 3B). Differences in DON concentrations could not be evaluated with Welch's *t*-test or the Mann-Whitney *U* test because DON was only measured along transect 5. Nevertheless, the thaw front DON concentration was substantially higher compared to other sampling points (10-fold increase compared to the average palsa concentration). Since the trends in DOC and $Fe^{2+}_{(aq)}$ are consistent across all transects when aligned to the pulse of $Fe^{2+}_{(aq)}$ (i.e., the thaw front), we can conclude that the geochemical profiles of the transects are comparable. Therefore, we propose that results from more detailed molecular analyses (FT-ICR MS and NMR) that were performed on select transects can be applied to the general thaw transition at Stordalen Mire.

3.2. Thaw front DON has lower H/C and lower relative abundance of aliphatic formula compared to palsa and bog

Van Krevelen diagram analysis showed clear compositional differences between the palsa and thaw front sites (Fig. 4A) The palsa (P2), thaw front, and bog (B3) featured 11272, 10852, and 10024 total monoisotopic formulae, respectively. Higher relative abundance formulae in the thaw front had lower H/C and higher O/C ratios and were more aromatic-like than in the palsa (Fig. 4A and B). Specifically, the percentage of aromatic/polyphenols-like and condensed aromatic-like formulae increased from 23 % in the palsa to 27 % in the thaw front followed by a decrease to 23 % in the bog. Higher aromatic-like content in the thaw front could be attributed to microbial degradation of polyphenolic compounds (Patzner et al., 2022a). Despite a 7.5-fold increase in DOC and a tenfold increase in the DON concentration at the thaw front, the number of identified DOC and DON formulae underwent minimal change. Assigned DON formulae represented approximately 27 % of the total formulae across all conditions. As observed in the total formulae, when only nitrogen-containing formulae (referred from here as CHNO formulae) were compared, the highly abundant CHNO formulae in the

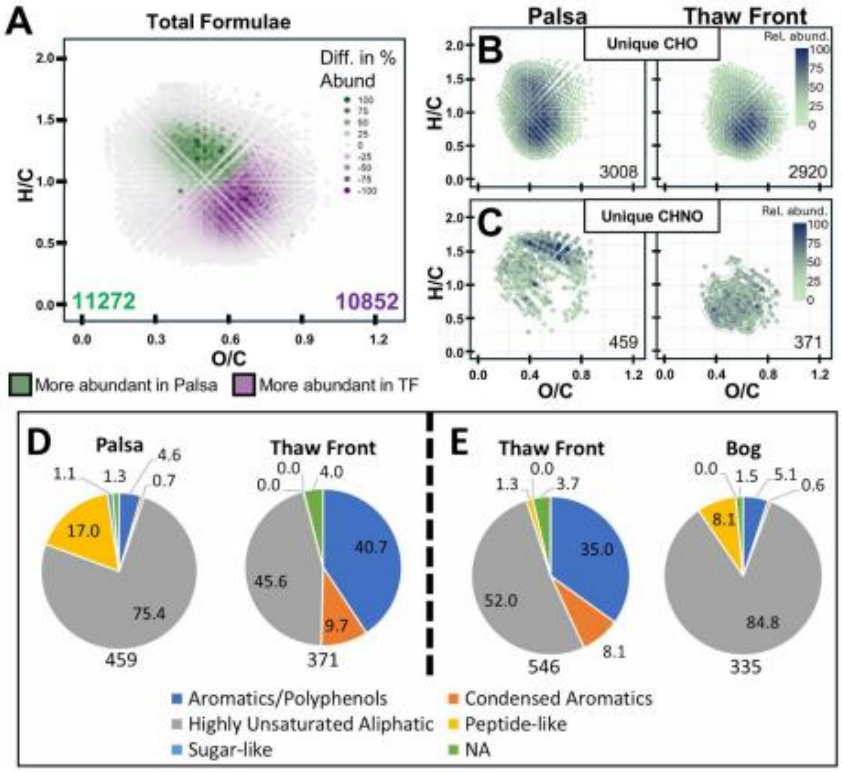

Fig. 4. Molecular formula characterization performed by FT-ICR MS of porewater samples. (A) Van Krevelen diagrams displaying comparisons between palsa (P2) and thaw front samples. Distribution of the total formula showing regions of higher abundance in palsa (green) and higher abundance in thaw front (purple). Color is determined by the difference in the relative abundance for a given formula between the palsa and the thaw front, with positive values having higher relative abundance in the palsa and negative values having higher relative abundance in the thaw front. The total count of identified formulae is inserted and color matched to palsa and thaw front. (B) Unique CHO formulae for palsa and thaw front and (C) unique CHNO formulae in palsa and thaw front colored by percent abundance of the formula. Inserted numbers in (B) and (C) are the number of formulae plotted in each plot. (D and E) Formula count of unique CHNO molecules shown as percentages of molecular class assigned by FT-ICR MS between (D) palsa (P2) and thaw front and (E) thaw front and bog (B3). The numbers of identified unique CHNO formulae for each thaw state are shown underneath each chart. Molecular class is defined by the heteroatom content of each molecular formula. Molecular class was defined according to Poulin et al. (2017). Unsaturated aliphatic and saturated fatty acid classes are not shown as there are no unique CHNO formulae in those classes.

thaw front also featured higher O/C and lower H/C ratios and were more aromatic-like than the palsa (Fig. 4C).

To further examine compositional differences in the assigned CHNO formulae, we isolated and compared formulae that were unique to each thaw state, hereafter referred to as the "unique pool". When comparing the unique CHNO pools between the palsa and thaw front, there is a clear compositional difference in CHNO formulae, which is distinct from the unique CHO pools. (Fig. 4B and C). Comparable to the total formulae pools, the unique CHNO formulae shifted from more aliphatic-like in the palsa to more aromatic-like in the thaw front. In the palsa, most unique CHNO formulae with high relative abundance feature H/C values around 1.5, with only a few formulae in the region of highest unique CHO. Conversely, the thaw front lacks unique formulae with H/C values near 1.5 but features a cluster of formulae in the more aromatic-like region, consistent with its unique CHO pool. The unique CHNO pools reveal a distinct pattern: many formulae found in the palsa are missing from the thaw front, and vice versa (Fig. 4C).

To determine which formulae contributed to the differences in the unique CHNO pools, we compared unique CHNO formulae by assigned molecular class (Table S3). The thaw front contained more aromatic-like and less peptide-like unique CHNO formulae when compared to either palsa or bog (Fig. 4D–Table S5). Notably, when comparing the palsa and thaw front, the proportion of unique CHNO formulae that were peptide-like decreased from 17 % to 0 %. Simultaneously, the aromatic/polyphenols-like and condensed aromatic-like formulae increased from 5 % to 50 %. Although the thaw front drains into the bog, the high proportions of condensed aromatic/polyphenol-like and low proportion of peptide-like unique CHNO formulae of the thaw front were not present in the bog. From the thaw front to the bog, the unique CHNO condensed aromatic and aromatic/polyphenol-like fraction decreased from 43 % to 6 %. Unique CHNO peptide-like formula increased from the thaw front to the bog, increasing from 1 % in the thaw front to 8 % in the bog, but did not return to palsa levels.

3.3. Carbohydrate- and peptide-like content was lowest at the thaw front

The FT-ICR MS results were complemented with solution-state ^{1}H NMR spectroscopy data to evaluate the molecular structure of porewater DOM throughout transect 4 (Fig. 5A, spectra shown in Fig. S1). The percentage of carbohydrates and peptides in the thaw front were approximately half of any other sample point (13 % in thaw front and 21–35 % in all other samples). The proportional decrease in carbohydrates and peptides correlated with a proportional increase in carboxylic rich alicyclic molecules (CRAM), considered an important product of microbial degradation (Hertkorn et al., 2006), which increased from 41 % in P1 to 60 % the thaw front. Like the FT-ICR MS results, the chemical composition in the thaw front did not persist into the bog. Notably the proportional CRAM content of the bog fell within the range of CRAM percentages in the palsa, and carbohydrate and peptide proportional content increased from thaw front to bog, although to only −75 % of the palsa average. The remaining fractions, materials derived from linear terpenoids (MDLT) and aromatic/phenolic, featured nominal proportional changes across the thaw transition.

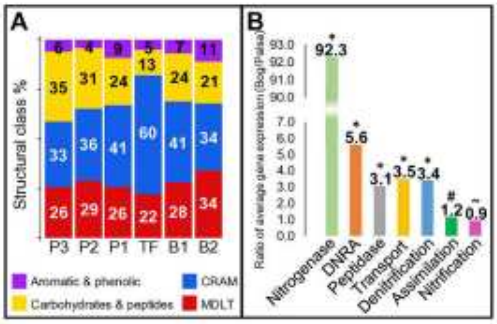

Fig. 5. (A) Relative abundance of general structural classes within porewater samples along the thaw transition determined by ^{1}H NMR. Sample position shown on the x-axis as P1-3 (palsa 1–3), TF (thaw front), B1-2 (bog 1–2). CRAM = carboxyl-rich alicyclic molecules, MDLT = materials derived from linear terpenoids. (B) Fold change in average metatranscriptome expression of microbial nitrogen cycling pathways between palsa (n = 3) and bog (n = 3) cores. The expression of pathways marked with (*) significantly (LIMMA, $p < 0.05$) increased, (#) increased but not significantly (LIMMA, $p > 0.05$), and (−) decreased but not significantly (LIMMA $p > 0.05$) when comparing gene expression in the bog to that in the palsa. Positive y-axis values indicate that the gene featured average greater expression in the bog than the palsa. See SI Data 1 for pathway information and statistics.

3.4. Microbial nitrogen cycling gene expression increased in the bog

To uncover the potential microbial processes contributing to nitrogen cycling in the palsa and bog, we mapped field metatranscriptome reads to a database of Stordalen Mire microbial metagenome assembled genomes (Woodcroft et al., 2018). We then aggregated genes into nitrogen cycling pathways and looked for altered gene expression levels between the palsa and bog (Fig. 5B–Supplementary Data 1). In the anoxic bog, several gene pathways were significantly upregulated (LIMMA, $p < 0.05$) including nitrogenase (*nifDKH*), dissimilatory nitrate reduction to ammonia (DNRA, *nrfA* and *nirBD*), nitrogen transporters, denitrification enzymes (*narGH*, *nirK*, *norB*), and peptidase pathways. Additionally, expression of genes in nitrogen assimilation (*nirA*, *nasA*) were upregulated in the bog but not to a significant extent (LIMMA, $p > 0.05$). Expression of nitrification (*hao*) was the only pathway to have lower expression in the bog than the palsa, but the decrease was not significant (LIMMA, $p > 0.05$).

4. Discussion

4.1. Thaw-induced conversion of DON to inorganic nitrogen

Several modeling studies suggest that the main factor controlling the production of inorganic nitrogen in thawing permafrost is the release of organic nitrogen (Hansen and Elberling, 2023; Ramm et al., 2022; Salmon et al., 2018). This release occurs due to the deepening of the active layer and the subsequent transformation of DON into ammonium (Lacroix et al., 2022; Mao et al., 2020; Ramm et al., 2022). When there is limited ammonium, which is the case for the active layer in most arctic soils, plant and microbial immobilization of nitrogen is dominant (Fiencke et al., 2022; Hansen and Elberling, 2023; Jones and Kielland, 2002; Salmon et al., 2018; Wegner et al., 2022). However, two *in situ* studies of permafrost thaw collapse linked DON release to elevated nitrate concentrations due to the improved drainage and oxic conditions after thaw (Mao et al., 2019; Wegner et al., 2022). Unlike these studies, the soil during and after the thaw front at our site remained saturated and at or below water level. At the thaw front we observed a large pulse of DON and significantly higher levels of ammonium compared to palsa and bog (Fig. 3). Despite the substantial ammonium within the thaw front, there was no significant change in nitrate concentrations across the thaw transition. In the well drained and oxic palsa, the limited nitrate is likely due to the low concentrations of DON and the lack of ammonium, which acts as substrate for nitrification. Conversely, in the thaw front and bog, the high saturation and anoxic conditions were likely the main limiters of nitrification (Fiencke et al., 2022; Kuypers et al., 2018; Olefeldt and Roulet, 2012; Wegner et al., 2022). Therefore, it is likely that the DON released during thaw is primarily mineralized to ammonium and any further nitrification is limited by the anoxic conditions. Our findings align with reported seasonal saturation of thaw slump floors, which observed increased ammonium concentrations and DON without

accumulating nitrate (Fiencke et al., 2022; Wegner et al., 2022). We propose that, confirming our first hypothesis, the high levels of ammonium within the thaw front are likely the result of rapid ammonification of DON.

4.2. Shifting composition of dissolved organic nitrogen at the thaw front

Within the thaw front, both NMR and FT-ICR MS results indicated the lowest proportions of peptide-like and carbohydrate molecules throughout the thaw transition (Figs. 3 and 4), despite a tenfold increase in DON concentration (Fig. 3). FT-ICR MS analysis of nitrogen-containing formulae showed the highest proportions of aromatics/polyphenols and condensed aromatics within the thaw front. NMR analysis of the total DOM pool revealed little change in aromatic and phenolic structures along the thaw transition, but it showed a substantial increase in CRAM structures at the thaw front. This increase likely reflects the overall oxidation and condensation of the DOM pool observed in previous studies (Patzner et al., 2022a), a pattern not captured in the nitrogen-specific FT-ICR MS analysis. The shift toward more condensed, less labile structures in both analyses, coupled with the decrease in peptide-like compounds, suggests active degradation of the nitrogen pool at the thaw front (D'Andrilli et al., 2015; Hertkorn et al., 2006). This interpretation aligns with soil amendment and incubation studies showing preferential mineralization of peptides and amino acids over larger nitrogen-containing organic molecules under conditions with abundant labile organic carbon (e.g., glucose) (Chen et al., 2018; Wild et al., 2013, 2014). Furthermore, arctic plant communities can preferentially uptake amino acids over nitrate, further increasing demand for labile DON (Jones and Kielland, 2002; Kielland, 1994; Schimel and Stuart Chapin, 1996; Wild et al., 2018). High nutrient demand in thaw fronts is expected as they have been identified as points of elevated microbial activity and active organic matter decomposition (Fiencke et al., 2022; Patzner et al., 2022a; Voigt et al., 2020). While we did not directly measure DON transformation, multiple lines of evidence suggest selective degradation is occurring. We observed a simultaneous decrease in labile peptide-like compounds and enrichment of less labile aromatic or cyclic molecules. This selective transformation of the DON pool parallels patterns documented in anoxic marine sediments, where peptides undergo selective deamination and microorganisms preferentially utilize free amino acids for cellular synthesis (Abdulla et al., 2018). The increased microbial activity previously reported at the thaw front (Patzner et al., 2022a; Patzner et al., 2022) would create higher demand for cellular building blocks, driving the observed depletion of available peptides. These findings confirm our second hypothesis and align with previous studies of permafrost nutrient cycling and DOC transformation (AminiTabrizi et al., 2020; Hodgkins et al., 2016; Mao et al., 2019; Ramm et al., 2022; Ward and Cory, 2015; Wild et al., 2014).

4.3. Organic nitrogen consumption at the thaw front leaves the bog nitrogen-limited

Metatranscriptomic data revealed an upregulation of gene expression for enzymes in nitrogen scavenging pathways in the bog (Fig. 5B). These pathways include nitrogen fixation, DNRA (a process often overlooked in permafrost studies) (Ramm et al., 2022), and mineralization via peptidases. Furthermore, in the water-saturated and anoxic bog, denitrification gene expression was significantly higher than in the palsa. Notably, we saw expression of genes encoding nitrate reductase (*narGH*), nitrite reductase (*nirK*), and nitric oxide reductase (*norB*) but not nitrous oxide reductase (*nosZ*), hinting that incomplete denitrification occurred in the bog. This could represent a pathway of nitrogen loss in the bog and N_2O generation, further contributing to nitrogen limitation (Ramm et al., 2022). However, saturated wetlands in the arctic have been found to have negligible N_2O emissions, due to the high water table acting as a diffusion barrier (Voigt et al., 2020). Anaerobic ammonia oxidation and complete ammonia oxidation could be additional pathways of nitrogen loss from the system, yet we did not detect gene expression for either of these processes.

At the thaw front, we observed a substantial increase in total DON concurrent with a reduction in the proportion of peptide-like molecular content. The adjacent bog showed a greater proportional decrease in DON concentration compared to DOC concentration (Fig. 3), indicating either preferential removal of nitrogen-containing molecules from solution or subsequent DOC release. This decrease in the proportion of nitrogen-containing organic matter in the bog corresponds with our metatranscriptomic results showing increased expression of nitrogen scavenging genes, suggesting a microbial response to reduced bioavailable DON.

After the pulse of ammonium at the thaw front, the anoxic conditions in the bog would limit nitrification, an aerobic process, which explains the persistence of low nitrate concentrations from thaw front to bog (Fig. 3). Furthermore, this limited nitrification would in turn limit denitrification by restricting production of nitrate (Fiencke et al., 2022; Voigt et al., 2020; Wegner et al., 2022). The observed decrease in DON, ammonium, and nitrate concentrations between the thaw front and bog suggests that the most labile and bioavailable nitrogen was likely transformed into ammonium and subsequently immobilized through biomass incorporation or removed though denitrification to N_2O (Kuypers et al., 2018; Voigt et al., 2017). However, contrary to our third hypothesis, denitrification increased in the bog despite the restricted nitrate substrate availability. This unexpected finding may reflect either increased denitrification activity or, more likely, upregulation of denitrification pathways as a mediating response to limited nitrate availability - similar to the upregulation of nitrogen scavenging pathways observed more broadly in the bog gene expression (Fig. 5). Although we did not collect metatranscriptome samples from the thaw front, our previous study documented increased activity of iron reducers and methanogens within it (Patzner et al., 2022a). Therefore, we propose the rapid appearance of high ammonium concentrations in this zone suggests similarly elevated nitrogen cycling activity, particularly ammonification. Although porewater and metatranscriptome samples were collected from different locations within Stordalen Mire, the consistent thaw conditions and ecology across sites (Holmes et al., 2022) allow these complementary datasets to inform our understanding of nitrogen transformations across the thaw transition.

4.4. Nitrogen availability is influenced by peptide content during permafrost thaw

Our data reveal an inverse relationship between peptide-like DON and ammonium concentrations along the permafrost thaw transition. At the thaw front, we observe depletion of labile peptide-like DON alongside enrichment of aromatic DON and elevated ammonium levels. In contrast, both the bog and palsa show higher peptide content with limited ammonium (Figs. 3–5). The consistent inverse relationship between peptide content and ammonium levels across sites suggests that peptide availability may act as a control point for nitrogen cycling, with peptide degradation regulating the ammonium pool available for subsequent nitrogen transformations. Although we did not directly measure nitrogen transformations at the thaw front, our metatranscriptomic analysis of the bog revealed increased expression of bioavailable nitrogen scavenging genes. These metatranscriptomic results support the role of microbial communities in driving nitrogen transformations at the thaw front. The relationship between nitrogen and carbon cycling in thawing permafrost remains poorly characterized, though nitrogen availability is expected to influence carbon mineralization and permafrost carbon feedback through both cellular synthesis and DOC mineralization priming (Abdulla et al., 2018; Schuur et al., 2022; Voigt et al., 2020). Based on our findings, we propose that components of Ramm's model (Ramm et al., 2022), particularly the controls on ammonification rates, can be applied to thaw fronts and bogs, with our suggested extensions illustrated in Fig. 6. Future studies directly examining metatranscriptomic activity at the thaw front will be crucial for fully understanding the fate of nitrogen-containing organic matter during permafrost thaw.

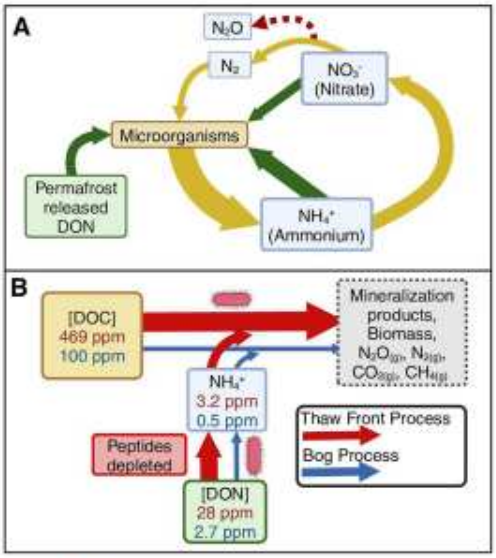

Fig. 6. (A) Modified conceptual model for nitrogen cycling within permafrost soils based on Ramm et al. (2022)(Ramm et al., 2022). Green arrows show uptake processes, yellow arrows show mineral N turnover processes, and red arrows show caseous losses. (B) Adapted model to show palsa vs. thaw front organic matter and nutrient transformation supported by empirical data reported herein. Data shows that high concentrations of organic nitrogen within the thaw front correlate to high ammonium concentrations and reduced peptide content. The production of ammonia can prime the microbial degradation of highly abundant DOC, potentially elevating the production of GHGs and biomass. Arrows are sized to indicate the expected relative amount of the transformation process based on previous GHG emission and nitrogen priming findings (Keuper et al., 2012; Mao et al., 2020; Voigt et al., 2017). Fig. 6(A) is based on Fig. 1 in "A review of the importance of mineral nitrogen …" by Ramm et al. (Ramm et al., 2022) and is licensed under a Creative Commons Attribution 4.0 International License (CC BY 4.0).

4.5. Conclusions

Our results provide some of the first detailed characterization of organic nitrogen dynamics within a permafrost thaw transition, revealing that the composition of organic nitrogen released during thaw significantly impacts nutrient cycling and creates biogeochemical hotspots within the thaw front environment. Notably, permafrost collapse and soil saturation resulted in high ammonium concentrations localized to the thaw front. Among nitrogen-containing molecules, the thaw front exhibited lower fractions of peptide and carbohydrate molecules and a higher fraction of aromatic molecules, aligning with previously reported selective degradation patterns of the total organic matter pool (Patzner et al., 2022a; Ramm et al., 2022; Wild et al., 2014). Nitrogen transformation during and after thaw appeared limited to DON mineralization, with no significant changes in nitrate concentration. However, the upregulation of denitrification under anoxic conditions in the bog suggests microbial metabolism could either contribute to N_2O emissions via incomplete denitrification (nitrate to N_2O) or mitigate N_2O release through complete denitrification (nitrate to N_2) (McGuire; et al., 2018; Mueller et al., 2015; Wegner et al., 2022). The absence of genes encoding N_2O reductase in the bog suggests thaw fronts may serve as previously underrepresented N_2O sources in climate models. Future studies combining metatranscriptome data from the thaw front with N_2O flux measurements would further elucidate nitrogen dynamics and improve our understanding of nitrogen mass balance in these systems. Our findings emphasize that future permafrost peatland studies and GHG models should incorporate thaw transitions due to their rapid and highly localized nitrogen dynamics.

CRediT authorship contribution statement

Merritt N. Logan: Writing – review & editing, Writing – original draft, Methodology, Investigation, Formal analysis, Conceptualization. **Monique S. Patzner:** Writing – review & editing, Methodology, Investigation, Conceptualization. **Jacob P. VanderRoest:** Writing – review & editing, Formal analysis. **Bridget B. McGivern:** Writing – review & editing, Methodology, Investigation, Formal analysis. **Myrna J. Simpson:** Writing – review & editing, Resources, Methodology, Investigation, Formal analysis. **Amy M. McKenna:** Writing – review & editing, Methodology, Investigation, Formal analysis, Conceptualization. **Kelly C. Wrighton:** Writing – review & editing, Methodology, Investigation, Funding acquisition, Formal analysis. **Casey Bryce:** Writing – review & editing, Resources, Project administration, Methodology, Investigation, Funding acquisition, Formal analysis, Conceptualization. **Andreas Kappler:** Writing – review & editing, Writing – original draft, Visualization, Supervision, Resources, Project administration, Methodology, Investigation, Funding acquisition, Formal analysis, Conceptualization. **Thomas Borch:** Writing – review & editing, Writing – original draft, Validation, Supervision, Project administration, Methodology, Investigation, Funding acquisition, Formal analysis, Conceptualization.

Data and code availability

All FT-ICR mass spectral data are publicly available through the Open Science Framework at DOI 10.17605/OSF.IO/TZKWN. R package used to process FT-ICR MS peak lists and produce figures is available at (https://github.com/robertyoung3/MSanalyzeNOM).

Funding sources

FT-ICR MS analyses were performed at the National High Magnetic Field Laboratory, which is supported by National Science Foundation Division of Chemistry and Division of Materials Research through Cooperative Agreement No. DMR-2128556 and the State of Florida. The sampling and field work conducted at the Abisko Scientific Research Station were made possible by The Swedish Polar Research Secretariat and The Swedish Infrastructure for Ecosystem Science (SITES). SITES is supported by the Swedish Research Council's grant 4.3-2021-00164. The authors acknowledge infra-structural support by the Deutsche Forschungsgemeinschaft (DFG, German Research Foundation) under Germany's Excellence Strategy, cluster of Excellence EXC2124, project ID 390838134. This work was supported by the University of Tuebingen (Programme for the Promotion of Junior Researchers award to Casey Bryce) and by the German Academic Scholarship Foundation (scholarship to Monique Patzner). The Natural Sciences and Engineering Research Council (NSERC) of Canada is thanked for their support via a Discovery Grant and the Tier 1 Canada Research Chair in Integrative Molecular Biogeochemistry to Myrna J. Simpson. Bridget B. McGivern and Kelly C. Wrighton were partially supported by awards from the National Science Foundation Biology Integration Institutes Program, Award #2022070, and from the Genomic Science Program of the United States Department of Energy Office of Biological and Environmental Research, award #DE-SC0023456. These funding sources had no role in the study design; collection, analysis and interpretation of data; in the writing of the report; and decision to submit the article for publication. Fig. 6 and graphical abstract were created with BioRender.com.

Declaration of Competing Interest

The authors declare the following financial interests/personal relationships which may be considered as potential competing interests: Andreas Kappler reports financial support was provided by German Research Foundation. Thomas Borch reports equipment, drugs, or supplies was provided by The National High Magnetic Field Laboratory, which is supported by National Science Foundation Division of Chemistry and Division of Materials Research through Cooperative Agreement No. DMR-2128556 and the State of Florida. Myrna Simpson reports financial support was provided by National Research Council Canada. Kelly Wrighton reports financial support was provided by National Science Foundation. If there are other authors, they declare that they have no known competing financial interests or personal relationships that could have appeared to influence the work reported in this paper.

Acknowledgements

We are especially grateful for the assistance of Jennie Wikström, Eric Lundin, Niklas Rakos, and Alexander Meire at the Abisko Scientific Research Station during the field campaign. We thank Eva Voggenreiter for her assistance collecting and analyzing porewater for DON concentrations after the completion of our campaign.

Appendix A. Supplementary data

Supplementary data to this article can be found online at https://doi.org/10.1016/j.seh.2025.100148.

References

Abbott, B.W., Jones, J.B., 2015. Permafrost collapse alters soil carbon stocks, respiration, CH4, and N2O in upland tundra. Glob. Change Biol. 21 (12), 4570–4587. https://doi.org/10.1111/gcb.13069.

Abbott, B.W., Brown, M., Carey, J.C., Ernakovich, J., Frederick, J.M., Guo, L., et al., 2022. We must stop fossil fuel emissions to protect permafrost ecosystems. Front. Environ. Sci. 10 (June), 1–13. https://doi.org/10.3389/fenvs.2022.899428.

Abdulla, H.A., Burdige, D.J., Komada, T., 2018. Accumulation of deaminated peptides in anoxic sediments of Santa Barbara Basin. Geochem. Cosmochim. Acta 223, 245–258. https://doi.org/10.1016/j.gca.2017.11.021.

AMAP, 2021. Arctic climate change update 2021: Key Trends and Impacts. Summary for Policy-makers. Arctic Monitoring and Assessment Programme (AMAP), Tromsø, Norway, p. 16.

AminiTabrizi, R., Wilson, R.M., Fudyma, J.D., Hodgkins, S.B., Heyman, H.M., Rich, V.I., et al., 2020. Controls on soil organic matter degradation and subsequent greenhouse gas emissions across a permafrost thaw gradient in northern Sweden. Front. Earth Sci. 8 (September). https://doi.org/10.3389/feart.2020.557961.

Bäckstrand, K., Crill, P.M., Jackowicz-Korczyński, M., Mastepanov, M., Christensen, T.R., Bastviken, D., 2010. Annual carbon gas budget for a subarctic peatland, Northern Sweden. Biogeosciences 7 (1), 95–108. https://doi.org/10.5194/bg-7-95-2010.

Bäckstrand, Kristina, Crill, P.M., Mastepanov, M., Christensen, T.R., Bastviken, D., 2008. Non-methane volatile organic compound flux from a subarctic mire in Northern Sweden. Tellus Ser. B Chem. Phys. Meteorol. 60 B (2), 226–237. https://doi.org/10.1111/j.1600-0889.2007.00331.x.

Bahureksa, W., Tfaily, M.M., Boiteau, R.M., Young, R.B., Logan, M.N., McKenna, A.M., Borch, T., 2021. Soil organic matter characterization by fourier transform ion cyclotron resonance mass spectrometry (fticr MS): a critical review of sample preparation, analysis, and data interpretation. Environ. Sci. Technol. 55 (14), 9637–9656. https://doi.org/10.1021/acs.est.1c01135.

Bahureksa, W., Borch, T., Young, R.B., Weisbrod, C., Blakney, G.T., McKenna, A.M., 2022. Improved dynamic range, resolving power, and sensitivity achievable with FT-ICR mass spectrometry at 21 T reveals the hidden complexity of natural organic matter. Anal. Chem. 94 (32), 11382–11389. https://doi.org/10.1021/acs.analchem.2c01377.

Batjes, N.H., 1996. Total carbon and nitrogen in the soils of the world. Eur. J. Soil Sci. 47, 151–163. https://doi.org/10.1111/j.1365-2389.1996.tb01386.x.

Bockheim, J.G., Munroe, J.S., 2014. Organic carbon pools and genesis of alpine soils with permafrost: a review. Arctic Antarct. Alpine Res. 46 (4), 987–1006. https://doi.org/10.1657/1938-4246-46.4.987.

Burke, E., Chadburn, S., Huntingford, C., 2022. Thawing permafrost as a nitrogen fertiliser: implications for climate feedbacks. Nitrogen 3 (2), 353–375. https://doi.org/10.3390/nitrogen3020023.

Butterbach-Bahl, K., Baggs, E.M., Dannenmann, M., Kiese, R., Zechmeister-Boltenstern, S., 2013. Nitrous oxide emissions from soils: how well do we understand the processes and their controls? Phil. Trans. Biol. Sci. 368 (1621). https://doi.org/10.1098/rstb.2013.0122.

Chen, H., Yang, Z., Chu, R.K., Tolić, N., Liang, L., Graham, D.E., et al., 2018. Molecular insights into arctic soil organic matter degradation under warming. Environ. Sci. Technol. 52, 4555–4564. https://doi.org/10.1021/acs.est.7b05469.

Cooper, M.D.A., Estop-Aragonés, C., Fisher, J.P., Thierry, A., Garnett, M.H., Charman, D.J., et al., 2017. Limited contribution of permafrost carbon to methane release from thawing peatlands. Nat. Clim. Change 7 (7), 507–511. https://doi.org/10.1038/nclimate3328.

D'Andrilli, J., Cooper, W.T., Foreman, C.M., Marshall, A.G., 2015. An ultrahigh-resolution mass spectrometry index to estimate natural organic matter lability. Rapid Commun. Mass Spectrom. 29 (24), 2385–2401. https://doi.org/10.1002/rcm.7400.

Dittmar, T., Koch, B., Hertkorn, N., Kattner, G., 2008. A simple and efficient method for the solid-phase extraction of dissolved organic matter (SPE-DOM) from seawater. Limnol Oceanogr. Methods 6 (6), 230–235. https://doi.org/10.4319/lom.2008.6.230.

Elder, C.D., Thompson, D.R., Thorpe, A.K., Chandanpurkar, H.A., Hanke, P.J., Hasson, N., et al., 2021. Characterizing methane emission hotspots from thawing permafrost. Glob. Biogeochem. Cycles 35 (12), 1–22. https://doi.org/10.1029/2020GB006922.

Ellenbogen, J.B., Borton, M.A., McGivern, B.B., Cronin, D.R., Hoyt, D.W., Freire-Zapata, V., et al., 2023. Methylotrophy in the Mire: direct and indirect routes for methane production in thawing permafrost. mSystems 9 (1). https://doi.org/10.1128/msystems.00698-23.

Fiencke, C., Marushchak, M.E., Sanders, T., Wegner, R., Beer, C., 2022. Microbiogeochemical traits to identify nitrogen hotspots in permafrost regions. Nitrogen 3 (3), 458–501. https://doi.org/10.3390/nitrogen3030031.

Fofana, A., Anderson, D., McCalley, C.K., Hodgkins, S., Wilson, R.M., Cronin, D., et al., 2022. Mapping substrate use across a permafrost thaw gradient. Soil Biol. Biochem. 175 (August), 108809. https://doi.org/10.1016/j.soilbio.2022.108809.

Grosse, G., Goetz, S., McGuire, A.D., Romanovsky, V.E., Schuur, E.A.G., 2016. Changing permafrost in a warming world and feedbacks to the Earth system. Environ. Res. Lett. 11 (4). https://doi.org/10.1088/1748-9326/11/4/040201.

Hansen, H.F.E., Elberling, B., 2023. Spatial distribution of bioavailable inorganic nitrogen from thawing permafrost. Glob. Biogeochem. Cycles 37 (2), 1–12. https://doi.org/10.1029/2022GB007589.

Harden, J.W., Koven, C.D., Ping, C.L., Hugelius, G., David McGuire, A., Camill, P., et al., 2012. Field information links permafrost carbon to physical vulnerabilities of thawing. Geophys. Res. Lett. 39 (15), 1–6. https://doi.org/10.1029/2012GL051958.

Harms, T.K., Jones, J.B., 2012. Thaw depth determines reaction and transport of inorganic nitrogen in valley bottom permafrost soils. Glob. Change Biol. 18 (9), 2958–2968. https://doi.org/10.1111/j.1365-2486.2012.02731.x.

Harris, S.A., French, H.M., Heginbottom, J.A., Johnston, G.H., Ladanyi, B., Sego, D.C., Everdingen, R.O., 1988. Glossary of Permafrost and Related Ground-Ice Terms Harris. Technical Memorandum (National Research Council of Canada. Associate Committee on Geotechnical Research). https://doi.org/10.4224/20386561.

Hawkes, J.A., Kew, W., 2020. High-resolution Mass Spectrometry Strategies for the Investigation of Dissolved Organic Matter. Multidimensional Analytical Techniques in Environmental Research. Elsevier Inc. https://doi.org/10.1016/b978-0-12-818896-5.00004-1.

Hendrickson, C.L., Quinn, J.P., Kaiser, N.K., Smith, D.F., Blakney, G.T., Chen, T., et al., 2015. 21 Tesla fourier transform ion cyclotron resonance mass spectrometer: a national resource for ultrahigh resolution mass analysis. J. Am. Soc. Mass Spectrom. 26 (9), 1626–1632. https://doi.org/10.1007/s13361-015-1182-2.

Hertkorn, N., Benner, R., Frommberger, M., Schmitt-kopplin, P., Witt, M., Kaiser, K., et al., 2006. Characterization of a Major Refractory Component of Marine Dissolved Organic Matter, vol. 70, pp. 2990–3010. https://doi.org/10.1016/j.gca.2006.03.021.

Hodgkins, S.B., Tfaily, M.M., McCalley, C.K., Logan, T.A., Crill, P.M., Saleska, S.R., et al., 2014. Changes in peat chemistry associated with permafrost thaw increase greenhouse gas production. Proc. Natl. Acad. Sci. USA 111 (16), 5819–5824. https://doi.org/10.1073/pnas.1314641111.

Hodgkins, Suzanne B., Tfaily, M.M., Podgorski, D.C., McCalley, C.K., Saleska, S.R., Crill, P.M., et al., 2016. Elemental composition and optical properties reveal changes in dissolved organic matter along a permafrost thaw chronosequence in a subarctic peatland. Geochem. Cosmochim. Acta 187, 123–140. https://doi.org/10.1016/j.gca.2016.05.015.

Holmes, M.E., Crill, P.M., Burnett, W.C., McCalley, C.K., Wilson, R.M., Frolking, S., et al., 2022. Carbon accumulation, flux, and fate in stordalen mire, a permafrost peatland in transition. Glob. Biogeochem. Cycles 36 (1). https://doi.org/10.1029/2021gb007113.

Hugelius, G., Strauss, J., Zubrzycki, S., Harden, J.W., Schuur, E.A.G., Ping, C.L., et al., 2014. Estimated stocks of circumpolar permafrost carbon with quantified uncertainty ranges and identified data gaps. Biogeosciences 11 (23), 6573–6593. https://doi.org/10.5194/bg-11-6573-2014.

Hugelius, Gustaf, Loisel, J., Chadburn, S., Jackson, R.B., Jones, M., MacDonald, G., et al., 2020. Large stocks of peatland carbon and nitrogen are vulnerable to permafrost thaw. Proc. Natl. Acad. Sci. U. S. A 117 (34), 20438–20446. https://doi.org/10.1073/pnas.1916387117.

Johansson, T., Malmer, N., Crill, P.M., Friborg, T., Åkerman, J.H., Mastepanov, M., Christensen, T.R., 2006. Decadal vegetation changes in a northern peatland, greenhouse gas fluxes and net radiative forcing. Glob. Change Biol. 12 (12), 2352–2369. https://doi.org/10.1111/j.1365-2486.2006.01267.x.

Jones, D.L., Kielland, K., 2002. Soil amino acid turnover dominates the nitrogen flux in permafrost-dominated taiga forest soils. Soil Biol. Biochem. 34 (2), 209–219. https://doi.org/10.1016/S0038-0717(01)00175-4.

Jorgenson, M.T., Racine, C.H., Walters, J.C., Osterkamp, T.E., 2001. Permafrost degradation and ecological changes associated with a warming climate in central Alaska. Clim. Change 48 (4), 551–579. https://doi.org/10.1023/A:1005667424292.

Keuper, F., van Bodegom, P.M., Dorrepaal, E., Weedon, J.T., van Hal, J., van Logtestijn, R.S.P., Aerts, R., 2012. A frozen feast: thawing permafrost increases plant-available nitrogen in subarctic peatlands. Glob. Change Biol. 18 (6), 1998–2007. https://doi.org/10.1111/j.1365-2486.2012.02663.x.

Kielland, K., 1994. Amino acid absorption by Arctic plants: implications for plant nutrition and nitrogen cycling. Ecology 75, 2373–2383. https://doi.org/10.2307/1940891.

Kim, S., Kim, D., Jung, M.J., Kim, S., 2022. Analysis of environmental organic matters by Ultrahigh-Resolution mass spectrometry—a review on the development of analytical methods. Mass Spectrom. Rev. 41 (2), 352–369. https://doi.org/10.1002/mas.21684.

Knoblauch, C., Beer, C., Liebner, S., Grigoriev, M.N., Pfeiffer, E., 2018. Methane production as key to the greenhouse gas budget of thawing permafrost. Nat. Clim. Change 8, 309–312. https://doi.org/10.1038/s41558-018-0095-z.

Koch, J.C., Ewing, S.A., Striegl, R., McKnight, D.M., 2013. Rapid runoff via shallow throughflow and deeper preferential flow in a boreal catchment underlain by frozen silt (Alaska, USA). Hydrogeol. J. 21 (1), 93–106. https://doi.org/10.1007/s10040-012-0934-3.

Kuypers, M.M.M., Marchant, H.K., Kartal, B., 2018. The microbial nitrogen-cycling network. Nat. Rev. Microbiol. 16 (5), 263–276. https://doi.org/10.1038/nrmicro.2018.9.

Lacroix, F., Zaehle, S., Caldararu, S., Schaller, J., Stimmler, P., Holl, D., et al., 2022. Mismatch of N release from the permafrost and vegetative uptake opens pathways of increasing nitrous oxide emissions in the high Arctic. Glob. Change Biol. 28 (20), 5973–5990. https://doi.org/10.1111/gcb.16345.

Lakomiec, P., Holst, J., Friborg, T., Crill, P., Rakos, N., Kljun, N., et al., 2021. Field-scale CH4 emission at a subarctic mire with heterogeneous permafrost thaw status. Biogeosciences 18 (20), 5811–5830. https://doi.org/10.5194/bg-18-5811-2021.

Li, Y., Harir, M., Lucio, M., Kanawati, B., Smirnov, K., Flerus, R., et al., 2016. Proposed guidelines for solid phase extraction of suwannee river dissolved organic matter. Anal. Chem. 88 (13), 6680–6688. https://doi.org/10.1021/acs.analchem.5b04501.

MacDonald, E.N., Tank, S.E., Kokelj, S.V., Froese, D.G., Hutchins, R.H.S., 2021. Permafrost-derived dissolved organic matter composition varies across permafrost end-members in the western Canadian Arctic. Environ. Res. Lett. 16 (2). https://doi.org/10.1088/1748-9326/abd971.

Malmer, N., Johansson, T., Olsrud, M., Christensen, T.R., 2005. Vegetation, climatic changes and net carbon sequestration in a North-Scandinavian subarctic mire over 30 years. Glob. Change Biol. 11 (11), 1895–1909. https://doi.org/10.1111/j.1365-2486.2005.01042.x.

Mann, B.F., Chen, H., Herndon, E.M., Chu, R.K., Tolic, N., Portier, E.F., et al., 2015. Indexing permafrost soil organic matter degradation using high-resolution mass spectrometry. PLoS One 10 (6), 1–16. https://doi.org/10.1371/journal.pone.0130557.

Mao, C., Kou, D., Wang, G., Peng, Y., Yang, G., Liu, F., et al., 2019. Trajectory of topsoil nitrogen transformations along a thermo-erosion gully on the Tibetan plateau. J. Geophys. Res.: Biogeosciences 124 (5), 1342–1354. https://doi.org/10.1029/2018JG004805.

Mao, C., Kou, D., Chen, L., Qin, S., Zhang, D., Peng, Y., Yang, Y., 2020. Permafrost nitrogen status and its determinants on the Tibetan Plateau. Glob. Change Biol. 26 (9), 5290–5302. https://doi.org/10.1111/gcb.15205.

Marushchak, M.E., Kerttula, J., Diáková, K., Faguet, A., Gil, J., Grosse, G., et al., 2021. Thawing Yedoma permafrost is a neglected nitrous oxide source. Nat. Commun. 12 (1). https://doi.org/10.1038/s41467-021-27386-2.

McGuire, A.D., Lawrence, D.M., Koven, C., Clein, J.S., Burke, E., Chen, G., et al., 2018. Dependence of the evolution of carbon dynamics in the northern permafrost region on the trajectory of climate change. Proc. Natl. Acad. Sci. USA 115 (15), 3882–3887. https://doi.org/10.1073/pnas.1719903115, 2.

Mishra, U., Drewniak, B., Jastrow, J.D., Matamala, R.M., Vitharana, U.W.A., 2017. Spatial representation of organic carbon and active-layer thickness of high latitude soils in CMIP5 earth system models. Geoderma 300, 55–63. https://doi.org/10.1016/j.geoderma.2016.04.017.

Mitchell, P.J., Simpson, A.J., Soong, R., Simpson, M.J., 2018. Nuclear magnetic resonance analysis of changes in dissolved organic matter composition with successive layering on clay mineral surfaces. Soil Systems 2 (1), 1–17. https://doi.org/10.3390/soils2010008.

Moore, M.R.N., Tank, S.E., Kurek, M.R., Taskovic, M., McKenna, A.M., Smith, J.L.J., et al., 2023. Ultrahigh resolution dissolved organic matter characterization reveals distinct permafrost characteristics on the Peel Plateau, Canada. Biogeochemistry (123456789). https://doi.org/10.1007/s10533-023-01101-3.

Mueller, C.W., Rethemeyer, J., Kao-Kniffin, J., Löppmann, S., Hinkel, K.M., Bockheim, J.G., 2015. Large amounts of labile organic carbon in permafrost soils of northern Alaska. Glob. Change Biol. 21 (7), 2804–2817. https://doi.org/10.1111/gcb.12876.

Nebbioso, A., Piccolo, A., 2013. Molecular characterization of dissolved organic matter (DOM): a critical review. Anal. Bioanal. Chem. 405 (1), 109–124. https://doi.org/10.1007/s00216-012-6363-2.

Norby, R.J., Sloan, V.L., Iversen, C.M., Childs, J., 2019. Controls on fine-scale spatial and temporal variability of plant-available inorganic nitrogen in a polygonal tundra landscape. Ecosystems 22, 528–543. https://doi.org/10.1007/s10021-018-0285-6.

Obu, J., 2021. How much of the earth's surface is underlain by permafrost? J. Geophys. Res.: Earth Surf. 126 (5), 1–5. https://doi.org/10.1029/2021JF006123.

Olefeldt, D., Roulet, N.T., 2012. Effects of permafrost and hydrology on the composition and transport of dissolved organic carbon in a subarctic peatland complex. J. Geophys. Res.: Biogeosciences 117 (1), 1–15. https://doi.org/10.1029/2011JG001819.

Olefeldt, D., Roulet, N.T., Bergeron, O., Crill, P., Bäckstrand, K., Christensen, T.R., 2012. Net carbon accumulation of a high-latitude permafrost palsa mire similar to permafrost-free peatlands. Geophys. Res. Lett. 39 (3). https://doi.org/10.1029/2011GL050355.

Olm, M.R., Brown, C.T., Brooks, B., Banfield, J.F., 2017. DRep: a tool for fast and accurate genomic comparisons that enables improved genome recovery from metagenomes through de-replication. ISME J. 11 (12). https://doi.org/10.1038/ismej.2017.126.

Patzner, M., Logan, M., McKenna, A., Young, R., Zhou, Z., Joss, H., et al., 2022a. Microbial iron cycling during palsa hillslope collapse promotes greenhouse gas emissions before complete permafrost thaw. Communications Earth and Environment 3 (76). https://doi.org/10.1038/s43247-022-00407-8.

Patzner, M.S., Mueller, C.W., Malusova, M., Baur, M., Nikeleit, V., Scholten, T., et al., 2020. Iron mineral dissolution releases iron and associated organic carbon during permafrost thaw. Nat. Commun. 11 (1), 1–39. https://doi.org/10.1038/s41467-020-20102-6.

Patzner, M.S., Kainz, N., Lundin, E., Barczok, M., Smith, C., Herndon, E., et al., 2022. Seasonal fluctuations in iron cycling in thawing permafrost peatlands. Environ. Sci. Technol. https://doi.org/10.1021/acs.est.1c06937.

Payandi-Rolland, D., Shirokova, L.S., Labonne, F., Bénézeth, P., Pokrovsky, O.S., 2021. Impact of freeze-thaw cycles on organic carbon and metals in waters of permafrost peatlands. Chemosphere 279. https://doi.org/10.1016/j.chemosphere.2021.130510.

Poulin, B.A., Ryan, J.N., Nagy, K.L., Stubbins, A., Dittmar, T., Orem, W., et al., 2017. Spatial dependence of reduced sulfur in everglades dissolved organic matter controlled by sulfate enrichment. Environ. Sci. Technol. 51 (7), 3630–3639. https://doi.org/10.1021/acs.est.6b04142.

Ramm, E., Liu, C., Ambus, P., Butterbach-Bahl, K., Hu, B., Martikainen, P.J., et al., 2022. A review of the importance of mineral nitrogen cycling in the plant-soil-microbe system of permafrost-affected soils—changing the paradigm. Environ. Res. Lett. 17 (1), 013004. https://doi.org/10.1088/1748-9326/ac417e.

Rosswall, T., Granhall, U., 1980. Nitrogen cycling in a subarctic ombrotrophic mire. Ecol. Bull. (30), 63–95.

Rosswall, T., Flower-Ellis, J.G.K., Johansson, L.G., Jonsson, S., Rydén, B.E., Sonesson, M., 1975. Stordalen (abisko), Sweden. Ecol. Bull. (20), 265–294. Retrieved from. https://www.jstor.org/stable/45331782.

Salmon, V.G., Schädel, C., Bracho, R., Pegoraro, E., Celis, G., Mauritz, M., et al., 2018. Adding depth to our understanding of nitrogen dynamics in permafrost soils. J. Geophys. Res.: Biogeosciences 123 (8), 2497–2512. https://doi.org/10.1029/2018JG004518.

Schädel, C., Schuur, E.A.G., Bracho, R., Elberling, B., Knoblauch, C., Lee, H., et al., 2014. Circumpolar assessment of permafrost C quality and its vulnerability over time using long-term incubation data. Glob. Change Biol. https://doi.org/10.1111/gcb.12417.

Schaefer, K., Lantuit, H., Romanovsky, V.E., Schuur, E.A.G., Witt, R., 2014. The impact of the permafrost carbon feedback on global climate. Environ. Res. Lett. 9. https://doi.org/10.1088/1748-9326/9/8/085003.

Schimel, J.P., Stuart Chapin, F., 1996. Tundra plant uptake of amino acid and NH4+ nitrogen in situ: plants compete well for amino acid N. Ecology 77 (7), 2142–2147. https://doi.org/10.2307/2265708.

Schuur, E.A.G., Abbott, B.W., Bowden, W.B., Brovkin, V., Camill, P., Canadell, J.G., et al., 2013. Expert assessment of vulnerability of permafrost carbon to climate change. Clim. Change 119 (2), 359–374. https://doi.org/10.1007/s10584-013-0730-7.

Schuur, E.A.G., McGuire, A.D., Schädel, C., Grosse, G., Harden, J.W., Hayes, D.J., et al., 2015. Climate change and the permafrost carbon feedback. Nature 520 (7546), 171–179. https://doi.org/10.1038/nature14338.

Schuur, Edward A.G., Crummer, K.G., Vogel, J.G., MacK, M.C., 2007. Plant species composition and productivity following permafrost thaw and thermokarst in Alaskan tundra. Ecosystems 10 (2), 280–292. https://doi.org/10.1007/s10021-007-9024-0.

Schuur, Edward A.G., Abbott, B.W., Commane, R., Ernakovich, J., Euskirchen, E., Hugelius, G., et al., 2022. Permafrost and climate change: carbon cycle feedbacks from the warming arctic. Annu. Rev. Environ. Resour. 47, 343–371. https://doi.org/10.1146/annurev-environ-012220-011847.

Shaffer, M., Borton, M.A., McGivern, B.B., Zayed, A.A., La Rosa, S.L., Solden, L.M., et al., 2020. DRAM for distilling microbial metabolism to automate the curation of microbiome function. Nucleic Acids Res. 48 (16). https://doi.org/10.1093/nar/gkaa621.

Sleighter, R.L., Hatcher, P.G., 2007. The application of electrospray ionization coupled to ultrahigh resolution mass spectrometry for the molecular characterization of natural organic matter. J. Mass Spectrom. 42 (5), 559–574. https://doi.org/10.1002/jms.1221.

Smith, D.F., Podgorski, D.C., Rodgers, R.P., Blakney, G.T., Hendrickson, C.L., 2018. 21 Tesla FT-ICR mass spectrometer for ultrahigh-resolution analysis of complex organic Mixtures. Anal. Chem. 90 (3), 2041–2047. https://doi.org/10.1021/acs.analchem.7b04159.

Stookey, L.L., 1970. Ferrozine-A New Spectrophotometric Reagent for Iron, vol. 42, pp. 779–781. https://doi.org/10.1021/ac60289a016.

Stricheli, P.E., Niggemann, J., Schubert, C.J., 2018. Comparison of different solid phase extraction sorbents for the qualitative assessment of dissolved organic nitrogen in freshwater samples using FT-ICR-MS. J. Limnol. 77 (3), 400–411. https://doi.org/10.4081/jlimnol.2018.1791.

Textor, S.R., Wickland, K.P., Podgorski, D.C., Johnston, S.E., Spencer, R.G.M., 2019. Dissolved organic carbon turnover in permafrost-influenced watersheds of interior Alaska: molecular insights and the priming effect. Front. Earth Sci. 7 (October), 1–17. https://doi.org/10.3389/feart.2019.00275.

Tong, H., Simpson, A.J., Paul, E.A., Simpson, M.J., 2021. Land-use change and environmental properties alter the quantity and molecular composition of soil-derived dissolved organic matter. ACS Earth Space Chem. 5 (6), 1395–1406. https://doi.org/10.1021/acsearthspacechem.1c00033.

Treat, C.C., Wollheim, W.M., Varner, R.K., Bowden, W.B., 2016. Longer thaw seasons increase nitrogen availability for leaching during fall in tundra soils. Environ. Res. Lett. 11 (6). https://doi.org/10.1088/1748-9326/11/6/064013.

Varner, R.K., Crill, P.M., Frolking, S., McCalley, C.K., Burke, S.A., Chanton, J.P., et al., 2022. Permafrost thaw driven changes in hydrology and vegetation cover increase trace gas emissions and climate forcing in Stordalen Mire from 1970 to 2014. Phil. Trans. Math. Phys. Eng. Sci. 380 (2215). https://doi.org/10.1098/rsta.2021.0022.

Voigt, C., Marushchak, M.E., Lamprecht, R.E., Jackowicz-Korczyński, M., Lindgren, A., Mastepanov, M., et al., 2017. Increased nitrous oxide emissions from Arctic peatlands after permafrost thaw. Proc. Natl. Acad. Sci. U. S. A 114 (24), 6238–6243. https://doi.org/10.1073/pnas.1702902114.

Voigt, C., Marushchak, M.E., Abbott, B.W., Biasi, C., Elberling, B., Siciliano, S.D., et al., 2020. Nitrous oxide emissions from permafrost-affected soils. Nat. Rev. Earth Environ. 1 (8), 420–434. https://doi.org/10.1038/s43017-020-0063-9.

Walker, D.A., Raynolds, M.K., Daniels, F.J.A., Einarsson, E., Elvebakk, A., Gould, W.A., et al., 2005. The circumpolar Arctic vegetation map. J. Veg. Sci. 16, 267–282. https://doi.org/10.1111/j.1654-1103.2005.tb02365.x.

Ward, C.P., Cory, R.M., 2015. Chemical composition of dissolved organic matter draining permafrost soils. Geochem. Cosmochim. Acta 167, 63–79. https://doi.org/10.1016/j.gca.2015.07.001.

Wegner, R., Fiencke, C., Knoblauch, C., Sauerland, L., Beer, C., 2022. Rapid permafrost thaw removes nitrogen limitation and rises the potential for N2O emissions. Nitrogen 3 (4), 608–627. https://doi.org/10.3390/nitrogen3040040.

Wild, B., Schnecker, J., Capek, P., Guggenberger, G., Hofhansl, F., Kaiser, C., et al., 2013. Nitrogen dynamics in turbic cryosols from siberia and Greenland c. Soil Biol. Biochem. 67, 85–93. https://doi.org/10.1016/j.soilbio.2013.08.004.

Wild, B., Schnecker, J., Alves, R.J.E., Barsukov, P., Bárta, J., Čapek, P., et al., 2014. Input of easily available organic C and N stimulates microbial decomposition of soil organic matter in arctic permafrost soil. Soil Biol. Biochem. https://doi.org/10.1016/j.soilbio.2014.04.014.

Wild, B., Alves, R.J.E., Bárta, J., Čapek, P., Gentsch, N., Guggenberger, G., et al., 2018. Amino acid production exceeds plant nitrogen demand in Siberian tundra. Environ. Res. Lett. 13 (3). https://doi.org/10.1088/1748-9326/aaa4fa.

Wilson, R.M., Hopple, A.M., Tfaily, M.M., Sebestyen, S.D., Schadt, C.W., Pfeifer-Meister, L., et al., 2016. Stability of peatland carbon to rising temperatures. Nat. Commun. 7, 13723. https://doi.org/10.1038/ncomms13723.

Wilson, Rachel M., Hough, M.A., Verbeke, B.A., Hodgkins, S.B., Chanton, J.P., Saleska, S.D., et al., 2022. Plant organic matter inputs exert a strong control on soil organic matter decomposition in a thawing permafrost peatland. Sci. Total Environ. 820, 152757. https://doi.org/10.1016/j.scitotenv.2021.152757.

Woodcroft, B.J., Singleton, C.M., Boyd, J.A., Evans, P.N., Emerson, J.B., Zayed, A.A.F., et al., 2018. Genome-centric view of carbon processing in thawing permafrost. Nature 560 (7716), 49–54. https://doi.org/10.1038/s41586-018-0338-1.

Woods, G., Simpson, A., 2011. HILIC-NMR: toward the identification of individual molecular components in dissolved organic matter. Environ. Sci. Technol. 45 (13), 5910. https://doi.org/10.1021/es201716u.

Zark, M., Dittmar, T., 2018. Universal molecular structures in natural dissolved organic matter. Nat. Commun. 9 (1), 1–8. https://doi.org/10.1038/s41467-018-05665-9.

Zhang, T., Barry, R.G., Knowles, K., Heginbottom, J.A., Brown, J., 2008. Statistics and characteristics of permafros and ground-ice distribution in the Northen Hemisphere. Polar Geogr. 23 (2), 132–154. https://doi.org/10.1080/10889370802175895.

Zherebker, A., Podgorski, D.C., Kholodov, V.A., Orlov, A.A., Yaroslavtseva, N.V., Kharybin, O., et al., 2019. The molecular composition of humic substances isolated from yedoma permafrost and alas cores in the eastern siberian arctic as measured by ultrahigh resolution mass spectrometry. J. Geophys. Res.: Biogeosciences. https://doi.org/10.1029/2018jg004743.

Supporting Information

Role of permafrost thaw transitions in biogeochemical nitrogen cycling

Merritt N. Logan[1], Monique S. Patzner[2], Jacob P. VanderRoest[1], Bridget B. McGivern[1], Nivetha Srikanthan[3], Myrna J. Simpson[3], Amy M. McKenna[1,5], Kelly C. Wrighton[1], Casey Bryce[4], Andreas Kappler[2,6], and Thomas Borch[1]*

Affiliations:

[1]Department of Soil & Crop Sciences and Department of Chemistry, Colorado State University, 307 University Ave, Fort Collins, CO 80523-1170, USA.

[2]Geomicrobiology, Department of Geosciences, University of Tuebingen, Schnarrenbergstrasse 94-96, 72076 Tuebingen, Germany.

[3]Environmental NMR Centre and Department of Physical & Environmental Sciences, University of Toronto Scarborough, Toronto, Ontario, Canada, M1C 1A4.

[4] School of Earth Sciences, University of Bristol, Bristol, BS8 1RL, UK.

[5]Ion Cyclotron Resonance Facility, National High Magnetic Field Laboratory, Florida State University, Tallahassee, FL 32310-4005, USA

[6]Cluster of Excellence EXC 2124: Controlling Microbes to Fight Infections, Tübingen, Germany

*Corresponding author email: thomas.borch@colostate.edu

Supporting Information includes 1 Figure, 2 Sections, 5 Tables, and 13 Pages

Contents

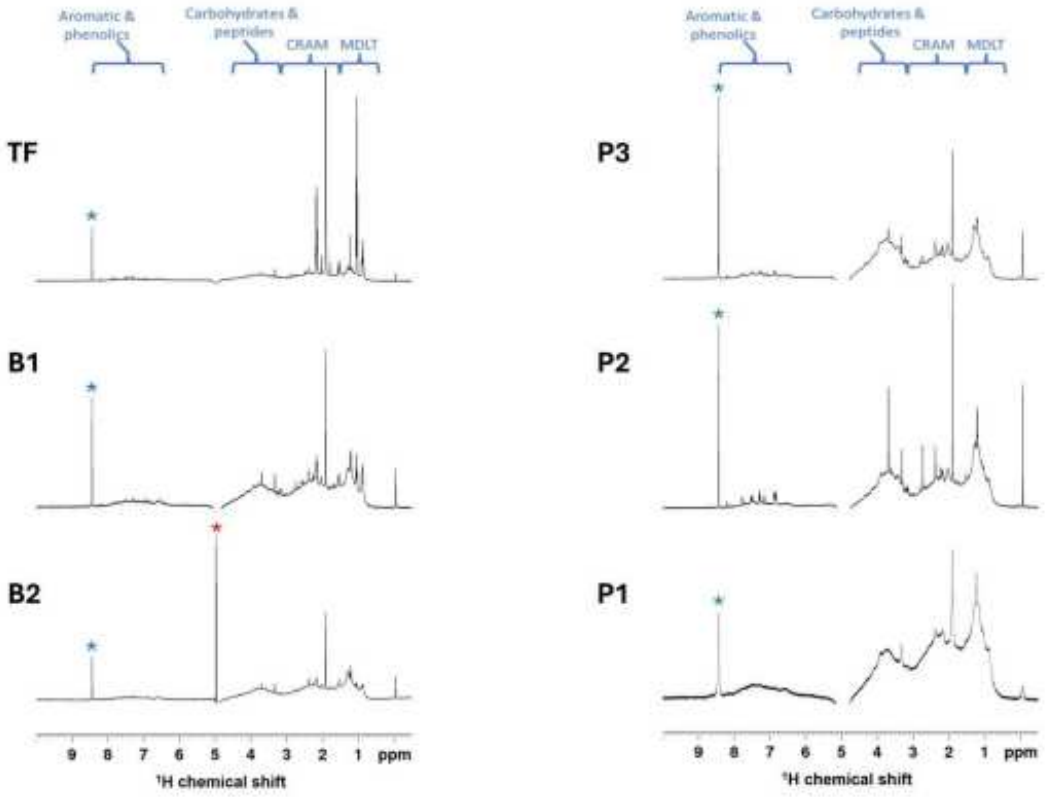

1. Figure S1. Solution state ^{1}H NMR spectra of dissolved organic matter samples

Samples are labeled as TF (thaw front), B1-2 (bog 1-2), P1-3 (palsa 1-3). All samples are from transect 4. Carboxyl-rich alicyclic molecules (CRAM) region also includes acetic acid (~1.90 ppm) and residual water is marked with a red asterisk and formic acid (~8.44 ppm) is marked with a blue asterisk. The palsa and bog samples exhibited higher proportions of carbohydrates and peptides compared to the thaw front. In contrast, the thaw front was characterized by a lower proportion of carbohydrates and peptides and a higher proportion of CRAM. Chemical shift integration regions and assignments are based on Woods, 2011(Woods & Simpson, 2011).

2. Section 1. Metatranscriptome library and read assignments

Metatranscriptome libraries were prepared for the six palsa and bog samples using the QIAseq FastSelect −5S/16S/23S (Qiagen) kit following the kit protocol with the following modifications: addition of probes for plant and yeast and using one-third the probe volumes. Then, the TruSeq Stranded Library Preparation kit (Illumina) was used to prepare the sequencing library. Libraries were sequenced on an Illumina NovaSeq 6000 system at the Genomics Core at the University of Colorado Anschutz Medical Campus.

Raw metatranscriptome reads were quality trimmed and adapters removed using bbduk(Bushnell, n.d.) with the following flags: k=23 mink=11 hdist=1 qtrim=rl trimq=20 minlength=75. Reads were filtered with rqcfilter2(Bushnell, n.d.) using the following flags: jni=t rna=t trimfragadapter=t qtrim=r trimq=0 maxns=1 maq=10 minlen=51 mlf=0.33 phix=t removeribo=t removehuman=t removedog=t removecat=t removemouse=t khist=t removemicrobes=t mtst=t sketch kapa=t clumpify=t tmpdir=null barcodefilter=f trimpolyg=5. Filtered and trimmed reads were mapped against the 99% dereplicated MAGs using bowtie2(Langmead & Salzberg, 2012) (v2.4.5) using the following settings: (-D 10 -R 2 -N 1 -L 22 -i S,0,2.50). The output SAM file was converted to BAM using samtools(Li et al., 2009) (v1.9), and filtered using the reformat.sh script in the bbtools package using: (idfilter=0.95 pairedonly=t primaryonly=t). Mapped reads were counted using featureCounts(Liao et al., 2014) (v1.5.3) using the following flags: (-t CDS -g ID -s 2 -p). Read counts were filtered to remove counts <3, and were converted to geTMM(Smid et al., 2018) in R. To curate nitrogen cycling reactions, geTMM values of genes annotated as enzymes involved in the nitrogen cycle were summed within samples at a pathway level (Supporting Data 1). Differences in pathway expression between palsa and bog samples were analyzed using LIMMA(Smyth, 2005) in R.

3. Section 2. FT-ICR MS instrument details

The sample solution was infused through a microelectrospray source(Emmett et al., 1998) (50 μm i.d. fused silica emitter) at 500 nL / min using a syringe pump. Typical conditions for negative ion formation were as follows: emitter voltage, -2.8-3.2 kV; S-lens RF level: 40%; and heated metal capillary temperature, 350°C. DOM extracts were analyzed with a custom-built hybrid linear ion trap FT-ICR mass spectrometer equipped with a 21 T superconducting solenoid magnet(Hendrickson et al., 2015; Smith et al., 2018). Ions were initially accumulated in an external multipole ion guide (1-5 ms) and released m/z-dependently by decrease of an auxiliary radio frequency potential between the multipole rods and the end-cap electrode(Kaiser et al., 2013). Ions were excited to m/z-dependent radius to maximize the dynamic range and number of observed mass spectral peaks (32-64%)(Kaiser et al., 2013), and excitation and detection were performed on the same pair of electrodes(Chen et al., 2014). The dynamically harmonized ICR cell in the 21 T FT-ICR is operated with 6 V trapping potential(Boldin & Nikolaev, 2011; Kaiser et al., 2013). Time-domain transients of 3.1 seconds were conditionally co-added and acquired with the Predator data station that handled excitation and detection only, initiated by a TTL trigger from the commercial Thermo data station with 100 time-domain acquisitions averaged for all experiments(Blakney et al., 2011). Mass spectra were phase-corrected(Xian et al., 2010) and internally calibrated with 10-15 highly abundant homologous series that span the entire molecular weight distribution based on the "walking" calibration method(Savory et al., 2011). Experimentally measured masses were converted from the International Union of Pure and Applied Chemistry (IUPAC) mass scale to the Kendrick mass scale(Kendrick, 1963) for rapid identification of homologous series for each heteroatom class (i.e., species with the same non carbon or hydrogen heteroatom content, differing only in degree of alkylation)(Hughey et al.,

2001). For each elemental composition, the heteroatom class, double bond equivalents (DBE = number of rings plus double bonds to carbon, DBE = C –h/2 + n/2 +1) and carbon number, C, were tabulated for subsequent generation of the relative abundance distributions and the graphical relative-abundance weighted images and van Krevelen diagrams(van Krevelen, 1950). Peaks with signal magnitude greater than six times the baseline root-mean-square (rms) noise at m/z 400 were exported to peak lists, and molecular formula assignments and data visualization were performed with PetroOrg © software(Bahureksa et al., 2022; Corilo, n.d.; Kim et al., 2003). Molecular formula assignments with an error >0.3 parts-per-million were discarded, and only chemical classes with a combined relative abundance of ≥0.15% of the total were considered.

4. Table S1. Porewater sample volumes

Porewater volumes collected across the thaw transition. While the exact volumes from transect 1 and transect 5 (marked with *) were not documented, they featured comparable volumes to that of transects 2-4 and provided sufficient volume for the required analyses. Cells marked with "-" indicate the transect did not feature that corresponding location.

	Transect 1 (mL)	Transect 2 (mL)	Transect 3 (mL)	Transect 4 (mL)	Transect 5 (mL)
Palsa 3	-	-	22	24	*
Palsa 2	*	26	24	44	*
Palsa 1	*	18	42	48	*
Thaw Front	*	17	21	26	*
Bog 1	*	14	19	16	*
Bog 2	*	29	23	15	-
Bog 3	*	30	-	-	-

5. Table S2. Transect porewater chemistry

Porewater chemistry of each transect and sampling point. Transects (T) are aligned to thaw front position. Sample name (P3, P2, P1, thaw front, B1, B2, B3) refers to the position in the transect relative to the thaw front. The letter refers to the thaw state (P for palsa and B for bog), and the number refers to the number of meters from the thaw front. N-values for each thaw state include all samples across all transects. Cells marked with "-" indicate the transect did not feature that corresponding location.

SAMPLE NAME		P3	P2	P1	Thaw front	B1	B2	B3
DOC [mg C/L]	T1	-	38.72	40.80	558.25	362.68	292.90	171.23
Palsa n=13	T2	-	52.93	450.89	638.94	324.11	221.78	328.08
Thaw front n=5	T3	69.63	44.72	77.68	322.27	149.36	158.13	-
Bog n=11	T4	46.32	25.38	261.22	386.13	159.89	104.36	-
	T5	67.0	64.0	58.8	440.1	214.1	-	-
Nitrite [mg/L]	T1	-	0.03	0.02	0.03	0.02	0.02	0.02
Palsa n=10	T2	-	0.03	0.02	0.03	0.02	0.02	0.02
Thaw front n=4	T3	0.01	0.01	0.01	0.01	0.01	0.01	-
Bog n=10	T4	0.01	0.01	0.01	0.01	0.01	0.01	-
	T5				N/A			
Nitrate [mg/L]	T1	-	1.27	0.41	0.35	0.23	0.17	0.19
Palsa n=10	T2	-	0.14	0.12	0.12	0.12	0.14	0.15
Thaw front n=4	T3	0.19	0.15	0.12	0.08	0.11	0.12	-
Bog n=10	T4	0.11	0.13	0.14	0.17	0.14	0.15	-
	T5				N/A			
Ammonium [mg/L]	T1	-	1.62	0.37	6.39	1.44	0.55	0.19
Palsa n=13	T2	-	0.15	3.33	4.27	1.04	0.21	0.48
Thaw front n=5	T3	0.25	0.13	0.10	1.07	0.71	0.48	-
Bog n=11	T4	0.31	0.11	0.09	2.01	1.19	1.48	-
	T5	0.29	0.04	0.04	2.12	0.25	-	-
Fe^{2+} [mg/L]	T1	-	0	2.23	136.84	67.02	46.92	18.99
Palsa n=13	T2	-	1.68	76.52	225.09	82.66	62.00	143.54
Thaw front n=5	T3	6.70	2.79	10.61	122.32	27.93	65.91	-
Bog n=11	T4	2.18	2.94	1.08	109.25	80.24	104.25	-
	T5	1.5	0.85	0.39	95.1	67.78	-	-
DON [mg N/L]	T1							
	T2				N/A			
	T3							
	T4							
	T5	4.34	2.59	1.25	27.88	7.5	-	-

6. Table S3. FT-ICR MS molecular class assignment

FT-ICR MS molecular class assignments based on atomic composition of the assigned formula, adapted from Poulin *et al* 2017(Poulin et al., 2017).

Condensed Aromatic-like	$Ai_{mod} > 0/67$
Aromatic/Polyphenol-like	$0.5 > Ai_{mod} > 0.67$
Highly Unsaturated Aliphatic-like	$Ai_{mod} < 0.5$; H/C <1.5; O/C <0.9
Unsaturated Aliphatic-like	H/C = 1.5-2.0; O/C < 0.9; N = 0
Saturated Fatty Acid-like	H/C ≥ 2.0; O/C ≤ 0.9
Peptide-like	H/C = 1.5-2.0; O/C < 0.9; N > 0
Sugar-like	O/C > 0.9

7. Table S4. FT-ICR MS total identified peaks

Total identified peaks from FT-ICR MS analysis for samples discussed herein. Total identified peaks include all ^{13}C peaks that were not included in sample comparison as they mirror the higher relative abundance ^{12}C peaks.

Sample Name	Total Identified Peaks	RMS error (ppm)
Palsa 2	18908	0.062219
Thaw Front	17370	0.055763
Bog 2	18782	0.063072
Bog 3	16314	0.070826

8. Table S5. FT-ICR MS assigned total and unique monoisotopic formulae

Counts of FT-ICR MS assigned total and unique monoisotopic formula for samples P2, thaw front, and B3 in transect one.

	SAMPLE	TOTAL FORMULAE	AROMATIC/ POLYPHENOL-LIKE	CONDENSED AROMATIC-LIKE	HIGHLY UNSATURATED ALIPHATIC-LIKE	PEPTIDE-LIKE	SUGAR-LIKE	UNSATURATED ALIPHATIC-LIKE	NA	SATURATED FATTY ACID-LIKE
FORMULAE COUNT (% OF TOTAL)	Palsa (P2)	11272	1972(17.5%)	606(5.4%)	7904(70.1%)	110(1.0%)	28(0.2%)	429(3.8%)	223(2.0%)	0(0%)
	Thaw front	10852	2192(20.2%)	694(6.4%)	7239(66.7%)	32(0.3%)	44(0.4%)	411(3.8%)	240(2.2%)	0(0%)
	Bog (B3)	10024	1833(18.3%)	491(4.9%)	6997(69.8%)	52(0.5%)	27(0.3%)	414(4.1%)	210(2.1%)	0(0%)
CHNO FORMULAE COUNT (% OF TOTAL)	Palsa (P2)	3008	551(18.3%)	69(2.3%)	2188(72.7%)	110(3.7%)	5(0.2%)	0(0%)	85(2.8%)	0(0%)
	Thaw front	2920	681(23.3%)	102(3.5%)	2011(68.9%)	32(1.1%)	0(0%)	0(0%)	94(3.2%)	0(0%)
	Bog (B3)	2709	507(18.7%)	60(2.2%)	2011(74.2%)	52(1.9%)	0(0%)	0(0%)	79(2.9%)	0(0%)
PALSA/THAW FRONT COMPARISON UNIQUE CHNO (% OF GROUP)	Palsa (P2)	459	21(4.6%)	3(0.7%)	346(75.4%)	78(17.0%)	5(1.1%)	0(0%)	6(1.3%)	0(0%)
	Thaw front	371	151(40.7%)	36(9.7%)	169(45.6%)	0(0%)	0(0%)	0(0%)	15(4.0%)	0(0%)
THAW FRONT/BOG COMPARISON UNIQUE CHNO (% OF GROUP)	Thaw front	546	191(35.0%)	44(8.1%)	284(52.0%)	7(1.3%)	0(0%)	0(0%)	20(3.7%)	0(0%)
	Bog (B3)	335	17(5.1%)	2(0.6%)	284(84.8%)	27(8.1%)	0(0%)	0(0%)	5(1.5%)	0(0%)

References

Bahureksa, W., Borch, T., Young, R. B., Weisbrod, C., Blakney, G. T., & McKenna, A. M. (2022). Improved Dynamic Range, Resolving Power, and Sensitivity Achievable with FT-ICR Mass Spectrometry at 21 T Reveals the Hidden Complexity of Natural Organic Matter. *Analytical Chemistry*, *94*(32), 11382–11389. https://doi.org/10.1021/acs.analchem.2c02377

Blakney, G. T., Hendrickson, C. L., & Marshall, A. G. (2011). Predator data station: A fast data acquisition system for advanced FT-ICR MS experiments. *International Journal of Mass Spectrometry*, *306*(2–3), 246–252. https://doi.org/10.1016/j.ijms.2011.03.009

Boldin, I. A., & Nikolaev, E. N. (2011). Fourier transform ion cyclotron resonance cell with dynamic harmonization of the electric field in the whole volume by shaping of the excitation and detection electrode assembly. *Rapid Communications in Mass Spectrometry*, *25*(1), 122–126. https://doi.org/10.1002/rcm.4838

Bushnell, B. (n.d.). BBtools. Retrieved from https://jgi.doe.gov/data-and-tools/software-tools/bbtools/

Chen, T., Beu, S. C., Kaiser, N. K., & Hendrickson, C. L. (2014). Note: Optimized circuit for excitation and detection with one pair of electrodes for improved Fourier transform ion cyclotron resonance mass spectrometry. *Review of Scientific Instruments*, *85*(6), 2012–2015. https://doi.org/10.1063/1.4883179

Corilo, Y. E. (n.d.). PetroOrg Software. The Florida State University, Tallahassee, Fl, USA 2012.

Emmett, M. R., White, F. M., Hendrickson, C. L., Shi, D. H., & Marshall, A. G. (1998). Application of micro-electrospray liquid chromatography techniques to FT-ICR MS to enable high-sensitivity biological analysis. *Journal of the American Society for Mass Spectrometry*, *9*(4), 333–340. https://doi.org/10.1016/S1044-0305(97)00287-0

Hendrickson, C. L., Quinn, J. P., Kaiser, N. K., Smith, D. F., Blakney, G. T., Chen, T., et al. (2015). 21 Tesla Fourier Transform Ion Cyclotron Resonance Mass Spectrometer: A National Resource for Ultrahigh Resolution Mass Analysis. *Journal of the American Society for Mass Spectrometry*, *26*(9), 1626–1632. https://doi.org/10.1007/s13361-015-1182-2

Hughey, C. A., Hendrickson, C. L., Rodgers, R. P., Marshall, A. G., & Qian, K. (2001). Kendrick Mass Defect Spectroscopy: A Compact Visual Analysis for Ultrahigh-Resolution Broadband Mass Spectra. *Analytical Chemistry*, *73*, 4676–4681.

Kaiser, N. K., McKenna, A. M., Savory, J. J., Hendrickson, C. L., & Marshall, A. G. (2013). Tailored ion radius distribution for increased dynamic range in FT-ICR mass analysis of complex mixtures. *Analytical Chemistry*, *85*(1), 265–272. https://doi.org/10.1021/ac302678v

Kendrick, E. (1963). A mass scale based on CH2 = 14.0000 for high resolution mass spectrometry of organic compounds. *Analytical Chemistry*, *35*(13), 2146–2154.

Kim, S., Kramer, R. W., & Hatcher, P. G. (2003). Graphical Method for Analysis of Ultrahigh-Resolution Broadband Mass Spectra of Natural Organic Matter, the Van Krevelen Diagram. *Analytical Chemistry*. https://doi.org/10.1021/ac034415p

van Krevelen, D. W. (1950). "Graphical-statistical method for the study of structure and reaction processes of coal." *Fuel*, *29*, 269–284.

Langmead, B., & Salzberg, S. L. (2012). Fast gapped-read alignment with Bowtie 2. *Nature Methods*, *9*(4). https://doi.org/10.1038/nmeth.1923

Li, H., Handsaker, B., Wysoker, A., Fennell, T., Ruan, J., Homer, N., et al. (2009). The Sequence Alignment/Map format and SAMtools. *Bioinformatics*, *25*(16). https://doi.org/10.1093/bioinformatics/btp352

Liao, Y., Smyth, G. K., & Shi, W. (2014). FeatureCounts: An efficient general purpose program for assigning sequence reads to genomic features. *Bioinformatics*, *30*(7). https://doi.org/10.1093/bioinformatics/btt656

Poulin, B. A., Ryan, J. N., Nagy, K. L., Stubbins, A., Dittmar, T., Orem, W., et al. (2017). Spatial Dependence of Reduced Sulfur in Everglades Dissolved Organic Matter Controlled by Sulfate Enrichment. *Environmental Science and Technology*, *51*(7), 3630–3639. https://doi.org/10.1021/acs.est.6b04142

Savory, J. J., Kaiser, N. K., Mckenna, A. M., Xian, F., Blakney, G. T., Rodgers, R. P., et al. (2011). Parts-Per-Billion Fourier Transform Ion Cyclotron Resonance Mass Measurement Accuracy with a "Walking" Calibration Equation. *Analytical Chemistry*, *83*, 1732–1736.

Smid, M., Coebergh van den Braak, R. R. J., van de Werken, H. J. G., van Riet, J., van Galen, A., de Weerd, V., et al. (2018). Gene length corrected trimmed mean of M-values (GeTMM) processing of RNA-seq data performs similarly in intersample analyses while improving intrasample comparisons. *BMC Bioinformatics*, *19*(1). https://doi.org/10.1186/s12859-018-2246-7

Smith, D. F., Podgorski, D. C., Rodgers, R. P., Blakney, G. T., & Hendrickson, C. L. (2018). 21 Tesla FT-ICR Mass Spectrometer for Ultrahigh-Resolution Analysis of Complex Organic Mixtures. *Analytical Chemistry*, *90*(3), 2041–2047. https://doi.org/10.1021/acs.analchem.7b04159

Smyth, G. K. (2005). limma: Linear Models for Microarray Data. In *Bioinformatics and Computational Biology Solutions Using R and Bioconductor*. https://doi.org/10.1007/0-387-29362-0_23

Woods, G., & Simpson, A. (2011). HILIC-NMR: Toward the identification of individual

molecular components in dissolved organic matter. *Environmental Science and Technology*, *45*(13), 5910. https://doi.org/10.1021/es201716u

Xian, F., Hendrickson, C. L., Blakney, G. T., Beu, S. C., & Marshall, A. G. (2010). Automated broadband phase correction of fourier transform ion cyclotron resonance mass spectra. *Analytical Chemistry*, *82*(21), 8807–8812. https://doi.org/10.1021/ac101091w

APPENDIX H: 2025 LOS ANGELES FIRES FIELDWORK

From February 4th to February 6th, 2025, I participated in a field sampling campaign in the aftermath of the 2025 Los Angeles Fires alongside Dr. Thomas Borch, Dr. Srinidhi Lokesh, Dr. Sean Fettrow, Dr. Ali Namayandeh, Katie Ann Huy, Frida Garcia-Ledezma, and Austen Michael Lambert. The 2025 Los Angeles Fires were comprised of multiple fires, including the Palisades Fire and Eaton Fire, that collectively burned ~20,000 ha and destroyed ~18,000 buildings in January 2025.[1,2] Due to this destruction, ~179,000 people were forced to evacuate, making these fires some of the most devastating urban fires in U.S. history.[1] Now that post-fire debris removal and reconstruction efforts are underway, residents are beginning to repopulate these areas, potentially exposing themselves to dangerous metals and toxic organic molecules in soil and dust. I was a part of a multi-institutional team comprised of scientists from Colorado State University, Stanford University, Chapman University, and NASA's Jet Propulsion laboratory to sample soil and debris from the Los Angeles Fires and determine what contaminants may have been released during the fires. We sampled from 11 destroyed, 5 partially damaged, and 13 undamaged properties within the Eaton Fire burn scar with permission granted directly by the individual property owners. At each property, we collected three soil samples in which surface debris, vegetation, and/or ash were cleared and mineral soil was collected to a depth of ~5 cm (**Figure J1**). The three soil samples were combined to make a composite soil sample for each property. At each destroyed property, a debris composite sample was prepared combining three debris samples collected within the destroyed building (**Figure J2**). Additionally, debris samples were collected from recognizable household objects (e.g. washing machine, dishwasher, microwave) and were referred to as "point source" samples (**Figure J3**). My responsibilities for this field sampling campaign included

crafting the itinerary for each sampling day, prioritizing sampling locations, photographing all locations and sampling, collecting soil and debris samples, and recording all observations. Samples from this field campaign were included in a publication submitted to *Environmental Science & Technology Water* titled "Enrichment of Disinfection Byproduct Precursors in Fire-Affected Soils from the 2025 Eaton Fire in Los Angeles, California." These samples will also be included in a manuscript evaluating per- and polyfluoroalkyl substances contamination in soil and building debris. **Figures J4-J11** feature additional photos from this sampling campaign.

Figure J1. Sampling soil from undamaged property.

Figure J2. Sampling debris from destroyed property.

Figure J3. Sampling debris next to microwave as a “point source” sample.

Figure J4. Photo of myself from the first destroyed property that we sampled from.

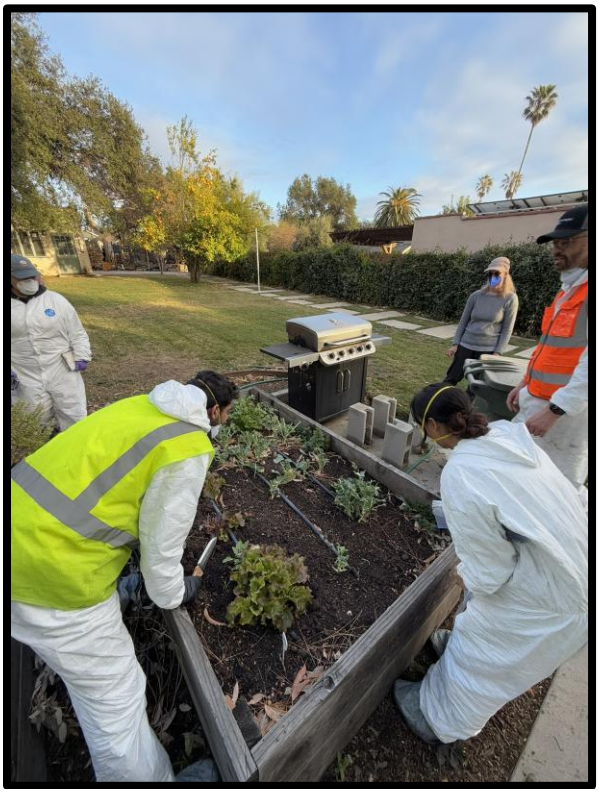

Figure J5. Collecting soil samples from a vegetable garden at an undamaged property.

Figure J6. Photo of one of the destroyed properties that we sampled from.

Figure J7. Dishwasher in debris from destroyed property.

Figure J8. Collecting "point source" sample next to washing and drying machines within destroyed property.

Figure J9. Collecting "point source" debris sample next to burned car.

Figure J10. Burned car labelled “NOT EV” to designate it as a non-electric vehicle.

Figure J11. Burned electric vehicle.

APPENDIX H REFERENCES

(1) McKoy, J. Death Count for 2025 LA County Wildfires Likely Hundreds Higher than Official Records Show. *Boston University School of Public Health*. August 7, 2025. https://www.bu.edu/sph/news/articles/2025/death-count-for-2025-la-county-wildfires-likely-hundreds-higher-than-official-records-show/.

(2) Schollaert, C.; Connolly, R.; Cushing, L.; Jerrett, M.; Liu, T.; Marlier, M. Air Quality Impacts of the January 2025 Los Angeles Wildfires: Insights from Public Data Sources. *Environ. Sci. Technol. Lett.* **2025**, *12* (8), 911–917. https://doi.org/10.1021/acs.estlett.5c00486.

APPENDIX I: EDUCATIONAL OUTREACH AND EXTRACURRICULARS

My extracurricular involvement in sustainability and educational outreach influenced local to global communities. Starting at the local to regional scale, I started the Graduate Student Chapter of the Student Sustainability Center within the School of Global Environmental Sustainability during my first year of graduate school at Colorado State University. This was a group of ~30 graduate students conducting sustainability-related research who were interested in participating in educational outreach. We regularly presented our research to classes of undergraduate students at Colorado State University and to classes of high schoolers at Timnath Middle-High School, showcasing what it's like studying sustainability-related topics as a graduate student (**Figure K1**). Furthermore, we participated in Climate Leadership Summits: climate conferences at Colorado State University for high school attendees. At these summits, hundreds of high school students from across northern Colorado came to Colorado State University and learned about various climate-related topics via presentations given by Colorado State University professors (**Figure K2**). I was responsible for helping coordinate these summits and recruit graduate students to chat with the high school attendees during the lunchtime session, facilitating novel interactions between high school and graduate students. As a part of the Graduate Student Chapter of the Student Sustainability Center, I also organized workshops for graduate students where I invited Colorado State University professors to present on relevant academic topics such as applying for grant funding.

My local outreach extended beyond my involvement with the School of Global Environmental Sustainability at Colorado State University. During my first year of graduate school, I was a tutor and outreach coordinator for local elementary schools. Specifically, I was a

Figure K1. Some members of the Graduate Student Council of the Student Sustainability Center and I discussing our research to a class of high school students.

Figure K2. The opening keynote address of the 2022 Climate Leadership Summit at Colorado State University. The audience is comprised of high school students from schools across northern Colorado.

tutor in the Triunfo program in which elementary students from Harris Bilingual Elementary School would come to Colorado State University and receive one-on-one mentoring. I was partnered with a fifth-grade student and helped him develop foundational scientific skills such as practicing multiplication, using a microscope, and refining his English reading and writing skills

(**Figure K3**). Additionally, a group of Colorado State University graduate students and I coordinated hands-on chemistry outreach events for fifth-grade students at Irish Elementary Escuela Bilingüe. For example, I taught 40 elementary students how to clean corroded pennies with a vinegar-based mixture, using the experiment to highlight the chemical concepts of solutions and oxidation. My educational efforts have been directed at homeschooled children as well. Working with the Heart-J Center in Loveland, CO, I organized an outreach event in which Dr. Sean Fettrow (a postdoctoral scholar in the Borch lab) and I gave a presentation about wildfires to a group of ~20 homeschooled children, led the children to our Alexander Mountain Fire field site, and showed them how to sample soil and measure soil temperature and pH (**Figure K4**). I have also been an invited speaker to multiple community events in northern Colorado. I have been a panelist for two "Managing the Planet" events hosted by the School of Global Environmental Sustainability at Colorado State University where experts discuss diverse topics related to relevant sustainability issues in front of a public audience (**Figure K5**). I was invited to give a presentation about my wildfire research to the Boulder, CO chapter of Citizens' Climate Lobby. Lastly, I was an invited speaker at a Latino Conservation Week in Fort Collins, CO where I delivered a five-minute "lightning talk" about my wildfire research which was actively translated to Spanish (**Figure K6**). Such experiences reinforced the importance of allocating time to community engagement and presenting to non-technical audiences.

Extending my participation to the national level, I was invited to be the keynote speaker at the Faithfully Advancing Sustainability Together conference hosted at Calvin University in Michigan (**Figure K7**). This was a conference for undergraduate students to learn more about how they can get involved and advance sustainability initiatives at their respective schools. Here, I delivered the keynote address and led a workshop titled "Make Your Idea a Reality" in which I

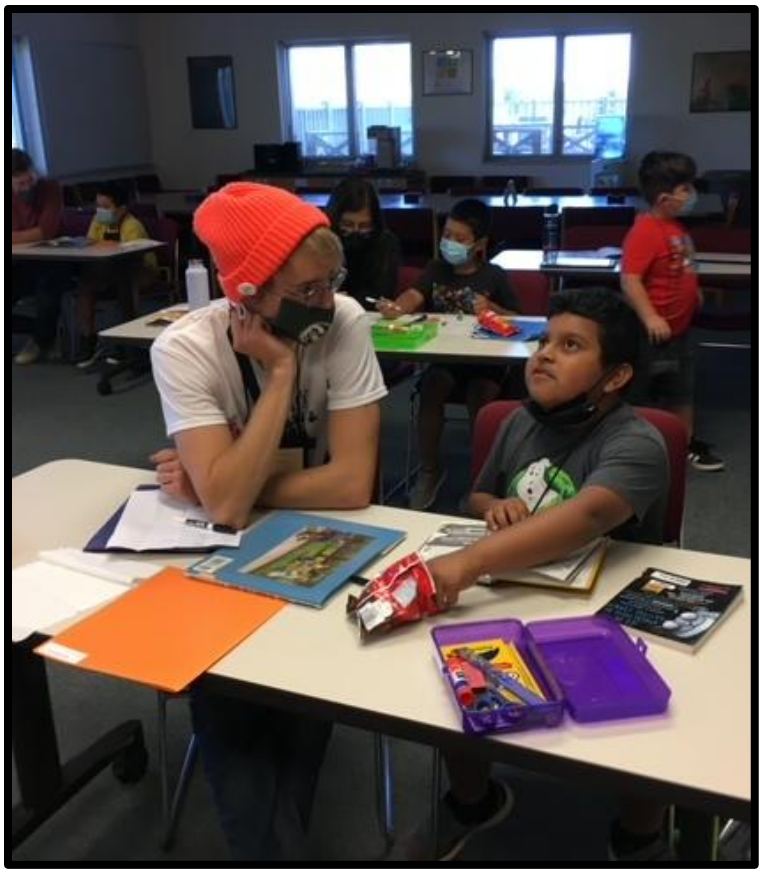

Figure K3. Tutoring a fifth-grade student through the Colorado State University Triunfo program.

Figure K4. Answering a homeschooled child's question during my wildfire presentation (left) and teaching homeschooled children how to measure soil temperature (right).

Figure K5. Speaking at a "Managing the Planet" event organized by the School of Global Environmental Sustainability at Colorado State University.

Figure K6. Speaking at a Latino Conservation Week community event at Fort Collins, CO.

guided students on how to design a sustainable initiative for their school and how to effectively implement it. Beyond Michigan, I lobbied on capitol hill in Washington, D.C. as a part of Citizens' Climate Lobby (**Figure K8**). Here, I spoke with staffers from the offices of Senator John Hickenlooper, Representative Joe Neguse, and Representative Brittany Pettersen advocating for

the Seedlings for Sustainable Habitat Restoration Act which sought to provide aid for tree nurseries to support post-fire reforestation efforts.

Figure K7. Delivering the keynote address at the 2023 Faithfully Advancing Sustainability Together conference at Calvin University.

Figure K8. Lobbying at Washington D.C. through Citizens' Climate Lobby.

Lastly, on the global scale, I was a Colorado State University delegate at the 2023 United Nations Climate Change Conference (COP28) at Dubai, United Arab Emirates (**Figure K9**). Here I sat in on climate negotiations featuring negotiators from dozens of countries discussing climate financing, supporting developing countries, and tracking greenhouse gas emissions. I also gave a presentation titled "Youth Engagement on College Campuses: How to Spark Efficacious Involvement" to an audience of early career researchers describing the lessons that I've learned about how to encourage and foster effective climate action from younger generations (**Figure K10**).

Figure K9. Participating in the 2023 United Nations Climate Change Conference (COP28) at Dubai, United Arab Emirates as a Colorado State University delegate.

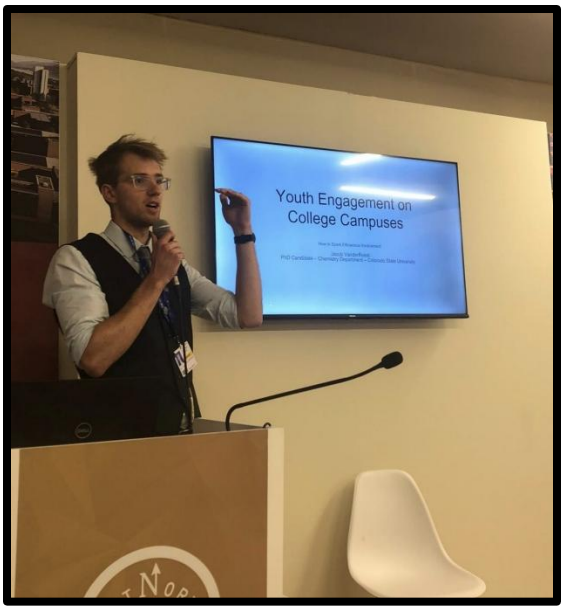

Figure K10. Presenting at the 2023 United Nations Climate Change Conference (COP28) at Dubai, United Arab Emirates.

These experiences from teaching homeschooled children how to sample soil to presenting at a global climate change conference broadened my perspective as a PhD student beyond my own research and graduate program. Due this extracurricular engagement, I am a more well-rounded scientist who will continue to engage with the public in the next stages of my career.

APPENDIX J: ADVICE FOR PHD STUDENTS

I wanted to conclude this dissertation with some advice for current PhD students. While I enjoy discussing this topic and would do so for a long time, I will narrow down my advice here to just three suggestions. 1). Practice asking questions. Asking questions is an essential skill for graduate students. Asking questions makes you a more curious and inquisitive student, can help you stand out in a crowd at a conference, develop new research ideas, and is essential for job interviews. Push yourself to ask questions at conferences or in seminars at your home institution. The more you practice, the easier asking questions becomes.

2). First learn how to say "yes" followed by learning when to say "no." To me, saying "yes" doesn't just mean signing up for additional classes or pursuing a graduate certificate; saying "yes" means advocating for yourself and positioning yourself as someone who takes the initiative. It means saying "yes" to asking a question in a crowded seminar lecture, saying "yes" to walking up to a respected scientist in your field and introducing yourself, and saying "yes" to the opportunity to organize a conference symposium. These are skills that can be developed. The more you say "yes" to opportunities and establish yourself as a go-getter, it becomes easier to be an engaged scientist. I advise that the first few years of one's PhD experience should be focused on getting comfortable with saying "yes." However, saying "yes" to too much can lead to overload, exhaustion, and burnout. Once you've mastered saying "yes," focus on prioritizing by saying "no." Rather than going to another conference, maybe say "no" and prioritize working on publishing a key manuscript. Instead of traveling to share your research, reschedule that for another time and prioritize meeting your dissertation defense deadlines. Of course, learning to say "yes" precedes learning when to say "no;" you can't say "no" to opportunities unless you position yourself to

receive opportunities by saying “yes” in the first place. But, learning when to say “no” during the latter years of your PhD will help you prioritize and prevent burnout and overextending yourself.

3). Write handwritten thank-you letters to collaborators. Expressing gratitude is very important in graduate school. While we technically lead papers, us graduate students often receive an abundance of support from advisors, collaborators, and fellow graduate students. To recognize that support, I believe that writing handwritten letters for collaborators effectively demonstrates one’s appreciation and admiration for others. After the contents of Chapter 3 were published, I wrote individual letters for every co-author on the publication. Not only did that let my collaborators know how much I appreciated their help, but it also reminded me how blessed I was to work with a generous, selfless team. Overall, thanking others helps you realize how much support you truly receive and helps to communicate your appreciation, and handwritten letters are a unique, personal way to express that gratitude.